Metal-insulator transitions

Masatoshi Imada

Institute for Solid State Physics, University of Tokyo, Roppongi, Minato-ku, Tokyo, 106, Japan

Atsushi Fujimori

Department of Physics, University of Tokyo, Hongo, Bunkyo-ku, Tokyo, 113, Japan

Yoshinori Tokura

Department of Applied Physics, University of Tokyo, Hongo, Bunkyo-ku, Tokyo, 113, Japan

Metal-insulator transitions are accompanied by huge resistivity changes, even over tens of orders of magnitude, and are widely observed in condensed-matter systems. This article presents the observations and current understanding of the metal-insulator transition with a pedagogical introduction to the subject. Especially important are the transitions driven by correlation effects associated with the electron-electron interaction. The insulating phase caused by the correlation effects is categorized as the Mott Insulator. Near the transition point the metallic state shows fluctuations and orderings in the spin, charge, and orbital degrees of freedom. The properties of these metals are frequently quite different from those of ordinary metals, as measured by transport, optical, and magnetic probes. The review first describes theoretical approaches to the unusual metallic states and to the metal-insulator transition. The Fermi-liquid theory treats the correlations that can be adiabatically connected with the noninteracting picture. Strong-coupling models that do not require Fermi-liquid behavior have also been developed. Much work has also been done on the scaling theory of the transition. A central issue for this review is the evaluation of these approaches in simple theoretical systems such as the Hubbard model and t-J models. Another key issue is strong competition among various orderings as in the interplay of spin and orbital fluctuations.

Experimentally, the unusual properties of the metallic state near the insulating transition have been most extensively studied in d-electron systems. In particular, there is revived interest in transition-metal oxides, motivated by the epoch-making findings of high-temperature superconductivity in cuprates and colossal magnetoresistance in manganites. The article reviews the rich phenomena of anomalous metallicity, taking as examples Ti, V, Cr, Mn, Fe, Co, Ni, Cu, and Ru compounds. The diverse phenomena include strong spin and orbital fluctuations, mass renormalization effects, incoherence of charge dynamics, and phase transitions under control of key parameters such as band filling, bandwidth, and dimensionality. These parameters are experimentally varied by doping, pressure, chemical composition, and magnetic fields. Much of the observed behavior can be described by the current theory. Open questions and future problems are also extracted from comparison between experimental results and theoretical achievements. [S0034-6861(98)00103-2]

CONTENTS

I. INTRODUCTION

A. General remarks

The first successful theoretical description of metals, insulators, and transitions between them is based on noninteracting or weakly interacting electron systems. The theory makes a general distinction between metals and insulators at zero temperature based on the filling of the electronic bands: For insulators the highest filled band is completely filled; for metals, it is partially filled. In other words, the Fermi level lies in a band gap in insulators while the level is inside a band for metals. In the noninteracting electron theory, the formation of band structure is totally due to the periodic lattice structure of atoms in crystals. This basic distinction between metals and insulators was proposed and established in the early years of quantum mechanics (Bethe, 1928; Sommerfeld, 1928; Bloch, 1929). By the early 1930s, it was recognized that insulators with a small energy gap between the highest filled band and lowest empty band would be semiconductors due to thermal excitation of the electrons (Wilson, 1931a, 1931b; Fowler, 1933a, 1933b). More than fifteen years later the transistor was invented by Shockley, Brattain, and Bardeen.

Although this band picture was successful in many respects, de Boer and Verwey (1937) reported that many transition-metal oxides with a partially filled d-electron band were nonetheless poor conductors and indeed often insulators. A typical example in their report was NiO. Concerning their report, Peierls (1937) pointed out the importance of the electron-electron correlation: Strong Coulomb repulsion between electrons could be the origin of the insulating behavior. According to Mott (1937), Peierls noted

> “it is quite possible that the electrostatic interaction between the electrons prevents them from moving at all. At low temperatures the majority of the electrons are in their proper places in the ions. The minority which have happened to cross the potential barrier

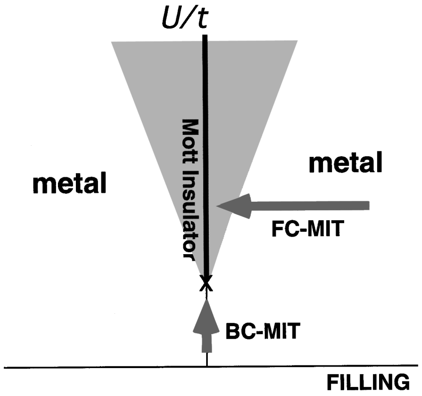

FIG. 1. Metal-insulator phase diagram based on the Hubbard model in the plane of U/t and filling n. The shaded area is in principle metallic but under the strong influence of the metal-insulator transition, in which carriers are easily localized by extrinsic forces such as randomness and electron-lattice coupling. Two routes for the MIT (metal-insulator transition) are shown: the FC-MIT (filling-control MIT) and the BC-MIT (bandwidth-control MIT).

> find therefore all the other atoms occupied, and in order to get through the lattice have to spend a long time in ions already occupied by other electrons. This needs a considerable addition of energy and so is extremely improbable at low temperatures.''

These observations launched the long and continuing history of the field of strongly correlated electrons, particularly the effort to understand how partially filled bands could be insulators and, as the history developed, how an insulator could become a metal as controllable parameters were varied. This transition illustrated in Fig. 1 is called the *metal-insulator transition* (MIT). The insulating phase and its fluctuations in metals are indeed the most outstanding and prominent features of strongly correlated electrons and have long been central to research in this field.

In the past sixty years, much progress has been made from both theoretical and experimental sides in understanding strongly correlated electrons and MITs. In theoretical approaches, Mott (1949, 1956, 1961, 1990) took the first important step towards understanding how electron-electron correlations could explain the insulating state, and we call this state the *Mott insulator*. He considered a lattice model with a single electronic orbital on each site. Without electron-electron interactions, a single band would be formed from the overlap of the atomic orbitals in this system, where the band becomes full when two electrons, one with spin-up and the other with spin-down, occupy each site. However, two electrons sitting on the same site would feel a large Coulomb repulsion, which Mott argued would split the band in two: The lower band is formed from electrons that occupied an empty site and the upper one from electrons that occupied a site already taken by another electron. With one electron per site, the lower band would be full, and the system an insulator. Although he discussed the magnetic state afterwards (see, for example, Mott, 1990), in his original formulation Mott argued that the existence of the insulator did not depend on whether the system was magnetic or not.

Slater (1951), on the other hand, ascribed the origin of the insulating behavior to magnetic ordering such as the antiferromagnetic long-range order. Because most Mott insulators have magnetic ordering at least at zero temperature, the insulator may appear due to a band gap generated by a superlattice structure of the magnetic periodicity. In contrast, we have several examples in which spin excitation has a gap in the Mott insulator without magnetic order. One might argue that this is not compatible with Slater's band picture. However, in this case, both charge and spin gaps exist similarly to the band insulator. This could give an adiabatic continuity between the Mott insulator and the band insulator, which we discuss in Sec. II.B.

In addition to the Mott insulating phase itself, a more difficult and challenging subject has been to describe and understand metallic phases near the Mott insulator. In this regime fluctuations of spin, charge, and orbital correlations are strong and sometimes critically enhanced toward the MIT, if the transition is continuous or weakly first order. The metallic phase with such strong fluctuations near the Mott insulator is now often called the *anomalous metallic phase*. A typical anomalous fluctuation is responsible for mass enhancement in V_2O_3, where the specific-heat coefficient γ and the Pauli paramagnetic susceptibility χ near the MIT show substantial enhancement from what would be expected from the noninteracting band theory. To understand this *mass enhancement*, the earlier pioneering work on the MIT by Hubbard (1964a, 1964b) known as the Hubbard approximation was reexamined and treated with the Gutzwiller approximation by Brinkmann and Rice (1970).

Fermi-liquid theory asserts that the ground state and low-energy excitations can be described by an adiabatic switching on of the electron-electron interaction. Then, naively, the carrier number does not change in the adiabatic process of introducing the electron correlation, as is celebrated as the Luttinger theorem. Because the Mott insulator is realized for a partially filled band, this adiabatic continuation forces the carrier density to remain nonzero when one approaches the MIT point in the framework of Fermi-liquid theory. Then the only way to approach the MIT in a continuous fashion is the divergence of the single-quasiparticle mass m^* (or more strictly speaking the vanishing of the renormalization factor Z) at the MIT point. Therefore mass enhancement as a typical property of metals near the Mott insulator is a natural consequence of Fermi-liquid theory.

If the symmetries of spin and orbital degrees of freedom are broken (either spontaneously as in the magnetic long-range ordered phase or externally as in the case of crystal-field splitting), the adiabatic continuity assumed in the Fermi-liquid theory is not satisfied any more and there may be no observable mass enhancement. In fact, a MIT with symmetry breaking of spin and orbital degrees of freedom is realized by the vanishing of the single-particle (carrier) number, as in the transition to a band insulator. For example, this takes place in the transition from an antiferromagnetic metal to an antiferromagnetic Mott insulator, where the folding of the Brillouin zone due to the superstructure of the magnetic periodicity creates a completely filled lower band. Carriers are doped into small pockets of Fermi surface whose Fermi volume vanishes at the MIT.

From this heuristic argument, one can see at least two distinct routes to the Mott insulator when one approaches the MIT point from the metallic side, namely, the *mass-diverging type* and *carrier-number-vanishing type*. The diversity of anomalous features of metallic phases near both types of MIT is a central subject of this review. Mass enhancement or carrier-number reduction as well as more complicated features have indeed been observed experimentally. The experiments were examined from various, more or less independently developed theoretical approaches, as detailed in Sec. II. In particular, anomalous features of correlated metals near the Mott insulator appear more clearly when the MIT is continuous. Theoretically, this continuous MIT has been a subject of recent intensive studies in which unusual metallic properties are understood from various critical fluctuations near the quantum critical point of the MIT.

A prototype of theoretical understanding for the transition between the Mott insulator and metals was achieved by using simplified lattice fermion models, in particular, in the celebrated *Hubbard model* (Anderson, 1959; Hubbard, 1963, 1964a, 1964b; Kanamori, 1963). The Hubbard model considers only electrons in a single band. Its Hamiltonian in a second-quantized form is given by

$$\mathcal{H}_H=\mathcal{H}_t+\mathcal{H}_U-\mu N, \tag{1.1a}$$

$$\mathcal{H}_t=-t\sum_{\langle ij\rangle}(c^\dagger_{i\sigma}c_{j\sigma}+\text{H.c.}), \tag{1.1b}$$

$$\mathcal{H}_U=U\sum_i(n_{i\uparrow}-\tfrac{1}{2})(n_{i\downarrow}-\tfrac{1}{2}), \tag{1.1c}$$

and

$$N\equiv\sum_{i\sigma}n_{i\sigma}, \tag{1.1d}$$

where the creation (annihilation) of the single-band electron at site i with spin σ is denoted by $c^\dagger_{i\sigma}(c_{i\sigma})$ with $n_{i\sigma}$ being the number operator $n_{i\sigma}\equiv c^\dagger_{i\sigma}c_{i\sigma}$. In this simplification, various realistic complexities are ignored, as we shall see in Sec. II.A. However, at the same time, low-energy and low-temperature properties are often well described even after this simplification since only a small number of bands (sometimes just one band) are crossing the Fermi level and have to do with low-energy excitations. The parameters of the simplified models in this case should be taken as effective values derived from renormalized bands near the Fermi level.

One of the most drastic simplification in the Hubbard model is to consider only electrons in a single orbit, say the s orbit. In contrast, the experimental study of the MIT in correlated metals has been most thorough and systematic in d-electron systems, namely, transition-metal compounds. Many examples will be reviewed in this article. In d-electron systems, *orbital degeneracy* is an important and unavoidable source of complicated behavior. For example, under the cubic crystal-field symmetry of the lattice, any of the threefold degenerate t_{2g} bands, d_{xy}, d_{yz}, and d_{zx} as well as twofold degenerate e_g bands, $d_{x^2-y^2}$ and $d_{3z^2-r^2}$, can be located near the Fermi level, depending on transition-metal ion, lattice structure, composition, dimensionality, and so on. In addition to strong spin fluctuations, effects of orbital fluctuations and orbital symmetry breaking play important roles in many d-electron systems, as discussed in Secs. II.H and IV. The orbital correlations are frequently strongly coupled with spin correlations through the usual relativistic spin-orbit coupling as well as through orbital-dependent exchange interactions and quandrupole interactions. An example of this orbital effect known as the double-exchange mechanism is seen in Mn oxides (Sec. IV.F), where strong Hund's-rule coupling between the e_g and t_{2g} orbitals triggers a transition between the Mott insulator with antiferromagnetic order and the ferromagnetic metal. *Colossal negative magnetoresistance* near the transition to this ferromagnetic metal phase has been intensively studied recently.

Another aspect of orbital degeneracy is the overlap or the closeness of the d band and the p band of ligand atoms which bridge the elements in transition-metal compounds. For example, as clarified in Secs. II.A and III.A, in the transition-metal oxides, the oxygen $2p_\sigma$ level becomes close to that of the partially filled $3d$ band near the Fermi level for heavier transition-metal elements such as Ni and Cu. Then the charge gap of the Mott insulator cannot be accounted for solely with d electrons, but p-electron degrees of freedom have also to be considered. In fact, when we could regard the Hubbard model as a description of a d band only, the charge excitation gap is formed between a singly occupied d band (the so-called lower Hubbard band) and a doubly occupied (with spin up and down) d band (the so-called upper Hubbard band). However, if the p_σ level becomes closer, the character of the minimum charge excitation gap changes to that of a gap between a singly occupied d band with fully occupied p band and a singly occupied d band with a p_σ hole. This kind of insulator, which was clarified by Zaanen, Sawatzky, and Allen (1985), is now called a *charge-transfer* (CT) *insulator* as contrasted to the former case, the *Mott-Hubbard* (MH) *insulator*, which we discuss in detail in Secs. II.A and III.A, and the distinction is indeed observed in high-energy spectroscopy. Correspondingly, compounds that have the MH insulating phase are called *MH compounds* while those with the CT insulating phase are called *CT compounds*. The term "Mott insulator" is used in this review in a broad sense which covers both types. Recent achievements in the field of strongly correlated electrons, especially in d-electron systems, have brought us closer to understanding more complicated situations in which there is an interplay between orbital and spin fluctuations and lattice degrees of freedom. Although we focus on the d-electron systems in this article, other systems also provide many interesting aspects in terms of strong-correlation effects. For example, organic systems with π-electron conduction such as BEDT-TTF compounds show two-dimensional (2D) anisotropy with an interesting interplay of MIT and transition to superconducting state (see, for example, Kanoda, 1997). Another example is seen in f-electron systems, where, for instance, non-Fermi-liquid properties due to orbital degeneracy effects have been extensively studied.

Most theoretical effort has been concentrated on simplified single-orbital systems such as the Hubbard and t-J models, in which the interplay of strong quantum fluctuations and correlation effects has been reexamined. In fact, the single-band model was originally derived, as we mentioned above, to discuss low-energy excitations of renormalized simple bands near the Fermi level even in the presence of a complicated structure of high-energy bands far from the Fermi level. This trend was clearly motivated and greatly accelerated by the discovery of *high-T_c cuprate superconductors* (Bednorz and Müller, 1986). In the cuprate superconductors, the low-energy electronic structure of the copper oxide is rather well described only by the $d_{x^2-y^2}$ band separated from the $d_{3z^2-r^2}$ and t_{2g} bands. Although the $2p_\sigma$ band is close to the $d_{x^2-y^2}$ band, as the copper oxides are typical CT compounds, the $2p_\sigma$ band is strongly hybridized with the $d_{x^2-y^2}$ band and consequently forms a single antibonding band near the Fermi level. This again lends support for a description by an effective single-band model (Anderson, 1987; Zhang and Rice, 1988).

Mother compounds of the cuprate superconductors are typical Mott insulators with antiferromagnetic order where the Cu atom is in a d^9 state with a half-filled $d_{x^2-y^2}$ orbital. A small amount of carrier doping to this Mott insulating state drives the MIT and directly results in the superconducting transition at low temperatures for low carrier doping. Because 2D anisotropy is prominent in cuprates due to the layered perovskite structure, strong quantum fluctuations with suppression of antiferromagnetic long-range order are the key aspects. One- and two-dimensional systems without orbital degeneracy are the extreme cases to enhance this quantum fluctuation, where high-T_c superconductivity was discovered. This has strongly motivated studies of the ground state and low-temperature properties of simple low-dimensional models such as the 2D Hubbard model beyond the level of mean-field approximations, taking account of strong fluctuations of spin and charge. It is widely recognized that reliable treatments of normal-state properties with strong low-dimensional anisotropy near the MIT are imperative for an understanding of this type of superconductivity, while low dimensionality makes various mean-field treatments very questionable The importance of strong correlation to our understanding of cuprate superconductors was stressed in the early stage by Anderson (1987).

In fact, the normal state of the cuprate superconductors shows many unusual properties which are far from the standard Fermi-liquid behavior. A typical anomalous property is the temperature dependence of the resistivity, which is linearly proportional to the temperature T, in contrast with the T^2 dependence expected in the Fermi-liquid theory. The optical conductivity roughly proportional to the inverse frequency is another unusual aspect, because it contradicts the well-known Drude theory. These indicate that the charge dynamics have a strongly incoherent character. Another example is the so-called pseudogap behavior observed in the underdoped region near the Mott insulating phase. The pseudogap is a frequency threshold for the strong excitation of spin and charge modes. We review basic features of these unusual properties observed in a number of experimental probes, such as photoemission, nuclear magnetic resonance, neutron scattering, transport measurements, and optical measurements, in Sec. IV.C, while we discuss various theoretical approaches to understanding them in Sec. II. We concentrate on properties in the normal state related to the MIT, while the properties in the superconducting phase are not reviewed in this article.

Strong incoherence actually turned out to be a common property of most transition-metal compounds near the Mott transition point, as discussed in Sec. IV. We call these *incoherent metals*. The incoherent charge dynamics as well as other anomalies in spin, charge, and orbital fluctuations all come from almost localized but barely itinerant electrons in the critical region of transition between metals and the Mott insulator. These critical regions are not easy to understand from either the metal or the insulator side, but their critical properties can be analyzed by the techniques for *quantum critical phenomena* discussed in Sec. II.

The two important parameters in the Hubbard model are the electron correlation strength U/t and the band filling n. The schematic metal-insulator phase diagram in terms of these parameters is presented in Fig. 1. In the case of a nondegenerate band, the $n=0$ and $n=2$ fillings correspond to the band insulator. For the half-filled case ($n=1$), it is believed that the change of U/t drives the insulator-to-metal transition (Mott transition) at a critical value of U/t except in the case of perfect nesting, where the critical value U_c is zero. This transition at a finite U_c is called a *bandwidth control* (BC)-MIT. Mott argued that the BC-MIT becomes a first-order transition when we consider the long-range Coulomb force not contained in the Hubbard model (Mott, 1956, 1990). He reasoned supposing that the carrier density decreases with increasing U/t. Then screening of long-range Coulomb forces by other carriers becomes ineffective, which results in the formation of an electron-hole bound pair at a finite U. This causes the first-order transition to the insulating state. Here we note that the validity of Mott's argument is still an open question because, as mentioned above, the Mott transition is not necessarily of the carrier-number-vanishing type but can be of the mass-diverging type, in contrast to the transition to the band insulator. We shall discuss this later in greater detail. Irrespective of Mott's argument the coupling to lattice degrees of freedom also favors the first-order transition by discontinuously increasing the transfer amplitude t in the metallic phase. The coupling of spin and orbital may also favor the first-order transition in real materials. In the region adjacent to the $n=1$ insulating line (a thick line in Fig. 1), the spin-ordered phase is frequently observed, that is, an antiferromagnetic insulating or metallic phase.

The filling at noninteger n usually leads to the metallic phase. The phase of particular interest is that of metals near the $n=1$ insulating line which is derived by *filling control* (FC) from the parent Mott insulator ($n=1$). Since the discovery of high-temperature superconductors, the concept of "*carrier doping*" or FC in the parent Mott insulators has been widely recognized as one of the important aspects of the MIT in the $3d$ electron systems. In contrast to the BC-MIT, the above two mechanisms for a first-order transition are not effective for the FC-MIT. The reason is that the electron-hole bound states cannot make an insulator by themselves due to the absence of carrier compensation. The coupling to the lattice is also ineffective because usually it does not couple to the electron filling. Therefore the transition can easily be continuous for an FC-MIT. In a relatively large-U/t region near the insulating phase of $n=0$, 1, and 2, however, the compounds occasionally suffer from the carrier localization effect arising from the static random potential and/or electron-lattice interaction. In addition, at some fractional but commensurate fillings such as $n=1/8$, 1/3, and 1/2, the compounds sometimes undergo the *charge-ordering phase transition*. We shall see ample examples in Sec. IV.E, associated with the commensurate charge-density and spin-density waves. The latter phenomenon is related not only with the short-ranged electron correlation as represented by U/t but also with the inter-site Coulomb interaction. Keeping these phenomena in mind, we shall review in Sec. III these electronic control parameters and how they are varied in actual materials.

B. Remarks on theoretical descriptions (Introduction to Sec. II)

Section II describes different theoretical approaches for strongly correlated electron systems and their MITs. A conventional way of describing the correlation effects is to assume the adiabatic continuity of the paramagnetic metallic phase with the noninteracting system based on the Fermi-liquid description. The Mott insulating phase is interpreted as in the pioneering work of Slater as a consequence of a charge gap's opening due to symmetry breaking of spin or orbit. In the other approaches, qualitatively different aspects which are claimed to be inaccessible from the Fermi-liquid-type approach are stressed. Since the proposals by Mott and Slater, these two viewpoints have played complementary roles sometimes in understanding the correlation effects, even though they provide contradicting scenarios in many cases, as we discuss in Sec. II in detail. A typical example of the controversy is seen in recent debates on high-temperature cuprate superconductors. Several attempts have been made, along the lines of Slater's approach, to account for the ground state of Mott insulators such as La_2CuO_4 and other transition-metal oxides as well as metallic phases, as we shall see in Sec. II.D. Some recent developments to treat the correlation effects in the framework of Fermi-liquid theory are reviewed in Sec. II.D.1 together with descriptions of the basic phenomenology of this theory. Effects of fluctuation in spin and charge responses can be taken into account on the level of the mean-field approximation by the random-phase approximation (RPA). When the symmetry is broken, the *Hartree-Fock* (HF) *theory* is the simplest way to describe the ordered state as well as the phase transition. The basic content of these mean-field approximations is summarized in Sec. II.D.2. Theoretical description beyond the mean-field level is the subject of later sections, Secs. II.E and II.F. To understand the correlation effect in d-electron systems on a more quantitative level, one has to go beyond the tight-binding approximation implicit in the Hubbard Hamiltonian. When the correlation effect is not important, the *local-density approximation* (LDA) is a useful tool for calculating the band structure of metals in the ground state. However, it is well known that the simple LDA is poor at reproducing the Mott insulating state as well as anomalous metallic states near the Mott insulator. Refinements of the LDA are then an important issue. These attempts include the *local spin-density approximation* (LSDA), *generalized (density) gradient approximation* (GGA), the *GW approximation*, the so-called LDA+U *approximation*, and *self-interaction correction* (SIC), which are reviewed in Sec. II.D.3. At finite temperatures, a mode-mode coupling theory [the *self-consistent renormalization* (SCR) *approximation*] was developed in metals to consistently take into account weak-amplitude spin fluctuations, which are ignored in the Hartree-Fock calculation (Moriya, 1985). This theory may be viewed as a self-consistent one-loop approximation in the weak-correlation approach. It is briefly reviewed in Sec. II.D.8. The basic assumption of the approaches initiated by Slater is that the perturbation expansion or the Hartree-Fock approximation and RPA in terms of spin correlations of electron quasiparticles is valid at least at zero temperature and well describes metals and the Mott insulator separately. On the other hand, in the approaches that go back to the original idea of Mott, several attempts have been made to take account of strong-correlation effects through strong charge correlations in a nonperturbative way. These attempts include the *Hubbard approximation* (Hubbard, 1964a, 1964b), the *Gutzwiller approximation* (Gutzwiller, 1965; Brinkman and Rice, 1970), various *slave-particle approximations* (Barnes, 1976, 1977; Coleman, 1984), and the *infinite-dimensional approach* (Kuramoto and Watanabe, 1987; Metzner and Vollhardt, 1989, Müller-Hartmann, 1989). In general, these approaches do not seriously take account of the wave-number dependence (or spatial dependence) of the correlation. In addition, they usually neglect effects of spin fluctuations. One coherent-potential approximation that does not assume magnetic order was developed by Hubbard (1964a, 1964b) and is summarized in Sec. II.D.4. This approach first succeeded in substantiating the appearance of the Mott insulating state along the lines of the original idea by Mott. Another approach on a basically mean-field level is the Gutzwiller approximation. This approximation, first applied to the MIT by Brinkman and Rice (1970), is discussed in Sec. II.D.5. These two approaches, by Hubbard and by Brinkman and Rice, have close connections to recently developed treatments in infinite dimensions and the slave-particle approximation. On the metallic side, the Gutzwiller approximation, the original slave-boson approximation, and the solution in infinite dimensions give essentially the same results for the low-energy excitations, indicating the basic equivalence of these three approximations for a description of the coherent part. In fact, the Gutzwiller and slave-particle approximations treat only the coherent part and neglect the incoherent part. On the insulating side, the Hubbard approximation and the infinite-dimensional approach provide similar results, because the Hubbard approximation considers only the incoherent excitations. Sections II.D.6 and II.D.7 discuss the results of the infinite-dimensional and slave-particle approximations, respectively. The infinite-dimensional approach is sometimes called the *dynamic mean-field theory* and treats the dynamic fluctuation correctly when spatial fluctuations can be ignored.

Aside from the above more or less biased approaches, numerical methods have been developed for the purpose of obtaining insights without approximations. A number of numerical studies are discussed in Sec. II.E.

To discuss this problem further, we should keep the following point in mind: When we consider the ground state of metals and insulators separately far away from the transition point, each of the ground states may in many cases be correctly expressed by adiabatic continuations of the fixed-point solutions obtained from rather simple Hartree-Fock approximations or perturbative expansions in terms of the correlation. However, an example is known in 1D interacting systems where the usual perturbation expansions and Hartree-Fock approximations clearly break down and the correct ground state is not reproduced from the weak-coupling approach. Its correct fixed point is believed to be the Tomonaga-Luttinger liquid. The analysis of 2D systems in terms of the Fermi-liquid fixed point is still controversial. In any case, aside from a few exceptional cases such as the 1D systems and systems under strong magnetic fields, the single-particle description of electrons is generally robust. However, even in the cases where the fixed point is more or less reproduced by the single-particle picture of electrons, weak-coupling approaches based on the perturbation expansion and/or Hartree-Fock-type analysis have serious difficulties in describing correlated metals.

The first serious problem is in describing excitations. For example, if one wants to ascribe the insulating nature of the Mott insulator to antiferromagnetic ordering, this attempt is immediately faced with the difficulty of describing properties above the Néel temperature T_N, because the insulating behavior is robust well above T_N in many cases, such as La_2CuO_4 and MnO. In fact, in La_2CuO_4, the charge excitation gap of the order of 2 eV, clearly observed in optical measurements above T_N, is two orders of magnitude larger than the energy scale of T_N. To understand this, a formalism to allow the formation of electron-hole bound states well above T_N is necessary. This is similar to the separation of the Bose condensation temperature and the energy scale of bound boson formation as in ^{4}He. An efficient way of describing phenomena below the electron-hole excitation energy, namely, the charge excitation gap, is to derive an effective Hamiltonian of Heisenberg spins, as is discussed in Sec. II.A. The formation of electron-hole bound states well above T_N is a clear indication of the breakdown of the single-particle picture. Of course since the low-energy collective excitations enhance the quantum spin fluctuations even at the level of zero-point oscillations, quantitatively reliable description of the ground state cannot be achieved by the usual single-particle description with a Hartree-Fock-type approximation.

The second serious problem is in describing the MIT. The breakdown of the single-particle description of electrons is most clearly observed when the MIT is continuous because the metallic ground state must be reconstructed from the low-energy states of the insulator when the insulator undergoes a continuous transition to a metal. There, critical fluctuations can only be treated by taking account of relevant collective excitations and growth of short-ranged correlations. Continuous MITs are the subject of extensive work in recent theoretical and experimental studies.

The critical fluctuation is not observable as a true divergence if the MIT is of first order. Therefore, in this case, whether interesting anomalous fluctuations in metals appear or not relies on whether the first-order transition is weak or not. Experimental aspects of first-order transitions are considered in Sec. IV.

As is discussed in Sec. IV, many compounds, such as some titanium oxides and vanadium oxides with the 3D perovskite structure, some of the sulfides and selenides, as well as 2D systems including high-T_c cuprates, appear to show a continuous MIT. To understand critical fluctuations near the MIT, it is crucial to extract the major driving force of the transition. One of the driving forces is the Anderson localization, and another is the correlation effect toward the Mott insulator. One may also argue the role of the electron-phonon interaction. In realistic situations, the effect of randomness, namely, the Anderson localization, must be seriously considered when the system is sufficiently close to the transition point. However, in many cases such as high-T_c cuprates, several other transition-metal oxides, and 2D ^{3}He, the strong-correlation effect appears to be the dominant driving force of the MIT. As a prototype, the nature of the transition from (to) the Mott insulator in clean systems, if clarified, provides a good starting point and is helpful in establishing new concepts. Theoretical understanding of the MIT caused by pure strong-correlation effects is an important subject of this review.

To understand the *continuous MIT*, the idea of scaling was first applied to the Anderson localization problem in the 1970s (Wegner, 1976; Abrahams, Anderson, Licciardello, and Ramakrishnan, 1979). As we discuss in Sec. II.F, it is now established that the scaling concept and renormalization-group analysis are useful especially in 2D. The *scaling theory* was also developed for understanding the transition between a Mott insulator and a superfluid of single-component bosons (see Sec. II.F.12). In the case of transitions between metals and Mott insulators in pure systems, a scaling theory has also been formulated recently and several new features of the MIT clarified (Imada, 1994c, 1995b). We discuss this recent achievement in Sec. II.F.

The difficulty of quasiparticle descriptions and mean-field approximations of electrons appear most seriously in non Fermi liquids. One-dimensional interacting systems showing the *Tomonaga-Luttinger liquid* behavior provide a prototype of non Fermi liquids due to strong-correlation effects. Its basic properties are summarized in Sec. II.G.1. To explain several anomalous properties of high-T_c cuprates, the *marginal Fermi-liquid theory* was proposed on phenomenological grounds. It is discussed in Sec. II.G.2.

Section II.H is devoted to recent attempts to describe more complicated situations. Transition-metal compounds have rich structures of phases due to spin and orbital fluctuations. Among them, the interplay of spin and orbital ordering is the subject of Sec. II.H.1. Due to the interplay of these two fluctuations, several d-electron systems have phases of ferromagnetic and antiferromagnetic metals. In particular, Mn and Co compounds show the MIT accompanied by the appearance of ferromagnetic metals due to strong Hund's-rule coupling. This is discussed in Sec. II.H.2. Other complexities such as the effects of charge ordering are also discussed in Sec. II.H.3.

C. Remarks on material systematics (Introduction to Sec. III)

In order to study Mott transitions and associated phenomena in real materials, microscopic models such as the Hubbard model [Eq. (1.1)] and its extended versions are necessary to formulate and to solve problems. Those models include parameters that are to be determined so as to reproduce experimentally measured physical properties of real systems as closely as possible. For example, the Hubbard model has the parameters U and t while the d-p model [Eq. (2.1)] also has $\varepsilon_d - \varepsilon_p \equiv \Delta$. There are more parameters when the degeneracy of the d orbitals has to be taken into account. In order to check the validity of theoretical ideas through comparison with experiment, however, it is often desirable not only to adjust the model parameters but also to have independent estimates of those parameters *a priori*. Section III describes such methods and the results of parameter estimates. Once we know the parameter values, especially how they change when the chemical composition of materials is changed, we are able to predict to some extent the physical properties of those materials using the parameter values as an input to theoretical calculations.

The current status of our understanding of the electronic structures of transition-metal compounds is heavily based on spectroscopic methods that have been developed in the last decade. A very useful approach for strongly correlated transition-metal compounds has been the configuration-interaction (CI) treatment of metal-ligand cluster models, in which correlation and hybridization effects within the local cluster are quite accurately taken into account. On the other hand, first-principles calculations have also greatly contributed to our understanding of electronic structures, especially to our estimates of the parameter values. In Sec. III.A, the local description of electronic structure based on the configuration-interaction picture of a metal-ligand cluster model is described. Basic parameters that characterize the electronic structure, namely, the charge-transfer energy Δ, the Coulomb repulsion U [see Eq. (1.1)], etc., are introduced together with the important concept of Mott-Hubbard-type versus charge-transfer-type insulators.

In Sec. III.B, methods used to derive those parameters are described: They are spectroscopic methods, first-principles methods, and more classical methods based on the ionic point-charge model. The spectroscopic methods are largely based on the configuration-interaction cluster model. Systematic variations of the model parameters have been deduced and employed to predict physical properties of the transition-metal compounds. The first-principles methods are based on the local-density approximation. The LDA with certain constraints (constrained LDA method) is used to calculate U and other parameters. Fits of first-principles band structures to the tight-binding model Hamiltonian give such parameters as the t and Δ.

In Sec. III.C we describe how to control the electronic parameters of the model for real materials systems. Two fundamental parameters of a strongly correlated electron system are the one-electron bandwidth W (or hopping interaction t of the conduction particle) and the band filling n (or doping level). The conventional method of bandwidth control (BC) is application of external or internal (chemical) pressure. In Sec. III.C.1 we show some examples of the metal-insulator phase diagram afforded by such bandwidth control. As a typical example of chemical pressure, we describe the general relation between the ionic radii of the composing atomic element (or the so-called tolerance factor) and the metal-oxygen-metal bond angle in a perovskite-type structure. The d-electron hopping interaction t is mediated by the oxygen $2p$ state (supertransfer process) and hence sensitive to the bond angle. This offers the opportunity to control W by variation of the perovskite tolerance factor. The example of $R\mathrm{NiO}_3$, is described in that section, where R is the rare-earth ion with varying ionic radius. The band filling or doping level can be controlled by modifying the chemical composition, as described in Sec. III.C.2, such as introducing extra oxygen or its vacancies and/or alloying the heterovalent ions other than on the tradition metal site. The perovskites and their analogs are again the most typical for such filling control (FC) and the FC range in the actual pseudocubic and layered perovskites of $3d$ transition-metal oxide is depicted. The last subsection (III.C.3) is devoted to a description of some homologous series compounds in which electronic dimensionality can be controlled to some extent. The cuprate ladder-type compounds and the Ruddlesden-Popper series (the so-called layered perovskite) structures represent the dimensional crossover from 1D to 2D and from 2D to 3D, respectively. These systematics are helpful in connecting the rather general theoretical descriptions in Sec. II to specific experimental examples in Sec. IV. They are also useful for classifying experimental results.

D. Remarks on experimental results of anomalous metals (Introduction to Sec. IV)

Section IV is devoted to experimentally observed features of correlated metals and related MITs in d-electron systems (mostly oxides), which are mostly derived from the Mott insulators by bandwidth control (BC) or filling control (FC). As we mentioned above, other systems, including the organic and f-electron systems, show similar MIT properties, but we do not cover them in this article. Concerning the work done before the mid-1980s, comprehensive reviews on d-electron compounds have been given in the literature, e.g., the book written by Mott (1990) himself and one in honor of the 80th anniversary of Mott's birth (Edwards and Rao, 1985). The review given here would be biased in favor of the late advance on the FC-MITs.

In Sec. IV.A, we try to update the experimental understanding of the BC-MIT systems, V_2O_3 (IV.A.1), NiS (IV.A.2), $NiS_{2-x}Se_x$ (IV.A.3) and RNiO$_3$ (IV.A.4). The first two compounds have long been known as the prototypical systems that show the Mott insulator-to-metal transition by application of pressure or by chemical substitution. The MIT induced by some nonstoichiometry or by Ti doping should rather be considered as FC-MIT, yet all the features of the MIT in V_2O_3 are comprehensively described in this section. In the modern view of the Zaanen-Sawatzky-Allen scheme, the insulating states of NiS and $NiS_{2-x}Se_x$ should be classified as charge-transfer insulators with the charge gap between the filled chalcogen $2p$ state and Ni $3d$ upper Hubbard band, in which the chalcogen $2p$ state bandwidth or the hybridization between the two states can be changed by applying pressure or alloying S site with Se. A similar BC-MIT has been recently recognized in a series of RNiO$_3$, R being a rare-earth element from La to Lu, and the BC acting by the bond distortion of the orthorhombic perovskite. In this case, the nominal valence of Ni is $3+$ with $3d^7$ electron configuration, indicating the insulating phase with $S=1/2$ in contrast to the former Ni-based conventional Mott insulators with $S=1$. In Sec. IV.A.5, we describe the electron spectroscopy of $Ca_{1-x}Sr_xVO_3$, in which the bandwidth control can be similarly achieved by perovskite distortion.

In Sec. IV.B we describe the features of the metallic state derived from the Ti^{3+}- and V^{3+}-based Mott-Hubbard insulators by FC-MIT. $R_{1-x}A_xTiO_3$ (IV.B.1) is a relatively new but prototypical Mott-Hubbard system, in which both BC and FC have been proven to be possible. The FC-MIT on the V^{3+}-based compound is also observed in $La_{1-x}Sr_xVO_3$ (IV.B.2) with perovskite structure, which has long been known but is yet to be investigated from the modernized view.

Concerning the high-temperature superconducting cuprates, there have been numerous publications on their anomalous metallic properties. They are the most important example of the FC-MIT. Here, we focus on the filling dependence of the normal-state properties in prototypical hole-doped superconductors (IV.C.1. $La_{2-x}Sr_xCuO_4$ and IV.C.3. $YBa_2Cu_3O_{6+y}$) and electron-doped ones (IVC.2 $R_{2-x}Ce_xCuO_4$).

In Sec. IV.D, we briefly describe the recent attempts to derive the metallic state via carrier doping or FC in the *quasi-1D cuprate compounds* as well as the thermally induced BC-MIT in $BaVS_3$. In particular, the search for the FC-MIT in the quasi-1D cuprates have recently been fruitful for one of the *spin-ladder compounds*, $(Sr,Ca)_{14}Cu_{24}O_{41}$, and 10 K superconductivity was found under pressure, a finding which is described in a little more detail in Sec. IV.D.1.

The part of the Coulomb repulsion between electrons on different sites occasionally helps the periodic real-space ordering of the charge carriers in narrow-band systems, although even without the intersite Coulomb repulsion, this real-space ordering may be stabilized due to the kinetic-energy gain (see Sec. II.H.3). These phenomena are called *charge ordering* in the d-electron oxides and are widely observed for systems with simple fractional filling. A classic example is the Verwey transition in magnetite, Fe_3O_4 (Sec. IV.E.1), with spinel structure. The resistivity jump at $T_V \approx 120$ K was assigned to the onset of the charge ordering, namely a real-space ordering of the Fe^{2+} and Fe^{3+} on the spinel B site in the ferrimagnetic state, where the spins on the A sites (Fe^{3+}) and on the B sites (Fe^{2+}/Fe^{3+}) direct oppositely. The magnetic phase-transition temperature is 858 K, much higher than T_V. Thus we can only consider the charge degree of freedom decoupled from the spin degree of freedom upon the charge-ordering transition. In contrast, versatile phenomena take place in the d-electron oxides arising from simultaneous or strongly correlated changes of the charge ordering and spin ordering. One such example is the case of $La_{1-x}Sr_xFeO_3$ (Sec. IV.E.2) with $x=2/3$, in which the MIT at 220 K is associated with simultaneous charge ordering and antiferromagnetic spin ordering. In the layered $(n=1)$ perovskite $La_{2-x}Sr_xNiO_4$ (Sec. IV.E.3) with $x=1/3$ or 1/2, the charge-ordered phase shows up at higher temperatures (220–240 K), accompanying the resistivity jump, and subsequently antiferromagnetic spin ordering takes place. It is now believed that similar charge-ordering phenomena in quasi-2D systems are present in the layered perovskites of manganites (Sec. IV.E.4) and cuprates (Sec. IV.C.1) with specific fillings. In particular, the cases of the superconducting cuprates $La_{2-x}Sr_xCuO_4$ and $La_{2-x}Ba_xCuO_4$, with $x=1/8$, are known as "the 1/8 problem:" The superconductivity disappears singularly at this filling even though 1/8 is near the optimum doping level ($x=0.15$) at which T_c is maximum. The phenomenon accompanies a structural change, as confirmed in $La_{2-x}Ba_xCuO_4$, and perhaps also spin ordering.

Sec. IV.F is devoted to a review of *double-exchange* systems, which are of revived interest due to the large magnetoresistance and other magnetic-field-induced phenomena. The ferromagnetic interaction between the local d-electron spins is mediated by the transfer of the conduction d electron (double-exchange interaction): The itinerant carriers are coupled with the local spin via the strong on-site exchange interaction (Hund's-rule coupling). The metallic phase is derived by hole doping from the parent insulators, e.g., $LaMnO_3$ and $LaCoO_3$. In the perovskite manganites (Sec. IV.F.1), the strong Hund's-rule coupling works between the e_g electron and the t_{2g} local spin ($S=3/2$). The e_g electrons are strongly correlated, which gives rise to various competing interactions with the double-exchange interaction. In particular, we shall see that competing interactions, such as electron-lattice (Jahn-Teller), superexchange, and charge-ordering interactions, cause a variety of magnetic-field-induced metal-insulator phenomena in the manganites with controlled bandwidth and filling. The attempt at dimension control in manganites is reviewed, taking examples of layered perovskite structures ($n=2$; Sec IV.F.2). Hole-doped cobalt oxides with the perovskite structure (Sec. IV.G.4) are other examples of double-exchange ferromagnets, although the itinerancy of the conduction electrons is considerably larger than in the manganites.

The systems associated with gaps for both charge and spin are conceptually difficult to distinguish from the band insulators, as discussed above. However, some d-electron compounds are considered to be strongly correlated insulators with a spin gap and undergo the transition to correlated metals usually by increasing temperature or by applying pressure (BC-MIT). Some examples are given in Sec. IV.G. FeSi (Sec. IV.G.1) has been pointed out to show similarities to a Kondo insulator. The nonmagnetic ground state of VO_2 (Sec. IV.G.2) arises from the dimerization of V sites. Nevertheless, the Cr-doped compound takes the structure of a homogeneous stack but remains insulating, i.e., is a Mott insulator. Thus the spin-dimerized state in VO_2 may be viewed as a spin Peierls state and the compound undergoes an insulator-metal transition with increasing temperature. $LaCoO_3$ (Sec. IV.G.4) undergoes a spin-state transition and the ground state corresponds to the low-spin ($S=0$) state. The thermally induced MIT in this compound has recently been revisited and some unconventional features arising from electron correlation have been found. We further consider the recent investigation of the misfit compounds, $La_{1.17-x}Pb_xVS_{3.17}$ (Sec. IV.G.5), which are nonmagnetic in the insulating state ($x=0.17$) where both electron doping and hole doping are possible. Section IV.H is devoted to other interesting *4d transition-metal oxides*, for example Sr_2RuO_4 (Sec. IV.H.1). This transition-metal oxide, which is isostructural with $La_{2-x}Sr_xCuO_4$, was recently found to be superconducting below 0.9 K and to show a highly anisotropic Fermi-liquid behavior.

II. THEORETICAL DESCRIPTION

A. Theoretical models for correlated metals and Mott insulators in *d*-electron systems

1. Electronic states of *d*-electron systems

The atomic orbitals of transition-metal elements are constructed as eigenstates under the spherical potential generated by the transition-metal ion. When the solid is formed, the atomic orbital forms bands due to the periodic potential of atoms. The bandwidth is basically determined from the overlap of two d orbitals on two adjacent transition metals each. The overlap comes from the tunneling of two adjacent so-called virtual bound states of d orbitals. Because of the relatively small radius of the wave function as compared to the lattice constant in crystals, d-electron systems have in general smaller overlap and hence smaller bandwidths than alkaline metals. In transition-metal compounds, the overlap is often determined by indirect transfer between d orbitals through ligand p orbitals. This means that the bandwidth is determined by the overlap (in other words, hybridization) of the d wave function at a transition-metal atom and the p wave function at the adjacent ligand atom if the ligand atoms make bridges between two transition-metal atoms. Because of this indirect transfer through ligand atomic orbitals, the d bandwidth becomes in general even narrower. Another origin of the relatively narrow bandwidth in transition-metal compounds is that $4s$ and $4p$ bands are pushed well above the d band, where screening effects by $4s$ and $4p$ electrons do not work well. This makes the interaction relatively larger than the bandwidth. In any case, because of the narrow bandwidth, the tight-binding models constructed from atomic Wannier orbitals provide a good starting point. For historic and seminal discussions on this point, readers are referred, to the textbook edited by Rado and Suhl (1963), particularly the articles by Herring (1963) and Anderson (1963a, 1963b).

The bands that are formed are under the strong influence of anisotropic crystal fields in solids. Because the $3d$ orbital has the total angular momentum $L=2$, it has fivefold degeneracy ($L_z=2,1,0,-1,-2$) for each spin and hence a total of tenfold degeneracy including spins. This degeneracy is lifted by the anisotropic crystal field. In transition-metal compounds, a transition-metal atom is surrounded by ligand atoms to help in the formation of a solid through the increase in cohesive energy by covalent bonds of the two species. Because the ligand atoms have a strong tendency towards negative valence,

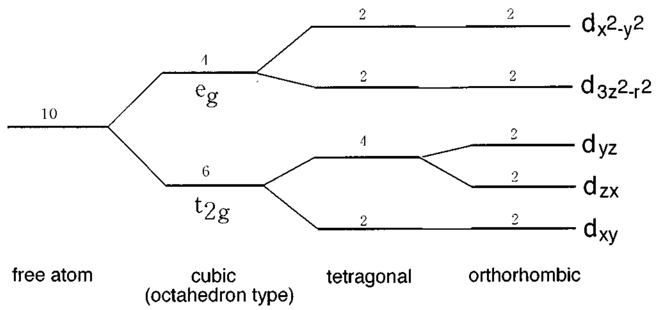

FIG. 2. Crystal-field splitting of $3d$ orbitals under cubic, tetragonal, and orthorhombic symmetries. The numbers cited near the levels are the degeneracy including spins.

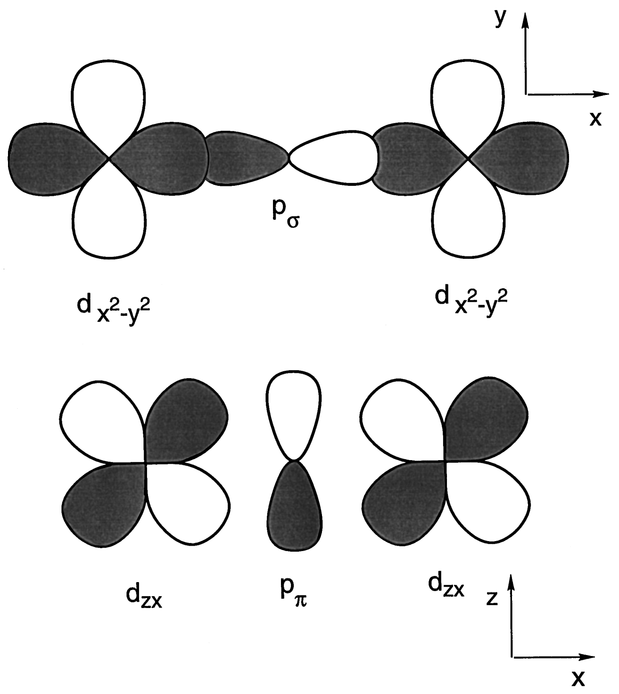

FIG. 3. Examples of configurations for transition-metal $3d$ orbitals which are bridged by ligand p orbitals.

the crystal field of electrons in the direction of the ligand atom is higher than in other directions. Figure 2 shows an example of the crystal field splitting, where the cubic lattice symmetry leads to a higher energy level of fourfold degenerate e_g (or d_γ) orbital and sixfold degenerate lower orbitals, t_{2g} (or d_ε). When a transition-metal atom is surrounded by ligand atoms with an octahedron configuration, the e_g orbital has anisotropy with larger amplitude in the direction of the principle axes, namely, toward neighboring ligand atoms. The basis of these orbitals may be expanded by $d_{x^2-y^2}$ and $d_{3z^2-r^2}$ orbitals. On the other hand, the t_{2g} orbital has anisotropy with larger amplitude of the wave function toward other directions and may be represented by d_{xy}, d_{yz}, and d_{zx} orbitals. For other lattice structures with other crystal symmetries, such as tetragonal or orthorhombic as in the case of 2D perovskite structure, similar crystal field splitting appears. In the case of tetrahedral surroundings of ligand ions, e_g orbitals lie lower than t_{2g}, in contrast to cubic symmetry or octahedron surroundings. Readers are referred to Sec. III for more detailed discussions of each compound.

In general, the relevant electronic orbitals for low-energy excitations transition-metal compounds with light transition-metal elements are different from those with heavy ones. In the compounds with light transition-metal elements such as Ti, V, Cr, . . . , only a few bands formed from $3d$ orbitals are occupied by electrons per atom. Therefore the t_{2g} orbital (more precisely, the t_{2g} band under the periodic potential) is the relevant band for low-energy excitations in the case of the above-mentioned octahedron structure because the Fermi level crosses bands mainly formed by t_{2g} orbitals. By contrast, in transition-metal compounds with heavy transition-metal elements such as Cu and Ni, the t_{2g} band is fully occupied far below the Fermi level, and low-energy excitations are expressed within the e_g band, which is formed mainly from e_g atomic orbitals. If degenerate t_{2g} or e_g orbitals are filled partially, it generally leads again to degeneracy of the ground state, which frequently induces the Jahn-Teller effect to lift the degeneracy.

Another important difference between light and heavy transition-metal compounds is the level of ligand p orbitals. For example, in the transition-metal oxides, the levels of the relevant $3d$ orbitals and oxygen $2p_\sigma$ orbitals, illustrated in Fig. 3, become closer when the transition-metal element is changed from Sc to Cu. This is mainly because the positive nuclear charge increases with this change, which makes the chemical potential of d electrons lower and closer to the p orbital. In fact, in the high-T_c cuprates, the $2p_\sigma$ orbital has a level close to the $3d_{x^2-y^2}$ orbital of Cu. This tendency, as well as the larger overlap of the e_g wave function with the ligand p_σ orbital for geometric reasons, causes a strong hybridization of the e_g and ligand p bands in the late transition metals. Therefore, to understand low-energy excitations on a quantitative level, we have to consider these strong hybridization effects. In contrast, for light transition-metal oxides, the oxygen p level becomes far from the $3d$ orbital and additionally the overlap of t_{2g} and p orbitals is weak. Then the oxygen p band is not strongly hybridized with $3d$ band at the Fermi level, and the formal valence of oxygen is kept close to O^{2-}. (More correctly speaking, the oxygen p band is nearly full. However, the real valence of oxygen itself may be larger than -2 because the oxygen p band is hybridized with $3d$, $4s$, and $4p$ orbitals.) Consequently the contribution from the oxygen p band to the wave function at the Fermi level may be ignored in the first stage. When the ligand atoms are replaced with S and Se, in general, the level of the $2p$ band becomes higher and can be closer to the d band. This systematic change can be seen, for example, in NiO, NiS, and NiSe, as we shall see in Secs. III.A and IV.A.

The electronic correlation effect is in general large when two electrons with up and down spins each occupy the same atomic d orbital of a transition-metal atom. The Coulomb repulsion energy of two electrons at the same atomic orbital is determined by the spatial extension of the orbital. The Coulomb energy thus determined is relatively large for the d orbital as compared to the small bandwidth. Of course, since the Coulomb interaction is long ranged, the interatomic Coulomb interaction up to the screening radius also has to be considered in realistic calculations.

2. Lattice fermion models

Much progress has been made in our theoretical understanding of d-electron systems through the tight-binding Hamiltonian. In this section we introduce several lattice fermion systems derived from the tight-binding approximation, for use and further discussion in later sections.

Considering all the above aspects of electronic wave functions in d-electron systems, we obtain several simplified tight-binding models. The most celebrated and simplified model is the Hubbard model (Anderson, 1959; Hubbard, 1963; Kanamori, 1963) defined in Eqs. (1.1a)–(1.1d). The kinetic-energy operator $\mathcal{H}_t$ in (1.1b) is obtained from the overlap of two atomic Wannier orbitals, $\varphi_{i\sigma}(\mathbf{r})$ on site i and $\varphi_{j\sigma}(\mathbf{r})$ on site j as

$$t=\int d\mathbf{r}\ \varphi^*_{i\sigma}(\mathbf{r})\frac{1}{2m}\nabla^2\varphi_{j\sigma}(\mathbf{r}), \tag{2.1}$$

where m is the electron mass and the Planck constant $\hbar$ is set to unity. The on-site term $\mathcal{H}_U$ in (1.1c) describes the Coulomb repulsion of two electrons at the same site, as derived from

$$U=\int d\mathbf{r}\ d\mathbf{r}'\ \varphi^*_{i\sigma}(\mathbf{r})\varphi_{i\sigma}(\mathbf{r})\frac{e^2}{|\mathbf{r}-\mathbf{r}'|}\varphi^*_{i-\sigma}(\mathbf{r}')\varphi_{i-\sigma}(\mathbf{r}'). \tag{2.2}$$

Cleary this Hamiltonian neglects multiband effects, a simplification that is valid in the strict sense only when the atom has only one s orbital, as in hydrogen atoms. When this model is used as a model of d-electron systems, it implicitly assumes that orbital degeneracy is lifted by the strong anisotropic crystal field so that relevant low-energy excitations can be described by a single band near the Fermi level. It also assumes that the ligand p band in transition-metal compounds is far from the relevant d band or that they are strongly hybridized to form an effective single band. This Hamiltonian also neglects the intersite Coulomb force. The screening effect makes the long-range part of the Coulomb force exponentially weak, which justifies neglect of the Coulomb interaction far beyond the screening radius. However, ignoring the intersite interaction in the short-ranged part of the Coulomb force is a simplification that sometimes results in failure to reproduce important features, such as the charge-ordering effect, as we shall discuss in Sec. II.H. In the literature, the electron hopping term $\mathcal{H}_t$ is often restricted to the sum over pairs of nearest-neighbor sites $\langle ij\rangle$.

In spite of these tremendous simplifications, the Hubbard model can reproduce the Mott insulating phase with basically correct spin correlations and the transition between Mott insulators and metals. The Mott insulating phase appears at half-filling where the average electron number $\langle n_{i\sigma}\rangle$ is controlled at $\langle n_{i\sigma}\rangle=1/2$. For the nearest-neighbor Hubbard model on a hypercubic lattice, the band structure of the noninteracting part is described as

$$\mathcal{H}_t=\sum_{k\sigma}\ \varepsilon_0(k)c^\dagger_{k\sigma}c_{k\sigma}, \tag{2.3a}$$

$$\varepsilon_0(k)=-2t\sum_{v=x,y,\cdots}\ \cos k_v, \tag{2.3b}$$

where we have taken the lattice constant to be unity. Here, the Fourier transform of the electron operator is introduced as

$$c^\dagger_{\mathbf{k}\sigma}=\sum_j\ e^{i\mathbf{k}\cdot\mathbf{r}_j}c^\dagger_{j\sigma}. \tag{2.4}$$

The spatial coordinate of the j site is denoted by $\mathbf{r}_j$. At half-filling under electron-hole symmetry, the Fermi level lies at $\mu=\varepsilon_F=0$. Because the band is half-filled at $\mu=0$, the appearance of the insulating phase is clearly due to the correlation effect arising from the term $\mathcal{H}_U$.

Although both the Mott insulating state and the MIT (metal-insulator transition) are reproduced in the Hubbard model, many aspects on quantitative levels with rich structure have to be discussed by introducing more complex and realistic factors. To discuss the charge-ordering effect, at least the near-neighbor interaction effect should be considered as

$$\mathcal{H}=\mathcal{H}_H+\mathcal{H}_V, \tag{2.5a}$$

$$\mathcal{H}_V=V\sum_{\langle ij\rangle}\ n_in_j, \tag{2.5b}$$

$$n_i=\sum_\sigma\ n_{i\sigma}. \tag{2.5c}$$

For light elements of transition metal, such as V and Ti, the Fermi level is on the t_{2g} bands, which are threefold degenerate under the cubic crystal field with possible weak splitting of this degeneracy under the Jahn-Teller distortion in the perovskite structure. When the Fermi level is on the e_g bands, as in Ni and Cu compounds, the degeneracy is twofold in the absence of the Jahn-Teller distortion. If the Jahn-Teller splitting is weak, we have to consider explicitly three orbitals, d_{xy}, d_{yz}, and d_{zx}, for the t_{2g} band and two orbitals, $d_{x^2-y^2}$ and $d_{3z^2-r^2}$, for the e_g band in addition to the spin degeneracy. This leads to the degenerate Hubbard model denoted by

$$\mathcal{H}_{DH}=\mathcal{H}_{Dt}+\mathcal{H}_{DU}+\mathcal{H}_{DV}+\mathcal{H}_{DUJ}, \tag{2.6a}$$

$$\mathcal{H}_{Dt}=-\sum_{\substack{\langle ij\rangle\\ \sigma,\nu,\nu'}}\ k(t_{ij}^{\nu,\nu'}c^\dagger_{i\sigma\nu}c_{j\sigma\nu'}+\mathrm{H.c.}), \tag{2.6b}$$

$$\mathcal{H}_{DU}=\sum_{\substack{i\nu\nu'\\ \sigma,\sigma'}}\ (1-\delta_{\nu\nu'}\delta_{\sigma\sigma'})U_{\nu\nu'}n_{i\sigma\nu}n_{i\sigma'\nu'}, \tag{2.6c}$$

$$\mathcal{H}_{DV}=\sum_{\substack{\sigma,\sigma'\\ \nu,\nu'\langle ij\rangle}}\ V_{ij}^{\nu\nu'}n_{i\sigma\nu}n_{j\sigma'\nu'}, \tag{2.6d}$$

$$\mathcal{H}_{DUJ}=-\sum_{\substack{\nu\nu'\\ i\sigma\sigma'}} J_{0\nu\nu'}[(1-\delta_{\nu\nu'})c^{\dagger}_{i\nu\sigma}c_{i\nu\sigma'}c^{\dagger}_{i\nu'\sigma'}c_{i\nu'\sigma}$$
$$-(1-\delta_{\nu\nu'})(1-\delta_{\sigma\sigma'})c^{\dagger}_{i\nu'\sigma'}c^{\dagger}_{i\nu'\sigma}c_{i\nu\sigma}c_{i\nu\sigma'}] \tag{2.6e}$$

where ν and ν' describe orbital degrees of freedom. $\mathcal{H}_{DUJ}$ is the contribution of the intrasite exchange interaction with

$$J_{0\nu\nu'}=\int d\mathbf{r}\, d\mathbf{r}'\ \varphi_i^{\nu}(\mathbf{r})\varphi_i^{\nu'}(\mathbf{r})\frac{e^2}{|\mathbf{r}-\mathbf{r}'|}\varphi_i^{\nu}(\mathbf{r}')\varphi_i^{\nu'}(\mathbf{r}'), \tag{2.7}$$

where φ is taken to be real. The intersite exchange term is neglected here for simplicity. The term $\mathcal{H}_{DUJ}$ generates a Hund's-rule coupling, since two electrons on different atomic orbitals feel higher energy for opposite spins due to the first term. In this orbitally degenerate model, in addition to spin correlations, we have to consider orbital correlations that can lead to orbital long-range order. The term $\mathcal{H}_{DU}$ represents the intra-orbital Coulomb energy $U_{\nu,\nu}$ as well as the interorbital one $U_{\nu,\nu'}$ with $\nu\neq\nu'$ for the on-site repulsion. The intersite repulsion is given in $\mathcal{H}_{DV}$.

For the case with orbital degeneracy as in Eq. (2.6a), the effective Hamiltonian may be derived from the orbital exchange coupling in analogy with the spin exchange coupling Eq. (2.12) (Castellani *et al.*, 1978a, 1978b, 1978c; Kugel and Khomskii, 1982). However, the orbital exchange coupling has important differences from the spin exchange. One such difference is that the orbital exchange may have large anisotropy.

As in the derivation of the usual superexchange interaction for the single-orbital system, we can derive the strong-coupling Hamiltonian by introducing pseudospin representation by τ_i for the orbital degrees of freedom in addition to the $S=1/2$ operator $\mathbf{S}_i$ for the spins (τ_i has the same representation as the spin-1/2 operators for doubly degenerate orbitals). More explicitly, $\tau_i^{\dagger}=c^{\dagger}_{i\nu}c_{i\nu'}$, $\tau_i^{-}=c^{\dagger}_{i\nu'}c_{i\nu}$ and $\tau_i^{z}=\frac{1}{2}(c^{\dagger}_{i\nu}c_{i\nu}-c^{\dagger}_{i\nu'}c_{i\nu'})$, respectively, for doubly degenerate orbits. In the simplest case of twofold degenerate orbitals with a single electron per site on average, the Hilbert space of the two-site problem is expanded by four states, as shown in Fig. 4, when the doubly occupied site is excluded due to a strong intrasite Coulomb interaction. Here we consider the transfer of two e_g orbitals between two sites located along the x or y directions. The transfers between two x^2-y^2 orbitals, t_{x1}, between two $3z^2-r^2$ orbitals, t_{x2}, and between x^2-y^2 orbital and $3z^2-r^2$ orbital, t_{x12}, respectively, satisfy $t_{x1}>t_{x12}>t_{x2}$ while $t_{z2}\gg t_{z1}$ and $t_{z12}=0$ are expected along the z direction. In fact, because of the anisotropy of the d wave function, these are scaled by a single parameter as

$$t_{x1}=\frac{3}{4}t_0,\quad t_{x2}=\frac{1}{4}t_0,\quad t_{x12}=-t_{y12}=-\frac{\sqrt{3}}{4}t_0,$$
$$t_{z1}=t_{z12}=0,\quad\text{and}\quad t_{z2}=1.$$

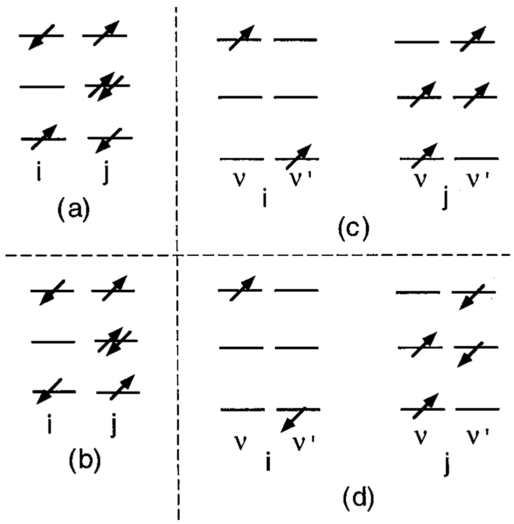

FIG. 4. Examples of various second-order processes of two-site systems with the sites i and j. The orbitals are specified by ν and ν'. The upper, middle, and lower states are the initial, intermediate, and final states in the second-order perturbation expansion in terms of t/U: (a) off-diagonal contribution to the spin-exchange process for the case without orbital degeneracy; (b) diagonal contribution for the case without orbital degeneracy; (c) twofold orbital degeneracy yielding off-diagonal orbital exchange process; (d) same situation as (c) yielding both orbital and spin exchange.

Therefore the Hamiltonian becomes highly anisotropic for τ operators. A general form of the exchange Hamiltonian in the strong-coupling limit in this case is given by

$$\mathcal{H}=\sum_{\langle ij\rangle}[\mathbf{S}_i\cdot\mathbf{S}_j\{J_s+J^z_{s\tau}\tau^z_i\tau^z_j+2J^{+-}_{s\tau}(\tau^+_i\tau^-_j+\tau^-_i\tau^+_j)$$
$$+2J^{++}_{s\tau}(\tau^+_i\tau^+_j+\tau^-_i\tau^-_j)+2J^{zx}_{s\tau}(\tau^+_j+\tau^-_j)$$
$$-2iJ^{zy}_{s\tau}(\tau^+_j-\tau^-_j)+K^z_{\tau s}\tau^z_i+K^x_{\tau s}\tau^x_i\}$$
$$+J^x_{\tau}\tau^z_i\tau^z_j+2J^{+-}_{\tau}(\tau^+_i\tau^-_j+\tau^-_i\tau^+_j)+2J^{zx}_{\tau}\tau^z_i(\tau^+_j+\tau^-_j)$$
$$-2iJ^{zy}_{\tau}\tau^z_i(\tau^+_j-\tau^-_j)+2J^{++}_{\tau}(\tau^+_i\tau^+_j+\tau^-_i\tau^-_j)$$
$$+K^z_{\tau}\tau^z_i+K^x_{\tau}\tau^x_i]. \tag{2.8}$$

Here, the parameters depend on the direction of $\vec{i}-\vec{j}$. It should be noted that XY-type or Ising-type anisotropy for the spin exchange easily occurs, and this anisotropy depends on the pair (i,j). When the system is away from the integer filling or the on-site interaction is not large enough to make the system Mott insulating, the transfer term has to be considered explicitly. As we saw above, the transfer itself is also highly anisotropic, depending on the orbital. For example, the transfer for the x^2-y^2 orbital is in general large in the x and y directions but small in the z direction. The opposite is true in the $3z^2-r^2$ orbital. This makes for complicated orbital-dependent band structure in contrast with the spin dependence. Another complexity is that the orbital exchange coupling of the bonds in the x direction is large for d_{xy}, d_{zx}, or $d_{x^2-y^2}$ orbitals, while it is small for the exchange including d_{yz} or $d_{3z^2-r^2}$ orbital. For the bonds in other directions, y and z, different combinations have large exchange coupling. In addition, orbital ordering strongly couples with magnetic ordering. The coupling of orbital and spin degrees of freedom is apparently different from the usual spin-orbit coupling because it is a nonrelativistic effect. For d-electron systems, the usual spin-orbit interaction is relatively weak as compared to rare-earth compounds. In general, in systems with orbital degeneracy, we have to consider couplings of orbital occupancy to the Jahn-Teller distortion, quadrupole interaction, and spin-orbit interaction. Orbital degeneracy also yields intersite orbital exchange coupling as in Eq. (2.8). These will lead to a rich structure of physical properties, as is discussed in Sec. II.H.l.

For Mn and Co compounds, the d electrons may occupy high-spin states because of Hund's-rule coupling. In this case, the t_{2g} bands are occupied by three spin-aligned electrons with additional electrons in the e_g bands ferromagnetically coupled with t_{2g} electrons due to Hund's-rule coupling. This circumstance is sometimes modeled by the double-exchange model (Zener, 1951; Anderson and Hasegawa, 1955; de Gennes, 1960):

$$\mathcal{H}_{DE}=\mathcal{H}_t+\mathcal{H}_{Hund}, \tag{2.9a}$$

$$\mathcal{H}_t=-t\sum_{\substack{\langle ij\rangle\\ \sigma}}(c_{i\sigma}^{\dagger}c_{j\sigma}+\mathrm{H.c.}), \tag{2.9b}$$

$$\mathcal{H}_{Hund}=-J_H\sum_i \vec{S}_i\cdot\vec{\sigma}_i, \tag{2.9c}$$

where $\vec{S}_i=(S_i^x,S_i^y,S_i^z)$ is defined from the e_g-electron operator $c_{i\sigma}$ as

$$S_i^+=S_i^x+iS_i^y=c_{i\uparrow}^{\dagger}c_{i\downarrow}, \tag{2.10a}$$

$$S_i^-=S_i^x-iS_i^y=c_{i\downarrow}^{\dagger}c_{i\uparrow}, \tag{2.10b}$$

$$S_i^z=\frac{1}{2}(c_{i\uparrow}^{\dagger}c_{i\uparrow}-c_{i\downarrow}^{\dagger}c_{i\downarrow}), \tag{2.10c}$$

whereas $\vec{\sigma}_i$ represents the localized t_{2g} spin operators. A strong Hund's-rule coupling J_H larger than t may lead to a wide region of ferromagnetic metal, as is observed in Mn and Co compounds. In Co compounds, a subtle balance of low-spin and high-spin states is realized, as we shall see later in Sec. IV.G.4. More generally, the interplay of the Hund's-rule coupling and exchange couplings with strong-correlation effects as well as orbital and Jahn-Teller fluctuations can lead to complicated phase diagrams with ferromagnetic and various types of antiferromagnetic phases in metals, as well as in the Mott insulator, as will be discussed in Secs. II.H.2 and IV.F.1.

In the compounds with heavy transition-metal elements such as Ni and Cu, t_{2g} bands are fully occupied with additional e_g electrons. In particular, in the high-T_c cuprates, two-dimensional perovskite structure leads to highly 2D anisotropy with crystal field splitting of d_γ bands to the lower orbit, $d_{3z^2-r^2}$, and the upper one, $d_{x^2-y^2}$, due to the Jahn-Teller distortion for the case of a $\mathrm{CuO_6}$ octahedron. The Mott insulating phase of the high-T_c cuprates as in $\mathrm{La_2CuO_4}$ is realized in the Cu d^9 configuration, where three t_{2g} bands as well as the $d_{3z^2-r^2}$ band are fully occupied, whereas the $d_{x^2-y^2}$ band is half filled. This makes the single-band description more or less valid because the low-energy excitation can be described only through the isolated $d_{x^2-y^2}$ band. This is the reason why the Hubbard model can be a good starting point for discussing physics in the cuprate superconductors. However, another feature of heavy transition-metal oxides is the strong hybridization effect of the d orbital and the oxygen p orbital. Because the conduction network is constructed from an oxygen $2p_\sigma$ orbital and a $3d_{x^2-y^2}$ orbital in this case, strong covalency pushes the oxygen $2p_\sigma$ orbital closer to the Fermi level. The d-p model is the full description of these $3d_{x^2-y^2}$ and $2p_\sigma$ orbitals in the copper oxides where the Hamiltonian takes the form

$$\mathcal{H}_{dp}=\mathcal{H}_{dpt}+\mathcal{H}_{dpU}+\mathcal{H}_{dpV}, \tag{2.11a}$$

$$\mathcal{H}_{dpt}=-\sum_{\langle ij\rangle\sigma}t_{pd}(d_{i\sigma}^{\dagger}p_{j\sigma}+\mathrm{H.c.})+\varepsilon_d\sum_i n_{di}+\varepsilon_p\sum_j n_{pj}, \tag{2.11b}$$

$$\mathcal{H}_{dpU}=U_{dd}\sum_i n_{di\uparrow}n_{di\downarrow}+U_{pp}\sum_i n_{pi\uparrow}n_{pi\downarrow}, \tag{2.11c}$$

$$\mathcal{H}_{dpV}=V_{pd}\sum_{\langle ij\rangle}n_{pi}n_{dj}. \tag{2.11d}$$

When the oxygen p_σ level, ε_p, is much lower than ε_d, the oxygen p orbital contributes only through virtual processes. The second-order perturbation in terms of $\varepsilon_d-\varepsilon_p$ generates the original Hubbard model. This type of transition-metal oxide in which $\varepsilon_d-\varepsilon_p$ is assumed to be larger than U_{dd} is called a Mott-Hubbard-type compound. Because of $U_{dd}<|\varepsilon_d-\varepsilon_p|$, the charge gap in the Mott insulating phase is mainly determined by U_{dd}.

In contrast, if $|\varepsilon_d-\varepsilon_p|$ is smaller than U_{dd}, the charge excitation in the Mott insulating phase is mainly determined by the charge transfer type where an added hole in the Mott insulator mainly occupies the oxygen p_σ band. The difference between these two cases is schematically illustrated in Fig. 5. The importance of the oxygen p_σ band in this class of material was first pointed out by Fujimori and Minami (1984). This type of compound is called a charge-transfer-type or CT compound (Zaanen, Sawatzky, and Allen, 1985).

The character of low-energy charge excitations changes from d in the Mott-Hubbard type to strongly hybridized p and d in the charge-transfer type. However, it may be affected by an adiabatic change in the parameter space of $\Delta=\varepsilon_d-\varepsilon_p$ and U, as long as the insulating phase survives at half-filling of d electrons. At least in the Mott insulating phase, these two types of compounds show similar features described by the Heisenberg model, as is discussed below. In the metallic phase, one may also expect a similarity when the strong hybridization of the d and ligand p band forms well separated bonding, nonbonding, and antibonding bands

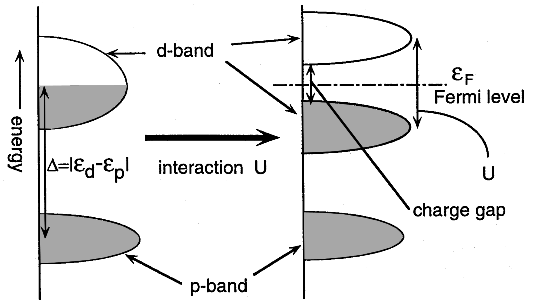

(a) Mott-Hubbard Insulator

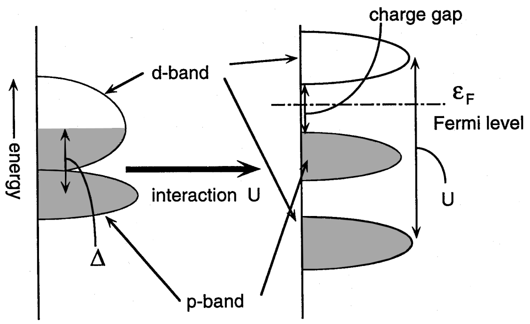

(b) Charge Transfer Insulator

FIG. 5. Schematic illustration of energy levels for (a) a Mott-Hubbard insulator and (b) a charge-transfer insulator generated by the d-site interaction effect.

and the Fermi level lies near one of them. However, it has been argued that some low-energy excitations display differences between the Mott-Hubbard and CT types (Emery, 1987; Varma, Schmitt-Rink, and Abrahams, 1987). With a decrease in Δ, the MIT may occur even at half-filling. This is probably the reason why Ni compounds become more metallic when one changes the ligand atom from oxygen, sulfur to selenium.

Low-energy excitations of the Mott insulating phase in transition-metal compounds are governed by the Kramers-Anderson superexchange interaction, in which only collective excitations of spin degrees of freedom are vital (Kramers, 1934; Anderson, 1963a, 1963b). The second-order perturbation in terms of t/U in the Hubbard model, as in Figs. 4(b) and 4(c), or the fourth-order perturbation in terms of $t_{pd}/|\varepsilon_d-\varepsilon_p|$ or t_{pd}/U_{dd} in the d-p model yield the spin-1/2 Heisenberg model at half band filling of d electrons:

$$\mathcal{H}_{\text{Heis}}=J\sum_{\langle ij\rangle}\mathbf{S}_i\cdot\mathbf{S}_j, \tag{2.12}$$

where $S_i^+=S_i^x+iS_i^y=c_{i\uparrow}^\dagger c_{i\downarrow}$, $S_i^-=S_i^x-iS_i^y=c_{i\downarrow}^\dagger c_{i\uparrow}$ and $S_i^z=\frac{1}{2}(n_{i\uparrow}-n_{i\downarrow})$. Here J is given in the perturbation expansion as $J=4t^2/U$ for the Hubbard model and

$$J=\frac{8t_{pd}^4}{(|\varepsilon_d-\varepsilon_p|+V_{pd})^2(|\varepsilon_d-\varepsilon_p|+U_{pp})}+\frac{4t_{pd}^4}{(|\varepsilon_d-\varepsilon_p|+V_{pd})^2U_{dd}}$$

for the d-p model. The exchange between two d orbitals, 1 and 2, in the presence of the ligand p orbital 3, is indeed derived from the direct exchange between the d orbital 1 and the neighboring p orbital 3, which is hybridized with the other d orbital 2 or vice versa. This generates a "superexchange" between 1 and 2 in the order shown above (Anderson, 1959). Even for doped systems, a second-order perturbation in terms of t/U in the Hubbard model leads to the so-called t-J model (Chao, Spalek, and Oles, 1977; Hirsch, 1985a; Anderson, 1987),

$$\mathcal{H}_{t\text{-}J}=-\sum_{\substack{\langle ij\rangle\\ \sigma}}P_d(t_{ij}c_{i\sigma}^\dagger c_{j\sigma}+\text{H.c.})P_d+J\sum_{\langle ij\rangle}\mathbf{S}_i\cdot\mathbf{S}_j, \tag{2.13}$$

where P_d is a projection operator to exclude the double occupancy of particles at the same site. To derive Eq. (2.13), we neglect the so-called three-site term given by

$$\mathcal{H}'_{t-J}\propto\sum_{\langle ilj\rangle}c_{i\sigma}^\dagger(S_l)_{\sigma\sigma'}c_{j\sigma'} \tag{2.14}$$

from the assumption that the basic physics may be the same. However, this is a controversial issue, since it appears to make a substantial difference in spectral properties (Eskes *et al.*, 1994) and superconducting instability (Assaad, Imada, and Scalapino, 1997). It was stressed that the t-J model (2.13) represents an effective Hamiltonian of the d-p model (2.11a) by extracting the singlet nature of a doped p hole and a localized d hole coupled with it (Zhang and Rice, 1988). Of course, for highly doped system far away from the Mott insulator, it is questionable whether Eq. (2.13) with doping-independent J can be justified as the effective Hamiltonian.

B. Variety of metal-insulator transitions and correlated metals

In order to discuss various aspects of correlated metals, insulators, and the MIT observed in d-electron systems, it is important first to classify and distinguish several different types. To understand anomalous features in recent experiments, we must keep in mind the important parameter, dimensionality. We should also keep in mind that both spin and orbital degrees of freedom play crucial roles in determining the character of the transition. Metal-insulator transitions may be broadly classified according to the presence or the absence of symmetry breaking in the component degrees of freedom on both the insulating and the metallic side, because different types of broken-symmetry states cannot be adiabatically connected. Here we employ the term "component" to represent both spin and orbital degrees of freedom in d-electron systems. Symmetry breaking in Mott insulators as well as in metals is due to the multiplicity of the particle components. For example, for antiferromagnetic order, the symmetry of multiple spin degrees of freedom is broken.

The Mott insulator itself in the usual sense is realizable only in a multicomponent system. This is because the Mott insulating state is defined when the band is at integer filling but only partially filled, which is possible only in multicomponent systems. In this context, the Mott insulator, in the sense discussed in the Introduction, is the insulator caused by intrasite Coulomb repulsion, as in the Hubbard model. This definition is generalized in the last part of this section to allow intersite Coulomb repulsion as the origin of generalized Mott insulator. For the moment, we restrict our discussion to the usual "intrasite" Mott insulator, as in the Hubbard model. When intrasite repulsion causes the Mott insulator, energetically degenerate multiple states coming from a multiplicity of components are only partially occupied by electrons because of strong mutual intrasite repulsion of electrons. This origin of an insulator does not exist when the multiplicity of states on a site is lost.

Although a multiplicity of components is necessary to realize a Mott insulator, it does not uniquely fix the behavior of the component degrees of freedom. Namely, the insulator itself may or may not be a broken-symmetry state of the component. To be more specific, consider, for example, the spin degree of freedom as the component. In the antiferromagnetic or the ferromagnetic state, the spin-component symmetry is broken and hence the spin entropy is zero in the ground state, as it should be. Because of the superexchange interaction, antiferromagnetic long-range order is the most widely observed symmetry-broken state in the Mott insulator; we shall see many examples in Sec. IV.

When continuous symmetry is broken, as in SU(2) symmetry breaking of the isotropic Heisenberg model, only the Goldstone mode of the component, such as the spin wave, survives at low energies accompanied by a gap in the charge excitation. We show in Sec. II.E.5 that this low-energy excitation of the Goldstone mode is neither relevant nor singular at the MIT point. Here the SU(2) symmetry is defined as the rotational symmetry of the Pauli matrix S_x, S_y, and S_z.

Another possible symmetry breaking may be caused by the orbital order. For example, because the t_{2g} orbital is threefold degenerate in the cubic symmetry, the Mott insulator may have either staggered orbital order (similar to antiferromagnetic order in the case of spins) or uniform orbital order (similar to ferromagnetic order) or even helical (spiral) and more complicated types of order to lift the orbital degeneracy. In general, the orbital order can be accompanied by static lattice anomalies, such as staggered Jahn-Teller-type distortion as discussed in Sec. II.H.1. From the experimental point of view, detection of the orbital order is not easy when it does not strongly couple with the lattice anomaly. When orbital and magnetic order take place simultaneously or take place only partially, interesting and rich physics is expected, as we discuss in Secs. II.H.1 and IV.

When the component order is not broken in the ground state, it implies that a highly quantum mechanical state like a total singlet state should be the ground state to satisfy the third thermodynamic law, which asserts zero entropy as the normal condition of the ground state. The total singlet ground state of the Mott insulator is observed in many spin-gapped insulators. Examples can be seen in spin Peierls insulators such as $CuGeO_3$, Peierls insulators with dimerization such as in TTF-TCNQ and DCNQ salts, one-dimensional spin-1 chains as in NENP, ladder systems (for example $Sr_{n-1}Cu_nO_{2n-1}$), two-dimensional systems as in CaV_4O_9 and the Kondo insulator. The appearance of spin gaps in these cases may be understood in a unified way from the geometric structure of the underlying lattice (see, for example, Hida, 1992; Katoh and Imada, 1993, 1994). Here, the spin gap Δ_s is defined as the difference between ground-state energies for the singlet and the triplet state:

$$\Delta_s \equiv E_g\left(\frac{N}{2}+1, \frac{N}{2}-1\right) - E_g\left(\frac{N}{2}, \frac{N}{2}\right), \tag{2.15}$$

where $E_g(N,M)$ is the total ground-state energy of N electrons with up spin and M electrons with down spin. The charge gap Δ_c for the hole doping into the singlet ground state is given by

$$\Delta_c \equiv \frac{1}{2}\left[E_g\left(\frac{N}{2}, \frac{N}{2}\right) - E_g\left(\frac{N}{2}-1, \frac{N}{2}-1\right)\right]. \tag{2.16}$$

When the spin excitation has a gap and the orbital excitation is not considered, this Mott insulator has both spin and charge gaps. In this it is actually similar to a band insulator, in which spin and charge have the same electron-hole excitation gap. Although the spin gap can be much smaller than the charge gap due to collective spin excitations in the above correlated insulators, in this category of spin gapped insulators, it is hard to draw a definite boundary between the band insulator and the Mott insulator. Indeed, they may be adiabatically connected by changes in the parameters when one concentrates only on the insulating phase apart from metals.

There is another type of Mott insulator in which neither symmetry breaking of the components nor a component excitation gap exists. Two well-known examples of this category are the 1D Hubbard model at half-filling and the 1D Heisenberg model in which the spin excitation is gapless due to algebraic decay of antiferromagnetic correlation. These examples indicate the absence of magnetic order because of large quantum fluctuations inherent in low-dimensional systems. To realize this type, low dimensionality appears to be necessary.

In terms of a quantum phase transition, this type of gapless spin unbroken-symmetry insulator appears just at the lower critical dimension d_{il} of the Mott insulator for component order, or, in other words, just at the magnetic critical point. As we discuss in detail in Sec. II.F, below the lower critical dimension of the relevant component order, $d<d_{il}$, insulators with a disordered component appear while order appears for $d>d_{il}$. The dimension $d=d_{il}$ is marginal with gapless spin and unbroken-symmetry behavior. The lower critical dimension may depend on details of the system under consideration such as lattice structure and number of components. For example, if lattice dimerization increases in the Heisenberg model, the ground state changes from the antiferromagnetic state to a spin-gapped singlet at a critical strength of dimerization in 2D (Katoh and Imada, 1993, 1994). A strongly dimerized lattice in 2D corresponds to $d<d_{il}$ while, in the case of a uniform square lattice, d_{il} is below 2.

In metals near the Mott insulator, a similar classification scheme is also useful. Here, we define two types of component order. One is diagonal, where there is a density wave such as the spin density wave in antiferromagnetic and ferromagnetic phases or an orbital density wave. The other is off-diagonal, in which superconductivity is the case. Above the lower critical dimension of metal for diagonal component order, d_{ml}, a diagonal component order exists, as in antiferromagnetic metals and ferromagnetic metals. By contrast, for $d\leqslant d_{ml}$, the diagonal component order disappears due to quantum fluctuations. d_{ml} may depend on the number of components. In principle, the insulating state can be realized through a diagonal component order of an arbitrarily incommensurate periodicity at the Fermi level, if the nesting condition is satisfied. This is indeed the case with the stripe phase in the Hartree-Fock approximation, as is discussed in Sec. II.D.2 and II.H.3. However, in the Hartree-Fock approximation dynamic quantum fluctuations are ignored. Usually, in reality, the ordering takes place only at some specific commensurate filling for a such large electron density of the order realizable in solids. Incommensurate order is hardly realized due to quantum fluctuations. When the quantum fluctuation is large enough, and the impurity-localization effect and the effect of anisotropic gap (in other words, discrete symmetry breaking as in the Ising-like anisotropic case) are not serious, usually metal appears just adjacent to the Mott insulator.

If this metal has a diagonal component order, the most plausible case is the same order with the same periodicity, like the order in the Mott insulating state. In this case, a small pocket of the Fermi surface is expected if the metal is obtained by carrier doping of the Mott insulator. This may be realized in the antiferromagnetic metallic state near the Mott insulator. Another important case of this class is that of ferromagnetic metals, as observed in Mn and Co compounds such as (La,Sr)MnO_3. Here the symmetry breaking is quite different between the antiferromagnetic order in the Mott insulator and the ferromagnetic order in the doped system. The appearance of ferromagnetic metals is theoretically argued in connection with Nagaoka ferromagnetism (Nagaoka, 1966), where the ferromagnetism is proven when a hole is doped into the Hubbard model at half filling in a special limit of infinite U. Ferromagnetism is also proven in some special band structures with a flat dispersion at the Fermi level. In the above argument the orbital degrees of freedom are ignored. In some cases, the formation of the ferromagnetic order is tightly connected with the double-exchange mechanism, which is made possible by the strong Hund's-rule coupling. Some of theoretical and experimental aspects of this class are discussed in Secs. II.H.2 and IV.F, respectively.

For the case $d\leqslant d_{ml}$, order in the diagonal component is lost. This class is further divided into three cases. In the first case, the component excitation has a gap due to formation of a bound state. A typical example is singlet Cooper pairing, where the ground state has an off-diagonal order, namely, superconducting for $d\geqslant 2$, while gap formation only leads to algebraic decay of the pairing correlation at $d=1$ because long-range order is destroyed by quantum fluctuations. A known example of this class in 1D is the Luther-Emery-type liquid (Luther and Emery, 1974; Emery, 1979). Although no example is known to date, the possibility is not excluded in principle that the superconducting ground state could dominate or coexist with diagonal component-order in a part of the region $d>d_{ml}$ near the Mott insulator. This class does not exclude the case of an anisotropic gap with nodes as in d-wave pairing, where the true excitation gap is lost.

The second case for $d\leqslant d_{ml}$ is the formation of a large Fermi surface consistent with the Luttinger sum rule. This case is possible, for example, when the Fermi-liquid state is retained close to the Mott insulating state. Here, the Fermi liquid is defined as an adiabatically continued state with the ground state of the noninteracting system, in which the interaction is gradually switched on. Then the Fermi surface in momentum space is retained in the Fermi liquid with the same volume as in a noninteracting system, which is the statement of the Luttinger theorem (Luttinger, 1963). The formation of a large "Fermi surface" is not necessarily restricted to the Fermi liquid. In the case of the Tomonaga-Luttinger liquid in 1D, the Fermi surface is characterized by singularity of the momentum distribution function, and there is a large Fermi volume consistent with the Luttinger theorem.

The third case is the formation of small pockets of Fermi surface. This is basically the same as what happens in a band insulator upon doping. Therefore no clear distinction from the doping into the band insulator is expected.

We summarize three cases of insulators and four cases of metals near the Mott insulator:

(I-1) insulator with diagonal order of components
(I-2) insulator with disordered component and component excitation gap
(I-3) insulator with disordered component and gapless component excitations
(M-1) metal with diagonal order of components and small Fermi volume
(M-2) metal or superconducting state with the bound-state formation dominated by off-diagonal component order (frequently with component excitation gap)
(M-3) metal with disordered component and "large" Fermi volume consistent with the Luttinger theorem

TABLE I. Rough and simplified sketch for types of metal-insulator transitions in overall phase diagram observed in various compounds. In parentheses, section numbers where discussions may be found in Sec. IV are given.

Insulator Metal	I-1 Component order	I-2 Component gap
M-1 diagonal component-order	$V_{2-y}O_3$(IV.A.1) $Ni_{2-y}S_{2-x}Se_x$(IV.A.2) $R_{1-x}A_xMnO_3$(IV.F.1)	$La_{1-x}Sr_xCoO_3$ (IV.G.4)
M-2 bound state (superconductor)	high-T_c cuprates (IV.C) BEDT-TTF compounds	$(Sr,Ca)_{14}Cu_{24}O_{41}$ (IV.D.1)
M-3 component disorder (large Fermi volume)	$La_{1-x}Sr_xTiO_3$ (IV.B.1) RNiO$_3$ $La_{1-x}Sr_xVO_3$ (IV.A.3) (IV.B.2)	
M-4 component disorder (small Fermi volume)		Kondo insulator (IV.G)

(M-4) metal with disordered component and "small" Fermi volume as in a doped band insulator

In d-electron systems experimentally and also in theoretical models, a variety of MITs are observed. Here we classify them in the form $[I\text{-}i \leftrightarrow M\text{-}j]$ ($i=1,2,3$, $j=1,2,3,4$) where a transition from an insulator of the type I-i to a metal of the type M-j takes place. We list below both cases of filling control (FC-MIT) and bandwidth control (BC-MIT) and summarize examples of the compounds in Table I.

$[I\text{-}1 \leftrightarrow M\text{-}1]$: A typical example is the transition between an antiferromagnetic insulator and an antiferromagnetic metal. Examples are seen in V_2O_{3-y} (BC-MIT or FC-MIT) and in $NiS_{2-x}Se_x$ (BC-MIT). Although the Hartree-Fock approximation usually gives this class of behavior for the MIT, it is important to note that in systems with strong 2D anisotropy, no example of this class is known to date. This lends support to the idea that d_{ml} is larger than two for the antiferromagnetic order, at least in single orbital systems. Quantum Monte Carlo results in 2D for a single band system also support the absence of antiferromagnetic order in metals. Even in 3D, all the examples of antiferromagnetic metals known to date are found when orbital degeneracy exists. For doped spin-1/2 Mott insulators, antiferromagnetic order quickly disappears by metallization upon doping or bandwidth widening, and no antiferromagnetic metals are scarcely found, as is known in $La_{1-x}Sr_xTiO_3$ (FC-MIT) and RNiO$_3$ (BC-MIT), although they have orbital degeneracy. Therefore d_{ml} for antiferromagnetic order without orbital degeneracy can be larger than three, although we do not have a reliable theory. With increasing component degeneracy due to orbital degrees of freedom, d_{ml} may become smaller than three. Quite different spin orderings can be realized between insulating and metallic phases in this category. A good example is the double-exchange system, such as $La_{1-x}Sr_xMnO_3$, where the Mott insulating state at $x=0$ has a type of antiferromagnetic order with orbital and Jahn-Teller orderings, whereas the metallic phase has ferromagnetic order. As for the orbital order, this compound has the character of $[I\text{-}1 \leftrightarrow M\text{-}3]$, because it is speculated that the orbital order is lost upon metallization.

$[I\text{-}1 \leftrightarrow M\text{-}2]$: This is the case of high-T_c cuprates at low temperatures. Recent studies appear to support that the superconducting phase directly undergoes transition to a Mott insulator (Fukuzumi *et al.*, 1996) by the route of FC-MIT. No normal metallic phase is seen between superconductor and insulator at zero temperature in the cuprates. Another example of this type of transition is that of BEDT-TTF compounds (BC-MIT; for a review, see Kanoda, 1997).

$[I\text{-}1 \leftrightarrow M\text{-}3]$: This class can be observed for $d_{ml} > d > d_{il}$. As we have already discussed, in 3D, $La_{1-x}Sr_xTiO_3$ (FC-MIT) and RNiO$_3$ may be examples, although the possible existence of a tiny antiferromagnetic-metal region cannot be ruled out. When the effect of orbital degeneracies becomes important, even for doped spin-1/2 insulators, rather complicated behavior may appear, as in (Y,Ca)TiO$_3$ (FC-MIT) where a wide region of orbital ordered insulator is speculated. In 2D, the second layer registered phase of ^{3}He adsorbed on graphite may also be interpreted as a Mott insulator (Greywall, 1990; Lusher *et al.*, 1993; Imada, 1995b). Solidification of 3D ^{3}He has been discussed before in analogy with the Mott transition in the Gutzwiller approximation (Vollhardt, 1984). However, the 3D solid of ^{3}He should not be categorized as a Mott insulator, because commensurability with the underlying periodic potential is crucial for a Mott insulator while it is absent in 3D ^{3}He. In contrast, the second layer of adsorbed ^{3}He on graphite indeed undergoes a transition between a quantum liquid and a Mott insulator. In this case, the Mott insulator is formed on the van der Waals periodic potential of the triangular lattice of the ^{3}He solid in the first layer. The second-layer Mott insulator appears to be realized at a commensurate density on a triangular lattice. The anomalous quantum liquid state of ^{3}He observed upon doping can basically be classified as belonging to this class, $[I\text{-}1 \leftrightarrow M\text{-}3]$, though the transition is of weakly first order (Imada, 1995b). An advantage of the ^{3}He system (FC-MIT) is that one can investigate a prototype system without orbital degeneracies, impurity scattering, interlayer coupling, or long-range Coulomb interactions. Although the Anderson localization effect appears to be serious, $La_{1.17+x}VS_{3.17}$ also belongs to this class (Nishikawa, Yasui, and Sato, 1994; Takeda *et al.*, 1994). In this compound there exists a subtlety related to dimerization and spin gap formation in the insulating phase, and hence it can also be characterized as $[I\text{-}2 \leftrightarrow M\text{-}4]$. The 2D Hubbard model clarified by quantum Monte Carlo calculations appears to belong to a theoretical model of this class as we shall see in Sec. II.E. In general, a new universality class of transition is expected in this category, as we discuss in Sec. II.F.

$[I\text{-}2 \leftrightarrow M\text{-}1]$: An example is seen in $La_{1-x}Sr_xCoO_3$, where the low-spin state of $LaCoO_3$ at low temperatures becomes a ferromagnetic metal under doping.

$[I\text{-}2 \leftrightarrow M\text{-}2]$: Extensive effort has been made to realize this class of transition experimentally, as in doping of dimerized, spin-1, or ladder systems (Hiroi and Takano, 1995; McCarron *et al.*, 1988; Siegrist *et al.*, 1988). This is based on a proposal of the pairing mechanism for doped spin-gapped systems and theoretical results where the spin gap remains finite and pairing correlation becomes dominant when carriers are doped into various spin-gapped 1D systems such as dimerized systems (Imada, 1991, 1993c), spin-1 systems (Imada, 1993c), the frustrated t-J model (Ogata *et al.*, 1991), ladder systems (Dagotto, Riera, and Scalapina, 1992; Rice *et al.*, 1993, Tsunetsugu *et al.*, 1994; Dagotto and Rice, 1996). These apparently different systems are continuously connected in the parameter space of models (Katoh and Imada, 1995). Although a ladder system $LaCuO_{2.5}$ was metallized upon doping, the metallic state appears to be realized from the 3D network by changing the geometry of the ladder network. Therefore it is questionable whether it can be classified as a doped ladder system. One clear origin of the difficulty in realizing superconductivity is the localization effect, which must be serious with 1D anisotropy. Doping of a spin-gapped Mott insulator in 2D would therefore be desirable. The recent discovery of a superconducting phase in a spin ladder system $(Sr,Ca)_{14}Cu_{24}O_{41}$ by Uehara *et al.* (1996) may belong to this category. At the moment, it is not clear enough whether this superconductivity is realized by carrier doping of a quasi-1D spin-gapped insulator via the mechanism described above or by a mechanism like that for the high-T_c cuprates, ascribed to the more general anomalous character of metals near the Mott insulator, as discussed in Secs. II.E, II.F, and II.G. We discuss experimental details of this category in Sec. IV.D.1.

$[I\text{-}2 \leftrightarrow M\text{-}4]$: This is basically the same as the transition between a band insulator and a normal metal. Kondo insulators are also supposed to belong to this class. For d-electron systems, spin excitation gaps or low-spin configurations appear in the insulating phase in, for example, FeSi, TiO_2, Ti_2O_3, and $LaCoO_3$. Recently, it was found that several other systems also show spin-gapped excitations in the insulating phase. Examples are spin Peierls compounds such as $CuGeO_3$ (Hase *et al.*, 1993), NaV_2O_5 (Isobe and Ueda, 1996), spin-1 chain compounds such as Y_2BaNiO_5 (Buttrey *et al.*, 1990), ladder compounds as already discussed above, CaV_4O_9 (Taniguchi, *et al.*, 1995) and $La_{1.17+x}VS_{3.17}$ (Takeda *et al.*, 1994). Carrier doping of these compounds has not been successful so far, except in the ladder compounds, and it is not clear whether spin excitation becomes gapless or not in these cases upon metallization.

$[I\text{-}3 \leftrightarrow M\text{-}3]$: Experimentally this class has not been observed in the strict sense. In theoretical models, examples are 1D systems such as the 1D Hubbard model. Although it is not Fermi liquid, the singularity of the momentum distribution clearly specifies the formation of "large Fermi volume" in the metallic region.

When the electron density is commensurate to the number of lattice sites, charge ordering may occur. This is observed in the cases of Fe_3O_4, Ti_4O_7, and several perovskite oxides (see Sec. IV). This class of charge-ordering transition has often been called (for example, by Mott, 1990) the Wigner transition or the Verwey transition. However, this type of charge ordering usually takes place only at simple commensurate filling. In the case of d-electron systems, the Wigner crystal in the usual sense of an electron gas cannot be realized because the electron density is too great. The commensurability of the electron filling is crucial for realizing charge ordering. Although the intersite Coulomb repulsion helps the charge ordering, the gain in kinetic energy could be enough to stabilize the charge-ordered state. In this sense, a charge-ordered insulator may also be viewed as a generalized Mott insulator where the electron density is kept constant at a commensurate value and it is incompressible. The charge-ordering transition is discussed in Sec. II.H.3. Another mechanism for charge ordering is the Peierls transition when the nesting condition is well satisfied. In this case, the periodicity can be incommensurate to the lattice periodicity.

C. Field-theoretical framework for interacting fermion systems

In this section, a basic formulation for treating interacting fermions based on the path-integral formalism is summarized for use in later sections. To show how the formulation is constructed, we take the Hubbard model as an example. Since this section discusses only the basic formalism needed to understand the content of later sections, readers are referred to other references (for example, Negele and Orland, 1988) for a more complete and rigorous description.

1. Coherent states

Fermion Fock space can be represented by a basis of Slater determinants. However, Fock space can alternatively be represented by a basis of coherent states, as we show below. The coherent states are defined as eigenstates of the fermion annihilation operator. This is expressed as

$$c_\alpha|\psi\rangle=\psi_\alpha|\psi\rangle, \tag{2.17}$$

where c_α is the fermion annihilation operator with the quantum number α, whereas $|\psi\rangle$ is a coherent state with the eigenvalue ψ_α. When one operates more than one annihilation operator to $|\psi\rangle$, one gets the commutation relation for ψ_α from that of c_α:

$$\psi_\alpha\psi_\gamma+\psi_\gamma\psi_\alpha=0. \tag{2.18}$$

This means that ψ_α's are not c numbers. Actually, this commutation relation constitutes the Grassmann algebra.

In order to demonstrate that the basic Grassmann algebra given below is indeed useful and necessary to represent the Fock space, we first introduce the explicit form of the coherent state. Because ψ_α's are not c numbers, we are forced to enlarge the original Fock space by including Grassmann variables ψ_α as coefficients. Any vector $|\phi\rangle$ in the generalized Fock space is given by the linear combination of vectors in the original Fock space with Grassmann variables as coefficients:

$$|\phi\rangle=\sum_\alpha \psi_\alpha|\varphi_\alpha\rangle, \tag{2.19}$$

where ψ_α is a Grassmann variable with $\{|\varphi_\alpha\rangle\}$ being the complete set of vectors in the original Fock space. In the generalized Fock space, the fermion coherent state is given as

$$|\psi\rangle=\exp\left[-\sum_\alpha \psi_\alpha c_\alpha^\dagger\right]|0\rangle=\prod_\alpha (1-\psi_\alpha c_\alpha^\dagger)|0\rangle. \tag{2.20}$$

For the coherent state $|\psi\rangle$ defined in Eq. (2.20), it is necessary to require the commutation relations

$$\psi_\alpha c_\beta^\dagger+c_\beta^\dagger\psi_\alpha=0, \tag{2.21a}$$

$$\psi_\alpha c_\beta+c_\beta\psi_\alpha=0. \tag{2.21b}$$

Since $\psi_\alpha c_\alpha^\dagger$ and $\psi_\beta c_\beta^\dagger$ commute from Eqs. (2.21a) and (2.21b), we can show that

$$\begin{aligned}c_\alpha|\psi\rangle&=\prod_{\beta\neq\alpha} (1-\psi_\beta c_\beta^\dagger)c_\alpha(1-\psi_\alpha c_\alpha^\dagger)|0\rangle\\&=\prod_{\beta\neq\alpha} (1-\psi_\beta c_\beta^\dagger)\psi_\alpha|0\rangle\\&=\prod_{\beta\neq\alpha} (1-\psi_\beta c_\beta^\dagger)\psi_\alpha(1-\psi_\alpha c_\alpha^\dagger)|0\rangle=\psi_\alpha|\psi\rangle,\end{aligned} \tag{2.22}$$

where we have used Eq. (2.18).

2. Grassmann algebra

The basic algebra of the Grassmann variable $\{\psi_\alpha\}$ is given by Eq. (2.18). In addition, several other relations are summarized here. From the adjoint state of (2.20),

$$\langle\psi|=\langle 0|\exp\left[-\sum_\alpha c_\alpha\bar{\psi}_\alpha\right]=\langle 0|\prod_\alpha (1+\bar{\psi}_\alpha c_\alpha), \tag{2.23}$$

we can define the conjugation of ψ_α as $\bar{\psi}_\alpha$. From this definition, it is clear that the conjugation operation follows:

$$\bar{\bar{\psi}}_\alpha=\psi_\alpha, \tag{2.24a}$$

$$\overline{\lambda\psi_\alpha}=\lambda^*\bar{\psi}_\alpha, \tag{2.24b}$$

$$\overline{\psi_\alpha\psi_\beta\psi_\gamma\cdots}=\cdots\bar{\psi}_\gamma\bar{\psi}_\beta\bar{\psi}_\alpha \tag{2.24c}$$

where λ is a complex number with its complex conjugate λ^*.

The operation of $c_\alpha^\dagger$ can be associated with the derivative of Grassmann variables as

$$\begin{aligned}c_\alpha^\dagger|\psi\rangle&=c_\alpha^\dagger(1-\psi_\alpha c_\alpha^\dagger)\prod_{\beta\neq\alpha} (1-\psi_\beta c_\beta^\dagger)|0\rangle\\&=c_\alpha^\dagger\prod_{\beta\neq\alpha} (1-\psi_\beta c_\beta^\dagger)|0\rangle=-\frac{\partial}{\partial\psi_\alpha}(1-\psi_\alpha c_\alpha^\dagger)\\&\quad\times\prod_{\beta\neq\alpha} (1-\psi_\beta c_\beta^\dagger)|0\rangle=-\frac{\partial}{\partial\psi_\alpha}|\psi\rangle,\end{aligned} \tag{2.25}$$

where the derivative of ψ_α is defined in a natural way as

$$\frac{\partial}{\partial\psi_\alpha}[a_0+a_1\psi_\alpha+a_2\bar{\psi}_\alpha+a_3\bar{\psi}_\alpha\psi_\alpha]=a_1-a_3\bar{\psi}_\alpha \tag{2.26}$$

for c number constants a_0, a_1, a_2, and a_3. Note that $(\partial/\partial\psi_\alpha)(\bar{\psi}_\alpha\psi_\alpha)=-(\partial/\partial\psi_\alpha)(\psi_\alpha\bar{\psi}_\alpha)=-\bar{\psi}_\alpha$. Equation (2.25) is indeed easily shown from the definitions (2.20) and (2.26). One can verify the conjugation of (2.25):

$$\langle\psi|c_\alpha=\frac{\partial}{\partial\bar{\psi}_\alpha}\langle\psi|. \tag{2.27}$$

The overlap of two coherent states is shown from Eqs. (2.20) and (2.27) as

$$\begin{aligned}\langle\psi|\psi'\rangle&=\langle 0|\prod_\alpha (1+\bar{\psi}_\alpha c_\alpha)(1-\psi'_\alpha c_\alpha^\dagger)|0\rangle\\&=\prod_\alpha (1+\bar{\psi}_\alpha\psi'_\alpha)=\exp\left[\sum_\alpha \bar{\psi}_\alpha\psi'_\alpha\right].\end{aligned} \tag{2.28}$$

The matrix element of a *normal-ordered* operator $H(c_\alpha^\dagger, c_\alpha)$ between two coherent states immediately follows from Eq. (2.28) as

$$\langle\psi|H(c_\alpha^\dagger, c_\alpha)|\psi'\rangle = \exp\left[\sum_\alpha \bar{\psi}_\alpha \psi'_\alpha\right] H(\bar{\psi}_\alpha, \psi_\alpha). \tag{2.29}$$

Through Eq. (2.29), operators are represented only by the Grassmann variables.

To calculate matrix elements of operators as well as trace summations, it is useful to introduce a definite integral in terms of ψ_α. Any regular function of ψ_α may be expanded as

$$f(\psi_\alpha) = a_0 + a_1 \psi_\alpha \tag{2.30}$$

because of $\psi_\alpha^2 = 0$. Therefore it is sufficient to define $\int d\psi_\alpha 1$ and $\int d\psi_\alpha \psi_\alpha$. When we assume the same properties as those of ordinary integrals from $-\infty$ to $+\infty$ over functions which vanish at infinity, it is natural to define the definite integral so as to satisfy vanishing integral of a complete differential form:

$$\int d\psi_\alpha \frac{\partial}{\partial \psi_\alpha} f(\psi_\alpha) = 0. \tag{2.31}$$

Then, because of $1 = (\partial/\partial\psi_\alpha)\,\psi_\alpha$, we have

$$\int d\psi_\alpha 1 = \int d\bar{\psi}_\alpha 1 = 0. \tag{2.32a}$$

The definite integral of ψ_α can be taken as a constant. Only for convenience, to avoid annoying coefficients in later matrix elements, we take this constant to be unity:

$$\int d\psi_\alpha \psi_\alpha = \int d\bar{\psi}_\alpha \bar{\psi}_\alpha = 1. \tag{2.32b}$$

From the definition of the integrals, we obtain the useful closure relation

$$\int \prod_\alpha d\bar{\psi}_\alpha \, d\psi_\alpha \exp\left[-\sum_\alpha \bar{\psi}_\alpha \psi_\alpha\right] |\psi\rangle\langle\psi| = 1. \tag{2.33}$$

If we restrict the Hilbert space to single-particle states with particle number 0 or 1, Eq. (2.33) is proven as

$$\begin{aligned}
(2.33) &= \int d\bar{\psi}_\alpha \, d\psi_\alpha \exp[-\bar{\psi}_\alpha \psi_\alpha] \\
&\quad \times (1 - \psi_\alpha c_\alpha^\dagger)|0\rangle\langle 0|(1 + \bar{\psi}_\alpha c_\alpha) \\
&= \int d\bar{\psi}_\alpha d\psi_\alpha [(1 + \psi_\alpha \bar{\psi}_\alpha)|0\rangle\langle 0| - \psi_\alpha c_\alpha^\dagger |0\rangle\langle 0| \\
&\quad + |0\rangle\langle 0| \bar{\psi}_\alpha c_\alpha + \psi_\alpha \bar{\psi}_\alpha c_\alpha^\dagger |0\rangle\langle 0| c_\alpha] \\
&= [|0\rangle\langle 0| + c_\alpha^\dagger |0\rangle\langle |0| c_\alpha] = 1.
\end{aligned}$$

The generalization of this proof to many-particle states $|\psi\rangle = \Pi_\alpha (1 - \psi_\alpha c_\alpha^\dagger)|0\rangle$ is straightforward.

From Eqs. (2.20), (2.23), and (2.33), the trace of an operator A is

$$\begin{aligned}
\mathrm{Tr}\, A &= \sum_i \langle \varphi_i | A | \varphi_i \rangle \\
&= \int \prod_\alpha d\bar{\psi}_\alpha d\psi_\alpha \exp\left[-\sum_\alpha \bar{\psi}_\alpha \psi_\alpha\right] \\
&\quad \times \sum_i \langle \varphi_i | \psi \rangle \langle \psi | A | \varphi_i \rangle \\
&= \int \prod_\alpha d\bar{\psi}_\alpha \, d\psi_\alpha \exp\left[-\sum_\alpha \bar{\psi}_\alpha \psi_\alpha\right] \\
&\quad \times \sum_i \langle -\psi | A | \varphi_i \rangle \langle \varphi_i | \psi \rangle \\
&= \int \prod_\alpha d\bar{\psi}_\alpha \, d\psi_\alpha \exp\left[-\sum_\alpha \bar{\psi}_\alpha \psi_\alpha\right] \langle -\psi | A | \psi \rangle .
\end{aligned} \tag{2.34}$$

A Gaussian integral of a pair of conjugate Grassmann variables is

$$\int d\bar{\psi}_\alpha \, d\psi_\alpha \, e^{-\bar{\psi}_\alpha a \psi_\alpha} = \int d\bar{\psi}_\alpha \, d\psi_\alpha (1 - \bar{\psi}_\alpha a \psi_\alpha) = a. \tag{2.35}$$

Similarly, a Gaussian integral in matrix form is proven to be

$$\begin{aligned}
&\int \prod_{\alpha=1}^{n} d\bar{\psi}_\alpha \, d\psi_\alpha \exp[-\bar{\psi}_\alpha A_{\alpha\beta} \psi_\beta + \bar{\zeta}_\alpha \psi_\alpha + \zeta_\alpha \bar{\psi}_\alpha] \\
&\quad = (\det A) \exp[\bar{\zeta}_\alpha A^{-1}_{\alpha\beta} \zeta_\beta],
\end{aligned} \tag{2.36}$$

where $\bar{\zeta}_\alpha$ and ζ_α are another pair of Grassmann variables. Using Eqs. (2.29), (2.34), and (2.36), we can calculate the partition function and other functional integrals in the path-integral formalism.

3. Functional integrals, path integrals, and statistical mechanics of many-fermion systems

In the case of the Hubbard model (1.1a), the matrix element of the Hamiltonian H_H in the coherent state representation reads from Eq. (2.29) as

$$\mathcal{H}_H[\bar{\psi}, \psi] = \mathcal{H}_t + \mathcal{H}_U - \left(\mu + \frac{U}{2}\right) \mathcal{N}, \tag{2.37a}$$

$$\mathcal{H}_t = -t \sum_{\langle ij \rangle} (\bar{\psi}_{i\sigma} \psi_{j\sigma} + \bar{\psi}_{j\sigma} \psi_{i\sigma}), \tag{2.37b}$$

$$\mathcal{H}_U = U \sum_i \bar{\psi}_{i\uparrow} \bar{\psi}_{i\downarrow} \psi_{i\downarrow} \psi_{i\uparrow}, \tag{2.37c}$$

$$\mathcal{N}=\sum_{i\sigma}\bar{\psi}_{i\sigma}\psi_{i\sigma}, \tag{2.37d}$$

which is obtained by replacing $c^{\dagger}_{i\sigma}$ and $c_{i\sigma}$ with Grassmann variables $\bar{\psi}_{i\sigma}$ and $\psi_{i\sigma}$, respectively, after proper normal ordering. The partition function for a many-particle system is

$$\begin{aligned}Z&=\mathrm{Tr}\, e^{-\beta\mathcal{H}}\\&=\int d\bar{\psi}_{\alpha}\, d\psi_{\alpha}\exp\left[-\sum_{\alpha}\bar{\psi}_{\alpha}\psi_{\alpha}\right]\langle-\psi|e^{-\beta\mathcal{H}}|\psi\rangle.\end{aligned} \tag{2.38}$$

When one divides $e^{-\beta\mathcal{H}}$ into L imaginary-time slices (Trotter slices) by keeping the inverse temperature $(\Delta\tau)L=\beta$ constant and inserts the closure relation Eq. (2.33) in each interval of slices, using Eqs. (2.28) and (2.33), one obtains the standard path-integral formalism in the limit $L\to\infty$ in the form

$$Z=\lim_{L\to\infty}\int\left[\prod_{l=1}^{L}d\bar{\psi}^{(l)}_{\alpha}\, d\psi^{(l)}_{\alpha}\right]\exp[-S[\bar{\psi},\psi]], \tag{2.39a}$$

$$S[\bar{\psi},\psi]=\sum_{l=1}^{L}\sum_{m=1}^{L}\mathcal{S}_{lm}[\bar{\psi},\psi], \tag{2.39b}$$

$$\begin{aligned}\mathcal{S}_{lm}[\bar{\psi},\psi]=\Delta\tau\sum_{\alpha}\Bigg[&\bar{\psi}^{(l)}_{\alpha}\psi^{(m)}_{\alpha}\left[\frac{\delta_{lm}-\delta_{l-1,m}}{\Delta\tau}\right]\\&+\mathcal{H}[\bar{\psi}^{(l)}_{\alpha},\psi^{(m)}_{\alpha}]\,\delta_{l-1,m}\Bigg]\end{aligned} \tag{2.39c}$$

with $\psi^{(0)}_{\alpha}=-\psi^{(L)}_{\alpha}$. By defining the functional integration

$$\mathcal{D}[\bar{\psi},\psi]=\lim_{L\to\infty}\prod_{l=1}^{L}\prod_{\alpha}d\bar{\psi}^{(l)}_{\alpha}d\psi^{(l)}_{\alpha}, \tag{2.40}$$

one obtains the partition function

$$Z=\int\mathcal{D}[\bar{\psi},\psi]e^{-S[\bar{\psi},\psi]}, \tag{2.41a}$$

with the action

$$\begin{aligned}S[\bar{\psi},\psi]=&\int_{0}^{\beta}d\tau\sum_{\alpha}\bar{\psi}_{\alpha}(\tau)\frac{\partial}{\partial\tau}\psi_{\alpha}(\tau)\\&+\int_{0}^{\beta}d\tau\,\mathcal{H}[\bar{\psi}_{\alpha}(\tau),\psi_{\alpha}(\tau)]\end{aligned} \tag{2.41b}$$

under the constraint $\psi_{\alpha}(0)=-\psi_{\alpha}(\beta)$.

The Fourier transforms of the Grassmann variables are

$$\psi(k)=\int d\mathbf{r}\int_{0}^{\beta}d\tau\, e^{-i(\mathbf{k}\cdot\mathbf{r}-\omega_n\tau)}\psi(x), \tag{2.42a}$$

$$\psi(x)=\frac{1}{\beta V}\sum_{k,\omega_n}e^{i(\mathbf{k}\cdot\mathbf{r}-\omega_n\tau)}\psi(k), \tag{2.42b}$$

where x and k are Euclidean four-dimensional vectors $x\equiv(\mathbf{r},\tau)$ and $k\equiv(\mathbf{k},\omega_n)$, with ω_n being the Matsubara frequency $\omega_n\equiv2\pi T(n+\frac{1}{2})$, $n=0,\pm1,\pm2,\ldots$. Hereafter the volume V and the number of sites N_s will have the same meaning for lattice systems. The Fourier-transformed form of the action is

$$S[\bar{\psi},\psi]=\sum_{n}\left[-i\omega_n\int d\mathbf{k}\,\bar{\psi}(k)\psi(k)+\mathcal{H}[\bar{\psi}(k),\psi(k)]\right]. \tag{2.43}$$

4. Green's functions, self-energy, and spectral functions

The τ-dependent thermal Green's function for systems with translational symmetry is defined by

$$\mathcal{G}(\mathbf{k},\tau)=-\int d\mathbf{r}\, e^{-i\mathbf{k}\cdot\mathbf{r}}\langle Tc(\mathbf{r},\tau)c^{\dagger}(0,0)\rangle, \tag{2.44}$$

with the time-ordered product T and the thermodynamic average $\langle\cdots\rangle$. The spectral representation of $\mathcal{G}(\mathbf{k},\tau)$ is

$$\begin{aligned}\mathcal{G}(\mathbf{k},\tau)\equiv\sum_{mn}&e^{\beta(F-E_m(N))+(E_m(N)-E_n(N-1)+\mu)\tau}\\&\times\langle\Phi_m(N)|c^{\dagger}_{k}|\Phi_n(N-1)\rangle\\&\times\langle\Phi_n(N-1)|c_{k}|\Phi_m(N)\rangle\end{aligned} \tag{2.45}$$

for $\tau>0$, and for $\tau<0$ the same but with $c^{\dagger}_{\mathbf{k}}$ and $c_{\mathbf{k}}$ exchanged. Here, F is the free energy $F\equiv-(1/\beta)\ln\mathrm{Tr}\, e^{-\beta\mathcal{H}}$ and $\{E_m(N)\}$ are eigenvalues of a complete set of eigenstates $\{\Phi_m(N)\}$ in an N-electron system with the chemical potential μ. Although we do not explicitly take the summation over N in the grand canonical ensemble with a fixed μ, it is hereafter implicitly assumed. Because the spectral representation of $\mathcal{G}$ proves to satisfy $\mathcal{G}(\mathbf{k},\tau+\beta)=-\mathcal{G}(\mathbf{k},\tau)$, it can be expanded in the Fourier series as

$$\mathcal{G}(\mathbf{k},\tau)=\frac{1}{\beta}\sum_{n}\mathcal{G}(\mathbf{k},\omega_n)e^{-i\omega_n\tau}, \tag{2.46}$$

$$\mathcal{G}(\mathbf{k},\omega_n)=\int_{0}^{\beta}d\tau\,\mathcal{G}(\mathbf{k},\tau)e^{i\omega_n\tau}. \tag{2.47}$$

The thermal Green's function of the free-fermion system is obtained with the help of the Grassmann representation as

$$\begin{aligned}\mathcal{G}_0(\xi,\tau_1;\eta,\tau_2) &\equiv -\frac{1}{Z_0}\,\mathrm{Tr}\left[T\ \exp\left[-\int_0^\beta d\tau\ \mathcal{H}_0\right] c_\xi(\tau_1)c_\eta^\dagger(\tau_2)\right]\\ &= -\delta_{\xi\eta}\frac{\int\mathcal{D}[\overline{\psi},\psi]\exp[-\int d\tau_3\ d\tau_4\ \mathcal{S}_{\tau_3,\tau_4}[\overline{\psi},\psi]]\psi_\xi(\tau_1)\overline{\psi}_\eta(\tau_2)}{\int\mathcal{D}[\overline{\psi},\psi]\exp\left[-\int d\tau_3\ d\tau_4\ \mathcal{S}_{\tau_3\tau_4}[\overline{\psi},\psi]\right]}\\ &= -\delta_{\xi\eta}\frac{\partial^2}{\partial J^*(\tau_1)\partial J(\tau_2)}\left.\frac{\int\mathcal{D}[\overline{\psi},\psi]\exp[-\int d\tau_3\ d\tau_4\ \mathcal{S}_{\tau_3\tau_4}[\overline{\psi},\psi]+\int d\tau J^*(\tau)\psi(\tau)+\overline{\psi}(\tau)J(\tau)]}{\{\int\mathcal{D}[\overline{\psi},\psi]\exp[-\int d\tau_3\ d\tau_4\ \mathcal{S}_{\tau_3\tau_4}[\overline{\psi},\psi]]\}}\right|_{J=J^*=0}\\ &= -\delta_{\xi\eta}\frac{\partial^2}{\partial J^*(\tau_1)\partial J(\tau_2)}\exp\left.\left[\int d\tau_3\ d\tau_4\ J^*(\tau_3)[\mathcal{S}[\overline{\psi},\psi]]^{-1}_{\tau_3\tau_4}J(\tau_4)\right]\right|_{J=J^*=0} = -\delta_{\xi\eta}[\mathcal{S}^{-1}]_{\tau_1\tau_2}, \qquad (2.48)\end{aligned}$$

where $\mathcal{S}$ is the matrix whose (l,m) component is $\mathcal{S}_{l,m}[\overline{\psi},\psi]$. After the Fourier transformation, the thermal Green's function for the noninteracting Hamiltonian $\mathcal{H}_0$ is easily obtained from Eqs. (2.43) and (2.48) as

$$\mathcal{G}_0(\mathbf{k},\omega_n)=\frac{1}{i\omega_n-\varepsilon_0(\mathbf{k})}, \qquad (2.49)$$

where $\varepsilon_0(\mathbf{k})$ is the dispersion of H_0 as in Eq. (2.3b).

The real-time-displaced retarded Green's function is defined by

$$G^R(\mathbf{r},t)=-i\theta(t)\langle\{c(\mathbf{r},t),c^\dagger(0,0)\}\rangle, \qquad (2.50)$$

with the anticommutator $\{A,B\}\equiv AB+BA$, the Heaviside step function θ, and the Heisenberg representation $A(t)=e^{i\mathcal{H}t}Ae^{-i\mathcal{H}t}$. The causal Green's function is similarly defined by

$$G^C(\mathbf{r},t)=-i\langle Tc(\mathbf{r},t)c^\dagger(0,0)\rangle. \qquad (2.51)$$

The thermal Green's function is analytically continued to a complex variable z,

$$\mathcal{G}(\mathbf{k},-iz)=\int_{-\infty}^{\infty}\frac{A(\mathbf{k},\omega')}{z-\omega'}d\omega', \qquad (2.52)$$

with the spectral function

$$\begin{aligned}A(\mathbf{k},\omega)\equiv\sum_{n,m} & e^{\beta(F-E_m(N))}(e^{\beta(\omega-\mu)}+1)\\ &\times|\langle\Phi_n(N-1)|c_\mathbf{k}|\Phi_m(N)\rangle|^2\\ &\times\delta(\omega-E_m(N)+E_n(N-1)). \qquad (2.53)\end{aligned}$$

At zero temperature the spectral function is reduced to

$$\begin{aligned}A(\mathbf{k},\omega)=\sum_n & |\langle\Phi_n(N-1)|c_\mathbf{k}|\Phi_g(N)\rangle|^2\\ &\times\delta(\omega+E_n(N-1)-E_g(N))\\ &+\sum_n|\langle\Phi_n(N+1)|c_\mathbf{k}^\dagger|\Phi_g(N)\rangle|^2\\ &\times\delta(\omega-E_n(N+1)+E_g(N)), \qquad (2.54)\end{aligned}$$

where g specifies the ground state. From a comparison of the spectral representation of $G^R(\mathbf{k},\omega)$ and the analytic continuation, we find that

$$\begin{aligned}G^R(\mathbf{k},\omega) &= \lim_{\delta\to+0}\int_{-\infty}^{\infty}\frac{A(\mathbf{k},\omega')}{\omega-\omega'+i\delta}d\omega'\\ &= \lim_{\delta\to+0}\mathcal{G}(i(\omega+i\delta)) \qquad (2.55)\end{aligned}$$

is satisfied, where G^R is analytic in the upper half plane of complex ω.

$A(\mathbf{k},\omega)$ is the imaginary part of the single-particle Green's function and therefore contains full information about the temporal and spatial evolution of a single electron or a single hole in the interacting many-electron system. Using the Fourier transform $G^R(\mathbf{k},\omega)$ of the retarded Green's function (2.50), we find the spectral function

$$A(\mathbf{k},\omega)=-\frac{1}{\pi}\,\mathrm{Im}\ G^R(\mathbf{k},\omega). \qquad (2.56)$$

This directly follows from Eq. (2.55).

The $\mathbf{k}$-integrated spectral function or the density of states is defined by

$$\rho(\omega)\equiv\sum_\mathbf{k}A(\mathbf{k},\omega). \qquad (2.57)$$

If we integrate $A(\mathbf{k},\omega)$ with respect to ω up to the chemical potential μ, we obtain the electron momentum distribution function

$$n(\mathbf{k})=\int_{-\infty}^{\mu} d\omega\, A(\mathbf{k},\omega). \tag{2.58}$$

If we integrate $A(\mathbf{k},\omega)$ above and below the chemical potential, then

$$\int_{-\infty}^{\infty} d\omega\, A(\mathbf{k},\omega)=1, \tag{2.59}$$

per energy band.

In a noninteracting system, we derive

$$G^R(\mathbf{k},\omega)=\frac{1}{\omega-\varepsilon_0(\mathbf{k})-i\delta},$$

$$G^C(\mathbf{k},\omega)=\frac{1}{\omega-\varepsilon_0(\mathbf{k})+i\delta\,\mathrm{sgn}(\varepsilon_0(\mathbf{k})-\varepsilon_F)}.$$

The Green's function of an interacting electron system G^R or $\mathcal{G}$ is related to that of the noninteracting system $G_0^R(\mathbf{k},\omega)=1/[\omega-\varepsilon_0(\mathbf{k})-i\delta]$, or $\mathcal{G}_0(\mathbf{k},\omega_n)=1/[i\omega_n-\varepsilon_0(\mathbf{k})]$ where $\varepsilon_0(\mathbf{k})$ is the energy of a noninteracting Bloch electron, through the Dyson equation

$$\mathcal{G}(\mathbf{k},\omega_n)=\mathcal{G}_0(\mathbf{k},\omega_n)+\mathcal{G}_0(\mathbf{k},\omega_n)\Sigma(\mathbf{k},\omega_n)\mathcal{G}(\mathbf{k},\omega_n). \tag{2.60}$$

Here $\Sigma(\mathbf{k},\omega_n)$ is the self-energy into which all of the interaction effects are squeezed. The solution of the Dyson equation formally reads

$$\mathcal{G}(\mathbf{k},\omega_n)=\frac{1}{i\omega_n-\varepsilon_0(\mathbf{k})-\Sigma(\mathbf{k},\omega_n)}. \tag{2.61}$$

After analytic continuation of the Matsubara frequency $i\omega_n$ to the real ω, the Green's function is

$$G^R(\mathbf{k},\omega)=\frac{1}{\omega-\varepsilon_0(\mathbf{k})-\Sigma(\mathbf{k},\omega)}. \tag{2.62}$$

The pole $\omega=\varepsilon_0(\mathbf{k})$ for the noninteracting system is modified to $\omega=\varepsilon_0(\mathbf{k})+\Sigma(\mathbf{k},\omega)$.

For simplicity, we consider the case in which there is only one energy band in the Brillouin zone. The self-energy $\Sigma(\mathbf{k},\omega)$ gives the change of $\varepsilon_0(\mathbf{k})$ caused by electron-electron interaction, electron-phonon interaction, and/or any kind of interaction that cannot be incorporated in the noninteracting energy spectrum $\varepsilon_0(\mathbf{k})$. In this article, we implicitly assume that the self-energy correction is due to electron-electron interaction. In a noninteracting system, the spectral function has a δ-function peak at $\omega=\varepsilon_0(\mathbf{k})$: $A(\mathbf{k},\omega)=\delta(\omega-\varepsilon_0(\mathbf{k}))$. With interaction,

$$\begin{aligned}A(\mathbf{k},\omega)&=-\frac{1}{\pi}\,\mathrm{Im}\,G^R(\mathbf{k},\omega)\\&=\frac{1}{\pi}\frac{-\mathrm{Im}\,\Sigma(\mathbf{k},\omega)}{[\omega-\varepsilon_0(\mathbf{k})-\mathrm{Re}\,\Sigma(\mathbf{k},\omega)]^2+[-\mathrm{Im}\,\Sigma(\mathbf{k},\omega)]^2}.\end{aligned} \tag{2.63}$$

Therefore $\mathrm{Re}\,\Sigma(\mathbf{k},\omega)$ and $-\mathrm{Im}\,\Sigma(\mathbf{k},\omega)$ give, respectively, the energy shift and the broadening of the one-electron eigenvalue $\omega=\varepsilon_0(\mathbf{k})$ due to the interaction.

Because the Green's function $G^R(\mathbf{k},t)$ is a linear response function to an external perturbation at $t=0$, the imaginary part and the real part of its Fourier transform $G^R(\mathbf{k},\omega)$ should satisfy causality, i.e., the Kramers-Kronig relation:

$$\mathrm{Re}\,G^R(\mathbf{k},\omega)=\frac{1}{\pi}\mathcal{P}\int_{-\infty}^{\infty}\frac{\mathrm{Im}\,G^R(\mathbf{k},\omega')}{\omega-\omega'}d\omega', \tag{2.64}$$

$$\mathrm{Im}\,G^R(\mathbf{k},\omega)=-\frac{1}{\pi}\mathcal{P}\int_{-\infty}^{\infty}\frac{\mathrm{Re}\,G^R(\mathbf{k},\omega')}{\omega-\omega'}d\omega'. \tag{2.65}$$

That is, $G^R(\mathbf{k},\omega)$ has to be an analytic function of ω in the complete upper ω half-plane.

Then, $\Sigma(\mathbf{k},\omega)$ should also be analytic in the same ω region and satisfy the Kramers-Kronig relation:

$$\mathrm{Re}\,\Sigma(\mathbf{k},\omega)=\frac{1}{\pi}\mathcal{P}\int_{-\infty}^{\infty}\frac{\mathrm{Im}\,\Sigma(\mathbf{k},\omega')-\mathrm{Im}\,\Sigma(\mathbf{k},\infty)}{\omega-\omega'}d\omega' \tag{2.66}$$

$$\mathrm{Im}\,\Sigma(\mathbf{k},\omega)-\mathrm{Im}\,\Sigma(\mathbf{k},\infty)=-\frac{1}{\pi}\mathcal{P}\int_{-\infty}^{\infty}\frac{\mathrm{Re}\,\Sigma(\mathbf{k},\omega')}{\omega-\omega'}d\omega'. \tag{2.67}$$

Equations (2.53) and (2.54) for $\omega<\mu$ and $\omega>\mu$ can be measured by photoemission and inverse photoemission spectroscopy, respectively, in the angle-resolved (**k**-resolved) mode using single-crystal samples. Here ω is related to the kinetic energy $\varepsilon_{\mathrm{kin}}$ of the emitted (absorbed) electron through $\omega=\varepsilon_{\mathrm{kin}}-h\nu$, where $h\nu$ is the energy of the absorbed (emitted) photon. $\rho(\omega)$, given by Eq. (2.57), is measured by the angle-integrated mode of photoemission and inverse photoemission experiments. Here it should be noted that the photoemission and inverse photoemission spectra are not identical to the spectral function $A(\mathbf{k},\omega)$ due to several experimental conditions, e.g., the spectral function is modulated by dipole matrix elements for the optical transitions to yield measured spectra; finite mean free paths of photoelectrons violate the conservation of momentum perpendicular to the sample surface, $\mathbf{K}_\perp$, making it difficult to determine $(\mathbf{K})_\perp$, etc. [see the text book on photoelectron spectroscopy by Hüfner (1995)]. The latter problem does not exist for quasi-1D or 2D materials, in which the dispersions of energy bands in one or two directions is negligibly small and hence the nonconservation of $(\mathbf{K})_\perp$ does not cause any inconvenience.

D. Fermi-liquid theory and various mean-field approaches: Single-particle descriptions of correlated metals and insulators

To understand the fundamental significance of strong-correlation effects, as well as the difficulties in treating them, it is helpful first to recollect basic and established single-particle theories. This section discusses several single-particle theories of metals. In particular, the achievements to date of weak-correlation approaches and mean-field methods, as well as their limitations and difficulties, are surveyed in this section in order to understand the motivation for the strong-correlation approaches presented in later sections.

1. Fermi-liquid description

In Fermi-liquid theory, adiabatic continuation of the correct ground state in the interacting system from that in its noninteracting counterpart is assumed (Landau, 1957a, 1957b, 1958; Anderson, 1984). In this subsection, we mainly discuss basic statements of the Fermi-liquid theory. The reader is also referred to references for further detail (Pines and Nozières, 1989). In Fermi-liquid theory, the Green's function G defined by Eq. (2.61) or (2.62) has basically the same structure of poles as in a noninteracting system. The interaction term of the Hamiltonian may be considered in the perturbation expansion. The Green's function can be expressed in a self-consistent fashion using the self-energy introduced in Sec. II.C.4, which includes terms in the perturbation expansion summed to infinite order. If the Fermi-liquid description is valid, the self-energy Σ remains finite and G is characterized by a pole at $\omega=\varepsilon_0(\mathbf{k})+\Sigma(\mathbf{k},\omega)$. Because Fermi-liquid theory is meaningful only near the Fermi level, we may restrict our consideration to small ω and $\mathbf{k}$ measured from the Fermi surface. Then the real and imaginary parts of the self-energy can be expanded as

$$\begin{aligned}\mathrm{Re}\,\Sigma(\mathbf{k},\omega)=&\mathrm{Re}\,\Sigma(\mathbf{k}=\mathbf{k}_F,\omega=\mu)-b_{\mathbf{k}_F}(\omega-\mu)\\&-O((\omega-\mu)^2)+a(\mathbf{k}_F)(\mathbf{k}-\mathbf{k}_F)\\&+O((\mathbf{k}-\mathbf{k}_F)^2),\end{aligned}\tag{2.68a}$$

$$\begin{aligned}\mathrm{Im}\,\Sigma(\mathbf{k},\omega)=&-\Gamma(\omega-\mu)^2+O((\omega-\mu)^3)\\&+\zeta(\mathbf{k}_F)(\mathbf{k}-\mathbf{k}_F)^2+O((\mathbf{k}-\mathbf{k}_F)^3).\end{aligned}\tag{2.68b}$$

Here we have neglected possible logarithmic corrections. The fact that the interaction term generates only quadratic or higher-order terms for Im Σ in terms of ω is the central assumption of Fermi-liquid theory. In the Fermi liquid, the quasiparticle decays through excitations of electron-hole pairs across the chemical potential. The lifetime of the quasiparticle is proportional to the number of available electron-hole pairs and is therefore proportional to $(\omega-\mu)^2$ in the $\omega\to\mu$ limit: $\mathrm{Im}\,\Sigma(\mathbf{k},\omega)\propto-(\omega-\mu)^2$. Then the real part of the self-energy should be proportional to $-(\omega-\mu)+\mathrm{const}$ in the vicinity of $\omega=\mu$. The renormalized Green's function has the form

$$G^R(\mathbf{k},\omega)\simeq\frac{Z_{\mathbf{k}_F}}{\omega-\varepsilon^*(\mathbf{k}-\mathbf{k}_F)+i(Z_{\mathbf{k}_F}\Gamma(\omega-\mu)^2-Z_{\mathbf{k}_F}\zeta(\mathbf{k}_F)(\mathbf{k}-\mathbf{k}_F)^2)},\tag{2.69}$$

for small $\omega-\mu$ and $\mathbf{k}-\mathbf{k}_F$ where

$$Z_{\mathbf{k}_F}=1/(1+b_{\mathbf{k}_F})\tag{2.70}$$

is the renormalization factor, whereas

$$\varepsilon^*(\mathbf{k}-\mathbf{k}_F)\simeq Z_{\mathbf{k}_F}[\varepsilon_0(\mathbf{k})+a(\mathbf{k}_F)(\mathbf{k}-\mathbf{k}_F)]\tag{2.71}$$

is the renormalized dispersion. $\mathrm{Re}\,\Sigma(\mathbf{k}=\mathbf{k}_F,\omega=\mu)$ can be absorbed into a constant shift of $\varepsilon_0(\mathbf{k})$, which should keep the constraint of fixed density. The necessary condition for the validity of the Fermi-liquid description is $\varepsilon^*-\mu\gg\mathrm{Im}\,\Sigma(\mathbf{k},\omega)$ for small $\omega-\mu$ and $\mathbf{k}-\mathbf{k}_F$, which is indeed satisfied in this case if $Z_{\mathbf{k}_F}>0$. The renormalization factor $Z_{\mathbf{k}_F}$ scales basically all the other quantities. From this Green's function, other physical quantities are derived. If the spectral function $A(\mathbf{k},\omega)$ and the renormalization factor $Z_{\mathbf{k}}(\omega)$ [or $\mathrm{Re}\,\Sigma(\mathbf{k},\omega)$] are known, $Z_{\mathbf{k}}(\omega)^{-1}A(\mathbf{k},\omega)$ gives the energy distribution function of quasiparticles with momentum $\mathbf{k}$, in which each quasiparticle carries weight 1 instead of Z of the spectral function. Hence the density of states of quasiparticles $N^*(\omega)$ is given by

$$N^*(\omega)=\sum_{\mathbf{k}}Z_{\mathbf{k}}(\omega)^{-1}A(\mathbf{k},\omega).\tag{2.72}$$

The renormalization of the quasiparticle density of states, as compared to that of the noninteracting system at the Fermi level, is

$$\frac{N^*(\mu)}{\rho_0(\mu)}=\int_{\mathbf{k}=\mathbf{k}_F}\frac{\partial\mathbf{k}}{\partial\varepsilon^*}d\mathbf{k}\Big/\int_{\mathbf{k}=\mathbf{k}_F}\frac{\partial\mathbf{k}}{\partial\varepsilon_0}d\mathbf{k}\tag{2.73a}$$

$$=\frac{m^*}{m_b}=\frac{m_\omega}{m_b}\cdot\frac{m_k}{m_b}\tag{2.73b}$$

where

$$m_b=\int_{\mathbf{k}=\mathbf{k}_F}\frac{\partial\mathbf{k}}{\partial\varepsilon_0}d\mathbf{k},\tag{2.73c}$$

$$m_\omega=m_b/Z_{\mathbf{k}_F},\tag{2.73d}$$

and

$$m_k=(v_{F0}+a(\mathbf{k}_F))^{-1}v_{F0}m_b,\tag{2.73e}$$

with the bare Fermi velocity $v_{F0}=(\partial\varepsilon_0/\partial\mathbf{k})|_{\mathbf{k}=\mathbf{k}_F}$ and the bare band mass m_b. We employ the notation m_b instead of m_0 to specify the band mass of the noninteracting Bloch electrons, although the noninteracting band dispersion is denoted by ε_0. Here, m_ω and m_k are often called the ω mass and the k mass, respectively, with the total effective mass $m^* = m_k m_\omega / m_b$. The ratio of the specific-heat coefficient γ to that of noninteracting system, γ_b, is also scaled by the effective mass enhancement m^*/m_b:

$$\frac{\gamma}{\gamma_b} = \frac{m^*}{m_b}. \tag{2.74}$$

The charge compressibility $\kappa = (1/n^2)\, \partial n / \partial \mu$ is scaled as

$$\kappa = \frac{1}{n^2} \frac{m^*}{m_b} \frac{1}{1 + F_0^s}, \tag{2.75}$$

where a Landau parameter F_0^s is introduced phenomenologically as the spin-independent and spatially isotropic part of the quasiparticle interaction. Similarly, the uniform magnetic susceptibility has the scaling form

$$\chi_s = \frac{m^*}{m_b} \frac{1}{1 + F_0^a}, \tag{2.76}$$

where the spin antisymmetric and spatially isotropic part of the quasiparticle interaction is described by F_0^a.

The renormalization factor $Z_{\mathbf{k}_F}$ can be interpreted as follows: From Eqs. (2.54), (2.55), and (2.69), $Z_{\mathbf{k}_F}$ is rewritten as

$$Z_{\mathbf{k}_F} = |\langle \Phi_g(N+1) | c^\dagger_{\mathbf{k}_F,\sigma} | \Phi_g(N) \rangle|^2, \tag{2.77}$$

where $Z_{\mathbf{k}_F}$ is interpreted as the overlap between the true ground state of the $(N+1)$-particle system and the wave function for a bare single particle at $\mathbf{k}_F$ is added to the true N-particle ground state. $Z_{\mathbf{k}_F}$ is also given as the jump of the momentum distribution function $\langle n(\mathbf{k}) \rangle \equiv \langle c^\dagger_{\mathbf{k}\sigma} c_{\mathbf{k}\sigma} \rangle$ at $T=0$. The spectral representation

$$\begin{aligned} G^C(\mathbf{k},\omega) = \lim_{\delta \to +0} \sum_n & \frac{|\langle \Phi_g(N) | c_{\mathbf{k}} | \Phi_n(N+1) \rangle|^2}{\omega - E_n + i\delta} \\ & + \frac{|\langle \Phi_g(N) | c^\dagger_{\mathbf{k}} | \Phi_n(N-1) \rangle|^2}{\omega + E_n - i\delta} \end{aligned} \tag{2.78}$$

leads to

$$\langle n(\mathbf{k}) \rangle = \frac{1}{2\pi i} \lim_{t \to +0} \int_{-\infty}^{\infty} d\omega\, G^C(\mathbf{k},\omega) e^{i\omega t}. \tag{2.79}$$

Using the renormalized form

$$G^C(\mathbf{k},\omega) = \frac{Z_{\mathbf{k}}}{\omega - \varepsilon^*(\mathbf{k} - \mathbf{k}_F) + i\gamma\, \mathrm{sgn}(\varepsilon^* - \varepsilon_F)}, \tag{2.80}$$

the jump of $\langle n(\mathbf{k}) \rangle$ at $\mathbf{k}_F$, is given by

$$\begin{aligned} & \langle n(\mathbf{k}) \rangle_{\mathbf{k}=\mathbf{k}_F-\delta} - \langle n(\mathbf{k}) \rangle_{\mathbf{k}=\mathbf{k}_F+\delta} \\ & = -\frac{i}{2\pi} \lim_{t \to +0} \int_{-\infty}^{\infty} d\omega\, e^{i\omega t} \\ & \quad \times \left(\frac{Z_{\mathbf{k}}}{\omega - \varepsilon^*(\mathbf{k}-\mathbf{k}_F) - i\gamma} - \frac{Z_{\mathbf{k}}}{\omega - \varepsilon^*(\mathbf{k}-\mathbf{k}_F) + i\gamma} \right) \\ & = Z_{\mathbf{k}}. \end{aligned} \tag{2.81}$$

The spectral function defined in Eq. (2.63) becomes

$$\begin{aligned} A(\mathbf{k},\omega) \simeq & -\frac{Z_{\mathbf{k}}(\varepsilon^*(\mathbf{k}))}{\pi} \\ & \times \frac{Z_{\mathbf{k}}(\varepsilon^*(\mathbf{k}))\, \mathrm{Im}\, \Sigma(\mathbf{k},\varepsilon^*(\mathbf{k}))}{[\omega - \varepsilon^*(\mathbf{k})]^2 + [Z_{\mathbf{k}}(\varepsilon^*(\mathbf{k}))\, \mathrm{Im}\, \Sigma(\mathbf{k},\omega)]^2}, \end{aligned} \tag{2.82}$$

where $Z_{\mathbf{k}_F}$ is generalized to $Z_{\mathbf{k}}(\omega) \equiv [1 - \partial\, \mathrm{Re}\, \Sigma(\mathbf{k},\omega)/\partial \omega]^{-1} (<1)$ to allow ω dependence. Equation (2.82) indicates that the quasiparticle peak at $\omega = \varepsilon^*(\mathbf{k})$ has approximately a Lorentzian line shape with a width of $Z_{\mathbf{k}}(\varepsilon^*(\mathbf{k}))\, \mathrm{Im}\, \Sigma(\mathbf{k},\varepsilon^*(\mathbf{k}))$. It also indicates that the quasiparticle weight is $Z_{\mathbf{k}}(\varepsilon^*(\mathbf{k}))$ instead of one as in the noninteracting case.

In the transport process, it is known that the mass m, which appears in the conductivity formula, $\sigma \propto n e^2 \tau / m$ and the Drude weight $D \propto n/m$, is not scaled by the effective mass m^* but by the bare mass m_0 for systems with Galilean invariance. This is because the electron-electron interaction conserves the total momentum and hence the current does not change under an adiabatic switching of the interaction. However, the transport of electrons in solid is associated with Umklapp scattering and impurity scattering. In particular, the Drude weight in perfect crystals may be strongly affected by Umklapp scattering, which may be regarded as the origin of the Mott transition in the perturbational framework. This effect of the discrete lattice, not seen in the Galilean invariant system, may cause a renormalization of the transport mass from the bare value to m_D^*, which may in general be different from m^* and m_b. When the electron correlation is large, electron-electron scattering is the dominant decoherence process of the electron wave function. This decoherence process is believed to govern the electron relaxation time τ, although Umklapp scattering is necessary to cause inelastic relaxation. The quasiparticle-quasiparticle scattering time is given by $1/\tau = Z_{\mathbf{k}}\, \mathrm{Im}\, \Sigma$. Then, in the usual Fermi liquid, the ω dependence $Z_{\mathbf{k}}\, \mathrm{Im}\, \Sigma \propto (\omega - \mu)^2$ may be transformed to temperature dependence by replacing $\omega - \mu$ with T because the thermal excitation has a characteristic energy scale of T from the Fermi surface. Therefore the resistivity at low temperatures in strongly correlated systems in general has the temperature dependence

$$\rho = A T^2 + \rho_0, \tag{2.83}$$

where ρ_0 is the residual resistivity determined from the impurity scattering process. The temperature dependence (2.83) is widely observed in many d and f electron compounds at low temperatures. We discuss some examples, $\mathrm{NiS}_{2-x}\mathrm{Se}_x$, NiS, $R\mathrm{NiO}_3$, $\mathrm{Ca}_{1-x}\mathrm{Sr}_x\mathrm{VO}_3$, $R_{1-x}\mathrm{S}_x\mathrm{TiO}_3$, $R_{1-x}A_x\mathrm{MnO}_3$, etc., in Sec. IV. However, we also discuss how T^2 dependence is replaced with other temperature dependences in cases such as the high-T_c cuprates and NiSSe. The origin of these unusual properties is one of the important issues to be discussed in this article. On empirical grounds, it has been suggested that A seems to be proportional to γ^2 in many

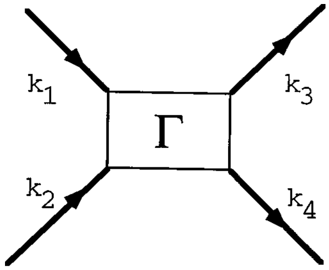

FIG. 6. Diagrammatic representation of the four-point vertex function $\Gamma(k_1,k_2,k_3,k_4)$.

heavy-fermion compounds, that is, A/γ^2 seems to be a universal constant in many cases (Kadowaki and Woods, 1986). This constant is also similar in some perovskite Ti and V compounds ($Ca_{1-x}Sr_xVO_3$, $R_{1-x}A_xTiO_3$ etc.; see Secs. IV.A.5 and IV.B.1). However, this empirical rule is not satisfied near antiferromagnetic transition, as in $NiS_{2-x}Se_x$ (Sec. IV.A.2), as well as in the high-T_c cuprates.

To derive thermodynamic as well as dynamic properties based on the Fermi-liquid theory, it is necessary to include self-consistently the vertex correction in the self-energy. For this purpose, the Ward-Takahashi identity provides a useful relation between the self-energy and the vertex function under spin-rotational invariance (Koyama and Tachiki, 1986; Yamada and Yosida, 1986; Kohno and Yamada, 1991). The Ward-Takahashi identity leads to

$$\frac{\partial\Sigma_\sigma(\mathbf{k},i\omega)}{\partial(i\omega)}=\frac{\partial\Sigma_\sigma(\mathbf{k},i\omega)}{\partial\mu}-\sum_{\mathbf{k}',\sigma'}A(\mathbf{k}',\omega=\mu)\times\Gamma_{\sigma\sigma'}(\mathbf{k},\mathbf{k}';\mathbf{k}',\mathbf{k}) \tag{2.84}$$

and

$$\frac{\partial\Sigma_\sigma(\mathbf{k},i\omega)}{\partial(i\omega)}=\frac{\partial\Sigma_\sigma(\mathbf{k},i\omega)}{\partial H_\sigma}-\sum_{\mathbf{k}'}A(\mathbf{k}',\omega=\mu)\times\Gamma_{\sigma\sigma}(\mathbf{k},\mathbf{k}';\mathbf{k}',\mathbf{k}) \tag{2.85}$$

with $H_\sigma=g\mu_B H\sigma/2$ under a magnetic field H where the four-point vertex function $\Gamma_{\sigma\sigma'}$ is defined in Fig. 6 and where all of ω are taken zero. We note the identity $\partial\Sigma_\sigma/\partial\mu=\partial\Sigma_\sigma/\partial H_\sigma+\partial\Sigma_\sigma/\partial H_{-\sigma}$. Below we neglect the wave-number dependence of the self-energy for the time being. Because

$$Z_{\mathbf{k}}=\left(1-\frac{\partial\Sigma}{\partial\omega}\right)^{-1} \tag{2.86}$$

is satisfied from Eqs. (2.68a), (2.68b), and (2.70), we obtain

$$\frac{\gamma}{\gamma_b}=1-\sum_{\mathbf{k}\sigma}\left.\frac{\partial\Sigma_\sigma(\mathbf{k},\omega)}{\partial\omega}\right|_{\omega=\mu}. \tag{2.87}$$

Similarly, the enhancement of the uniform magnetic susceptibility and charge susceptibility as compared to the noninteracting band values χ_b and κ_b satisfies

$$\frac{\chi}{\chi_b}=1-(X_{\uparrow\uparrow}-X_{\uparrow\downarrow}), \tag{2.88}$$

$$\frac{\kappa}{\kappa_b}=1-(X_{\uparrow\uparrow}+X_{\uparrow\downarrow}), \tag{2.89}$$

with

$$X_{\uparrow\uparrow}(\mathbf{k})=\left.\frac{\partial\Sigma_\sigma(\mathbf{k},\omega=\mu)}{\partial H_\sigma}\right|_{H_\sigma=0}, \tag{2.90}$$

$$X_{\uparrow\downarrow}(\mathbf{k})=\left.\frac{\partial\Sigma_\sigma(\mathbf{k},\omega=\mu)}{\partial H_{-\sigma}}\right|_{H_{-\sigma}=0}. \tag{2.91}$$

From Eqs. (2.84) and (2.85), $X_{\uparrow\downarrow}$ can be expressed as

$$X_{\uparrow\downarrow}(\mathbf{k})=\sum_{\mathbf{k}'}A(\mathbf{k}',\omega=\mu)\Gamma_{\uparrow\downarrow}(\mathbf{k},\mathbf{k}';\mathbf{k}',\mathbf{k}). \tag{2.92}$$

In this notation, the mass enhancement is basically ascribed to the enhancement of $\Sigma_{\mathbf{k}'}\Gamma_{\uparrow\downarrow}(\mathbf{k}=0,\mathbf{k}';\mathbf{k}',\mathbf{k}=0)$. Up to the order of T^2 and ω^2, Im $\Sigma(\mathbf{k},\omega)$ is calculated as

$$\begin{aligned}\mathrm{Im}\sum(\mathbf{k},\omega)=&-\frac{\omega^2+(\pi T)^2}{2}\pi\sum_{\mathbf{k}',q}A(\mathbf{k}-\mathbf{q},\omega=\mu)\\&\times A(\mathbf{k}',\omega=\mu)A(\mathbf{k}'+\mathbf{q},\omega=\mu)\\&\times\Bigg[\Gamma^2_{\uparrow\downarrow}(\mathbf{k},\mathbf{k}';\mathbf{k}'+\mathbf{q},\mathbf{k}-\mathbf{q})\\&+\frac{1}{2}\Gamma^2_{\uparrow\uparrow A}(\mathbf{k},\mathbf{k}';\mathbf{k}'+\mathbf{q},\mathbf{k}-\mathbf{q})\Bigg]\end{aligned} \tag{2.93}$$

with the antisymmetrized vertex function

$$\begin{aligned}&\Gamma_{\uparrow\uparrow A}(\mathbf{k}_1,\mathbf{k}_2;\mathbf{k}_3,\mathbf{k}_4)\\&\quad=\Gamma_{\uparrow\uparrow}(\mathbf{k}_1,\mathbf{k}_2;\mathbf{k}_3,\mathbf{k}_4)-\Gamma_{\uparrow\uparrow}(\mathbf{k}_1,\mathbf{k}_2;\mathbf{k}_4,\mathbf{k}_3).\end{aligned} \tag{2.94}$$

Using the damping factor

$$\tilde{\Gamma}(\mathbf{k})=-Z(\mathbf{k})\mathrm{Im}\sum(\mathbf{k},\omega), \tag{2.95}$$

we can express the coherent part of the conductivity as

$$\sigma_{\mathrm{coh}}(\omega)\sim e^2\sum_{\mathbf{k}}A^*(\mathbf{k},\omega=\mu)J_{\mathbf{k}}\frac{k^2}{\Sigma_i(\mathbf{K}_i\cdot\mathbf{k})}J_{\mathbf{k}}\frac{i}{\omega+i\tilde{\Gamma}(k)} \tag{2.96}$$

with the sum Σ_i over the internal product of k and all the reciprocal lattice vectors $\mathbf{K}_i$ coming from Umklapp scattering. It should be noted that the electron-electron interaction itself does not generate a nonzero resistivity because of momentum conservation, and Umklapp scattering is needed to yield a momentum relaxation process (Yamada and Yosida, 1986). Yamada and Yosida succeeded in deriving the momentum conservation by taking account of proper vertex and self-energy corrections utilizing the Ward-Takahashi identity. This guarantees zero resistivity in the absence of Umklapp scattering. Because the inverse of the quasiparticle spectral weight A^{*-1}, the current $J_{\mathbf{k}}$, and $\tilde{\Gamma}(k)$ are all renormalized by $Z_{\mathbf{k}}(\omega)$, they are canceled in $\sigma(\omega=0)$. Therefore $\sigma(\omega$

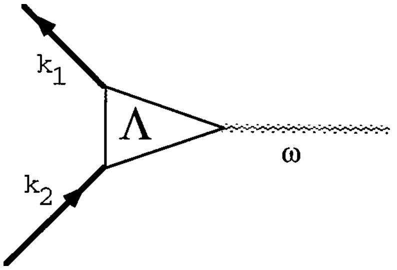

FIG. 7. Diagrammatic representation of the three-point vertex function $\Lambda(k_1,k_2,k_3,k_4)$.

$=0$) is basically scaled by $[\mathrm{Im}\,\Sigma(\mathbf{k},\omega)]^{-1}$, which may be then related to γ and χ through $\Gamma_{\uparrow\downarrow}$.

It was argued that if the charge fluctuation could be assumed to be suppressed as $\kappa\to 0$, as compared with spin fluctuations, we might take

$$X_{\uparrow\uparrow}\simeq 1-X_{\uparrow\downarrow}, \tag{2.97}$$

which leads to

$$\frac{\chi}{\chi_b}=2\sum_{\mathbf{k}} X_{\uparrow\downarrow}=2\sum_{\mathbf{k},\mathbf{k}'} A(\mathbf{k}',\omega=\mu)\Gamma_{\uparrow\downarrow}(\mathbf{k},\mathbf{k}';\mathbf{k}',\mathbf{k}), \tag{2.98}$$

$$\begin{aligned}\frac{\gamma}{\gamma_b}&=\sum_{\substack{\mathbf{k},\mathbf{k}'\\ \sigma'}} A(\mathbf{k}',\omega=\mu)\Gamma_{\sigma\sigma'}(\mathbf{k},\mathbf{k}';\mathbf{k}',\mathbf{k})\\ &=\frac{1}{2}\frac{\chi}{\chi_b}+2\sum_{\mathbf{k},\mathbf{k}'} A(\mathbf{k}',\omega=\mu)\Gamma_{\uparrow\uparrow}(\mathbf{k},\mathbf{k}';\mathbf{k}',\mathbf{k}).\end{aligned} \tag{2.99}$$

Therefore the Wilson ratio is given by

$$\begin{aligned}R_W&=\frac{\chi}{\chi_b}\frac{\gamma_b}{\gamma}\\ &=\frac{2}{1+\dfrac{4\chi_b}{\chi}\Sigma_{\mathbf{k},\mathbf{k}'}A(\mathbf{k}',\omega=\mu)\Gamma_{\uparrow\uparrow}(\mathbf{k},\mathbf{k}';\mathbf{k}',\mathbf{k})}.\end{aligned} \tag{2.100}$$

If the Wilson ratio is close to two, it gives

$$\sum_{\mathbf{k}\mathbf{k}'} A(\mathbf{k}',\omega=\mu)\Gamma_{\uparrow\uparrow}(\mathbf{k},\mathbf{k}';\mathbf{k}',\mathbf{k})\simeq 0. \tag{2.101}$$

The static susceptibility $\chi(\mathbf{q})$ is expressed as

$$\chi(\mathbf{q})=-\sum_{\mathbf{k}}\int_{-\infty}^{\infty}\frac{d\omega}{2\pi i}\Lambda(\mathbf{k},\mathbf{k}+\mathbf{q};0)G(\mathbf{k},i\omega)G(\mathbf{k}+\mathbf{q},i\omega) \tag{2.102}$$

with the three-point vertex function Λ illustrated in Fig. 7. The Λ and four-point vertex functions Γ are related as

$$\begin{aligned}\Lambda(\mathbf{k},\mathbf{k}+\mathbf{q},0)=1-T\sum_n\sum_{\mathbf{k}'}\Gamma_{\uparrow\downarrow}(\mathbf{k}+\mathbf{q},\mathbf{k}';\mathbf{k},\mathbf{k}'+\mathbf{q})\\ \times G_{\uparrow}(\mathbf{k}'+\mathbf{q},i\omega_n)G_{\downarrow}(\mathbf{k}',i\omega_n).\end{aligned} \tag{2.103}$$

Therefore, if $\chi(\mathbf{q})$ is strongly peaked around $\mathbf{k}=\mathbf{Q}$ due to spin fluctuations, this enhancement must be due to Λ. Thus neglecting $\mathbf{k}$ and ω dependence of $\Lambda(\mathbf{k},\mathbf{k}+\mathbf{Q};i\omega)$, we obtain

$$\chi(\mathbf{q}+\mathbf{Q})\sim\Lambda(\mathbf{q}+\mathbf{Q})\chi_b(\mathbf{q}+\mathbf{Q}), \tag{2.104}$$

where we employed simplified notation $\Lambda(\mathbf{q})\sim\Lambda(\mathbf{k},\mathbf{k}+\mathbf{q};i\omega)$ and where χ_b is the susceptibility without the vertex correction. From Eq. (2.103), if we neglect $\mathbf{k}$ and $\mathbf{k}'$ dependence of $\Gamma_{\uparrow\downarrow}(\mathbf{k}+\mathbf{q},\mathbf{k}';\mathbf{k},\mathbf{k}'+\mathbf{q})$ as denoted by $\Gamma_{\uparrow\downarrow}(\mathbf{q})$, we obtain

$$\chi(\mathbf{Q}+\mathbf{q})\sim\chi_b^2(\mathbf{Q}+\mathbf{q})\Gamma_{\uparrow\downarrow}(\mathbf{Q}+\mathbf{q}). \tag{2.105}$$

When the strong peak structure of $\chi(\mathbf{Q}+\mathbf{q},\omega)$ can be approximated as

$$\chi(\mathbf{Q}+\mathbf{q},\omega)\sim\frac{1}{-i\omega+D_s(K^2+q^2)}\chi_b(\mathbf{Q}+\mathbf{q},0), \tag{2.106}$$

we have

$$\begin{aligned}\frac{\chi(\mathbf{Q}+\mathbf{q},\omega=0)}{\chi_b(\mathbf{Q}+\mathbf{q},\omega=0)}&\sim\chi_b(\mathbf{Q}+\mathbf{q},\omega=0)\Gamma_{\uparrow\downarrow}(\mathbf{Q}+\mathbf{q})\\ &\sim\frac{1}{D_s(K^2+q^2)}.\end{aligned} \tag{2.107}$$

This type of susceptibility is justified for an order parameter that is not a conserved quantity of the Hamiltonian and that is coupled to metallic and gapless Stoner excitations. Because of the coupling to the Stoner excitation Eq. (2.106) contains an ω-linear term in the denominator, which comes from the overdamped nature of the spin fluctuation. The antiferromagnetic transition at $\mathbf{Q}\neq 0$ may indeed belong to this class, as we discuss in Sec. II.D.9. Then the NMR relaxation rate is given as

$$(T_1T)^{-1}\sim\lim_{\omega\to 0}\sum_{\mathbf{k}} f(\mathbf{k})\frac{\mathrm{Im}\,\chi(\mathbf{k},\omega=0)}{\omega}\sim\sum_{\mathbf{k}} f(\mathbf{k})\Gamma_{\uparrow\downarrow}^2(\mathbf{k}), \tag{2.108}$$

while from Eqs. (2.93), (2.95), and (2.96), neglecting $\Gamma_{\uparrow\uparrow}$, we obtain

$$\sigma(\omega)\propto\frac{1}{-i\omega+\tilde{\Gamma}}, \tag{2.109}$$

$$\tilde{\Gamma}\sim\mathrm{Im}\sum\propto[\omega^2+(\pi T)^2]\sum_{\mathbf{k}}\Gamma_{\uparrow\downarrow}^2(\mathbf{k}). \tag{2.110}$$

Therefore, when we assume weak $\mathbf{k}$ dependence of χ_b, the basic scaling of these two quantities is determined from

$$\Xi\equiv\sum_{\mathbf{k}}[\Gamma_{\uparrow\downarrow}(\mathbf{k})]^2\propto\int dk\frac{k^{d-1}}{(K^2+k^2)^2}\propto K^{d-4}. \tag{2.111}$$

This leads to

$$(T_1T)^{-1}\propto A\propto K^{d-4} \tag{2.112}$$

for the resistivity coefficient A defined by $\rho=AT^2$. Here we have neglected $\mathbf{q}$ dependences of the nuclear form factor $f(\mathbf{q})$ by assuming weak $\mathbf{q}$ dependence. As we see from Eqs. (2.99) and (2.107) the specific-heat coefficient γ and the local susceptibility χ for the singular part follow the scaling

$$\gamma \propto \chi \propto \int dq \frac{q^{d-1}}{K^2+q^2} \propto \begin{cases} 1/K & \text{for 1D} \\ -\ln K & \text{for 2D} \\ -\sqrt{K} & \text{for 3D.} \end{cases} \tag{2.113}$$

When the susceptibility can be described by a Curie-Weiss law

$$\chi(\mathbf{Q}) \sim \frac{C}{T+\Theta} \tag{2.114}$$

where C is the Curie-Weiss constant and Θ the Curie-Weiss temperature, then Eq. (2.107) implies $K \propto (T+\Theta)^{1/2}$, leading to

$$(T_1 T)^{-1} \propto A \propto (T+\Theta)^{d/2-2}. \tag{2.115}$$

Similarly, we obtain for the singular part

$$\gamma \propto \chi \propto \begin{cases} -\ln(T+\Theta) & \text{for 2D} \\ -\sqrt{T+\Theta} & \text{for 3D.} \end{cases} \tag{2.116}$$

We note that, aside from the singular part given in Eq. (2.116), the leading term is a constant for 3D. These comprise the basic framework of the antiferromagnetic spin-fluctuation theory based on the Fermi-liquid theory, as we discuss in detail in Secs. II.D.8 and II.D.9. In three dimensions, at the critical point $\Theta=0$ of the magnetic transition, it leads to

$$(T_1 T)^{-1} \propto T^{-1/2}, \tag{2.117}$$

$$\rho \propto T^{3/2}, \tag{2.118}$$

$$\gamma \propto \chi \propto \text{const} - \sqrt{T} \tag{2.119}$$

while in two dimensions at $\Theta=0$ it leads to

$$T_1^{-1} \propto \text{const}, \tag{2.120}$$

$$\rho \propto T, \tag{2.121}$$

and

$$\gamma \propto \chi \propto -\ln T, \tag{2.122}$$

as is known in the self-consistent renormalization theory (Ueda, 1977; Moriya, 1985; Moriya, Takahashi, and Ueda, 1990). In particular, at the antiferromagnetic transition point in some 3D metals such as β-Mn, $NiS_{2-x}Se_x$, and $Ni_{1-x}Co_xS_2$ this behavior is indeed observed (Watanabe, Môri, and Mitsui, 1976; Katayama, Akimoto, and Asayama, 1977; Miyasaka *et al.*, 1997). In 2D, it was claimed that Eqs. (2.120) and (2.121) reproduce the anomalous behavior in the high-T_c cuprates, as we discuss in Sec. IV.C.1.

As is evident from the above arguments, spin-fluctuation theory alone fails to reproduce physical properties near the Mott transition point if the MIT is of the continuous type. This is because the above treatment of spin fluctuations takes into account only the coherent part of the charge excitations. We also discuss in Secs. II.E.3 and II.F why the neglect of charge fluctuation, assumed above through vanishing charge compressibility $\kappa \sim 0$, is not justified in metals near the Mott insulator.

Let us consider the resistivity and the frequency-dependent conductivity by considering the dependence on the renormalization factor Z explicitly. As we discussed above, the optical conductivity given by Eqs. (2.109) and (2.96) can be rewritten from the fact that A^{*-1}, $J_{\mathbf{k}}$, and $\tilde{\Gamma}(k)$ are all scaled by the renormalization factor $Z(\omega)$:

$$\text{Re}\,\sigma(\omega) \propto \frac{\tilde{\Gamma}(\omega) n Z(\omega)}{\omega^2+\tilde{\Gamma}(\omega)^2} \tag{2.123}$$

with

$$\begin{aligned} \tilde{\Gamma}(\omega) &\sim Z(\omega)\,\text{Im}\,\Sigma \propto \int dz\, Z(z)\,\text{Im}\,\chi(q,z) \\ &\quad \times \text{Im}\,\chi_b(Q,\omega-z)[n_B(z)-n_B(z-\omega)] \\ &\propto \frac{Z(\omega)}{nD_s} G(\omega) \end{aligned} \tag{2.124}$$

in the Born approximation at $T \ll \omega$. Here χ_b is the susceptibility of the noninteracting band electrons while the Bose distribution n_B is defined by $n_B(z)=1/(e^{\beta z}-1)$; $G(\omega)$ is proportional to ω^2 in a simple Fermi liquid, while it may have ω dependence $G(\omega) \propto \omega^{d/2}$ in a wide range of ω if the spin-fluctuation effect is important. This dependence is easily understood when we replace the T dependence of $\tilde{\Gamma}$ discussed above with ω dependence. Note that the temperature dependence of $\tilde{\Gamma}$ is obtained from Eqs. (2.110), (2.111), (2.114), and (2.107) as $\tilde{\Gamma} \sim T^2 K^{d-4} \sim T^{d/2}$ at $T > \omega$ and $\Theta \sim 0$. Then the ω-integrated conductivity, that is, the Drude weight $D = \int_0^\infty \sigma_{coh}(\omega) d\omega$, can be sensitively dependent on the doping concentration near the Mott insulator only through the renormalization factor Z in the region without magnetic order when a singular $\mathbf{k}$-dependent mass m_k is absent. This is because the spin-diffusion constant D_s is not critically dependent on the doping concentration and n must remain finite near the Mott insulator in the Fermi-liquid theory due to the Luttinger theorem. In fact, because the spin-diffusion constant D_s should be connected with the overdamped mode of the spin wave, it should remain finite near the antiferromagnetic Mott insulator. Therefore, the Drude weight decreases to vanish toward the Mott transition only when Z^{-1} is critically enhanced at small ω. In this case, the total Drude weight derived from Eq. (2.123) depends on the doping concentration δ mainly in the form $D \propto Z$. This necessarily leads to critical enhancement of γ through Eqs. (2.73a)–(2.73e) and (2.74) provided that the $\mathbf{k}$ mass is not critically suppressed. At least for the paramagnetic metal region, the reduction of D near the Mott insulator transition is necessarily accompanied by enhancement of γ in the Fermi-liquid description if m_k does not have singular $\mathbf{k}$ dependence. As we discuss in Sec. IV, such behavior in D and γ contrasts with that observed in high-T_c cuprates because D decreases while γ is not enhanced. In the region where antiferromagnetic order exists, of course, D can be reduced to zero without the

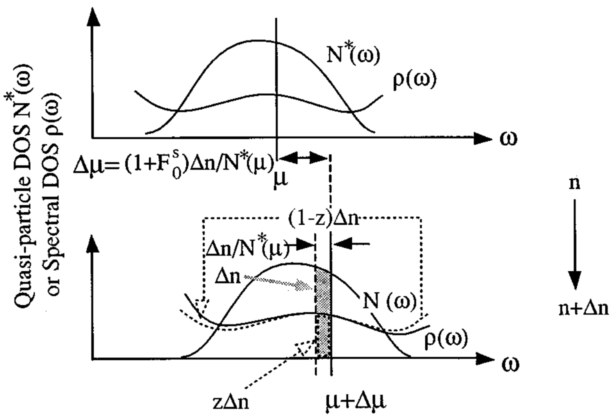

FIG. 8. Schematic representation of the chemical potential shift $\Delta\mu$ induced by a change Δn in the electron concentration n and spectral weight transfer near the chemical potential in an isotropic Fermi liquid. $N^*(\omega)$ is the quasiparticle density and $\rho(\omega)$ is the (spectral) density of states. Note that $\rho(\omega)=ZN^*(\omega)$ near the chemical potential.

enhancement of γ because small pockets of the Fermi surface can be arbitrarily small. This, however, is not the case in the high-T_c cuprates. In contrast to the Drude weight, the resistivity depends mainly on δ through Im Σ while the dependence on Z is canceled. Therefore critical enhancement of A has to be ascribed to Im Σ. It was argued that if Z were not reduced and the **k** dependence of $\Gamma_{\uparrow\downarrow}$ could be neglected, the Kadowaki-Woods relation would result from $\gamma\propto\Gamma_{\uparrow\downarrow}$ and $A\propto\Gamma_{\uparrow\downarrow}^2$.

Aside from all the above phenomenological and rather sketchy arguments, as far as the authors know, no theoretical studies have been attempted in this Fermi-liquid description with a self-consistent treatment of spin and charge fluctuations to discuss the paramagnetic region near the Mott insulator. This remains for further studies. In particular, the **k** dependence of the self-energy has to be considered seriously near a Mott insulator with magnetic order, while all the above arguments basically neglect this dependence. In Sec. II.F, we discuss how the singular **k** dependence of the self-energy should be considered to satisfy the scaling relation of the Mott transition.

The shift of the electron chemical potential μ as a function of electron concentration n defines the charge susceptibility χ_c through $\chi_c^{-1}\equiv\partial\mu/\partial n$, as discussed above. This quantity can be measured by photoemission spectroscopy as a shift of the Fermi level as a function of band filling n. Experimentally, the energies of photoelectrons are usually referenced to the electron chemical potential of the spectrometer, which is in electrical contact with the sample. A chemical potential shift would therefore cause a uniform shift of all the core-level and valence-band spectra if there were no interaction between electrons.

Now we consider the spectral weight transfer caused by the change Δn, referring to Fig. 8 (Ino *et al.*, 1997a, 1997b). As the electron concentration increases by Δn, spectral weight Δn should be transferred from above to below the chemical potential, a condition imposed by the sum rule, Eq. (2.58). If the line shape of the spectral function $\rho(\omega)$ did not change with the increase of electron concentration Δn, the spectral weight that could be transferred from above to below the chemical potential would be $\rho(\mu)\Delta\mu'=ZN^*(\mu)\Delta\mu'$ [Eq. (2.126)], which is less than $\Delta n=N^*(\mu)\Delta\mu'$ by the renormalization factor Z, and would violate the sum rule. The rest of the spectral weight $(1-Z)\Delta n$ is necessarily transferred from well above the chemical potential to well below it through a change in the line shape of $\rho(\omega)$. It is therefore concluded that, if there is electron correlation, i.e., if $Z=[1-\partial\ \mathrm{Re}\ \Sigma/\partial\omega|_{\omega=\mu}]^{-1}<1$, a change in the band filling necessarily leads to a change in the line shape of the spectral function.

Here it should be noted that carrier doping in real compounds such as transition-metal oxides has to be carried out under the condition of charge neutrality because of the presence of the long-range Coulomb interaction in real systems. That is, in the case of perovskite-type transition-metal oxides, in order to dope the system with electrons (holes), one must usually replace A-site metal ions by ions with higher (lower) valencies or oxygen vacancies (excess oxygens). Therefore the "particle" in the definition of the chemical potential, the derivative of the Gibbs free energy with respect to the particle number, is not the bare electron or hole but an electron or hole whose long-range Coulomb interaction is screened by the positive background charges of the substituted ions or oxygen defects. This implies that microscopic models which neglect the long-range Coulomb interaction, such as the Hubbard model, may be relevant for analysis of the chemical potential shift and the charge susceptibility, although the long-range Coulomb interaction should influence the dynamic (spectroscopic) behaviors through $\Sigma(\mathbf{k},\omega)$.

Below we discuss in some detail a phenomenological way of analyzing experimentally observed line shapes of spectral weight. We discuss the case in which the self-energy is local and hence $a(\mathbf{k})=0$, and $Z_{\mathbf{k}_F}=Z$ independent of the direction of $\mathbf{k}_F$. In this case, $\Delta^*\equiv1/Z\Gamma$, called the quasiparticle coherence energy, defines the energy scale below which ($|\omega-\mu|\ll\Delta^*$) the quasiparticle is well defined. The quasiparticle dispersion is given by $\omega-\mu=Z[\varepsilon_0(\mathbf{k})-\mu]$: The band is uniformly narrowed by the renormalization factor $Z(<1)$, meaning that the density of states (per unit energy) of the quasiparticles, or equivalently the effective mass m^* of the conduction electrons, is enhanced by the factor $1/Z(>1)$ compared with the noninteracting case. Thus the mass enhancement factor m^*/m_b, where m_b is the noninteracting conduction-band mass at the chemical potential, is equivalent to $1/Z$.

The quasiparticle peak carries spectral weight Z, and the remaining spectral weight $1-Z$ is distributed as an "incoherent" background mostly at higher energies, i.e., at larger $|\omega-\mu|$, as schematically shown in Fig. 9. It should be noted that the **k**-integrated spectral function $\rho(\omega)$ at $\omega\sim\mu$ is not affected by the local self-energy correction, i.e., $\rho(\mu)=N_b(\mu)$, where $N_b(\omega)$ is the density of states of the noninteracting band, because the mass

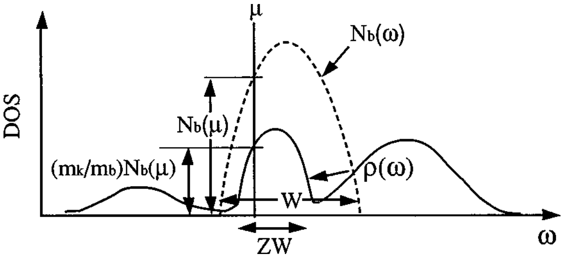

FIG. 9. Spectral function $\rho(\omega)$ for a constant renormalization factor Z. $N_b(\omega)$ is the band density of states, m_b is the band mass, and m_k is the k mass.

enhancement factor $1/Z$ is canceled out by the quasiparticle spectral weight Z. Therefore one can claim that if $\rho(\mu)$ is different from $N_b(\mu)$ there must be **k** dependence in the self-energy, i.e., the self-energy should be nonlocal. This is the case not only for a Fermi liquid but also for a non-Fermi liquid. Therefore, as shown in Fig. 9, if Z is **k** independent throughout the quasiparticle band, the quasiparticle band in the spectral function $\rho(\omega)$ is narrowed by a factor Z with the peak height unchanged, resulting in the loss of spectral weight $1-Z$ from the coherent quasiparticle band region. The lost spectral weight $1-Z$ is distributed as incoherent weight at higher $|\omega-\mu|$.

Although the original Fermi-liquid theory assumes a structureless incoherent part and neglects its contribution to low-energy excitations, recent studies described below in Secs. II.D.4, II.D.6, II.E, II.F, and II.G have clarified the importance of the growing weight of incoherent contributions. Based on the Fermi-liquid description, a phenomenological treatment of coherent and incoherent parts on an equal footing has been given (Kawabata, 1975; Kuramoto and Miyake, 1990; Miyake and Narikiyo, 1994a, 1994b; Narikiyo and Miyake, 1994; Narikiyo, 1996; Okuno, Narikiyo, and Miyake, 1997). This approach may be justified when the incoherent part described by “upper” and “lower” Hubbard bands give serious renormalization to the quasiparticle coherent part.

In discussing Eq. (2.72) above, we ignored the **k** dependence of the self-energy for simplicity. However, the effect of electron correlation is not restricted to each atomic site but is generally extended over many atomic sites, necessitating a **k**-dependent self-energy. The degree of nonlocality of the self-energy generally increases as the range of interaction increases. Nevertheless, even the on-site Coulomb interaction included in the Hubbard model leads to some **k** dependence in the self-energy through the intersite hybridization term. In particular, in cases where there is a nesting feature in the Fermi surface, the self-energy should show an anomaly for **k** around the nesting wave vector. Because of this, the **k** dependence of the self-energy is more pronounced for low (one or two) dimensions, since the nesting condition is more easily satisfied. The effect of antiferromagnetic fluctuation on the spectral function arising from Fermi-surface nesting was discussed for the 2D Hubbard model originally by Kampf and Schrieffer (1990) and more recently by Langer *et al.* (1995) and Deisz *et al.* (1996).

The density of states at the chemical potential $\rho(\mu)$ is modified from the noninteracting value $N_b(\mu)$ as

$$\rho(\mu)/N_b(\mu)=m_k/m_b, \tag{2.125}$$

which means that **k** dependence of the self-energy is necessary to have $\rho(\mu)\neq N_b(\mu)$ (Greef, Glyde, and Clements, 1992). The ratio between the density of states $\rho(\mu)$ and the density of states of quasiparticles $N^*(\mu)=(m^*/m_b)N_b(\mu)$ is given by Z (Allen *et al.*, 1985),

$$\rho(\mu)=ZN^*(\mu). \tag{2.126}$$

That is, the density of states at the chemical potential is reduced from the quasiparticle density of states by the quasiparticle residue Z. This is a special case of the relationship between the spectral function and the energy distribution function of quasiparticles, Eq. (2.72).

In the limit of large dimensionality or large lattice connectivity, the **k** dependence of the self-energy is lost because the fluctuation of the neighboring sites is averaged out and the central atom feels only the average field from the neighboring sites without fluctuation. This is described in greater detail in Sec. II.D.6. In that case, the spectral weight at the chemical potential, $\rho(\mu)$, is not influenced by electron correlation. It is also expected that the **k** dependence of the self-energy will become less important for a large orbital degeneracy (Kuramoto and Watanabe, 1987).

In the definition of the **k** dependence of the self-energy, one must define the reference mean-field state to which the self-energy correction is applied. Such a mean-field state is either the band structure calculated using the local-(spin-)density approximation (LDA or LSDA) or that calculated using the Hartree-Fock approximation. In the Hartree-Fock approximation, the nonlocality of the exchange interaction is properly dealt with and the nonlocality of the electron-electron interaction is already included on the mean-field level (and not beyond the mean-field level) in the one-electron energy $\varepsilon_0(\mathbf{k})$, so that $\Sigma(\mathbf{k},\mu)\sim 0$. In the L(S)DA, on the other hand, the exchange potential is approximated by a local potential. That is, the potential at a spatial point **r** is a function of the electron (and spin) densities at this **r**, i.e., $V_\sigma(\mathbf{r})=f_\sigma[n_\uparrow(\mathbf{r}),n_\downarrow(\mathbf{r})]$. Therefore $\Sigma(\mathbf{k},\mu)$ may be substantially different from zero, meaning that $\Sigma(\mathbf{k},\mu)$ will have to be taken into account if one analyzes photoemission spectra starting from the LDA band structure.

For the free-electron gas, the LDA gives $\varepsilon_0(\mathbf{k})$ almost identical to the noninteracting dispersion $\varepsilon_0(\mathbf{k})=\hbar^2k^2/2m_e$, while the Hartree-Fock approximation yields

$$\varepsilon_0(\mathbf{k})=\frac{\hbar^2k^2}{2m_e}-\frac{2e^2}{\pi}k_F\left(\frac{1}{2}+\frac{1-x^2}{4x}\ln\left|\frac{1+x}{1-x}\right|\right), \tag{2.127}$$

where $x\equiv k/k_F$ (Ashcroft and Mermin, 1976). Therefore, if one starts from the LDA, $\Sigma(\mathbf{k}_F,\mu)-\Sigma(0,\mu)=2e^2k_F/\pi$, meaning that the occupied bandwidth is increased by $\sim 2e^2k_F/\pi$ compared to the LDA band structure due to the effect of nonlocal exchange. In fact, the screening effect, which is completely neglected in the Hartree-Fock approximation and can be treated in the RPA, will reduce the $\Sigma(\mathbf{k}_F,\mu)-\Sigma(0,\mu)$ to some extent, but such a screening effect would be weak when the electron density is low, as is the case in most of the metallic transition-metal oxides. Since $k_F=(3n/8\pi)^{1/3}\sim 1/2\overline{r}$, where $\overline{r}$ is the average distance between nearest electrons, $\Sigma(\mathbf{k}_F,\mu)-\Sigma(0,\mu)\sim e^2/\pi\overline{r}$. That is, the total bandwidth is increased by $\sim\Sigma(\mathbf{k}_F,\mu)-\Sigma(0,\mu)\sim e^2/\overline{r}$ due to the exchange contribution from the long-range Coulomb interaction. If we consider that the long-range Coulomb interaction is screened by the electric polarization of constituent ions, represented by the optical dielectric constant ε_∞, which is $\sim 3-5$ in oxides, the band widening becomes $\sim e^2/\varepsilon_\infty\overline{r}\sim 0.5$ eV (Morikawa *et al.*, 1996). Equation (2.127) means that for small k_F the second term (exchange energy $\propto k_F$) dominates the first term (kinetic energy $\propto k_F^2$), i.e., for large $\overline{r}$. Therefore the nonlocal exchange is important in systems with low carrier density. In ordinary metals and alloys, the carrier density is high enough (k_F is large) that the kinetic energy dominates Eq. (2.127) and the nonlocal exchange contribution is negligible, explaining why the LDA works well in ordinary metals and alloys. The increase of the bandwidth due to nonlocal exchange is also found using a tight-binding Hamiltonian if one treats the intersite Coulomb interaction in the Hartree-Fock approximation: It contributes through $-V_{ij}\langle c_i^\dagger c_j\rangle$ to the transfer integral t_{ij}, where V_{ij} is the intersite Coulomb energy, thereby effectively increasing $|t_{ij}|$.

2. Hartree-Fock approximation and RPA for phase transitions

The Hubbard Hamiltonian (1.1a) is rewritten as

$$\mathcal{H}=\mathcal{H}_K+\mathcal{H}_U, \tag{2.128a}$$

$$\mathcal{H}_K=\sum_\sigma\sum_{ij}c_{i\sigma}^\dagger\{\mathcal{K}_{ij}-[\mu+(2-y)U/4]\delta_{ij}\}c_{j\sigma}, \tag{2.128b}$$

$$\mathcal{H}_U=\frac{U}{4}\sum_i[y(c_{i\uparrow}^\dagger c_{i\uparrow}+c_{i\downarrow}^\dagger c_{i\downarrow}-1)^2 +2(2-y)c_{i\uparrow}^\dagger c_{i\downarrow}^\dagger c_{i\downarrow}c_{i\uparrow}], \tag{2.128c}$$

where $\mathcal{K}_{ij}$ is $-t$ for the pair (i,j) summed in Eq. (2.37b). Here y is an arbitrary constant and we have omitted a constant term $U/4$. For this Hamiltonian, the partition function (2.41a) can be expressed in the path integral of a noninteracting system through the Stratonovich-Hubbard (SH) transformation. Several formally different but equivalent representations through different SH transformations are possible. In a simple and ordinary mean-field approximation, one can introduce only $\tilde{\Delta}_s$ by taking $y=0$ to discuss magnetic ordering. Below we show a general choice of SH transformations in which both $\tilde{\Delta}_c$ and $\tilde{\Delta}_s$ are introduced to represent possible charge and spin fluctuations separately. We use the identity

$$1=\int\mathcal{D}\tilde{\Delta}_{si}^*\mathcal{D}\tilde{\Delta}_{si}\exp\left[-\frac{2-y}{2U}\sum_i(2\tilde{\Delta}_{si}^*-Uc_{i\uparrow}^\dagger c_{i\downarrow})\times(2\tilde{\Delta}_{si}-Uc_{i\downarrow}^\dagger c_{i\uparrow})\right], \tag{2.129a}$$

and

$$1=\int d\tilde{\Delta}_{ci}\exp\left[-\frac{y}{4U}\sum_i(4\tilde{\Delta}_{ci}-iU(c_{i\uparrow}^\dagger c_{i\uparrow}+c_{i\downarrow}^\dagger c_{i\downarrow}-1))\times(4\tilde{\Delta}_{ci}-iU(c_{i\uparrow}^\dagger c_\uparrow+c_{i\downarrow}^\dagger c_{i\downarrow}-1))\right], \tag{2.129b}$$

for complex c-number $\tilde{\Delta}_{si}$ and real variable $\tilde{\Delta}_{ci}$. Then we can rewrite the partition function in the coherent-state representation using the Grassmann variables,

$$Z=\int\mathcal{D}[\overline{\psi},\psi]\mathcal{D}\tilde{\Delta}_{si}(\tau)\mathcal{D}\tilde{\Delta}_{si}^*(\tau)\mathcal{D}\tilde{\Delta}_{ci}(\tau)\exp\Bigg(-\int_0^\beta d\tau\Bigg[\sum_i\overline{\psi}_{i\sigma}\frac{\partial}{\partial\tau}\psi_{i\sigma}-\sum_{ij}\overline{\psi}_{i\sigma}(\mathcal{K}_{ij}-\mu\delta_{ij})\psi_{j\sigma} +\frac{2}{U}(2-y)\sum_i\tilde{\Delta}_{si}^*(\tau)\tilde{\Delta}_{si}(\tau)+\frac{4y}{U}\sum_i\tilde{\Delta}_{ci}(\tau)^2-(2-y)\sum_i[\tilde{\Delta}_{si}^*(\tau)\overline{\psi}_{i\downarrow}\psi_{i\uparrow}+\tilde{\Delta}_{si}(\tau)\overline{\psi}_{i\uparrow}\psi_{i\downarrow}] -2iy\sum_i\tilde{\Delta}_{ci}(\tau)(\overline{\psi}_{i\uparrow}\psi_{i\uparrow}+\overline{\psi}_{i\downarrow}\psi_{i\downarrow}-1)\Bigg]\Bigg). \tag{2.130}$$

The variables $\tilde{\Delta}_s$ and $\tilde{\Delta}_c$ are called Stratonovich fields or Stratonovich variables. The normalization constants in Eqs. (2.129a) and (2.129b) are absorbed in $\mathcal{D}\tilde{\Delta}_c$ and $\mathcal{D}\tilde{\Delta}_s^*\mathcal{D}\tilde{\Delta}_s$. Although this is an identical transformation, a Stratonovich transformation of this type readily takes account of magnetic symmetry breaking, as we shall see below. The partition function may also be expressed only through $\tilde{\Delta}_{si}$ without introducing $\tilde{\Delta}_{ci}$ by using Eqs. (2.129a) and (2.37a)–(2.37d). These different choices should give the same result if the integration over the

SH variables Δ is rigorously performed. However, approximations like the mean-field approximation lead in general to different results.

In the Fourier-transformed form, the partition function is further rewritten by using the spinor notation

$$\bar{\Psi} \equiv (\bar{\psi}_\uparrow, \bar{\psi}_\downarrow), \tag{2.131a}$$

$$\Psi \equiv \begin{pmatrix} \psi_\uparrow \\ \psi_\downarrow \end{pmatrix}, \tag{2.131b}$$

in the form

$$Z = \int \mathcal{D}[\bar{\Psi}, \Psi]\, \mathcal{D}\tilde{\Delta}_s^* \mathcal{D}\tilde{\Delta}_s \mathcal{D}\tilde{\Delta}_c\, e^{-S}, \tag{2.132a}$$

$$S = \bar{\Psi} Q \Psi + \frac{2(2-y)}{U} \tilde{\Delta}_s^* \tilde{\Delta}_s + \frac{4y}{U} \tilde{\Delta}_c^2 + 2iy\tilde{\Delta}_c, \tag{2.132b}$$

$$Q = \begin{pmatrix} Q_{\uparrow\uparrow} + Q'_{\uparrow\uparrow} & Q_{\uparrow\downarrow} \\ Q_{\downarrow\uparrow} & Q_{\downarrow\downarrow} + Q'_{\downarrow\downarrow} \end{pmatrix}, \tag{2.132c}$$

with

$$Q_{\uparrow\uparrow}(k,k') = \delta_{kk'}(-i\omega_n + \varepsilon_0(\mathbf{k}) - \mu), \tag{2.133a}$$

$$Q_{\downarrow\downarrow}(k,k') = \delta_{kk'}(-i\omega_n + \varepsilon_0(\mathbf{k}) - \mu), \tag{2.133b}$$

$$Q_{\uparrow\downarrow}(k,k') = -(2-y)\tilde{\Delta}_s(k-k'), \tag{2.133c}$$

$$Q_{\downarrow\uparrow}(k,k') = -(2-y)\tilde{\Delta}_s^*(k-k'), \tag{2.133d}$$

$$Q'_{\uparrow\uparrow}(k,k') = Q'_{\downarrow\downarrow}(k,k') = -2iy\tilde{\Delta}_c(k-k'), \tag{2.133e}$$

where $k \equiv (\mathbf{k}, i\omega_n)$. In Eqs. (2.132a), (2.132b), and (2.132c), the products $\bar{\Psi} Q \Psi$ and $\tilde{\Delta}^* \tilde{\Delta}$ are abbreviated forms of the matrix products

$$\bar{\Psi} Q \Psi \equiv \frac{1}{(\beta V)} \sum_{\mathbf{k},\mathbf{k}'} \sum_{n,n'} \bar{\Psi}(\mathbf{k},\omega_n) Q(\mathbf{k},\omega_n;\mathbf{k}',\omega_{n'}) \times \Psi(\mathbf{k}',\omega_{n'})$$

and

$$\tilde{\Delta}^* \tilde{\Delta} \equiv \frac{1}{\beta V} \sum_{\mathbf{k}} \sum_{n} \tilde{\Delta}^*(\mathbf{k},\omega_n) \tilde{\Delta}(\mathbf{k},\omega_n),$$

respectively. The noninteracting dispersion $\varepsilon_0(\mathbf{k})$ is the Fourier transform of $\mathcal{K}$.

After Fourier transformation, $\tilde{\Delta}_c(k) = \tilde{\Delta}_c^*(-k)$ is satisfied. Therefore the functional integration over $\tilde{\Delta}_c(k)$ may be written as

$$\mathcal{D}\tilde{\Delta}_c \equiv \prod_k d\tilde{\Delta}_c(k) = d\Delta_c(\mathbf{k}=0, \omega_n=0) \times \prod_{\mathbf{k}} \prod_{\omega_n>0} d\tilde{\Delta}_c^*(\mathbf{k},\omega_n) d\tilde{\Delta}_c(\mathbf{k},\omega_n).$$

After integrating the Grassmann variables Ψ and $\bar{\Psi}$, we are led to

$$Z(\tilde{\Delta}) \equiv \int \mathcal{D}\tilde{\Delta}_s^* \mathcal{D}\tilde{\Delta}_s \mathcal{D}\tilde{\Delta}_c\, Z_Q(\tilde{\Delta}) e^{-S_\Delta}, \tag{2.134a}$$

$$\begin{aligned} Z_Q(\tilde{\Delta}) &\equiv \int \mathcal{D}\Psi\, \mathcal{D}\bar{\Psi}\, e^{-\bar{\Psi} Q \Psi} \\ &= \det Q = \exp[\ln \det Q_0 + \ln \det(1 + Q_0^{-1} Q_1)] \\ &= \exp[-\mathrm{Tr}\ \ln(-G_0) + \mathrm{Tr}\ \ln(1 - G_0 Q_1)], \end{aligned} \tag{2.134b}$$

$$S_\Delta \equiv \frac{2(2-y)}{U} \tilde{\Delta}_s^* \tilde{\Delta}_s + \frac{4y}{U} \tilde{\Delta}_c^2 + 2iy\tilde{\Delta}_c, \tag{2.134c}$$

where $\mathrm{Tr}\ \ln A = \ln \det A$ is used. In Eq. (2.132c), the matrix Q is decomposed to

$$Q = Q_0 + Q_1, \tag{2.135a}$$

$$Q_0 \equiv \begin{pmatrix} Q_{\uparrow\uparrow}(k,k'), & 0 \\ 0, & Q_{\downarrow\downarrow}(k,k') \end{pmatrix}, \tag{2.135b}$$

$$Q_1 \equiv \begin{pmatrix} Q'_{\uparrow\uparrow}(k,k') & Q_{\uparrow\downarrow}(k,k') \\ Q_{\downarrow\uparrow}(k,k') & Q'_{\downarrow\downarrow}(k,k') \end{pmatrix}. \tag{2.135c}$$

The noninteracting Green's function is defined as

$$G_0 = \begin{pmatrix} G_{0\uparrow} & 0 \\ 0 & G_{0\downarrow} \end{pmatrix}, \tag{2.136a}$$

$$G_{0\sigma}(k,k') = \delta_{kk'}(i\omega_n - \xi_0(\mathbf{k}))^{-1}, \tag{2.136b}$$

$$\xi_0 \equiv \varepsilon_0(\mathbf{k}) - \mu. \tag{2.136c}$$

$\tilde{\Delta}$ or $\tilde{\Delta}^*$-dependent terms of S have the form

$$\frac{2(2-y)}{U} \sum_k \tilde{\Delta}_s^*(k) \tilde{\Delta}_s(k) + \frac{4y}{U} \sum_{\substack{\mathbf{k} \\ \omega_n>0}} \tilde{\Delta}_c^*(k) \tilde{\Delta}_c(k) + \frac{4y}{U} \tilde{\Delta}_c(0)^2 + 2iy\tilde{\Delta}_c(0) - \mathrm{Tr}\ \ln[1 - G_0 Q_1]. \tag{2.137}$$

The mean-field (Hartree-Fock) approximation of the magnetic ordering is based on several approximations. The first important assumption is that only static fluctuations of $\tilde{\Delta}_s$ or $\tilde{\Delta}_c$ are important, so that $\tilde{\Delta}_{c,s}(\mathbf{k},\omega_n)$ at $\omega_n \neq 0$ may be ignored. This static approximation discards dynamic fluctuations though they are crucial in understanding anomalous features of metals near the Mott insulator. Another approximation in the Hartree-Fock theory is that it determines the static values $\tilde{\Delta}_c(\omega_n=0)$ and $\tilde{\Delta}_s(\omega_n=0)$ by the saddle-point approximation. More precisely, it is obtained by replacing the functional integral of e^{-S} over $\tilde{\Delta}$ and $\tilde{\Delta}^*$ with the saddle-point estimation of e^{-S} at $\Delta(0)$ and $\Delta^*(0)$ obtained from $\partial S/\partial \Delta^* = 0$. So far, we have discussed possible spin and charge fluctuations by introducing $\tilde{\Delta}_c$ and $\tilde{\Delta}_s$. Hereafter, for simplicity, we take $\Delta_c(0) \equiv y\tilde{\Delta}_c(0)$ and $\Delta_s(0) \equiv (2-y)\tilde{\Delta}_s(\mathbf{K})$ with the staggered antiferromagnetic ordering wave vector $\mathbf{k} = \mathbf{K}$. The condition of extremum is explicitly written as

$$\frac{\partial S}{\partial \Delta_s^*} = \frac{2\Delta_s}{U} + \mathrm{Tr}\left[(1 - G_0 Q_1)^{-1} G_0 \frac{\partial Q_1}{\partial \Delta_s^*(0)}\right] = 0 \tag{2.138a}$$

and

$$\frac{\partial S}{\partial \Delta_c^*}=\frac{4\Delta_c}{U}+\mathrm{Tr}(1-G_0Q_1)^{-1}G_0\frac{\partial Q_1}{\partial \Delta_c(0)}+2i=0. \tag{2.138b}$$

Equation (2.138a) is nothing but the self-consistent equation for magnetic ordering at the wave vector **K**, which may be rewritten as

$$\frac{\Delta_s(0)}{U}=\frac{1}{\beta V}\sum_{\mathbf{k},\omega_n}\frac{\Delta_s(0)}{(-i\omega_n+\varepsilon_0-\mu)(-i\omega_n-\varepsilon_0-\mu)-|\Delta_s(0)|^2} \tag{2.139}$$

or

$$\frac{\Delta_s(0)}{U}=\frac{1}{\beta V}\sum_{\mathbf{k},\omega_n}\frac{\Delta_s(0)}{(-i\omega_n+\sqrt{\varepsilon_0(\mathbf{k})^2+|\Delta_s(0)|^2}-\mu)}\times\frac{1}{(i\omega_n-\sqrt{\varepsilon_0(\mathbf{k})^2+|\Delta_s(0)|^2}-\mu)}. \tag{2.140}$$

where we have assumed $\varepsilon_0(\mathbf{k}+\mathbf{K})=-\varepsilon_0(\mathbf{k})$ as in the case of the antiferromagnetic order of the nearest-neighbor Hubbard model. The extension to more general cases is straightforward. The quasiparticle excitation from this broken-symmetry state is given by the dispersion

$$E(\mathbf{k})=\pm\sqrt{\varepsilon_0(\mathbf{k})^2+|\Delta_s(0)|^2}-\mu. \tag{2.141}$$

The saddle-point solution of $\Delta_c(0)$ for Eq. (2.138b) gives

$$\Delta_c(0)=\frac{Ui}{4}(\langle n\rangle-1) \tag{2.142}$$

where $\langle n\rangle$ is the average electron density. The single-particle Green's function in the Hartree-Fock approximation is

$$G_{\sigma\sigma'}(\mathbf{k},\omega_n;\mathbf{k}',\omega_{n'})\equiv -Q^{-1}=\frac{-1}{[-i\omega_n+\varepsilon_0(\mathbf{k})-\mu][-i\omega_n-\varepsilon_0(\mathbf{k})-\mu]-|\Delta_s(0)|^2}\times\begin{pmatrix}(-i\omega_n-\varepsilon_0-\mu)\,\delta_{\mathbf{k},\mathbf{k}'}\delta_{n,n'}, & \Delta_s(0)\,\delta_{\mathbf{k}',\mathbf{k}+\mathbf{K}}\delta_{n,n'}\\ \Delta_s(0)\,\delta_{\mathbf{k}',\mathbf{k}+\mathbf{K}}\delta_{n,n'}, & (-i\omega_n+\varepsilon_0-\mu)\,\delta_{\mathbf{k},\mathbf{k}'}\delta_{n,n'}\end{pmatrix},$$

where

$$G\equiv\begin{pmatrix}G_{\uparrow\uparrow} & G_{\downarrow\uparrow}\\ G_{\uparrow\downarrow} & G_{\downarrow\downarrow}\end{pmatrix}. \tag{2.143}$$

After the Bogoliubov transformation

$$\Gamma=\begin{pmatrix}\gamma_{\uparrow(k)}\\ \gamma_{\downarrow(k)}\end{pmatrix}=U\begin{pmatrix}\psi_\uparrow(k)\\ \psi_\downarrow(k)\end{pmatrix} \tag{2.144a}$$

with

$$U=\begin{pmatrix}u(k), & v(k)\\ -v(k), & u(k)\end{pmatrix}, \tag{2.144b}$$

and

$$u(k)^2=\frac{1}{2}\left(1+\frac{\varepsilon_0(k)}{E(k)}\right), \tag{2.144c}$$

$$v(k)^2=\frac{1}{2}\left(1-\frac{\varepsilon_0(k)}{E(k)}\right), \tag{2.144d}$$

the action (2.132b) in the Hartree-Fock approximation is diagonalized, using the quasiparticles γ, into the form

$$S_\gamma=\overline{\Gamma}Q_\gamma\Gamma+\frac{2}{U}|\Delta_s(0)|^2-\frac{U}{4}(n-1)(\langle n\rangle-1) \tag{2.145a}$$

$$Q_\gamma=\begin{pmatrix}Q_{\gamma\uparrow\uparrow} & 0\\ 0 & Q_{\gamma\downarrow\downarrow}\end{pmatrix}, \tag{2.145b}$$

$$Q_{\gamma\sigma\sigma}=\delta_{kk'}(-i\omega_n-\mu+\sigma E(\mathbf{k})). \tag{2.145c}$$

The Green's function for the quasiparticle is therefore

$$G_{\gamma\sigma\sigma'}(k,k')\equiv-\langle\gamma_\sigma(k)\overline{\gamma_\sigma}(k')\rangle=\delta_{\sigma\sigma'}\delta_{kk'}\frac{1}{i\omega_n+\mu-\sigma E(\mathbf{k})}. \tag{2.146}$$

We next discuss how the random-phase approximation is given by the Gaussian approximation for $\tilde{\Delta}_s$. The dynamic spin susceptibility defined by

$$\chi(q,\omega_m)=\frac{1}{4}\langle TS^+(q,\omega_m)S^-(q,\omega_m)\rangle \tag{2.147}$$

$$=\frac{1}{4\beta VZ}\int \mathcal{D}\tilde{\Delta}_s^*\mathcal{D}\tilde{\Delta}_s$$

$$\times e^{-S_\Delta}\frac{\partial^2}{\partial\tilde{\Delta}_s^*(q,\omega_m)\partial\tilde{\Delta}_s(q,\omega_m)}Z_Q(\tilde{\Delta}) \tag{2.148}$$

$$=\frac{1}{2\beta VU}\left(\frac{2}{U}\langle\tilde{\Delta}_s^*(q,\omega_m)\tilde{\Delta}_s(q,\omega_m)\rangle-\beta V\right) \tag{2.149}$$

is obtained from Eqs. (2.134a)–(2.134c) after partial integration. In the paramagnetic phase, up to second order in Q_1 for Eq. (2.134), we obtain

$$Z_Q(\tilde{\Delta})\simeq\exp[-\mathrm{Tr}\ \ln(-G_0)-\mathrm{Tr}\ G_0Q_1 -\mathrm{Tr}\ G_0Q_1G_0Q_1]. \tag{2.150}$$

The term linearly proportional to Q_1 (the second term) vanishes and the last term is

$$\mathrm{Tr}\ G_0Q_1G_0Q_1=8\sum_{\mathbf{q},m}\chi_b(\mathbf{q},\omega_m)\tilde{\Delta}_s^*(\mathbf{q},\omega_m)\tilde{\Delta}_s(\mathbf{q},\omega_m), \tag{2.151}$$

where $\chi_b(\mathbf{q},\omega_m)$ is the spin susceptibility at $U=0$. Therefore, combined with the term S_Δ in Eq. (2.134), $\langle\tilde{\Delta}_s^*\tilde{\Delta}_s\rangle$ is estimated as

$$\langle\tilde{\Delta}_s^*(\mathbf{q},\omega_m)\tilde{\Delta}_s(\mathbf{q},\omega_m)\rangle=\frac{U}{2}\beta V\frac{1}{1-2U\chi_b(\mathbf{q},\omega_m)}, \tag{2.152}$$

which leads to

$$\chi(\mathbf{q},\omega_m)=\frac{\chi_b(\mathbf{q},\omega_m)}{1-2U\chi_b(\mathbf{q},\omega_m)}. \tag{2.153}$$

This is nothing but the RPA result. The Hartree-Fock phase diagram calculated by using the above procedure is shown in Fig. 10 for the 3D nearest-neighbor Hubbard model (Penn, 1966) and in Fig. 11 for the 2D Hubbard model (Hirsch, 1985b). Here it is assumed that the ordering vector $\mathbf{K}$ is either antiferromagnetic [$\mathbf{K}=(\pi,\pi)$ or (π,π,π)] or ferromagnetic [$\mathbf{K}=(0,0)$ or $(0,0,0)$] with the lattice constant unity. The characteristic feature is a rather wide region of antiferromagnetic and ferromagnetic metals near the Mott insulator, $n=1$. We discuss more complicated types of spin or charge orderings in Sec. II.H.3 and IV.

So far we have restricted our choice of the Stratonovich-Hubbard transformation with Δ_s corresponding to the decoupling of $c_{i\uparrow}^\dagger c_{i\downarrow}^\dagger c_{i\downarrow}c_{i\uparrow}$ into $c_{i\uparrow}^\dagger c_{i\downarrow}$ and $c_{i\downarrow}^\dagger c_{i\uparrow}$ as in Eq. (2.129a). However, this transformation makes possible symmetry breaking only in the xy plane of the spin space. To retain the SU(2) symmetry even after the SH transformation, a vector SH field $\vec{\tilde{\Delta}}_s$ may be introduced (C. Herring, 1952; Capellmann, 1974, 1979; Korenman, Murray, and Prange, 1977a, 1977b, 1977c; Schulz, 1990c), in which case the partition function Z given in Eq. (2.130) is rewritten as

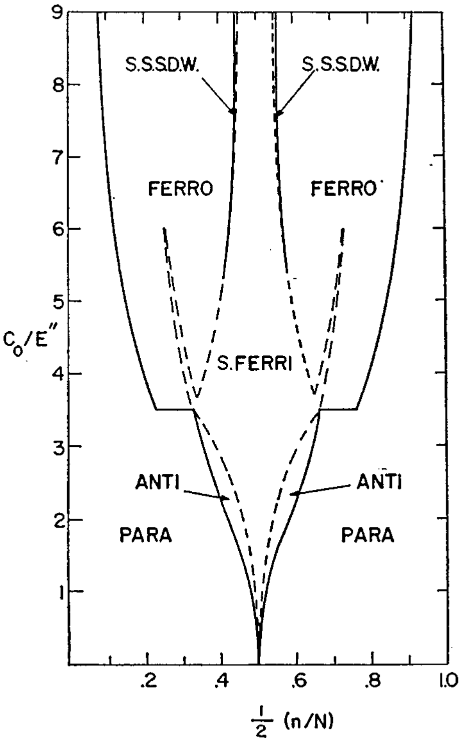

FIG. 10. Hartree-Fock phase diagram of three-dimensional nearest-neighbor Hubbard model in the plane of U and a half of filling $\langle n\rangle$ (Penn, 1966). Here the ordinate C_0/E'' represents $U/2t$ in our notation. ANTI, antiferromagnetic; PARA, paramagnetic; FERRO, ferromagnetic; S. FERRI, spiral ferrimagnetic; and S.S.SDW, spiral spin-density-wave phases.

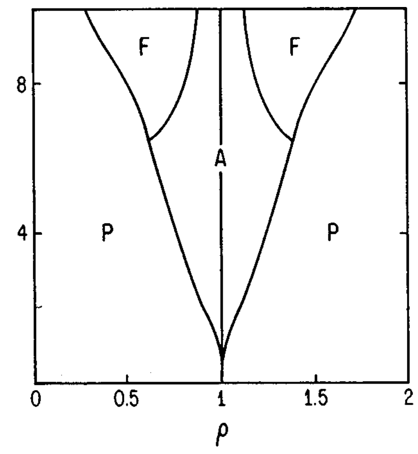

FIG. 11. Hartree-Fock phase diagram of two-dimensional nearest-neighbor Hubbard model in the plane of U/t and filling $\langle n\rangle\equiv\rho$ (Hirsch, 1985a, 1985b). P, A, and F represent paramagnetic, antiferromagnetic, and ferromagnetic phases, respectively. The possibility of incommensurate order is not considered here.

$$
\begin{aligned}
Z=\int & \mathcal{D}[\overline{\psi},\psi]\mathcal{D}\vec{\tilde{\Delta}}_{si}(\tau)\mathcal{D}\vec{\tilde{\Delta}}^{*}_{si}(\tau)\mathcal{D}\tilde{\Delta}_{ci}(\tau) \\
& \times\exp\Bigg[-\int_0^\beta d\tau\Bigg(\sum_i \overline{\psi}_{i\sigma}\frac{\partial}{\partial\tau}\psi_{i\sigma} \\
& -\sum_{ij} \overline{\psi}_{i\sigma}(\mathcal{K}_{ij}-\mu\delta_{ij})\psi_{j\sigma} \\
& +\frac{2(2-y)}{3U}\sum_i \vec{\tilde{\Delta}}^{*}_{si}(\tau)\cdot\vec{\tilde{\Delta}}_{si}(\tau) \\
& -\frac{(2-y)}{3}\sum_i (\vec{\tilde{\Delta}}^{*}_{si}\cdot\overline{\psi}_{i\sigma}\mathbf{S}_{\sigma\sigma'}\psi_{i\sigma'} \\
& +\vec{\tilde{\Delta}}_{si}(\tau)\cdot\overline{\psi}_{i\sigma}\mathbf{S}_{\sigma'\sigma}\psi_{i\sigma'})+\frac{4y}{U}\sum_i \tilde{\Delta}_{ci}(\tau)^2 \\
& -2iy\sum_i \tilde{\Delta}_{ci}(\tau)(\overline{\psi}_{i\uparrow}\psi_{i\uparrow}+\overline{\psi}_{i\downarrow}\psi_{i\downarrow}-1)\Bigg)\Bigg]
\end{aligned}
\tag{2.154}
$$

where $\vec{\tilde{\Delta}}_s\cdot\mathbf{S}_{\sigma\sigma'}$ is an internal product with

$$(\mathbf{S}_{\sigma\sigma'})_x=\delta_{\sigma\uparrow}\delta_{\sigma'\downarrow}+i\,\delta_{\sigma\downarrow}\delta_{\sigma\uparrow}\,, \tag{2.155a}$$

$$(\mathbf{S}_{\sigma\sigma'})_y=\delta_{\sigma\uparrow}\delta_{\sigma'\downarrow}-i\,\delta_{\sigma\downarrow}\delta_{\sigma\uparrow}\,, \tag{2.155b}$$

$$(\mathbf{S}_{\sigma\sigma'})_z=\frac{1}{2}(\delta_{\sigma\uparrow}\delta_{\sigma'\uparrow}-\delta_{\sigma\downarrow}\delta_{\sigma'\downarrow}). \tag{2.155c}$$

Here we note that Δ_{ci} is real while $\vec{\tilde{\Delta}}_{si}$ is a complex three-dimensional vector. In particular, $\vec{\tilde{\Delta}}_{si}$ is rewritten as

$$\vec{\tilde{\Delta}}_{si}=\Delta_{s0}e^{i\theta_i}\vec{n}_i \tag{2.156}$$

where Δ_{s0} is a scalar for the amplitude of this Hartree-Fock field while θ_i is the phase and $\vec{n}$ is the unit vector to specify the direction of $\vec{\tilde{\Delta}}_s$ in the 3D spin space. In the magnetically ordered phase, Δ_{s0} has a finite amplitude, so that the excitation of this amplitude mode has a finite gap. In contrast, θ_i and $\vec{n}_i$ represent the gapless excitation mode. Therefore low-energy excitations are exhausted by the excitations through θ and $\vec{n}$. Even when there is no symmetry breaking, provided that the correlation length is sufficiently long, the low-energy excitation can be described only through θ and $\vec{n}$. This is indeed the case for low-dimensional systems below the mean-field transition temperature T_{MF} where quantum fluctuations destroy the symmetry breaking while the amplitude itself is developed below T_{MF}. The low-energy action described by θ and $\vec{n}$ frequently contains topological terms that cause singular and nonlinear excitations in the continuum limit (for example, for 1D; Haldane, 1983a, 1983b). Except in the 1D case, the role of these topological terms, such as the Berry phase term, has not been fully clarified yet. We discuss the low-energy effective Hamiltonian for this case later.

The Hartree-Fock approximation is a self-consistent approach which satisfies microscopic conservation laws for particle number, energy, and momentum. Some higher-order diagrams were also considered in addition to the Hartree-Fock diagram so as to retain the above conservation laws (Bickers and Scalapino, 1989; Bickers and White, 1991), which may be viewed as an attempt to include perturbatively fluctuation effects that are ignored in the Hartree-Fock approximation. This is called the fluctuation exchange (FLEX) approximation.

3. Local-density approximation and its refinement

In a number of ways, as we see in this article, theoretical understanding of strongly correlated systems has been made possible through studies on effective lattice Hamiltonians derived from the tight-binding approximation for a small number of bands near the Fermi level. Although the simplification to effective tight-binding Hamiltonians is useful to elucidate many universal features of correlation effects, detailed experimental data such as those from photoemission often have to be analyzed from a more original Hamiltonian which contains more or less all the electronic orbitals in the continuum space under the periodic potential of the real lattice. This is because high-energy spectroscopy reflects the individual character of the compounds. Electronic structure calculations starting from atoms and electrons with their mutual Coulomb interactions in the continuum space are sometimes called first-principles calculations or *ab initio* calculations. The expected role of these first-principles calculations is not restricted to quantitative analyses of high-energy spectroscopy and the structural stability of lattices but is also extended to derive or justify starting effective Hamiltonians of simplified lattice fermion models for each compound and to bridge the gap between high- and low-energy physics. For example, band-structure calculations provide a generally accepted way of determining parameters of effective lattice models if carefully examined. It is also expected that the phase of the ground state will be correctly reproduced without introducing any parameter fitting. In fact, we describe below several treatments that have been successful in reproducing correct ground states of transition-metal compounds.

As it stands, “first-principles” calculation does not mean a rigorous, practical way of determining electronic structure, contrary to what one might imagine from its terminology. Basically, three types of approximations have been employed to make the “first principles” calculation tractable in practice.

One is the configuration-interaction (CI) method, in which small clusters under the atomic potential with all the relevant electronic orbitals are solved by the diagonalization of a Hamiltonian matrix. This method is exact but applicable only for small clusters, typically a few unit cells. Therefore it frequently underestimates the effect of electronic kinetic energy and coherence. We further discuss details of the configuration-interaction method in Sec. III.A.1. This method has a computational similarity to the exact diagonalization method reviewed in Sec. II.E.

The second type of approximation is the Hartree-Fock approximation, which is one of the best ways to approximate a true many-body fermion state by a single Slater determinant. By taking a single Slater determinant as a variational state of the many-body Hamiltonian

$$\mathcal{H} = -\sum_i \frac{\hbar^2}{2m_e}\Delta_i + \sum_i V_{lat}(\mathbf{r}_i) + \sum_{\langle ij\rangle} \frac{e^2}{|\mathbf{r}_i - \mathbf{r}_j|}, \tag{2.157}$$

one determines the single-particle state $\psi_l(\mathbf{r}_i)$ from the minimization of energy by solving the self-consistent equation

$$\left[-\frac{\hbar^2}{2m}\Delta + V_{lat}(\mathbf{r}) + \sum_{l'} \int d\mathbf{r}' \frac{e^2}{|\mathbf{r}-\mathbf{r}'|}|\psi_{l'}(\mathbf{r}')|^2\right]\psi_l(\mathbf{r}) - \sum_{l'}{}' \left[\int d\mathbf{r} \frac{e^2}{|\mathbf{r}-\mathbf{r}'|}\psi^*_{l'}(\mathbf{r}')\psi_l(\mathbf{r}')\right]\psi_{l'}(\mathbf{r}) = \varepsilon_l \psi_l(\mathbf{r}). \tag{2.158}$$

Here, l and l' specify quantum numbers including orbital degrees of freedom, and the sum Σ' is taken only over l', which has the same spin as that of l. The atomic periodic potential of the lattice is denoted as an external one by V_{lat}. The electron-electron Coulomb interaction is considered through the third term, the Hartree term, and the fourth (last) term, the exchange term. The exchange term can be rewritten as

$$V^l_{ex}(\mathbf{r})\psi_l(\mathbf{r}), \tag{2.159}$$

$$V^l_{ex}(\mathbf{r}) = \int d\mathbf{r}' \rho^l_{ex}(\mathbf{r},\mathbf{r}') \frac{e^2}{|\mathbf{r}-\mathbf{r}'|} \tag{2.160}$$

with

$$\rho^l_{ex}(\mathbf{r},\mathbf{r}') = -\frac{\psi^*_l(\mathbf{r})\psi_l(\mathbf{r}')\Sigma'_{l'}\psi^*_{l'}(\mathbf{r}')\psi_{l'}(\mathbf{r})}{|\psi_l(\mathbf{r})|^2} \tag{2.161}$$

where the exchange interaction is expressed as if it were a static Coulomb term. A computational difficulty of the Hartree-Fock approximation is that the exchange potential $V^l_{ex}(\mathbf{r})$ depends on the solution $\psi_l(\mathbf{r})$ itself, and different exchange potentials must be taken for each quantum number l while the number of states l to be considered increases linearly with the system size. It should be noted that the Hartree-Fock approximation does not take into account correlations between electrons with different spins and hence an up-spin electron behaves independently of the down-spin electrons if there is no symmetry breaking of spins such as the spin-density wave state as in Sec. II.D.2. To take into account short-ranged correlation effects of opposite-spin electrons, which is important in strongly correlated systems, one has to go beyond the Hartree-Fock approximation.

The third approximation is the local-density approximation, which gives a basic starting point for widely used band-structure calculations. The local-density approximation is based on the density-functional theory of Hohenberg, Kohn, and Sham (Hohenberg and Kohn, 1964; Kohn and Sham, 1965). A general and exact statement of the density-functional theory is that the true ground-state energy is obtained by two steps: First, one finds the many-body state $\Psi[n(\mathbf{r})]$ that minimizes the expectation value of the total many-body Hamiltonian, $E_g[n(\mathbf{r})]$, under given single-particle density $n(\mathbf{r})$. Second one minimizes $E_g[n(\mathbf{r})]$ as a functional of $n(\mathbf{r})$. An important point is the existence of the energy functional $E_g[n(\mathbf{r})]$. Of course these two steps are difficult to perform in practice. A basic underlying assumption in practical applications of the Kohn-Sham theory is that $E_g[n(\mathbf{r})]$ can be calculated by starting from single-particle states given by a single Slater determinant that reproduces $n(\mathbf{r})$, with this single-particle state being obtained as a solution of the Schrödinger equation

$$\left(-\frac{\hbar^2}{2m}\Delta + V(\mathbf{r})\right)\psi_l(\mathbf{r}) = \varepsilon_l\psi_l(\mathbf{r}) \tag{2.162}$$

with $V(\mathbf{r})$ chosen to give

$$n(\mathbf{r}) = \sum_l |\psi_l(\mathbf{r})|^2. \tag{2.163}$$

We discuss this procedure in greater detail below. In the original many-body problem, the ground-state energy is obtained through minimization of the energy expectation value

$$E[n(\mathbf{r})] = \langle\Psi[n(\mathbf{r})]|\mathcal{H}_K + \mathcal{H}_{ext} + \mathcal{H}_U|\Psi[n(\mathbf{r})]\rangle \tag{2.164}$$

with respect to variations of both $\Psi[n(\mathbf{r})]$ and the density functional $n(\mathbf{r})$, where $\Psi[n(\mathbf{r})]$ is a many-body wave function $\Psi(\mathbf{r}_1,\mathbf{r}_2,\ldots,\mathbf{r}_N)$ that satisfies

$$\int d\mathbf{r}_2\, d\mathbf{r}_3,\ldots,d\mathbf{r}_N|\Psi[n(\mathbf{r})]|^2 = n(\mathbf{r}_1). \tag{2.165}$$

The kinetic energy, interaction energy, and external atomic potential are denoted as $\mathcal{H}_K$, $\mathcal{H}_U$, and $\mathcal{H}_{ext}$, respectively. After minimization with respect to Ψ with fixed $n(\mathbf{r})$, the minimum in terms of $n(\mathbf{r})$ is obtained from

$$\frac{\delta E_g[n(\mathbf{r})]}{\delta n(\mathbf{r})} = 0, \tag{2.166}$$

where $E_g[n(\mathbf{r})]$ is the minimized value with respect to Ψ. An important point here is that, in this step, the ground-state energy is calculated only from the energy functional $E_g[n(\mathbf{r})]$ without any detailed knowledge of the many-body wave function. Of course, the functional form of E_g is not easy to obtain.

When we can assume that the first minimization procedure to obtain $E_g[n(\mathbf{r})]$ may be performed within the single Slater determinant under an appropriate fictitious external potential $V(\mathbf{r})$, the minimization may be performed from the minimization of the energy functional,

$$E[n(\mathbf{r})] = E_K[n(\mathbf{r})] + \int d\mathbf{r}\, V_{lat}(\mathbf{r})n(\mathbf{r}) + \frac{e^2}{2}\int d\mathbf{r}\, d\mathbf{r}' \frac{n(\mathbf{r})n(\mathbf{r}')}{|\mathbf{r}-\mathbf{r}'|} + \int d\mathbf{r}\, V_{ex}(\mathbf{r})n(\mathbf{r}), \tag{2.167}$$

with

$$V_{ex}(\mathbf{r}) \equiv \int d\mathbf{r}'\, \rho_{ex}(\mathbf{r},\mathbf{r}')\, \frac{e^2}{|\mathbf{r}-\mathbf{r}'|}, \tag{2.168}$$

$$\rho_{ex}(\mathbf{r},\mathbf{r}') \equiv \sum_l \frac{|\psi_l(\mathbf{r})|^2}{n(\mathbf{r})} \rho^l_{ex}(\mathbf{r},\mathbf{r}'). \tag{2.169}$$

Here, the first term of Eq. (2.167), E_K, is the kinetic-energy term written as a functional of $n(\mathbf{r})$. For example, E_K is given from Eq. (2.162) as

$$E_K = \sum_l \, [\varepsilon_l - \langle \psi_l | V(\mathbf{r}) | \psi_l \rangle]. \tag{2.170}$$

The sum over l in Eq. (2.170) is taken to fill the lowest N levels of ε_l for an N-particle system.

However, the assumption that $E_g[n(\mathbf{r})]$ may be obtained within the single Slater determinant is in general not justified in correlated systems. Therefore we leave the form of $V_{ex}(\mathbf{r})$ unknown and just define it as the difference between the true ground-state energy and the contribution from the first three terms in Eq. (2.167). The point is that $V_{ex}(\mathbf{r})$ is still represented by a functional of $n(\mathbf{r})$. We also note, however, that there exists no proof that $V(\mathbf{r})$ always exists, though its existence is necessary in this procedure, and in this approach it is assumed to exist. The minimization of Eq. (2.167) in terms of the functional $n(\mathbf{r})$ gives the condition

$$-\frac{\delta E_K}{\delta n(\mathbf{r})} = V_{lat}(\mathbf{r}) + e^2 \int d\mathbf{r}'\, \frac{n(\mathbf{r}')}{|\mathbf{r}-\mathbf{r}'|} + \frac{\delta}{\delta n(\mathbf{r})} \int d\mathbf{r}\, V_{ex}(\mathbf{r}) n(\mathbf{r}). \tag{2.171}$$

The ground-state energy is obtained by solving the Kohn-Sham equations (2.162), (2.163), and (2.171) self-consistently, if we know the functional dependence of $V_{ex}(\mathbf{r})$ on $\{n(\mathbf{r})\}$. In general, the exchange potential $V_{ex}(\mathbf{r})$ depends on $n(\mathbf{r}')$ for $\mathbf{r} \neq \mathbf{r}'$ in a nonlocal fashion. The local-density approximation (LDA) assumes that $V_{ex}(\mathbf{r})$ is determined only by $n(\mathbf{r}')$ at $\mathbf{r}'=\mathbf{r}$. This assumption may be justified when effects of spatial variations of the electron density may be neglected in the exchange potential, so that $V_{ex}(\mathbf{r})$ is calculated from the uniform electron gas with density $n(\mathbf{r})$. This condition for justification is explicitly given as

$$\frac{\nabla n(\mathbf{r})}{k_F(\mathbf{r}) n(\mathbf{r})} \ll 1 \tag{2.172}$$

provided that the Fermi wave number k_F can be described as a local variable under the same assumption of slow modulation of the electron density.

Because we have left $V_{ex}(\mathbf{r})$ just as the difference of the true ground-state energy and the contribution from the first three terms in Eq. (2.167), it has to be calculated from other explicit calculations taking account of the correlation effects honestly. This is usually done by using the quantum Monte Carlo result (Ceperley and Alder, 1980) of the ground-state energy for a uniform electron gas with density $n(\mathbf{r})$ (Perdew and Zunger, 1981). From the difference between the Monte Carlo result and the corresponding energy for the first three terms of Eq. (2.167), V_{ex} is estimated.

The practical difficulties of applying the density-functional procedure to strongly correlated systems can be appreciated from the difficulty of calculating $V_{ex}(\mathbf{r})$, into which all the many-body effects are squeezed. The assumption that $V_{ex}(\mathbf{r})$ is determined from the local density $n(\mathbf{r})$ is in general not satisfied in strongly correlated systems.

Failure of the LDA calculation is widely observed in the Mott insulating phase of many transition-metal compounds as well as in phases of correlated metals near the Mott insulator. MnO, NiO, NiS, $YBa_2Cu_3O_6$, and La_2CuO_4 are well known examples of the LDA's inability to reproduce the insulating (or semiconducting) phase (Terakura, Oguchi, Williams, and Küller, 1984; Pickett, 1989; Singh and Pickett, 1991).

To improve the LDA, several different approaches have been taken. The local spin-density approximation (LSDA) explicitly introduces the spin-dependent electron densities $n_\uparrow(\mathbf{r})$ and $n_\downarrow(\mathbf{r})$ separately, to allow for possible spin-density waves or antiferromagnetic states (von Barth and Hedin, 1972; Perdew and Zunger, 1981). Instead of Eq. (2.167), the exchange-correlation energy $\int d\mathbf{r} V_{ex}(\mathbf{r}) n(\mathbf{r})$ is replaced with $\int d\mathbf{r}[n_\uparrow(\mathbf{r}) + n_\downarrow(\mathbf{r})] V_{ex}[n_\uparrow(\mathbf{r}), n_\downarrow(\mathbf{r})]$ in the LSDA, where V_{ex} is taken as a functional of both $n_\uparrow(\mathbf{r})$ and $n_\downarrow(\mathbf{r})$. Correspondingly, the Kohn-Sham equations (2.162), (2.163), (2.170), and (2.171), which need to be solved self-consistently, are replaced with spin-dependent forms,

$$\left(-\frac{\hbar^2}{2m} \Delta + V_\sigma(\mathbf{r}) \right) \psi_{l\sigma}(\mathbf{r}) = \varepsilon_{l\sigma} \psi_{l\sigma}(\mathbf{r}), \tag{2.173}$$

$$n_\sigma(\mathbf{r}) = \sum_l |\psi_{l\sigma}(\mathbf{r})|^2, \tag{2.174}$$

$$n(\mathbf{r}) = \sum_\sigma n_\sigma(\mathbf{r}), \tag{2.175}$$

$$E_K = \sum_{l\sigma} (\varepsilon_{l\sigma} - \langle \psi_{l\sigma} | V_\sigma(\mathbf{r}) | \psi_{l\sigma} \rangle), \tag{2.176}$$

$$-\frac{\delta_{E_K}}{\delta n_\sigma(\mathbf{r})} = V_{lat}(\mathbf{r}) + e^2 \int d\mathbf{r}'\, \frac{n(\mathbf{r}')}{|\mathbf{r}-\mathbf{r}'|} + \frac{\delta}{\delta n_\sigma(\mathbf{r})} \int d\mathbf{r}\, V_{ex}(\mathbf{r}) n(\mathbf{r}). \tag{2.177}$$

In the LSDA, $V_{ex}(\mathbf{r})$ is assumed to be determined only from the local spin densities $n_\uparrow(\mathbf{r}')$ and $n_\downarrow(\mathbf{r}')$ at $\mathbf{r}'=\mathbf{r}$, and usually V_{ex} is given from the energy difference between the quantum Monte Carlo result and the single-particle solution as in the LDA. For example, the LSDA succeeds in reproducing the presence of the band gap at the Fermi level for MnO by allowing antiferromagnetic order (Terakura, Oguchi, Williams, and Küller, 1984). It also succeeds in reproducing the antiferromagnetic insulating state of $LaMO_3$ (M=Cr,Mn,Fe,Ni) (Sarma *et al.*, 1995).

However, the LSDA fails to reproduce the antiferromagnetic ground state of many strongly correlated compounds such as NiS, La_2CuO_4, $YBa_2Cu_3O_6$, $LaTiO_3$, and $LaVO_3$. Even in MnO, strongly insulating behavior observed well above the Néel temperature implies that the charge-gap structure is not a direct consequence of antiferromagnetic order, although antiferromagnetic order is needed to open a gap in the LSDA calculation.

The LDA band-structure calculation makes a drastic approximation in that the exchange-correlation energy $V_{ex}(\mathbf{r})$ is determined only from the local electron density $n(\mathbf{r})$. When the electron density $n(\mathbf{r})$ has a strong spatial dependence, this approximation breaks down. This is indeed the case for strongly fluctuating spin and charge degrees of freedom in correlated metals. To improve this local-density approximation, the gradient expansion of $n(\mathbf{r})$ may be considered to take into account the nonlocal dependence of $V_{ex}(\mathbf{r})$ on $n(\mathbf{r}')$, where $\mathbf{r}' \neq \mathbf{r}$. Langreth and Mehl (1983), Perdew and Wang (1986), Perdew (1986), and Becke (1988) developed a way of including the gradient expansion of $n(\mathbf{r})$ in the exchange energy by keeping the constraint of negative density of the exchange hole everywhere in space with a total deficit of exactly one electron. This is called the generalized gradient approximation (GGA) method. It was applied to reproduce the bcc ferromagnetic phase of Fe by Bagno, Jepsen, and Gunnarson (1989). Recently this method was applied to the transition-metal compounds FeO, CoO, FeF_2, and CoF_2 with partial improvements of the LDA results. It was also applied to transition-metal oxides with 3D perovskite structure, $LaVO_3$, $LaTiO_3$, and YVO_3 (Sawada, Hamada, Terakura, and Asada, 1996). It showed improvements in reproducing the band gap in $LaVO_3$, but the ground state was not correct for YVO_3 and $LaTiO_3$.

A serious problem in LDA and LSDA calculations is that the self-interaction is not canceled between the contributions from the Coulomb term and the exchange interaction term because of the drastic approximation in the exchange-interaction term. This produces a physically unrealistic self-interaction, which makes the approximation poor for strongly correlated systems. Perdew and Zunger (1981) proposed imposing a constraint to remove the self-interaction. This method of self-interaction correction (SIC) was applied to the Hubbard model as well as to models of transition-metal oxides with quantitative improvement of the band gap and the magnetic moment for MnO, FeO, CoO, NiO, and CuO (Svane and Gunnarsson, 1988a, 1988b, 1990).

In principle, the Kohn-Sham equation provides the procedure to calculate exactly the ground state at the Fermi level. However, it does not guarantee that excitations will be well reproduced. A possible way of improving estimates for the excitation spectrum is to combine the Kohn-Sham equation with a standard technique for many-body systems by introducing the self-energy correction to the single-particle Green's function obtained from LDA-type calculations. This attempt is called the "GW" approximation (Hedin and Lundqvist, 1969). It was applied to NiO (Aryasetiawan, 1992), although systematic studies on transition-metal compounds are not available so far (for a review, see Aryasetiawan and Gunnarsson, 1997). Effects of local three-body scattering on the self-energy correction have also been examined (Igarashi, 1983).

To counter the general tendency to underestimate the band gap of the Mott insulator in LDA-type calculations, a combination of the LDA and a Hartree-Fock-type approximation called the LDA+U method was proposed (Anisimov, Zaanen, and Andersen, 1991). The Coulomb interaction for double occupancy of the same site as in the Hubbard model requires a large energy U if the eigenstate is localized as compared to extended states. This is not correctly taken into account in the LDA calculation, which estimates the exchange interaction using information from the uniform electron gas, which is appropriate only for extended wave functions. In the LDA+U approach the contribution of the interaction proportional to U is added to the LDA energy in an *ad hoc* way when the orbital is supposed to be localized. The method thus combines arbitrariness in specifying the localized orbital with a drastic approximation in the treatment of the U term (for example, the Hartree-Fock approximation was used.) The LDA+U method has the same difficulty as the other many-body approaches in the tight-binding Hamiltonian because it does not necessarily provide a reliable way of treating U term, while, in a sense, all the important effects of strong correlation are relegated to this term. Another problem of this method is that the estimate of U may depend on the choice of the basis (Pickett *et al.*, 1996). Different choices of local atomic orbitals such as the linear muffin-tin orbital (LMTO) and linear combination of atomic orbitals (LCAO) give different U because the definition of the orbital becomes ambiguous whenever there is strong hybridization.

To take account of frequency-dependent fluctuations ignored in the LDA method, Anisimov *et al.* combined the LDA method with the dynamic mean-field approximation (the $d=\infty$ method described in Sec. II.D.6; Anisimov *et al.*, 1997). They treated strongly correlated bands by the dynamic mean-field approximation and described other itinerant bands by the LDA with a linear muffin-tin orbital basis. Recently, the exchange-correlation energy functional was calculated as the sum of the exact exchange energy and a correlation energy given from the RPA without introducing the local-density approximation (Kotani, 1997).

As we have seen above, in this decade substantial progress has been achieved in the band-structure calculation of transition-metal compounds. However, it is still not sufficient to reproduce the Mott insulator correctly in strongly correlated materials such as La_2CuO_4 and $YBa_2Cu_3O_6$. A more serious problem lies in the description of the metallic state near the Mott insulator, where spin and charge fluctuations play crucial roles even in the ground state, while the band-structure calculation has difficulty in including such fluctuation effects. For example, the continuous MIT should be described by the continuous reduction of coherent excitation when approaching the insulator, while the available approaches mentioned in this subsection fail to describe important contributions from the increasing weight of incoherent part.

4. Hubbard approximation

To gain insight into the original suggestion by Mott, Hubbard (1963) developed the coherent-potential approximation (CPA), which is combined with a Hartree-Fock-type approximation to address the problem of the metal-insulator transition. The CPA is a technique developed to treat the effects of random potentials (see, for example, Lloyd and Best, 1975), which Hubbard had already developed before its widespread application (see also Kawabata, 1972). In the Hubbard approximation, the Stratonovich-Hubbard transformation, using only the charge fluctuations $\tilde{\Delta}_{ci}(\tau)$ in Eq. (2.130), is employed to obtain a static approximation represented by the Stratonovich-Hubbard field; the static field is regarded as a random potential in the CPA. Below some details of the Hubbard approximation are given.

In the CPA, the τ dependence of $\tilde{\Delta}_c(r,\tau)$ is neglected in the same way as in the Hartree-Fock approximation. After integrating out the Grassmann variables, one replaces $\tilde{\Delta}_c(r,\tau)$ with the τ-independent constants $\Delta_c(r)$, which is called the static approximation. In contrast to the Hartree-Fock approximation, $\Delta_c(r)$ is assumed to take more than one value $\tilde{\Delta}_c^{(l)}$ $(l=1,2,\ldots)$ in a random way from site to site. In fact, in the Hubbard approximation, two values 0 and $U_i/4$ are assumed for $\tilde{\Delta}_c$. These two values are obtained from the saddle-point solution (2.142) if we take either $\langle n\rangle=1$ or $\langle n\rangle=2$. These two values can intuitively be understood because an electron at a doubly occupied site feels a static interaction potential U while its potential is absent for a singly occupied site if all the other electrons are frozen so that dynamic effects can be neglected. (As we shall see later in this subsection, in the CPA, dynamic effects are partially taken into account in another way by introducing afterwards an ω-dependent self-energy Σ as determined variationally in the single-particle excitation spectrum.) As in Eq. (2.130) the partition function is first assumed to have the form

$$Z=\sum_l Z_l, \tag{2.178a}$$

$$Z_l=P_l\prod_\sigma \int \mathcal{D}\psi_\sigma \mathcal{D}\bar{\psi}_\sigma \exp\bigg[-\int dx\,\bar{\psi}_\sigma(x)\frac{\partial}{\partial\tau}\psi_\sigma(x) -\int dx\,\bar{\psi}_\sigma(x)(\mathcal{K}-\mu)\psi_\sigma(x) +4i\tilde{\Delta}_c^{(l)}(n_\uparrow(x)+n_\downarrow(x)-1)-\frac{4}{U}\tilde{\Delta}_c^{(l)2}\bigg], \tag{2.178b}$$

where the spatial (or wave-number) dependence of the self-energy is neglected. The probability to have the value $\tilde{\Delta}_c^{(l)}$ is denoted by P_l. Originally, P_l was determined from the Gaussian approximation obtained from $\exp[-S_\Delta]$ with S_Δ in Eq. (2.134c). However, in the Hubbard approximation, as we describe below, P_l is taken rather differently, in order to consider nonlinear fluctuations ignored in the Gaussian approximation. We shall see in Sec. II.D.6 that Σ is not dependent on wave number in infinite dimensions, although, in general, it is wave-number dependent in finite dimensions. Although $\Sigma(\tau)$ is exactly calculated in infinite dimensions in Sec. II.D.6, the Hubbard approximation calculates it only approximately as follows: The partition function (2.178a) is rewritten in the same manner as Eq. (2.134),

$$Z_l=P_l\exp[-\mathrm{Tr}\,\ln(-G_0)+\mathrm{Tr}\,\ln(1-G_0Q_{1l})] \tag{2.179}$$

with

$$Q_{1l}=-4i\begin{pmatrix}\tilde{\Delta}_c^{(l)} & 0\\ 0 & \tilde{\Delta}_c^{(l)}\end{pmatrix}. \tag{2.180}$$

This may be rewritten as

$$Z_l=P_l\exp\{-\mathrm{Tr}[\ln(-G)-\ln(1-G(Q_{1l}-\Sigma))]\}, \tag{2.181}$$

where the Green's function G has the form

$$G^{-1}(\mathbf{k},\omega_n)=G_0^{-1}(\mathbf{k},\omega_n)-\Sigma(\omega_n), \tag{2.182}$$

with ω-dependent self-energy Σ. Now the on-site Green's function $G_{loc}(\omega_n)$ is defined as

$$G_{loc}(\omega_n)=\sum_{\mathbf{k}} G(\mathbf{k},\omega_n). \tag{2.183}$$

Then, to include locally tractable and averaged effects in the second term of Eq. (2.181), we rewrite it as

$$Z_l=P_l\exp[-\mathrm{Tr}\{\ln(-G)-\ln[1-G_{loc}(Q_{1l}-\Sigma)] -\ln[1-(G-G_{loc})\mathcal{T}_l]\}], \tag{2.184}$$

where $\mathcal{T}_l$ is a t matrix,

$$\mathcal{T}_l=(Q_{1l}-\Sigma)[1-G_{loc}(Q_{1l}-\Sigma)]^{-1}. \tag{2.185}$$

The CPA is regarded as the lowest-order expansion of the t matrix, since it neglects the last term in (2.184). Since it determines Σ in a variational way, the condition for determining Σ is $\partial Z/\partial\Sigma=0$. This leads to

$$\sum_l Z_l\mathrm{Tr}\left\{\left(G_{loc}^2-\frac{\partial G_{loc}}{\partial\Sigma}\right)\mathcal{T}_l\right\}=0, \tag{2.186}$$

from which we obtain the self-consistent equation for the self-energy,

$$\Sigma=\sum_{l} Z_l Q_{1l}\{1-G_{loc}(Q_{1l}-\Sigma)\}^{-1} \Big/ \sum_{l} Z_l\{1-G_{loc}(Q_{1l}-\Sigma)\}^{-1}. \tag{2.187}$$

In the case of the Hubbard approximation for the nearest-neighbor Hubbard model at half filling, $Q_{11}=0$, $Q_{12}=U$, $P_1=1/2$, and $P_2=1/2$, where the number of l's is taken as two. When Σ is determined by solving Eq. (2.187), Z is obtained from Eq. (2.184) by putting $\mathcal{T}_l=0$. The procedure of the Hubbard approximation is summarized as follows:

(1) Take a variational form of G and Σ.

(2) Calculate G_{loc} using Eq. (2.183) and Z_l using Eq. (2.184).

(3) Calculate Σ from Eq. (2.187) by substituting the present form of Σ, G_{loc}, and Z_l in the right-hand side.

(4) Using the form of Σ obtained in step (3), calculate G from Eq. (2.182).

(5) From the form of G and Σ determined in steps (3) and (4), repeat the process from step (2) again until the iteration converges.

Because an electron feels the static potential of 0 or U in the static approximation, it is rather obvious that it succeeds in splitting the band into the so-called upper and lower Hubbard bands for the Mott insulating phase, as shown in the bottom of Fig. 13 for large U, while it merges to a singly connected band for small U, as shown in the top panel of Fig. 13.

We shall see in Sec. II.D.6 that the solution in infinite dimensions is similar for the insulating phase, i.e., for large U. This is because dynamic charge fluctuations neglected in the Hubbard approximation are irrelevant in the insulating phase. We shall also see in Sec. II.D.6 that Σ can be determined rigorously in infinite dimensions by introducing dynamic mean fields instead of static charge-Stratonovich variables. In the metallic phase, neglect of the dynamic charge fluctuations in the Hubbard approximation is not at all justified.

A related problem in the Hubbard approximation is that spin fluctuations are not taken into account because it starts from the Stratonovich-Hubbard transformation, in which there is decomposition only in the charge density. In Sec. II.D.8, we discuss a similar type of CPA developed for the case of decomposition into spin density fluctuations. A crucial drawback of the Hubbard approximation in the metallic phase is that the Fermi volume is small for small doping away from the Mott insulator, which does not satisfy the Luttinger requirement of large Fermi volume for the Fermi-liquid description.

5. Gutzwiller approximation

The Gutzwiller approximation (Gutzwiller, 1965) was first applied to the MIT problem by Brinkman and Rice (1970). This approach is based on two stages of approximation. We discuss the case of the Hubbard model [Eqs. (1.1a)–(1.1d)] here. First, it employs a variational wave function of the form

$$|\Psi\rangle=\prod_{j}(1-gn_{j\uparrow}n_{j\downarrow})|\Phi\rangle, \tag{2.188}$$

where Φ is a single-particle state represented by a Slater determinant and g is a variational parameter to take into account the reduction of double occupancy of electrons at the same site. The free-fermion determinant was originally taken as the Slater determinant. It may be generalized to cases with other types of single Slater determinant where some symmetry is broken, as in the spin-density wave state or in the superconducting state. The ground-state energy

$$E_g=\langle\Psi|\mathcal{H}|\Psi\rangle/\langle\Psi|\Psi\rangle \tag{2.189}$$

is estimated from optimization of the parameter g and the choice of a single Slater determinant. This estimate satisfies the variational principle and hence gives the upper bound of the ground-state energy.

Then an additional approximation is introduced to estimate the ground state. When one assumes the number of doubly occupied sites D, the interaction energy is exactly given by $\langle\Psi|\mathcal{H}_U|\Psi\rangle/\langle\Psi|\Psi\rangle=DU$. However, the kinetic energy $\langle\Psi|\mathcal{H}_t|\Psi\rangle/\langle\Psi|\Psi\rangle$ is difficult to estimate analytically. By neglecting the spin and charge short-ranged correlation, one can calculate the energy as a function of D and g for a given system size N and number of up spins $N_\uparrow$ and down spins $N_\downarrow$. With $\overline{\varepsilon_\sigma}=\langle\Phi|\mathcal{H}_t|\Phi\rangle$, the optimization in terms of g at half filling gives

$$\frac{E_g}{N}=q(\overline{\varepsilon_\uparrow}+\overline{\varepsilon_\downarrow})+Ud, \tag{2.190}$$

where $d\equiv D/N$ and $q=8d(1-2d)$. From minimization with respect to d, we obtain

$$\frac{E_g}{N}=-|(\overline{\varepsilon_\uparrow}+\overline{\varepsilon_\downarrow})|(1-U/U_c)^2 \tag{2.191}$$

with $U_c=8|\overline{\varepsilon_\uparrow}+\overline{\varepsilon_\downarrow}|$ at $U<U_c$, while at $U>U_c$, the insulating state with $g=1$ is stabilized with $E_g=0$. As the MIT point $U=U_c$ is approached, the renormalization factor $Z=q=m/m^*$ is renormalized to zero as $q=1-(U/U_c)^2$. For details of the derivation, readers are referred to Vollhardt (1984). In the Gutzwiller approximation, the uniform magnetic susceptibility χ_s, the charge susceptibility χ_c, and the effective mass m^* follow

$$\chi_s\propto(1-U/U_c)^{-1}, \tag{2.192}$$

$$m^*/m_b\propto(1-U/U_c)^{-1}, \tag{2.193}$$

$$\chi_c\propto(1-U/U_c), \tag{2.194}$$

in the metallic region $U<U_c$. The MIT scenario of the Gutzwiller approximation is described by mass divergence within the Fermi liquid. The Gutzwiller approxi-

mation ignores the wave-number dependence of the self-energy as well as the incoherent part of the excitations.

Away from half filling, for the doping concentration δ (i.e., $n_\uparrow \equiv N_\uparrow/N = n_\downarrow \equiv N_\downarrow/N = \frac{1}{2} - \delta$), E_g is given by

$$\frac{E_g}{N} = q(\overline{\varepsilon_\uparrow} + \overline{\varepsilon_\downarrow}) + Ud \tag{2.195}$$

with

$$q = \frac{(1/2 + \delta - d)(\sqrt{-2\delta + d} + \sqrt{d})^2}{1/4 - \delta^2}. \tag{2.196}$$

This is minimized at $d = r\delta$ with $r = [(\gamma+2)y - 1]/2$ and $y = [-(\gamma+2) + 2\sqrt{\gamma^2 + 4\gamma + 1}]/[\gamma(\gamma+4)]$ where $\gamma = 4(U/U_c - 1)$. At $U > U_c$, we obtain

$$\frac{E_g}{N} = (\overline{\varepsilon_\uparrow} + \overline{\varepsilon_\downarrow})(r + 1 + y)(4\delta + 8(1+r)\delta^2) - Ur\delta + O(\delta^3) \tag{2.197}$$

for $\delta \ll 1$. Therefore the FC-MIT takes place at $U > U_c$ at $\delta = 0$ with a change in δ. At $U > U_c$, q has the form $q = q_1\delta + q_2\delta^2$ with

$$q_1 \propto (U - U_c)^{-1/2} \tag{2.198}$$

near $U = U_c$. The charge susceptibility

$$\chi_c = \left[\frac{1}{N}(\partial^2 E_g/\partial\delta^2)\right]^{-1}$$

remains finite at $\delta \neq 0$ and $\lim_{\delta\to+0}\chi_c = p/[16(\overline{\varepsilon_\uparrow} + \overline{\varepsilon_\downarrow})]$ with $p = \gamma^2/[(1+\gamma)^2 - \sqrt{\gamma^2 + 4\gamma + 1}]$ for $U > U_c$. At $U = U_c$, the charge susceptibility has an exponent given by $\chi_c \propto \delta^{2/3}$. The above mean-field exponents are not the same as the exponent in 1D and 2D, as is discussed in Sec. II.E and Sec. II.F.

The second step of the Gutzwiller approximation does not satisfy the variational principle. Alternatively, the energy of this Gutzwiller wave function may be estimated numerically from Eq. (2.189) by Monte Carlo sampling (Yokoyama and Shiba, 1987a, 1987b) without introducing the second step of the Gutzwiller approximation. This Monte Carlo method satisfies the variational principle and gives the upper bound of the ground-state energy. Variational Monte Carlo results correctly predict the absence of MIT in the 1D Hubbard model at half filling, that is, the insulating state for all $U > 0$.

As we see below in Sec. II.D.6, the Gutzwiller approximation reproduces to some extent the coherent part of the spectral weight, while it fails to treat the incoherent part, in contrast to the Hubbard approximation.

6. Infinite-dimensional approach

In a simple model of phase transitions such as the Ising model for the ferromagnetic transition, the universality class and critical exponents are correctly reproduced by the mean-field theory when the system is above the upper critical dimension d_c. For sufficiently large dimensional systems, fluctuations are in general suppressed and hence the mean-field approximation becomes valid. In fermionic systems with metallic spin and charge excitations, however, the situation is much more complicated because dynamic quantum fluctuations are important even in large dimensions. In infinite dimensions, the number of spatial dimension is infinite, so spatial fluctuations are suppressed, while the number of temporal dimension is always one with an inherent quantum dynamics. Therefore the mean-field theory must be constructed in a dynamic way to describe metallic states in large dimensions. In the dynamic mean-field theory, the spatial degrees of freedom are replaced with a single-site problem, while dynamic fluctuations must be fully taken into account. In the path-integral approach, the "mean field" determined self-consistently should be dynamically fluctuating in the temporal direction.

To understand how the dynamical fluctuation is exactly taken into account in infinite dimensions, it is important to notice that the self-energy of the single-particle Green's function has no wave-number dependence and hence is site diagonal (Müller-Hartman, 1989). By using the site-diagonal self-energy, one can obtain a set of self-consistent equations for the exact solution of the Green's function in infinite dimensions. The MIT has been extensively studied with the help of numerical or perturbational solutions of the self-consistent equations. Below we first define the Hubbard model in infinite dimensions. Next the self-energy of the Green's function is shown to be site diagonal. The self-consistent equations are derived and several different ways of solving them are discussed. Consequences obtained from the results are then discussed. For more detailed discussions of the infinite-dimensional approach, readers are referred to the review article of Georges, Kotliar, Krauth, and Rozenberg (1996).

In infinite dimensions, the Hubbard model defined in Eqs. (1.1a)–(1.1d) with nearest-neighbor hopping characterized by the dispersion in Eqs. (2.3a)–(2.3b) has the same form. The dispersion of Eq. (2.3b) in d dimensions is explicitly written as

$$\varepsilon_0(k) = -2t\sum_{j=1}^{d} \cos k_j \tag{2.199}$$

for a simple hypercubic lattice. For $d \to \infty$, we have to take a proper limit to yield a nontrivial model (Metzner and Vollhardt, 1989), because the on-site interaction term (1.1c) is still well defined in $d = \infty$ while the kinetic-energy term $\mathcal{H}_t$ has to be rescaled. This is easily understood from the density of states $\rho(E)$ in the noninteracting limit $U = 0$, which has the form

$$\rho(E) = \lim_{d\to\infty} \frac{1}{2t(\pi d)^{1/2}} \exp[-(E/2t\sqrt{d})^2]. \tag{2.200}$$

in the case of a hypercubic lattice. This density of states is derived from the equivalence between $\rho(E)$ and the probability distribution function of the x coordinate of a random walker in 2D after d steps of length $2t$ each with a uniform and random choice of direction in the 2D

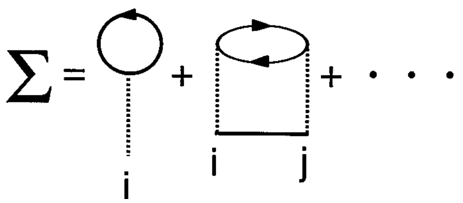

FIG. 12. The lowest-order diagrams of the intersite self-energy. The interaction is denoted by a black dotted line, while G_0 is given by a full curve. The sites are denoted by i and j.

plane (x,y). Equation (2.200) is simply the solution of the diffusion equation for $d\rightarrow\infty$ as it should be in the case of a long time limit of the random walk. To take the limit with a finite density of states, one must scale t as $t=t^*/2\sqrt{d}$ with a finite t^*. Therefore the bare t is scaled to zero as d increases.

As we see in Eq. (2.200), the density of states for a simple hypercubic lattice has a Gaussian distribution of width t^*. A drawback of this density of states is that the MIT does not take place at finite U in the strict sense, because the exponential but finite tail of the density of states blocks charge-gap formation at any finite U. To get around this difficulty, van Dongen (1991) considered replacing the simple hypercubic lattice by the Bethe lattice, where the density of states has a semicircular form:

$$\rho(E)=\frac{2}{\pi t^*}\sqrt{1-(E/t^*)^2}. \tag{2.201}$$

In an explicit calculation of the Green's function and the self-energy described below, we use only the density of states as input, while the calculation does not depend on more detailed knowledge of the actual lattice structure. This indicates that, in $d=\infty$, lattice structure, connectivity for the hopping transfer, and a measure of the distance are all irrelevant. In other words, spatial correlations are completely ignored in $d=\infty$.

When t is scaled as $t\propto 1/\sqrt{d}$, one can show that the intersite self-energy of the Green's function $\Sigma_{ij}(\omega)$ $(i\neq j)$ is a higher order of the $1/d$ expansion than on-site self-energy $\Sigma_{ii}(\omega)$ (Müller-Hartman, 1989). In the diagrammatic expansion of the self-energy as in Fig. 12, the lowest order is a part of the on-site term Σ_{ii}, which contains one bare Green's function G_{0ii}. In contrast, the lowest-order term of the intersite self-energy is second order in U with three bare Green's functions, as in Fig. 12. The intersite bare Green's function G_{0ij} is scaled as

$$G_{0ij}\sim t^{|R_i-R_j|},$$

where $|R_i-R_j|$ is the Manhattan distance of the i and j sites. Then the lowest-order term of Σ_{ij} for the nearest-neighbor pair (i,j) is at most scaled by t^3. Therefore the self-energy which contains the i site has contributions from the on-site term $\Sigma_{ii}\sim O(1)$, the nearest-neighbor term $\Sigma_{ij}\sim$(number of nearest neighbors)$\times t^3\sim dt^3$, and the next-nearest-neighbor term $\Sigma_{ij}\sim$(number of next-nearest neighbors)$\times t^6\sim d^2t^6\cdots$. Because of $t\sim 1/\sqrt{d}$, these are reduced to $\Sigma_{\text{on-site}}\sim O(1)$, $\Sigma_{\text{nearest-neighbor}}\sim 1/\sqrt{d}$, $\Sigma_{\text{next-nearest-neighbor}}\sim 1/d$ etc. In the limit $d\rightarrow\infty$, we see that the intersite terms vanish as compared to Σ_{ii}. This heuristic argument can be extended to all the higher-order terms in U, which guarantees that all the intersite terms of the self-energy can be neglected in $d=\infty$.

We rewrite the functional integral of the Hubbard model introduced in Eqs. (2.41a) and (2.41b) with (2.37a)–(2.37d) as

$$Z=\int \mathcal{D}\bar{\Psi}\mathcal{D}\Psi\ \exp[-S], \tag{2.202a}$$

$$S=\int_0^\beta d\tau\sum_{i,j,\sigma}\left[\bar{\psi}_{i\sigma}(\tau)\left(\delta_{ij}\frac{\partial}{\partial\tau}+t_{ij}-\mu\delta_{ij}\right)\psi_{j\sigma}(\tau)\right]+S_U, \tag{2.202b}$$

$$S_U=\sum_i S_{Ui}=\sum_i\int_0^\beta d\tau\mathcal{H}_{Ui}(\tau), \tag{2.202c}$$

$$\mathcal{H}_{Ui}(\tau)=U\bar{\psi}_{i\uparrow}(\tau)\bar{\psi}_{i\downarrow}(\tau)\psi_{i\downarrow}(\tau)\psi_{i\uparrow}(\tau). \tag{2.202d}$$

Here Ψ is a vector which depends upon site i (or wave number $\mathbf{k}$), imaginary time τ (or the Matsubara frequency ω_n), and spin σ. The matrix product, such as the $\bar{\Psi}A\Psi$ used below, follows the same notation as that from Eqs. (2.131a)–(2.131b) through (2.134a)–(2.134c). The nointeracting Green's function at $U=0$ is defined as

$$G_{0ij}\equiv\left(\delta_{ij}\frac{\partial}{\partial\tau}+t_{ij}+\mu\delta_{ij}\right)^{-1}, \tag{2.203}$$

which is transformed in Fourier space as

$$G_0(\mathbf{k},\omega)=\frac{1}{i\omega_n-\varepsilon_0(\mathbf{k})+\mu}. \tag{2.204}$$

When we use G_0, the action has the form

$$S=S_{G_0}+S_U, \tag{2.205a}$$

$$S_{G_0}\equiv-\mathrm{Tr}\ \bar{\Psi}G_0^{-1}\Psi, \tag{2.205b}$$

where $\mathrm{Tr}\equiv\int_0^\beta d\tau\Sigma_i$. The Green's function G at $U\neq 0$ is formally given by introducing the self-energy Σ as

$$G^{-1}=G_0^{-1}-\Sigma, \tag{2.206}$$

from which the action is rewritten as

$$S=S_G-S_\Sigma+S_U, \tag{2.207a}$$

$$S_\Sigma=\mathrm{Tr}\ \bar{\Psi}\hat{\Sigma}\Psi. \tag{2.207b}$$

Here, in the real-space and imaginary-time representation, $\hat{\Sigma}$ is a diagonal matrix given by σI with the identity matrix I, since Σ is site diagonal in $d=\infty$. Then the partition function may be given as

$$\begin{aligned}Z&=\int\mathcal{D}\bar{\Psi}\mathcal{D}\Psi\ \exp[-S_G+S_\Sigma-S_U]\\&=Z_G\langle\exp[S_\Sigma-S_U]\rangle_G\end{aligned} \tag{2.208a}$$

with

$$Z_G\equiv\int\mathcal{D}\bar{\Psi}\mathcal{D}\Psi\ \exp[-S_G], \tag{2.208b}$$

$$\langle \cdots \rangle_G \equiv \frac{1}{Z_G} \int \mathcal{D}\overline{\Psi}\mathcal{D}\Psi \, \exp[-S_G] \cdots . \tag{2.208c}$$

Because Σ and U are site diagonal, for an N-site system, the average over G may be replaced with the average over the on-site Green's function $G_{ii} \equiv G_{loc}$ after integration over $\overline{\psi}_j$ and ψ_j with $j \neq i$ first, as

$$Z_G \langle \exp[S_\Sigma - S_U] \rangle_G = Z_{G_{loc}} \langle \exp[S_{\Sigma i} - S_{Ui}] \rangle_{G_{loc}}, \tag{2.209}$$

where

$$S_{\Sigma i} = \int_0^\beta d\tau' d\tau \, \overline{\psi}_i(\tau) \Sigma(\tau - \tau') \psi_i(\tau'). \tag{2.210}$$

Here, $\langle \cdots \rangle_{G_{loc}}$ is defined by a local average,

$$\langle \cdots \rangle_{G_{loc}} = \int \mathcal{D}\overline{\psi}_i \mathcal{D}\psi_i \langle \exp[\overline{\psi}_i G_{ii}^{-1} \psi_i] \cdots \rangle / Z_{G_{loc}}, \tag{2.211a}$$

$$Z_{G_{loc}} = \int \mathcal{D}\overline{\psi}_i \mathcal{D}\psi_i \exp[\overline{\psi}_i G_{ii}^{-1} \psi_i], \tag{2.211b}$$

and we have used the identity

$$\exp[\overline{\psi}_i G_{ii}^{-1} \psi_i] = \int \prod_{j \neq i} d\overline{\psi}_j d\psi_j \exp[-S].$$

The on-site Green's function is related to its Fourier transform as

$$G_{ii}(\tau) = \frac{1}{N\beta} \sum_{\omega_n} \sum_{\mathbf{k}} G(\mathbf{k}, i\omega_n) e^{-i\omega_n \tau}. \tag{2.212}$$

Then from Eqs. (2.208a)–(2.208c) and (2.209), the partition function has the form

$$Z = \int \mathcal{D}\overline{\psi}_i \mathcal{D}\psi_i \times \exp\left[-\int_0^\beta d\tau' d\tau \{ -\overline{\psi}_i(\tau) \tilde{G}^{-1}(\tau - \tau') \psi_i(\tau') + \mathcal{H}_{Ui} \} \right] \tag{2.213}$$

with

$$\tilde{G}^{-1}(\tau) \equiv G_{ii}^{-1}(\tau) - \Sigma(\tau). \tag{2.214}$$

In dynamic mean-field theory, $\tilde{G}^{-1}$ plays a role corresponding to the Weiss mean field in the usual mean-field theory. Now the problem is reduced to solving a single-site problem (2.213), where G and Σ are exactly obtained in a self-consistent fashion as follows:

(1) Calculate the Green's function G_{ii} from the single-site partition function (2.213) by assuming a trial form of $\tilde{G}$. This is possible because Eq. (2.213) is a single-site problem. We discuss several different ways of solving Eq. (2.213) later.

(2) From the obtained result G_{ii} in step (1) and the assumed $\tilde{G}$, obtain $\Sigma(\tau)$ from Eq. (2.214).

(3) From the Fourier transform $\Sigma(\omega_n)$ derived from $\Sigma(\tau)$ in step (2), calculate the on-site Green's function from

$$G_{ii}(\omega_n) = \sum_{\mathbf{k}} \frac{1}{i\omega_n - \varepsilon_0(\mathbf{k}) - \Sigma(\omega_n)} = \int d\epsilon \frac{\rho(\epsilon)}{i\omega_n - \epsilon - \Sigma}. \tag{2.215}$$

(4) From $G_{ii}(\omega_n)$ and $\Sigma(\omega_n)$ obtained in step (3), calculate $\tilde{G}(\tau)$ from Eq. (2.214).

(5) Use $\tilde{G}(\tau)$ obtained in step (4) as the input to solve Eq. (2.213) and repeat the process from step (1) again until the iteration converges so that self-consistency is satisfied.

From this iteration, the single-site problem with dynamical fluctuations is solved exactly. The lattice structure enters the procedure only through the density of states in Eq. (2.215). The basic idea of this self-consistent procedure was first proposed by Kuramoto and Watanabe (1987) for the periodic Anderson model and extended to the Falikov-Kimball model by Brandt and Mielsch (1989). This self-consistent procedure may be compared with the coherent-potential approximation employed in the Hubbard approximation and the self-consistent renormalization approximation. While they are similar, an important difference of the $d = \infty$ approach from the Hubbard approximation and the self-consistent renormalization approximation is that the mean field is dynamic and the dynamic fluctuations are taken into account exactly in ω dependence of Σ.

It is difficult to solve Eq. (2.213) in an analytical way. Several different numerical ways for solving Eq. (2.213) have been proposed. One is the quantum Monte Carlo method (Jarrell, 1992; Rozenberg, Zhang, and Kotliar, 1992), in which a single-site problem with dynamically fluctuating $\tilde{G}$ is solved numerically in the path-integral formalism following the algorithm for the impurity Anderson model developed by Hirsch and Fye (1986). Although this is a numerically exact procedure, within statistical errors, it is rather difficult to apply in the low-temperature region. Another approach is the perturbation expansion in which Eq. (2.213) is solved perturbatively in terms of U (Georges and Kotliar, 1992). This is called the iterative perturbation method. Among several different approaches, the most precise way of estimating physical quantities in the low-energy scale seems to be the numerical renormalization-group method (Sakai and Kuramoto, 1994). The MIT of the Hubbard model in $d = \infty$ has been extensively studied using these procedures.[1] Other strongly correlated models, such as the degenerate Hubbard models, the periodic Anderson model, the d-p model, and the double-exchange model have also been studied (Jarrell, Akhlaghpour, and Prus-

---

[1] Studies of $d = \infty$ include those of Georges and Kotliar, 1992; Georges and Krauth, 1992; Jarrell, 1992; Rozenberg, Zhang, and Kotliar, 1992; Jarrell and Pruschke, 1993; Pruschke, Cox, and Jarrell, 1993; Zhang, Rozenberg, and Kotliar, 1993; Caffarell and Krauth, 1994; Jarrell and Pruschke, 1994; Sakai and Kuramoto, 1994; Moeller *et al.*, 1995.

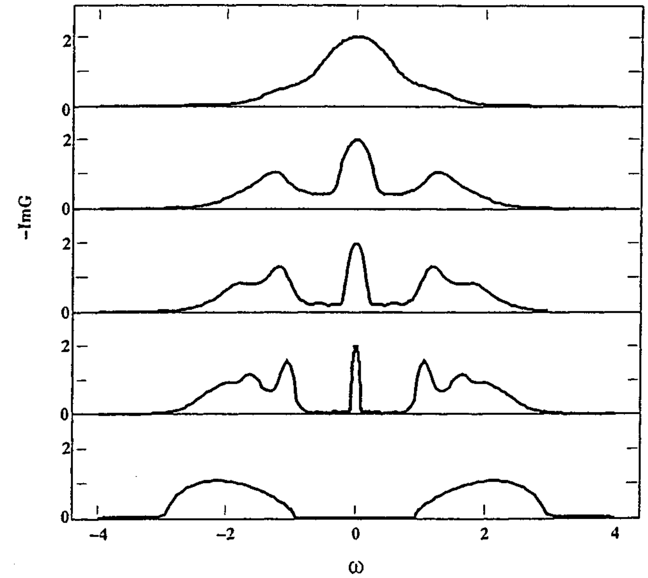

FIG. 13. Density of states $\rho(\omega)=-\mathrm{Im}\,G$ by the $d=\infty$ approach at $T=0$ for the half-filled Hubbard model at $U/t^*=1$, 2, 2.5, 3, and 4 from top to bottom. The calculation is done by iterative perturbation in terms of U. The bottom one ($U/t^*=4$) is an insulator. From Georges, Kotliar, Krauth, and Rozenberg, 1996.

chke, 1993; Si and Kotliar, 1993; Furukawa, 1995a, 1995b, 1995c; Kajueter and Kotliar, 1996; Rozenberg, 1996a; Mutou and Hirashima, 1996; Mutou, Takahashi, and Hirashima, 1997)

Here basic results for the $d=\infty$ Hubbard model are summarized below. We first discuss the case of the BC-MIT. In the metallic phase, the Fermi-liquid state with Luttinger sum rule is realized in the solution in $d=\infty$ if one considers only the paramagnetic phase (Georges and Kotliar, 1992). A remarkable property of the solution in $d=\infty$ is seen in the density of states $\rho(\omega)$ as illustrated in Fig. 13. At half filling it has basically the same structure as the Hubbard approximation in the insulating region $U>U_c$, where the Fermi level lies in the Hubbard gap sandwiched between the upper and lower Hubbard bands. The reason why the Hubbard approximation can treat the dynamics more or less properly has been discussed in Sec. II.D.4. In the metallic phase $U<U_c$ but near U_c, a resonance peak appears around the Fermi level in addition to the upper and lower Hubbard bands. The peak height is kept constant in the metallic region, while the width of the peak becomes smaller and smaller as the MIT point $U=U_c$ is approached. The peak at the Fermi level eventually disappears with a vanishing width at $U=U_c$. This is associated with a vanishing renormalization factor Z and hence a diverging effective mass m^*. In the metallic phase this critical divergence of m^* is essentially the same as what happens in the Gutzwiller approximation (Brinkman and Rice, 1970), that is, Z^{-1}, m^* and the specific-heat coefficient γ are enhanced in proportion to $|U-U_c|^{-1}$ while the compressibility κ decreases until it vanishes at the transition point. The Drude weight is also proportional to $|U-U_c|$ in the $d=\infty$ approach. The magnetic susceptibility χ_s is enhanced but approaches a constant $\sim 1/J$ at the transition, in contrast with the divergence in the Gutzwiller approximation. Here J is the energy scale of the exchange interaction. This difference comes from the fact that χ_s has contributions from the incoherent part, namely, upper and lower Hubbard bands, while the incoherent contribution is ignored in the Gutzwiller approximation. Even for the filling-control MIT, results in $d=\infty$ show behavior similar to that of the Gutzwiller approximation where Z^{-1}, m^*, and γ are also enhanced while κ remains finite. As we shall see in Secs. II.E and II.F, κ appears to diverge at the transition point in 2D in contrast to the $d=\infty$ result.

Comparisons of the spectral weight and the density of state with experimental data on $\mathrm{Ca}_{1-x}\mathrm{Sr}_x\mathrm{VO}_3$, $\mathrm{La}_{1-x}\mathrm{Sr}_x\mathrm{TiO}_3$, and other compounds are made in later sections. A controversy exists concerning the BC-MIT. The coherence peak at the Fermi level seems to disappear when the metal-insulator transition in $\mathrm{Ca}_{1-x}\mathrm{Sr}_x\mathrm{VO}_3$ and other series of compounds such as VO_2, LaTiO_3, and YTiO_3 takes place with the incoherent upper and lower Hubbard band kept more or less unchanged, yet the optical conductivity shows that the charge gap closes continuously at the transition. The $d=\infty$ results are consistent with the former but appear to contradict the optical data, as will be discussed in Sec. IV. Although the mass enhancement in $d=\infty$ is similar to that in some experimental systems such as $\mathrm{La}_{1-x}\mathrm{Sr}_x\mathrm{TiO}_3$, in the $d=\infty$ result, the Wilson ratio $R_W\equiv\chi_s/\gamma$ vanishes at the transition while experimentally it remains constant around 2 in $\mathrm{La}_{1-x}\mathrm{Sr}_x\mathrm{TiO}_3$, as is discussed in Sec. IV.B.1. However, quantitatively this discrepancy is not remarkable.

The solution in $d=\infty$ seems to combine two approaches, the Hubbard approximation and the Gutzwiller approximation, in a natural way. In the insulating phase, the Hubbard approximation provides similar results, whereas, in the metallic phase, many of properties have similarities with the Gutzwiller approximation This merging of the Gutzwiller and Hubbard approximations was pointed out in an early work of Kawabata (1975). He showed that the inelasticity of quasiparticle scattering is crucial for realization of a sharp Fermi surface, which is not considered in the Hubbard approximation. The $d=\infty$ approach further makes it possible to discuss dynamics and excitations such as spectral weight. Thus one of the mean-field pictures of the MIT, when combined with the $d=\infty$ results, has become clearer.

The original solution in $d=\infty$ contains only a paramagnetic phase with complete ignorance of the antiferromagnetic order. However, by introducing two sublattices A and B, one can reproduce the antiferromagnetic order even in $d=\infty$ (Jarrell, 1992; Jarrell and Pruschke, 1993). The solution in this case indicates an antiferromagnetic order which persists not only in the insulating phase but also in a wide region of metals similarly to the simple Hartree-Fock-RPA results. Therefore the MIT observed by excluding magnetic order is usually interrupted and masked by the appearance of the magnetic transition in reality at $d=\infty$. It was pointed out that the

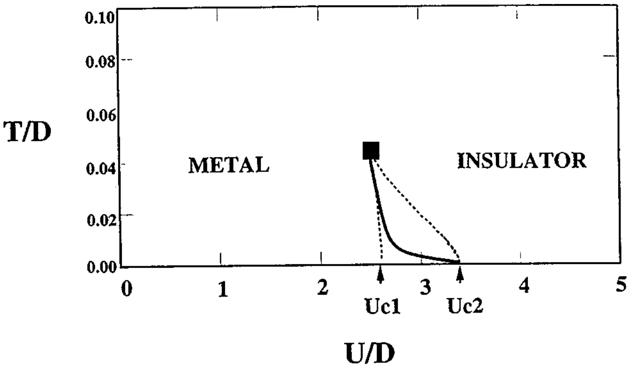

FIG. 14. Phase diagram of the $d=\infty$ Hubbard model at half filling in the plane of temperature T/t^* and interaction U/t^* in the case where the magnetic order is entirely suppressed by frustration. The solid curve is the first-order transition line with the critical point at the black square. The region surrounded by dotted curve shows the coexistence of metal and insulator, while the transition at $T=0$ is a continuous transition. From Georges, Kotliar, Krauth, and Rozenberg, 1996.

original MIT in the paramagnetic phase could be more or less recovered by introducing frustrations because the magnetic order could be suppressed by the frustration (Georges and Krauth, 1993; Rozenberg, Kotliar, and Zhang, 1994).

The phase diagram of metals and insulators in the plane of U and temperature T shown in Fig. 14 was argued to be similar to that of V_2O_3 under pressure or doping (Rozenberg, Kotliar, and Zhang, 1994). Although the first-order transition appears to take place in $d=\infty$ at finite temperatures even with the transfer t being fixed, in the experimental situation observed in the case of V_2O_3, the change in the lattice parameter at the transition may also be an origin of the strong first-order transition where discontinuous reduction of the lattice constant may stabilize the metallic state through the increase in the bandwidth. In the $d=\infty$ approach, the first-order transition at $T\neq 0$ is replaced with a continuous transition at $T=0$ (Moeller *et al.*, 1995).

At half filling, when a two-sublattice structure is introduced, the antiferromagnetic transition temperature T_N as a function of U shows a peak at a moderate U (see Fig. 15), whose structure is similar to the SCR result as well as to the quantum Monte Carlo results in 3D (Scalettar *et al.*, 1989), although temperature and energy scales have an ambiguity in $d=\infty$ due to the rescaling of t to t^*. It is clear that 2D systems show quite different behavior because T_N should always be zero. Away from half filling, T_N still shows similar behavior to RPA results with a wide region of antiferromagnetic metal. A serious problem in $d=\infty$ with antiferromagnetic order is that the short-ranged spin fluctuation inherent in lower-dimensional systems is completely ignored.

As we shall see in Sec. II.F the scenarios of the MIT in $d=\infty$ have some similarity, such as the mass divergence, to the low-dimensional case while they are rather different from the predictions of the scaling theory in many respects, such as the critical exponents themselves and the role of antiferromagnetic correlations. If we compare the results in $d=\infty$ with those in realistic low-dimensional systems including 3D, the region of the antiferromagnetic ordered phase may extend beyond those for $d=2$ and 3. In the case without orbital degeneracy, the antiferromagnetic order can be remarkably suppressed due to quantum fluctuations in finite dimensions, while it requires some other origin, such as frustration, to suppress magnetic order in $d=\infty$. In the limit $d=\infty$, each exchange coupling is scaled to vanish, and hence we do not expect spin-glass-like order. However, in this case we have nonzero entropy at $T=0$. Another more important difference between low-dimensional systems and $d=\infty$ occurs in the paramagnetic metallic phase due to difference in the universality class of the MIT as well as the absence of magnetic short-range correlations in $d=\infty$. For example the Drude weight D appears to scale linearly with δ for the FC-MIT at $d=\infty$, while it can be suppressed as $D\propto\delta^p$, $p>1$ in the scaling theory. The $d=\infty$ approach may be justified only above the upper critical dimension d_c, as we shall discuss in Sec. II.F. Although some attempts have been made to calculate $1/d$ corrections to compare with the Gutzwiller results in finite dimensions (Schiller and Ingersent, 1995), as it stands, the convergence properties of the $1/d$ expansions are not clear. To make connections to finite-dimensional results, it would be desirable to develop a systematic approach in terms of the $1/d$ expansion. In the Mott insulating phase, the Heisenberg spin model has been treated by an approach similar to that in this section (Kuramoto and Fukushima, 1998). The expansion can be calculated up to the order of $1/d$ (or up to the order of $1/z_n$ where z_n is the number of nearest neighbors), because the polarization function remains site diagonal up to this order in the quantum spin model. This approximation goes beyond the one-loop level and corresponds to the spherical approximation known in spin systems.

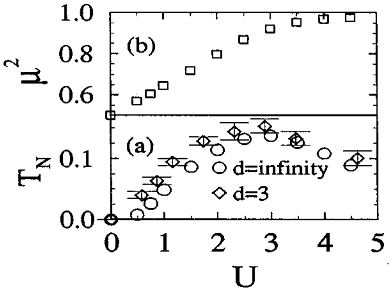

FIG. 15. U dependence in the $d=\infty$ Hubband model. (a) Antiferromagnetic transition temperature as a function of U: ○, $d=\infty$ Hubbard model; ◇, $d=3$ at half-filling. (b) U dependence of the square of the local moment μ^2. From Jarrell and Pruschke, 1993.

7. Slave-particle approximation

In strongly correlated systems, the strong-coupling limit is frequently a good starting point for understanding the basic physics. The strong-coupling limit is defined in the single-band model as the limit where double occupation of the same orbital is strictly prohibited. The t-J model (2.13) offers an example of this limit. To implement this local constraint, the slave-particle method has been developed. As an example, we discuss the case of the slave-boson method (Barnes, 1976, 1977; Coleman, 1984; Baskaran, Zou, and Anderson, 1987; Affleck and Marston, 1988; Kotliar and Liu, 1988; Suzumura, Hasegawa, and Fukuyama, 1988) where the electron operator $c_{i\sigma}$ is decoupled as

$$c_{i\sigma}=f_{i\sigma}b_i^\dagger . \tag{2.216}$$

Here $f_{i\sigma}$ is a fermion operator called a spinon, which carries spin degrees of freedom, while a boson operator $b_i^\dagger$ called a holon represents a charged hole. The local constraint prohibiting double occupancy is represented as

$$\sum_\sigma f_{i\sigma}^\dagger f_{i\sigma}+b_i^\dagger b_i=1 \tag{2.217}$$

at all the sites i.

Another way of decoupling is to assign fermion statistics for charge degrees of freedom and boson statistics for spins. Aside from minor differences, this reduces to the spin-wave theory at half filling where the spins are represented by Schwinger bosons. This formalism is called the slave-fermion method (Arovas and Auerbach, 1988; Yoshioka, 1989a, 1989b). The advantage of the slave-fermion method is that it is easier to implement antiferromagnetic order at half filling than with the slave-boson method. Away from half filling, however, the mean-field solution of the slave-fermion method generally predicts a wide region of incommensurate antiferromagnetic order, in contrast with the rapid disappearance of magnetic order believed to occur in 2D. A related formalism was also developed in the spin-fermion model in a rotating reference frame of antiferromagnetic correlations (Kübert and Muramatsu, 1996). We do not discuss the details of the slave-fermion approximation here.

In the slave-boson method, the t-J model defined in Eq. (2.13) is represented using these operators as

$$\mathcal{H}=-t\sum_{\substack{\langle i,j\rangle\\ \sigma}} b_i f_{i\sigma}^\dagger f_{j\sigma} b_j^\dagger-\frac{J}{2}\sum_{\substack{\langle ij\rangle\\ \sigma\sigma'}}[f_{i\sigma}^\dagger f_{j\sigma'}^\dagger f_{j\sigma'} f_{i\sigma} + f_{i\sigma}^\dagger f_{j\sigma'}^\dagger f_{j\sigma} f_{j\sigma'}]. \tag{2.218}$$

When the local constraint (2.217) is rigorously enforced, (2.218) is equivalent to the original t-J model. However, in practical treatments, as we shall see below, this local constraint is in many cases replaced by a global, averaged one. In addition to this approximation, various types of mean-field decoupling have been attempted to discuss the phase diagram of this Hamiltonian, including flux phase, commensurate flux phase, dimer phase, and the so-called resonating valence bond (RVB) state. As a typical example, here we discuss the case of RVB decoupling. The uniform RVB state introduces three order parameters for mean-field decoupling:

$$\chi_{ij}=J\sum_\sigma \langle f_{i\sigma}^\dagger f_{j\sigma}\rangle \tag{2.219}$$

and

$$\Delta_{ij}=\langle b_i b_j^\dagger\rangle \tag{2.220}$$

to decouple the transfer term proportional to t, whereas

$$D_{ij}=\langle f_{i\uparrow}f_{j\downarrow}-f_{i\downarrow}f_{j\uparrow}\rangle \tag{2.221}$$

and χ_{ij} for decoupling of the exchange term proportional to J. By using the mean-field approximation $\langle b_i^\dagger b_j\rangle \propto \delta$ to replace the local constraint with an averaged one, we can reduce the transfer term to

$$\mathcal{H}_t=-t\delta\sum_{\substack{\sigma\\ \langle ij\rangle}} f_{i\sigma}^\dagger f_{j\sigma} . \tag{2.222}$$

This leads to an approximation that is similar to the Gutzwiller result but not strictly identical, in which the bandwidth becomes narrow in proportion to the doping concentration δ and hence the mass is enhanced critically. It should be noted that the holon degrees of freedom are frozen in the approximation $\langle b_i^\dagger b_j\rangle =$ constant and a Fermi liquid of spinons is realized. When we further decouple the exchange term by using the RVB order parameter χ_{ij}, the bandwidth becomes proportional to $\Delta_{ij}+\chi_{ij}$, which is proportional to J even in the limit of $\delta\to 0$. When the charge degrees of freedom are retained in a dynamical manner, with the assumption that χ_{ij} is frozen below the mean-field temperature for χ_{ij}, the transfer term may be rewritten as

$$\mathcal{H}_t=-t\sum_{\substack{\sigma\\ \langle ij\rangle}} \chi_{ij} b_i^\dagger b_j . \tag{2.223}$$

Then, if χ_{ij} is assumed to be a mean-field constant $\bar{\chi}$, it leads to Bose condensation, $\langle b_i\rangle \neq 0$, below the transition temperature when a weak interaction of the bosons is assumed. On the other hand, if the Bose condensation of b_i takes place, by neglecting the strict local constraint, the Fermi-liquid state of f_i is realized again with finite mean-field order parameters for χ_{ij} and $\langle b_i\rangle$. This gives a bandwidth proportional to $t\langle b_i\rangle^2+(J/2)\langle \chi_{ij}\rangle$. When we neglect J, we obtain a bandwidth proportional to $\langle b_i\rangle^2 \propto \delta$ again, as in the Gutzwiller approximation. Therefore, at $T=0$, this mean-field framework always leads to the same level of approximations as the Gutzwiller approximation for the MIT. As discussed in Secs. II.D.6 and II.F, this approximation of course gives only mean-field exponents with no information on the incoherent part of the charge excitation.

In the large-N limit, where the SU(2) symmetry of the original spin-1/2 models is generalized to SU(N) with arbitrary integer N, this mean-field solution becomes exact in any dimension and the incoherent part disappears in the leading order of $1/N$ (see the reviews of Newns and Read, 1987; Kotliar, 1993; see also Jichu, Matsuura, and Kuroda, 1989).

Mean-field solutions of the slave-particle formalism give various phases such as the dimer phase, flux phase, and RVB phase. When the dimer and flux phases are suppressed, the metallic state at $T=0$ is the Fermi liquid, and the MIT near $\delta\to 0$ in this framework is characterized by $Z \propto \delta$ and $D \propto \delta$ where Z is the renormalization factor and D is the Drude weight. The specific-heat coefficient γ is given by $\gamma \propto 1/(\delta + \alpha J/t)$ with a constant α of order unity (Grilli and Kotliar, 1990). The effective mass m^* is enhanced but remains finite, $m^* \sim (t/J) m_b$ in the limit $\delta \rightarrow 0$.

Above the Bose condensation temperature of b_i, when using the Hamiltonian (2.218) as a starting point, one must treat the dynamic fluctuation of χ_{ij} with strongly coupled spinons and holons if one wishes to go beyond the mean-field approximation. A gauge-field approach (Ioffe and Larkin, 1989; Ioffe and Kotliar, 1990; Nagaosa and Lee, 1990; Lee and Nagaosa, 1992) can in principle treat this fluctuation, where the local constraint and the fluctuation of χ_{ij} are represented by a gauge field coupled to both spinon and holon. This may be implemented through the fluctuation of θ which is similar to Eq. (2.156) but actually uses the Stratonovich-Hubbard field to decouple Eq. (2.218), where the coupling of holon to spinon is represented by chirality fluctuations of θ. Recently this approach was extended to reproduce the SU(2) symmetry at half filling. The π-flux state at half filling is connected to the RVB phase upon doping (Wen and Lee, 1996).

In the gauge-field approach, it has been claimed that the linear-T resistivity is reproduced from the dynamics of holes (slave bosons) strongly coupled to the gauge field. So far, in this gauge-field theory, the T-linear resistivity has been ascribed to the incoherence of slave bosons due to low boson concentration together with the speculated retraceable nature of bosons under the coupling to the dynamic gauge field. However, the gauge fluctuation has been considered mostly within the Gaussian approximation without a self-consistent treatment. Self-consistent treatment of holons and spinons coupled by the gauge field has not been attempted so far, and it is not clear whether the above claims will be confirmed by a self-consistent treatment. In fact, the energy scale of the dynamic fluctuation of spinons is only J, which yields incoherent charge dynamics only on the same energy scale through the spinon-holon coupling by the gauge field. This appears to contradict the experimental and numerical observations to be described in Secs. II.E.1 and IV.C, where $\sigma(\omega) \propto 1/\omega$ extends to the order of the bare bandwidth in the absence of the characteristic crossover energy scale. The energy scale for the appearance of incoherence is of the order of the Mott gap and much larger than J near the Mott insulator. In Secs. II.E.1 and II.F, we shall see that the incoherence may be ascribed to different origins near the MIT.

The description of the MIT $\delta \rightarrow 0$ by the slave-particle approach including the gauge-field method is rather primitive in many other respects: First, it does not properly take account of the growth of (short-ranged) antiferromagnetic correlation, which plays an important role in the incoherent dynamics. [The RPA level of antiferromagnetic correlation was additionally considered within a uniform RVB treatment (Tanamoto, Kohno, and Fukuyama, 1992)]. Secondly, at $T=0$, as mentioned above, this approach gives only a simple mean-field result similar to that of a Gutzwiller-type approximation, due to Bose condensation of b_i. In the limit $T \rightarrow 0$, this treatment ignores the incoherent part of the excitations although the incoherence becomes important near the Mott transition even at $T=0$. This incoherence is considered in the above scenario only partially via gauge-field fluctuations at finite temperatures. It is also difficult in this approach to explain the small amplitude of R_H observed in the high-T_c cuprates at high temperatures (see Secs. II.E.1 and IV.C). Diverging compressibility at $T=0$ near $\delta=0$ (see Secs. II.E.3 and IV.C.1) is also difficult to explain in this scheme. All these problems are of fundamental importance and contribute to the failure of this approach in treating the Mott transition in finite dimensions in a manner similar to the Gutzwiller approximation.

One of many serious difficulties of the slave-particle model is that it is not clear whether the gauge-field coupling is weak enough to justify the original spin-charge separation. Without a weak enough coupling, spinons and holons recombine to the original electrons, which would invalidate the model. Because this approach is based on a very strong statement, namely, an explicit spin-charge separation, it is highly desirable to find direct evidence for or against it. From a theoretical point of view, the 2D Hubbard model at low concentration has been extensively investigated and, although it is still controversial (see for example, Narikiyo, 1997; Castellani *et al.*, 1998), the conclusion appears to be that the Fermi-liquid state is stable and hence the spin-charge separation does not take place. In general, in 2D, the Fermi liquid is destroyed only when there is a singular interaction between quasiparticles.

When we take into account the J term, below the mean-field temperature of D_{ij}, the spin degrees of freedom may have a pseudogap structure on the mean-field level. It was claimed that this may be relevant to the pseudogap anomaly observed in the high-T_c cuprates (Kotliar and Liu, 1988; Suzumura, Hasegawa, and Fukuyama, 1988). The basic mechanism could be closely related to superconducting pairing due to antiferromagnetic fluctuations. However, the formation of pseudogaps above the superconducting transition temperature T_c, expected at low doping in this framework, is rather difficult to explain from antiferromagnetic spin-fluctuation theory, while it may have an interesting connection to the pairing mechanism for doped spin-gap Mott insulators. Pseudogap formation may be just a consequence of the preformed singlet pair (fluctuations) of electrons due to some pairing force, for example, and is not necessarily the consequence of this particular formalism of spin-charge separation. Indeed, on general grounds, it is natural to have a separation of T_c and the pseudogap formation temperature T_{PG} at low doping, as we shall discuss in Secs. II.F and IV.C. The critical temperature must go to zero as $\delta \rightarrow 0$ because the coherence temperature T_{coh} should go to zero when the system approaches the continuous MIT point, while T_{PG} may remain finite due to a finite pairing energy even close to the MI transition point.

Although the slave-particle approach provides in principle an attractive way to describe the problem if the local constraint is reliably implemented and the fluctuation around the starting mean-field solution is properly estimated, its practical realization is rather difficult and the approximations employed so far are unfortunately not well controlled. As in all the mean-field theories, the way of decoupling the original Hamiltonian by assuming order parameters in the mean-field treatment of the constraint (2.217) is not unique and we can argue many possibilities. Mean-field results give a criterion for local stability of the solution while it is hard to show global stability. It is also hard to estimate fluctuation effects in a controlled way. Generally speaking, in low-dimensional systems, this is a serious problem because of large quantum fluctuations. In fact, if the dimensionality is below the upper critical dimension, phase transitions must be described beyond the mean-field theories. The slave-particle approximation does not reproduce the large dynamic exponent $z=4$ observed in 2D numerical studies, discussed in Secs. II.E and II.F, because of the neglect of strong wave-number dependence. Therefore it does not reproduce important physical quantities associated with the MIT in 2D. For qualitatively correct descriptions of the problem, the slave-particle approach is useful for limited use on a mean-field level, but it is important to consider the overall consistency of the obtained results with those of other theoretical approaches and with experimental indications.

8. Self-consistent renormalization approximation and two-particle self-consistent approximation

When electron correlation effects become stronger, in general, spin fluctuations have to be considered seriously. In the Hubbard approximation and Gutzwiller approximation, as well as in the infinite-dimensional approach, wave-number- and frequency-dependent spin fluctuations are not taken into account. Although the RPA, discussed in Sec. II.D.2, provides a formalism to deal with spin fluctuations perturbatively, its validity is restricted to cases of sufficiently weak spin fluctuations, as is easily understood from its derivation. It describes magnetic transitions only at the mean-field level with uncontrolled treatment of fluctuations. To consider wave-number-dependent spin fluctuation of any amplitude, large or small, and especially to improve the RPA and the Hartree-Fock approximations at finite temperatures, the self-consistent renormalization (SCR) approximation was developed by Moriya (1985). In the SCR theory, as we see below, wave-number-dependent spin fluctuations of large amplitude can be taken into account more completely, while dynamic fluctuations are more or less neglected because of the static approximation employed to treat the strong-correlation regime. In the original terminology of SCR, it was a mode-coupling theory developed for weak ferromagnetic or antiferromagnetic systems with small-amplitude spin fluctuations within the Gaussian approximation. In addition to the RPA diagrams of bubbles, within the one-loop approximation, the polarization function contains diagrams whose bubbles are coupled to the spin fluctuations with different wave numbers. This generates mode couplings, which are treated self-consistently. This is basically a self-consistent treatment of the one-loop approximation. The original mode-coupling treatment takes account of dynamic fluctuations but is justified only for weakly correlated systems at the one-loop level and at the level of minor vertex corrections. On the other hand, our main interest in this review is strongly correlated systems. Therefore we shall use the terminology of the SCR approximation for more generalized treatments, formulated later, with the static approximation of the Stratonovich-Hubbard variable, to cover both small and large amplitudes (Moriya, 1985). This may be viewed as an extrapolation of the original SCR to the strong-correlation regime but within the static approximation of the Stratonovich-Hubbard variables. As we shall see below, in principle, the mode-coupling contribution to the additionally introduced self-energy can be implemented so as to include the original SCR treatment as a special case, although it has not been done seriously. Though there exist several different ways of formulating the SCR theory, the level of approximations used is similar. A typical formulation of the SCR theory (Moriya and Hasegawa, 1980) is reviewed below. We also briefly review a more or less equivalent renormalization-group approach by Millis (1993) in Sec. II.D.9.

To calculate the partition function in the path-integral formalism with the Stratonovich-Hubbard transformation, we need to calculate Eq. (2.132a). Like the Hartree-Fock formulation for the strong-correlation regime, the SCR approximation for the strong-correlation regime employs a static approximation in which dynamic fluctuations of $\tilde{\Delta}_s$ and $\tilde{\Delta}_c$ are ignored. This static approximation becomes a serious drawback in treating anomalous metals with fluctuations related to correlated insulators.

Instead of the saddle-point approximation of a single mode of $\tilde{\Delta}$ in the Hartree-Fock approximation, the SCR theory employs a mode-coupling theory for Gaussian fluctuations combined with a coherent potential approximation (CPA) which regards the wave-number-dependent static Stratonovich fields $\tilde{\Delta}_s$ as random potentials. The framework of the CPA is quite similar to that for the Hubbard approximation discussed in Sec. II.C.4. Instead of the $\tilde{\Delta}_c$ considered in the Hubbard approximation, the fields $\tilde{\Delta}_s$ are mainly taken into account in SCR. The first goal is to calculate the Green's function

$$G_{\sigma\sigma'}(k,k') \equiv -Q^{-1}_{\sigma\sigma'}(k,k'). \tag{2.224}$$

Instead of using Eq. (2.143) for the quasiparticle Green's function in the Hartree-Fock approximation, we consider the self-energy correction in the form

$$G_\gamma^{-1}=-Q_\gamma=\begin{pmatrix} -Q_{\gamma\uparrow\uparrow}-\Sigma_1, & 0 \\ 0, & -Q_{\gamma\downarrow\downarrow}-\Sigma_2 \end{pmatrix}, \tag{2.225}$$

with $Q_{\gamma\sigma\sigma}$ given in Eq. (2.145c). The self-energy is described as Σ_1 and Σ_2. In the absence of symmetry breaking, namely, in the paramagnetic phase, the self-energy correction may be written in the original single-particle Green's function (2.143) in the form

$$G^{-1}=-Q_0-\begin{pmatrix} \Sigma_1 & 0 \\ 0 & \Sigma_2 \end{pmatrix}. \tag{2.226}$$

The self-energy is determined by the CPA combined with some approximations such as the Gaussian approximation for the static fluctuation $\tilde{\Delta}_s(\mathbf{k},\omega_n=0)$. The coherent potential approximation neglects the wave-number dependence of the self-energy and considers only $\Sigma_1(\mathbf{k}=0)=\Sigma_2(\mathbf{k}=0)$ in the absence of magnetic fields. In other words, the CPA condition is to take into account the effect of Q_1 (or effects of dynamic $\tilde{\Delta}_s$) by the local on-site self-energy on average. This may be achieved by solution of the self-consistent equation

$$\Sigma=\frac{\left\langle Q_1(k)\left[1-\left(\frac{1}{N}\sum_{\mathbf{k}} G(\mathbf{k},\omega)\right)(Q_1(\mathbf{k})-\Sigma)\right]^{-1}\right\rangle}{\left\langle\left[1-\left(\frac{1}{N}\sum_{\mathbf{k}} G(\mathbf{k},\omega)\right)(Q_1(\mathbf{k})-\Sigma)\right]^{-1}\right\rangle}. \tag{2.227}$$

as in Eq. (2.187). Here $\langle\cdots\rangle$ is the average over the distribution of $\tilde{\Delta}_s$ corresponding to $\Sigma_l Z_l\cdots/\Sigma_l Z_l$ in Eq. (2.187). In this case, the probability P_l is taken as $\exp[-S_\Delta]$ defined in Eq. (2.134).

After one has determined the wave-number-independent but frequency-dependent $\Sigma(\omega)$, a systematic t-matrix expansion is in principle possible to allow for corrections coming from the wave-number dependence. The effective action for Δ obtained from Eqs. (2.134a)–(2.134c),

$$S_{eff}(\Delta)=[-\mathrm{Tr}\ \ln(-G_0)+\mathrm{Tr}\ \ln(1-G_0Q_1)], \tag{2.228}$$

is rewritten as

$$\begin{aligned} S_{eff}(\Delta)&=\mathrm{Tr}\ \ln(-G_0^{-1}+Q_1)=\mathrm{Tr}\ \ln(-G^{-1}+Q_1-\Sigma)\\ &=-\mathrm{Tr}[\ln(-G)-\ln(1-G(Q_1-\Sigma))]\\ &=-\mathrm{Tr}[\ln(-G)-\ln\{1-G_{loc}(Q_1-\Sigma)\}\\ &\quad-\ln\{1-(G-G_{loc})\mathcal{T}\}], \end{aligned} \tag{2.229}$$

where the t matrix is defined as

$$\mathcal{T}=(Q_1-\Sigma)[1-G_{loc}(Q_1-\Sigma)]^{-1} \tag{2.230}$$

with the local Green's function

$$G_{loc}(\omega_n)=\frac{1}{N}\sum_{\mathbf{k}} G(\mathbf{k},\omega_n). \tag{2.231}$$

The CPA condition (2.227) is solved in some approximation, while charge fluctuations are neglected. Then a further approximation such as the Gaussian approximation of $\tilde{\Delta}_s$ is taken to cut off the t-matrix expansion (Moriya and Hasegawa, 1980). The formal procedure for solving the problem in this approximation is rather similar to that explained in the Hubbard approximation (Sec. II.D.4). The result in the paramagnetic phase is

$$\begin{aligned} \Sigma(\omega_n)\equiv\Sigma_1=\Sigma_2=-\Bigg[&\Sigma^2(\omega_n)-2\pi\left(\frac{1}{N\beta}\right)^2\\ &\times\sum_{\mathbf{k}\neq 0}\langle\tilde{\Delta}_s(\mathbf{k})\tilde{\Delta}_s(-\mathbf{k})\rangle\Bigg]G_{loc}(\omega_n). \end{aligned} \tag{2.232}$$

It should be noted that, in contrast to the infinite-dimensional approach, the CPA self-consistent equation (2.227) cannot be exactly solved because of its explicit wave-number dependence. Since $\Sigma_{\mathbf{k}\neq 0}\Delta_s(\mathbf{k})\Delta_s(-\mathbf{k})$ becomes β linear at low temperatures, Re $\Sigma\propto T$ is obtained. From the Kramers-Kronig relation, this implies Im $\Sigma\propto T^2$, which is consistent with the Fermi-liquid description.

When $\Sigma=0$, the static approximation with only a single mode of $\tilde{\Delta}_s$ retained leads directly to the Hartree-Fock approximation, while the Gaussian approximation for $\tilde{\Delta}_s$ leads to the RPA result. Therefore, at $T=0$, the SCR approximation is reduced to the Hartree-Fock-RPA result. The most important contribution of the SCR approximation is an improvement in the prediction of temperature dependence for various physical quantities in weak ferromagnetic or antiferromagnetic metals. One of them is the Curie-Weiss-like temperature dependence of the susceptibility derived in metallic magnetism. In contrast to the critical behavior of the Mott insulating systems, in which the local magnetic moment is temperature independent, the Curie-Weiss-like susceptibility in this case is mainly ascribed to temperature dependence of the squared local moment, which becomes T-linear at the critical coupling constant for $T>T_c=0$. The Curie-Weiss-like susceptibility obtained in this framework is not so surprising because in the SCR approximation we reproduce the critical behavior of the Gaussian treatment, as we discuss in Sec. II.D.9. For analyses of experimental results in weakly correlated materials, readers are referred to the review article of Moriya (1985). The basic predictions of this treatment for transport, magnetic, and thermodynamic properties, especially temperature dependences, have already been described in Sec. II.D.1, where the basic temperature dependences are derived from rather simple dimensional analyses. Experimentally, an example that follows the basic predictions of the SCR approximation near the magnetic transition is discussed in Sec. IV.A. Several f-electron systems also appear to follow this prediction, while some systems such as $\mathrm{CeCu}_{6-x}\mathrm{Au}_x$ show different criticality at the antiferromagnetic transition (von Löhneysen, 1996), where the specific heat C, the resistivity ρ, and the uniform magnetic susceptibility χ follow $C/T\propto-\ln(T)$, $\rho=\rho_0+A'T$, and $\chi=\chi_0(1-\alpha\sqrt{T})$, respectively. Other f-electron systems such as $\mathrm{U}_x\mathrm{Y}_{1-x}\mathrm{Pd}_3$

and $\mathrm{CeCu_2Si_2}$ also show a variety of anomalous features, which we do not discuss in detail here.

The most serious drawback of the SCR approximation in treating strongly correlated systems is the combination of the Gaussian approximation with the static approximation. First, dynamic spin fluctuations beyond the Gaussian level (one-loop level) are neglected. The prescription for the vertex correction is also insufficient. Second, since the static approximation employed in the strong-correlation regime is justified only when the temperature is much higher than all the characteristic spin fluctuation energies, various interesting quantum fluctuations may be ignored. Intrinsically quantum-mechanical phenomena have to be treated beyond the static approximation.

The metal-to-Mott-insulator transition, one of the main subjects in this article, is a good example in which the above drawbacks become serious. MITs are essentially quantum phase transitions at $T=0$ controlled by quantum fluctuations such as the band-width and the filling. There quantum dynamics plays a crucial role. In fact, near the Mott insulator, the characteristic spin-fluctuation energy remains at a finite value even in the insulating phase, whereas the characteristic charge excitation energy has to vanish toward the MIT point if the transition is of continuous type. Therefore the temperature range at which the static approximation is justified lies outside the interesting temperature range of charge dynamics. In addition, the existing framework of SCR on the one-loop level does not properly take into account the contribution from incoherent excitations or the reduction of the renormalization factor, which is a dominant effect near the continuous MIT.

Another point to be discussed with SCR is the treatment of magnetic transitions at finite temperatures as well as at zero. Self-consistent renormalization leads to a mean-field prediction for critical exponents near the transition point, because it is based on the Gaussian approximation in the paramagnetic region. This is only valid when the system is above the upper critical dimension of the $T=0$ quantum transition. In terms of critical phenomena, a proper treatment beyond the mean-field level becomes necessary in low dimensions. Recently, an equivalent approach to the weak-coupling SCR approximation was formulated by Hertz (1976) and Millis (1993), using renormalization-group (RG) analysis, as we review in the next subsection (Sec. II.D.9). This RG approach is also justified only above the upper critical dimension. A basic point there is that the dynamic exponent z is 2 for an antiferromagnetic transition in the metallic phase while $z=3$ for a ferromagnetic transition in metals. These dynamic exponents are derived from the low-energy action for an overdamped spin-wave due to the continuum of the Stoner excitation coupled to the spin wave. From the renormalization-group study, it was suggested that the upper critical dimension appears to be $d=3$ for antiferromagnetic transitions provided that the Fermi surface does not satisfy the nesting condition, while it is controversial for the ferromagnetic case (see the next subsection). As we discuss in Secs. II.D.9 and II.F in detail, such mean-field predictions are no longer justified in low dimensions. The mean-field prediction also ceases to be satisfied near the Mott transition point because the nesting condition has to be considered. Low dimensionality and the proximity of the Mott insulating phase are two typical cases in which quantum fluctuations are crucially important in deriving various features beyond the level of the SCR approximation, as is detailed in Sec. II.F.

Recently, an approximation at the same level as the SCR but extended to allow explicit charge fluctuations simultaneously and to allow an incommensurate periodicity of order has been developed as the two-particle self-consistent approach (Vilk, Chen, and Tremblay, 1994; Daré, Vilk, and Tremblay, 1996). In this approach, the same functional forms as for the RPA for χ_s and χ_c are assumed, but with renormalized interactions U_s and U_c. These parameters U_s and U_c are determined self-consistently to satisfy the constraint on a relation to $\langle n_\uparrow n_\downarrow \rangle$. This constitutes a conserving one-loop approximation at the two-particle level, in contrast to the one-particle level in the fluctuation exchange (FLEX) approximation. FLEX is regarded as the same level of approximation as the original weak-coupling SCR approximation without the vertex correction.

In the strong-coupling limit, that is, in localized spin systems, it appears that the SCR approximation in this subsection can be extended to reproduce the spherical approximation of spin systems. Kuramoto and Fukushima (1997) clarified the level of approximation needed to reproduce the spherical approximation in more detail.

9. Renormalization-group study of magnetic transitions in metals

In this subsection, renormalization-group studies of the Gaussian fixed point of magnetic transitions in the metallic phase, developed by Hertz (1976) and Millis (1993), are reviewed. As is mentioned in Sec. II.D.8, this treatment of the Gaussian fixed point essentially leads to equivalent results to the SCR approximation. We start with the path-integral formalism with the Stratonovich-Hubbard transformation introduced in Sec. II.D.2. When we neglect the charge fluctuation part by taking $y=0$ in Eq. (2.132b), the Δ_s-dependent part of the action derived in Eq. (2.137) is rewritten as

$$S=\frac{4}{U}\sum_k \tilde{\Delta}_s^*(k)\tilde{\Delta}_s(k)-\mathrm{Tr}\ \ln[1-G_0Q_1]. \qquad (2.233)$$

Since Q_1 is linear in $\tilde{\Delta}_s$, as defined in Eqs. (2.135c) and (2.133c)–(2.133e), we are able to expand S in terms of $\tilde{\Delta}_s$ and $\tilde{\Delta}_s^*$. Hereafter, for simplicity, we employ the notation Δ_s for $2\tilde{\Delta}_s$. Up to the fourth order of Δ_s, it is written as

$$S=\sum_k v_2(k)\Delta_s^*(k)\Delta_s(k)+\sum_{k_1\cdots k_4} v_4(k_1,k_2,k_3,k_4) \times\delta\left(\sum_{i=1}^{4} k_i\right)\Delta_s^*(k_1)\Delta_s^*(k_2)\Delta_s(k_3)\Delta_s(k_4)+\cdots \qquad (2.234)$$

where

$$v_2(k)=\frac{1}{U}-\chi_b(k) \tag{2.235}$$

while

$$\chi_b(k)=-\frac{1}{\beta}\sum_q G_0(q)G_0(k+q)$$
$$=-\sum_q \frac{f(\varepsilon_q)-f(\varepsilon_{k+q})}{\varepsilon_q-\varepsilon_{k+q}+\omega} \tag{2.236}$$

is the magnetic susceptibility of the noninteracting system. The coefficient v_4 is given by the fourth-order loop and can be expressed using G_0. The Gaussian coefficient $v_2(k)$ is expanded in terms of $\mathbf{k}$ and ω_n by using

$$\chi_b(\mathbf{k},i\omega_n)=\rho(\varepsilon_F)\left[1-\frac{1}{3}\left(\frac{\mathbf{k}}{2k_F}\right)^2-\frac{\pi}{2}\frac{|\omega_n|}{|\mathbf{k}|v_F}+\cdots\right] \tag{2.237}$$

for the case of ferromagnetic transitions with isotropic Fermi sphere. It should be noted that this expansion is possible only for $d>3$. In $d=1$ and $d=2$, the susceptibility is singular at $|\mathbf{k}|=2k_F$ even for an isotropic Fermi surface and cannot be expanded regularly (Kittel, 1968). A crucial assumption of the Gaussian treatment described in this subsection is that the dispersion in v_2 has nonzero coefficient for the quadratic k dependence and this is the leading contribution at small k. Recently, the nonanalyticity of χ_b in k for $d\leqslant 3$ in the leading order was considered more seriously (Vojta *et al.*, 1996; Kirkpatrick and Belitz, 1997), which led to the conclusion that, for the ferromagnetic case, the mean-field description is incorrect at $d=2$ and 3, in contrast with the results obtained from Eq. (2.237).

If the above assumption for the regular expansion in (2.237) is allowed, we obtain

$$v_2(k)=\Delta+\mathbf{k}^2+\frac{|\omega_n|}{|\mathbf{k}|}, \tag{2.238}$$

where we have assumed nonzero and finite coefficients for Δ, $\mathbf{k}^2$, and $|\omega_n|/|\mathbf{k}|$, which can be taken to be unity in appropriate units. Here Δ is the parameter measuring the distance from the critical point ($\Delta=0$ at the transition point) and should not be confused with the order parameter Δ_s. In the antiferromagnetic case, $v_2(k)$ is similarly expanded around the ordering wave number $\mathbf{Q}$ through $\chi_b(\mathbf{Q}+\mathbf{k},i\omega_n)$ for small $\mathbf{k}$ and ω_n if the nesting condition is not satisfied and the spatial dimension d satisfies $d\geqslant 3$. When the nesting condition is satisfied, as in the case of transitions to the Mott insulating state, this type of simple expansion is not possible, because v_n in the expansion (2.234) has higher-order singularities for larger n. We do not discuss this case here. The Mott transition is the subject of Sec. II.F, and we discuss this problem in Sec. II.F.11. After taking proper units, we have

$$v_2(k)=\Delta+\mathbf{k}^2+|\omega_n|\tau \tag{2.239}$$

for the antiferromagnetic case, where we have again assumed that coefficients for Δ, $\mathbf{k}^2$, and $|\omega_n|$ are nonzero and finite. We discuss the possible breakdown of this assumption in Sec. II.F. The difference between the ferromagnetic and antiferromagnetic cases arises from the fact that the order parameter, that is, the magnetization, commutes with the Hamiltonian and hence is conserved for the ferromagnetic case while this is not so for the staggered magnetization in the antiferromagnetic case. Because of the conserved magnetization, the inverse lifetime τ^{-1} of the ferromagnetic fluctuation becomes k linear for small k and hence the lifetime diverges in the limit $k\rightarrow 0$. The ω_n-linear dependence of the action is the consequence of the overdamped nature of the fluctuation due to coupling to the continuum Stoner excitations of metal.

Next we consider the scaling properties of these actions. When we take the scale transformation $k'=kb$ and $\omega'=\omega b^z$, the Gaussian terms

$$S_{2F}=\sum_k (\Delta+\mathbf{k}^2+|\omega_n|/|\mathbf{k}|)|\Delta_s(k)|^2 \tag{2.240}$$

for the ferromagnetic case and

$$S_{2AF}=\sum_k [\Delta+\mathbf{k}^2+|\omega_n|\tau]|\Delta_s(k)|^2 \tag{2.241}$$

for the antiferromagnetic case are transformed as

$$S'_{2F}=\sum_{k'} [\Delta+\mathbf{k}'^2 b^{-2}+(|\omega'_n|/|\mathbf{k}'|)\,b^{1-z}]|\Delta_s(k)|^2 \tag{2.242}$$

and

$$S'_{2AF}=\sum_{k'} [\Delta+\mathbf{k}'^2 b^{-2}+(|\omega'_n|\tau)\,b^{-z}]|\Delta_s(k)|^2, \tag{2.243}$$

respectively. The action can be kept in the same form after this scaling if the dynamic exponent z is given by $z=3$ for the ferromagnetic case and $z=2$ for the antiferromagnetic case with the following scaling taken simultaneously:

$$\Delta'=\Delta b^2 \tag{2.244}$$

and

$$\Delta'_s=\Delta_s b^{-(d+z+2)/2}. \tag{2.245}$$

The k dependence of the fourth-order coefficient v_4 is not important for critical properties and may be replaced with the value $u\equiv v_4(k=0)$ because $v_4(k=0)>0$ is assumed to be finite to make the transition from paramagnetic phase $\langle\Delta_s\rangle=0$ to the magnetic phase $\langle\Delta_s\rangle\neq 0$ possible at $\Delta=0$, as in the usual Landau free-energy expansion for Δ_s. Then the fourth-order term is scaled as

$$S_4=b^{4-(d+z)}u\sum_{k'_1\cdots k'_4}\delta\left(\sum_{i=1}^{4}k'_i\right)$$
$$\times\Delta_s'^{*}(k'_1)\Delta_s'^{*}(k'_2)\Delta'_s(k'_3)\Delta'_s(k'_4). \tag{2.246}$$

Therefore, the scaling of u should be

$$u'=ub^{4-(d+z)} \tag{2.247}$$

to keep the scale-invariant form for S_4. This means that the quartic term is scaled to zero for $d+z>4$ after repeating the renormalization. This is the reason why the mean-field approximation is justified for $d+z>4$ because the term S_4 becomes irrelevant. [Strictly speaking, as usual, the term S_4 is dangerously irrelevant. See, for example, Ma (1976)]. In this case, in the paramagnetic phase, the Gaussian approximation retaining only the quadratic term S_2 is justified in describing the quantum phase transition at $T=0$. We note, however, that if the dispersion itself in Eq. (2.240) or (2.241) is given by higher-order k^{ζ} such as k^4 instead of k^2, the above criterion $d+z>4$ for the justification of the mean-field treatment must be replaced with $d+z>2\zeta$. This is indeed the case for the Mott transition, discussed in Sec. II.F, where hyperscaling is justified.

If only the Gaussian part of S_{2F} or S_{2AF} is considered, the partition function $Z=e^{-\beta F}\equiv\int\mathcal{D}\Delta_s^*\mathcal{D}\Delta_s e^{-S}$ is given by

$$F=V\int_0^{\Lambda}\frac{d^d\mathbf{k}}{(2\pi)^d}\int_0^{\Gamma_k}\frac{d\varepsilon}{\pi}\coth\frac{\varepsilon}{2T}\tan^{-1}\left[\frac{\varepsilon/\Gamma_k}{\Delta+k^2}\right], \tag{2.248}$$

where we introduce a cutoff Λ for the momentum and Γ for the energy, with $\Gamma_k=\Gamma$ for antiferromagnets and $\Gamma_k=\Gamma k$ for ferromagnets. When we first integrate out the rapidly varying part of a thin frequency-momentum shell defined by the region $\Lambda\geqslant k\geqslant\Lambda/b$ and $\Gamma_k\geqslant\varepsilon\geqslant\Gamma_k/b^z$, we obtain

$$F=V\int_0^{\Lambda/b}\frac{d^dk}{(2\pi)^d}\int_0^{\Gamma_k/b^z}\frac{d\varepsilon}{\pi}\coth\frac{\varepsilon}{2T}\tan^{-1}\frac{\varepsilon/\Gamma_k}{\Delta+k^2}+F_1\ln b, \tag{2.249}$$

$$F_1=V\Lambda^dK_d\int_0^{\Gamma_\Lambda}\frac{d\varepsilon}{\pi}\coth\frac{\varepsilon}{2T}\tan^{-1}\frac{\varepsilon/\Gamma_\Lambda}{\Delta+\Lambda^2}+\frac{Vz}{\pi}\int_0^{\Lambda}\frac{d^dk}{(2\pi)^d}\coth\frac{\Gamma_k}{2T}\tan^{-1}\frac{1}{\Delta+k^2}. \tag{2.250}$$

After the rescaling of k to $k'=bk$ and ε to $\varepsilon'=\varepsilon b^z$ to recover the original range of k and ε, we need the rescaling

$$\Delta=\Delta'/b^2, \tag{2.251}$$

$$T=T'/b^z \tag{2.252}$$

to keep the same form for F as

$$F=V'b^{-(d+z)}\int_0^{\Lambda}\frac{d^dk'}{(2\pi)^d}\int_0^{\Gamma_{k'}}\frac{d\varepsilon'}{\pi}\times\coth\frac{\varepsilon'}{2T'}\tan^{-1}\frac{\varepsilon'/\Gamma_{k'}}{\Delta'+k'^2}. \tag{2.253}$$

Then the renormalization-group equation of Δ and u for S_2 is $d\Delta/d\ln b=2\Delta$ and $dT/d\ln b=zT$. The non-Gaussian term S_4 can be treated perturbatively, when we treat only Gaussian behavior. The free energy can be easily calculated up to first order in u, and rescalings of Δ, T, and u are determined to keep the same form for F after the scale transformation b. The resultant renormalization-group equations up to first order in u are

$$\frac{d\Delta}{d\ln b}=2\Delta+\Xi(T,\Delta)u, \tag{2.254}$$

$$\frac{dT}{d\ln b}=zT, \tag{2.255}$$

$$\frac{du}{d\ln b}=[4-(d+z)]u \tag{2.256}$$

with

$$\Xi(T,\Delta)=2(n+2)\Bigg[\frac{2}{\pi}\int_0^{\Lambda}\frac{d^dk}{(2\pi)^d}k^{z-2}\times\coth\frac{k^{z-2}}{2T}\frac{1}{1+(\Delta+k^2)^2}+K_d\int_0^1\frac{d\varepsilon}{\pi}\coth\frac{\varepsilon}{2T}\frac{\varepsilon}{\varepsilon^2+(\Delta+1)^2}\Bigg], \tag{2.257}$$

where

$$K_d=(2\pi)^{-d/2}/(d-2)!!$$

for even d and

$$K_d=2(2\pi)^{-(d+1)/2}/(d-2)!!$$

for odd d. The solution of these equations is

$$T=T_0b^z, \tag{2.258}$$

$$u=u_0b^{4-(d+z)}, \tag{2.259}$$

$$\Delta=b^2\left(\Delta_0+u_0\int_0^{\ln b}dxe^{[2-(d+z)]x}F(T_0e^{zx},\Delta_0e^{2x})\right). \tag{2.260}$$

From the solution for u, it is clear that the Gaussian treatment is justified in the paramagnetic phase when $4-(d+z)<0$. Two regimes exist when the scaling stops at $\Delta\sim1$. One is the quantum regime, where $T\ll1$ is satisfied when the scaling stops at $\Delta\sim1$. The other is the classical regime, where $T\gg1$ for $\Delta\sim1$. The boundary of these two regimes is obtained by putting $T=0$ and $\Delta=1$ into Eq. (2.260) to get b and substituting the resultant b into Eq. (2.258). The condition for the occurrence of the quantum regime is

$$1\gg T_0/r^{z/2}, \tag{2.261}$$

$$r=\Delta_0+\frac{uF(T=0,\Delta_0)}{z+d-2}, \tag{2.262}$$

where T_0 and Δ_0 are the bare values of the temperature and the control parameter. In the quantum regime, as is usual in the Gaussian model, the correlation length is given by

$$\xi=r^{-1/2}. \tag{2.263}$$

When T is scaled large, the renormalization-group equation should be rewritten with a new variable $v=uT$ because $\Xi(T)\sim CT$ for $T\gg1$, and the right-hand side of Eq. (2.254) is a function of the single variable uT. Then the renormalization-group equation reads

$$\frac{d\Delta}{d\ln b}=2\Delta+Cv, \tag{2.264}$$

$$\frac{dv}{d\ln b}=(4-d)v \tag{2.265}$$

up to linear order in v. The initial condition for these equations is obtained from a solution of the original equations (2.254)–(2.256) when the renormalization stops at $T=1$, as

$$\bar{\Delta}=T_0^{-2/z}[r+Bu_0T_0^{(d+z-2)/z}], \tag{2.266}$$

$$\bar{v}=u_0T_0^{(d+z-4)/z}, \tag{2.267}$$

where

$$B=\frac{1}{2z}\int_0^1 dT\,T^{(2-d-2z)/z}[\Xi(T)-\Xi(0)]/(n+2). \tag{2.268}$$

The renormalization-group equations (2.264) and (2.265) are solved using the initial conditions (2.266) and (2.267). The Ginsburg criterion, which is the condition for justification of Gaussian treatment, is given by $v\ll1$ when the scaling stops at $\Delta=1$. This criterion is

$$\frac{uT^{1+1/z}}{r+(B+C)uT^{1+1/z}}\ll1, \tag{2.269}$$

which is always justified at $T=0$ and is violated only in a narrow critical region near the critical point $r+(B+C)uT^{1+1/z}=0$ for $T\neq0$. We note that this derivation of the Ginsburg criterion is justified only when $d+z-4>0$ and u remains small after renormalization.

The free energy can be computed from the solution of the renormalization-group equation. The specific heat coefficient $\gamma=C/T$ at low T is calculated as

$$\gamma\propto\gamma_0+O(T^2) \tag{2.270}$$

in the quantum regime with a constant γ_0, while

$$\gamma\propto\ln T \tag{2.271}$$

for $z=d$ and

$$\gamma\propto\gamma_0+\alpha T^{1/z} \tag{2.272}$$

for $z<d$ in the classical regime. These are indeed the results obtained in the SCR approximation, which is essentially a treatment by the Gaussian fixed point with self-consistent determination of the coefficients of the Gaussian term. When this description is justified, it is natural to expect that $\chi(q)$ follows the criticality of the mean-field theory and hence the Curie-Weiss law $\chi(q)\sim C/(T+\theta)$, although the coefficients C and θ may be renormalized from the bare values. This is related to the Curie-Weiss law derived in the SCR approximation, where treatment by the Gaussian fixed point is justified around $\Delta\sim0$ even at low temperatures $T\sim0$. In this region, as pointed out by the SCR approximation, the temperature dependence of the local moment $\sim T$ plays an important role in deriving the Curie-Weiss behavior. Consequences of the Gaussian treatment for other quantities such as the susceptibility, spin correlations, and resistivity are discussed from intuitive picture in Secs. II.D.1 and II.D.8. In the strong-correlation regime, the amplitude of the order parameter grows faster than the weak-correlation regime above the transition temperature, where the low-energy excitation is described through $\vec{n}_i$ and θ_i by Eq. (2.156). In this region, the Gaussian treatment described in this subsection is no longer justified, even in the disordered phase. The Gaussian treatment also becomes invalid when the dispersion of the relevant gapless excitation becomes flatter in low-dimensional systems. In this case we have to consider the scaling analysis. We discuss in Sec. II.F when and how the Gaussian treatment breaks down.

E. Numerical studies of metal-insulator transitions for theoretical models

Algorithms for numerical computation of strongly correlated systems have recently been developed and applied extensively. Several comprehensive articles in the literature are available on these algorithms and their applications (Scalapino, 1990; von der Linden, 1992; Hatano and Suzuki, 1993; Imada, 1993d, 1995d; Dagotto, 1994). Two different algorithms have been widely studied and applied, so far. One is the exact diagonalization of the Hamiltonian matrix including the Lanczos method. Using this method, one can obtain physical quantities with high accuracy but only for small clusters. Tractable system size is strictly limited because the necessary memory size increases exponentially with system size. For instance, for the Hubbard model, the largest tractable number of sites for the ground state is around 20. The exact diagonalization method has close ties with the configuration-interaction method, which is the subject of Sec. III.A.1.

Rigorous treatments of finite-temperature properties as well as dynamic properties are possible only when the Hamiltonian matrix is fully diagonalized. However, full diagonalization by, for example, the Householder method is possible only for even smaller-sized system than the Lanczos method for the ground state only. To relax the severe limitation of tractable size for treating finite-temperature and dynamic properties, a combination of diagonalization and statistical sampling was introduced a decade ago (Imada and Takahashi, 1986). In this method, the trace summation is replaced by a sampling of randomly generated basis states, while the imaginary-time or real-time evolution, $e^{-\tau\mathcal{H}}$ or $e^{i\mathcal{H}t}$, is computed exactly as in the power method. In this quantum transfer Monte Carlo method and the quantum molecular dynamics method, the tractable system size is extended to sizes comparable to the Lanczos method. A very similar method was also applied recently to the t-J model by replacing the power method with Lanczos diagonalization (Jaklič and Prelovšek, 1994).

The quantum Monte Carlo method provides another way of calculating strong-correlation effects for relatively larger systems. A frequently used algorithm of quantum Monte Carlo calculation is based on the path-integral formalism combined with the Stratonovich-Hubbard transformation. This takes a similar starting point to that of the method described in Secs. II.C and II.D. The Stratonovich-Hubbard variable employed in the Monte Carlo calculation is usually chosen to break up the interaction into two diagonal operators. A crucial difference from the Hartree-Fock-type treatment is that dynamic and spatial fluctuations of the Stratonovich-Hubbard variables are taken into account numerically in an honest fashion in contrast to saddle-point estimates, static approximations, or Gaussian approximations employed in the mean-field-type treatments. Therefore, in terms of interaction effects, the quantum Monte Carlo study provides a controlled method of calculation. A drawback of the numerical methods is that they can treat only finite-size systems. Thus careful analyses of finite-size effects are important in numerical studies, especially for low-energy excitations.

There exist various types of algorithms for quantum Monte Carlo simulations. For the algorithm for fermion systems with the Stratonovich-Hubbard transformation described above, readers are referred to the literature (von der Linden, 1992; Hatano and Suzuki, 1993; Imada, 1993d, 1995d). In addition to this algorithm, several different methods are known. The so-called world-line algorithm is a powerful method for nonfrustrated quantum spin systems as well as for fermion models in one dimension. Recently for the world-line method, two useful algorithms have been introduced. One is the cluster updating algorithm or the loop algorithm (Evertz, Lana, and Marcu, 1993; Evertz and Marcu, 1993), which was developed based on the original cluster algorithm for classical systems (Swendsen and Wang, 1987). By using the cluster algorithm, one can update the configuration of a large cluster at once, so that the sample can be more efficiently updated with shorter autocorrelation time. This is especially powerful for example, when the critical slowing down is serious near the critical point. The other useful algorithm is for continuous time simulation, where the path integral can be simulated without taking a discrete time slice, so that the procedure to take the continuum limit of the breakup in the time slice can be avoided (Beard and Wiese, 1996). In 1D systems, some other efficient methods of numerical calculation have also been developed. The density-matrix renormalization-group (DMRG) method developed by White (1993) is a typical example, where the numerical renormalization-group method originally developed by Wilson (1975) is successfully extended to a study of the ground state of 1D lattice models using a renormalization-group scheme applied to the density matrix by properly considering the boundary condition of the system. It was recently applied, as well, to a lattice of stripe such as $6\times n$ and $8\times n$ square lattices to discuss 2D systems (White and Scalapino, 1996). The recently developed constrained path-integral method also appears to give high accuracy in any dimension, although it relies on a variational estimate (Zhang, Carlson, and Gubernatis, 1997).

There is an enormous literature on the numerical investigation of strongly correlated systems, especially on models for high-T_c cuprates. Because extensive reviews of numerical results on strongly interacting lattice fermion models are available elsewhere (Scalapino, 1990; von der Linden, 1992; Imada, 1993d, 1995d; Dagotto, 1994), here we give only a brief summary of results directly related to the metal-insulator transition and the anomalous metallic states near it. We do not discuss in detail the superconducting properties studied by numerical methods. The reader is referred to other reviews (Scalapino, 1995, and the references cited above).

Near the MIT point, various quantities exhibit critical fluctuations. Here we discuss calculated results for the Hubbard model, the d-p model, and the t-J model. Most of the effort in numerical studies is concentrated in 1D and 2D systems without orbital degeneracy, partly due to the interest in these systems in relation to the high-T_c cuprates and partly due to the feasibility of estimating finite-size effects within present computer capabilities. Another important motivation for investigating low-dimensional systems is that they show a variety of interesting and anomalous quantum fluctuations. To understand real complexity in d-electron systems with orbital degeneracy, an algorithm for the degenerate Hubbard model, treating the MIT and orbital and spin-fluctuation effects, was developed and applied by Motome and Imada (1997, 1998).

1. Drude weight and transport properties

As we discuss in Sec. II.F.3, the Drude weight and the charge compressibility are the most basic and relevant quantities for discussing the Mott transition. The Drude weight D for periodic systems is defined from the frequency-dependent conductivity $\sigma(\omega)$ as

$$\sigma(\omega)=D\,\delta(\omega)+\sigma_{\rm reg}(\omega) \qquad (2.273)$$

at $T=0$ where $\sigma_{\rm reg}$ describes the contribution from incoherent excitations and must be smooth as a function of ω.

The Drude weight has been calculated by the exact diagonalization method for the 1D and 2D Hubbard models as well as for the t-J models.[2] Although the extrapolation to the thermodynamic limit is difficult because of small system sizes, it appears to show that the

---

[2] Exact diagonalization studies include those of Moreo and Dagotto, 1990; Sega and Prelovšek, 1990; Stephen and Horsch, 1990, 1992; Fye *et al.*, 1991; Wagner, Hanke, and Scalapino, 1991; Dagotto, Moreo, Ortolani, Riera, and Scalapino, 1991; Tohyama and Maekawa, 1992; Tsunetsugu and Imada, 1997.

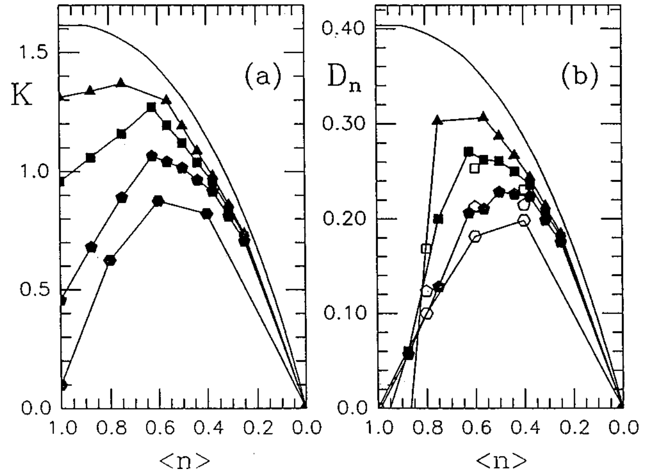

FIG. 16. Diagonalization result for the total kinetic energy K in (a) and Drude weight D in (b) as a function of electron filling $\langle n\rangle$ in the ground state for the 4×4 cluster of the Hubbard model: triangles, $U/t=4$; squares, $U/t=8$; pentagons, $U/t=20$; hexagons, $U/t=100$. The curves without symbols are for $U=0$. From Dagotto *et al.*, 1992.

Drude weight decreases continuously and vanishes at half filling. The vanishing Drude weight clearly shows the appearance of the Mott insulator at half filling. The Hubbard model and the t-J model show similar behaviors, as can be seen in Figs. 16 and 17. In 1D systems, exactly solvable models follow $D\propto\delta$, as we show in Sec. II.F. In constrast, 2D systems seem to follow $D\propto\delta^2$ (Tsunetsugu and Imada, 1998).

Experimental results on the cuprate superconductors and several other transition-metal oxides such as $La_{1-x}Sr_xTiO_3$ appear to show similar continuous reduction of the Drude weight with decreasing doping concentration (see Sec. IV). In the strict sense, the Drude weight is defined as the singularity of the conductivity at $\omega=0$ and $T=0$, but experimental results always suffer from finite-temperature broadening as well as lifetime effects from the impurity scattering. This issue is further discussed in Secs. II.F and IV.

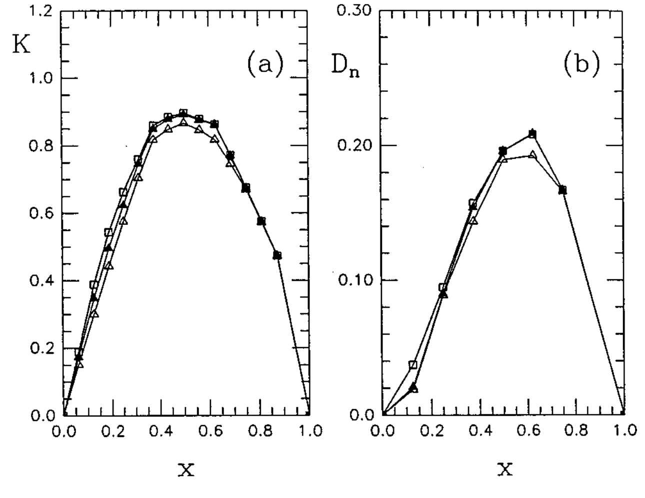

FIG. 17. The same as Fig. 16 as a function of hole doping concentration $\delta\equiv x=1-\langle n\rangle$ for the 4×4 cluster of the t-J model: squares, $J/t=0.1$; solid triangles, $J/t=0.4$; open triangles, $J/t=1$. From Dagotto *et al.*, 1992.

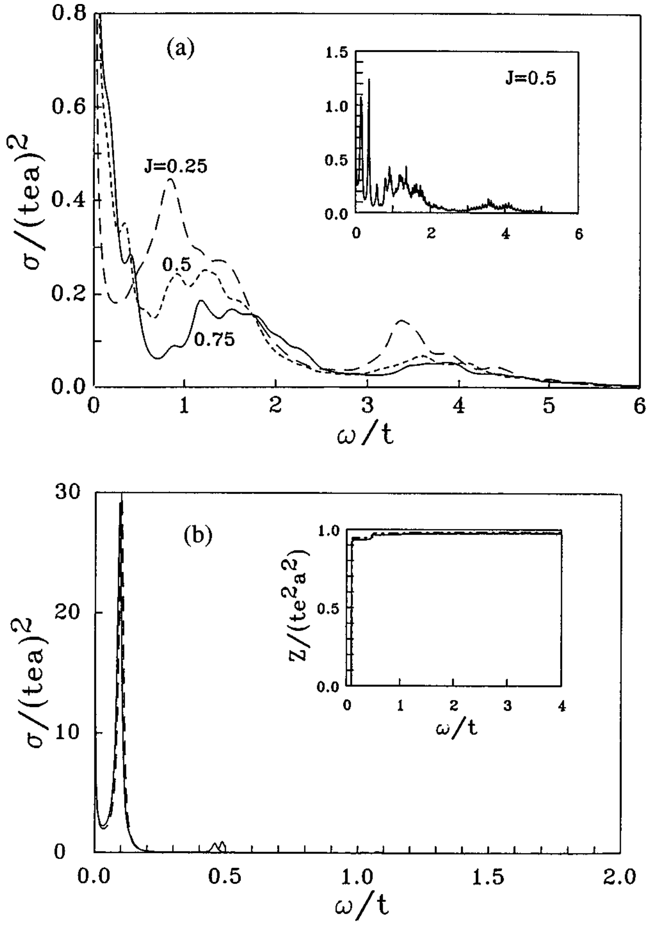

FIG. 18. Optical conductivity $\sigma(\omega)$ of the t-J model with one hole at $T=0$: (a) two-dimensional 4×4 cluster for three choices of $J/t=0.25$, 0.5, and 0.75; (b) one-dimensional 16-site cluster at $J/t=0.5$ for the $S=1/2$ ground state (solid curve) and the $S=15/16$ ferromagnetic state (dashed curve). Note that the Drude peak appears at a finite frequency $\omega\sim0.1$ due to the open boundary condition. The spectra are broadened with width 0.1. The inset in (a) shows the case with a higher resolution (the broadening is 0.02). The inset in (b) shows the weight integrated from 0 to ω. From Stephan and Horsch, 1990.

The frequency-dependent conductivity $\sigma(\omega)$ has also been calculated in the Hubbard and t-J models (Inoue and Maekawa, 1990; Moreo and Dagotto, 1990; Sega and Prelovšek, 1990; Stephen and Horsch, 1990). It was pointed out that the 2D system under doping has large weight in the incoherent part $\sigma_{reg}(\omega)$ inside the original charge gap. Upon doping, in addition to the growth of the Drude-like part, the weight is progressively transferred from the higher ω region above the charge gap of the insulator to the region inside the gap as shown in Fig. 18. This is similar to what happens in the cuprate superconductors (see, for example, Uchida *et al.*, 1991) as discussed in Sec. IV.C. It was also pointed out that the long tail of $\sigma(\omega)$ at large ω seen in the numerical

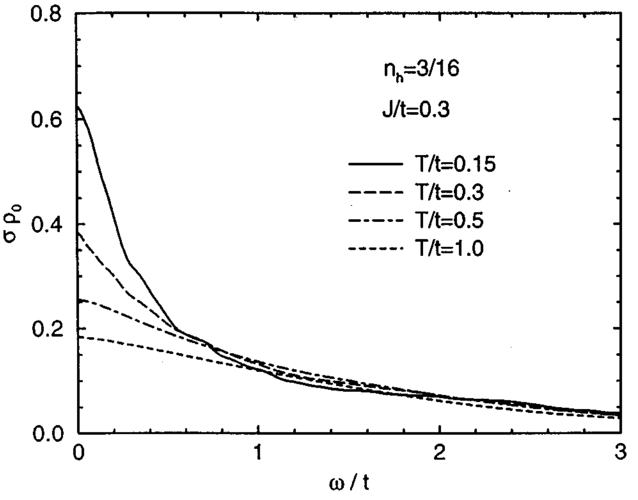

FIG. 19. Optical conductivity at finite temperatures for 4×4 cluster of the t-J model at $J/t=0.3$ and $\delta=3/16$ where $\rho_0=\hbar/e^2$, with e being the electronic charge and $n_h\equiv\delta$ the doping concentration. From Jaklič and Prelovšek, 1995a.

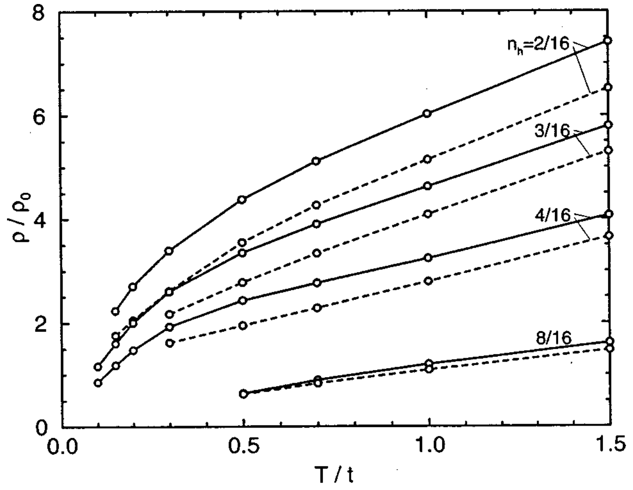

FIG. 20. Temperature dependence of resistivity ρ for 4×4 cluster of the t-J model for various doping concentrations: dashed curves, $J/t=0$; solid curves, $J/t=0.3$. The same notation as Fig. 19. From Jaklič and Prelovšek, 1995a.

results is similar to the experimental results (Azrak *et al.*, 1994). In contrast with 2D systems, the incoherent part of the charge excitation is not clearly seen in 1D systems under doping, as shown in Fig. 18 (Stephen and Horsch, 1990). The transferred weight from the region above the gap is exhausted only in the coherent Drude part. Recently, it was suggested that the integrable model in 1D has a finite Drude weight with the δ-function peak at $\omega=0$ in $\sigma(\omega)$, even at finite temperatures (Zotos and Prelovšek, 1996). It should be noted that the overall feature of $\sigma(\omega)$ of the single ladder system shows an incoherent tail similar to the 2D case, in contrast to the naive expectation of similarity to 1D systems (Tsunetsugu and Imada, 1997).

For the t-J model in 2D, in the temperature range of the superexchange interaction and lower, $\sigma(\omega)$ shown in Fig. 19 and calculated by Jaklič and Prelovšek (1995a) appears to follow

$$\sigma(\omega)=\frac{1-e^{-\beta\omega}}{\omega}C(\omega) \tag{2.274}$$

and the current correlation function

$$C(\omega)\equiv\int_{-\infty}^{\infty}dt\, e^{i\omega t}\langle j(0)j(t)\rangle\simeq\frac{\sigma_0/\tau}{\omega^2+(1/\tau)^2} \tag{2.275}$$

with temperature-independent σ_0 and τ. The scale of $1/\tau$ seems to be larger than or comparable to the transfer t (Jaklič and Prelovšek, 1995a). This form implicitly assumes that the carrier dynamics are totally incoherent. We discuss this problem in Secs. II.F.9 and II.G.2, as well as a related problem in Sec. II.E.3. Jaklič and Prelovšek claimed the similarity of this result to the experimentally observed transport properties in the normal state of high-T_c cuprates. From the above form, $\sigma(\omega)$ has a rather long tail proportional to $1/\omega$ in the range $0<\omega<1/\tau$, while the dc conductivity is proportional to β, consistent with experimental results on cuprates and the marginal Fermi-liquid hypothesis (for the marginal Fermi liquid, see Sec. II.G.2, and for experimental aspects of the cuprates, see Sec. IV.C). The dc resistivity has indeed been calculated at relatively high temperatures (Jaklič and Prelovšek, 1995a, 1995b; Tsunetsugu and Imada, 1997). What should be noted here is that the linear-T resistivity $R\propto T$ characteristic in the high-temperature limit with totally incoherent dynamics (Ohata and Kubo, 1970; Rice and Zhang, 1989) seems to be retained even in the temperature region below the superexchange interaction for the planar t-J model (see Fig. 20). This seems to be related to the suppression of coherence due to the anomalous character of the Mott transition (see Secs. II.F.9 and II.G.2). Broad incoherent tails roughly scaled by $1/\omega$ are seen not only in the high-T_c cuprates but also in many transition-metal compounds near the Mott transition point. We discuss examples of this unusual feature in Sec. IV, for example in Secs. IV.B and IV.D. The optical conductivity of the Mn and Co compounds discussed in Secs. IV.F and IV.G shows even more incoherent ω dependence.

The Hall coefficient is another interesting subject of the transport properties. The frequency-dependent Hall coefficient $R_H(B,\omega)$ in a magnetic field B is defined by

$$R_H(B,\omega)=\frac{1}{B}\frac{\sigma_{x,y}(\omega)}{\sigma_{x,x}(\omega)\sigma_{y,y}(\omega)-\sigma_{x,y}(\omega)\sigma_{y,x}(\omega)}, \tag{2.276}$$

where

$$\sigma_{\alpha,\gamma}(\omega)=\frac{ie^2}{\omega+i\eta}D_{\alpha,\gamma}(\omega) \tag{2.277}$$

with

$$D_{\alpha,\gamma}(\omega)=\frac{1}{L^d}\left(-\frac{\langle K\rangle}{d}\delta_{\alpha,\gamma}-\int_0^{\infty}dt\; e^{-i\omega t}\langle j_\alpha(t);j_\gamma(0)\rangle\right) \tag{2.278}$$

for a linear system of size L and the infinitesimal convergence factor η (Shastry, Shraiman, and Singh, 1993; Assaad and Imada, 1995). The canonical correlation $\langle P;Q\rangle$ is defined by

$$\langle P;Q\rangle \equiv \int_0^\beta \frac{d\lambda}{\beta}\,\mathrm{Tr}[e^{-\beta\mathcal{H}}e^{\lambda\mathcal{H}}Pe^{-\lambda\mathcal{H}}Q]. \tag{2.279}$$

Here the averaged kinetic energy is denoted by $\langle K\rangle$ and the current operator is given by

$$j_\alpha = -i\sum_{\vec{i},\sigma}[t_{\vec{i},\vec{a}_\alpha}(\vec{A})c^\dagger_{\vec{i},\sigma}c_{\vec{i},+\vec{a}_\alpha,\sigma} - t_{\vec{i}+\vec{a}_\alpha,-\vec{a}_\alpha}(\vec{A})c_{\vec{i}+\vec{a}_\alpha,\sigma}c_{\vec{i},\sigma}] \tag{2.280}$$

and

$$t_{\vec{i},\vec{a}}(\vec{A}) = -t\,\exp\left(\frac{2\pi i}{\Phi_0}\int_{\vec{i}}^{\vec{i}+\vec{a}}\vec{A}\cdot d\vec{l}\right), \tag{2.281}$$

with the flux quantum Φ_0 and the vector potential $\vec{A}$. Here, a hypercubic lattice structure is assumed for simplicity. Since the effect of the lifetime τ of the charge is washed out in the frequency $\omega \gg 1/\tau$, R_H at large ω represents a simpler and more intrinsic property of strong correlations than the zero-frequency Hall coefficient. In fact it is a better probe to measure the carrier density, as pointed out by Shastry *et al.* (1993). At $\omega\to\infty$, one can show

$$R_H^* \equiv R_H(\omega\to\infty) = -\frac{4L^d}{e^2B}\frac{i\langle(j_x,j_y)\rangle}{\langle K\rangle^2} \tag{2.282}$$

with the commutator $(a,b)=ab-ba$. Recently the ω-dependent Hall coefficient was measured experimentally (Kaplan *et al.*, 1996).

The temperature dependence of the Hall coefficient R_H^* as well as its frequency dependence has been calculated by several authors (Shastry, Shraimann, and Singh, 1993; Assaad and Imada, 1995; Tsunetsugu and Imada, 1997). In the strong-correlation regime of 2D systems, it shows that, at small hole doping, R_H^* is electronlike ($R_H^*<0$) with small amplitude at $T>U$, while it becomes hole-like ($R_H^*>0$) with large amplitude at $J<T<U$ where U and J are the energy scales of the repulsive interaction and the superexchange interaction, respectively. When T is smaller than the energy scale of J, R_H^* again decreases and becomes negative (electron-like; see Fig. 21).

These two crossovers are explained by the following simple physical picture: At $T>U$, the Hall coefficient approaches the value of noninteracting electrons because the interaction effect may be neglected. In the region $J<T<U$, the interaction effect becomes important, while the spin degrees of freedom are still degenerate, so that the particles behave essentially as spinless fermions. In terms of the spinless fermions, the band is completely filled for the filling corresponding to the Mott insulator. Therefore a system with small hole doping is indeed expected to behave as hole-like with small carrier number (that is, R_H has large amplitude). When the temperature is further lowered to $T<J$, the spin entropy is gradually released with the growth of antiferromagnetic correlations and up- and down-spin electrons start forming large Fermi surface consistently with the Luttinger volume. This state with large carrier number leads to a small amplitude of the Hall coefficient. The sign of R_H itself may depend on details of the Fermi surface. If the curvature of the Fermi surface is hole-like, R_H^* may be positive.

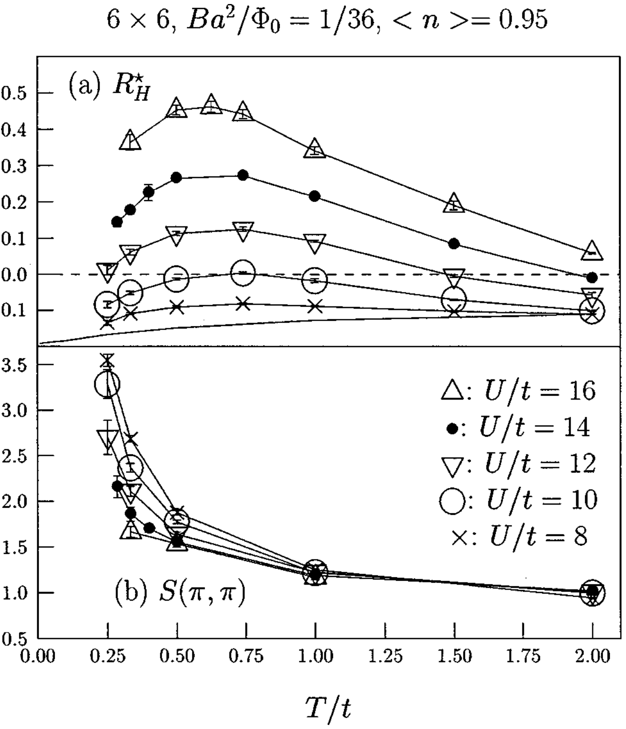

FIG. 21. Temperature dependence of high-frequency Hall coefficient R_H^* and equal-time spin structure factor $S(\pi,\pi)$ at $\delta=0.05$ for 6×6 cluster of the 2D Hubbard model. Solid line with no symbols corresponds to the $U/t=0$ result. From Assaad and Imada, 1995.

Another interesting crossover happens when a spin gap or pseudogap due to singlet pairing is formed. Although the tractable system size is limited to small clusters, this was numerically studied by explicitly forming a spin gap in a ladder structure of the lattice. Below the spin-gap temperature, R_H^* becomes large and generally positive (Tsunetsugu and Imada, 1997), and the system is transformed essentially to single-component bosons near the Mott insulator, although coexistence of singlet pairs and quasiparticles with dynamic fluctuations may show aspects different from simple bosons. Because the hard-core bosons near the Mott insulator are mapped to the case of dilute bosons near the vacuum by the electron-hole transformation, the single-component bosons near the Mott insulator behave as dilute holes. This is the basic reason for hole-like R_H^* with large amplitude.

All the above seem to be consistent with the measured temperature dependence of R_H in the high-T_c cuprates if the R_H at large and small frequencies are qualitatively similar. As is discussed in Secs. IV.C.1 and

IV.C.3, the experimentally measured R_H in the underdoped region showed strong temperature dependence from small amplitude at higher temperatures to large and positive values basically scaled by the inverse hole concentration $1/\delta$ at low temperatures. The crossover occurred at the temperature T_{cr} where the uniform magnetic susceptibility decreased remarkably with decreasing temperature (Nishikawa *et al.*, 1993; Hwang *et al.*, 1994; Nakano *et al.*, 1994). All of these properties can be explained by gradual and progressive pseudogap formation (preformed singlet pair fluctuation) below the crossover temperature T_{cr}, which decreases from the value $\sim 500 \sim 600$ K at small doping to 0 K in the overdoped region ($\delta \sim 0.2 \sim 0.3$).

In the case of ladder systems, with the lattice structure of two chains coupled by rungs, however, the particular geometry of the ladder leads to a large negative value of R_H^* below the temperature of spin-gap formation, although it has been shown in a small cluster study that a substantial interladder coupling generally drives R_H^* to a large positive value (Tsunetsugu and Imada, 1997). In most of the above cases, the frequency dependence of $R_H(\omega)$ has not yet been examined systematically. However, the calculated ω dependence available so far appears to show similar behavior between small and large ω. It is not clear whether $R_H(\omega)$ has a strong ω dependence at the frequency scale of the inverse relaxation time τ^{-1} of carriers.

2. Spectral function and density of states

Two other quantities important to our understanding of the MIT and anomalous metallic states are the spectral function $A(\mathbf{k},\omega)$ and the density of states $\rho(\omega)$ defined from Eqs. (2.50), (2.56), and (2.57) as

$$\rho(\omega) = \sum_{\mathbf{k}} A(\mathbf{k},\omega), \tag{2.283}$$

$$A(\mathbf{k},\omega) = -\frac{1}{\pi} \operatorname{Im} G^R(\mathbf{k},\omega), \tag{2.284}$$

$$G^R(\mathbf{k},\omega) = -i \int_{-\infty}^{\infty} dt\, e^{i\omega t} \theta(t) \langle \{ c_{\mathbf{k}\sigma}(t), c_{\mathbf{k}\sigma}^{\dagger}(0) \} \rangle, \tag{2.285}$$

where the thermodynamic average $\langle \cdots \rangle$ and the Heisenberg representation $O(t) = e^{-i\mathcal{H}t} O e^{i\mathcal{H}t}$ are introduced. In the ground state, $A(\mathbf{k},\omega)$ may be rewritten as Eq. (2.54). Experimentally, $A(\mathbf{k},\omega)$ is measured by angle-resolved photoemission and inverse photoemission experiments as described in Sec. II.C.4. The angle-integrated intensity gives $\rho(\omega)$. Numerically, $A(\mathbf{k},\omega)$ and $\rho(\omega)$ have been calculated either by the exact diagonalization method or by quantum Monte Carlo calculations combined with the maximum-entropy method.

Numerical results on $A(\mathbf{k},\omega)$ and $\rho(\omega)$ for the Hubbard model and the *t*-*J* model show drastic but continuous change upon doping (Dagotto, Moreo, *et al.*, 1991, 1992; Stephen and Horsch, 1991; Tohyama and Maekawa, 1992; Bulut, Scalapino, and White, 1994a; Moreo, Haas, Sandvik, and Dagotto, 1995; Preuss, Hanke, and W. von der Linden, 1995; Preuss *et al.*, 1997). Figure 22 shows an example of the doping concentration dependence of $\rho(\omega)$. The density of states at half filling clearly shows the opening of the charge gap, as we discuss below. The chemical potential shifts immediately upon doping to the edge of the "Hubbard gap." The chemical potential slowly shifts upon further doping within a large density of states observed near the gap edge. This shift is accompanied by a drastic and continuous reconstruction from "upper" and "lower" Hubbard band structure to a single merged band structure. When the doping concentration is low, in the 2D Hubbard or *t*-*J* models, $A(\mathbf{k},\omega)$ shows dispersive quasiparticle-like structure with a bandwidth comparable to that of J in addition to broad incoherent backgrounds, as in Fig. 23. This basic and overall structure seems to be robust in some interval of doping range. The dispersive part has a flat band structure with stronger damping around $\mathbf{k} = (\pi,0)$ and three other equivalent points (Bulut, Scalapino, and White, 1994b; Dagotto, Nazarenko, and Boninsegni, 1994). The dispersions there appear to be flatter than that expected from the usual van Hove singularity. This flatter dispersion could be related to other unusual properties observed numerically, such as incoherent charge transport (Sec. II.E.1), singular charge compressibility (Sec. II.E.3), and incoherent spin dynamics (Sec. II.E.4). This idea is discussed in Sec. II.F.11. Recently, it was shown that the dispersion around $(\pi,0)$ follows quartic dispersion ($\sim k^4$) in agreement with the picture in Sec. II.F.11 (Imada, Assaad, *et al.*, 1998). Although the numerical results of clusters have suggested the existence of a quasiparticle band of width $\sim J$, this "band" itself could be dominantly incoherent near the Fermi level. Because these numerical results are results on simplified models, more complicated features can also be observed in realistic situations. Effects of impurity levels and the long-range Coulumb interaction are among these complexities. We compare these results on theoretical models with photoemission results on transition-metal oxides in Secs. IV.C.3, IV.C.4 and IV.D.1. In particular, in a recent comparison of 1D and 2D systems by Kim *et al.* (1996), it was suggested that weakly dispersive bands with incoherent character in 2D be contrasted with a clearer dispersion in 1D, as is discussed in Sec. IV.D.1. This difference between 1D and 2D is related with the difference in the Drude weight discussed in Sec. II.E.1.

Angle-resolved photoemission spectra of a model compound of the parent insulator of high-T_c superconductors, $Sr_2CuCl_2O_2$ (Wells *et al.*, 1995), can be compared with the Monte Carlo simulations of the Hubbard as well as of the *t*-*J* model (Dagotto, 1994), since the single-band Hubbard model and the *t*-*J* model are effective Hamiltonians for the CuO_2 plane. (The top of the occupied band is derived from the $d^9 \rightarrow d^9\underline{L}$ local-singlet spectral weight and the bottom of the unoccupied band forms the $d^9 \rightarrow d^{10}$ spectral weight). Figure 24 shows that in going away from $\mathbf{k} = (0,0)$ a peak disperses towards lower binding energies; along the (π,π) direction, the peak reaches closest to E_F at $\sim(\pi/2,\pi/2)$ and then is shifted back toward higher binding energies, in good

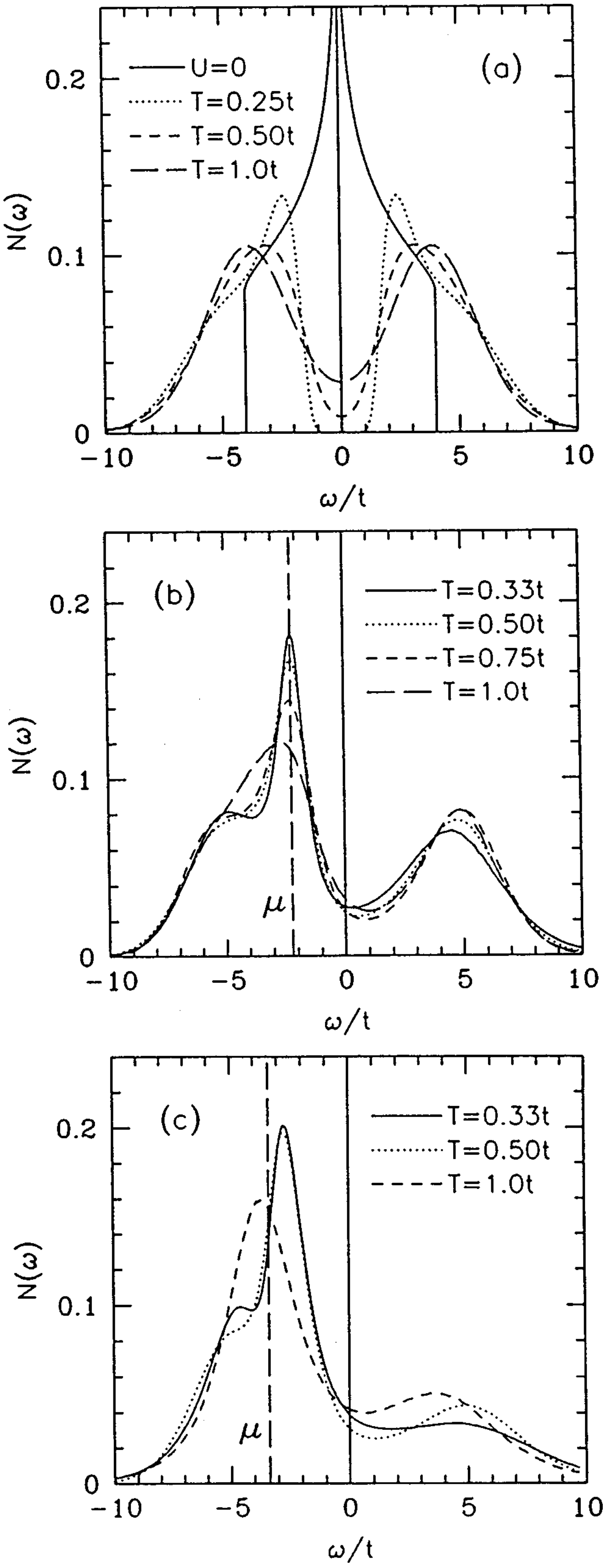

FIG. 22. Doping concentration and temperature dependence of the density of states $\rho(\omega)$ for 8×8 Hubbard model at $U/t=8$ for (a) $\delta=0$, (b) $\delta=0.13$, and (c) $\delta=0.3$. The ordinate $N(\omega)$ is the density of states $\rho(\omega)$ in our notation. From Bulut, Scalapino, and White, 1994a.

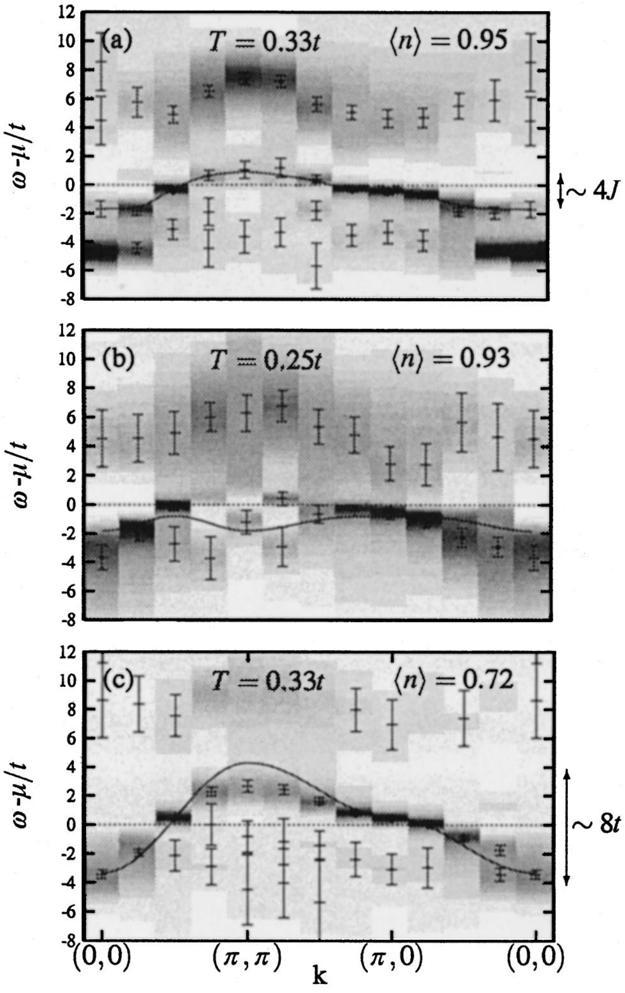

FIG. 23. The spectral weight $A(k,\omega)$ by quantum Monte Carlo calculations of the 8×8 Hubbard model at $U=8t$. Dark areas correspond to large spectral weight, white areas to small spectral weight. The solid lines in (a) and (c) are tight-binding fits of the data while in (b) they are the quantum Monte Carlo result at $\langle n\rangle=1.0$. Preuss *et al.*, 1997.

agreement with the prediction of the Monte Carlo simulations using the *t*-*J* model and the Hubbard model. Along the (π,0) direction, on the other hand, the peak does not disperse so close to E_F, although the *t*-*J* and Hubbard-model calculations predict a peak position nearly equal to the $\sim(\pi/2,\pi/2)$ point. That the occupied band has maxima along the (π,0)-(0,π) line as in the Monte Carlo study is a generic feature of the single-band Hubbard model and is also the case in the weak-coupling spin-density wave picture (Bulut *et al.*, 1994b). The discrepancy between theory and experiment around the (π,0) point remains unexplained. Around (π,0) the peak is rather broad due to large incoherent character, leading to uncertainty that might be the origin of the discrepancy. Another possibility is that a more realistic model, such as the t-t'-J model or d-p model including apex oxygens, will be necessary (see, for example, Nazarenko *et al.*, 1995).

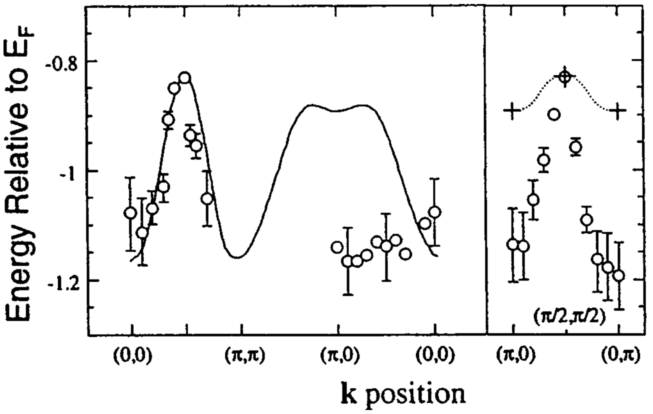

FIG. 24. Quasiparticle dispersions in angle-resolved photoemission spectra of $Sr_2CuCl_2O_2$ (Wells *et al.*, 1995) compared with *t-J* model calculations given by solid curve (left panel) and crosses with an interpolation of crosses by dotted curve (right panel). From Bulut, Scalapino, and White, 1994a, 1994b.

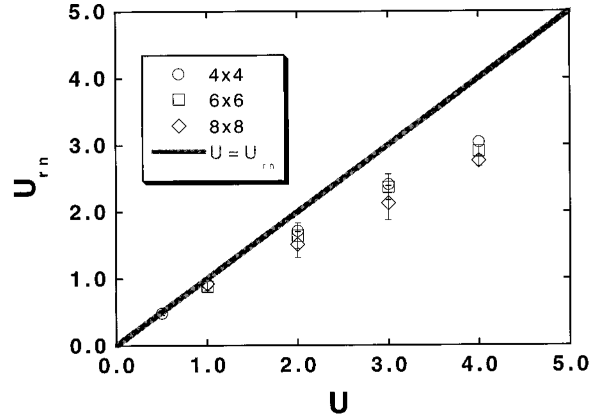

FIG. 25. The renormalized interaction U_{rn} derived so as to reproduce the numerically observed charge gap by the Hartree-Fock calculation is plotted against the bare U for the 2D Hubbard model (from N. Furukawa and M. Imada, unpublished). This indicates that the Hartree-Fock gap becomes correct for small U.

3. Charge response

In connection with the vanishing Drude weight, a charge excitation gap opens at half filling. This is directly observed in the density of states at half filling (White, 1992). A direct estimate of the charge gap is also possible from Eq. (2.16). Both the quantum Monte Carlo finite-temperature algorithm applied by Moreo, Scalapino, and Dagotto (1991) and the projector algorithm for $T=0$ applied by Furukawa and Imada (1991b, 1991c, 1992) to the nearest-neighbor Hubbard model at $U/t=4$ show the charge gap $\Delta_c \sim 0.6$. Recently a more elaborate algorithm for estimating zero-temperature properties in the Mott insulating phase was developed using stabilized matrix calculations (Assaad and Imada, 1996a). The application of this algorithm to the Hubbard model at $U/t=4$ showed $\Delta_c/t=0.66\pm 0.015$ (Assaad and Imada, 1996b). The amplitude of the charge gap examined as a function of U in the 2D Hubbard model agreed with the prediction of the Hartree-Fock approximation for small U but deviated for larger U, as is expected. Figure 25 shows how the charge gap scaled as a function of U. In Fig. 25, U_{ren} is the interaction with which the Hartree-Fock equation of the Hubbard model gives the same charge gap as the numerically observed value in the quantum Monte Carlo. The Hartree-Fock result predicts that Δ_c is scaled as $\Delta_c \sim t\exp[-2\pi\sqrt{t/U}]$, while Hirsch (1985b) suggested a slight modification, namely, replacing the prefactor t with $\sqrt{tU}$.

The charge compressibility κ is essentially the same as the charge susceptibility χ_c and is defined as

$$\chi_c = n^2\kappa = \partial n/\partial\mu \tag{2.286}$$

where n is the electron density and μ is the chemical potential. The charge susceptibility vanishes in the Mott insulating phase because of incompressibility. However, quantum Monte Carlo results on 2D systems show that doped systems can be very compressible near the MIT on the metallic side (Otsuka, 1990; Furukawa and Imada, 1991b, 1992, 1993). In 2D systems, in contrast to the Drude weight, the charge susceptibility χ_c does not gradually and continuously vanish when one controls the doping concentration from the metallic phase to the MIT point $\delta=0$. The scaling plot of χ_c even shows a singular divergence in the form

$$\chi_c \propto 1/|\delta| \tag{2.287}$$

for $\delta \neq 0$, as illustrated in Fig. 26 (Furukawa and Imada, 1992, 1993). The singular divergence in the form of (2.287) is observed not only in the nearest-neighbor Hubbard model (1.1a) but also in a model extended by adding a finite next-nearest-neighbor transfer t'. This indicates that the origin of this scaling has nothing to do either with electron-hole symmetry, perfect nesting, or with the Van Hove singularity because they are absent in a model with nonzero t'. Similar behavior is also observed in the 2D *t-J* model (Jaklič and Prelovšek, 1996; Kohno, 1997). In 1D systems the same scaling $\chi_c \propto \delta^{-1}$ is derived in exactly solvable cases, as we shall see in Sec. II.F.6. There we shall discuss how the 1D and 2D systems differ in terms of the quantum phase transition de-

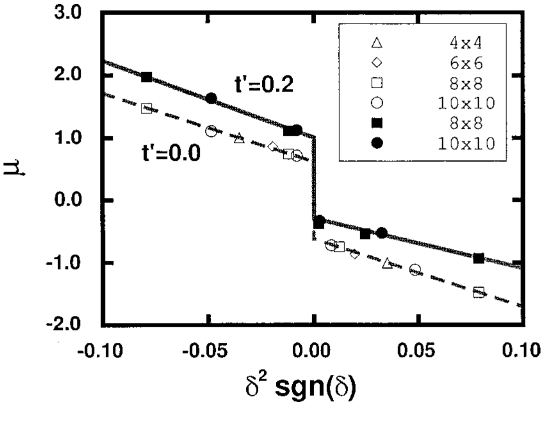

FIG. 26. Chemical potential vs δ^2 for the 2D Hubbard model of various sizes at $T=0$: open symbols, without next-nearest-neighbor transfer t'; filled symbols, with $t'=0.2$. From Furukawa and Imada, 1993.

spite their seemingly identical behavior. This is due to the difference in universality class. Experimental aspects of χ_c and the chemical-potential shift upon doping of a 2D MIT are discussed in Secs. IV.C.1 and IV.G.5 and interpretation in terms of Fermi-liquid theory is given in Sec. II.D.1.

When the charge susceptibility is singularly divergent as a power law of δ for $\delta \to +0$, the single-particle description of low-energy excitations is made possible only by the divergence of the effective mass of a relevant particle. This is in contrast with the usual transition between metals and band insulators, in which the number of carriers goes to zero as the effective mass of the quasiparticle remains finite. This numerical study by Furukawa and Imada prompted subsequent theoretical studies of continuous MITs based on the scaling theory, the main subject of Sec. II.F.

When the charge susceptibility is scaled by Eq. (2.287), it may be regarded as tending strongly toward phase separation as $\delta \to 0$ although real phase separation is not achieved. In fact, a continuous transition to a phase-separated state may be probed by the singularity $\chi_c \to \infty$. The growth of charge-density fluctuations, observed when χ_c is enhanced is reminiscent of the proposal of phase separation by Visscher (1974) and Emery, Kivelson, and Lin (1990). The possibility of phase separation in the 2D t-J model was examined recently by Hellberg and Manousakis (1997), who claimed to find a phase separation for any J/t at close to half filling. This result contradicts the observation of Kohno mentioned above. The numerical methods of these two studies are similar, while Hellberg *et al.* derived the opposite conclusion basically by relying on a single data point near half filling. Further studies in the t-J model are clearly needed, including a reexamination of the convergence to the ground state for this region. The quantum Monte Carlo results in the Hubbard model imply that χ_c diverges only for $\delta \to +0$, and there the transition to a Mott insulator takes place without a real phase separation. If a phase separation took place at finite doping concentration, the quantum Monte Carlo method could indeed detect it, as we shall see later in the case of the Ising-like boson t-J model in Sec. II.E.12. We of course have to note here the limitation of the numerical study for the ultimate limit of $\delta \to 0$, because the numerical results can be obtained only at finite δ in finite-size systems. In any case, the overall numerical results indicate that rapid growth of the charge compressibility and the tendency towards phase separation do exist near half filling. It is interesting to regard the critical enhancement of χ_c at small δ as a general tendency not of static but of dynamic fluctuation toward the phase separation. In fact, static phase separation is suppressed due to the long-range Coulomb force, ignored in this discussion, and the above controversy is not so serious in real materials. The dynamic phase separation provides an alternative view to Eq. (2.287). We discuss this issue further in Secs. II.H.3, IV.C., and IV.E.

4. Magnetic correlations

Effects of spin fluctuations are another intensively studied issue. In low-dimensional systems, the antiferromagnetic correlation is under the strong influence of quantum fluctuations. The one-dimensional spin-1/2 Heisenberg model and the Hubbard model at half filling show a power-law decay of the antiferromagnetic correlation at $T=0$, $\langle \mathbf{S}(r)\cdot\mathbf{S}(0)\rangle \propto 1/r$. For spin-1/2 systems, the spin-wave theory in 2D predicts the existence of antiferromagnetic order (Anderson, 1952; Kubo, 1952). Although the existence of long-range order is proven for a spin $S \geqslant 1$ on a square lattice (Neves and Perez, 1986; Kubo and Kishi, 1988), at the moment, no rigorous proof for long-range order exists at $S=1/2$, even for nearest-neighbor coupling on a square lattice. Quantum Monte Carlo results on the square-lattice Heisenberg model appear to show antiferromagnetic order at $T=0$ (Okabe and Kikuchi, 1988; Reger and Young, 1988; Makivić and Ding, 1991). In the 2D Hubbard model, quantum Monte Carlo results also suggest the existence of antiferromagnetic long-range order in the Mott insulating phase, $\delta=0$ (White *et al.*, 1989). The existence of long-range order is also inferred in a parameter region of the d-p model (Dopf, Wagner, *et al.*, 1992).

In the 2D Hubbard model, long-range order appears to be lost immediately upon doping (Furukawa and Imada, 1991b, 1992). The Fourier transform of the equal-time spin-spin correlation function

$$S(\mathbf{k})=\frac{1}{3}\int e^{-i\mathbf{k}\cdot\mathbf{r}}\langle \mathbf{S}(\mathbf{r})\cdot\mathbf{S}(0)\rangle d\mathbf{r} \tag{2.288}$$

shows a short-ranged incommensurate peak at $\mathbf{k}=\mathbf{Q}$ away from the antiferromagnetic Bragg point $\mathbf{k}=(\pi,\pi)$ when the doping proceeds as we see in Fig. 27 (Imada and Hatsugai, 1989; Moreo, Scalapino, *et al.*, 1990; Furukawa and Imada, 1992). Similar incommensurate peaks are observed in the 2D t-J model (Moreo and Dagotto, 1990) and in the d-p model (Dopf, Muramatsu, and Hanke, 1992). Figure 28 indicates that this peak value $S(\mathbf{Q})$ becomes finite for $\delta \neq 0$, which means the disappearance of long-range order in the whole metallic region, $\delta \neq 0$. The scaling of $S(\mathbf{Q})$ appears to follow

$$S(\mathbf{Q}) \propto 1/\delta, \tag{2.289}$$

which can be interpreted as the antiferromagnetic correlation length ξ_m scaled by $\xi_m \propto \delta^{-1/2}$ (Furukawa and Imada, 1993). Here it should be noted that the existence of an antiferromagnetic correlation length in the metallic phase is nontrivial because the correlation at an asymptotically long distance should follow a power-law decay in the usual spin gapless metals and, naively, this should lead to divergence of the correlation length. The Monte Carlo results in 2D suggest that the spin correlation of the period given by the wave number $\mathbf{Q}$ is constant as in the Heisenberg model for the distance $1 \ll r \ll \xi_m$ while it decays as a power law $\propto 1/r^{\gamma}$ with $\gamma > 2$ in the region $r \gg \xi_m$. In the 1D doped Hubbard model, it has been established that the incommensurate spin correlation decays as $1/r$ for $1 \ll r \ll \xi_m$ while as $1/r^{1+K_\rho}$ for

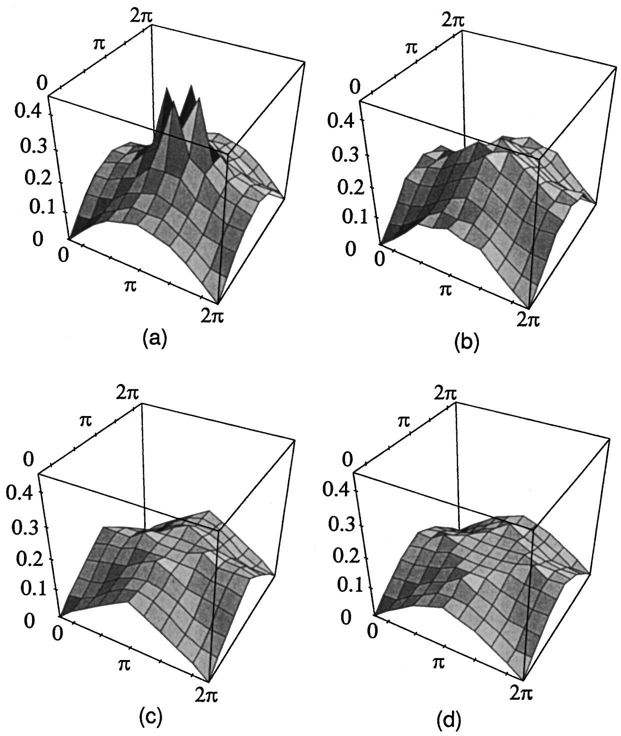

FIG. 27. Incommensurate peak in the momentum space of equal-time magnetic structure factor $S(q,t=0)$ for the 2D Hubbard model of a 10×10 cluster at $T=0$: (a) $\delta=0.18$; (b) $\delta=0.26$; (c) $\delta=0.42$; and (d) $\delta=0.5$ at $U/t=4$. From Furukawa and Imada, 1992.

$r \gg \xi_m$ with $\xi_m \propto \delta^{-1}$ (Imada, Furukawa, and Rice, 1992; Iino and Imada, 1995). K_ρ is the exponent of the Tomonaga-Luttinger liquid given in Sec. II.G.1. This nontrivial way of defining ξ_m in 1D and 2D is further discussed in Sec. II.F.10. We note that the immediate destruction of antiferromagnetic order, which is numerically observed, may be a characteristic feature in *single-band* 2D systems.

Experimentally, so far we have no definite example of an antiferromagnetic metal near the Mott insulator in highly 2D single-band systems, in agreement with the above numerical studies. As is well known and discussed in Sec. IV.C, the cuprate superconductors in general lose antiferromagnetic order upon small doping without any indication of antiferromagnetic metals. Antiferromagnetic order survives up to $\delta=0.02$, while insulating behavior persists until $\delta=0.05$ for $La_{2-\delta}Sr_\delta CuO_4$. The MIT at small but finite δ is clearly due to Anderson localization under random potentials.

In 3D systems, however, antiferromagnetic metals may exist, although no numerical study is available so far. They have been found adjacent to the Mott insulator in limited examples, such as $NiS_{2-x}Se_x$ with pyrite structure and V_2O_{3-y}, as will be discussed in Sec. IV.A. However, it should also be noted that these two materials have orbital degeneracies with spins larger than 1/2 in the insulator, which may stabilize the antiferromagnetic metals. In the weak-correlation regime, other examples of antiferromagnetic metals are known, for instance in such d-electron systems with orbital degeneracy as V_3Se_4, V_5Se_8, and V_3S_4. Even in 3D, so far, antiferromagnetic metals are observed only in cases with strong orbital degeneracy. From both theoretical and experimental viewpoints, the stability of antiferromagnetic and metallic phases near the Mott insulator for single-band systems, even in 3D, calls for further study. It is not clear whether the lower critical dimension of antiferromagnetism in metals, d_{ml}, is even higher than three for systems without orbital degeneracy, that is, two-component systems. This uncertainty is due in part to the difficulty of finding an effectively single-band system in 3D.

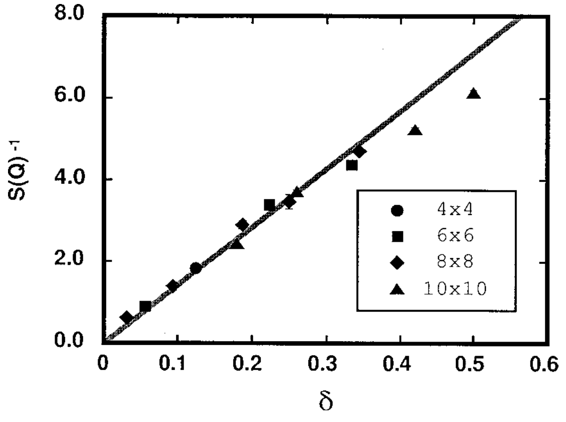

FIG. 28. Inverse of equal-time spin structure factor $S^{-1}(Q,t=0)$ at the peak point $q=Q$ as a function of doping δ for the 2D Hubbard model at $U/t=4$ with various sizes. From Furukawa and Imada, 1992.

The temperature dependence of the antiferromagnetic correlation length ξ_m has also been studied extensively by numerical approaches. In the undoped case, ξ_m continuously and rapidly increases until $T \rightarrow 0$ because the antiferromagnetic transition takes place at $T=0$ in 2D. Chakraverty, Halperin, and Nelson (1989) pointed out the relation of the quantum Heisenberg model in 2D to the O(3) nonlinear sigma model in 3D and suggested the existence of two regions, namely, where $\xi_m \propto 1/T$ at higher temperatures (the quantum critical regime) and where ξ_m increases exponentially at lower temperatures in the renormalized classical regime. This basic picture has been more or less confirmed numerically (for example, Makivić and Ding, 1991).

At finite doping, $\xi_m(T)$ was also computed for the 2D Hubbard model (Imada, 1994a). It displayed a sharp contrast with the undoped case. Both ξ_m and the peak value of the equal-time spin structure factor $S(Q)$ started growing at high temperatures, $T>J$. With decreasing temperature, however, they showed rapid saturation at rather high temperatures, as in Fig. 29. For example, at $\delta \sim 0.15$, ξ_m more or less saturated at $T \sim J$ and did not grow below it. This means that ξ_m quickly approaches the intrinsic correlation length $\sim 1/\sqrt{\delta}$ given from Eq. (2.289). The temperature below which ξ_m becomes more or less temperature independent is denoted as $T_{\rm scr}$. $T_{\rm scr}$ rapidly increases from 0 at $\delta=0$ to $T_{\rm scr} \sim J$ at

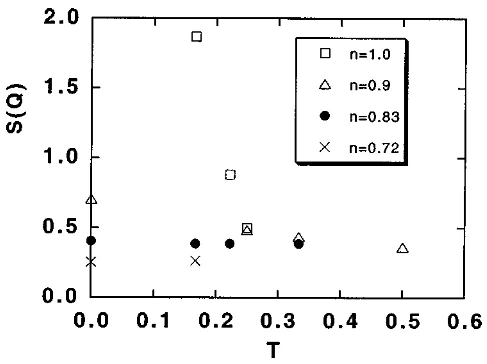

FIG. 29. Temperature dependence of $S(Q,t=0)$ for various fillings $n=1-\delta$ of the 2D Hubbard model at $U/t=4$. From Imada, 1994a.

$\delta\sim 0.15\sim 0.2$. A similar and consistent result was also obtained in the 2D t-J model by Jaklič and Prelovšek (1995b), who applied the finite-temperature Lanczos method mentioned above and found that Im $\chi(q,\omega)/\omega$ has a peak around (π,π) and grows with decreasing temperature, while the width in ω and q is temperature independent at $T<J$ for the doping $\delta\sim 0.15$; see Fig. 30. This peak structure is associated with the "incoherent part" of the spin correlation, while the "coherent part" has only a low weight at lower frequencies when the doping concentration becomes low. This coherent part may give rise to the Fermi-surface effect at low temperatures, which is associated with a power-law decay of the spin correlation at long distances in metals.

These numerical results are consistently interpreted by the following picture, as discussed by Imada (1994a) and Jaklič and Prelovšek (1995b): Although it is not completely correct, it is useful to analyze the spin correlation as the sum of incoherent and coherent parts. As the doping concentration decreases, the weight of the coherent part decreases to zero and the incoherent weight becomes dominant. The coherent part comes from an asymptotically long-time and long-distance part beyond $\tau_m(\equiv\xi_m^z)$ and ξ_m, where the correlation decays as a power law at $T=0$. Here z is the dynamic exponent discussed in detail in Sec. II.F. The incoherent part arises from the short-time and short-distance part ($\tau<\xi_m^z$ and $r<\xi_m$). As $\xi_m\to\infty$ with decreasing δ, it is clear that the incoherent spin correlation dominates and the coherent weight vanishes. The spin structure factor

$$S(\mathbf{q},\omega)\equiv\int_{-\infty}^{\infty} d\mathbf{r}\,dt\,e^{-i\omega t}e^{i\mathbf{q}\cdot\mathbf{r}}\langle\mathbf{S}(\mathbf{r},t)\cdot\mathbf{S}(0,0)\rangle \qquad (2.290)$$

may be given as the sum of the coherent and incoherent contributions,

$$S(\mathbf{q},\omega)\simeq S_{\mathrm{inc}}(\mathbf{q},\omega)+S_{\mathrm{coh}}(\mathbf{q},\omega). \qquad (2.291)$$

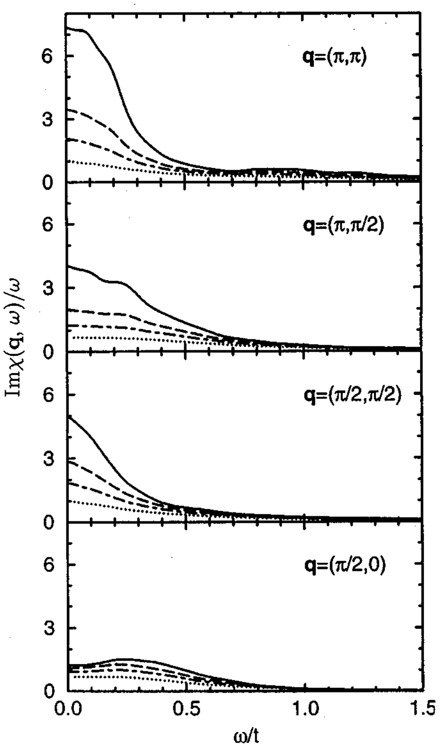

FIG. 30. Dynamic spin susceptibility Im $\chi(q,\omega)/\omega$ for a 4×4 cluster of the t-J model at $\delta=3/16$: solid line, $T/t=0.1$; dashed line, $T/t=0.2$; dashed-dotted line, $T/t=0.3$; dotted line, $T/t=0.5$. From Jaklič and Prelovšek, 1995b.

This phenomenological way of writing $S(q,\omega)$ with coherent and incoherent contributions was also suggested by Narikiyo and Miyake (1994). The incoherent contribution S_{inc} has typical widths ξ_m^{-1} in q space and ξ_m^{-z} in ω space. The essential features of the numerical results may be written, approximately and phenomenologically, for $\omega>0$ as

$$S_{\mathrm{inc}}(\mathbf{q},\omega)\sim\frac{C}{\omega^2+[D_s(\mathbf{q}^2+K^2)]^2}, \qquad (2.292)$$

with $K\equiv\xi_m^{-1}$, $D_s\propto\xi_m^{2-z}$, $C\propto\xi_m^d$. Here we take the dimension $d=2$. The important point is that ξ_m has to be temperature independent at $T<T_{\mathrm{scr}}$ to be consistent with numerical results. The coherent part S_{coh} may have strong temperature dependence even below T_{scr}. In fact, S_{coh} represents the long-ranged power-law decay of the spin correlation and reflects the Fermi-surface effect at low temperatures. Therefore S_{coh} grows in general as incommensurate and rather sharp non-Lorentzian peaks below the coherence temperature $T_{\mathrm{coh}}\equiv T_F$. The total structure factor S is schematically illustrated in Fig. 31 as the sum of these two parts. Although neutron scattering may detect this structure coming from S_{coh} at low temperatures, the weight of S_{coh} becomes smaller at lower doping. Therefore q-integrated or ω-integrated values are generally dominated by S_{inc} at low doping. Because K and D_s are temperature independent below T_{scr},

$$\mathrm{Im}\,\chi(q,\omega)=(1-e^{-\beta\omega})S(q,\omega) \qquad (2.293)$$

for $\omega>0$ has a temperature dependence coming mainly from the Bose factor $(1-e^{-\beta\omega})$. We note that Im χ and S at $\omega<0$ are determined from the requirement

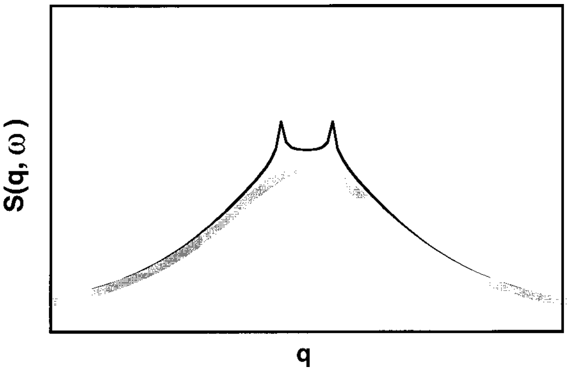

FIG. 31. Total typical and schematic structure of $S(q,\omega)$ around the antiferromagnetic peak point. The incoherent contribution is illustrated as a bold gray curve and the total amplitude is given by a black solid curve.

$\mathrm{Im}\,\chi(q,-\omega)=-\mathrm{Im}\,\chi(q,\omega)$, leading to the result that $\int dq\ \mathrm{Im}\,\chi(q,\omega)$ is universally scaled as

$$\int dq\ \mathrm{Im}\,\chi(q,\omega)\propto(1-e^{-\beta\omega}) \qquad (2.294)$$

at $\omega<\xi_m^{-z}$ when the incoherent contribution is dominant. It was pointed out (Imada, 1994a) that this explains the neutron and NMR results in high-T_c cuprates where $\int dq\ \mathrm{Im}\,\chi(q,\omega)$ is reported to be universally scaled by ω/T (Hayden *et al.*, 1991a; Keimer *et al.*, 1992; Sternlieb *et al.*, 1993) while the NMR relaxation rate $T_1\sim$const at $T>T_{\mathrm{coh}}$ (Imai *et al.*, 1993). The coherence temperature T_{coh} is estimated to be $\sim100\sim300$ K at the optimal doping $\delta\sim0.15$. More detailed analysis of the antiferromagnetic correlation based on scaling theory is given in Sec. II.F.10. Experimental aspects of high-T_c cuprates are discussed in Secs. IV.C.1 and IV.C.3.

5. Approach from the insulator side

So far we have discussed the Mott transition from the metallic side. Recently, a method of probing the transition from the insulator side was developed (Assaad and Imada, 1996a, 1996b). If the transition is continuous, it can be shown that critical exponents in both sides should be the same. Therefore, any information gained about the transition from the insulator side also helps to clarify its character on the metallic side. A large advantage of observing the transition from the insulator side is that we can avoid the negative-sign problem, which has plagued the quantum Monte Carlo method (Loh *et al.*, 1990; Furukawa and Imada, 1991a). For the case of electron-hole symmetry, as in the nearest-neighbor Hubbard model on a bipartite lattice, the negative sign does not appear at half filling (Hirsch, 1983).

The insulator undergoes a transition to a metal when the chemical potential μ approaches the critical point μ_c from the region of the charge gap. The ground-state wave function $|\Phi_g\rangle$ in the insulating phase should not change when μ changes because the number of particles is fixed at N within the gap, while the Hamiltonian contains μ only through the term μN irrespective of the eigenvectors in the Hilbert space of N particles. The two-body correlation function is also independent of μ within the charge gap. However, the single-particle Green's function defined in Eq. (2.44) as

$$\mathcal{G}(r,\tau)=\langle Tc(r,\tau)c^{\dagger}(0,0)\rangle \qquad (2.295)$$

depends on μ because it propagates a particle created above the gap in the $N+1$-particle sector for the interval of $\tau>0$. This Green's function yields a factor of $e^{-\tau(E_n-\mu)}$ in Eq. (2.295) for a created particle with energy E_n. Then the μ dependence of $\mathcal{G}(r,\tau)$ is simply $e^{\mu\tau}$. Therefore, when $\mathcal{G}(r,\tau)$ at $\mu=0$ is calculated, $\mathcal{G}(r,\tau)$ at $\mu\neq0$ is given as $\mathcal{G}(r,\tau,\mu\neq0)=\mathcal{G}(r,\tau,\mu=0)e^{\mu\tau}$. This means that all the $\mathcal{G}(r,\tau)$ for μ within the charge gap can be obtained by calculating $\mathcal{G}(r,\tau)$ once at $\mu=0$. Because there may be numerical instability for large τ due to the factor $e^{\mu\tau}$, a numerical stabilization technique for the matrix calculation is necessary (Assaad and Imada, 1996a).

In any case, the calculated Green's function provides the localization length ξ_l defined by

$$\mathcal{G}(r,\omega=\mu)\equiv\int_0^{\infty}\mathcal{G}(r,\tau,\mu)d\tau\sim e^{-r/\xi_l}. \qquad (2.296)$$

Here ξ_l may be regarded as the localization length of the wave function of the virtually created state at the chemical potential. The localization length ξ_l has to diverge at the MIT. The scaling of ξ_l near μ_c calculated by the above method for the two-dimensional Hubbard model shows

$$\xi_l\sim|\mu-\mu_c|^{-\nu},$$

$$\nu=0.26\pm0.05, \qquad (2.297)$$

as in Fig. 32 (Assaad and Imada, 1996a, 1996b). In Sec. II.F, we compare this exponent $\nu\sim1/4$ with the exponent of the compressibility analysis given in Eq. (2.287) in the metallic side, assuming hyperscaling, and find them to be consistent. The confirmation of the large dynamic exponent has prompted subsequent studies on the t-U-W model in which the two-particle process defined in Eq. (2.347) is introduced explicitly and added to the Hubbard model because of its greater relevance than that of the irrelevant single-particle process characterized by $z=4$ (Assaad, Imada, and Scalapino, 1996, 1997; Assaad and Imada, 1997; see also Sec. II.F.9). The (t-U-W) model has made it possible to study directly the quantum transition between an antiferromagnetic Mott insulator and a d-wave superconductor and thereby to clarify the character of the obtained d-wave superconductor at $T=0$. Antiferromagnetic correlation is extremely compatible in the superconducting phase with divergence of the staggered susceptibility. Finite temperature fluctuations were also studied as well.

6. Bosonic systems

Transitions between Mott insulators and superfluids in bosonic systems have been the subject of recent inten-

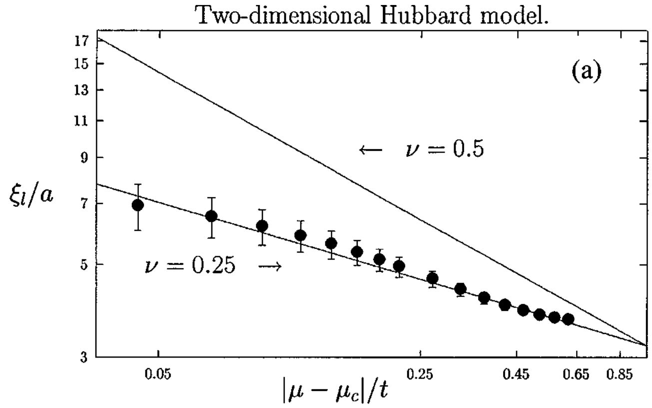

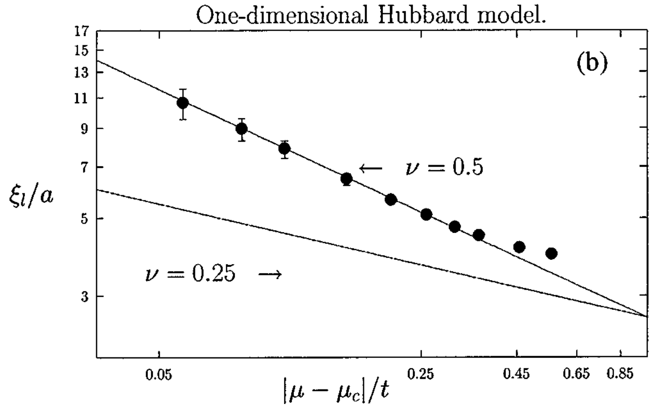

FIG. 32. Localization length ξ_l vs $|\mu-\mu_c|$ for the Hubbard model at $U/t=4$ for (a) two-dimensional systems, (b) one-dimensional systems. Monte Carlo data are illustrated by solid circles. From Assaad and Imada, 1996b.

sive studies. When disorder drives the transition in bosonic systems, a superfluid undergoes a transition to a Bose glass phase. Studies of the critical exponents of the transition from superfluid to Bose glass were motivated by the proposal of the scaling theory (Fisher *et al.*, 1989). The results of quantum Monte Carlo calculations appear to support the scaling theory, as discussed in Sec. II.F.12 (Sørensen *et al.*, 1992; Wallin *et al.*, 1994; Zhang *et al.*, 1995).

In the transition between a superfluid and a Mott insulator, an interesting case is that of multicomponent bosons. In analogy with the fermion *t-J* model (2.13), the boson *t-J* model of two-component hard-core bosons was investigated by Imada (1994b). In the case of Ising-exchange for J, Monte Carlo results clearly show a phase separation into the Mott insulating phase at $\delta=0$ and another component-ordered phase at a finite δ_c near the Mott insulator (Motome and Imada, 1996). A remarkable fact is that the component correlation length diverges at the continuous transition point $\delta=\delta_c$ when the filling is changed from $\delta>\delta_c$ to $\delta\rightarrow\delta_c$ while phase separation takes place for $\delta<\delta_c$. Strong mass enhancement and vanishing superfluid density are observed with $\delta\rightarrow\delta_c$. This appears to come from a mechanism of mass enhancement at finite δ which is different from the mechanism of the mass divergence in the 2D Hubbard model discussed above. The origin of the mass enhancement was speculated to be the persistence of the Ising-like component order for $\delta\leq\delta_c$.

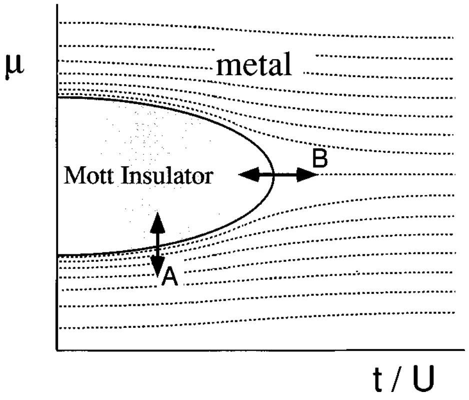

FIG. 33. Schematic phase diagram of a metal and a Mott insulator in the plane of μ/t and t/U. Route A shows filling-control transition, FC-MIT (generic transition), while route B is the bandwidth-control transition, BC-MIT (multicritical transition). Dotted curves illustration density contour lines.

F. Scaling theory of metal-insulator transitions

The Mott transition defined as the transition between a metal and a Mott insulator, has two types, the filling-control transition (FC-MIT) and the bandwidth-control transition (BC-MIT), as explained in Sec. I and illustrated in Fig. 33. Both of these transitions are controlled by quantum fluctuations rather than by temperatures. The FC-MIT has as control parameters the electron concentration or the chemical potential. The BC-MIT has as a control parameter the ratio of the bandwidth to the interaction, t/U. The quantum fluctuation is enhanced for large t/U, which stabilizes the metallic phase, namely, the quantum liquid state of electrons, while large U/t makes the localized state more stable. Because these control parameters are intrinsically quantum mechanical, the MIT is the subject of research in the more general field of quantum phase transitions. The transition itself can take place either through continuous phase transitions or through a first-order transition accompanied by hysteresis. Critical fluctuations of metallic states can be observed more easily near the continuous transition point. In this section, we look more closely at continuous transitions.

In Sec. II.D, various theoretical approaches to the Mott transition and correlated metals are described, including the Gutzwiller approximation, the Hubbard approximation, the infinite-dimensional approach, slave-particle methods, and spin-fluctuation theories. Although their physical consequences vary and sometimes conflict with each other, these methods share a common limitation in that they all rely on the mean-field approximation. The level of mean-field approximations used ranges from dynamically correct treatments that neglect spatial correlations, as in the $d=\infty$ approach, to simple static approximations on the Hartree-Fock level. In Sec. II.D.9, we have seen that the magnetic transition in metals independent of the MIT seems to be described by mean-field fixed points for antiferromagnetic transitions at $d \geqslant 3$ and for ferromagnetic transitions at $d \geqslant 2$ or $d \geqslant 3$ under certain assumptions. However, in this section, we discuss some rather different features of the Mott transition.

In general, mean-field approximations are justified if the dimension is high enough. However, in the Mott transition of fermionic models, the upper critical dimension beyond which the mean-field approximation is justified is not so straightforwardly estimated as in simple magnetic transitions of the Ising model. As we saw in Sec. II.D.6, the infinite-dimensional approach provides an example where the mean-field approximation becomes exact at $d=\infty$ by taking account of dynamic fluctuations correctly. On the other hand, other mean-field approximations do not take account of on-site dynamic fluctuations and incoherent excitations correctly, leading to failure of the method even in the limit of large dimensions, because incoherent excitations become overwhelming near the transition point.

In low-dimensional systems, temporal as well as spatial fluctuations from both thermal and quantum origins become important. A generally accepted view is that the mean-field theories for phase transitions become invalid below the upper critical dimension due to large spatial fluctuations.

Below the upper critical dimension, where the mean-field description breaks down, phase transitions are believed in general to be described by scaling theory, with hyperscaling assumed. In this subsection we review the scaling theory of the Mott transition and examine its validity based on recent numerical work. Its consequences and experimental relevance are also discussed. Among various Mott transitions categorized in Sec. II.B, $[I\text{-}1 \leftrightarrow M\text{-}1]$, $[I\text{-}1 \leftrightarrow M\text{-}2]$, $[I\text{-}2 \leftrightarrow M\text{-}2]$, and $[I\text{-}2 \leftrightarrow M\text{-}4]$ are basically characterized by vanishing carrier number as the MIT is approached. In this case, the universality class of the MIT may be characterized as the same as that for a transition between a band insulator and a standard metal, as will be discussed in Sec. II.F.8. On the other hand, for the case of $[I\text{-}1 \leftrightarrow M\text{-}3]$, an unusual type of MIT can take place with an anomalous metallic phase. In this case the MIT is characterized by diverging single-particle mass (Imada, 1993a). As we shall see below and also in Sec. II.E, critical properties of the MIT are observed numerically in a wide region around the critical point. The existence of such a wide critical region also leads to a wide region of an anomalous metallic state near the MIT with strongly incoherent charge dynamics. In this sense, the scaling argument for the MIT discussed in this section is not limited to a narrow region but appears to be relevant for a wide region of unusual metallic behavior observed in transition-metal compounds.

In 2D systems, numerical analyses support the assumption of hyperscaling and the mean-field description breaks down. This observation may be related to the strong and singular wave-number dependence of the renormalized charge excitations near the Mott insulator. The universality class obtained in 2D is characterized by an unusually large dynamic exponent $z=4$. An important consequence of this new universality class is the suppression of coherence as compared to that in the transition between band insulators and metals. We discuss in Sec. II.F.9 how and why the coherence of charge and spin dynamics is suppressed for the Mott transition. We also discuss the instability of the large-z state to superconducting pairing. The success of the hyperscaling description is a nontrivial consequence for large z because, generally speaking, the upper critical dimension becomes low for large z. A possible microscopic origin for hyperscaling with $z=4$ in 2D is discussed in Sec. II.F.11. In Sec. II.F.12, superfluid-insulator transitions are discussed.

1. Hyperscaling scenario

Continuous MITs were first analyzed in terms of the scaling concept in the Anderson localization problem in the 70s. Scaling has proven to be useful in establishing the marginal nature of 2D systems for localization by disorder (Wegner, 1976; Abrahams *et al.*, 1979). The underlying assumption in this approach is the hyperscaling hypothesis. In this subsection, we introduce the hyperscaling description of the MIT caused by the electron correlation from more general point of view following recent developments (Continentino, 1992, 1994; Imada, 1994c, 1995a, 1995b). Because the MIT is controlled by quantum fluctuations, we may use control parameters such as the electron chemical potential μ or the bandwidth t and measure the distance from the critical point by Δ. The control parameter can either be the chemical potential to control the filling or the bandwidth (or the interaction), as can be seen in Fig. 33. The scaling theory assumes the existence of a single characteristic length scale ξ, which diverges as $|\Delta| \rightarrow 0$, and a single characteristic frequency scale Ω, which vanishes as $|\Delta| \rightarrow 0$. The correlation length ξ is assumed to follow

$$\xi \sim |\Delta|^{-\nu} \tag{2.298}$$

as $\Delta \rightarrow 0$, which defines the correlation length exponent ν. The frequency scale Ω is determined from the quantum dynamics of the system independently of the length scale in general. The dynamical exponent z determines how Ω vanishes as a power of Δ,

$$\Omega \sim \xi^{-z} \sim |\Delta|^{z\nu}. \tag{2.299}$$

In critical phenomena, hyperscaling is believed to hold between the upper critical dimension d_c and the lower critical dimension d_l (see, for example, Ma, 1976). Above d_c, the mean-field description is justified and the hyperscaling description breaks down, whereas below d_l the transition itself disappears. Here, d_c and d_l should not be confused with d_{ml} and d_{il} defined in Sec. II.B. d_c and d_l are defined as the critical dimensions of the MIT and not of the magnetic transition. Hyperscaling asserts the homogeneity in the singular part of the free-energy density f_s in terms of an arbitrary length-scale transformation parameter b:

$$f_s(\Delta) \sim b^{-(d+z)} f_s(b^{1/\nu}\Delta) \sim \Delta^{\nu(d+z)}. \tag{2.300}$$

This scaling is derived, in the absence of anomalous dimensions, from dimensional analysis of the free-energy density defined by

$$f=-\lim_{\beta\to\infty}\lim_{N\to\infty}\frac{1}{\beta N}\ln Z, \tag{2.301}$$

which is proportional to [frequency]×[length]$^{-d}$. The scale transformation of the argument $\propto b^{1/\nu}\Delta$ in f_s is made dimensionless using the single characteristic length scale (2.298). When the inverse temperature β and the linear dimension of the system size L are both large but finite, a finite-size scaling function $\mathcal{F}$ is expected to hold as

$$f_s(\Delta)\sim\Delta^{\nu(d+z)}\mathcal{F}(\xi/L,\xi^z/\beta) \tag{2.302}$$

in the combination of dimensionless arguments.

Here, we confirm that the hyperscaling scenario is satisfied for the transition between a metal and a band insulator in any number of dimensions $1\leqslant d\leqslant\infty$. In a noninteracting fermion system, the control parameter Δ is the chemical potential that controls the filling, and the ground-state energy has the form

$$E_g\sim\int_0^{k_F}dk\,k^{d-1}\frac{k^2}{2m}\sim\frac{k_F^{d+2}}{2(d+2)m}$$
$$=\frac{(2m)^{d/2}}{d+2}\Delta^{(d+2)/2}, \tag{2.303}$$

where Δ is the chemical potential measured from the bottom of the band edge with a quadratic dispersion, $\varepsilon(k_F)=k_F^2/2m$. Comparison of Eqs. (2.303) and (2.300) clearly shows that the hyperscaling scenario is satisfied with $\nu=1/2$ and $z=2$. The characteristic length ξ and the characteristic energy Ω are nothing but the Fermi wavelength k_F^{-1} and the Fermi energy $E_F=\mu_F=\Delta$, respectively. The reason why hyperscaling holds in any dimension in this case is rather trivial, namely, the Hamiltonian is quadratic and it is always at the Gaussian fixed point.

2. Metal-insulator transition of a noninteracting system by disorder

The idea of scaling for the MIT in the form first introduced (Wegner, 1976, 1979; Abrahams *et al.*, 1979) for the Anderson localization problem is certainly equivalent to the assumption of hyperscaling (Abrahams and Lee, 1986). We introduce here the scaling function for an external field h relevant to the order parameter

$$f_s(\Delta,T,h)=b^{-(d+z)}\mathcal{F}_{sh}(b^{1/\nu}\Delta,b^{y_h}h) \tag{2.304}$$

with the exponent y_h. Since the order parameter for a disordered transition is the single-particle density of states ρ at the Fermi level, we obtain the scaling of the density of states as

$$\rho(\Delta)=\frac{1}{T}\frac{\partial f}{\partial h}\bigg|_{h=0}=b^{-(d-y_h)}\rho(b^{1/\nu}\Delta,b^{y_h}h)$$
$$\propto\Delta^{\nu(d-y_h)}. \tag{2.305}$$

Since the order parameter exponent is shown to be noncritical (McKane and Stone, 1981) for a transition controlled by disorder, Eq. (2.305) leads to the relation $y_h=d$. The order-parameter susceptibility also has the scaling form

$$\chi(\Delta)=\frac{1}{T}\frac{\partial^2 f}{\partial h^2}\bigg|_{h=0}=b^{2y_h-d}\chi(b^{1/\nu}\Delta,b^{y_h}h). \tag{2.306}$$

From the fluctuation dissipation theorem (Kubo, 1957), we see that Eq. (2.306) is equal to the density-density correlation function

$$C(\mathbf{k},\omega)=\frac{i\partial n/\partial\mu}{-i\omega+D_ck^2} \tag{2.307}$$

at $\omega=0$. Because of the noncriticality of the compressibility at a transition driven by disorder, we have

$$C(\mathbf{k},\omega=0)\propto D_c^{-1}k^{-2}. \tag{2.308}$$

Therefore C, which follows the same scaling form as Eq. (2.306),

$$C(\mathbf{k},\omega=0)=b^{2y_h-d}C(b\mathbf{k},\omega=0), \tag{2.309}$$

leads to scaling of the diffusion coefficient D_c as

$$D_c(\mathbf{k},\omega=0)=b^{2+d-2y_h}D_c(b\mathbf{k},\omega=0). \tag{2.310}$$

Combined with $d=y_h$, this is indeed consistent with the original scaling function of the conductivity $\sigma\propto D_c$ introduced by Wegner (1976) in the form

$$\sigma(\mathbf{k},\omega)=b^{2-d}\sigma(b\mathbf{k},b^z\omega). \tag{2.311}$$

This demonstrates that $d=2$ is marginal. This scaling form has inspired subsequent studies by perturbation expansion in terms of ε_F/τ in the weakly localized regime. The scaling form (2.310) is supported by numerical analysis (MacKinnon and Kramer, 1993).

In the case of the Anderson transition, the compressibility κ, γ, and the density of states are all nonsingular at the critical point, in contrast with the Mott transition. This is because a finite density of states exists on both sides of the mobility edge. As we shall see later, γ and κ are scaled by $\Delta^{\nu(d-z)}$, leading to $z=y_h=d$.

So far we have discussed the noninteracting case. To treat the Anderson transition with an interaction term, we can write the original action in the path-integral formalism. After making the Stratonovich-Hubbard transformation for the interaction part with the replica trick for the random potential, we can reduce the effective action to the nonlinear sigma model,

$$S[Q]=-\frac{1}{2G}\int d\mathbf{r}\,\mathrm{tr}(\vec{\boldsymbol{\nabla}}Q(\mathbf{r}))^2+2H\int d\mathbf{r}\,\mathrm{tr}(\Omega Q(\mathbf{r}))$$
$$+S_{int}(Q), \tag{2.312}$$

where Q is an infinite matrix with matrix element $Q_{nm}^{\alpha\beta}$ given by spin quarternions represented by 4×4 complex matrices (Finkelstein, 1983, 1984). The indices n,m are for the Matsubara frequencies, while α,β denote replica indices. The c-number variables Q are obtained as the Stratonovich variables from the interaction and the random potential combined, and $S_{int}(Q)$ represents the interaction part. The coupling constants $G=4/\pi N_F D_c$ and $H=\pi N_F/4$ are given from the density of states N_F and the diffusion constant D_c. The critical exponent ν for the transition by disorder is known to follow $\nu \geqslant 2/d$ (Chayes *et al.*, 1986). Experimentally and theoretically, the critical exponents are examined for various cases with and without magnetic field, magnetic impurities, and spin-orbit scattering. For example, under the spin-flip mechanism, as in magnetic fields, $\nu=1$ has been suggested experimentally [for example Dai, Zhang, and Sarachik (1992) and Bishop, Spencer, and Dynes (1985)]. When antiferromagnetic symmetry breaking exists on both sides of the MIT, it has been argued (Kirkpatrick and Belitz, 1995) that the effect of disorder can be mapped onto the random-field problem where the hyperscaling description is known to be modified even below the upper critical dimension.

So far the effect of interaction has been considered in this nonlinear sigma model only by the saddle-point approximation and hence at the Hartree-Fock level. The critical exponents have been calculated by perturbative renormalization-group analysis in the ε expansion. In the latter part of Sec. II.F, we shall see that the Mott transition must be treated by taking the interaction effect beyond the Hartree-Fock level because the critical behavior of the MIT itself is due to the critical fluctuation of interaction effects. Therefore qualitatively different aspects of scaling behavior at the Mott transition point appear, as we discuss later.

For more detailed discussions of the MIT caused by disorder in the case of minor contribution of electron correlation effects at the Hartree-Fock level, readers are referred to the extensive review articles of Lee and Ramakrishnan (1985) and Belitz and Kirkpatrick (1994). An important open question remains concerning the nature of the MIT when both correlation effects and disorder are crucially important near the Mott insulator. A dynamic mean-field theory (infinite-dimensional approach) was recently formulated to discuss the MIT when both electron correlation and disorder are strong (Dobrosavljević and Kotliar, 1997). It shows the appearance of a metallic non-Fermi-liquid phase near the MIT and strong effects of correlation even away from half filling. A recent experiment by Kravchenko *et al.* (1995) appears to show the existence of a true MIT in 2D interacting systems, in contrast with the conventional argument for noninteracting systems in which 2D systems become insulating even with weak disorder. The scaling properties of this transition have been discussed theoretically, for example, by Dobrosavljević *et al.* (1997).

3. Drude weight and charge compressibility

The Drude weight defined in Eq. (2.273) and the charge compressibility in Eq. (2.286) are the two important and relevant quantities needed to describe the Mott transition. A Mott insulator has two basic properties, one its insulating property and the other its incompressibility. In particular, incompressibility is a property that clearly distinguishes Mott insulators from Anderson-localized insulators, whose compressibility is generally nonzero, because incoherent states localized around impurities contribute to the compressibility. The Drude weight and the charge compressibility are both zero in the Mott insulating phase, whereas they are both nonzero in metallic phases. Therefore these two quantities must both be nonanalytic at the Mott transition point. The existence of nonanalyticities in these two quantities at the transition point is also common in the transition to a band insulator. However, as we shall see below, the way of reaching the transition point, in other words, the critical exponents and hence the universality class, can be different for a Mott transition and for the usual band-insulator/metal transition.

To understand the fundamental importance of the Drude weight and the charge compressibility, it is helpful to represent them as stiffness constants to the twist in boundary conditions in the path-integral formalism. The stiffness constant to the twist is in general useful in identifying phase transitions. One simple example is found in the ferromagnetic transition of the Ising model at the critical temperature. Suppose one imposes two different types of fixed boundary conditions at the boundaries in one spatial direction, x, in a system with a hypercubic structure. In one of the boundary conditions, one fixes all the up spins at the boundary $r_x=0$ and $r_x=L$, where r_x denotes the x coordinate of the spatial point $\mathbf{r}$. In the other boundary condition, one fixes all the up spins at $r_x=0$ and all the down spins at $r_x=L$. Let the averaged energy under the former boundary condition be E_u and under the latter, E_t. Then $\delta E=\lim_{L\to\infty}E_t-E_u$ must be zero in the paramagnetic phase because the spin correlation length is finite, whereas δE remains nonzero as $L\to\infty$ in the ferromagnetically long-range-ordered phase because a domain wall in the plane perpendicular to the x axis has to be introduced only for the latter boundary condition due to the twist. The latter boundary condition has higher energy coming from the formation energy of a domain wall.

When one wishes to establish similar criteria for the MIT, one has to work with the path-integral formalism because this transition is intrinsically quantum mechanical. Because of this quantum-mechanical nature, one has two ways of imposing twists in the $(d+1)$-dimensional space of the path integral. One way is to impose twist in the spatial direction while the other is to impose it in the temporal direction. Since the wave function in a metal is characterized by phase coherence, while that in an insulator is characterized by incoherence of the phase, these two types of wave functions respond differently to a twist of the phase in boundary conditions in terms of rigidity of the phase. In particular, in the Mott insulator, space-time localized wave functions result in the absence of phase rigidity in both the space and the time directions. Below it is shown that spatial and temporal rigidities are associated with nonzero Drude weight and nonzero charge compressibility, respectively (Continentino, 1992 Imada, 1994c, 1995a, 1995b).

An infinitesimally small twist of the phase, $\tilde{\phi}_L$, imposed between two boundaries $r_x=0$ and $r_x=L$ may alternatively be expressed by a transformation of the Grassmann variable introduced in Sec. II.C in the form

$$\psi_\sigma(\mathbf{r},\tau)\rightarrow\psi_\sigma(\mathbf{r},\tau)\exp[ir_x\nabla\phi], \tag{2.313}$$

where $\nabla\phi=\tilde{\phi}_L/L$ and r_x denotes the x coordinate of $\mathbf{r}$. It has been shown by Kohn (1964), Thouless (1974), and Shastry and Sutherland (1990) that this type of phase twist measures the stiffness, which is proportional to the Drude weight.

In a tight-binding Hamiltonian, the transformation (2.313) may equivalently be replaced by transforming the off-diagonal transfer term $t(r,r')\overline{\psi}(r)\psi(r')$ in the Hamiltonian as

$$t(r,r')\rightarrow t(r,r')\exp[i(r_x-r_x')\tilde{\phi}_L/L]. \tag{2.314}$$

This is nothing but the Peierls factor. In other words, Eq. (2.314) is the same as applying a vector potential

$$A_x=c\tilde{\phi}_L/Le \tag{2.315}$$

in the x direction. Because a small uniform phase twist and hence a uniform vector potential is imposed, it should be associated with the electromagnetic response at $\mathbf{k}=\omega=0$ in the second-order perturbation. This is indeed shown as follows: Under the vector potential (2.315), the change in the Hamiltonian up to the second order in $\tilde{\phi}_L$ reads

$$\delta\mathcal{H}=-\frac{j_x}{L}\,\tilde{\phi}_L-\frac{K_x}{2L^2}\,\tilde{\phi}_L^2+O(\tilde{\phi}_L^3), \tag{2.316}$$

where j_x and K_x are the current and the kinetic energy operator in the x direction, respectively. In the case of the nearest-neighbor Hubbard model (1.1a), these operators in the coherent-state representation have the form

$$j_x=2t\sum_{\mathbf{k},\sigma}\ \sin k_x\overline{\psi}_{k\sigma}\psi_{k\sigma}, \tag{2.317}$$

$$K_x=-2t\sum_{\mathbf{k},\sigma}\ \cos k_x\overline{\psi}_{k\sigma}\psi_{k\sigma}. \tag{2.318}$$

The change in the ground-state energy up to $\tilde{\phi}_L^2$ is obtained from the second-order perturbation as

$$\delta E=\tilde{D}\,\frac{\tilde{\phi}_L^2}{L^{2-d}}+O(\tilde{\phi}_L^4), \tag{2.319}$$

$$\tilde{D}=\frac{-1}{L^d}\left(\frac{1}{2d}\langle K\rangle+\sum_{\nu\neq0}\frac{|\langle0|j_x|\nu\rangle|^2}{E_\nu-E_0}\right), \tag{2.320}$$

for a d-dimensional hypercubic lattice. In Eq. (2.320), $|\nu\rangle$ denotes an eigenstate with the energy E_ν and $\nu=0$ denotes the ground state. The total average kinetic energy is $\langle K\rangle$.

Under the frequency-dependent vector potential $A_x=A_x^0e^{i\omega t}$, the electric field of the x component is given by

$$E_x=A_x^0i\omega/c. \tag{2.321}$$

When one uses the linear-response theory (Kubo, 1957), the current response to this electric field yields the conductivity as

$$\mathrm{Im}\ \sigma(\omega)=\frac{2e^2}{\omega}\,\tilde{D}. \tag{2.322}$$

From the Kramers-Kronig relation

$$\mathrm{Im}\ \sigma(\omega)=\int_{-\infty}^{\infty}d\omega'\,\frac{\mathcal{P}}{\omega-\omega'}\,\mathrm{Re}\ \sigma(\omega')d\omega',$$

the change in the energy density $\delta f=\delta E/L^d$ is given by using the Drude weight defined in Eq. (2.273) as

$$\delta f=\frac{1}{2\pi e^2}\,\frac{\tilde{\phi}_L^2}{L^2}D+O\left(\left(\frac{\tilde{\phi}_L}{L}\right)^4\right). \tag{2.323}$$

Equation (2.323) shows that the stiffness constant for the spatial phase twist is proportional to the Drude weight. An important point to keep in mind is that the Drude weight is obtained by taking the limit $\tilde{\phi}_L\rightarrow0$ first and $L\rightarrow\infty$ afterwards. If the opposite limit $\lim_{\phi_L\rightarrow0}\lim_{L\rightarrow\infty}$ is taken, one has to take account of possible level crossings at finite $\tilde{\phi}_L$ in the limit $L\rightarrow\infty$, which yields in principle a different quantity, namely, the superfluid density (Byers and Yang, 1961; Scalapino, White, and Zhang, 1993).

An infinitesimally small twist of the phase $\tilde{\phi}_\beta$ imposed between two boundaries $\tau=0$ and $\tau=\beta$ is equivalent to transforming the Grassmann variable as

$$\psi_\sigma(\mathbf{r},\tau)\rightarrow\psi_\sigma(\mathbf{r},\tau)\exp[i\tau\dot{\phi}] \tag{2.324}$$

with $\dot{\phi}=\tilde{\phi}_\beta/\beta$, where σ in general denotes quantum numbers other than the spatial coordinate. In case of the Hubbard model, σ is the spin. The transformation (2.324) may be replaced with the transformation of the Hamiltonian

$$\mathcal{H}\rightarrow\mathcal{H}+i\dot{\phi}\sum_{\mathbf{r},\sigma}\ \overline{\psi}_\sigma(\mathbf{r})\psi_\sigma(\mathbf{r}). \tag{2.325}$$

This equivalence is proven as follows: To calculate the partition function, one calculates the matrix element in a Trotter slice of the path integral:

$$\begin{aligned}\mathcal{L}(\tau,\psi,\mathcal{H})&=\langle\psi(\tau+\Delta\tau)|e^{-\Delta\tau\cdot\mathcal{H}[c^\dagger,c]}|\psi(\tau)\rangle\\&=\langle0|\prod_\alpha\ (1+\overline{\psi}_\alpha(\tau+\Delta\tau)c_\alpha)e^{-\Delta\tau\mathcal{H}[c^\dagger,c]}\\&\quad\times\prod_\gamma\ (1-\psi_\alpha(\tau)c_\alpha^\dagger)|0\rangle\\&=e^{-\Delta\tau\mathcal{H}[\overline{\psi}(\tau+\Delta\tau),\psi(\tau)]}.\end{aligned} \tag{2.326}$$

If one takes the transformation (2.325), this matrix element is transformed to

$$\begin{aligned}\mathcal{L}(\tau,\psi e^{i\tau\phi},\mathcal{H}) &= \mathcal{L}(\tau,\psi,\mathcal{H}) - i(\Delta\tau)\dot{\phi}\overline{\psi}_\alpha(\tau+\Delta\tau)\psi_\alpha(\tau)\\ &\quad + O((\Delta\tau)^2)\\ &= \langle\psi(\tau+\Delta\tau)|e^{-(\Delta\tau)\{\mathcal{H}[c^\dagger,c]+i\dot{\phi}c^\dagger c\}}|\psi(\tau)\rangle\\ &\quad + O((\Delta\tau)^2). \end{aligned} \qquad (2.327)$$

This proves equivalence to the transformation (2.325) in the functional integral limit $\Delta\tau\to 0$.

From Eq. (2.325) it turns out that $-i\phi$ is the same as an additional change in the chemical potential $\mu\to\mu-i\dot{\phi}$. Therefore the free energy as a function of the imposed small twist should have the form

$$f(\dot{\phi})=f(\dot{\phi}=0)+\frac{i\tilde{\phi}_\beta}{\beta}\rho+\frac{\tilde{\phi}_\beta^2}{2\beta^2}\kappa+O(\tilde{\phi}_\beta^3), \qquad (2.328)$$

where the electron density $\rho=-\partial f/\partial\mu$ and the charge compressibility $\kappa=\partial\rho/\partial\mu$ are obtained as expansion coefficients. Equation (2.328) shows that κ indeed measures the stiffness constant of the phase in the temporal direction.

4. Scaling of physical quantities

Combining Eqs. (2.323) and (2.328) for the Drude weight and the compressibility, respectively, with the finite-size scaling form derived from hyperscaling, one obtains useful scaling forms for physical quantities (Imada, 1994c, 1995a, 1995b; Continentino, 1994). This is because the finite-size scaling form (2.302) is also valid for δf, namely, the difference of the free energy between the cases in the presence and the absence of the twists. From a comparison of Eqs. (2.323) and (2.302) in the order of L^{-2}, the scaling of D is obtained:

$$D\propto\Delta^{\zeta} \qquad (2.329)$$

with $\zeta=\nu(d+z-2)$. Comparison of Eqs. (2.302) and (2.328) yields, in the order of β^{-1} and β^{-2},

$$\delta\propto\Delta^{-\alpha+1} \qquad (2.330)$$

and

$$\kappa\propto\Delta^{-\alpha} \qquad (2.331)$$

with $\alpha=\nu(z-d)$, where δ denotes the doping concentration, that is, the density measured from the Mott insulator.

When hyperscaling holds, scaling of other physical quantities can also be derived from Eqs. (2.300) and (2.302). In the insulating phase, the charge excitation gap E_g and the localization length ξ_l defined in Eq. (2.296) should be determined from the single characteristic energy and length scale Ω and ξ, respectively. Then,

$$E_g\propto|\Delta|^{z\nu} \qquad (2.332)$$

and

$$\xi_l\propto|\Delta|^{\nu} \qquad (2.333)$$

immediately follows, where we have used the fact that ν and z are identical on both sides of the transition point. This is shown by connecting the two sides via a route through the parameter space of Δ, temperature, and staggered magnetic fields. On the metallic side, the scaling of the specific heat $C=\beta^2\partial^2(\ln Z)/\partial\beta^2$ is given from Eq. (2.302):

$$C=\Delta^{\nu(d+z)}T\frac{\partial^2}{\partial T^2}\mathcal{F}(\xi/L=0,\xi^z T). \qquad (2.334)$$

At the critical point, the specific heat is given from the Δ-independent term as

$$C\propto T^{d/z}. \qquad (2.335)$$

If $C=\gamma T$ is satisfied at low temperatures in the metallic phase, the coefficient γ follows:

$$\gamma\propto\Delta^{\nu(d-z)}. \qquad (2.336)$$

In general, if C is not linear in T but proportional to T^q as $C\propto\sim\overline{\gamma}T^q$, $\overline{\gamma}$ is scaled as

$$\overline{\gamma}\propto\Delta^{\nu(d-qz)}. \qquad (2.337)$$

Another interesting quantity is the coherence temperature T_F below which the electron motion becomes quantum mechanical and degenerate. It is clear that T_F has to approach zero as $\Delta\to 0$ in a continuous transition. In case of the Fermi liquid, T_F is nothing but the Fermi temperature. The existence of a single characteristic energy scale with singularity at $\Delta=0$ leads to the scaling of T_F in the form

$$T_F\propto\Delta^{\nu z}. \qquad (2.338)$$

5. Filling-control transition

When the control parameter Δ is the chemical potential μ measured from the critical point μ_c, it represents the filling-control MIT (FC-MIT) and, in the terminology of critical phenomena, it is called a generic transition. In this case, it is possible to derive a useful scaling relation. Because the doping concentration is $\delta=-\partial f_s/\partial\mu=-\partial f_s/\partial\Delta$, it scales as

$$\delta\sim\Delta^{\nu(d+z)-1}. \qquad (2.339)$$

From the comparison of Eqs. (2.339) and (2.330), we derive

$$\nu z=1. \qquad (2.340)$$

The characteristic length scale is then

$$\xi\sim\delta^{-1/d}, \qquad (2.341)$$

which is the length scale of the "mean hole distance." This is a natural consequence because the mean hole distance is indeed a characteristic length scale which diverges at $\Delta=0$. From the scaling relation (2.340) the number of independent critical exponents is reduced to one in the above physical quantities. In the case of the FC-MIT, because the doping concentration δ is easier to control than the chemical potential, various exponents in terms of δ are summarized for convenience as follows:

$$\xi\sim\delta^{-1/d}, \qquad (2.342a)$$

$$\Delta\sim\delta^{z/d}, \qquad (2.342b)$$

$$\kappa \sim \delta^{1-z/d}, \tag{2.342c}$$

$$D \sim \delta^{1+(z-2)/d}, \tag{2.342d}$$

$$\gamma \sim \delta^{1-z/d}, \tag{2.342e}$$

$$T_F \sim \delta^{z/d}. \tag{2.342f}$$

6. Critical exponents of the filling-control metal-insulator transition in one dimension

In several 1D systems, we can derive rigorous estimates of various critical exponents for the cases of integrable models. After comparison of various cases, it turns out that the hyperscaling scenario holds for the MIT in 1D with $\nu=1/2$ and $z=2$ for all cases (Imada, 1995b; see also Stafford and Millis, 1993). This means that 1D is between the upper and lower critical dimensions of MIT. We start with the case of the Hubbard model. From the Bethe Ansatz solution, it is known that the compressibility (Usuki, Kawakami, and Okiji, 1989), the Drude weight (Shastry and Sutherland, 1990), and the specific-heat coefficient (Takahashi, 1972; Usuki, Kawakami, and Okiji, 1989) scale as

$$\chi_c \propto \delta^{-1}, \tag{2.343a}$$

$$D \propto \delta, \tag{2.343b}$$

$$\gamma \propto \delta^{-1}, \tag{2.343c}$$

for the 1D Hubbard model. For the supersymmetric t-J model, with $t=J$ in 1D, the Bethe Ansatz solution shows the same scaling as in Eqs. (2.343a)–(2.343c) (Kawakami and Yang, 1991). This is actually the same scaling form as we saw in Eq. (2.303) for noninteracting fermions near a band insulator. To understand the hyperscaling in 1D more intuitively, it is useful to consider the bosonized Hamiltonian derived after the asymptotic spin-charge separation. As will be derived in Sec. II.G.1, the Hamiltonian for the charge part has the form

$$H_\rho = \int dx \left(\frac{\pi v_\rho K_\rho}{2} \Pi_\rho^2 + \frac{v_\rho}{2\pi K_\rho} (\partial_x \phi_\rho)^2 \right), \tag{2.344}$$

where the charge-density phase field ϕ_ρ and the conjugate momentum Π_ρ satisfy the Bose commutation relation and constitute a noninteracting Hamiltonian with linear dispersion, $\omega_\rho(k)=v_\rho|k|$ (Emery, 1979; Haldane, 1980; Schulz, 1990b). This free-boson system indeed describes the case $z=1/\nu=2$ when $v_\rho \propto \xi^{-1}$. It should also be noted that, when the Hubbard model is mapped to the massive Thirring model, the transition to a Mott insulator with a Mott gap is mapped to the transition to a band insulator with a hybridization gap (Hida, Imada, and Ishikawa, 1983; Mori, Fukuyama, and Imada, 1994). This also shows that in 1D, the universality class should be the same between the metal Mott-insulator and metal band-insulator transitions. Even in bosonic systems, the Mott transition in 1D is characterized by the same universality class, $z=1/\nu=2$ (Imada, 1995b).

As for the MIT in 1D, the universality class is always the same irrespective of the character of low-energy excitations in the metallic phase. In the metallic phase, the low-energy spin and charge excitations can be characterized either by free fermions or by some type of Tomonaga-Luttinger liquid. However, the critical exponents of the MIT do not reflect this difference. In the metallic phase, the characteristic length and energy scales for the MIT are finite and always determine a crossover scale, while the character of a liquid is associated with behavior below this energy scale. The present scaling approach treats equally the zero-temperature transition for different types of metals, while the universality class of the transition does not necessarily specify the nature of coherent metals.

7. Critical exponents of the filling-control metal-insulator transition in two and three dimensions

In two or three dimensions, we have no exact solution for this problem. Therefore we have to rely on combined analyses of several numerical results. The most important question to be answered is whether 2D and 3D are lower than the upper critical dimension d_c or not. If $d_c<2$, some type of mean-field theory would be justified even in 2D, whereas we have to go beyond the mean-field level if $d_c>2$. We first review the predictions of various mean-field theories. In the Hartree-Fock approximation, the 2D and 3D Hubbard model in general has a phase diagram with an extended region of antiferromagnetic order in the metallic region around the Mott insulator, as in Figs. 10 and 11. Therefore the MIT takes place as a transition between insulating and metallic states, both with antiferromagnetic order. The solution of the unrestricted Hartree-Fock approximation shows that incommensurate periodicity at the wave-number $\mathbf{k} \neq (\pi,\pi)$ appears at finite doping. Irrespective of commensurate or incommensurate cases, the metal-insulator transition is in general achieved by the shrinking of hole pockets. This is the case for the transition [I-1↔M-1] discussed in Sec. II.B. It appears to be realized in some 3D compounds with orbital degeneracy, such as $\mathrm{NiS}_{2-x}\mathrm{Se}_x$, as will be discussed in Sec. IV.A.2.

Various experimental and numerical results, however, do not support this class in 2D. This is suggested by the absence of an antiferromagnetic metal in 2D. It means $d_{ml}>2$ at least unless the orbital degeneracy is too large. In this case possible types of transition in 2D would be [I-1↔M-2] and [I-1↔M-3]. Quantum Monte Carlo calculations first performed on the metallic side have shown $\chi_c \propto \delta^{-1}$ and an antiferromagnetic correlation length $\xi_m \propto \delta^{-1/2}$, which suggests a new universality class (Furukawa and Imada, 1992, 1993). This implication on the metallic side has been examined in terms of the scaling theory, leading to the conclusion that there does exist a new universality class $z=1/\nu=4$ in this case (Imada, 1994c, 1995b). Moreover, a localization length ξ_l scaled by $\xi_l \propto |\mu-\mu_c|^{-\nu}$ is predicted on the insulating side. This prediction for the insulating side has been critically tested by a quantum Monte Carlo calculation. The result is $\xi_l \propto |\mu-\mu_c|^{-\nu}$, $\nu=0.26\pm 0.05$. Therefore all the data are consistently explained by the scaling theory with a universality class of $z=4$ and $\nu=1/4$ for the case

[I-1↔M-3]. These two results can be explained neither by the Hartree-Fock approximation nor by the $d=\infty$ results. Indeed, neither the Hartree Fock approximation nor the $d=\infty$ results satisfies the assumption of hyperscaling [Eq. (2.300)]. For example, the Hartree-Fock approximation predicts $\nu=1/2$. Furthermore, scaling of the localization length ξ_l excludes the possibility that the MITs in 1D and 2D belong to the same universality class, because ξ_l scales following $\nu=1/2$ in 1D. Therefore numerical results on the 2D Hubbard model support the following four points for single-band systems in 2D on a square lattice:

(1) The upper critical dimension d_c of the MIT satisfies $d_c>2$ so that none of the mean-field approaches, including the Hartree-Fock approximation and the infinite-dimensional approach, is justified.

(2) Hyperscaling is satisfied in 2D with a new universality class of $\nu=1/4$ and $z=4$.

(3) $d_{ml}>2>d_{il}$, which means there are no antiferromagnetic metals close to the Mott insulator in 2D.

(4) The universality class is different for 1D and 2D because $z=1/\nu=2$ in 1D.

In 3D systems, the universality class of MIT for the case of [I-1↔M-3] is not well known. Experimental indications in (La,Sr)TiO$_3$ appear to support the mass-diverging-type MIT, will be as discussed in Sec. IV.B.1, and hence suggest that $z>2$ is also satisfied.

8. Two universality classes of the filling-control metal-insulator transition

Two different types of filling-control Mott transition have been shown to exist in the previous two subsections. One is characterized by $z=1/\nu=2$, which is the same as the band-insulator/metal transition. This is the case of all 1D systems as well as of several transitions at higher dimensions, where $z=1/\nu=2$ is expected for [I-1↔M-1], [I-1↔M-2], [I-2↔M-2], and [I-2↔M-4] in the classification scheme in Sec. II.B. In general, this class of transition appears when the component degrees of freedom do not contribute to low-energy excitations except in the Goldstone mode near the critical point. One way such contributions are realized is when both sides of the critical point are in broken-symmetry phases such as the magnetic ordered and superconducting ordered phases. The component degrees of freedom are also inert when an excitation gap such as a spin gap is formed. To understand the case [I-2↔M-2], it is helpful to consider the strong-coupling limit, where the problem is essentially reduced to single-component bosons because of the bound-state formation. Then it is equivalent to the problem of a superfluid-insulator transition, to be discussed in Sec. II.F.12.

The other case is characterized by values of z larger than two. This is seen in the case of [I-1↔M-3]. Two-dimensional systems with a single orbital, as in the Hubbard model on a square lattice, are shown in numerical calculations to follow $z=1/\nu=4$. Such a large dynamic exponent is associated with suppression of coherence, as we discuss in the next subsection, and this suppression in turn is associated with strong incoherent scattering of charge by a large degeneracy of component excitations. This degeneracy, coming from softened excitations of component degrees of freedom, is due to critical fluctuation of component correlations.

9. Suppression of coherence

In the new universality class discussed in the previous subsection (Sec. II.F.7), physical quantities show many anomalous features in terms of the standard MIT, the most important of which is the suppression of coherence. In this subsection we discuss several unusual aspects of this suppression for the new universality class.

Scaling theory predicts that the Drude weight is $D \propto \delta^{1+(z-2)/d}$. As is well known, $D\propto\delta$ is satisfied in the usual MIT, which is consistent with scaling theory when $z=2$. When the universality class is characterized by $z=1/\nu>2$, D is suppressed more strongly than δ-linear dependence at small δ. For example, when $z=4$ is satisfied in 2D, as suggested in numerical studies, $D\propto\delta^2$ is derived. This is one of the indications for the unusual suppression of coherence in this universality class and indeed supported by recent results for the *t-J* model (Tsunetsugu and Imada, 1998). Relative suppression of D as compared to the value D_0 for the metal band-insulator transition is given by $D/D_0, \propto\delta^{(z-2)/d}$.

From the sum rule, the ω-integrated conductivity gives the averaged kinetic energy

$$-\langle K\rangle=\int_0^\infty \sigma(\omega)d\omega. \tag{2.345}$$

In the strong-coupling limit, as in the *t-J* model, the total kinetic energy $\langle K\rangle=-(t/N)\Sigma_{\langle ij\rangle}\langle c_{i\sigma}^\dagger c_{j\sigma}+\mathrm{H.c.}\rangle$ is expected to be proportional to δ, that is, $-\langle K\rangle\propto\delta$. Therefore, from the above sum rule, the Drude part $D \propto\delta^{1+(z-2)/d}$ becomes negligibly small at small δ in the total weight $-\langle K\rangle\propto\delta$ if $z>2$. This means most of the total weight $-\langle K\rangle$ is exhausted in the incoherent part $\sigma_{\mathrm{reg}}(\omega)$ in Eq. (2.273). In scaling theory, the form of $\sigma_{\mathrm{reg}}(\omega)$ is not specified, and indeed it may depend on details of systems including the interband transition. However, for the intraband contribution, $\sigma(\omega)$ is expected to follow $\sigma(\omega)\sim(1-e^{-\beta\omega})/\omega$ at very high temperatures $t<T$ because the current correlation function $C(\omega)$ defined in Eq. (2.275) becomes temperature and frequency insensitive for $\omega<t$. In fact, $\sigma(\omega)\sim1/T$ for small ω and $\sigma(\omega)\sim1/\omega$ for larger ω is a general feature at high temperatures (Ohata and Kubo, 1970; Rice and Zhang, 1989; Metzner *et al.*, 1992; Kato and Imada, 1997). When the temperature is lowered, this incoherent part $\sim(1-e^{-\beta\omega})/\omega$ is in general transferred to the Drude part $\sim1/(-i\omega+\gamma)$ below the coherence temperature. In the usual band-insulator metal transition, this transfer can take place for the dominant part of the weight because $-\langle K\rangle$ and D both may be proportional to δ. Therefore the incoherent part is totally reconstructed to the Drude part with decreasing temperature. However, for $z>2$, this transfer takes place only in a tiny part of the total weight because the relative weight of the Drude part to the whole weight is $\delta^{(z-2)/d}$, which vanishes as $\delta\to0$ for $z>2$. Even at $T=0$, a large fraction of the conductivity weight must be exhausted in the incoherent part. Since scaling theory gives us no reason to expect a dramatic change of the form for $\sigma_{\rm reg}(\omega)$ at any temperature at the critical point, the optical conductivity more or less follows the form

$$\sigma_{\rm reg}(\omega)\sim C\frac{1-e^{-\beta\omega}}{\omega} \tag{2.346}$$

even for $t>\omega$ and $t>T$, where we have neglected model-dependent features such as the interband transition. The intraband part of the incoherent weight C may follow $C\propto\delta$. Such dominance of the incoherent part is consistent with the numerical results for 2D systems, as is discussed in Sec. II.E.1. It is also consistent with the experimental indications of high-T_c cuprates as will be discussed in Secs. IV.C.1 and IV.C.3. The scaling of $\sigma(\omega)$ by Eq. (2.346) is another argument in support of $z>2$ in 2D. We discuss in Sec. II.G.2 how the form of Eq. (2.346) is equivalent to the scaling of the marginal Fermi liquid. In contrast, the numerical results in 1D by Stephan and Horsch (1990), discussed in Sec. II.E.1, support a small incoherent part at low temperatures. This may be due to $z=2$ in 1D because the majority of the weight seems to be exhausted in the Drude weight. In 3D perovskite systems, the dominance of the incoherent part is a common feature, as we see in systems such as (La,Sr)TiO$_3$, (La,Sr)VO$_3$, and (La,Sr)MnO$_3$ (see Sec. IV for details). This seems to suggest $z>2$ in 3D, as well. In the high-T_c cuprates, it appears that the coherent part is almost absent, while in 3D systems, a small fraction of the coherent weight appears to exist which yields T^2 resistivity.

Another aspect of the suppression of coherence is seen in the coherence temperature T_{coh}. The scaling of T_{coh} is given by $T_{coh}\propto\delta^{z/d}$. Because the standard MIT is characterized by $T_{coh0}\propto\delta^{2/d}$, the relative suppression T_{coh}/T_{coh0} is again proportional to $\delta^{(z-2)/d}$. When $z=4$, as suggested by numerical results in 2D, we obtain $T_{coh}\propto\delta^2$ in 2D in contrast with $T_{coh0}\propto\delta$ for $z=2$.

In the Mott insulating phase, the charge degrees of freedom are not vital and only the spin or orbital degrees of freedom (that is, the component degrees of freedom) contribute to low-energy excitations. When symmetry is broken by the component degrees of freedom, the entropy coming from the components is reduced essentially to zero. The entropy is also reduced when the component excitation has a gap, as in the spin-gap phase. Even without such a clear phase change, the growth of short-ranged component correlation progressively reduces the entropy with decreasing temperature. For example, in 2D single-band systems, exponential growth of the antiferromagnetic correlations leads to exponentially small residual entropy at low temperatures, except for the contribution from the Goldstone mode. When carriers are doped, an additional entropy due to the charge degrees of freedom is expected proportional to δ. Of course, this additional entropy is assigned not solely to the charge but also to the spin entropy, because they are coupled, causing the destruction of antiferromagnetic long-range order and yielding a finite correlation length $\xi\propto 1/\delta^{1/d}$. This additional entropy $\propto\delta$ is released below the coherence temperature T_{coh}. Therefore we are led to a natural consequence that if T-linear specific heat characterizes the degenerate (coherent) temperature region, the coefficient γ should be given by $\gamma\sim\delta/T_{coh}\sim\delta^{1-z/d}$. This is indeed the scaling law we obtained in Eq. (2.336). From this heuristic argument, it turns out that the metallic phase near the Mott insulator is characterized by large residual entropy at low temperatures, which is also related to the suppression of the antiferromagnetic correlation. This large residual entropy again has numerical support in the 2D t-J model (Jaklič and Prelovšek, 1996). It may also be said that anomalous suppression of coherence at small δ is caused by short-ranged component correlations, which scatter carriers incoherently.

In a Mott insulator, because the single-particle process is suppressed due to the charge gap, we have to consider the two-particle process (electron-hole excitations) expressed by the superexchange interaction. Similarly, even in the metallic region, suppression of coherence for the single-particle process leads us to consider the relevance of two-particle processes. In contrast with the insulating phase, the two-particle processes in metals contain not only the particle-hole process (the exchange term) but also particle-particle processes through an effective pair hopping term. Such processes may be generically described by

$$\mathcal{H}_W=-t_W\sum_i\left(\sum_{\delta\sigma}(c^\dagger_{i\sigma}c_{i+\delta\sigma}+c^\dagger_{i+\delta\sigma}c_{i\sigma})\right)^2. \tag{2.347}$$

Coherence is not suppressed anomalously near the Mott insulator in the case of a two-particle process because the universality class of the two-particle transfer is given by $z=1/\nu=2$, making it more relevant than single-particle transfer for small δ. In fact, this term does not suffer from the mass enhancement effect. This new term added to the Hubband model, namely the t-U-W model leads to the appearance of the d-wave superconducting phase (Assaad, Imada, and Scalapino, 1996, 1997; Assaad and Imada, 1997), although it is not clear whether the bare Hubband model implicitly contains sufficiently large coupling of this form. The filling-control transition from superconductor to Mott insulator is indeed characterized by $z=1/\nu=2$. This shows an instability of metals near the Mott insulator to superconducting pairing or, more generally, an instability of the $z=4$ universality phase to a broken symmetry state.

A related but different view was proposed for the role of incoherence in the mechanism of superconductivity (Wheatley, Hsu, and Anderson, 1988). According to this proposal, lack of coherent transport in the interlayer direction occurs when electrons are confined due to spin-charge separation in 2D. The coherence recovers through interlayer tunneling after pair formation, which leads to a kinetic-energy gain in the interlayer direction. In the analysis given in this section, the driving force for recovering coherence by pair formation already exists in a single layer because of the novel universality class of the MIT. The enhancement of the pairing correlation for systems with a flat band near the Fermi level was also suggested in numerical studies (Yamaji and Shimoi, 1994; Kuroki, Kimura, and Aoki, 1996; Noack *et al.*, 1997).

10. Scaling of spin correlations

In the previous subsections, an unusually large z was obtained when the MIT was accompanied by a simultaneous component order transition, as in the 2D Hubbard model. In this case, a component correlation, such as the antiferromagnetic correlation or the orbital correlation, follows a particular scaling behavior near the transition point. Here as an example we discuss the scaling of the antiferromagnetic correlation in a single-band model. The destruction of magnetic order in the metallic region is ascribed to charge dynamics. In this case, the scaling of the magnetic correlation length ξ_m follows $\xi_m \sim \xi$, where ξ is the length scale of the MIT itself, and hence the mean distance of doped holes is given by Eq. (2.342a). In other words, the magnetic correlation length is controlled by ξ because long-range order is destroyed by the charge motion. We need to be careful about the definition of ξ_m in metals because they have gapless magnetic excitations, leading to a power-law decay at asymptotically long distances at $T=0$. In general, at the critical point of the magnetic transition, the spin correlation follows

$$\langle \mathbf{S}(0)\cdot\mathbf{S}(\mathbf{r})\rangle \sim r^{-(d+z-2+\eta)} e^{i\mathbf{Q}\cdot\mathbf{r}} \tag{2.348}$$

with the ordering vector $\mathbf{Q}$ and the exponent η. Here, the magnetic correlation in the insulating phase has to be kept unchanged up to the critical point as a function of the control parameter, the chemical potential. The reason is the following: The spectral representation of the spin correlation

$$\langle \mathbf{S}(0)\cdot\mathbf{S}(\mathbf{r})\rangle = \frac{1}{Z}\sum_m \langle m|\mathbf{S}(0)\cdot\mathbf{S}(\mathbf{r})|m\rangle e^{-\beta(E_m-\mu N)} \tag{2.349}$$

does not contain an explicit dependence on the chemical potential μ at $T=0$ because the number of particles is kept constant in the Mott insulating phase and $e^{\beta\mu N}$ in the numerator is canceled by the same factor in the partition function Z. This means that the staggered magnetization defined by

$$M_s = \frac{1}{N}\sum_i S_i^z e^{i\mathbf{Q}\cdot\mathbf{r}_i} \tag{2.350}$$

is a constant in the insulating phase. Therefore the magnetization exponent β_s, defined by

$$M_s \propto |\Delta_s|^{\beta_s}, \tag{2.351}$$

has to satisfy $\beta_s=0$ and $\eta=2-d-z$. Note that this is a continuous transition because ξ_m diverges continuously, although M_s jumps at $\Delta=0$. In the metallic region, this constant staggered magnetization is cut off at ξ_m and the antiferromagnetic correlation has to decay as a power law beyond ξ_m. The exponent for the power law at $r>\xi_m$ is determined from the Fermi-surface effect in the coherent region of metals. This nontrivial definition of the correlation length ξ_m is indeed known to exist in the 1D Hubbard model (Imada, Furukawa, and Rice, 1992), where the antiferromagnetic correlation decays as $\sim 1/r^{3/2}$ at $r>\xi_m$ while it decays as $\sim 1/r$ for $r<\xi_m$ excepting logarithmic corrections. The decay rate $\propto 1/r^{3/2}$ is indeed the asymptotic correlation in the metallic region for $\delta \to +0$, while the decay rate $\propto 1/r$ is the long-distance behavior in the insulating phase, because $\xi_m \propto 1/\delta$. In 2D, the insulating behavior at $r<\xi_m$ is characterized by a constant because of the presence of long-range order in a Mott insulator. The exponent of the power-law decay beyond ξ_m in 2D is not rigorously known. In a Fermi liquid, it has to follow $\langle \mathbf{S}(0)\cdot\mathbf{S}(\mathbf{r})\rangle \propto r^{-\gamma}$ with $\gamma=3$ at $r>\xi_m$ in 2D.

With this nontrivial definition of ξ_m in mind, the scaling form for the singular part of the free energy is generalized to include dependence on the staggered magnetic field h_s with wave number $\mathbf{Q}$ as

$$f_s(\Delta,h_s) \propto |\Delta|^{\nu(d+z)} Y(h_s/|\Delta|^{\varphi}) \tag{2.352}$$

at $T=0$, where φ is the exponent for h_s. From this expression, the staggered magnetization is derived as

$$M_s = \left.\frac{\partial f_s}{\partial h_s}\right|_{h_s\to 0} = |\Delta|^{\beta_s}. \tag{2.353}$$

with the exponent

$$\beta_s = \nu(d+z) - \varphi_s. \tag{2.354}$$

Therefore, from $\beta_s=0$, we obtain $\varphi_s=\nu(d+z)$. Then the staggered susceptibility $\chi(\mathbf{Q},\omega=0)$ is scaled as

$$\chi(\mathbf{Q},\omega=0) = \left.\frac{\partial M_s}{\partial h_s}\right|_{h_s\to 0} \sim \Delta^{-\gamma_s} \tag{2.355}$$

with $\gamma_s=\nu(d+z)$. Re $\chi(q,\omega)$ and Im $\chi(q,\omega)/\omega$ both have a peak around $q=\mathbf{Q}$ at $\omega=0$ with the same critical behavior of the peak height $\propto \Delta^{-\gamma_s}$ and widths $\sim \xi^{-z}$ in ω space and $\sim \xi^{-1}$ in k space. The dynamical structure factor is given from the fluctuation-dissipation theorem

$$\mathrm{Im}\,\chi(q,\omega) = (1-e^{-\beta\omega}) S(q,\omega). \tag{2.356}$$

At $T=0$, $S(q,\omega)$ also has a peak height $\propto \Delta^{-\gamma_s}$ with the widths ξ^{-z} and ξ^{-1} in ω and q spaces, respectively. The consistency of this scaling with the spin correlation $\langle \mathbf{S}(\mathbf{r})\mathbf{S}(0)\rangle$ discussed above is confirmed from the relation

$$S(\mathbf{Q},t=0) = \int_{-\infty}^{\infty} S(\mathbf{Q},\omega)\,d\omega$$
$$\propto \Delta^{-\gamma_s}\xi^{-z} \sim \Delta^{1-\gamma_s} \sim \xi^d \sim \delta^{-1}. \tag{2.357}$$

This is indeed the structure factor

$$S(\mathbf{Q},t=0) = \int \langle \mathbf{S}(\mathbf{r})\mathbf{S}(0)\rangle e^{i\mathbf{Q}\cdot\mathbf{r}} d\mathbf{r} \tag{2.358}$$

expected for spins with correlation length $\xi_m=\xi$, assuming the correlation is cut off at ξ_m.

However, from the nontrivial definition of ξ_m above, we should keep in mind that the power-law correlation beyond ξ_m is neglected in this argument. When the spin correlation follows the exponential form e^{-r/ξ_m}, $S(\mathbf{q},\omega)$ satisfies simple Lorentzian form, indeed with the width discussed above. However, if the correlation is not exponentially cut off but obeys a power-law decay beyond ξ_m, this contribution of the long-ranged part has to be superimposed around $q=\mathbf{Q}$ and $\omega=0$ in $S(\mathbf{q},\omega)$ as a non-Lorentzian contribution. We call this contribution the coherent part of the spin correlation, as discussed in Sec. II.E.4. Because of the presence of the coherent contribution, the width of the peak in q or ω space becomes ill defined, and the peak structure in general may have a singular structure such as a cusp at incommensurate positions, as schematically illustrated in Fig. 31. Such non-Lorentzian structure is due to the coherent contribution and grows below T_{coh}. We discuss temperature dependence later in greater detail. Although the width is not well defined, the total weight in q or ω space satisfies the above scaling because the weight in the coherent part does not exceed the incoherent contribution when the exponent of the power-law decay γ satisfies $\gamma>d$, as in the Fermi-liquid case (in a Fermi liquid, $\gamma=d+1$). Then the q-integrated and ω-integrated intensities at $T=0$ follow

$$\int dq \ \mathrm{Im}\ \chi(q,\omega)\propto\Delta^{\nu-\gamma_s}\sim\delta^{-1-(z-1)/d}, \tag{2.359}$$

$$\int d\omega \ \mathrm{Im}\ \chi(q,\omega)\propto\Delta^{1-\gamma_s}\sim\delta^{-1}. \tag{2.360}$$

Next we discuss the temperature dependence of the scaling. The intrinsic correlation length ξ_m is severely controlled by the hole concentration δ. However, the incoherent part at distance $r<\xi_m$ and time $t<\xi_m^z$ has basically the same structure as for a Mott insulator where there is no effect of holes. At finite temperatures, the thermal antiferromagnetic correlation length ξ_{mT} is a well-defined quantity because the correlation should decay exponentially at $T\neq0$ as $e^{-r/\xi_{mT}}$ in both metals and Mott insulators in 2D. If the temperature is lowered, this thermal correlation length diverges as $T\rightarrow0$. In the Mott insulating phase it leads to long-range order at $T=0$. In metals, although ξ_{mT} diverges, the intrinsic correlation length ξ_m cuts off the correlation even when ξ_{mT} exceeds ξ_m. It is rather trivial that the spin correlation shows essentially the same behavior at high temperatures if $\xi_{mT}<\xi_m$ whether in metals or in insulators. The crossover temperature T_{scr} where ξ_{mT} exceeds ξ_m was introduced in Sec. II.E.4 and is schematically shown in Fig. 34. At low doping concentration, T_{scr} is in general higher than T_{coh} because of the suppression of T_{coh}, as can be seen in Fig. 34. As is discussed in Sec. II.E.4, the dominant weight $S_{inc}(q,\omega)$ has no appreciable temperature dependence below T_{scr} with ξ_m unchanged. This leads to the scaling form

$$\mathrm{Im}\ \chi(q,\omega)=(1-e^{-\beta\omega})S_{inc}, \tag{2.361}$$

where S_{inc} has the temperature-insensitive widths $\sim\xi_m^{-1}$ in q and $\sim\xi_m^{-z}J$ in ω space. These widths are rather wide because they are of the order of $\sim2\pi\sqrt{\delta}$ in q and $(2\pi\sqrt{\delta})^zJ$ in ω. Therefore the dominant ω dependence at small ω in Im χ is given by the factor $1-e^{-\beta\omega}$. Due to this simplification, the neutron scattering weight $\int dq$ Im $\chi(q,\omega)$ follows

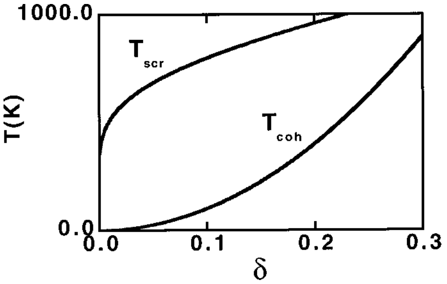

FIG. 34. Scaling of T_{scr} and T_{coh} in the plane of temperature and doping concentration in a typical situation of 2D systems.

$$\int dq \ \mathrm{Im}\ \chi(q,\omega)\sim1-e^{-\beta\omega} \tag{2.362}$$

and the NMR relaxation rate T_1 is given as

$$\frac{1}{T_1T}=\lim_{\omega\rightarrow0}\int\frac{\mathrm{Im}\ \chi(q,\omega)}{\omega}f(q)dq\sim\frac{1}{T} \tag{2.363}$$

when the atomic form factor $f(q)$ is a smooth function with an appreciable weight around $\mathbf{Q}$. Numerical results in accordance with the above scaling and also in agreement with experimental indications in the high-T_c cuprates are discussed in Sec. II.E.4 and IV.C. When the temperature is lowered to $T<T_{coh}$, complexity arises because of the growth of the coherent part. In the coherent temperature region, no microscopic calculation is available for the explicit temperature dependence. However, because the weight of the incoherent part is dominant over the coherent weight for small δ, the scaling for δ dependence given above at $T=0$ should be valid in this temperature range.

A qualitatively different feature may appear in the pseudogap region of underdoped high-T_c cuprates due to an increase in the coherent contribution from pairing fluctuations.

11. Possible realization of scaling

A microscopic description of the Mott transition which satisfies the scaling theory has not yet been fully worked out. Hyperscaling implies the existence of singular points at the MIT, around which charge excitations can be described. The large dynamic exponent $z=4$ implies that the relevant charge excitation has a flat dispersion $\varepsilon\propto k^4$ around those points near the MIT. This flat dispersion has to be realized around some point in **k** space near the large Fermi surface if the quasiparticle description is to be justified. We consider the case in which the paramagnetic phase is kept near the antiferromagnetic insulator ([I-1↔M-3] in the category of Sec. II.B). In this case, the Fermi surface must be renormalized to the completely nested one when the doping concentration decreases and the system approaches the antiferromagnetic insulator in a continuous fashion

(Miyake, 1996). This is because the shape of the Fermi surface changes continuously with doping while on the verge of the transition, it must coincide with the completely nested shape of the Fermi level of the antiferromagnetic insulator. Therefore at the Mott transition point on the metallic side, a flat dispersion should be observed around the completely nested surface. In numerical studies in the low-doping regime, as discussed in Sec. II.E.2, the spectral function $A(\mathbf{k},\omega)$ in 2D Hubbard and t-J models indeed shows a flat dispersion around $\mathbf{k}=(\pi,0)$ (Bulut *et al.*, 1994b; Dagotto *et al.*, 1994; Preuss *et al.*, 1997). In addition, there are several experimental indications from angle-resolved photoemission which suggest a flat dispersion around $\mathbf{k}=(\pi,0)$ (Liu *et al.*, 1992a; Dessau *et al.*, 1993; Gofron *et al.*, 1994; Marshall *et al.*, 1996), as is discussed in Secs. IV.C.3 and IV.C.4. This flat dispersion appears to be proportional to k^4, which means that the original Van Hove singularity present in the noninteracting case for the nearest-neighbor Hubbard model is not sufficient and the flatness must be much more enhanced by electron correlation (Imada, Assaad, *et al.*, 1998) The description "extended Van Hove singularity" inadequately describes this circumstance, which we call a "flat dispersion." A possible way to realize the $z=4$ universality class is, for example, for the dispersion to have the form $\varepsilon \sim q_x^4 - q_y^4$, around $\mathbf{k}_0=(\pi,0)$ with $\mathbf{q}=\mathbf{k}-\mathbf{k}_0$. In fact, this can occur if there is next-nearest-neighbor hopping but no nearest-neighbor hopping. It may occur if antiferromagnetic correlation is enhanced critically, because hopping to a different sublattice is suppressed by antiferromagnetic ordering. This flat dispersion may generate a strong channel of antiferromagnetic as well as Umklapp scattering with the momentum transfer $\mathbf{k}=(\pi,\pi)$ by scattering the quasiparticle around $\mathbf{k}=(\pi,0)$ to that around $\mathbf{k}=(0,\pi)$. Therefore spin degeneracies (correlations) are strongly coupled with the charge degeneracy in momentum space, which further enhances the incoherence of the charge excitations in a self-consistent fashion. The renormalization of the Fermi surface to a perfectly nested one, as well as the appearance of the flat dispersion around $(\pi,0)$, implies that the self-energy of the single particle has a singular k dependence around $(\pi,0)$. The instability of single-particle states against the two-particle process for this flat dispersion may result in the formation of bound states around $(\pi,0)$, as is discussed in Sec. II.F.9 which may be associated with the pseudogap phenomena in the high-T_c cuprates. Relationship between the scope here and experimental results is dicussed in Secs. IV.C.3 and IV.C.4. From both theoretical (numerical) and experimental points of view, the wave-number dependence of charge excitations with high-energy resolution is one of the hardest quantities to measure. Further studies are needed for a more accurate and quantitative picture.

12. Superfluid-insulator transition

The scaling theory of the superfluid-insulator transition is a closely related subject, which we review briefly in this subsection. The situation is simpler for this transition than for the fermionic Mott transition because it can be associated with the explicitly defined order parameter of the superfluid phase. This makes it possible to write down an effective action explicitly using the superfluid order parameter (Fisher *et al.*, 1989). The Hamiltonian for interacting bosons may be written as

$$\mathcal{H}=\mathcal{H}_0+\mathcal{H}_1, \tag{2.364}$$

$$\mathcal{H}_0=-\sum_{\langle ij\rangle} t_{ij}(b_i^\dagger b_j+\mathrm{H.c.}), \tag{2.365}$$

$$\mathcal{H}_1=U\sum_i n_i^2-\mu\sum_i n_i \tag{2.366}$$

with $n_i=b_i^\dagger b_i$ and the boson operators $b_i^\dagger$ and b_i. When U is large, the Mott insulating phase appears at integer fillings similarly to the fermionic case. The system undergoes the Mott transition from Mott insulator to superfluid when one changes filling or U/t_{ij}. The action is given as

$$S=\int_0^\beta d\tau[b_i^\dagger\partial_\tau b_i+\mathcal{H}]. \tag{2.367}$$

After making the Stratonovich-Hubbard transformation by introducing the c-number Stratonovich variable $\psi_i(\tau)$, we can expand the action in terms of ψ_i as

$$\begin{aligned}S=&\int dk\,d\omega\,r(k,\omega)|\psi(k,\omega)|^2\\&+g\int dk\,d\omega\,i\omega|\psi(k,\omega)|^2\\&+u\int dx\,d\tau|\psi(x,\tau)|^4+S_{phase}(\phi,\psi).\end{aligned} \tag{2.368}$$

The superfluid order is realized by $\langle|\psi_i(\tau)|\rangle\neq 0$, which is linearly related to the superfluid order parameter $\Phi(r,\tau)=|\Phi(r,\tau)|e^{i\phi(r,\tau)}$ with the amplitude mode $|\Phi|$ and the phase ϕ. The mean-field action is obtained by neglecting the phase fluctuation part $S_{phase}(\phi,\psi)$. However, low-energy fluctuations are generated from the phase mode after integrating out the amplitude mode as

$$S_{eff}=\int d\mathbf{r}\int_0^\beta d\tau\left(\rho(i\dot{\phi})+\kappa\dot{\phi}^2+\frac{\rho_s}{m}(\nabla\phi)^2\right), \tag{2.369}$$

where ρ, κ, m, and ρ_s are the average density, the compressibility, the mass, and the superfluid density, respectively. To derive Eq. (2.369), we used the fact that from the similar derivations to D and κ in the fermionic case, the superfluid density ρ_s and κ are related to the phase stiffness constant when twists are imposed in the boundary condition of the path integral. From a comparison of the hyperscaling form for the singular part of the free energy,

$$f_s\sim\Delta^{\nu(d+z)}\mathcal{F}(\xi/L,\xi^z/\beta), \tag{2.370}$$

with the form for κ and ρ_s, we obtain

$$\kappa\propto\Delta^{\nu(d-z)} \tag{2.371}$$

and

$$\rho_s \propto \Delta^{\zeta} \tag{2.372}$$

with $\zeta = \nu(d+z-2)$ similarly to the fermionic case. For a filling-control Mott transition (in other words, a generic transition) in a pure system, it was deduced that the exponents $z = 1/\nu = 2$ and $\zeta = 1$ hold in all dimensions (Fisher *et al.*, 1989). For a bandwidth-control Mott transition (that is, a multicritical transition) in a pure system, the effective action is mapped to the $(d+1)$-dimensional XY model. Because of space-time isotropy, $z = 1$ holds. The upper critical dimension d_c is thus given by $d_c = 3$ and at $d > 3$, $z = 1$ and $\nu = 1/2$ hold. For a disorder-driven transition between a Bose glass and a superfluid, the dynamic exponent z is considered to be $z = d$ as in the case of the disordered transition of fermions because the compressibility is nonsingular. The Bose-glass superfluid transition has been numerically studied by the Monte Carlo method. The conclusion $z = 2$ in 2D is consistent with scaling theory (Wallin *et al.*, 1994; Zhang, Kawashima, Carlson, and Gubernatis, 1995).

G. Non-fermi-liquid description of metals

1. Tomonaga-Luttinger liquid in one dimension

This article does not attempt to review recent progress in theoretical studies of interacting 1D systems. We summarize the elementary properties of the Tomonaga-Luttinger liquid in 1D theoretical systems only insofar as these are needed to discuss the present experimental situation in d-electron systems. It is well known and can be easily shown that a perturbation expansion in terms of the interaction breaks down in 1D systems. For instance, in a second-order perturbation expansion of the Hubbard model in terms of U, the momentum distribution function $n(k) \equiv \Sigma_\sigma \langle c^\dagger_{k\sigma} c_{k\sigma} \rangle$ shows logarithmic divergences at the Fermi level k_F even in the second order of U, which is an indication of the breakdown of the Fermi-liquid state. After summing the so-called parquet diagrams up to infinite order, we find that $n(k)$ at k_F has a power-law singularity. Other approaches such as the bosonization technique also support this singularity. The breakdown of the Fermi-liquid state in 1D was first suggested by Tomonaga (1950), who carried out the bosonization procedure for spinless interacting fermions in the continuum limit. The power-law singularity of $n(k)$ was analyzed in a similar model by Luttinger (1963). In the seventies, experimental studies on quasi-1D conductors further stimulated theoretical studies on 1D systems. Exact solutions by the Bethe ansatz, perturbation expansions, renormalization-group approaches, and bosonization techniques were developed (see, for example, Emery, 1979 Solyom, 1979). The Tomonaga-Luttinger liquid as a universal feature of interacting 1D systems was emphasized by Haldane (1980, 1981). The Bethe ansatz wave function for finite-size systems of the Hubbard model in the limit of $U = \infty$ was utilized to estimate numerically the singularity of metallic states (Ogata and Shiba, 1990). Recently, finite-size corrections to the Bethe ansatz solution have been combined with the conformal field theory to calculate the critical exponents of the Tomonaga-Luttinger liquid in the strongly correlated regime (Frahm and Korepin, 1990; Kawakami and Yang, 1990; Schulz, 1990b, 1991).

Here we summarize the case of simple systems such as the Hubbard model and the t-J model. In 1D interacting systems, the elementary excitation is not described by the electrons but by the spin density and charge-density degrees separately. When the spin and charge degrees of freedom both have gapless excitations, as in the case of the Hubbard model in the metallic phase, this quantum liquid is called a Tomonaga-Luttinger liquid, as compared to a Luther-Emery liquid, which we discuss later. The momentum distribution function $n(k)$ of a Tomonaga-Luttinger liquid is given by

$$\langle n(k) \rangle = \langle n_{k_F} \rangle - \mathrm{const} \times |k - k_F|^{\theta} \,\mathrm{sgn}(k - k_F), \tag{2.373}$$

where the exponent θ is related to the exponents for spin and charge correlation functions through K_ρ as

$$\theta = (K_\rho - 1)^2 / 4K_\rho . \tag{2.374}$$

It is clear that the renormalization factor Z of the Fermi liquid vanishes in a Tomonaga-Luttinger liquid because $\langle n(k) \rangle$ does not have a jump at $k = k_F$. The charge and spin correlation functions $\langle \rho(r)\rho(0) \rangle$ and $\langle s(r)s(0) \rangle$, respectively, are given at the asymptotically long distance r as

$$\begin{aligned}\langle \rho(r)\rho(0) \rangle \sim{}& \mathrm{const} + a_0 r^{-2} + a_2 r^{-(1+K_\rho)} \\ & \times \cos 2k_F r + a_4 r^{-4K_\rho} \cos 4k_F r\end{aligned} \tag{2.375}$$

and

$$\langle s(r)s(0) \rangle \sim b_0 r^{-2} + b_2 r^{-(1+K_\rho)} \cos 2k_F r . \tag{2.376}$$

The Fermi-liquid state is reproduced by taking $K_\rho = 1$. However, in 1D interacting systems, K_ρ is generally different from one. In the Hubbard model, K_ρ depends on U and filling in the range $\frac{1}{2} \leqslant K_\rho \leqslant 1$. In the limit of half filling, $\delta \to 0$, $K_\rho \to \frac{1}{2}$ irrespective of $U \neq 0$ while $K_\rho = \frac{1}{2}$ is satisfied at any filling in the limit $U \to \infty$. This power-law decay of spin and charge correlations is related to the branch cut in the single-particle Green's function given by

$$\begin{aligned}G(r,t) \sim{}& \frac{1}{[x - v_s t + (i/\Lambda)\mathrm{sgn}\, t]^{1/2}} \frac{1}{[x - v_c t + (i/\Lambda)\mathrm{sgn}\, t]^{1/2}} \\ & \times [\Lambda^2 (x - v_c t + i/\Lambda)(x + v_c t - i/\Lambda)]^{-\alpha_c},\end{aligned} \tag{2.377}$$

where Λ is a cutoff on the order of v_F/a, where a is the lattice constant, while $\alpha_c = \theta/2$. The spin and charge degrees of freedom are decoupled in the asymptotic low-energy scale to cause the separation of spin and charge group velocities v_s and v_c. An electron propagates with the group velocity v_F in a Fermi liquid at the Fermi level, while it separates into spin and charge degrees of freedom with different group velocities v_s and v_c in a Tomonaga-Luttinger liquid. Because of this separation, the single-particle spectral weight $G(q,\omega)$ does not have a pole structure as in the Fermi liquid. After taking the Fourier transform of Eq. (2.377), we find that it has the structure

$$G(q,\omega)=\frac{|q/k_F|^{\theta}}{qv_c}\mathcal{F}\left(\frac{\omega}{v_s q},\frac{v_s}{v_c}\right) \tag{2.378}$$

with power-law singularities.

Thus the spectral function $A(k,\omega)$ of the Tomonaga-Luttinger model shows power-law singularities instead of Lorentzian-like quasiparticle peaks. The thresholds of the power-law singularities for the Tomonaga-Luttinger model are at $\omega=v_\nu(k-k_F)+\mu$ and $-v_\nu(k+k_F)+\mu$, where $v_\nu=v_s$ and v_c (Meden and Schönhammer, 1993a, 1993b; Voit, 1993). The density of states near the chemical potential then behaves as

$$\rho(\omega)\propto|\omega-\mu|^{\theta}. \tag{2.379}$$

Thus the photoemission spectra do not show a Fermi edge but instead have an intensity that vanishes at the Fermi level as a power law.

The disappearance of the Fermi edge has been claimed for many organic and inorganic quasi-1D metals (Dardel *et al.*, 1992a, 1992b; Coluzza *et al.*, 1993; Nakamura *et al.*, 1994a). The photoemission spectra of quasi-1D metals near the Fermi level indeed show the disappearance of the Fermi edge, as predicted by Eq. (2.379). However, the exponent θ obtained from the experimental data is typically 0.7–2, which is much larger than the maximum value of 0.125 predicted for the Hubbard model (Kawakami and Yang, 1990). It has been suggested that this is related to long-ranged electron-electron interactions in these compounds because arbitrarily large θ is possible for long-range interactions (Luttinger, 1963). Another puzzling aspect of the experimental results is that the energy range in which the power-law fit is successful is as large as $\sim$0.5 eV, in spite of the fact that the power-law behavior of $\rho(\omega)$ is a result of spin-charge separation and therefore should be limited at most to the maximum spinon energy, which is of the order of the superexchange interaction $J\lesssim 0.1$ eV. Thus, at the moment, it is not clear whether the experimental indications mentioned above constitute evidence for the Tomonaga-Luttinger liquid.

The thermodynamic quantities of a Tomonaga-Luttinger liquid are at a first glance similar to those of a Fermi liquid. For example, the specific heat, the uniform magnetic susceptibility, and the charge susceptibility at low temperatures are given as

$$C\sim\gamma T, \tag{2.380}$$

$$\chi_s\sim\chi_{s0}\sim\text{const}, \tag{2.381}$$

$$\chi_c\sim\chi_{c0}\sim\text{const}, \tag{2.382}$$

respectively. At asymptotically low temperatures γ is actually given as the sum of spin and charge contributions,

$$\gamma=\gamma_c+\gamma_s, \tag{2.383}$$

where $\gamma_c\propto 1/v_c$ and $\gamma_s\propto 1/v_s$ while $\chi_{s0}\propto 1/v_s$ and $\chi_{c0}\propto 1/v_c$.

So far we have discussed the case of a quantum liquid for both spin and charge degrees of freedom. In some cases, such as the attractive Hubbard model with $U<0$, the spin degrees of freedom have an excitation gap due to the formation of a singlet or triplet bound state. When the spin gap is formed, the charge correlation has the asymptotic form

$$\begin{aligned}\langle\rho(r)\rho(0)\rangle\sim\text{const}&+a_0r^{-2}+a_2r^{-K_\rho}\cos 2k_Fr\\&+a_4r^{-4K_\rho}\cos 4k_Fr.\end{aligned} \tag{2.384}$$

This charge correlation function is compared with the singlet and triplet pair correlation functions given by

$$\langle O^{\dagger}(r)O(0)\rangle\sim c_1r^{-1/K_\rho} \tag{2.385}$$

(except for logarithmic corrections), where O is the Cooper pair order parameter. This class of quantum liquid with spin gap is called a Luther-Emery-type liquid. When $K_\rho>1$, the singlet pairing correlation dominates over the charge-density correlation at $k=2k_F$. This is the case for the attractive Hubbard model at $\delta\neq 0$. Several attempts at models for other interacting 1D systems such as the dimerized *t-J* model (Imada, 1991), a frustrated *t-J* model (Ogata *et al.*, 1991), and the ladder system (Dagotto, Riera, and Scalapino, 1992; Rice *et al.*, 1993; and for a review see Dagotto and Rice, 1996) also indicate that the singlet pairing correlation can be the dominant correlation at asymptotically long distance.

An interesting but controversial problem is the evolution of three dimensionality with increasing interchain transfer when we start from separate chains. This question was posed by Anderson (1991b) and prompted many studies, which appear to have reached a consensus that infinitesimally small interchain transfer is relevant and destroys the Tomonaga-Luttinger liquid in the sense of relevance in the renormalization group (Schulz, 1991; Castellani, di Castro, and Metzner, 1992; Fabrizio, Parola, and Tosatti, 1992; Haldane, 1994; Nersesyan, Luther, and Kusmartsev, 1993). This problem was readdressed by Clarke, Strong, and Anderson (1994), who claimed that the incoherence of the interchain hopping process still remains up to a finite critical value of interchain transfer. A related controversy concerns the question whether the Tomonaga-Luttinger liquid can be realized in 2D systems as hypothesized by Anderson (1990, 1997). We shall not discuss this controversy.

Below, we assume the relevance of interchain hopping and discuss dimensional crossover in quasi-1D systems with weak coupling between the chains. The problem here is how the physical properties change from those of low-dimensional systems to those of 3D ones as a function of temperature and excitation energy. If we denote the renormalized transfer integral between the chains (planes) by $t_\perp^*$, the spectral function will behave as that of a low-dimensional system at $|\omega-\mu|\gg t_\perp^*$ *or* at $\pi kT\gg t_\perp^*$ whereas it will show 3D character at $|\omega-\mu|<t_\perp^*$ and $\pi kT<t_\perp^*$. The photoemission spectra of the quasi-1D organic conductor (DCNQI)$_2$Cu salt, which is known to have considerable interchain coupling through intervening Cu atoms, exhibits such a behavior

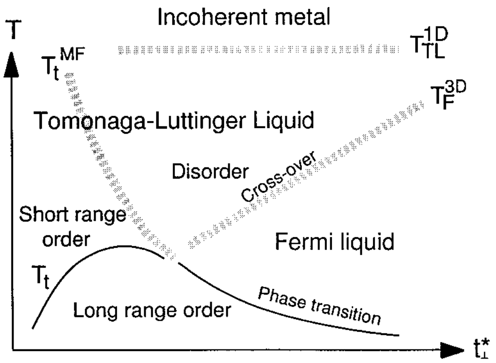

FIG. 35. A schematic phase diagram describing a dimensional crossover between 1D and 3D. $t_\perp^*$ is the (renormalized) interchain transfer integral. $T_F^{3D}\equiv t_\perp^*/\pi$ is the 3D "Fermi temperature," T_t^{MF} is the mean-field CDW or SDW transition temperature, T_t is the MIT temperature with long-range CDW or SDW order, and T_{TL}^{1D} is the characteristic temperature of the 1D Tomonaga-Luttinger liquid.

(Sekiyama *et al.*, 1995). The spectra show that the Fermi edge disappears at high temperatures, whereas a weak Fermi edge is observed at lower temperatures. On the other hand, in the temperature dependence of the photoemission spectra of $\mathrm{BaVS_3}$, which is thought to be more 1D like than the DCNQI-Cu salt, no sign of a Fermi edge has been observed, but rather a suppression of the intensity at the Fermi level even more pronounced than the power-law behavior at low temperatures just above the MIT (at ~70 K), as discussed in Sec. IV.D.2. The schematic $T-t_\perp^*$ phase diagram of Fig. 35 shows these experimental results in the context of dimensional crossover as a function of temperature: At low temperatures, $T\ll t_\perp^*/\pi k$, the charge transport between chains is coherent and the coupled chains behave as a 3D system (Kopietz, Meden, and Schönhammer, 1995). Therefore we denote the characteristic temperature of the 3D Fermi liquid $t_\perp^*/\pi k$ as T_F^{3D}. On the other hand, Fermi-surface nesting is more easily realized for smaller $t_\perp^*$, leading to increase of the charge-density-wave or spin-density-wave transition temperature in the mean-field sense, T_t^{MF}. Since true long-range order is possible in 3D but not in 1D, the MIT with CDW or SDW formation occurs at the lower of T_t^{MF} and T_F^{3D}. For small $t_\perp^*$, there is a temperature region $T_F^{3D}<T<T_t^{MF}$, where there is short-range order due to dynamical CDW or SDW fluctuations. The characteristic energy of the Tomonaga-Luttinger liquid T_{TL}^{1D} ($\gg T_F^{3D}$) is determined by intrachain coupling ($t_\parallel^*$, U, etc.) and is therefore independent of $t_\perp^*$. If $t_\perp^*$ is small, $T_F^{3D}<T_t^{MF}$ and no Fermi-liquid region exists, while $\mathrm{(DCNQI)_2Cu}$ may belong to the large-$t_\perp^*$ region, where the Fermi-liquid region exists. For small $t_\perp^*$, the short-range order at $T_F^{3D}<T<T_t^{MF}$ may create a pseudogap in the spectral function even if the system is metallic.

2. Marginal Fermi liquid

Since the discovery of the high-T_c cuprates, it has turned out that many electronic properties of the cuprates are unusual in the normal state in terms of the standard Fermi-liquid theory of metals. Aside from some unusual properties observed in the underdoped region associated with the so-called pseudogap formation, typical examples of these properties include the following, to be discussed in greater detail in Sec. IV.C:

(i) The resistivity has more or less linear dependence on T, $\rho\propto T$.

(ii) The optical conductivity $\sigma(\omega)$ has a long tail proportional to $1/\omega$ up to the order of several tenths or even 1 eV, while the true Lorentzian part of the Drude conductivity seems to have unusually low weight.

(iii) The Raman scattering intensity has a flat background extending to several tenths of an eV.

(iv) In photoemission experiments, the quasiparticle peak is unusually broad and accompanied by an intense incoherent background, leading to a very small spectral weight of the quasiparticle, if any exists.

(v) Nuclear magnetic resonance of Cu shows an unusually flat temperature dependence of the longitudinal relaxation time T_1 above room temperature for a certain range of doping, excepting the very low doping region.

On phenomenological grounds, Varma *et al.* (1989) proposed a form of single-particle self-energy Σ to explain all the above unusual features. This is substantiated by

$$\sum(\mathbf{k},\omega)\sim g^2N_b(\mu)^2\left[(\omega-\mu)\ln\frac{y}{\omega_c}-\frac{i\pi}{2}y\right], \qquad (2.386)$$

where y stands for $y\sim\max(|\omega-\mu|,T)$. Here g is a coupling constant and ω_c is a high-energy cutoff energy. Clearly, this form leads to breakdown of the Fermi-liquid theory in a marginal way. The imaginary part of the self-energy is proportional to $|\omega-\mu|$ or T so that the inverse lifetime of the quasiparticle is comparable to its energy. Because the quasiparticle can be defined as an elementary excitation only when its energy ω is much larger than the inverse lifetime τ^{-1}, this form makes the quasiparticle only marginally defined because ω and τ^{-1} are comparable. The form of the real part of the self-energy in Eq. (2.386) is a consequence of causality through the Kramers-Kronig relation. This self-energy is singular at $|\omega-\mu|=0$ but retains Fermi-liquid properties in a marginal way. That is, it conserves the "Fermi surface" (as in the 1D Tomonaga-Luttinger liquids), but the quasiparticle weight Z_k vanishes logarithmically as one approaches the Fermi surface, $|\omega-\mu|\to 0$. Because $|\mathrm{Im}\,\Sigma(\mathbf{k},\omega)|$ rises steeply with energy, i.e., rises linearly with $|\omega-\mu|$ rather than quadratically as in a Fermi liquid, the "quasiparticle" width dramatically increases as it disperses away from the chemical potential, in agreement with experimental results (Olson *et al.*, 1989; Dessau *et al.*, 1993).

This phenomenological description of excitation spectra does not assume explicit wave-number dependence. To understand the origin of this marginal behavior from more microscopic points of view, Virosztek and Ruvalds (1990) examined the effect of Fermi-surface nesting, expected near the antiferromagnetic instability, as a candidate for incoherent character. A nearly nested Fermi surface may have a strong scattering mechanism at the nesting wave vector. However, this proposal does not necessarily reproduce marginal behavior in a wide region of doping because the nesting condition is easily destroyed by doping and, in addition, in the YBCO compounds ($\mathrm{YBa_2Cu_3O_{7-y}}$), the nesting condition, meaningfully defined only from the weak-correlation approach, is clearly not satisfied even near the Mott insulator, because of these compounds' rather round Fermi surface (see Sec. IV.C.3).

As is discussed in Secs. II.E.1 and II.E.3, this marginal behavior has recently received support from numerical analyses of the t-J and Hubbard models. The frequency-dependent spin susceptibility and conductivity are given by Eqs. (2.274) and (2.293). According to the above numerical analyses, the spin-dynamical structure factor $\mathrm{Re}\, S(q,\omega)$ and the current-current correlation function $C(\omega)$, discussed in Secs. II.E.1 and II.E.3, are more or less temperature independent for the dominant part, with a broad peak around $\omega=0$ or $q=Q$, $\omega=0$ where their widths in ω space are on the order of eV for $C(\omega)$ and comparable or less than a tenth of an eV for $S(q,\omega)$ at $\delta\sim 0.1\sim 0.2$. This implies that the spin and charge dynamics are strongly incoherent with a short time scale of relaxation whose inverse is of the order of 1 eV for $C(\omega)$. In the conductivity this means that $C(\omega) = \Sigma_{\nu\mu}|\langle \nu|J|\mu\rangle|^2\delta(\varepsilon_\nu-\varepsilon_\mu-\omega)$ is ω insensitive at small ω. When we take the Kramers-Kronig transformation of $\mathrm{Im}\,\chi(q,\omega)$ or $\mathrm{Re}\,\sigma(\omega)$, it turns out that it necessarily leads to a form of "marginal Fermi liquid." For example, in the case of conductivity, one can show from Eq. (2.274)

$$\mathrm{Im}\,\sigma(\omega)\sim \frac{b\beta\omega}{\beta\omega+a}C(\omega), \tag{2.387}$$

where a and b are constants. When we wish to interpret this behavior by extending the Drude analysis and introducing an ω-dependent mass $m^*(\omega)$ and a relaxation time $\tau(\omega)$ in the form

$$\sigma(\omega)=\frac{\sigma_0(\omega)}{-i\omega+\tau^{-1}(\omega)},$$

$$\sigma_0(\omega)=\frac{ne^2}{m^*(\omega)},$$

we obtain $\tau^{-1}(\omega)\equiv\omega[\mathrm{Re}\,\sigma(\omega)/\mathrm{Im}\,\sigma(\omega)]\simeq(1/b)\,\omega + (a/b)\,T$. This leads to τ^{-1} that is linear in T at small ω, just as in the phenomenological description of a marginal Fermi liquid, in overall agreement with experiments in cuprates, as is discussed in Sec. IV.C (Thomas *et al.*, 1988; Schlesinger *et al.*, 1990; Uchida *et al.*, 1991; Cooper *et al.*, 1992; for a review see Tajima, 1997). This interpretation is based on the observation that the charge dynamics is totally incoherent because $C(\omega)$ has very broad structure with more or less ω-independent value C_0 up to the order of eV. The constant C_0 has a doping concentration dependence $C_0\propto\delta$, so that the ω-integrated conductivity up to the order of 1 eV shows the scaling $\int\sigma(\omega)d\omega\propto\delta$. However, it should be noted that this contribution comes from totally incoherent charge dynamics without any true Drude response, as we see from Eq. (2.274). The true Drude contribution has stronger δ dependence. This is closely related to the large dynamic exponent of the Mott transition. We further discuss this problem in Sec. II.F.9. In the case of spin correlations, $S(q,\omega)$ also has a strong incoherent contribution, as discussed in Sec. II.E.4. A point to be noted here is that the dominant incoherent contribution gives again marginal Fermi-liquid-like behavior because $S(q,\omega)$ has broad structure but the Bose factor $1-e^{-\beta\omega}$ yields marginal character. For example, the NMR relaxation rate T_1^{-1} follows $(T_1T)^{-1}\propto 1/T$ as in Eq. (2.363) for the contribution from the incoherent part. Another point to be stressed here is that although $S(q,\omega)$ has a broad peak structure at $\delta\geqslant 0.1$ as $C/[i\omega+D(q^2+\kappa^2)]$, as discussed in Sec. II.E.4, its widths in q and ω space become critically sharpened as $\delta\to 0$. Originally the marginal Fermi-liquid hypothesis was proposed without considering appreciable q dependence. This ω-dependent but q-independent structure is naturally understood from the form of Eqs. (2.274) and (2.293) when we ascribe this behavior to incoherent dynamics. The origin of this incoherence is discussed in Sec. II.F.

There are two different views concerning the microscopic origin of marginal behavior, or incoherent dynamics. Marginal behavior or more generally non-Fermi-liquid behavior can appear when charge is coupled to other degenerate degrees of freedom in addition to the Fermi degeneracy. This indeed happens at a critical point such as the magnetic instability point, where there is an arbitrarily small energy scale due to the degeneracy. In one view, the critical point exists at $\delta\neq 0$ while in the other the critical point is at $\delta=0$, the Mott transition point.

In the first view, degeneracy, arises at the critical point between the phases of normal metal and the superconducting state at $T=0$. For example, Varma (1996b) claimed that the critical point is at the optimal doping concentration for the highest superconducting T_c and that degeneracy is due to a double-well-type structure of potentials for local charge which comes from valence fluctuation.

Another possible origin of marginal behavior with incoherent charge dynamics is the Mott transition itself (Imada, 1995b). The Mott transition has a unique character with a large dynamic exponent $z=4$, as explained in Sec. II.F, which causes quantum critical behavior in a wide region of the (δ,T) plane. In consequence there is suppression of the coherence temperature $T_{coh}\propto\delta^2$, which leads to incoherent charge dynamics, consistent with the observation described in the first part of this subsection. This also naturally explains why the wave-number dependence is absent in the "marginal-Fermi-liquid" behavior.

H. Orbital degeneracy and other complexities

1. Jahn-Teller distortion, spin, and orbital fluctuations and orderings

In transition-metal compounds, various degrees of freedom combined together can play roles in physical properties. Roles of spin degrees of freedom are discussed in previous subsections in detail. However, in transition-metal compounds, as mentioned in Sec. II.A, the orbital degrees of freedom are degenerate in various ways depending on the crystal field coming from the basic lattice structure and Jahn-Teller distortions. This degeneracy produces a rich structure of low-energy excitations through orbital fluctuations and orbital orderings. In this subsection the role of orbital degeneracies, combined sometimes with the Jahn-Teller effect, is discussed. The degenerate Hubbard model defined in Eqs. (2.6a)–(2.6e) may be a good starting point, if we may neglect the coupling to the lattice. As is mentioned in Sec. II.A.2, the first term of $\mathcal{H}_{DUJ}$ is the origin of the Hund's-rule coupling, which is the strong driving force that aligns spins of d electrons on the same atom.

We discuss here the basic structure of degeneracy in a cubic crystal field. When three t_{2g} orbitals are degenerate, d^2 and d^3 states usually have spin quantum number $S=1$ and $S=3/2$ where two or three t_{2g} orbitals are occupied with parallel spins, as in V^{3+} and Cr^{3+}. If the crystal-field splitting between t_{2g} and e_g is smaller than the Hund's-rule coupling, d^4, and d^5 states are realized by occupying three spin-aligned t_{2g} orbitals and one or two electrons with the same spin in the e_g orbitals, as in Mn^{3+} and Fe^{3+}, respectively. As in Co^{3+}, there may be subtlety in d^6 due to competing states of fully occupied t_{2g} orbitals (a low-spin state), five electrons in the t_{2g} orbitals in addition to one e_g electron (an $S=1$ state), and four electrons in the t_{2g} orbital plus two spin-aligned e_g electrons ($S=2$ state). For the case of d^7 as in Ni^{3+}, the low-spin state is realized with fully occupied t_{2g} orbital and singly occupied e_g orbital with $S=1/2$, as in $R\mathrm{NiO}_3$. As in Ni^{2+}, d^8 is given by a state in which the t_{2g} orbitals are completely filled and two e_g orbitals are occupied by spin-aligned electrons ($S=1$ state) if the crystal-field splitting of $d_{x^2-y^2}$ and $d_{3z^2-r^2}$ is weak. In such ways, depending on these electron fillings, different physics appears. Dynamic coupling to the lattice is another source of complexity.

We start with the simplest degenerate case, with two orbitals with one electron (or one hole) occupied at each site on average. This is indeed the case, for example, in KCuF_3, in which the Cu d^9 state leads to one hole per site in the twofold degenerate e_g orbitals, under the cubic crystal field of the perovskite structure. $R\mathrm{NiO}_3$ ($R=\mathrm{La}$, Nd, Y, Sm) is another example, in which e_g orbitals are occupied with one electron per site although t_{2g} orbitals are fully occupied. If the intrasite Coulomb interaction $U_{\nu\nu'}$ in Eq. (2.6c) is large enough, as in KCuF_3, this integer filling state should be the Mott insulator. Here, we discuss the effective Hamiltonian for the strong-coupling limit to derive the orbital and spin exchange as in Eq. (2.8). To understand the basic physics, we make a drastic simplification to Eq. (2.8). We first assume only the diagonal transfer $t_{ij}^{\nu\nu'}=t\delta_{\nu\nu'}$ and ν-dependent interaction $U_{\nu\nu'}=U'$ for $\nu\neq\nu'$ and $U_{\nu\nu}=U$. Here J_H is the Hund's-rule coupling. Through the second-order perturbation, the exchange interaction is given by the simplified Hamiltonian

$$\mathcal{H}=\sum_{\langle i,j\rangle}(J_s\mathbf{S}_i\cdot\mathbf{S}_j+J_\tau\vec{\tau}_i\cdot\vec{\tau}_j+J_{s\tau}\mathbf{S}_i\cdot\mathbf{S}_j\vec{\tau}_i\cdot\vec{\tau}_j), \tag{2.388}$$

where the usual spin-orbit interaction $\mathbf{S}\tau$ is neglected (Inagaki and Kubo, 1973, 1975; Kugel and Khomskii, 1982). Here, the parameters are given by

$$J_s=t^2\left(-\frac{1}{U'-J_H}+\frac{1}{U'}+\frac{3}{U}\right), \tag{2.389a}$$

$$J_\tau=t^2\left(\frac{3}{U'-J_H}+\frac{1}{U'}-\frac{1}{U}\right), \tag{2.389b}$$

$$J_{s\tau}=4t^2\left(\frac{1}{U'-J_H}-\frac{1}{U'}+\frac{1}{U}\right). \tag{2.389c}$$

If $J_{s\tau}$ is positive and $J_\tau>J_s$, this leads to stabilization of the ferromagnetic state with the "antiferro-orbital" ordering (Roth, 1966, 1967; Inagaki, 1973). In more realistic cases, the transfer is anisotropic with finite off-diagonal hoppings, and hence J_τ and $J_{s\tau}$ become highly anisotropic depending on the direction.

The orbital degeneracy can be lifted by several on-site mechanisms, including the spin-orbit interaction and the Jahn-Teller distortion. In the case of spin-orbit interaction, splitting of orbital levels is usually accompanied by simultaneous spin symmetry breaking. For example, if the spins order along the z axis, then the LS interaction $\lambda\mathbf{L}\cdot\mathbf{S}$ immediately stabilizes the orbitals with the z component of the angular momentum $L_z=\pm1$ or $L_z=\pm2$ instead of $L_z=0$. Depending on the sign of λ, the orbitals are chosen so that L_z and the spin align in a parallel or antiparallel way. (Strictly speaking, the spin and orbital quantum numbers are not good quantum numbers separately, but the total angular momentum is conserved.) When a finite L_z state is chosen, it may also induce lattice distortion. For example, in the octahedron surroundings of the ligand atoms, a Jahn-Teller distortion occurs in such a way that the octahedron elongates in the z direction because the electrons occupy nonzero L_z states, such as yz and zx orbitals.

Coupling between orbital occupancy and the Jahn-Teller distortion can play a major role as a driving force of symmetry breaking, because the orbital occupation may strongly couple to the lattice in some cases. The simplest example of this coupling is seen in Fig. 36, where an electron in a $d_{3z^2-r^2}$ or $d_{x^2-y^2}$ orbital induces distortion of anions in the octahedron structure around the transition-metal elements. The static Jahn-Teller distortion of course lifts the original degeneracy of t_{2g} or e_g orbitals. The Jahn-Teller distortion occurs because the energy gain due to this splitting of the degeneracy, which is linear in the distortion, always wins in comparison to the loss of energy due to the lattice elastic energy, which is quadratic in the distortion. When the crystal lattice of these transition-metal elements and anions is formed, the static Jahn-Teller distortion frequently favors a specific type of distortion pattern. For example, in the configuration of Fig. 36, the Jahn-Teller distortion stabilizes the "antiferro-orbital" ordering of the pseudospin τ for $d_{x^2-y^2}$ and $d_{3z^2-r^2}$ orbitals. This induces the

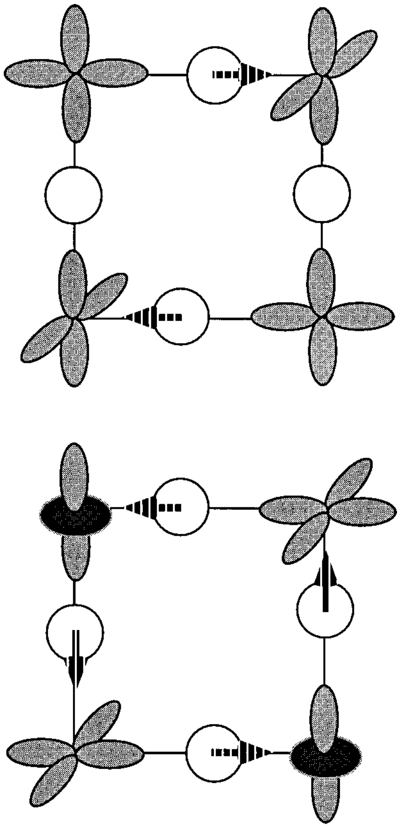

FIG. 36. Examples of the Jahn-Teller distortion by antiferro-orbital occupation of (upper panel) $d_{x^2-y^2}$ and $d_{y^2-z^2}$ orbitals and (lower panel) $d_{x^2-y^2}$ and $d_{3z^2-r^2}$ orbitals.

cooperative Jahn-Teller effect, accompanied by symmetry breaking of both lattice and orbitals (Kanamori, 1959). A typical example of such "antiferro-orbital" symmetry breaking can be seen in $KCuF_3$, as shown in Fig. 37. A general tendency of the cooperative Jahn-Teller effect is that some type of "antiferro-orbital" ordering takes place, usually in the perovskite structure. This is because the octahedron has corner-sharing structure for adjacent transition-metal elements, so that the displacement of an anion at the corner induces occupations of opposite orbitals for the transition-metal ion in the neighborhood of the distorted anion, as in Fig. 36. In contrast, an edge-sharing system such as the spinel structure has a tendency for "ferro-orbital" ordering.

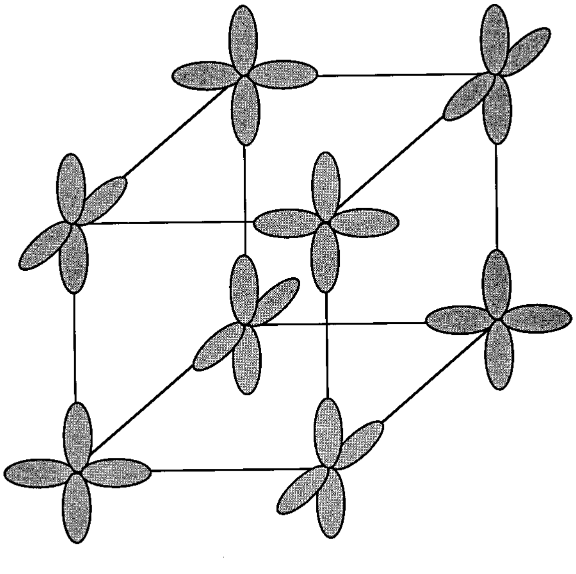

FIG. 37. Antiferro-orbital order in a phase of $KCuF_3$.

In addition to the static Jahn-Teller distortion, the dynamic process of virtual distortion also mediates the exchange interaction of pseudospins τ on adjacent sites through a coupling of the form $g_k^\alpha q_k \tau_k^\alpha$ where $g_k^\alpha(\alpha = x,y,z)$ is the coupling constant, q_k is the anion distortion (phonon), and τ_k^α is the Fourier transform of the pseudospin operator τ_i^α. By eliminating phonon degrees of freedom in the second-order perturbation, we obtain the pseudospin exchange in the form

$$\mathcal{H}=\sum_{\langle ij\rangle}[J_{ij}^z\tau_i^z\tau_j^z+J_{ij}^{xy}(\tau_i^+\tau_j^-+\tau_i^-\tau_j^+)]. \tag{2.390}$$

Direct quadrupole-quadrupole interaction between d electrons on adjacent sites also generates a similar effective Hamiltonian for τ. These exchange interactions between orbitals can be the origin of orbital ordering even without the static Jahn-Teller distortion. In realistic situations, exchange coupling of pseudospins through the dynamic Jahn-Teller interaction or the quadrupole-quadrupole interaction, and static Jahn-Teller distortions as well as super-exchange-type coupling as in Eq. (2.388) or (2.8) due to the strong-correlation effect may be entangled and compete or cooperate in rich ways. In this article, we do not go into a comprehensive description of such interplay. Readers are referred to the review article by Kugel and Khomskii (1982) for this problem. Below, a few typical examples of recent developments are described.

Several mean-field-level calculations have been done on models with orbital degeneracy. They include Hartree-Fock calculations (Roth, 1966, 1967; Inagaki and Kubo, 1973, 1975), the Gutzwiller approximation (Chao and Gutzwiller, 1971; Lu, 1994), slave-boson approximations (Frésard and Kotliar, 1997; Hasegawa, 1997a, 1997b), and the infinite-dimensional approach (Rozenberg, 1996a, 1996b; Kotliar and Kajueter, 1996; Kajueter and Kotliar, 1996). Quantum Monte Carlo calculations were also carried out to study MIT, and spin and orbital fluctuations (Motome and Imada, 1997, 1998).

In V_2O_3 compounds, as is discussed in Sec. IV.A.1, the t_{2g} levels may split into a single a_{1g} orbital and twofold-degenerate e_g orbitals due to the corundum structure. In particular, the strong orbital fluctuation combined with spin fluctuation can be the origin of the first-order transition between a paramagnetic insulator and an antiferromagnetic insulator (Rice, 1995). See Sec. IV.A.1 for further discussions. In terms of effects of orbital degeneracy, mechanisms of gapped spin excitations in the Mott insulating phase of another vanadium compound, CaV_4O_9, were examined (Katoh and Imada, 1997).

Recently, the interplay of electron correlation with spin orderings, orbital orderings, and the Jahn-Teller distortion has been examined in the end materials of 3D

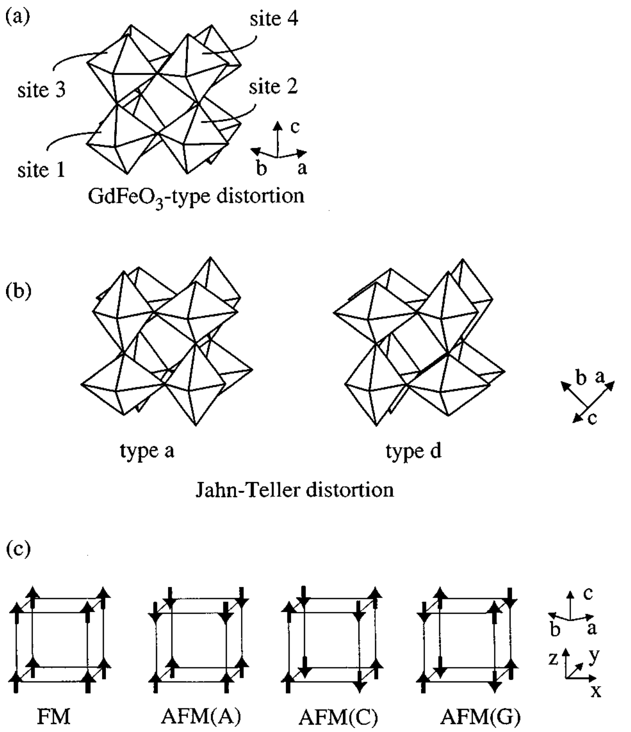

FIG. 38. Types of lattice distortion and antiferromagnetic order. (a) GdFeO$_3$-type tilting distortion of MO$_6$ octahedron; (b) types of Jahn-Teller distortion in 3D perovskite structure; (c) types of antiferromagnetic order in 3D perovskite structure.

perovskite compounds. In the 3D perovskite compounds, RMO_3, in addition to the Jahn-Teller distortion, tilting of the MO$_6$ octahedron, illustrated in Fig. 38(a), plays an important role in determining the hybridization of different orbitals on adjacent sites and consequently in controlling the bandwidth. Considering this tilting as well as the Jahn-Teller distortion and spin and orbital orderings, Mizokawa and Fujimori (1996a, 1996b) performed unrestricted Hartree-Fock calculations on RMO_3. In general, the spin and orbital orderings obtained were in good agreement with those of the experimentally observed results when the observed Jahn-Teller and tilting distortions were assumed. Electronic structure calculations with the local spin-density approximation (Hamada, Sawada and Terakura, 1995; Sarma *et al.*, 1995), with GGA (Sawada, Hamada, Terakura, and Asada, 1996) and with the LDA+U method (Solovyev, Hamada, and Terakura, 1996b) also succeeded in improving and reproducing general tendency of spin and orbital orderings by assuming the proper Jahn-Teller and tilting distortion. However, these two approaches show different tendencies for the band gap. The Hartree-Fock and LDA+U calculations in general overestimate the band gap, while the LSDA and GGA calculations tend to underestimate the gap, as is explained in Sec. II.D.3. At the moment, self-consistent determination of lattice distortion, orbital occupation, and spin ordering have not been attempted successfully except in the case of KCuF$_3$ by Liechtenstein, Anisimov, and Zaanen (1995). Detailed discussions of each compound are given in Secs. IV.A.3, IV.B.1, IV.B.2, and IV.F.1. Various types of Jahn-Teller distortions and antiferromagnetic order realized in 3D perovskite structure are shown in Figs. 38(b) and 38(c), respectively.

Although the spin degrees of freedom have been studied rather thoroughly on the level of their fluctuations in the paramagnetic phase, fluctuations of the orbital degrees of freedom have been neither experimentally nor theoretically well studied. These fluctuation effects may be important when the system is metallized away from the end material.

Orbital ordering phenomena are also widely observed in f-electron systems, where they are called quadrupole orderings. An example is seen in CeB$_6$. The interplay of spin and orbital fluctuations may be very similar in d- and f-electron systems, though it is not fully understood so far.

2. Ferromagnetic metal near a Mott insulator

When the Jahn-Teller distortion is absent in LaMnO$_3$, the antiferro-orbitally ordered $3x^2-r^2$ and $3y^2-r^2$ states strongly hybridize with the $3z^2-r^2$ orbital because of high symmetry and hence enhance the ferromagnetic coupling, basically the same as in the Hund mechanism. It has been argued that this is also the origin of ferromagnetism in metallic doped systems like La$_{1-x}$Sr$_x$MnO$_3$ because the static Jahn-Teller distortion seems to disappear in the metallic phase. The basic physics of this mechanism was pointed out by Kanamori (1959).

Although the underlying physics and the mechanism are similar, a slightly different way of explaining the ferromagnetism in metallic La$_{1-x}$Sr$_x$MnO$_3$ is the so-called double-exchange mechanism (Zener, 1951; de Gennes, 1960; Anderson and Hasegawa, 1955). Because the localized $3t_{2g}$ electrons are perfectly aligned due to the Hund's-rule coupling, the double-exchange Hamiltonian defined in Eqs. (2.9a)–(2.9c) may be a good starting point if degeneracy of the e_g orbitals can be neglected. In the completely ferromagnetic phase, e_g electrons can hop coherently without magnetic scattering by t_{2g} spins, while they become strongly incoherent due to scattering through the J_H term if the localized t_{2g} spins are disordered. In other words, if t_{2g} spins on adjacent sites have different directions, the e_g electron feels a higher energy on one of the two sites because of Hund's-rule coupling. The gain in kinetic energy due to coherence favors the ferromagnetic order in the metallic phase. When the t_{2g} orbital electrons are treated as a classical spin coupled with e_g electrons by very large Hund's-rule coupling, the spin axis of the quantization may be taken in the direction of the t_{2g} spins as in the discussion below Eq. (2.156). Then the transfer between the sites i and j in Eq. (2.9b) is modified through the relative angle of the t_{2g} spins at the i and j sites as

$$t_{ij}=t[\cos(\theta_i/2)\cos(\theta_j/2)+\sin(\theta_i/2)\sin(\theta_j/2)e^{i(\phi_i-\phi_j)}], \tag{2.391}$$

where ϕ is the phase of the wave function. Neglecting the phase fluctuations, this leads to

$$t_{ij}=t\cos(\theta_{ij}/2), \tag{2.392}$$

where θ_{ij} is the relative angle of the t_{2g} spins. In the Hartree-Fock treatment, the effective averaged transfer is given by

$$\tilde{t}=t\langle\cos(\theta_{ij}/2)\rangle. \tag{2.393}$$

Recently, giant or colossal negative magnetoresistance has attracted renewed interest in ferromagnetic metals in Mn and Co perovskite compounds. This is discussed in detail in Sec. IV.F. From the theoretical point of view, d electrons in Mn and Co compounds have strong coupling to Jahn-Teller-type distortions and fluctuations. These couplings as well as orbital degeneracy in e_g orbitals make magnetic and transport properties complicated, especially near the Mott insulating phase. The hardest and most challenging subject is to understand the interplay of spin, orbital, and lattice fluctuations when the critical fluctuations of the Mott transition, exemplified by incoherent charge dynamics, appear. We review the present status of this theoretical effort in Sec. IV.F.1 and compare theory with experimental indications.

3. Charge ordering

Periodic structures of spin and charge orderings are discussed within the framework of the Hartree-Fock approximation in Sec. II.D.2, where the periodicity of the spin or charge orderings is assumed to be commensurate to the lattice periodicity. This commensurate order, assumed in the above results, has been reexamined in 2D within the unrestricted Hartree-Fock approximation to allow an incommensurate ordering vector (Machida, 1989; Poilblanc and Rice, 1989; Schulz, 1990a; Inui and Littlewood, 1991; Vergés *et al.*, 1991). These analyses indicate that, within the Hartree-Fock approximation, antiferromagnetic ordering at the commensurate wave vector (π,π) gives way to incommensurate ordering if the filling deviates away from half filling. Incommensurate ordering may also be realized by introducing a stripe structure in real space, such as the periodic stripe of hole arrays (Zaanen and Gunarson, 1989). In this case, Hartree-Fock solutions give an insulating phase up to some finite doping concentration of holes even away from half filling. This problem was further explored by the variational Monte Carlo method by Giamarchi and Lhuiller (1990) and by a Monte Carlo method with fixed-node approximation by An and van Leeuwen (1991). The possibility of phase separation into hole-rich and hole-free phases was also examined, although calculational results are limited to small clusters (Emery, Kivelson, and Lin, 1990). As we discuss later, the problem with the above arguments is that the effects of quantum fluctuations, which may destroy the stripe phase and phase separation, have not been seriously considered. In Sec. II.E.6, we show that phase separation is clearly seen by numerical methods in some other models, as it should be, whereas it is not observed numerically in the 2D Hubbard model. Although the stability of incommensurate phases against quantum fluctuations is questionable, charge ordering with some commensurate periodicity to the lattice may occur. This commensurate charge order may indeed be stabilized in the presence of intersite Coulomb interactions, as in the extended Hubbard model [Eqs. (2.5b)–(2.5c) with $V\neq 0$]. The charge order at a simple commensurate filling may also be stabilized by the underlying mass enhancement due to the proximity of the Mott transition. In this sense, the charge ordering effect is enhanced in strongly correlated systems as a secondary effect of the Mott transition. Charge ordering at a commensurate filling leads to an *incompressible state*, which may have similarities to the most fundamental Mott insulator itself. Experimentally, charge orderings are observed for some simple commensurate periodicities, as will be discussed in Sec. IV.E. This is also related to the valence fluctuation problem in heavy-fermion compounds. We discuss theoretical aspects of charge ordering in each compound in connection with the experimental results in more detail in Sec. IV. Possible pairing mechanisms due to dynamic fluctuation of charge ordering or phase separation will be discussed in Sec. IV.C.3.

III. MATERIALS SYSTEMATICS

A. Local electronic structure of transition-metal oxides

1. Configuration-interaction cluster model

Prior to the early 1980s, the most widely accepted picture of band-gap formation in a Mott insulator was that the d band was split into lower and upper Hubbard bands, separated by the on-site d-d Coulomb interaction U, as discussed in Sec. II and shown in Fig. 5(a). Charge excitations across that band gap were thus realized by a charge transfer of the type $(d^n)_i+(d^n)_j\rightarrow(d^{n-1})_i+(d^{n+1})_j$, where i and j denote transition-metal sites, and cost energy U. This classical picture was first questioned by resonance photoemission studies of NiO (Oh *et al.*, 1982; Thuler *et al.*, 1983) and of a series of transition-metal halides (Kakizaki *et al.*, 1983). Until then the photoemission spectra of NiO had been interpreted within ligand-field theory (Sugano *et al.*, 1970) as due to transitions from the d^8 ground state of the Ni^{2+} ion to the d^7 final-state multiplet. As shown in Fig. 39, these transitions constitute the topmost part of the valence-band photoemission spectra of NiO, below which is located the oxygen $2p$ band. In addition to these "main" features, there is another structure below the O $2p$ band called a "shake-up satellite" or "multi-electron satellite." It was thought that the satellite arose from a transition from the filled oxygen p orbitals to the unoccupied metal d orbitals subsequent to the emission of the d electron from the d^8 ground state. If this assignment were correct, the satellite would be due to the $d^8\underline{L}$ final states as opposed to the d^7 final states of the main band, where $\underline{L}$ denotes a hole in the ligand O $2p$ band. Then photoemission spectra recorded using photons in the Ni $3p\rightarrow 3d$ absorption region should have shown enhancement of the main band derived from the $3d^8\rightarrow 3d^7$ spectral weight through the resonance photoemis-

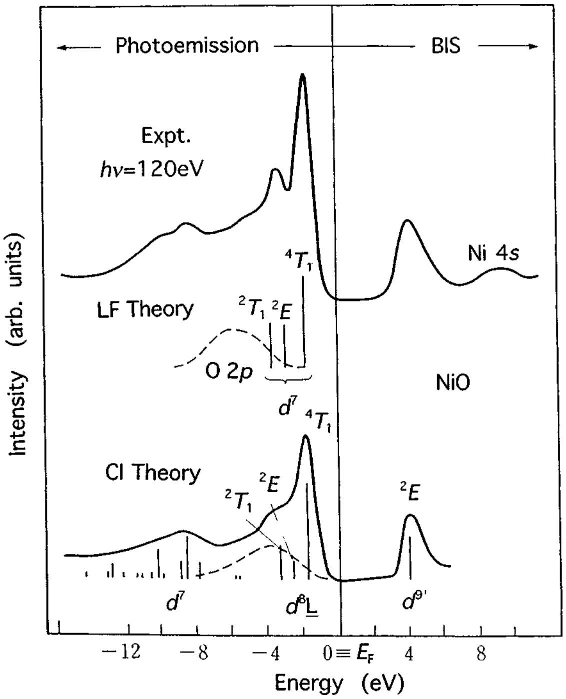

FIG. 39. Photoemission and inverse-photoemission (BIS) spectra of NiO (Sawatzky and Allen, 1984) and their analysis using ligand-field (LF) theory with the Ni^{2+} ion and that using CI theory for the NiO_6 cluster model (Fujimori, Minami, and Sugano, 1984).

sion process, $3p^63d^8+h\nu\rightarrow3p^53d^9\rightarrow3p^63d^7+\varepsilon l$, where εl is a photoelectron. However, the experimental results showed the enhancement of the satellite rather than the main band, which implied that the satellite was in fact due to the d^7 final states, that is, the lower Hubbard band is located below the O $2p$ band. Davis (1982) made an analysis of the resonance photoemission results of the Ni compounds by treating the configuration interaction (CI) within a simplified metal-ligand cluster model, in which one ligand $\underline{L}$ orbital and one d orbital are considered. He showed that the satellite should be due to d^7 final states rather than $d^8\underline{L}$ final states if it showed resonance enhancement at the $3p\rightarrow3d$ threshold. Subsequently, a more realistic CI cluster-model analysis of the photoemission spectra of NiO was made by Fujimori, Minami, and Sugano (1984), who took into account the multiplet structure of the Ni ion and symmetry-adopted molecular orbitals consisting of the ligand p orbitals. According to their analysis, shown in Fig. 39, it was confirmed that the satellite corresponds to the lower Hubbard band ($d^8\rightarrow d^7$ spectral weight) and is located below the O $2p$ band ($d^8\rightarrow d^8\underline{L}$ spectral weight), corresponding to the situation schematically depicted in Fig. 5(b). In NiO, the O $2p$-to-Ni $3d$ charge-transfer energy Δ ($\sim$4 eV) is smaller than the on-site d-d Coulomb energy U ($\sim$ 7 eV), which makes the p-to-d charge transfer, $(d^n)_i+(d^n)_j\rightarrow(d^n\underline{L})_i+(d^{n+1})_j$, the lowest-energy charge fluctuation and hence the band gap of the system (see Fig. 39). Here, the charge-transfer energy Δ is defined as the energy required to transfer an electron from the filled ligand p orbitals to the empty metal d orbitals, $d^n\rightarrow d^{n+1}\underline{L}$.

Because the on-site Coulomb energy U is often larger than the d bandwidths in $3d$ transition-metal compounds (U being typically as large as 4–8 eV), it is often more convenient to consider the total energies of a metal-ligand cluster such as NiO_6 within CI theory rather than as the energies of one-electron states, at least for insulating compounds. Figure 40 shows the total-energy diagram of the NiO_6 cluster in the neutral, positively ionized, and negatively ionized states, which we refer to as N-electron, $(N-1)$-electron, and $(N+1)$-electron states, respectively (Fujimori and Minami, 1984). Here, it should be noted that the "neutral" NiO_6 cluster has negative charges of 12- $[(NiO_6)^{12-}]$ in order

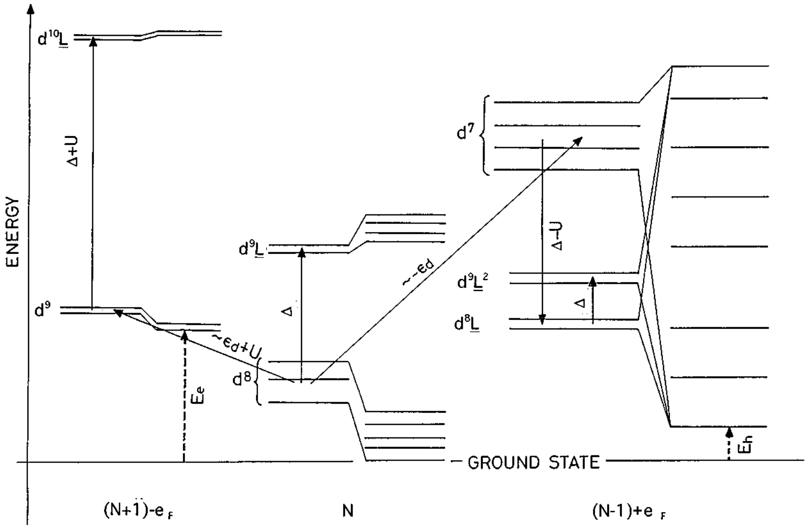

FIG. 40. Total-energy diagram of the NiO_6 cluster in the "neutral" (N-electron), positively ionized [$(N-1)$-electron], and negatively ionized [$(N+1)$-electron] states. E_h and E_e are the minimum energies required to create an electron and hole, respectively. e_F denotes an electron at the Fermi level.

to ensure the complete filling of the O $2p$ band and the d-band filling of eight as in bulk NiO. The ground state of the N-electron state primarily consists of the d^8 configuration (corresponding to the ionic Ni^{2+} and O^{2-} configurations) with admixture of charge-transfer configurations $d^9\underline{L}$ and to a lesser extent $d^{10}\underline{L}^2$:

$$\Phi_g(N)=\alpha_1|d^8\rangle+\alpha_2|d^9\underline{L}\rangle+\alpha_3|d^{10}\underline{L}^2\rangle. \tag{3.1}$$

The ground state of the N-electron state is split into multiplet terms due to intra-atomic Coulomb and exchange interactions. The lowest multiplet term ${}^3A_{2g}$ has a high-spin ($S=1$) $t_{2g}^6 e_g^2$ configuration, as predicted by ligand-field theory. Hybridization with the charge-transfer states $d^9\underline{L}$, which are located by $\sim\Delta$ higher, causes a "crystal-field splitting" of the d^8 multiplet as well as a lowering of the ground-state energy $E_g(N)$. This energy lowering signifies the covalency contribution to the cohesive energy of the ground state.

If there were no multiplet splitting and p-d hybridization, the total energy of the cluster with the central ion in the d^n configuration would be given by (Bocquet *et al.*, 1992a; Fujimori *et al.*, 1993)

$$E(d^n)=E_0+n\varepsilon_d^0+\frac{1}{2}n(n-1)U, \tag{3.2}$$

where E_0 is a reference energy and ε_d^0 is the energy of a bare d electron (including the Madelung potential at the cation site). The charge-transfer energy Δ is then given by

$$\Delta=E(d^{n+1})-\varepsilon_p-E(d^n)=\varepsilon_d^0-\varepsilon_p+nU\equiv\varepsilon_d-\varepsilon_p, \tag{3.3}$$

where ε_p is the energy of the ligand p orbital neglecting the finite p bandwidth. Here, the Coulomb interaction among the p electrons and that between neighboring p and d electrons are ignored. One can obtain the ground state Eq. (3.1) by solving a secular equation for the Hamiltonian,

$$\mathcal{H}=\begin{pmatrix} E(d^8)-\Delta E_8 & -\sqrt{2}T & 0 \\ -\sqrt{2}T & E(d^8)+\Delta & -\sqrt{2}T \\ 0 & -\sqrt{2}T & E(d^8)+2\Delta+U \end{pmatrix}, \tag{3.4}$$

for NiO. Here, $T\equiv-\sqrt{3}(pd\sigma)\equiv-2t_{pd}$ [with $(pd\sigma)$ being a Slater-Koster parameter (Harrison, 1989)] is a p-d transfer integral and $-\Delta E_8$ is the shift of the ${}^3A_{2g}$ term of the d^8 multiplet relative to the center of gravity $E(d^8)$ of the d^8 multiplet. In the present CI treatment, the crystal-field splitting between the t_{2g} and e_g orbitals is included not through an input parameter $10Dq$ as in ligand-field theory but as a result of the different p-d hybridization strengths for the t_{2g} and e_g orbitals. (One has also to consider a small nonorthogonality contribution to $10Dq$, typically $\sim$0.5 eV.)

The band gap E_{gap} of the system is given by the lowest energy of an electron plus that of a hole, which are created in the crystal independently. In the cluster model, therefore, one has to remove an electron from the N-electron ground state of one cluster and to add that electron to the N-electron ground state of another cluster and calculate the total energy difference:

$$E_{\mathrm{gap}}=E_g(N+1)+E_g(N-1)-2E_g(N), \tag{3.5}$$

where $E_g(N-1)$ and $E_g(N+1)$ denote the lowest energies of the $(N-1)$- and $(N+1)$-electron states, respectively. In Fig. 40 are plotted the total energies of the $(N-1)$- and $(N+1)$-electron states as well as those of the N-electron state of the NiO_6 cluster. In the $(N-1)$-electron state, the d^7 states are located above the charge-transfer $d^8\underline{L}$ states because $\Delta<U$, and the energy separation between the two configurations is $U-\Delta$. In analogy with Eq. (3.1), the $(N-1)$-electron state of a given spin and spatial symmetry is given by

$$\Phi_i(N-1)=\beta_{i1}|d^7\rangle+\beta_{i2}|d^8\underline{L}\rangle+\cdots . \tag{3.6}$$

In the $(N+1)$-electron state, the $d^{10}\underline{L}$ configuration is located well above d^9 because of the large energy separation $U+\Delta\gg 0$. From Fig. 40, one can also recognize that the magnitude of the band gap ($E_{\mathrm{gap}}=E_e+E_h$, where E_e and E_h are the lowest energies of the extra electron and the extra hole added to the N-electron ground state, respectively, as shown in the figure) is $\sim\Delta$ rather than $\sim U$.

2. Cluster-model analyses of photoemission spectra

To obtain the electronic structure parameters Δ, U, and T, the CI cluster model has been widely used to analyze photoemission spectra. The wave functions of the ground state, photoemission final states, and inverse-photoemission final states of the $M\mathrm{O}_m$ metal-oxygen cluster are given by

$$\begin{aligned} \Phi_g(N)&=\alpha_1|d^n\rangle+\alpha_2|d^{n+1}\underline{L}\rangle+\alpha_3|d^{n+2}\underline{L}^2\rangle+\cdots , \\ \Phi_i(N-1)&=\beta_{i1}|d^{n-1}\rangle+\beta_{i2}|d^n\underline{L}\rangle+\beta_{i3}|d^{n+1}\underline{L}^2\rangle+\cdots , \\ \Phi_i(N+1)&=\gamma_{i1}|d^{n+1}\rangle+\gamma_{i2}|d^{n+2}\underline{L}\rangle+\gamma_{i3}|d^{n+3}\underline{L}^2\rangle+\cdots . \end{aligned} \tag{3.7}$$

Here, each wave function is an eigenstate of the total spin S and S_z and has the proper point-group symmetry of the cluster. The d-derived spectral function (d-derived density of states) $\rho_d(\omega)$ is thus calculated using Eq. (2.54), with $c_{\mathbf{k}}$ and $c_{\mathbf{k}}^\dagger$ replaced by the annihilation and creation operators of the d electron, c_d and $c_d^\dagger$:

$$\begin{aligned} \rho_d(\omega)=\sum_i\ &|\beta_{i1}^*\alpha_1+\beta_{i2}^*\alpha_2+\beta_{i3}^*\alpha_3|^2 \\ &\times\delta(\omega+E_i(N-1)-E_g(N)) \\ &+\sum_i\ |\gamma_{i1}^*\alpha_1+\gamma_2^*\alpha_{i2}|^2 \\ &\times\delta(\omega-E_i(N+1)+E_g(N)). \end{aligned} \tag{3.8}$$

Since the energy levels of the cluster are discrete, the delta functions in Eq. (3.8) have to be appropriately broadened in order to be compared with experiment.

Let us consider the simplest case in which only two configurations are used as basis functions for each of the N- and $N-1$-electron states:

$$\begin{aligned}\Phi_g(N)&=\cos\theta|d^n\rangle+\sin\theta|d^{n+1}\underline{L}\rangle,\\ \Phi_-(N-1)&=\cos\phi|d^{n-1}\rangle+\sin\phi|d^n\underline{L}\rangle,\\ \Phi_+(N-1)&=-\sin\phi|d^{n-1}\rangle+\cos\phi|d^n\underline{L}\rangle,\end{aligned}\tag{3.9}$$

where $-\pi/2<\theta$, $\phi<\pi/2$. The Hamiltonian for the N-electron state is

$$\mathcal{H}=\begin{pmatrix}E(d^n) & -\sqrt{10-n}T\\ -\sqrt{10-n}T & E(d^n)+\Delta\end{pmatrix}.\tag{3.10}$$

Here, the multiplet structure and the different transfer integrals for the e_g and t_{2g} orbitals have been ignored. For the $(N-1)$-electron final states

$$\mathcal{H}=\begin{pmatrix}E(d^{n-1}) & -\sqrt{11-n}T\\ -\sqrt{11-n}T & E(d^{n-1})+\Delta-U\end{pmatrix},\tag{3.11}$$

whose lower and higher energy eigenvalues are denoted by $E_-(N-1)$ and $E_+(N-1)$, respectively. These final states correspond to the main feature and the satellite of the photoemission spectrum, respectively. Then the d-derived photoemission spectrum (the $\omega<\mu$ part of the d spectral function) is given by

$$\begin{aligned}\rho_d(\omega)=&|\cos\theta\cos\phi+\sin\theta\sin\phi|^2\\ &\times\delta(\omega+E_-(N-1)-E_g(N))\\ &+|-\cos\theta\sin\phi+\sin\theta\cos\phi|^2\\ &\times\delta(\omega+E_+(N+1)-E_g(N)),\end{aligned}\tag{3.12}$$

where the first term gives a peak at the lower binding energy $[\mu-\omega=E_-(N-1)-E_g(N)+\mu]$ and the second term at the higher binding energy $[\mu-\omega=E_+(N-1)-E_g(N)+\mu]$. The ratio between the spectral weight (I_+) of the higher final state $\Phi_+(N-1)$ and that (I_-) of the lower final state $\Phi_-(N-1)$ is given by $I_+/I_-\sim\tan^2(\theta-\phi)$ according to Eq. (3.12). Because the difference between θ and ϕ increases with decreasing $|T|$ or with increasing U, spectral weight transfers from the lower to the higher binding energy peak with increasing $U/|T|$.

The above spectral weight transfer may be viewed in a different way if we refer to the basis functions of fixed local configurations and regard the p-d transfer integrals as a perturbation. In this picture, T causes spectral weight transfer in the opposite direction, namely, from higher to lower energies. By increasing $|T|$, the difference between θ and ϕ becomes small, resulting in an increase in $I_+/I_-\sim\tan^2(\theta-\phi)$. Here, we point out that the p-d transfer integrals effectively increase due to electron correlation, i.e., in going from the one-electron Hartree-Fock picture to the many-body CI picture. If one treats the cluster model in the Hartree-Fock approximation, the one-electron Hamiltonian has off-diagonal matrix elements of $\sim T$, whereas in the CI treatment the off-diagonal matrix elements of the many-electron Hamiltonian are $\sqrt{10-n}T$, $\sqrt{11-n}T$, or $\sqrt{9-n}T$ in the N-electron, $(N-1)$-electron, or $(N+1)$-electron states [Eqs. (3.10) and (3.11)], respectively. Such enhanced off-diagonal matrix elements enhance spectral weight transfer from high-energy to low-energy states (satellites to main features) as well as enhance the energy splitting between them. This can be seen by comparing the Hartree-Fock band density of states (DOS) of NiO and the actual photoemission spectrum [or the Hartree-Fock band DOS corrected for the self-energy (Mizokawa and Fujimori, 1996a; Takahashi and Igarashi, 1996)], where the lower Hubbard band, well ($\sim$7 eV) below E_F in the Hartree-Fock approximation, is shifted further away from E_F and spread in energy and the spectral weight of the lower Hubbard band is transferred to the main band within $\sim$5 eV of E_F.

3. Zaanen-Sawatzky-Allen classification scheme

In the $(N-1)$-electron state of NiO, where $\Delta<U$, the $d^n\underline{L}$ configuration is located below the d^{n-1} configuration, resulting in a p-to-d band gap. If $\Delta>U$, on the other hand, the d^{n-1} configuration would lie below the $d^n\underline{L}$ configuration, leading to a d-to-d band gap. Zaanen, Sawatzky, and Allen (1985) and Hüfner (1985) extended this view of electronic structure to a wide range of $3d$ transition-metal compounds, including light transition-metal (Ti,V,...) compounds. For $\Delta<U$, the band gap is of the p-d type; the p band is located between the upper and lower Hubbard bands in the spectral function, as shown in Fig. 5(b). The gap is thus called a charge-transfer gap and the compound is called a charge-transfer insulator. It has a band gap of magnitude $\sim\Delta$. If $\Delta>U$, on the other hand, the band gap is of the d-d type as in the original Hubbard picture [Fig. 5(a)]. The gap is then called a Mott-Hubbard gap and the compound is called a Mott-Hubbard insulator. It has a band gap of magnitude $\sim U$. Figure 41 shows a two-dimensional plot, the so-called Zaanen-Sawatzky-Allen plot, of the transition-metal compounds according to the relative magnitudes of U and Δ. The straight line $U=\Delta$ separates the U-Δ space into Mott-Hubbard and charge-transfer regimes. It should be noted, however, that because of hybridization between the d and p states, the boundary $U=\Delta$ is not a sharp phase boundary but is a crossover line at which the character of the band gap changes continuously.

Whether doped carriers in a "filling-control" system have oxygen p character or transition-metal d character is an important question in considering the transport properties of the transition-metal oxides. Since the ground state of the N-electron state is usually dominated by the d^n configuration, the doped holes will have mainly d character if the lowest $(N-1)$-electron state is dominated by the d^{n-1} configuration and will have mainly p character if it is dominated by the $d^n\underline{L}$ configuration. That is, doped holes have mainly d character in a Mott-Hubbard insulator $(\Delta>U)$ and p character in a

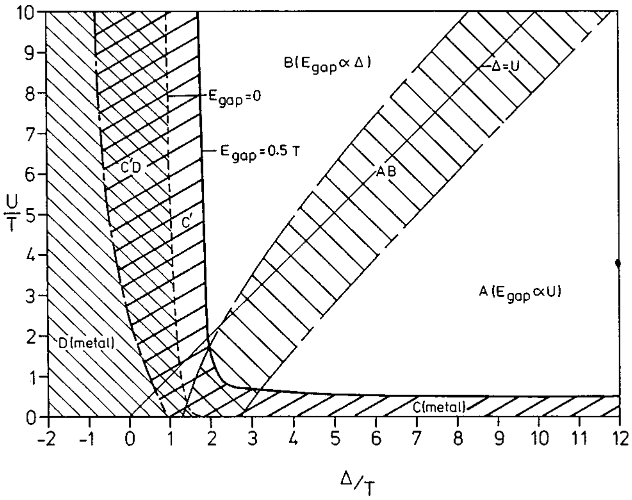

FIG. 41. Zaanen-Sawatzky-Allen plot for classifying $3d$ transition-metal compounds. The straight line $U=\Delta$ separates the Mott-Hubbard regime (A) and the charge-transfer regime (B). Between the two regimes is located an intermediate regime (AB). The shaded areas near $U=0$ and $\Delta=0$ are metallic regions where a Mott-Hubbard-type or charge-transfer-type band gap is closed. From Zaanen, Sawatzky, and Allen, 1985.

charge-transfer insulator $(\Delta<U)$. In either case, the doped electrons have mainly d character because the lowest unoccupied states are dominated by the d^{n+1} configuration, since the $d^{n+1}\rightarrow d^{n+2}\underline{L}$ charge-transfer energy $\Delta+U$ is always a large positive number.

In going from lighter to heavier transition-metal elements, the d level is lowered and therefore Δ is decreased, whereas U is increased because the spatial extent of the d orbital shrinks with atomic number. This means that early transition-metal compounds tend to become Mott-Hubbard type and late transition-metal compounds tend to become charge-transfer type. When the ligand atom becomes less electronegative, the p level is raised and hence Δ is decreased. For instance, transition-metal chalcogenides are more likely to become charge-transfer type than transition-metal oxides. Compounds to be plotted in Fig. 41 indeed follow this chemical trend, where Ti and V oxides are classified as typical Mott-Hubbard-type compounds and Cu oxides as typical charge-transfer compounds. Systematic variation of the electronic structure is described below in more detail.

The diagram of Fig. 41 contains a metallic region (shaded area) near the Δ- and U-axes, where the magnitude of the band gap, $\sim\Delta$ or $\sim U$, becomes small. Δ and U are defined with respect to the center of the p and d bands and therefore the actual band gap is smaller than Δ or U by the half widths of the p and d bands: If for simplicity, one ignores hybridization between the metal d and ligand p orbitals and multiplet effects, the magnitude of the band gap is given by $E_{\mathrm{gap}}\sim\Delta-\frac{1}{2}(W_p+W_d)$ for a charge-transfer insulator and $E_{\mathrm{gap}}\sim\Delta-W_d$ for a Mott-Hubbard insulator, where W_d and W_p are the bandwidths of d and p, respectively (see Fig. 5). If the energy shifts due to p-d hybridization are taken into account, $2\delta(N)-\delta(N-1)-\delta(N+1)$ should be added to the above E_{gap}, where $\delta(N)$ is the decrease in energy of the lowest N-electron state due to p-d hybridization.

The effect of the finite p bandwidth W_p can be incorporated by replacing the ligand molecular orbitals by a continuum of the p band (Zaanen *et al.*, 1985). The problem should then be formulated using the Anderson impurity model instead of the cluster model. The Hamiltonian of this model is given by

$$\mathcal{H}=\sum_{\nu}\varepsilon_{d\nu}n_{d\nu}+\frac{1}{2}\sum_{\nu\nu'\mu\mu'}\langle\nu\nu'\|\mu\mu'\rangle d^{\dagger}_{\nu'}d^{\dagger}_{\nu}d_{\mu}d_{\mu'}$$

$$+\sum_{\mathbf{k}}\varepsilon_{p\mathbf{k}}n_{p\mathbf{k}}-\sum_{\nu\mathbf{k}}(T_{\nu\mathbf{k}}d^{\dagger}_{\nu}p_{\mathbf{k}}+\mathrm{H.c.}),\tag{3.13}$$

where ν, μ, etc., denote the spin and orbital of the d states and $\langle\nu\nu'\|\mu\mu'\rangle\equiv\int d\mathbf{r}\int d\mathbf{r}'\,\phi^{*}_{\nu}(\mathbf{r})\phi^{*}_{\nu'}(\mathbf{r}')e^2/(|\mathbf{r}-\mathbf{r}'|)\,\phi_{\mu}(\mathbf{r})\phi_{\mu'}(\mathbf{r}')$. $d^{\dagger}_{\nu}$ and $p^{\dagger}_{\mathbf{k}}$ are the creation operators of localized d and bandlike p electrons, respectively. This Hamiltonian can be rewritten as

$$\mathcal{H}=\sum_{\nu}\varepsilon_{d\nu}n_{d\nu}+\frac{1}{2}\sum_{\nu\nu'\mu\mu'}\langle\nu\nu'\|\mu\mu'\rangle d^{\dagger}_{\nu'}d^{\dagger}_{\nu}d_{\mu}d_{\mu'}$$

$$+\int_{\varepsilon_p-W_p/2}^{\varepsilon_p-W_p/2}\varepsilon n_p(\varepsilon)d\varepsilon$$

$$-\sum_{\nu}\int_{\varepsilon_p-W_p/2}^{\varepsilon_p-W_p/2}d\varepsilon[T_{\nu}(\varepsilon)d^{\dagger}_{\nu}p(\varepsilon)+\mathrm{H.c.}],\tag{3.14}$$

where

$$|T_{\nu}(\varepsilon)|^2\delta_{\nu\nu'}\equiv\sum_{\mathbf{k}}T_{\nu\mathbf{k}}T^{*}_{\nu'\mathbf{k}}\delta(\varepsilon_{p\mathbf{k}}-\varepsilon).\tag{3.15}$$

The ground state of the formally d^8 impurity embedded in the filled p-band continuum is given by

$$\Phi_g(N)=A\left[|d^8\rangle+\int_{\varepsilon_p-W_p/2}^{\varepsilon_p+W_p/2}a(\varepsilon)|d^9\underline{L}(\varepsilon)\rangle d\varepsilon+\cdots\right],\tag{3.16}$$

where ε is the energy of an electron in the ligand p band. By inserting Eq. (3.16) into the Anderson impurity Hamiltonian (3.14) [neglecting the $|d^{10}\underline{L}(\varepsilon)^2\rangle$ term], we obtain an equation

$$\delta=\int_{\varepsilon_p-W_p/2}^{\varepsilon_p+W_p/2}\frac{2|T_{\nu}(\varepsilon)|^2d\varepsilon}{\delta-\varepsilon+\varepsilon_p+\Delta+\Delta E_8},\tag{3.17}$$

where ν is one of the e_g orbitals and $\sqrt{2}T_{\nu}(\varepsilon)\equiv\langle d^8|\mathcal{H}|d^9\underline{L}(\varepsilon)\rangle$, which satisfies $T^2_{pd}=\int_{\varepsilon_p-W_p/2}^{\varepsilon_p+W_p/2}|T_{\nu}(\varepsilon)|^2d\varepsilon$. The lowest-energy solution of Eq. (3.16) yields $\delta=\delta(N)$. Figure 42(a) shows that p-d hybridization lowers the energy of the d^8 multiplet component (the $^3A_{2g}$ term in the case of NiO). In the $(N-1)$-electron state, although the $d^8\underline{L}$ continuum lies below the discrete d^7 state, strong p-d hybridization creates a split-off state of predominantly $d^8\underline{L}$ character below the $d^8\underline{L}$ continuum, as shown in Fig. 42(b). The diagram of Fig. 41 was indeed calculated using such an Anderson impurity model for the N-, $(N-1)$-, and $(N$

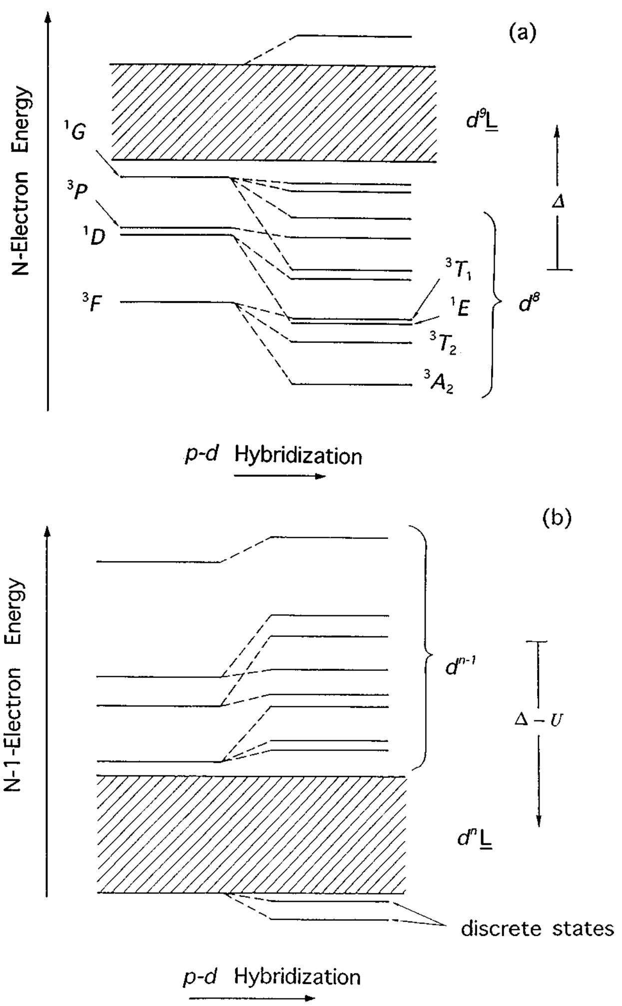

FIG. 42. Hybridization between discrete and continuum states in the impurity mode for a charge-transfer insulator: (a) Hybridized d^8 and $d^9\underline{L}$ configurations in the N-electron state for NiO; (b) d^7 and $d^8\underline{L}$ configurations in the $(N-1)$-electron state.

+1)-electron states (and assuming $W_p = 3T$). Because the effect of the finite d bandwidth cannot be included in the impurity model, a finite d bandwidth $W_d = 0.5T$ was assumed to produce the metal-insulator phase boundary shown in Fig. 41.

4. Multiplet effects

Multiplet splitting of the energy levels of a transition-metal ion is of a magnitude comparable to Δ, U, and T and is therefore important in characterizing electronic structure. Intra-atomic exchange and anisotropic Coulomb interactions are the cause of multiplet splitting and are represented by Racah parameters (B and C) or Slater integrals (F_2 and F_4). [The Racah parameter A or the Slater integral F_0 represents the isotropic part of the Coulomb interaction and therefore is close to U, which is a multiplet averaged value defined in Eq. (3.2).] Definitions of these parameters and the interrelation between them are given in Table II.

TABLE II. Relation between Kanamori parameters, u, u', and j, Racah parameters, A, B, and C, and Slater integrals, F_0, F_2, and F_4. Here $r_>$ and $r_<$ denote, respectively, the larger and smaller ones of r_1 and r_2.

$$A = F_0 - 49F_4, B = F_2 - 5F_4, C = 35F_4$$
$$F_0 = A + \tfrac{7}{5}C, U = A - \tfrac{14}{9}B + \tfrac{7}{9}C$$
$$u = A + 4B + 3C = F_0 + 4F_2 + 36F_4$$
$$u' = A - B + C = F_0 - F_2 - 4F_4$$
$$j = \tfrac{5}{2}B + C = \tfrac{5}{2}F_2 + \tfrac{45}{2}F_4$$
$$F_0 = F^0, F_2 = \tfrac{1}{49}F^2, F_4 = \tfrac{1}{441}F^4$$
$$F^k = \int_0^\infty r_1^2 dr_1 \int_0^\infty r_2^2 dr_2 (r_<^k / r_>^{k+1}) R_{3d}(r_1)^2 R_{3d}(r_2)^2$$

The energy $E(d^n)$ given by Eq. (3.2), where multiplet effect is neglected, yields the center of gravity of the multiplet terms of the d^n configuration. If we switch on the multiplet splitting in the above energy-level scheme, as shown in Fig. 43, each multiplet term $^{2S+1}\Gamma$ is shifted from the center of gravity $E(d^n)$ [Eq. (3.2)] by a "multiplet correction" $\Delta E(d^n\text{: } ^{2S+1}\Gamma)$. Then the energy of each multiplet term is given by $E(d^n\text{: } ^{2S+1}\Gamma) = E(d^n) + \Delta E(d^n\text{: } ^{2S+1}\Gamma)$. For the lowest term of the d^n multiplet, we denote the multiplet correction by $\Delta E(d^n\text{: } ^{2S+1}\Gamma) \equiv -\Delta E_n (<0)$. The charge-transfer energy Δ and the d-d Coulomb energy U can alternatively be defined using the lowest multiplet of each configuration instead of the center of gravity as described in Fig. 43. We denote the parameters thus redefined by Δ_{eff} and U_{eff}. Most of the physical properties

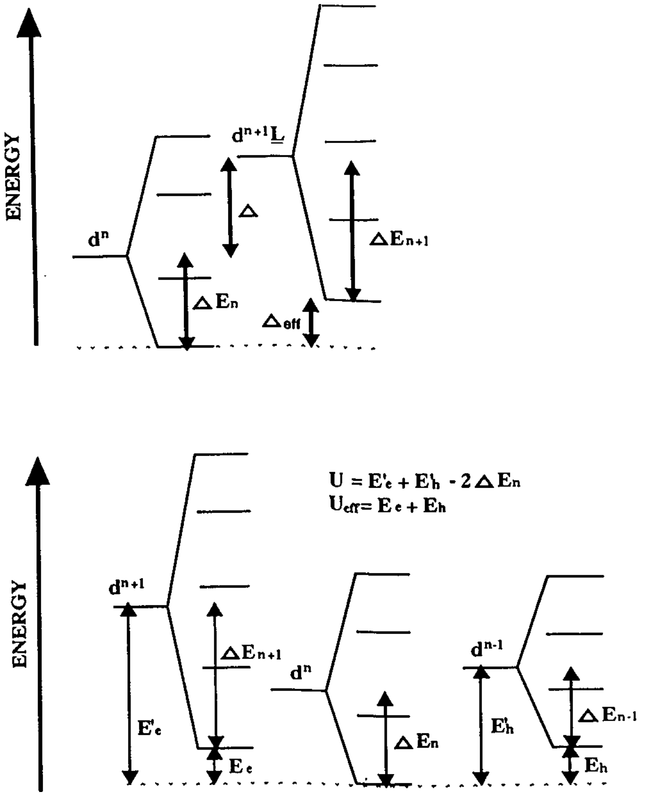

FIG. 43. Definition of Δ, U, Δ_{eff}, U_{eff}, and ΔE_n. From Fujimori *et al.*, 1993.

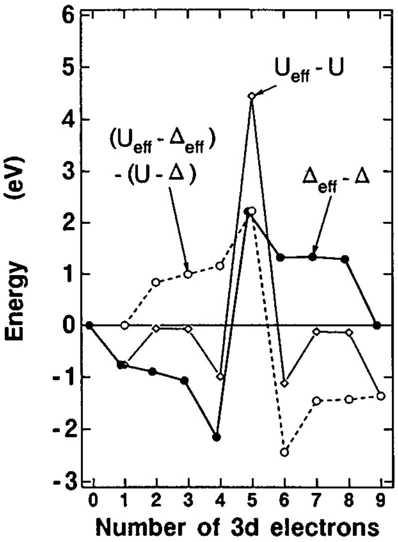

FIG. 44. Multiplet corrections $\Delta_{\mathrm{eff}}-\Delta$, $U_{\mathrm{eff}}-U$, and $(U_{\mathrm{eff}}-\Delta_{\mathrm{eff}})-(U-\Delta)$ for the high-spin states as functions of the d-electron number n. Racah parameters of divalent ions are used. From Fujimori *et al.*, 1993.

of $3d$ transition-metal compounds are determined by Δ_{eff} and U_{eff} rather than by Δ and U, since the lowest multiplet terms contribute most significantly to the ground state and the low-energy excited states of the system, including the magnitude of the band gap. Using the multiplet correction ΔE_n, we obtain

$$\Delta_{\mathrm{eff}}=\Delta+\Delta E_n-\Delta E_{n+1}, \tag{3.18}$$

$$U_{\mathrm{eff}}=U+2\Delta E_n-\Delta E_{n-1}-\Delta E_{n+1}. \tag{3.19}$$

In a free ion, the lowest multiplet term of each configuration is always a Hund's-rule high-spin state. This is not always the case in solids because p-d hybridization may lower the energy of the low-spin state below the high-spin state. We restrict the following argument to those cases in which the high-spin state is the lowest term of each multiplet.

As we shall show below, Δ and U are smooth functions of the atomic number Z and valence v of the transition-metal ion, whereas Δ_{eff} and U_{eff} are apparently irregular functions of these variables (Bocquet *et al.*, 1992c). The irregularity arises from the fact that the multiplet correction ΔE_n is a strongly nonmonotonic function of the nominal d-electron number n, showing a maximum at $n=5$, i.e., at half filling. Figure 44 shows the multiplet corrections for Δ and U as functions of n: $\Delta_{\mathrm{eff}}-\Delta$ $(\equiv\Delta E_n-\Delta E_{n+1})$ and $U_{\mathrm{eff}}-U$ $(\equiv 2\Delta E_n-\Delta E_{n-1}-\Delta E_{n+1})$. $\Delta_{\mathrm{eff}}-\Delta$ increases with n except for a sharp drop from $n=4$ to $n=5$, resulting in a minimum at $n=4$ and a maximum at $n=5$. $U_{\mathrm{eff}}-U$ exhibits a sharp maximum at $n=5$ and otherwise is a small negative number. In Fig. 44, the solid circles yield energies of full multiplet calculations using Racah parameters whereas the open circles yield energies calculated assuming a single Slater determinant of the type

$$\Phi(N)=|t_{2g\uparrow}^{m'}t_{2g\downarrow}^{m''}e_{g\uparrow}^{n'}e_{g\downarrow}^{n''}|, \tag{3.20}$$

i.e., calculated in the Hartree-Fock approximation (Brandow, 1977). Here, for simplicity, Kanamori's parameters u, u', and j are used instead of the more accurate Racah parameters or Slater integrals: $u\equiv\langle\nu\nu|H|\nu\nu\rangle\equiv U_{\nu\nu}$, $u'\equiv\langle\nu\nu'|H|\nu\nu'\rangle\equiv U_{\nu\nu'}$ [Eq. (2.6d)] and $j\equiv\langle\nu\nu'|H|\nu'\nu\rangle\equiv J_{0\nu\nu'}$ [Eq. (2.6e)] $(\nu\neq\nu')$, where ν and ν' denote different d orbitals. u and u' are Coulomb integrals and j is an exchange integral between d electrons. The relationship between Kanamori's parameters, Racah parameters, and Slater integrals is summarized in Table III.

The multiplet corrections to Δ and U modify the magnitudes of the band gaps as follows. From the behavior of $\Delta_{\mathrm{eff}}-\Delta$ and $U_{\mathrm{eff}}-U$ shown in Fig. 44: (i) for a charge-transfer insulator, the band gap is reduced for $n\leqslant 4$ whereas it increases for $n\geqslant 5$, with the most pronounced effect occurring at $n=4$ and 5; (ii) for a Mott-Hubbard insulator, the band gap greatly increases at $n=5$ and is slightly reduced otherwise. A dramatic manifestation of the multiplet effect is seen, for example, in Fe and Mn oxides, in which n is changed around 4 and 5 when the transition-metal atomic number and valence are varied: $\mathrm{LaFeO_3}$ (Fe^{3+}: d^5) is a wide-gap insulator because $n=5$. For $n=4$, $\mathrm{SrFeO_3}$ (Fe^{4+}: d^4) is a metal (Bocquet *et al.*, 1992b) and $\mathrm{CaFeO_3}$ (Fe^{4+}: d^4) has a small gap that is closed at high temperature or under high pressure (Takano *et al.*, 1991). As for Mn compounds, the band gap of $\mathrm{LaMnO_3}$ (Mn^{3+}: d^4) is smaller than that of $\mathrm{SrMnO_3}$ (Mn^{4+}: d^3) (van Santen and Jonker, 1950); MnO (Mn^{2+}: d^5) is a well-known wide-gap insulator.

Multiplet splitting also affects the character of the band gap and hence the character of doped carriers because now the relative magnitudes of Δ_{eff} and U_{eff}, instead of Δ and U, determines the character of doped holes and electrons. $U_{\mathrm{eff}}-\Delta_{\mathrm{eff}}$ $[\equiv-\Delta_{\mathrm{eff}}(d^{n-1})]$ may be taken as a measure of the p character of the top of the valence band, i.e., a measure of the p-hole character of doped holes. Multiplet corrections to $U-\Delta$ [i.e., $U_{\mathrm{eff}}-\Delta_{\mathrm{eff}}-(U-\Delta)$] are also shown in Fig. 44. From the sign of the correction, one can see that the multiplet effect tends to increase the p-hole character for $n\leqslant 5$ whereas it tends to increase the d-hole character for $n\geqslant 6$; the maximum of the p-hole character occurs at $n=5$. Indeed, it was found from the O $1s$ x-ray absorption spectroscopy (XAS) study of $\mathrm{La}_{1-x}\mathrm{Sr}_x\mathrm{FeO_3}$ that the p-hole character of holes doped into $\mathrm{LaFeO_3}$ is particularly pronounced (Abbate *et al.*, 1992). Another measure of the character of doped holes is the difference between the undoped ground state and the hole-doped state, i.e, the difference between the weight of the ligand hole $\underline{L}$ character in the undoped state and that in the hole-doped state. Since the p-hole character in the ground state decreases with Δ_{eff}, i.e., increases with $-\Delta_{\mathrm{eff}}$, and that in the doped state increases with $U_{\mathrm{eff}}-\Delta_{\mathrm{eff}}$, their difference $U_{\mathrm{eff}}-\Delta_{\mathrm{eff}}-(-\Delta_{\mathrm{eff}})=U_{\mathrm{eff}}$ may serve as a crude measure of the p-hole character of doped holes. From this viewpoint, the maximum p-hole character should occur at $n=5$ (see Fig. 44). In the case of electron doping, the difference between the p-hole ($d^{n+1}\underline{L}$) character in the ground state (measured by $-\Delta_{\mathrm{eff}}$) and that in

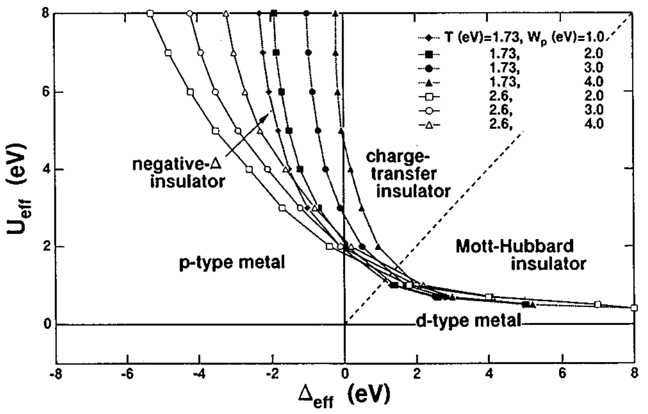

FIG. 45. Modified Zaanen-Sawatzky-Allen diagram including the effect of strong p-d hybridization in the region $\Delta\sim 0$ (Mizokawa *et al.*, 1994). In this region, the gap increases with increasing p-d transfer or decreasing p bandwidth w_p.

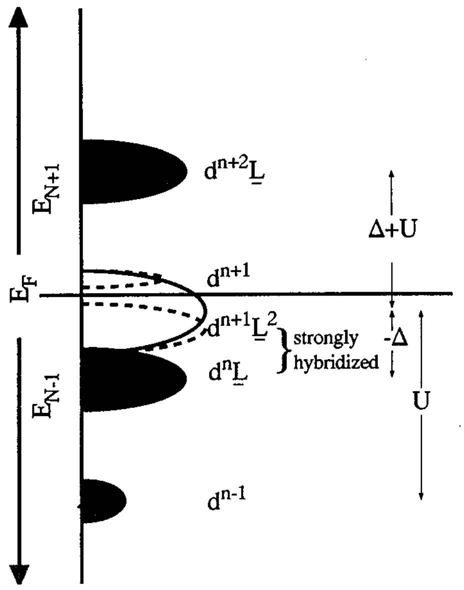

FIG. 46. Schematic picture of the one-electron density of states of the negative-Δ insulator (Mizokawa *et al.*, 1994).

the doped state (negligibly small $d^{n+2}\underline{L}$ character) yields the p-electron character of the doped electrons. Therefore one can conclude from Fig. 44 that $n=5$ compounds have maximum d character for doped electrons and that $n=4$ compounds have maximum p character for doped electrons. From this we expect that $SrFeO_3$ (Abbate *et al.*, 1992; Bocquet *et al.*, 1992b) would accommodate doped electrons predominantly in the ligand p orbitals to form the stable d^5 configuration.

5. Small or negative charge-transfer energies

In a charge-transfer insulator, if the charge-transfer energy Δ or Δ_{eff} is small compared to T, hybridization between the d^n and $d^{n+1}\underline{L}$ configurations becomes strong and the contribution of the $d^{n+1}\underline{L}$ configuration to the ground state becomes substantial. If Δ or Δ_{eff} <0, the weight of the $d^{n+1}\underline{L}$ configuration becomes dominant in the ground state. This situation is expected to occur when the valence of the transition-metal ion is unusually high because Δ is expected to decrease with metal valence. The $d^{n+1}\underline{L}$ configuration is a continuum. However, within the Anderson impurity model, it can be shown that sufficiently strong p-d hybridization causes a discrete state of $d^{n+1}\underline{L}$ character to be split off below the continuum in the same way as in the formation of a split-off state in the $(N-1)$-electron state of a charge-transfer insulator described above [see Fig. 42(b)]. The insulating region was restricted to positive Δ values in the original Zaanen-Sawatzky-Allen diagram (Fig. 41) because it was assumed that the p-d hybridization strength was small $T=\frac{1}{3}W_p$ (Zaanen *et al.*, 1985). In order to extend the Zaanen-Sawatzky-Allen framework to small and negative Δ values, the magnitude of the band gaps has been calculated using the Anderson impurity model for various sets of Δ, U, T $[\equiv -\sqrt{3}(pd\sigma)]$, and W_p as shown in Fig. 45 (Mizokawa *et al.*, 1994), where one can see that the insulating region is extended to negative Δ values for certain parameters. In the small or negative Δ regime, the magnitude of the band gap is proportional neither to Δ nor to U but is sensitively dependent on the p-d hybridization strength T. Therefore, as the ligand bandwidth W_p decreases or the transfer integral T increases, the band gap tends to increase. In Fig. 45 are plotted sets of U and Δ which give $E_{\text{gap}}=0.4$ eV as a measure of the metal-insulator phase boundary.

The effect of lattice periodicity is much more complicated in the case of negative Δ than in the case of positive Δ. In the periodic lattice, d orbitals at neighboring transition-metal atoms share intervening anion p orbitals, which leads to a complicated many-body problem, especially for a small or negative Δ. This will effectively decrease the $3d$-ligand hybridization strength T. Also, the dispersional widths of the $(N-1)$- and $(N+1)$-electron states resulting from intercluster hybridization would effectively increase the ligand bandwidth W_p. Therefore intercluster hybridization effectively decreases T or increases W_p, thereby shrinking the insulating region in the U-Δ phase diagram. The strength of the intercluster hybridization is dependent on the metal-oxygen-metal bond angle (see Sec. III B): It is maximized at 180° and minimized at 90°. This may explain why $LaCuO_3$, in which octahedral CuO_6 clusters are interconnected with ~180° Cu-O-Cu bond angles, is metallic and $NaCuO_2$, in which square-planar CuO_4 clusters are interconnected with ~ 90° Cu-O-Cu angles, is insulating, although the Cu is formally trivalent in both compounds (Mizokawa *et al.*, 1991). For a negative Δ, the lowest $(N-1)$-electron state is $d^{n+1}\underline{L}^2$ [because $E(d^{n+1}\underline{L}^2)=E(d^n\underline{L})+\Delta<E(d^n\underline{L})$; see Eq. (3.2)] and the lowest $(N+1)$-electron state is d^{n+1}. Since the main constituent of the ground state is the $d^{n+1}\underline{L}$ configuration, the charge transfer $(d^{n+1}\underline{L})_i+(d^{n+1}\underline{L})_j$ $\rightarrow(d^{n+1}\underline{L}^2)_i+(d^{n+1})_j$ gives the lowest-energy charge fluctuation and therefore the band gap has predominantly p-to-p character. This situation is illustrated in Fig. 46.

The fact that $NaCuO_2$ is a nonmagnetic insulator ($S=0$) was explained by the low-spin ($S=0$) solution of the CI cluster model, whereas band-structure calculations using the local-density approximation (LDA; Karlsson *et al.*, 1992; Singh, 1994) have also given a nonmagnetic insulating ground state. Therefore it is not obvious whether $NaCuO_2$ is a correlated insulator or a band insulator. According to the configuration-interaction picture, the nonmagnetic ground state dominated by the $d^9\underline{L}$ configuration may be viewed as a valence-bond state in which the local spin of the d hole (d^9) and that of the ligand hole ($\underline{L}$) form a local singlet. Therefore the negative Δ insulator with low-spin configuration may be called a "local-singlet lattice" or "valence-bond (Heitler-London) insulator." In this picture, the wave function of the ground state is quite different from a single Slater determinant without electron correlation. Such a lattice consisting of the local singlets is, however, analytically connected to the nonmagnetic band insulator. Because the origin of the band gaps in insulators with small or negative Δ is neither U nor Δ but rather the strong p-d hybridization. Sarma and coworkers referred to them as "covalent insulators" (Nimkar *et al.*, 1993). According to their Hartree-Fock band-structure calculations on the p-d model, the character of the band gap is of strongly hybridized pd-p type rather than pure p-p type. On the other hand, it is closer to the p-p type according to the LDA calculation of Singh (1994).

B. Systematics in model parameters and charge gaps

To understand the diverse physical properties of $3d$ transition-metal compounds from a unified point of view, it is important to clarify the systematics underlying changes in the electronic structure and hence in the model parameters, Δ, U, and T as functions of chemical environment, namely, as functions of the atomic number and valence of the transition-metal ion, the nature (electronegativity, ionic radius, etc.) of the ligand atom, and the crystal structure. In the following, we present three different approaches to this task, namely, (1) methods based on the ionic crystal model, (2) semiempirical methods based on the analysis of photoemission spectra, and (3) theoretical methods using first-principles electronic structure calculations.

1. Ionic crystal model

The simplest method of estimating values for the parameters Δ and U is the ionic crystal model, which was applied to $3d$ transition-metal oxides by Torrance *et al.* (1991). Assuming that each atom is a point charge having its formal ionic charge, they calculated the bare Madelung potential energy at each atomic site and estimated $\Delta_{\rm eff}$ and $U_{\rm eff}$ using the ionization potentials and electron affinities of the constituent ions. Here, the multiplet corrections are included in the parameters thus estimated since the experimental ionization potentials are used.

Using the ionization potential $I(M^{v+})$ and the electron affinity $A(M^{v+})$ of the transition-metal M^{v+} ion, $U_{\rm eff}$ is given by

$$U_{\rm eff}=I(M^{v+})-A(M^{v+})-\frac{e^2}{d_{M-M}}, \qquad (3.21)$$

where $e^2/(d_{M-M})$ is the attractive Coulomb energy between nearest-neighbor metal ions that are separated by d_{M-M}. Here, the inclusion of the $e^2/(d_{M-M})$ term corresponds to the optical excitation, where an electron and a hole are created on nearest-neighbor cation sites. Without the latter term, $U_{\rm eff}$ would correspond to photoemission and inverse photoemission, where the electron and hole are well separated from each other and do not interact. Correspondingly, $\Delta_{\rm eff}$ is given by

$$\Delta_{\rm eff}=e\Delta V_{\rm Mad}+I(\mathrm{O}^{2-})-A(M^{v+})-\frac{e^2}{d_{M-\mathrm{O}}}, \qquad (3.22)$$

where $\Delta V_{\rm Mad}$ is the difference in the Madelung potential between the metal site and the oxygen site and $d_{M-\mathrm{O}}$ is the nearest-neighbor metal-oxygen distance. The definition of $\Delta_{\rm eff}$ also contains the electron-hole interaction term relevant to optical transitions.

In Fig. 47 are plotted values for $\Delta_{\rm eff}$ and $U_{\rm eff}$ estimated using Eqs. (3.21) and (3.22). These $\Delta_{\rm eff}$ and $U_{\rm eff}$ values have been calculated using the bare electrostatic potential without screening and are therefore expected to overestimate the actual parameter values. Indeed, they range from -10 eV to $+20$ eV, extending over a much wider energy range than parameter values estimated using first-principles methods or the spectroscopic method. One can see from Fig. 47 that, although the absolute magnitudes of $\Delta_{\rm eff}$ and $U_{\rm eff}$ are overestimated, the qualitative trends are the same as those estimated using spectroscopic methods. The charge-transfer type ($\Delta_{\rm eff}<U_{\rm eff}$) versus Mott-Hubbard type ($\Delta_{\rm eff}>U_{\rm eff}$) seems almost correctly predicted by this method: Late transition-metal compounds fall into the charge-transfer regime and early transition-metal compounds into the Mott-Hubbard regime with some V compounds with high valences in the charge-transfer regime. According to the Zaanen-Sawatzky-Allen picture, a charge-transfer insulator becomes metallic when the charge-transfer gap of magnitude $\Delta_{\rm eff}-\frac{1}{2}(W_p+W_d)$ becomes negative, while a Mott-Hubbard-type insulator becomes metallic when the Mott-Hubbard-type gap of magnitude $U_{\rm eff}-W_d$ becomes negative. The vertical ($\Delta_{\rm eff}=\Delta_B$) and horizontal ($U_{\rm eff}=U_B$) lines in Fig. 47 are drawn in an attempt to separate metals from insulators. $\Delta_B\sim 10$ eV and $U_B\sim 11$ eV would mean that $W_p\sim W_d\sim 10$ eV. The latter values are, however, unrealistically large and would contain other contributions (such as incomplete screening of the bare electrostatic potentials in the ionic model).

The band gaps predicted by the ionic model were compared with the optical band gaps of perovskite-type $RM\mathrm{O}_3$ compounds, where R is La or Y, by Arima, Tokura, and Torrance (1993). The experimentally determined optical gaps are shown in Fig. 48. The figure shows that the lowest-energy gap is of the Mott-

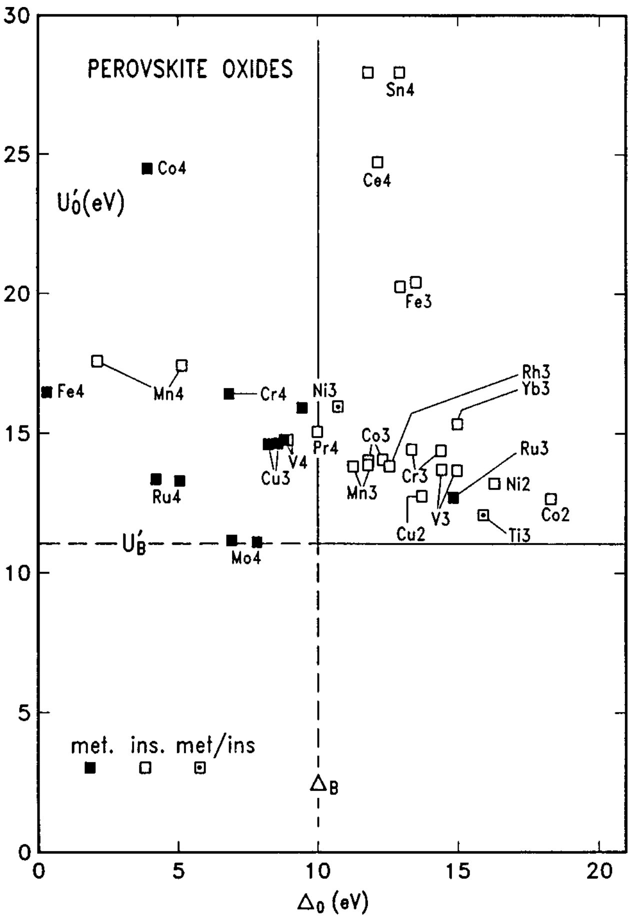

FIG. 47. Charge-transfer energies Δ_{eff} and on-site d-d Coulomb energies U_{eff} of transition-metal oxides calculated using the ionic model by Torrance *et al.* (1991). The vertical ($\Delta_{\mathrm{eff}}=\Delta_B$) and horizontal ($U_{\mathrm{eff}}=U_B$) lines are drawn to separate metals (solid symbols) and insulators (open symbols). The number next to each element gives its oxidation state, e.g., Fe3: α-Fe_2O_3 and $LaFeO_3$.

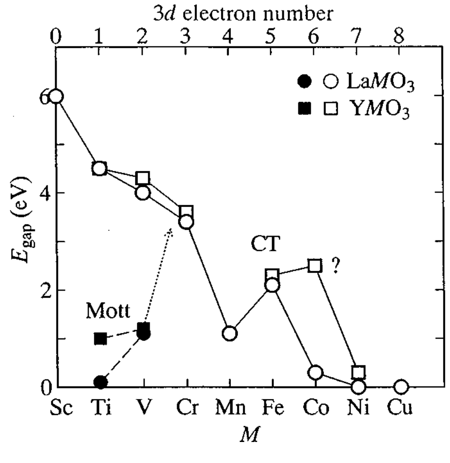

FIG. 48. Measured optical gaps for RMO_3 (R=La or Y) plotted against the transition-metal atom (Arima, Tokura, and Torrance, 1993). The open symbols give charge-transfer (p-to-d) gaps, while the solid symbols give Mott-Hubbard (d-to-d) gaps.

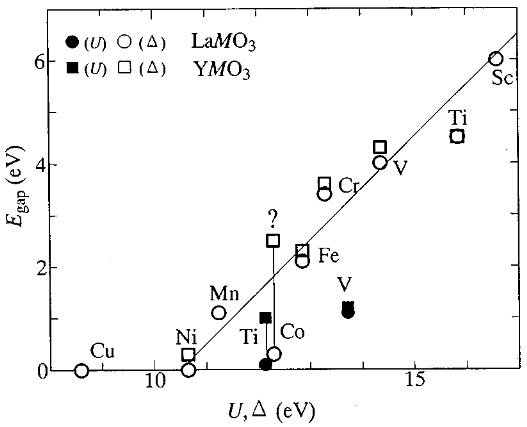

FIG. 49. Experimental optical gaps vs charge-transfer (open symbols, Δ) or Mott-Hubbard (solid symbols, U) gaps calculated using the ionic model. From Arima, Tokura, and Torrance, 1993.

Hubbard type for M=Ti and V and is of the charge-transfer type for M=Mn to Cu. The magnitude of the gap shows a maximum at $n=5$ (M=Fe), due to the maximum stabilization of the completely filled $t_{2g\uparrow}$ and $e_{g\uparrow}$ levels as shown in Fig. 44. The peak at $n=3$ (M=Cr) is due to the complete filling of the $t_{2g\uparrow}$ level. The dip at $n=4$ (M=Mn) seen in Fig. 48 can also be understood from the multiplet correction (Fig. 44). A comparison of the optical gap values with those calculated using the ionic model is made in Fig. 49, where one can see excellent correlation between the experimental and the calculated values except for the ~10 eV overestimate of the calculated values. The ~10 eV difference should have the same origin as the metal-insulator boundary $\Delta_{\mathrm{eff}}=\Delta_B$ and $U_{\mathrm{eff}}=U_B$ noticed in Fig. 47.

There are slightly different methods of estimating the parameters U and Δ using the ionic crystal model. Ohta *et al.* (1991a, 1991b) assumed that the Madelung term $e\Delta V_{\mathrm{Mad}}$ is screened by the optical dielectric constant ε_∞: $e\Delta V_{\mathrm{Mad}}/\varepsilon_\infty$. Zaanen and Sawatzky (1990) argued that the dielectric constant, which describes screening between charges separated by many lattice spacings, is not appropriate for describing the screening process considered here. Instead they added the polarization energies of surrounding atoms $-2E_{\mathrm{pol}}$ and $-4E_{\mathrm{pol}}$ to Eqs. (3.21) and (3.22), respectively. Here, E_{pol} is the polarization energy for a unit point charge $\pm e$ in the crystal and is given by $E_{\mathrm{pol}}=\frac{1}{2}\Sigma_j\alpha_j F_j^2$, where F_j is the electric field produced by the point charge at ion j and α is the polarizability of ion j. The Racah parameter A and charge-transfer energy Δ estimated by this method for various 3d transition-metal monoxides are listed in Table III. Here, in order to estimate E_{pol}, parameters for NiO have been determined so as to fit the photoemission spectra, and the empirical $1/d^4$ dependence of E_{pol} on the interatomic distance d has been used.

2. Spectroscopic methods

The valence-band photoemission spectra of a number of 3d transition-metal compounds have so far been ana-

TABLE III. On-site Coulomb (U) and exchange (J) energies estimated using the constrained LDA method (Anisimov *et al.*, 1991), compared with the empirical estimates for the Racah parameter A and charge-transfer energy Δ (Zaanen and Sawatzky, 1990). U_{eff} is the splitting between the d^{n-1} and d^{n+1} high-spin states. Energies are in eV.

	U	J	U_{eff}	A	Δ
CuO/CaCuO$_2$	7.5	0.98	6.5	4.0	4.0
NiO	8.0	0.95	7.1	(6.0)	(4.92)
CoO	7.8	0.92	6.9	5.02	5.53
FeO	6.8	0.89	5.9	4.46	6.21
MnO	6.9	0.86	10.3	5.43	8.23
VO	6.7	0.81	5.9	3.54	10.47
TiO	6.6	0.78	5.8	3.02	10.01

lyzed using the CI cluster model and the Anderson impurity model (Fujimori *et al.*, 1986, 1990; Eskes *et al.*, 1990; van Elp *et al.*, 1991) and the model parameters Δ, U, and T have been estimated. Having obtained N- and $(N-1)$-electron eigenstates, one calculates the photoemission spectrum by

$$\rho(\omega)=\sum_i |\langle\Phi_i(N-1)|d|\Phi_g(N)\rangle|^2 \times\delta(\omega+E_i(N-1)-E_g(N)), \qquad (3.23)$$

where $\Phi_g(N)$ and $\Phi_i(N-1)$ are the ground state and the final states of photoemission, $E_g(N)$ and $E_i(N-1)$ are their energies, d is the annihilation operator of a d electron and $\omega\equiv\varepsilon_{\text{kin}}-h\nu$. Therefore $\mu-\omega$, where μ is the electron chemical potential, i.e., the Fermi level, is the electron binding energy measured from the Fermi level and $\rho(\omega)$ with $\omega<\mu$ gives a photoemission spectrum. The summation in Eq. (3.23) runs over all final states that can be reached by the annihilation of one d electron. By inserting Eqs. (3.1) and (3.6) into Eq. (3.23), one obtains $\rho(\omega)=\Sigma_i|a_1b_{i1}+a_2b_{i2}+\cdots|^2\delta(\omega+E_i(N-1)-E_g(N))$. When one compares the calculated spectra with experiment, the delta function in Eq. (3.23) is replaced by a Gaussian function (broadened by a Lorentzian function) in order to represent the finite bandwidths, lifetime widths, and other broadening effects. In addition, the oxygen p band is superposed on the d-electron spectrum.

Figure 50 shows the photoemission spectra and the best-fit results for a series of transition-metal monoxides. Since CuO and NiO are charge-transfer insulators, the main band closer to the Fermi level is due to $d^n\underline{L}$ final states and the satellite at higher binding energies is due to d^{n-1} final states. The separation between the main and satellite features is given by $\sim U-\Delta$ (plus shifts due to p-d hybridization). In going from heavier to lighter transition-metal atoms, the separation between the main band and the satellite decreases, meaning that $U-\Delta$ decreases. The cluster-model analysis shown in Fig. 50 yields a systematic increase of Δ with decreasing atomic number, while the systematic decrease of U is not so significant. $U>\Delta$ for the charge-transfer-type CuO and NiO, and $U<\Delta$ for the Mott-Hubbard-type VO (although this compound is metallic). MnO with $U\sim\Delta$ is intermediate between the charge-transfer-type and Mott-Hubbard-type compounds.

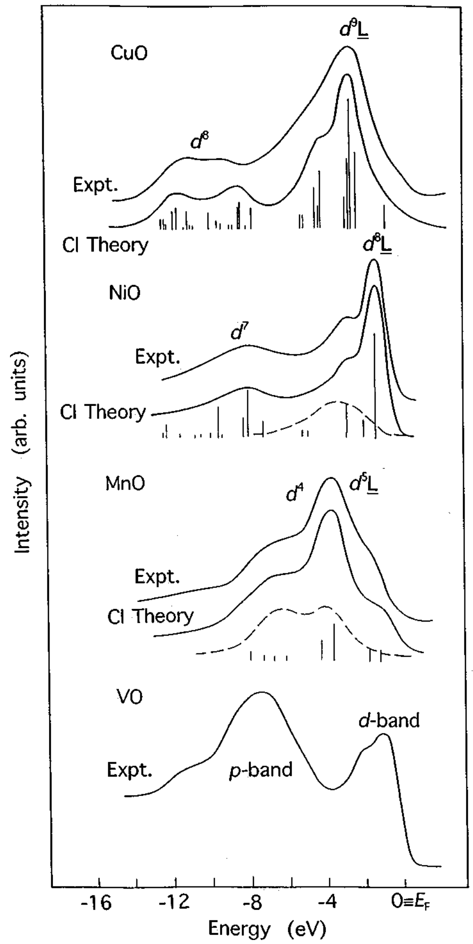

FIG. 50. Valence-band photoemission spectra of CuO (Eskes *et al.*, 1990), NiO (Fujimori and Minami, 1984), MnO (Fujimori *et al.*, 1990) and VO (Werfel *et al.*, 1981) and their cluster-model analyses. $\Delta\sim2.75$ eV and $U\sim6.5$ eV for CuO, $\Delta\sim4.0$ eV and $U\sim7.5$ eV for NiO, and $\Delta\sim7.0$ eV and $U\sim7.5$ eV for MnO. VO is metallic and no cluster-model analysis could be made.

The photoemission spectra of the core levels of the $3d$ transition-metal atom also yield nearly the same information as the valence-band spectra (van der Laan *et al.*, 1981). The core-level spectra have an advantage over the valence-band spectra in that there are no overlapping features, such as the O $2p$ band, that obscure the cluster-model analysis, while they have the disadvantage that the unknown strength of the core-hole potential introduces an additional parameter. The final state of core-level photoemission is given by

$$\Phi(\underline{c}N)=e_1|\underline{c}d^n\rangle+e_2|\underline{c}d^{n+1}\underline{L}\rangle+\cdots \qquad (3.24)$$

and the photoemission spectrum by

$$\rho(\omega)=\sum_i |a_1e_{i1}+a_2e_{i2}+\cdots|^2\delta(\omega+E_i(\underline{c}N)-E_g(N)) \qquad (3.25)$$

A systematic analysis of the metal $2p$ core-level spectra for a wide range of $3d$ transition-metal compounds was attempted by Bocquet *et al.* (1992a; 1996) using a simplified version of the CI cluster model, where wave functions of single Slater determinants [Eq. (3.20)] and Kanamori's parameters were employed for both the ground state and the final states. The parameter values thus obtained are not exactly the same as, but are reasonably close to, those obtained from analysis of the valence-band photoemission spectra. More elaborate full multiplet cluster-model calculations have been made for the transition-metal dihalides MX_2 and trivalent transition-metal oxides M_2O_3 by Kotani and co-workers (Okada *et al.*, 1992; Uozumi *et al.*, 1997). The Δ values thus obtained for M_2O_3 are generally smaller than those for the monoxides MO but show a tendency to increase with decreasing transition-metal atomic number, as in the case of the monoxides. Thus Δ seems to decrease systematically with atomic number Z and valence v of the transition-metal ion. This tendency is clearly seen in Fig. 51, where Δ values deduced from the $2p$ core-level spectra are plotted as a function of Z and v. In Fig. 52 are plotted U values, which weakly increase with the atomic number and valence of the transition-metal due to shrinkage of the spatial extent of the $3d$ orbitals. Figure 52 also shows that the decrease in the electronegativity of the ligand atom (in going from oxygen to sulfur) decreases the Δ value. The systematic variation of Δ and U with Z and v demonstrated above may be very crudely written as

$$\Delta \sim \Delta_0 - 0.6Z - 2.5v, \tag{3.26}$$

$$U \sim U_0 + 0.3Z + 0.5v, \tag{3.27}$$

where $\Delta_0 \sim 26$ eV and $U_0 \sim -2.5$ eV for oxides and $\Delta_0 \sim 23.5$ eV and $U_0 \sim -4.5$ eV for sulfides.

Figure 52 shows that light transition-metal compounds still have sizable U values, which in some cases exceed Δ. This means that many light transition-metal oxides are not ideal Mott-Hubbard-type compounds, in which Δ is larger than U and the magnitude of the band gap is $\sim U$. Indeed, recent cluster-model analyses of the metal $2p$ core levels of Ti and V oxides have shown that U is comparable to or larger than Δ (Uozumi *et al.*, 1993; Okada *et al.*, 1994; Bocquet *et al.*, 1996). The prefactor $\sqrt{10-n}$ in the off-diagonal matrix elements $T_{\rm eff} \equiv \sqrt{10-n}T$ increases with decreasing atomic number Z, not only because of the increase in T itself (Fig. 53), but also because of the increase in $(10-n)$. Therefore, in the light transition-metal oxides, $T_{\rm eff}$ is often larger than U and Δ and sets the largest energy scale. Then $T_{\rm eff}$ plays the most important role in determining the magnitude of the band gap, unlike in the original Zaanen-Sawatzky-Allen picture. This situation may be described as follows: For example, for the d^1 system Ti_2O_3, the occupied d band seen by photoemission is actually a split-off state of predominantly $d^1\underline{L}$ character rather than d^0 in the photoemission final state (Uozumi *et al.*, 1996) in a manner similar to that shown in Fig. 42(b). Figure 54 shows various transition-metal oxides plotted in the Zaanen-Sawatzky-Allen diagram (Fig. 41) but with $U/T_{\rm eff}$ and $\Delta/T_{\rm eff}$ shown in the plot instead of U/T and Δ/T. Most of the V and Ti oxides are found near the origin ($U/T_{\rm eff} \sim 0$ and $\Delta/T_{\rm eff} \sim 0$) because of the large $T_{\rm eff}$ values. The parameter values shown in Fig. 54 indicate that the Δ of compounds with high metal valencies, such as Ti^{4+}, V^{4+}, and V^{5+}, is comparable to or lower than U.

If there were no p-d hybridization and the bandwidths (W_p and W_d) were zero, the band gap would be given by $\Delta_{\rm eff}$ for a charge-transfer insulator and by $U_{\rm eff}$ for a Mott-Hubbard insulator. Values for $\Delta_{\rm eff}$ and $U_{\rm eff}$ deduced from the cluster-model analysis of the metal $2p$ core-level spectra are plotted for various transition-metal compounds in Fig. 55 as functions of n. Figure 55(a) demonstrates that $\Delta_{\rm eff}$ decreases monotonically with n except for the large discontinuity between $n=4$ and 5. This variation reflects both the smooth variation of Δ with n and its multiplet correction, $\Delta_{\rm eff}-\Delta$ (Fig. 44), which is a large negative value for $n=4$ and a large positive value for $n=5$. Figure 55 also shows that, for a fixed n, $\Delta_{\rm eff}$ (and hence Δ) decreases as the valence of the metal ion increases, reflecting the lowering of the $3d$ energy level due to the increasing positive charges at the transition-metal ion. Figure 55(b) shows that $U_{\rm eff}$ slowly and monotonically increases with n except for the sharp peak at $n=5$. Calculated band gaps are shown in Fig. 56. Due to p-d hybridization, the d-d and p-d characters of the band gaps are mixed with each other and the variation of the band gap with n reflects both that of $\Delta_{\rm eff}$ and that of $U_{\rm eff}$. The p-d hybridization weakens the degree of variation of the band gap compared to that of $\Delta_{\rm eff}$ or $U_{\rm eff}$. Moreover, p-d hybridization lowers the ground-state energy $E_g(N)$, thereby increasing $E_{\rm gap}$ [see, Eq. (3.5)]. In addition to the $E_{\rm gap}$ peak at $n=5$, which is derived from the peak in $\Delta_{\rm eff}$ and/or $U_{\rm eff}$, there is a small peak at $n=3$. This comes from the stabilization of the d^3 configuration due to intra-atomic exchange coupling (Hund's rule coupling), since the t_{2g} orbitals are half-filled by three electrons. The calculated $E_{\rm gap}$ for oxides of composition RMO_3 compare favorably with the experimental values (Fig. 48).

Using the cluster-model calculation, one can study whether doped carriers occupy the metal d or ligand p orbitals. We may define the p character of doped holes and the d character of doped electrons from the n_d values of the N-, $(N-1)$-, and $(N+1)$-electron states, $n_d(N)(\equiv n_d)$, $n_d(N-1)$, and $n_d(N+1)$, as $C^p_{\rm hole}=1-[n_d(N)-n_d(N-1)]$ and $C^d_{\rm el}=n_d(N+1)-n_d(N)$. The $C^p_{\rm hole}$ shown in Fig. 57(a) generally increases with n, reflecting the decrease in Δ. The curves have a peak at $n=5$ and a dip at $n=6$ due to the multiplet effect. In Fig. 57(b), $C^d_{\rm el}$ is plotted against n. The exchange stabilization and hence the reduced covalency for the d^5 configurations enhances the d character of doped electrons and the p character of doped holes. One can also see that the d character of doped electrons decreases with the valence of the transition-metal ion, reflecting the decrease in Δ with metal valence. In the above

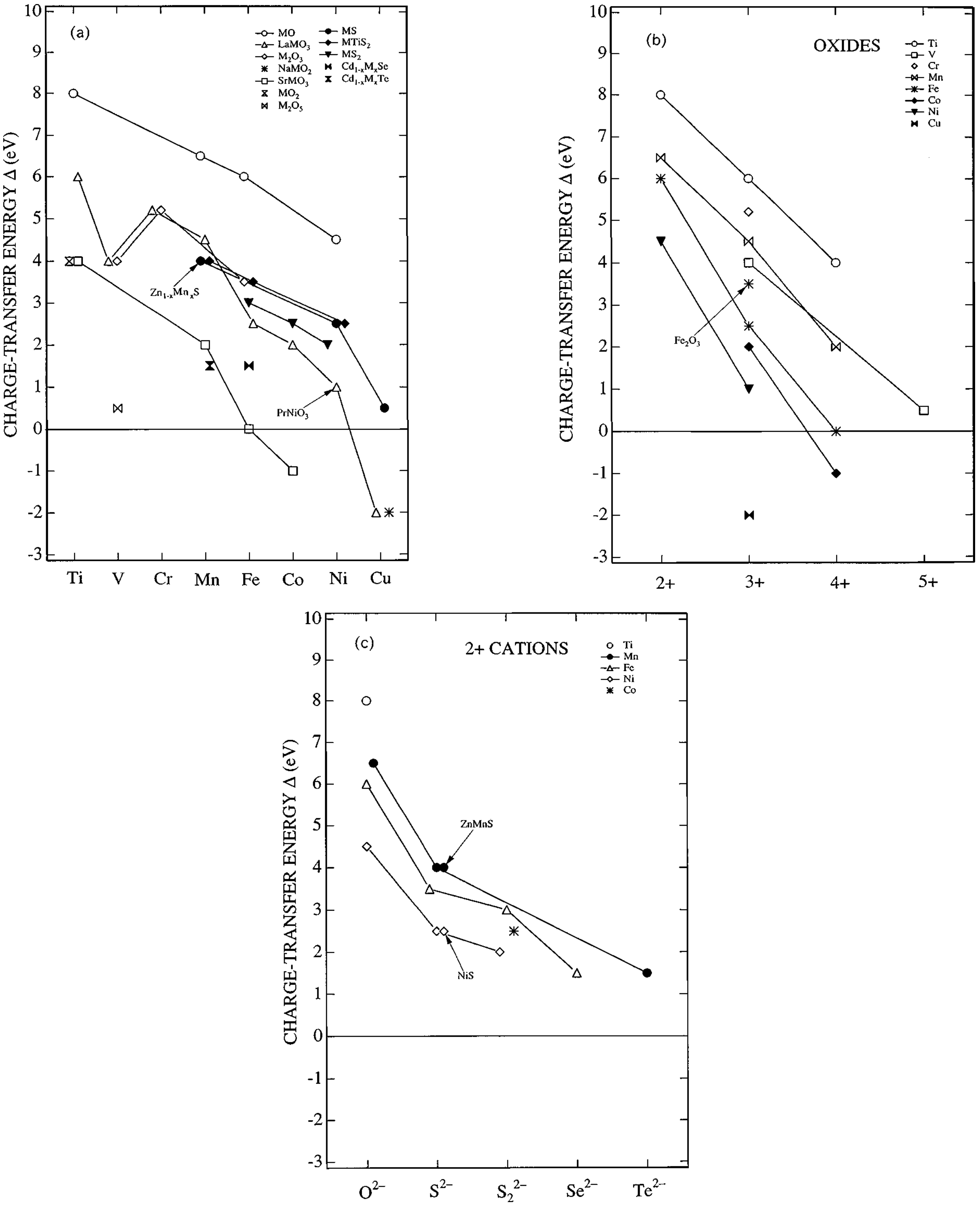

FIG. 51. Charge-transfer energies Δ of various $3d$ transition-metal compounds displayed with respect to (a) the transition-metal atomic number (b) its valence, and (c) the ligand electronegativity (Bocquet *et al.*, 1992a, 1992c, 1996).

definition those compounds which have C^p_{hole} smaller than 0.5 and C^d_{el} larger than 0.5 can be said to have d-d gaps, while those compounds which have C^p_{hole} larger than 0.5 and C^d_{el} larger than 0.5 can be said to have p-d gaps.

3. First-principles methods

There has also been considerable progress in first-principles methods for estimating the parameter values using the local(-spin)-density approximation [L(S)DA]. Although the L(S)DA often fails to predict the correct

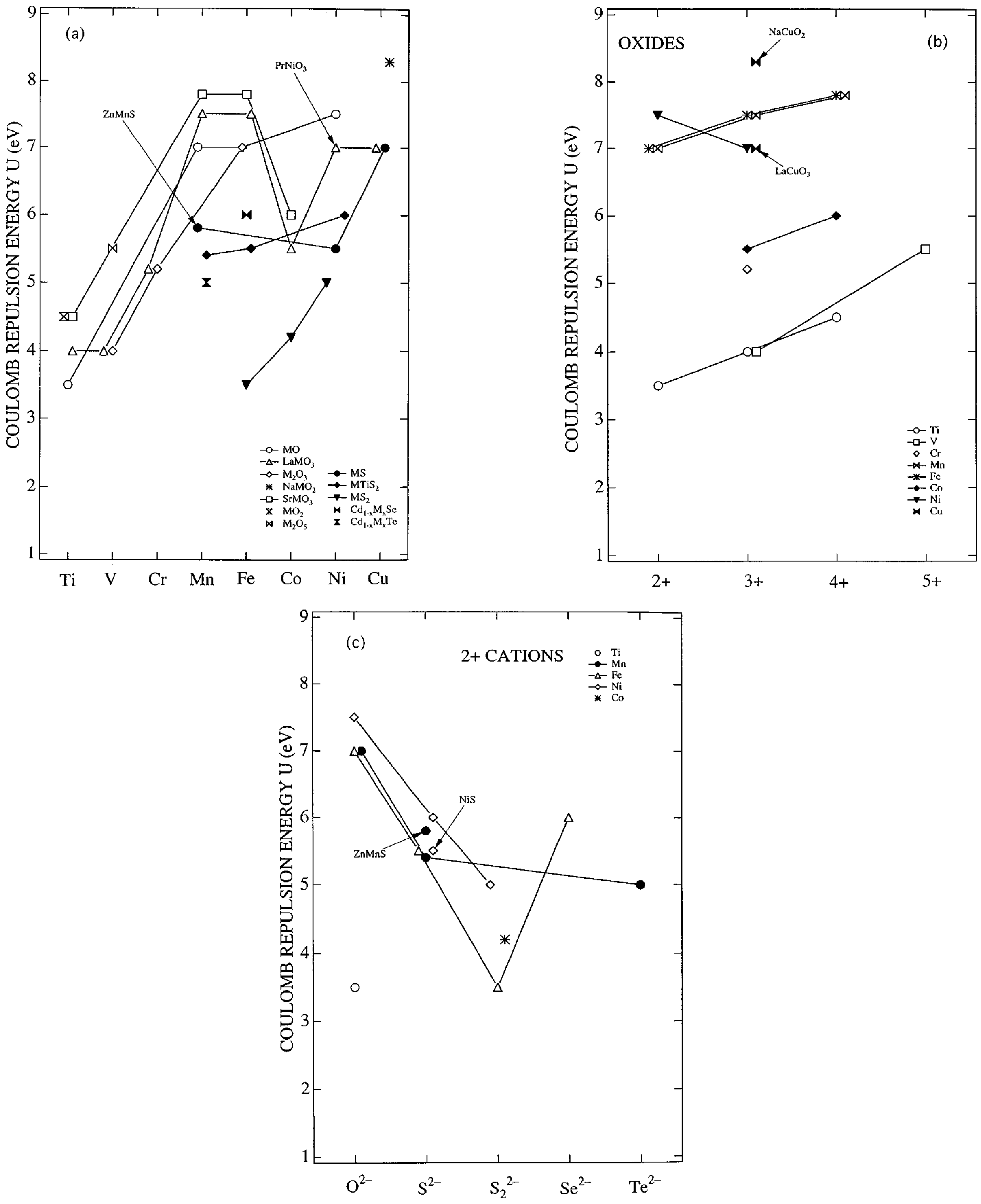

FIG. 52. On-site d-d Coulomb energies U of various $3d$ transition-metal compounds displayed with respect to (a) the transition-metal atomic number, (b) its valence and (c) the ligand electronegativity (Bocquet *et al.*, 1992a, 1992c, 1996).

ground-state properties of Mott insulators, it gives basically correct model parameters.

The p-d transfer integral T [or $(pd\sigma)$, $(pd\pi)$] can be estimated by fitting the LDA energy band structure using a tight-binding Hamiltonian, which contains the p-d transfer integrals as well as the p-p transfer integrals $[(pp\sigma)$, $(pp\pi)]$, the transition-metal d level ε_d, and the anion p level ε_p. Systematic changes of these parameters with transition-metal atomic number were found in an early study of $3d$ transition-metal monoxides (Mattheiss, 1972): Tight-binding fits to non-self-consistent band-structure calculations showed an in-

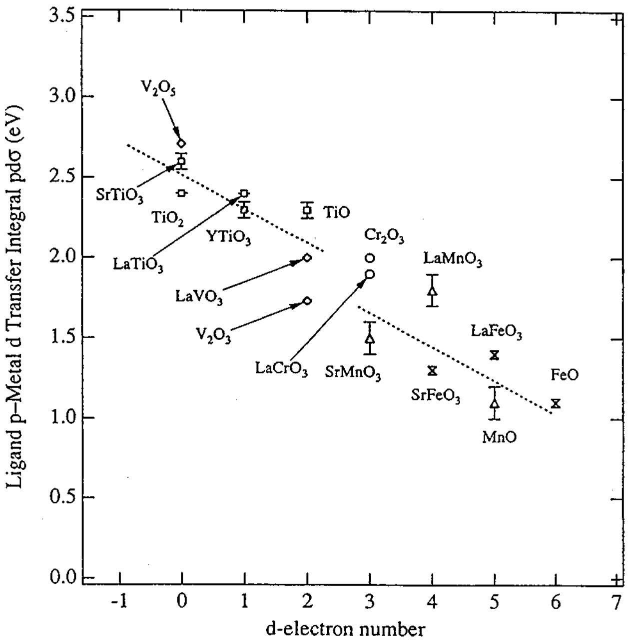

FIG. 53. p-d transfer integral $(pd\sigma)$ plotted against the nominal d-electron number n (Bocquet *et al.*, 1996).

crease in $\varepsilon_d - \varepsilon_p$ by $\sim$0.7 eV per unit increase in Z, in good agreement with the spectroscopic estimates described above.

Using the tight-binding fit approach to band structures calculated within the LDA, Mahadevan, Shanti, and Sarma (1996) systematically studied a series of LaMO$_3$ compounds. Figure 58 shows deduced values for various transfer integrals including $(pd\sigma)$ and $(pd\pi)$ between the metal and other oxygen orbitals. The decreasing trend of their magnitudes with atomic number is in accordance with the spectroscopic estimates shown in Fig. 53. Values for $\varepsilon_d - \varepsilon_p$ deduced simultaneously are plotted in Fig. 59, which again shows the same decreasing trend with metal atomic number as the Δ values deduced from electron spectroscopy (Fig. 51). One can see from the figures that Δ is generally larger than $\varepsilon_d - \varepsilon_p$ by a few eV. This can be understood from the definition of the LDA eigenvalue $\varepsilon_{\mathrm{LDA},d} \equiv \varepsilon_d^0 + (n - \frac{1}{2})U$ [see Eq. (3.29) below] and that of the d-electron affinity level $\varepsilon_d \equiv \varepsilon_d^0 + nU$ [see Eqs. (3.2) and (3.3)].

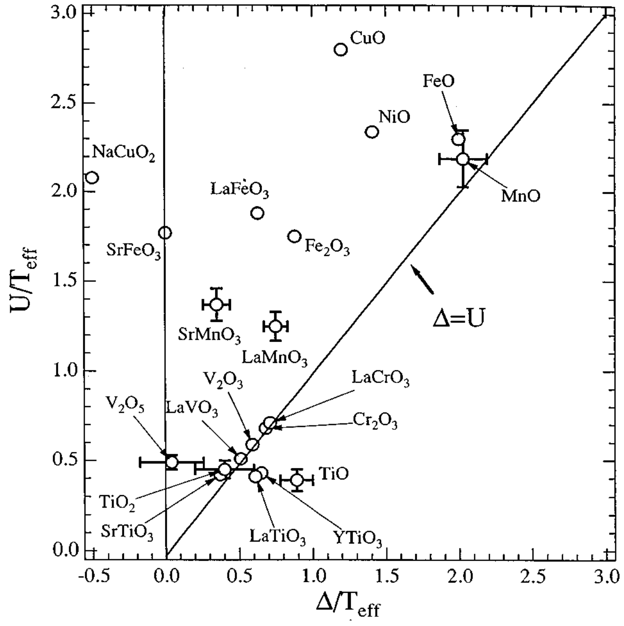

FIG. 54. Zaanen-Sawatzky-Allen U/T_{eff}-Δ/T_{eff} plot for $3d$ transition-metal oxides (Bocquet *et al.*, 1996).

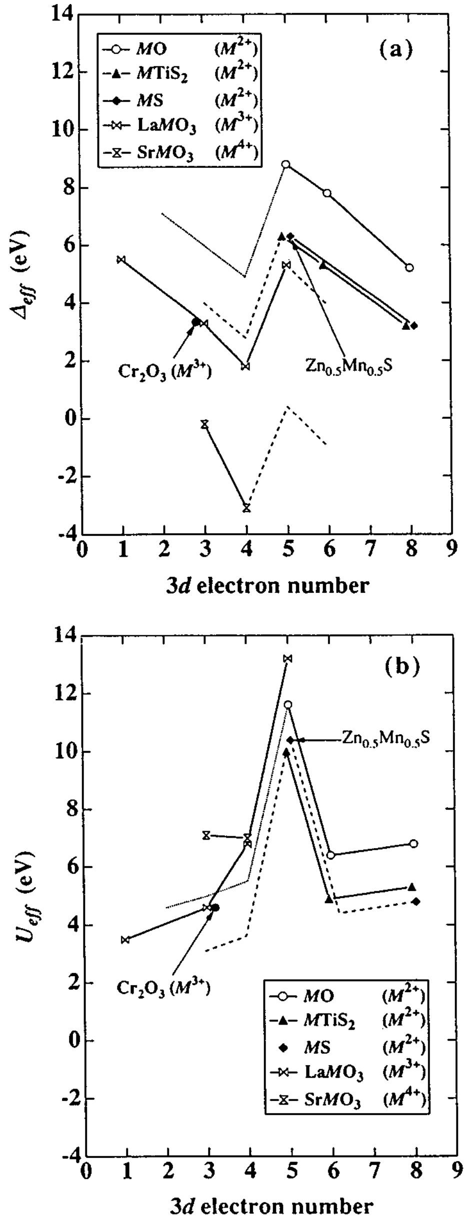

FIG. 55. Effective charge-transfer energy Δ_{eff} (a) and effective averaged d-d Coulomb energy U_{eff} (b) of $3d$ transition-metal oxides plotted against the nominal d-electron number n. The dotted line for MO is deduced from the extrapolated values of Δ and U for MO. Dashed lines represent behaviors expected from the systematic variation of the parameters. From Saitoh, Bocquet, *et al.*, 1995a.

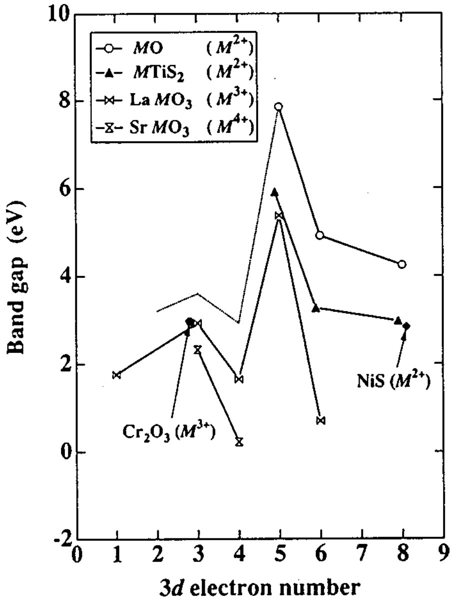

FIG. 56. Band gaps E_{gap} of $3d$ transition-metal compounds calculated using the cluster model. The dotted line for MO represents the calculated results using the extrapolated values of Δ and U for MO (Saitoh, Bocquet, *et al.*, 1995a).

The Coulomb interaction parameter U in solids can be calculated using constrained local-density functional techniques (McMahan *et al.*, 1989, 1990; Gunnarsson *et al.*, 1989; Hybertsen *et al.*, 1990). In the L(S)DA, the one-electron potential at a given spatial point $\mathbf{r}$ is approximated by a function of the charge density at that point $\mathbf{r}$, $\rho(\mathbf{r})$ [and the spin density $\sigma(\mathbf{r})\equiv\rho_{\uparrow}(\mathbf{r})-\rho_{\downarrow}(\mathbf{r})$]. If we use atomic orbitals as the basis set, the total energy of a transition-metal atom is given by the d-electron number n at the atomic site (which is here regarded as a continuous variable) as

$$E_{\mathrm{LDA}}(n)=E_0+n\varepsilon_d^0+\frac{1}{2}n(n-1)U, \tag{3.28}$$

when the orbitals are not spin polarized. The one-electron eigenvalue of the atomic d orbital is given by the derivative of the total-energy functional with respect to n:

$$\varepsilon_{\mathrm{LDA},d}(n)=\frac{\partial E_{\mathrm{LDA}}(n)}{\partial n}=\varepsilon_d^0+\left(n-\frac{1}{2}\right)U. \tag{3.29}$$

Therefore U is given by the n derivative of the eigenvalue $\varepsilon_{\mathrm{LDA}}$:

$$U=\frac{\partial\varepsilon_{\mathrm{LDA},d}}{\partial n}. \tag{3.30}$$

In order to evaluate this quantity, one calculates $\varepsilon_{\mathrm{LDA},d}$ for various fixed n values. To do so, one employs the constrained LDA method in the impurity model or the supercell model, in which the transfer integrals connecting the d atomic orbitals of the central transition-metal ion with surrounding orbitals (including anion p) are set to zero, making n a good quantum number. The surrounding orbitals are allowed to relax as a function of the change in n in order to include solid-state screening effects in self-consistent calculations for the U value.

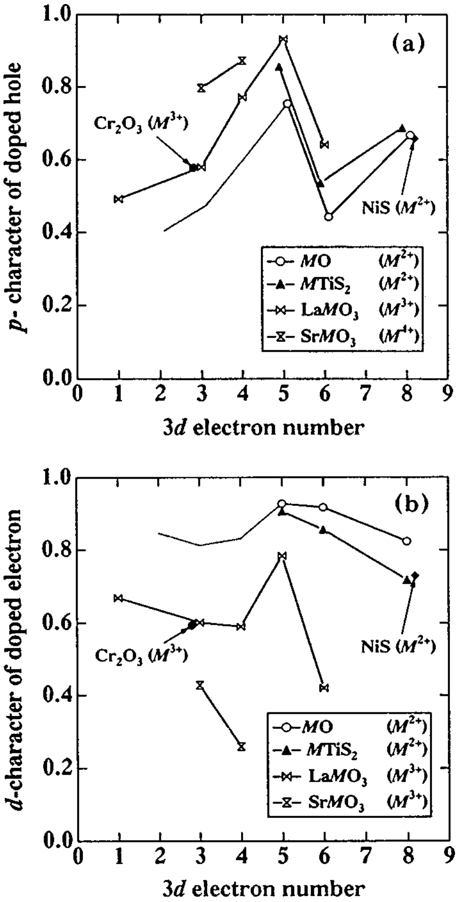

FIG. 57. Character of doped electron and hole in $3d$ transition-metal compounds: (a) p character of the doped hole C_{hole}^{p}; (b) d character of the doped electron C_{el}^{d}. From Saitoh, Bocquet, *et al.*, 1995a.

In order to deduce the charge-transfer energy Δ, the affinity level, $E(d^{n+1})-E(d^n)=\varepsilon_d$ [Eq. (3.3)], or the ionization level $E(d^n)-E(d^{n-1})=\varepsilon_d-U$ of the d orbital has to be evaluated. For this purpose, Slater's transition-state rule (Slater, 1974) is utilized:

$$\varepsilon_d\equiv E_{\mathrm{LDA}}(d^{n+1})-E_{\mathrm{LDA}}(d^n)=\varepsilon_{\mathrm{LDA},d}(n+\tfrac{1}{2}), \tag{3.31}$$

which also follows from Eqs. (3.28) and (3.29). Slater's transition-state rule can also be applied to evaluate U:

$$\begin{aligned}U&\equiv[E(d^{n+1})-E(d^n)]-[E(d^n)-E(d^{n-1})]\\&=\varepsilon_{\mathrm{LDA},d}(n+\tfrac{1}{2})-\varepsilon_{\mathrm{LDA},d}(n-\tfrac{1}{2}).\end{aligned} \tag{3.32}$$

The p-level energy ε_p is assumed to be correctly given by the LDA eigenvalue.

When the system is spin polarized, the LSDA functional becomes a function not only of $n\equiv n_{\uparrow}+n_{\downarrow}$ but also of the d-electron number of each spin, $n_{\uparrow}$ and $n_{\downarrow}$:

$$\begin{aligned}E_{\mathrm{LSDA}}(n_{\uparrow},n_{\downarrow})&=E_0+n\varepsilon_d^0+\frac{1}{2}n(n-1)U\\&\quad-\frac{1}{2}n_{\uparrow}(n_{\uparrow}-1)J-\frac{1}{2}n_{\downarrow}(n_{\downarrow}-1)J,\end{aligned} \tag{3.33}$$

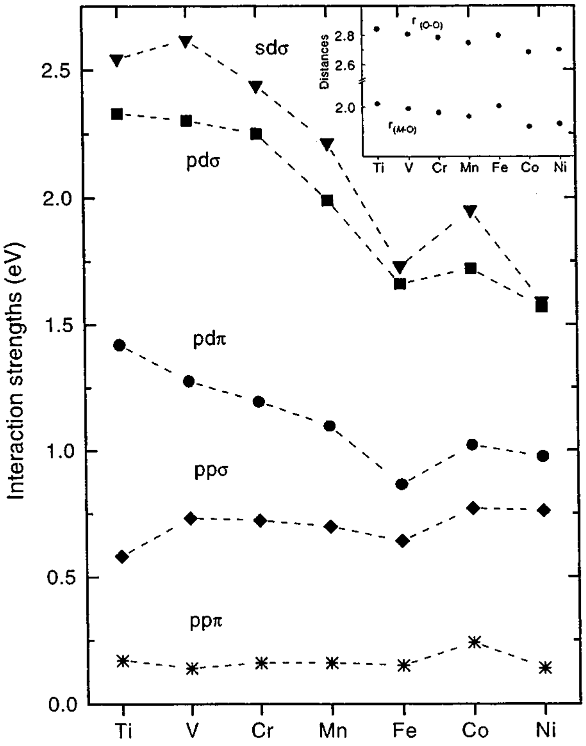

FIG. 58. Various p-d and p-p transfer integrals in the $3d$ transition-metal oxide series LaMO$_3$ derived from a tight-binding fit to the LDA band structures (Mahadevan *et al.*, 1996). The inset shows the metal-oxygen and oxygen-oxygen distances in Å.

where $J(\equiv j \equiv J_H/2)$ is the exchange integral between the d electrons. The one-electron eigenvalues of the spin-up and spin-down d levels are given by (Anisimov *et al.*, 1991)

$$\varepsilon_{\mathrm{LSDA},d\sigma}(n_\uparrow,n_\downarrow)=\frac{\partial E_{\mathrm{LSDA}}(n_\uparrow,n_\downarrow)}{\partial n_\sigma}$$

$$=\varepsilon_d^0+(n-\tfrac{1}{2})U-(n_\sigma-\tfrac{1}{2})J, \quad (3.34)$$

where $\sigma=\uparrow$ or $\downarrow$. Using this expression, one can estimate the parameters U and J by

$$U=\varepsilon_{\mathrm{LSDA},d\uparrow}\left(\frac{n}{2}+\frac{1}{2},\frac{n}{2}\right)-\varepsilon_{\mathrm{LSDA},d\uparrow}\left(\frac{n}{2}+\frac{1}{2},\frac{n}{2}-1\right), \quad (3.35)$$

$$J=\varepsilon_{\mathrm{LSDA},d\downarrow}\left(\frac{n}{2}+\frac{1}{2},\frac{n}{2}-\frac{1}{2}\right)-\varepsilon_{\mathrm{LSDA},d\uparrow}\left(\frac{n}{2}+\frac{1}{2},\frac{n}{2}-\frac{1}{2}\right). \quad (3.36)$$

Here, it should be noted that setting $n_\uparrow=n_\downarrow=\frac{1}{2}n$ in Eq. (3.35) does not reduce to Eq. (3.32), meaning that the definition of U is different between the two expressions. J in Eq. (3.36) is equal to j, and U in Eq. (3.35) is a certain average of u and u' (see Table II). Parameters thus estimated are listed in Table III for some $3d$ transition-metal monoxides (Anisimov *et al.*, 1991). A serious shortcoming of this method is that the Coulomb energy tends to be overestimated for light $3d$ transition-metal oxides: U's for TiO and VO were calculated too large, as shown in Table III, and hence these compounds are incorrectly predicted to be wide gap insulators. This is related to the problem of how well the constrained LDA works in describing the screening process in the solid state and also to the problem of how one can define localized orbitals in a strongly hybridized system.

C. Control of model parameters in materials

1. Bandwidth control

The electron correlation strength can be controlled by modifying the lattice parameters or the chemical composition while essentially maintaining the original lattice structure. The on-site (U) or intersite (V) Coulomb interaction is kept almost unchanged during the above procedure and hence control of electron correlation strength is usually achieved by control of the transfer interaction (t) or the one-electron bandwidth (W). One method of controlling W is the application of pressure. In general, an application of hydrostatic pressure decreases the interatomic distance and hence increases the transfer interaction. Pressure-induced Mott-insulator-to-metal transitions are observed typically for V$_2$O$_3$ (see Sec. IV.A.1) and RNiO$_3$ (R=Pr and Nd; see Sec. IV.A.3). Hydrostatic pressure is an ideal perturbation that modifies W and that is suitable for investigating the critical behavior of the phase transition. To derive a more quantitative picture of the transition, however, we need to know the lattice structural change under a pressure that is usually not so easy to determine. In particular, in the anisotropic crystals, such as a layered perovskite structure, anisotropic compressibility affects W in a complex manner.

Another method of W control is modification of the chemical composition using the solid solution or mixed-crystal effect. In the case of transition-metal compounds, the electron correlation arises from a narrow d band.

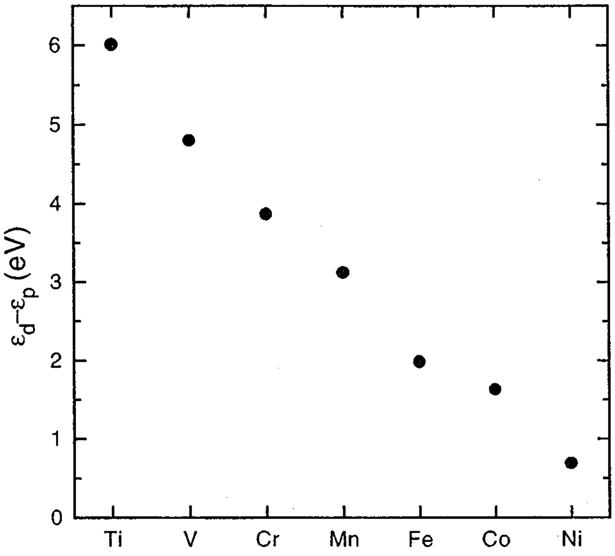

FIG. 59. Variation of $\varepsilon_d-\varepsilon_p$ for the LaMO$_3$ series with the metal M element. From Mahadevan *et al.*, 1996.

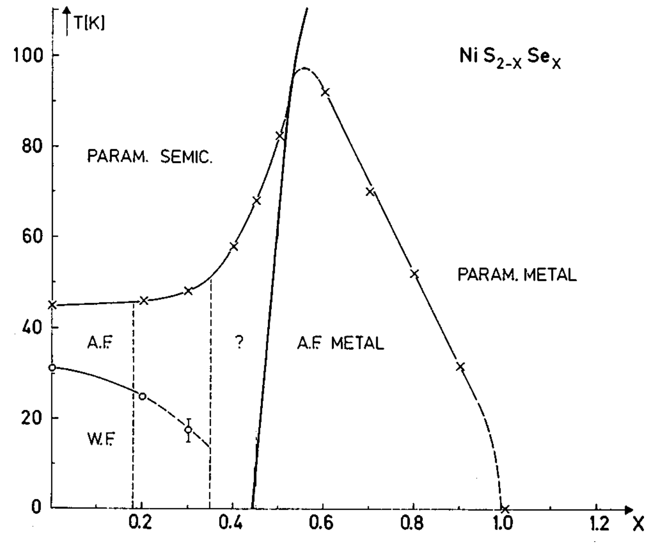

FIG. 60. Phase diagram of $NiS_{2-x}Se_x$ in the plane of temperature and x (Czjzek *et al.*, 1976; Wilson and Pitt, 1971).

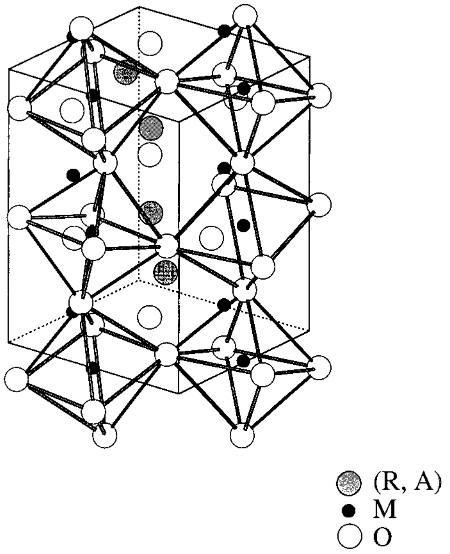

FIG. 61. Orthorhombically distorted perovskite ($GdFeO_3$-type) structure.

Therefore alloying of the transition-metal cations should be avoided for W control, and the solid solution in other chemical sites is usually attempted. One of the best-known examples of this W control is the case of $NiS_{2-x}Se_x$ crystals (Wilson, 1985). The schematic metal-insulator phase diagram for $NiS_{2-x}Se_x$ is shown in Fig. 60 (see Sec. IV.A.2 for the details and references). The parent compound NiS_2 is a charge-transfer insulator with the charge gap between the Ni $3d$-like state (upper Hubbard band) and the S_2 $2p$ band. The partial substitution of Se on the S site enlarges the amalgamated $2p$ band and increases d-p hybridization. Around $x=0.6$ the mixed crystal $NiS_{2-x}Se_x$ undergoes the insulator-metal transition at room temperature. At low temperatures, the antiferromagnetic metal (AFM) state exists in between the Pauli paramagnetic metal (PM) and antiferromagnetic insulator phase. It has been confirmed that an application of hydrostatic pressure near the AFM-PM phase boundary reproduces a change in the transport properties like that observed in the case of x control, indicating a nearly identical role of pressure and compositional control.

Another useful method of W control for a perovskite-type compound (ABO_3, see Fig. 61) is modification of the ionic radius of the A site. The lattice distortion of the perovskite ABO_3 is governed by the so-called tolerance factor f, which is defined as

$$f=(r_A+r_O)/\sqrt{2}(r_B+r_O). \tag{3.37}$$

Here, r_i ($i=A$, B, or O) represents the ionic size of each element. When f is close to 1, the cubic perovskite structure is realized, as shown in Fig. 62. As r_A or equivalently f decreases, the lattice structure transforms to rhombohedral and then to orthorhombic ($GdFeO_3$-type) structure (Fig. 61), in which the B-O-B bond is bent and the angle is deviated from 180°. In the case of the orthorhombic lattice (the so-called $GdFeO_3$-type lattice), the bond angle (θ) varies continuously with f (Marezio *et al.*, 1970; MacLean *et al.*, 1979), as shown in Fig. 62, nearly irrespective of the species of A and B. The bond angle distortion decreases the one-electron bandwidth W, since the effective d electron transfer interaction between the neighboring B sites is governed by the supertransfer process via the O $2p$ state. For example, let us consider the hybridization between the $3d$ e_g state and the $2p$ σ state in a $GdFeO_3$-type lattice composed of the quasi-right BO_6 octahedral tilting alternatively (see Fig. 61). In the strong-ligand-field approximation, the p-d transfer interaction t_{pd} is scaled as t_{pd}^0 $\cos(\pi-\theta)$, where

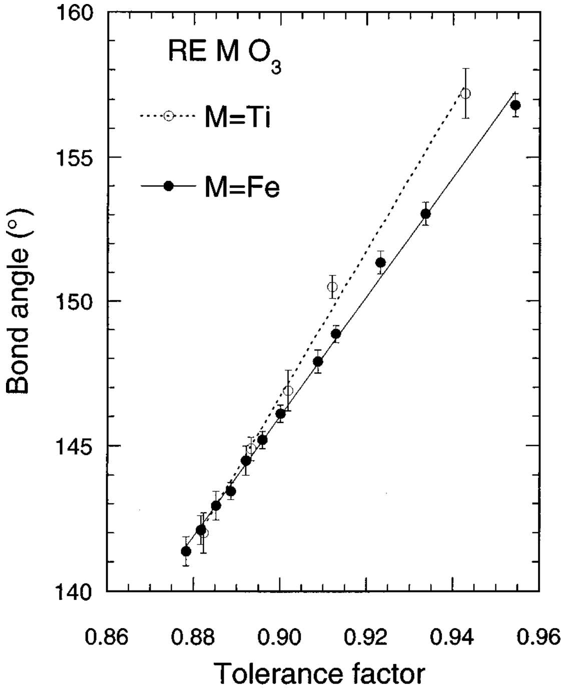

FIG. 62. The metal-oxygen-metal bond angles in an orthorhombically distorted perovskite ($GdFeO_3$-type) as a function of tolerance factor.

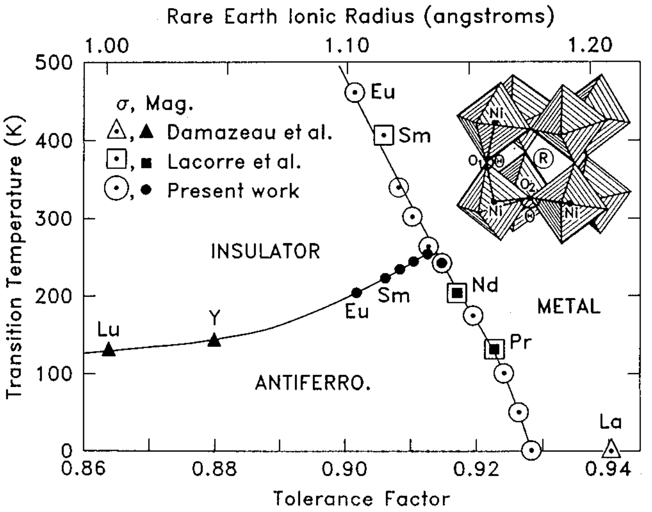

FIG. 63. Electronic phase diagram of RNiO$_3$ (Torrance *et al.*, 1992).

t_{pd}^0 is the value for the cubic perovskite. Thus W is approximately proportional to $\cos^2\theta$. A similar relation will hold approximately for the one-electron bandwidth of the t_{2g} electron state, although a more complicated calculation for distortion-induced mixing between the t_{2g} and $2p$ σ orbitals is necessary (Okimoto *et al.*, 1995b).

An advantage of using a distorted perovskite for W control is that the A site is not directly relevant to the electronic properties inherent in the B-O network and also that the W value can be varied to a considerable extent (by 30–40 %) by choice of different rare-earth or alkaline-earth cations as the A-site element. The best example of successful W control is the MIT for RNiO$_3$, with R being the trivalent rare-earth ions (La to Lu). The MI phase diagram for RNiO$_3$ derived by Torrance *et al.* (1992) is shown in Fig. 63. The tolerance factor f as the abscissa represents the variation of the one-electron bandwidth or the degree of p-d hybridization t_{pd}. The effective valence of Ni in RNiO$_3$ is $3+$ and hence the d electron configuration is $t_{2g}^6 e_g^1$ with $S=1/2$. LaNiO$_3$ with the maximal t_{pd} is metallic, while the other RNiO$_3$ compounds with smaller f or t_{pd} are charge-transfer insulators with an antiferromagnetic ground state. The MI phase boundary is slanting in the T-f plane, as shown in Fig. 63. For example, PrNiO$_3$ shows a first-order I-M transition around 200 K associated with an abrupt change in the lattice parameters and the sudden onset of antiferromagnetic spin ordering. For the smaller-f region, however, the paramagnetic insulating phase is present above the antiferromagnetic insulating phase, as in most of the correlated insulators. Again, an application of pressure increases t_{pd} and in fact drives the IM transition for PrNiO$_3$ and NdNiO$_3$ because these two compounds are located in the vicinity of the MI phase boundary. (See Sec. IV.A.3 for the details.)

Such a strategy for W control in the perovskite-type compounds has been widely used. In Sec. IV, we shall see ample examples of W control not only for the parent (integer-n) compounds but also for the carrier-doped compounds such as $R_{1-x}A_xM$O$_3$ ($M=$Ti, V, Mn, and Co), where the averaged ionic size of the rare-earth (R) and alkaline-earth (A) ions on the perovskite A sites can be systematically modified.

2. Filling control

The importance of filling control in correlated metals has been widely recognized since the discovery of high-temperature superconductivity as a function of filling in the layered cuprate compounds. The standard method of filling control is to utilize ternary or multinary compounds in which ionic sites other than the $3d$ ($4d$) or $2p$ electron related sites can be occupied by different-valence ions. For example, the band filling (n) of La$_{2-x}$Sr$_x$CuO$_4$ is controlled by substitution of divalent Sr on the trivalent La sites and is given by the relation; $n=1-x$. Similarly, a number of filling-controlled compounds can be made by forming the A-site mixed crystals of perovskites, such as La$_{1-x}$Sr$_x$$MO_3$, M being the $3d$ transition-metal element. Taking the correlated insulator (Mott or CT insulator with $n=$integer filling) as the parent compound, we customarily use the nomenclature "hole doping" when the band filling is decreased and "electron-doping" when it is increased, although the carriers are not necessarily hole-like or electron-like.

Among a number of ternary and multinary compounds, perovskite and related compounds are quite suitable for filling control since their structure is very tough in withstanding chemical modification on the A-site. We show in Fig. 64 a guide map for the synthesis of quasicubic and single-layered (K$_2$NiF$_4$-type) perovskite oxides of $3d$ transition-metals (Tokura, 1994), e.g., (La,Sr)MO$_3$ and (La,Sr)$_2$$MO_4$, with a variable number of $3d$ electrons (or with a variable filling of the $3d$-electron-related band). Black bars indicate the range of the solid solution (mixed-crystal) compounds that have so far been successfully synthesized. We can immediately see that quite a wide range of the band fillings can be achieved by A-site substitution of perovskite-related structures.

For the pseudocubic perovskites of $3d$ transition-metal oxides, we show in Fig. 65 a schematic metal-insulator phase diagram (Fujimori, 1992) with the relative electron correlation strength represented by U/W as an ordinate and the band filling of the 3d band as an abscissa. As described in the previous section, YMO$_3$ shows stronger electron correlation than LaMO$_3$ because of reduced W due to M-O-M bending in the distorted perovskite structure. The $n=$integer filled $3d$ transition-metal oxides with perovskite-type structure are mostly correlated insulators, as can be seen in Fig. 65, apart from LaCuO$_3$ and LaNiO$_3$. A fractional valence or filling drives the system metallic, yet in some cases the compounds remain insulating for large U/W.

Nonstoichiometry or altered stoichiometry for the element composition sometimes plays the role of filling control. A well-known example of this is the case of YBa$_2$Cu$_3$O$_{6+y}$ with variable oxygen content. The $y=1$ compound (YBa$_2$Cu$_3$O$_7$) is composed of CuO$_2$ sheets

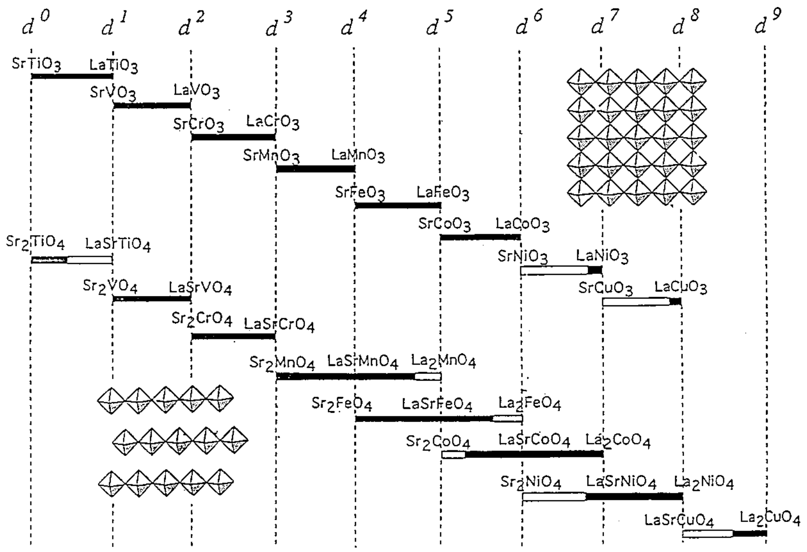

FIG. 64. A guide map for the synthesis of filling-controlled (FC) $3d$ transition-metal oxides with perovskite and layered perovskite (K_2NiF_4-type) structures.

and CuO chains. The nominal valence of Cu on the sheet and chain is estimated to be approximately +2.25 and 2.50, respectively (Tokura *et al.*, 1988). In other words, the holes are almost optimally doped into the sheet to produce superconductivity in this stoichiometric compound. The oxygen content on the chain site can be reduced, either partially ($0<y<1$) or totally ($y=0$), which results in a decrease in the nominal valence of Cu on the sheet, lowering the superconducting transition temperature T_c and finally ($y<0.4$) driving the system to a Mott insulator (or more rigorously, a CT insulator). The nominal valence of the chain-site Cu in the $y=0$ compound is +1 due to the twofold coordination, while that for the $y=1$ compounds is $\approx +2.5$. Thus the nominal hole concentration or Cu valence in the sheet can apparently be controlled by oxygen nonstoichiometry on the chain site, yet it bears a complicated relation to the oxygen content (y) and furthermore depends on the detailed ordering pattern of the oxygen on the chain sites.

Filling control by use of nonstoichiometry (offstoichiometry) has also been carried out for other systems, for example $V_{2-y}O_3$ (see Sec. IV.A.1) and $LaTiO_{3+y}$ (Sec. IV.B.1), which both show the Mott-insulator-to-metal transition with such slight offstoichiometry as $y \leqslant 0.03$. The advantage of utilizing oxygen nonstoichiometry is that one can accurately vary the filling on the same specimen by a post-annealing procedure under oxidizing or reducing atmosphere. Since vacancies or interstitials may cause an additional random potential, the above method is not appropriate for covering a broad range of fillings.

3. Dimensionality control

Anisotropic electronic structure and the resultant anisotropy in the electrical and magnetic properties of d electron systems arises in general from anisotropic network patterns of covalent bondings in the compounds.

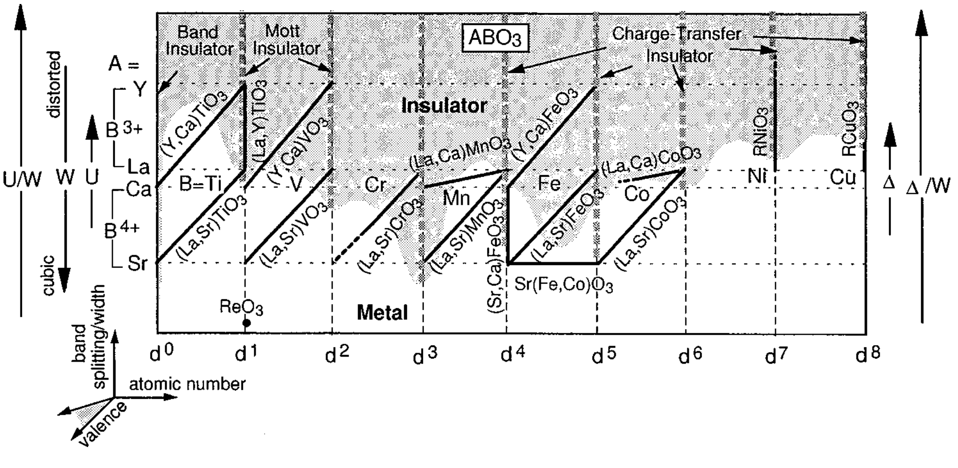

FIG. 65. A schematic metal-insulator diagram for the filling-control (FC) and bandwidth-control (BC) $3d$ transition-metal oxides with perovskite structure. From Fujimori, 1992.

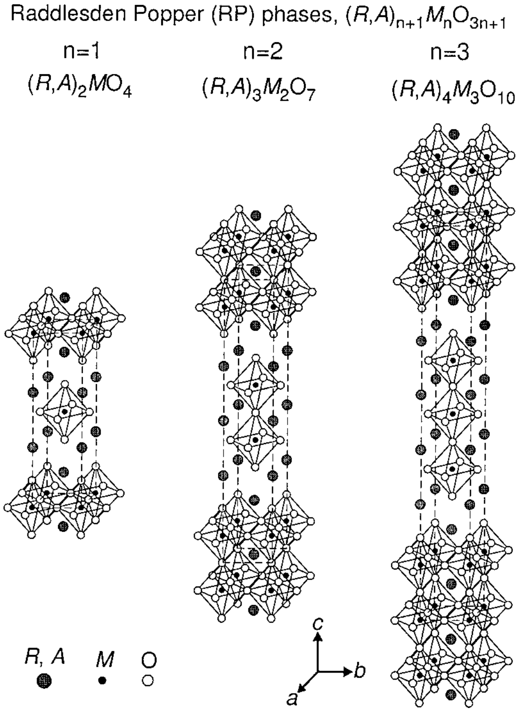

FIG. 66. Ruddlesden-Popper series (layered perovskite structures) $(R,A)_{n+1}M_nO_{3n+1}$ ($n=1$, 2, and 3).

The lowering of the electronic dimensionality causes a variety of essential changes in the electronic properties as well as changes in the interactions among the electron, spin, and lattice dynamics. Systematic control of the electronic dimensionality while keeping the fundamental electronic parameters is usually not so easy. In the ternary or multinary transition-metal oxide compounds, however, we may sometimes find a homologous series in which dimensionality control is possible to a considerable extent, as we show in the following examples.

Typical examples of such a homologous series are the transition-metal oxide compounds with layered perovskite structure (called the Ruddlesden-Popper phase), which are represented by the chemical formula $(R,A)_{n+1}M_nO_{3n+1-y}$, where R and A are the trivalent rare-earth and divalent alkaline-earth ions, respectively, and y is the oxygen vacancy. The layered perovskite structure, $(R,A)_{n+1}M_nO_{3n+1}$, includes in the unit cell two sets of n-MO_2 sheets, which are connected via apical oxygens and separated by an intergrowth (R,A)O layer of rock salt structure, as depicted for $n=1$, 2, and 3 in Fig. 66. The infinite-n analog of a layered perovskite is nothing but the conventional cubic perovskite. Filling control can be executed by alloying the (R,A)-sites, such as $R_{n+1-x}A_xM_nO_{3n+1-y}$. The nominal valence of the transition metal $M(v)$ is given by the relation $v=(3n+x-2y-1)/n$. Thus varying n in the layered perovskite structures corresponds to dimensionality control from two to three dimensions as far as the M-O network shape is concerned. However, the lifting of the d-electron orbital degeneracy in the (pseudo)tetragonal structure and/or the anisotropic distortion of the MO_6 octahedron (e.g., Jahn-Teller distortion) have to be taken into account when considering the anisotropic nature of the electronic states near the Fermi level.

A prototypical series of layered perovskites are the titanates, $Sr_{n+1}Ti_nO_{3n+1}$. They have Ti^{4+} valence (no $3d$ electron) irrespective of n, showing the fairly wide $2p-3d$ gap exceeding 3 eV. The best known example of a layered perovskite is $La_{2-x}A_xCuO_4$ ($A=$Ba, Sr, or Ca) with $n=1$ structure or the so-called K_2NiF_4 structure. This was the first compound of the high-temperature superconducting cuprates discovered by Bednorz and Müller (1986). The $n=2$ analogs of the cuprates are $La_{2-x}Ca_{1+x}Cu_2O_6$ or $(La_{2-x}Sr_x)CaCuO_6$, which are also superconducting for the appropriate doping range, e.g., at $x\sim0.3$ (Cava *et al.*, 1990). The compounds are regularly oxygen deficient ($y=1$) at the apical positions in between a pair of CuO_2 sheets and hence form a nearly isolated Cu-O sheet composed of CuO_5 pyramidal, not octahedral, units. Similar $n=1,2,3,\ldots$ analogs of the layered perovskite structure are often seen as essential building blocks of the high-temperature superconducting cuprates, e.g., in the compounds containing BiO, TlO, or HgO layers. In those cases, however, each CuO_2 sheet is always nearly isolated by the oxygen-deficient layer or by the absence of the apical oxygens and retains its essentially single-CuO_2-layer structure as well.

In contrast, a literally dimensional crossover with n (the number of MO_2 sheets) has been observed in some 3d transition-metal oxides with layered perovskite structure. One such example is $Sr_{n+1}V_nO_{3n+1}$ ($n=1$, 2, 3, and infinite), in which the nominal electronic configuration of the V ion is always $3d^1$ ($S=1/2$). The single-layered ($n=1$) compound shows an insulating behavior over the whole temperature region, whereas the $n\geqslant2$ compound is metallic down to near-zero temperature (Nozaki *et al.*, 1991). Another example of a layered perovskite family showing the insulator-metal transition with n is the case of $(La,Sr)_{n+1}Mn_nO_{3n+1}$. As described in detail in Sec. IV.F, the perovskite manganites undergo a phase change from antiferromagnetic insulator (Mott insulator) to ferromagnetic metal with hole doping, e.g., by partial substitution of Sr on the La sites. Such a ferromagnetic metallic state is stabilized to gain the kinetic energy of doped carriers under the so-called double-exchange interaction. The single-layered ($n=1$) compounds $La_{1-x}Sr_{1+x}MnO_4$ are insulators with antiferromagnetic or spin-glass-like ground states over the whole nominal hole concentration (x). (The $x=0$ corresponds to a parent Mott insulator with a nominal valence of Mn^{3+}). On the other hand, the ferromagnetic metallic state appears around $x=0.3-0.4$ in the double-layer ($n=2$) compounds, $La_{2-x}Sr_{1+x}Mn_2O_7$, perhaps due to an increased double-exchange interaction with effective increase of dimensionality, in which high anisotropy in magnetic and electronic properties is observed (see Sec. IV.F.2). A doped hole in the manganites has an orbital degree of freedom in the e_g state, and hence the lifting of orbital degeneracy as well as the

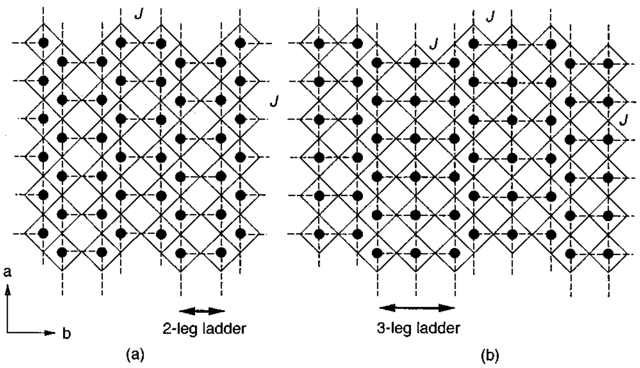

FIG. 67. Schematic structures of spin-ladder chain systems, $Sr_{n-1}Cu_{n+1}O_{2n}$ ($n=3$ and 5). From Azuma *et al.*, 1994.

effective decrease of W should be taken into account when considering the variation of electronic properties with n.

A new homologous series of the ladder chain systems of the copper oxides, $Sr_{n-1}Cu_{n+1}O_{2n}$, may be viewed as a successful example of dimensionality control between 1D and 2D. The structures are depicted for $n=3$ and 5 in Fig. 67. The $n=\infty$ compound corresponds to the so-called infinite-layer compound, $SrCuO_2$ (higher-pressure phase), which is composed of alternating sheets of CuO_2 and Sr. A strong antiferromagnetic exchange interaction (of the order of 0.1 eV) works between the $S=1/2$ spins on the Cu^{2+} sites connected via the corner oxygens (i.e., on the corner-sharing Cu sites) but not on the edge-sharing Cu sites. Thus the Cu-O networks shown in Fig. 67 can be viewed as representing the two-leg and three-leg antiferromagnetic Heisenberg spin-ladder systems. It was theoretically predicted (Dagotto, Riera, and Scalapino 1992; Rice *et al.*, 1993) that the even-leg chains would show the singlet ground-state with a spin gap, while the odd-leg chains would have no spin gap.

Takano and co-workers (Hiroi *et al.*, 1991; Azuma *et al.*, 1994; Hiroi and Takano, 1995) have succeeded in preparing a series of these spin-ladder compounds, $n=3$, 5, and infinite, with use of an ultrahigh-pressure furnace. In fact, they have observed a spin-gap behavior in the temperature dependence of the magnetic susceptibility and the NMR relaxation rate (T_1) for the $n=3$ compound, but not for the $n=5$ compound. Dagotto, Riera, and Scalapino (1992) and Rice *et al.* (1993) predicted theoretically that hole-doping in a spin-ladder system with a spin gap might produce the metallic state with a pseudo spin gap in the underdoped region and give rise to novel superconductivity. Unfortunately, carrier doping has not been successful up to now for the spin-ladder systems shown in Fig. 67. However, it is possible for somewhat modified spin-ladder systems, and in fact superconductivity was discovered (Uehara *et al.*, 1996), as detailed in Sec. IV.D.1.

IV. SOME ANOMALOUS METALS

In Table IV we summarize the basic properties of compounds discussed in this section.

A. Bandwidth-control metal-insulator transition systems

1. V_2O_3

Vanadium sesquioxide V_2O_3 and its derivatives have been extensively studied over the past three decades as the canonical Mott-Hubbard system. The discovery of high-temperature superconductivity in the doped cuprates has revived interest in the vanadium and titanium oxides with many similar ingredients for correlated metallic states in close proximity to insulating antiferromagnetic states. As for undoped and doped V_2O_3, the literature is vast (>500 papers), yet a review by Mott (1990) summarizes the basic features (see also Brückner *et al.*, 1983). Here, we should like to focus on recent advances in the study of V_2O_3 achieved in the 1990s.

V_2O_3 shows the corundum structure (Fig. 68), in which the V ions are arranged in V-V pairs along the c axis and form a honeycomb lattice in the ab plane. The oxidation state of V ions is V^{3+} with $3d^2$ configuration. Each V ion is surrounded by an octahedron of O atoms. The t_{2g} orbitals are subject to lifting of degeneracy due to trigonal distortion of the V_2O_3 lattice and splitting into nondegenerate a_{1g} and doubly degenerate e_g levels. This set of t_{2g} levels forms a group of subbands which are isolated in energy but do not decouple further within the subbands. A recent LDA band-structure calculation by Mattheiss (1994) confirms this feature. On the other hand, the c-axis V-V pairs have a large overlap of orbitals in the a_{1g} levels and hence it has been assumed in many theoretical studies that one electron per V atom resides in a singlet bond of a_{1g} levels and the remaining electron is accommodated in the doublet e_g levels. However, as we discuss below, the electronic state of this material is still controversial.

Direct information about the electronic structure of V_2O_3 has been obtained by photoemission and x-ray absorption spectroscopic studies since the 1970s. As shown in Fig. 69, the valence-band photoemission spectra of V_2O_3 show the O $2p$ band located from ~ -4 to ~ -10 eV and the V $3d$ band within ~ 3 eV of the Fermi level (E_F), apparently indicating a typical Mott-Hubbard-type electronic structure, i.e., $\Delta > U$ (Shin *et al.*, 1990). The peak of the V $3d$ band (at 1–1.5 eV below E_F) shows a weak dispersion of ~ 0.5 eV according to angle-resolved photoemission spectroscopy (Smith and Henrich, 1988). This assignment was confirmed by a resonant photoemission study, in which a strong enhancement of the near-E_F feature was observed for photon energies above the V $3p \rightarrow 3d$ core absorption threshold ($h\nu \gtrsim 45$ eV), as shown in the figure. However, hybridization between the O $2p$ and V $3d$ states is substantial, as indicated by their having nearly the same Δ and U values (~ 4 eV), as described in Sec. III.B (Bocquet *et al.*, 1996). If one applies the local-cluster configuration-interaction picture to V_2O_3, the V $3d$ band just below E_F in the photoemission spectra is described as made up of bonding states which are formed between the d^1 and $d^2\underline{L}$ configurations in the $(N-1)$-electron final state and are pushed out of the p-band continuum (i.e., $d^2\underline{L}$) due to strong p-d

TABLE IV. Basic physical properties near metal-insulator transitions for d-electron systems discussed in this article. The compounds are listed in the same order as their appearance in Sec. IV. The representative cases of the properties summarized here can be found in figures in the corresponding subsections of Sec. IV. The following abbreviations are used: Mott-Hubbard type (MH), charge-transfer type (CT), antiferromagnetic order (AF), ferrimagnetic order (Ferri), paramagnetic (P), superconducting (SC), spin-density wave (SDW), filling control (FC), bandwidth control (BC), temperature control (T), continuous transition (C), crossover (CR), accompanied by a change of structural symmetry (S), enhanced Pauli paramagnetic (ePp), enhanced specific heat $\gamma(e)$. The following notations are also used: T_{CO} (charge ordering transition temperature), T_c (superconducting transitions temperature), T_C (ferromagnetic Curie temperature), T_N (Néel temperature), x_c (critical concentration for MIT). The asterisks indicate that data are not available, while "text" indicates that details are given in the text (Sec. IV). The resistivity denoted as "diffuse" indicates that the temperature dependence is rather flat with weakly metallic dependence at high temperatures. The description of the magnetic susceptibility in metals is for the paramagnetic states outside the magnetically ordered state near the MIT. The unit of temperature T, the uniform magnetic susceptibility χ, and the specific-heat coefficient γ are K, 10^{-4} emu/(Avogadro's number of transition-metal ions), and (mJ/K^2)/(Avogadro's number of transition-metal ions), respectively.

	Mott insulator				MIT		Metals near MIT				Spatial dimension of anisotropy	
Compounds	Type		Spin order	T_N(K)	Control parameter	order	ρ	χ	γ	Spin order		Remark
					FC		T^2 for	ePp∼10	e	SDW for FC		strong mass enhancement
V_2O_{3-y}	d^2	MH	AF	∼180	BC	1	BC	for BC	⩽40	P for BC	3	
								∼30–40				
								for FC	for BC			
					T			($y=0.013$)	and FC		corundum	
$NiS_{2-x}Se_x$	d^8	CT	AF	40–80	BC	weakly	T^2	ePp	e	AF	3	$\rho \sim T^{1.5}$ at AF-P transition
	$S=1$				T	1		∼5 [1]	∼20		pyrite	R_H enhanced
RNiO$_3$	d^7	CT	AF	130–	BC	1	T^2	ePp	e	P	3	
	$S=1/2$			240	T			5	14		perovskite	
$NiS_{1-x}Se_x$	d^8	CT	AF	260	(FC)BC	1	T^2	ePp	e	P	3	
					T(260 at						NiAs	
	$S=1$				$x=0$)			1.6–2.4	∼6–7			
$Ca_{1-x}Sr_xVO_3$	—	—	—	—	—	—	T^2	ePp	e	P	3	
								∼2	∼9		perovskite	
$La_{1-x}Sr_xTiO_3$	d^1	MH	AF	140	FC	C	T^2	ePp	e	P	3	typical mass enhancement by FC
	$S=1/2$				$x_c=0.05$			⩽5	⩽17		perovskite	
$La_{1-x}Sr_xVO_3$	d^2	MH	AF	∼150	FC	C	$\sim T^{1.5}$	ePp	e	P	3	
	$S=1$				$x_c=0.2$			∼9.5 [2]	*		perovskite	
$La_{2-x}Sr_xCuO_4$	d^9	CT	AF	300	FC	C	$\sim T$	text		P	2	high-T_c superconductor
	$S=1/2$				$x_c \sim 0.05-$						K_2NiF_4	$T_c \leqslant 40$ K
					0.06				⩽14	SC		
$Nd_{2-x}Ce_xCuO_4$	d^9	CT	AF	∼240	FC	C	$\sim T^2$			P	2	high-T_c superconductor
	$S=1/2$				$x_c \sim 0.14$			*	*	SC		$T_c \leqslant 24$ K
								text				
$YBa_2Cu_3O_{7-y}$	d^9	CT	AF	∼400	FC	C	$\sim T$	(pseudo	⩽18	P	2	high-T_c superconductor
	$S=1/2$				$y_c \sim 0.6$			gap)		SC	perovskite-like	$T_c \leqslant 90$ K
$Bi_2Sr_2Ca_{1-x}R_xCu_2O_{8+\delta}$	d^9	CT	*	*	FC	C	$\sim T$		*	P	2	high-T_c superconductor
	$s=1/2$							⩽0.2 [3]		SC		$T_c \leqslant 90$ K
$La_{1-x}Sr_xCuO_{2.5}$	d^9	CT	AF	110	FC	C	$\sim T^2$	∼1	⩽4 [4]	P	1 (or 3)	near critical point between AF and gapped phase, spin-ladder system
	$S=1/2$				$x_c \sim 0.15$							
$Sr_{14-x}Ca_xCu_{24}O_{41}$	d^9	CT	gap	—	FC	C	$\sim T^2$	∼2	*	P	1 (or 2)	superconductor under pressure at $x \sim 13.5$ ($T_c \sim 10$ K), spin-ladder system
	$s=1/2$				$x_c \sim 13.5$					SC		

TABLE IV. (*Continued*).

	Mott insulator				MIT		Metals near MIT					
Compounds	Type		Spin order	T_N(K)	Control parameter	order	ρ	χ	γ	Spin order	Spatial dimension of anisotropy	Remark
$BaVS_3$	d^1 $S=1/2$	MH	AF	~ 35	T (74 K)	C	diffuse	CW	*	P	1 hexagonal	TL liquid?
Fe_3O_4	d^6,d^5 $S=2,5/2$		Ferri		T (121 K)	1 S	diffuse	—	—	P Ferri	3 spinel	ferrimagnetic $T_c=858$ K charge order $T_{co}=121$ K resistivity is metallic ($d\rho/dT>0$) only at $T>350$ K
$La_{1-x}Sr_xFeO_3$	d^5 $S=5/2$	CT	AF	$740(x=0)$ $134(x=1)$	FC T (at T_{co})	C	diffuse	CW	*	$P(x<0.7)$ or $AF(x=1)$	3 perovskite	charge order $x=0.66$ $T_{co}=210$ K, $d\rho/dT<0$ even at $T>T_{co}$
$La_{2-x}Sr_xNiO_{4+y}$	d^8	CT	AF	~ 500 at $x=y=0$ [5]	FC $x_c\sim 0.7-$ 0.8	C	diffuse	~ 4[6]	*	P	2 K_2NiF_4	charge order $y=0.125$ $T_N=110$ K $x=0.33$ $T_{co}=240$ K, $T_N=180$ K $x=0.5$ $T_{co}=340$ K, $d\rho/dT<0$ even at $T\geqslant T_{co}$
$La_{1-x}Sr_{1+x}MnO_4$	d^4 $S=2$	CT	AF	120	—	—	—	—	—	—	2 K_2NiF_4	charge order $x=0.5$ $T_{co}=217$ K, $T_N=110$ K
$La_{1-x}Sr_xMnO_3$	d^4 $S=2$	CT	AF	140	FC $(x_c\sim 0.17)$	C	T^2	—	$\sim 3-5$	F	3 perovskite	double-exchange system ferromagnetic $T_c\sim 370$ K ($x\sim 0.3$)
$La_{2-2x}Sr_{1+2x}Mn_2O_7$	d^4 $S=2$	CT	*	*	FC $(x_c\sim 0.3)$	C	*	—	*	F	2 perovskite	double-exchange system
FeSi			gap	—	T (300 K)	CR	diffuse	CW	—	P	3 distorted NaCl	
VO_2	d^1	(MH)	gap	—	T (340 K)	1 S	T?	ePp ~ 6	—	P	1 or 3 rutile	
Ti_2O_3	d^1	MH	gap	—	(FC) T 400 K–600 K	CR	diffuse	*	—	P	3 corundum	
$LaCoO_3$	d^6 $S=0,1,$ 2	CT	gap	—	T ~ 500 K	CR	diffuse	CW	—	P	3 perovskite	low-spin, intermediate-spin (high-spin) transition
$La_{1.17-x}A_xVS_{3.17}$	d^2	(MH)	gap	—	FC$(x_c\sim 0.35)$ T (280 K at $x=0.17$)	CR	diffuse	ePp 4.4	e <20	P	2 misfit	
Sr_2RuO_4	—	—	—	—	—	—	$\sim T^2$	ePp 9.7	39	P SC	2 K_2NiF_4	superconducting $T_c\sim 1$ K
$Ca_{1-x}Sr_xRuO_3$	—	—	—	—	—	—	T^2	CW $(x<0.4)$	30 $x=1$	$P(x<0.4)$ $F(x>0.4)$	3 perovskite	

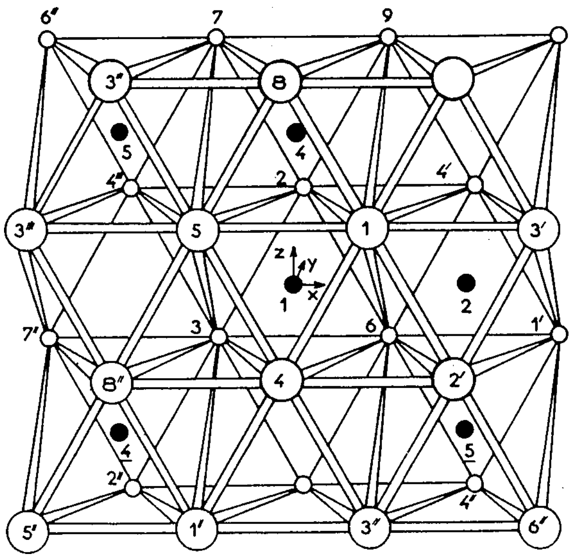

FIG. 68. Corundum structure of V_2O_3.

(d^1-$d^2\underline{L}$) hybridization (Uozumi *et al.*, 1993). Cluster-model analysis has revealed considerable weight of charge-transfer configurations, $d^3\underline{L}, d^4\underline{L}^2, \ldots$, mixed into the ionic d^2 configuration, resulting in a net d-electron number of $n_d \simeq 3.1$ (Bocquet *et al.*, 1996). This value is considerably larger than the d-band filling or the formal d-electron number $n=2$ and is in good agreement with the value ($n_d = 3.0$) deduced from an analysis of core-core-valence Auger spectra (Sawatzky and Post, 1979). If the above local-cluster CI picture is relevant to experiment, the antibonding counterpart of the split-off bonding state is predicted to be observed as a satellite on the high-binding-energy side of the O $2p$ band, although its spectral weight may be much smaller than the bonding state [due to interference between the $d^2 \rightarrow d^1 + e$ and $d^3\underline{L} \rightarrow d^2\underline{L} + e$ photoemission channels; see Eq. (3.12)]. Such a spectral feature was indeed observed in an ultraviolet photoemission study by Smith and Henrich (1988) and in a resonant photoemission study by Park and Allen (1997). In spite of the strong p-d hybridization and the resulting charge-transfer satellite mechanism described above, it is not only convenient but also realistic to regard the d^1-$d^2\underline{L}$ bonding band as an effective V $3d$ band (lower Hubbard band). The $3d$ wave function is thus considerably hybridized with oxygen p orbitals and hence has a relatively small effective U of 1–2 eV (Sawatzky and Post, 1979) instead of the bare value $U \sim 4$ eV. Therefore the effective d bandwidth W becomes comparable to the effective U: $W \sim U$. With these facts in mind, one can regard V_2O_3 as a model Mott-Hubbard system and the (degenerate) Hubbard model as a relevant model for analyzing the physical properties of V_2O_3.

The time-honored phase diagram for doped V_2O_3 systems, $(V_{1-x}Cr_x)_2O_3$ and $(V_{1-x}Ti_x)_2O_3$, is reproduced in Fig. 70. The phase boundary represented by the solid line is of first order, accompanied by thermal hysteresis (Kuwamoto, Honig, and Appel, 1980). In a Cr-doped system $(V_{1-x}Cr_x)_2O_3$, a gradual crossover is observed from the high-temperature paramagnetic metal (PM) to

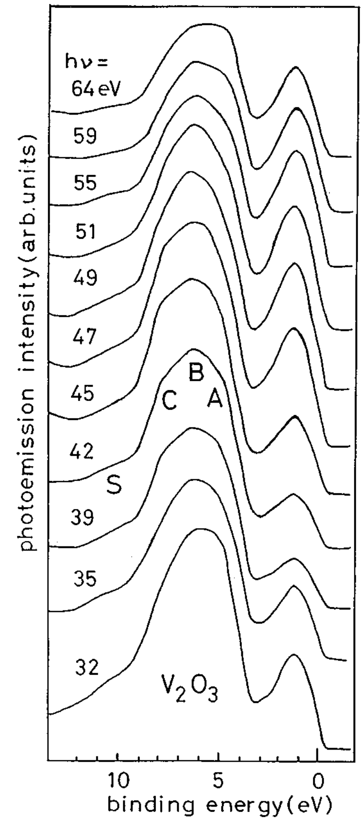

FIG. 69. Photoemission spectra of V_2O_3 in the metallic phase taken using photon energies in the $3p$-$3d$ core excitation region. From Shin *et al.*, 1990.

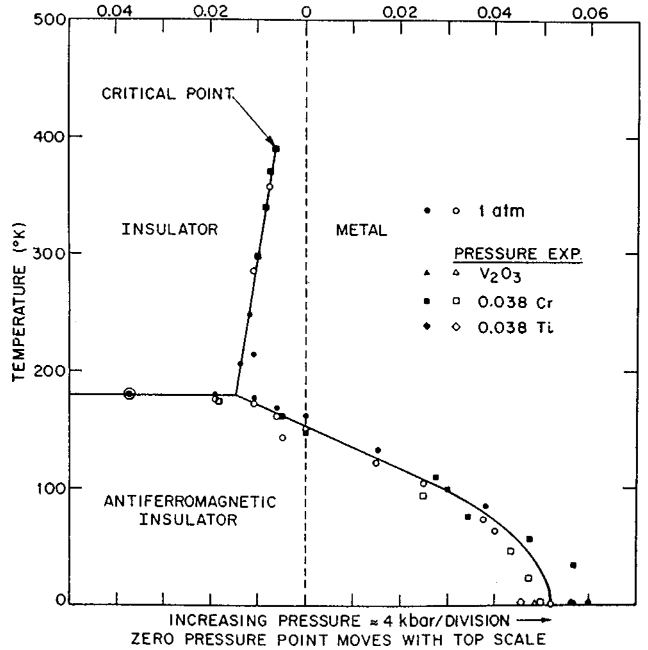

FIG. 70. Phase diagram for doped V_2O_3 systems, $(V_{1-x}Cr_x)_2O_3$ and $(V_{1-x}Ti_x)_2O_3$. From McWhan *et al.*, 1971, 1973.

the paramagnetic insulator (PI) with decreasing temperature from above the 500-K region. In a $(V_{1-x}Cr_x)_2O_3$ ($x=0.03$) crystal, for example, one encounters the three transitions from the high-temperature side: PM to PI, PI to PM, and PM to antiferromagnetic insulator, the last two of which are of first order. Such a reentrant MIT disappears for $x(\mathrm{Cr})<0.05$, and with $x(\mathrm{Ti})>0.05$ the metallic phase dominates over the whole temperature region.

As first theoretically demonstrated by Castellani *et al.* (1978a, 1978b, 1978c), orbital spin coupling of the type (2.8) is particularly important for our understanding of the ordered spin structure in the antiferromagnetic insulating (AFI) phase, since the sign and magnitude of the spin-spin superexchange couplings are dependent on the orbital occupancy. More recently, Rice (1995) stressed that the interaction between orbital and spin degrees of freedom is strong and mutually frustrating, so that the paramagnetic phases may have strong spin and orbital fluctuations which are unrelated to the ordered phase. This may explain the first-order nature of the magnetic order transition because, in general, two competing order parameters easily trigger a first-order transition, as can be seen in the Landau free-energy expansion. Rice's conjecture has been confirmed in a recent inelastic neutron scattering measurement by Bao *et al.* (1997). The momentum dependence of the spin fluctuation in the PM state is not related at all to that of the spin ordering in the AFI state, where the orbital ordering effect is supposed to be important.

The pioneering and extensive work by McWhan and coworkers (McWhan *et al.*, 1973) demonstrated that there is an empirical scaling relating the addition of Ti^{3+} (Cr^{3+}) and external pressures, 0.4 GPa per 0.01 addition of Ti^{3+} and 0.4 Gpa per 0.01 removal of Cr^{3+}. It had been anticipated that the doping of Cr or Ti would not alter the electron counting of the V sites but rather would affect the one-electron bandwidth via a slight modification of the lattice. In the case of Cr doping, the three $3d$ electrons on the impurity Cr-site may be tightly bound, so the above hypothesis holds fairly well. By contrast, the doped Ti atom can be in a mixed valence between $3+$ and $4+$, indicating a possible change in the band filling. Thus the Ti-doping-induced MIT is not purely a BC-MIT but has the character of an FC-MIT.

A difference between Ti doping and application of pressure is seen in the ground state of the metallic state: The Ti-doped metallic crystal ($0.06<x<0.30$) undergoes an antiferromagnetic transition at 10–50 K (Ueda *et al.*, 1979), though this is not shown in Fig. 70. Ueda, Kosuge, and Kachi (1980) also found that an electronic phase diagram similar to the case of Ti doping occurs for O-rich (or equivalently V-deficient) samples ($V_{2-y}O_3$): The AFI abruptly disappears with $y>0.02$ and instead the antiferromagnetic metal (AFM) phase is present below 8–10 K up to $y=0.05$, beyond which the sample shows a phase separation.

The spin structure in the AFM phase was recently determined by neutron scattering for an O-rich crystal (Bao *et al.*, 1993; Bao, Broholm, *et al.*, 1996). The phase diagram for a $V_{2-y}O_3$ system as a function of both pressure (P) and y is displayed in Fig. 71. Notably, the metallic $V_{2-y}O_3$ develops a spiral spin-density wave (SDW) below $T_N=9$ K (in the AFM phase), with incommensurate wave vector $q\approx 1.7c^*$. The incommensurate spin structure is depicted in Fig. 72: The ordered spin for $y=0.027$ is in the basal plane with a magnitude of $0.15\mu_B$, forming a perfect planar honeycomb antiferromagnet, and spins in the nearest-neighbor plane are almost perpendicular. More recently, a nearly identical

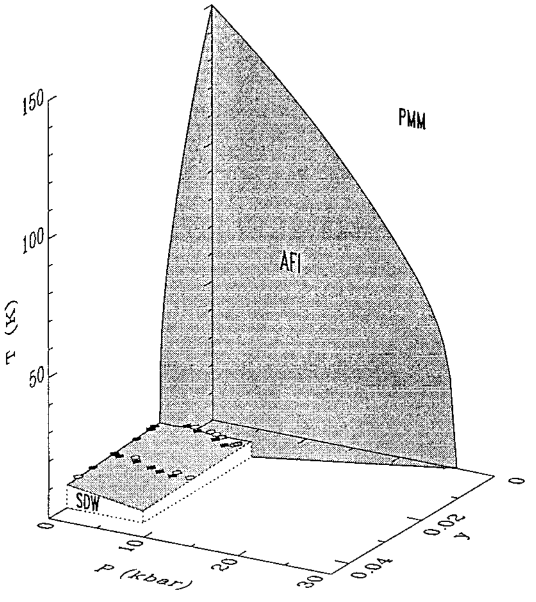

FIG. 71. Phase diagram for $V_{2-y}O_3$ system as a function of both pressure (P) and y (Carter *et al.*, 1993, 1994). From Bao *et al.*, 1993.

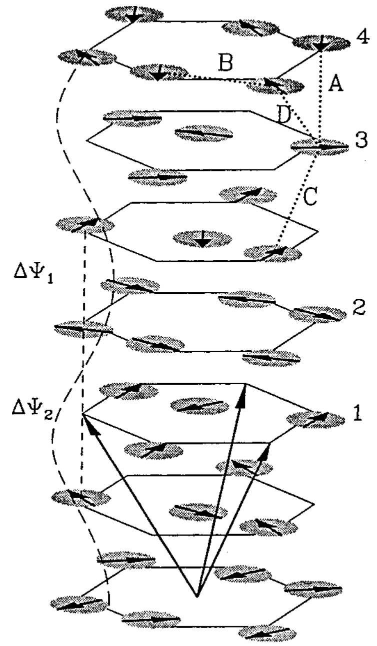

FIG. 72. Incommensurate spin structure of $V_{2-y}O_3$. From Bao *et al.*, 1993.

spin structure and moment were confirmed to be present in the AFM phase for a Ti-doped ($x = 0.05$) crystal.

In contrast with the robust helical SDW phase against y in $V_{2-y}O_3$, pressure above 2 GPa transforms a neat V_2O_3 crystal to the low-temperature metallic state without magnetic order (McWhan *et al.*, 1973; Carter *et al.*, 1994). Importantly, there is no sign of superconductivity down to 350 mK in this BC-MIT (Carter *et al.*, 1994). The magnetic properties of such a pressurized metallic state were investigated by measurements of the ^{51}V NMR Knight shift and the spin-lattice relaxation rate ($1/T_1$; Takigawa *et al.*, 1996). [At 1.83 GPa, the highest pressure attainable in that measurement, a major fraction of the sample showed the MIT around 70 K, while a finite fraction (about 4%) of the PM phase remained at the lowest temperature for unidentified reasons but not due to the presence of impurities or nonstoichiometry.] The spin susceptibility deduced from the Knight-shift data has a maximum at 40 K. Also, a peak was observed in the $1/T_1T$ versus T curve at 8 K. These phenomena resemble the spin-gap behavior observed in lightly doped (underdoped) cuprate superconductors (see Sec. IV.C.3), although the temperature scale differs by nearly one order of magnitude. At the moment, it is not clear whether this "gap" behavior arises from the spin contribution or the orbital one due to orbital degeneracy (Castellani *et al.*, 1978a, 1978b, 1978c; Rice, 1995). Such an anomalous metallic state in pressurized V_2O_3 is particularly interesting in light of the possibility of a spin-gapped metal or an orbital contribution and warrants further study.

The Ti-doping-induced or V-deficiency-induced MIT is easier to investigate experimentally than the undoped case, which needs relatively high pressure. However, the robust presence of the SDW in the AFM phase complicates the interpretation of $T = 0$ MIT in terms of the canonical Hubbard model. Nearly a quarter of a century ago, McWhan and co-workers (1971) found that the T-linear term in the heat capacity in the Ti-doped ($x = 0.08$) metallic state was very large ($\gamma = 80\,\mathrm{mJ\,K^{-2}}$ per mol. of V_2O_3) and that the Wilson ratio $\chi/\gamma = 1.8$. On the other hand, the Hall coefficient for the metallic V_2O_3 both under pressure (2 GPa, $T = 4.2$ K) and at ambient pressure ($T = 150$ K), is $+(3.5 \pm 0.4) \times 10^{-4}$ cm^3/C, indicating nearly one hole-type carrier per V site. Such a large mass enhancement effect has been interpreted as a clear manifestation of Brinkman-Rice-type mass renormalization on the verge of the BC-MIT. One may notice, however, that the low-temperature metallic state is different for the different cases, namely, those under pressures of more than 2 GPa and those induced by Ti doping (or V deficiency). The critical behavior of γ as well as of the Hall coefficient was reinvestigated recently by Carter and her co-workers (1993, 1994). Figure 73 shows the Hall coefficient versus temperature for (a) a series of barely metallic V-deficient crystals and (b) an insulating crystal driven to metallic under pressure. [Note that both cases show the SDW phase below about 10 K in the measured composition (y) and pressure region. See also the phase diagram in Fig. 71.] The respective Hall coefficient versus temperature curves show maxima at around the SDW transition temperature (~10 K). As the paramagnetic high-temperature state approaches the SDW transition with decrease of temperature, the Hall coefficient is critically enhanced from the high-temperature value ($3-4 \times 10^{-4}$ cm^3/C), which is comparable with the value observed for a pressure-driven metallic V_2O_3 (20 GPa, 4.2 K; McWhan *et al.*, 1973). Such an anomalous enhancement of the Hall coefficient is reminiscent of the high-temperature superconducting cuprates (see Sec. IV.C), although the enhanced amplitude is substantially smaller than that in the high-T_c cuprates. The enhancement ceases as the temperature is decreased below T_N.

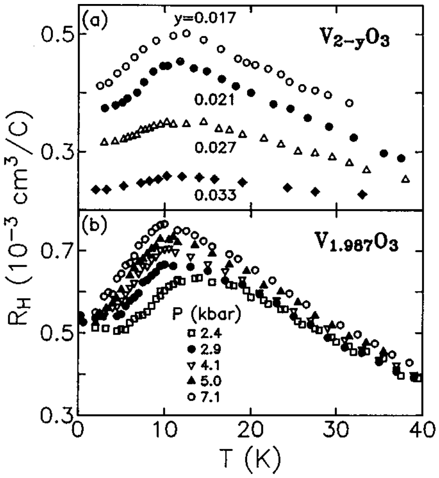

FIG. 73. Temperature dependence of Hall coefficient for (a) a series of V-deficient crystals in the metallic phase and (b) an insulating crystal driven to metallic with pressure. From Carter *et al.*, 1993, 1994.

Another notable feature in Fig. 73 is that the V deficiency y, or equivalently the change in the band filling, remarkably suppresses such an enhancement of the Hall coefficient, which is nearly linear with y around T_N. The observed behavior bears a qualitative resemblance to the case of the hole-doped cuprates, e.g., $La_{2-x}Sr_xCuO_4$ (see Sec. IV.D), in which the Hall coefficient shows a strong temperature dependence in the underdoped region and the enhanced coefficient nearly scales with $1/x$ rather than the inverse band filling $(1-x)^{-1}$. One might speculate that the two systems share a common underlying physics caused by strong antiferromagnetic spin fluctuations. However, we need careful and further analyses, because the enhanced amplitude is considerably different (typically by an order of magnitude).

The critical behavior of the electronic specific-heat coefficient γ is shown in Fig. 74 as a function of y (at ambient pressure) as well as of pressure P for the specific ($y = 0.013$) crystal (Carter *et al.*, 1993). In the light of the phase diagram depicted in Fig. 71, the metallic crystal whose γ is shown in Fig. 74 is in the SDW state and not in the paramagnetic phase. The aforementioned large γ for the Ti-doped ($x = 0.95$) crystal that was reported by McWhan *et al.* (1971) must also be for the SDW state. As seen in Fig. 74, the γ for the pressurized

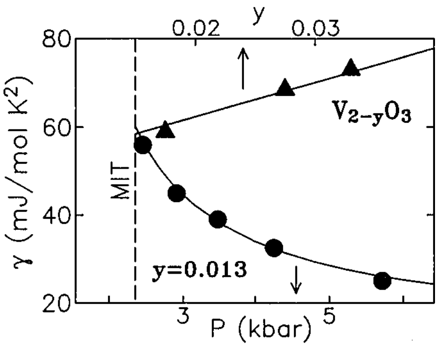

FIG. 74. T-linear electronic specific-heat coefficient γ vs the oxygen deficiency y at ambient pressure as well as vs the pressure P at $y=0.013$. From Carter *et al.*, 1993, 1994.

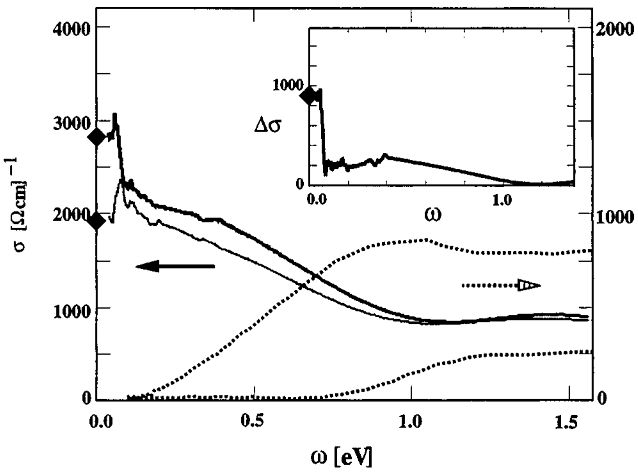

FIG. 75. Optical conductivity spectra of $V_{2-y}O_3$ in the metallic phase (full lines) at T=170 K (upper) and T=300 K (lower). The inset contains the difference of the two spectra $\Delta\sigma(\omega)=\sigma_{170\,\mathrm{K}}(\omega)-\sigma_{300\,\mathrm{K}}(\omega)$. Diamonds indicate the measured dc conductivity. Dotted lines indicate $\sigma(\omega)$ of insulating phase with y=0.013 at 10 K (upper) and y=0 at 70 K (lower). From Rozemberg *et al.*, 1995.

system is steeply increased as the compound approaches the metal-insulator (AFI-AFM) phase boundary. This was considered as a hallmark of Brinkman-Rice-type mass enhancement, although the Brinkman-Rice model does not consider the SDW-like spin order. The critical behavior is given by $\gamma=\gamma_0[1-(U/U_c)]^{-1}$, where γ_0 is the γ expected for the noninteracting V $3d$ in a band and U is the intra-atomic Coulomb interaction with the value U_c at the MIT (Brinkman and Rice, 1970). The data presented in Fig. 74 are consistent with the assumption that the ratio U/U_c varies linearly with P/P_c.

In the case of an FC-MIT, on the other hand, the γ decreases as the V deficiency y approaches the MI phase boundary. Carter *et al.* (1993) compared the different cases, variations of y and P, by sorting the γ into contributions from the spin-fluctuation term (Moriya, 1979) and the Brinkman-Rice term. Then the result could be explained by assuming that the spin-fluctuation term increases in proportion to the doping y, while the Brinkman-Rice term is nearly unchanged. However, it is not conceptionally clear whether the γ can be considered as a sum of the two terms, which must have the same physical origin, i.e., electron correlation. If further doping were possible, the γ would eventually show a peak at the AFM(spin-density wave)-PM phase boundary and then steeply decrease, as observed in another doped Mott-Hubbard system, $La_{1-x}Sr_xTiO_3$ (see Sec. IV.B.1). In a real $V_{2-y}O_3$ system, however, the spin ordering in the AFM phase is robust against y and no paramagnetic metallic state at $T=0$ K emerges up to the chemical phase separation ($y\approx0.06$; Ueda, Kosuge, and Kachi, 1980; Carter *et al.*, 1991). When the filling is controlled for the AFM phase to approach the Mott insulator by fixing U/t, γ should rather decrease because the electron and hole pockets with small Fermi surfaces shrink further. This is in contrast to the mass divergence expected for the MIT between the PM and AFI phases. As discussed in Secs. II.C, II.G.1, and II.G.8, metal-insulator transitions between the AFI and AFM phases are categorized as [I-1↔M-1] where the carrier number vanishes at the MIT, and γ may decrease toward the MIT in three dimensions due to a vanishing density of states at the band edge. When U/t is increased with fixed filling, on the other hand, the mass and γ may be quantitatively and strongly enhanced simply due to correlation effects. However, we know of no reason for divergence of γ at the AFM-AFI boundary. The experimental results shown in Fig. 74 appear to be consistent with these arguments.

The effect of electron correlation in V_2O_3 and the resultant temperature- and filling-dependent change in the electronic state are also manifested by the optical conductivity, as reported by Thomas *et al.* (1994) and Rozenberg *et al.* (1995). Figure 75 shows the optical conductivity spectra (essentially of the $T=0$ limit) for the insulating $V_{2-y}O_3$ phase with MIT critical temperatures $T_c=154$ K ($y=0$) and $T_c=50$ K (perhaps $y=0.13$, though not specified in the original report). Although the experimental data were analyzed based on the calculated result for a BC-MIT of the infinite-dimensional Hubbard model, the experimental conditions imply that the dominant character may not be BC-MIT but FC-MIT.

The temperature-dependent MIT in pure V_2O_3 between the low-temperature antiferromagnetic insulating phase and the high-temperature paramagnetic metallic phase was studied using a high-resolution photoemission technique as shown in Fig. 76 (Shin *et al.*, 1995). In the insulating phase below $T=155$ K, the total width of the lower Hubbard band was ~3 eV, considerably larger than that (~0.5–1 eV) deduced from the optical study by Thomas *et al.* (1994). The low-intensity region near E_F in the insulating phase has a width of ~0.2 eV, much smaller than the band gap (~0.6 eV) deduced from an optical study of a sample with the same transition temperature but twice the transport activation energy (~0.1 eV; McWhan and Remeika, 1970). Since the insulating phase of V_2O_3 is a p-type semiconductor due to a small number of V vacancies, the Fermi level should be located closer to the top of the occupied valence band than to the bottom of the unoccupied conduction band and should thus be separated from the top of the valence band by a p-type transport activation energy. The origin of the small discrepancy between the photoemission gap (~ 0.2 eV) and the activation energy ~ 0.1 eV is not clear but might be due to a polaronic effect, which generally increases the photoemission gap compared to the transport gap for p-type semiconductors. In the insulating phase, the spectrum shows a shoulder on the low-binding-energy side of the lower Hubbard band, i.e., at ~ 0.5 eV below E_F, which may correspond to the coherent part of the spectral function as predicted by Hubbard-model calculations for the Mott insulating phase (Shin *et al.*, 1995). In the metallic phase ($T > 155$ K), the gap is closed and finite spectral weight appears at E_F. However, the lower Hubbard band persists in the metallic phase without significant change in its line shape from that in the insulating phase, except for a broadening by ~ 0.5 eV. This indicates that electron correlation remains substantial even in the metallic phase, in accordance with the strong mass renormalization of conduction electrons. If we attribute the spectral weight near E_F, which appeared above the MIT temperature, to that of quasiparticles, the quasiparticle spectral weight $Z \equiv m_b/m_\omega$ [Eq. (2.73c)] is as small as ~ 0.05. On the other hand, the spectral intensity at E_F $[=(m_k/m_b)N_b(\mu)]$ is only 10–20 % of $N_b(\mu)$ deduced from the band-structure calculation (Ashkenazi and Weger, 1973). Thus the effective mass $m^*/m_b = (m_k/m_b)(m_\omega/m_b) \sim 2-4$, which is consistent with $m^*/m_b \simeq 5$ deduced from the electronic specific heat of the metallic phase of V_2O_3 (stabilized at low temperatures by pressure or V vacancies). The small quasiparticle weight $Z \sim 0.05$ indicates that the metallic carriers are largely incoherent in V_2O_3, consistent with the largely incoherent optical conductivity spectra (Thomas *et al.*, 1994).

The high-temperature MIT in Cr-doped samples between the high-temperature paramagnetic insulating (PI) phase and the low-temperature paramagnetic metallic (PM) phase was studied by photoemission by Smith and Henrich (1994). They found the spectral intensity at E_F to be reduced again above the transition, but the high-temperature insulating phase had a larger bandwidth than that of the low-temperature insulating phase, which would partly be due to thermal broadening and partly due to the absence of magnetic ordering.

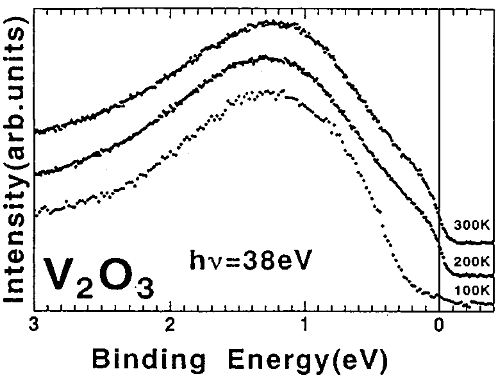

FIG. 76. High-resolution photoemission spectra of V_2O_3 above and below the MIT temperature (Shin *et al.*, 1995). The Fermi edge disappears below the transition temperature.

As mentioned above, most of the theoretical studies on V_2O_3 (Ashkenazi and Weger, 1973; Castellani, Natoli, and Ranninger, 1978a, 1978b, 1978c; Hertel and Appel, 1986) employed a model in which one electron occupied the e_g level and the other electron occupied the a_{1g} level. Here, the a_{1g} electrons were assumed to form a Heitler-London-type singlet bond between the two adjacent V atoms along the c axis (or equivalently, two electrons occupied the bonding state formed between the a_{1g} orbitals of the two V ions). Thus the remaining e_g electron contributed to the magnetic and transport properties and the Hubbard model, with one electron per site used as an appropriate starting point for V_2O_3. Recently, based on their LDA+U band-structure calculations, Czyzyk and Sawatzky (1997) proposed a new model in which the two d electrons occupy the e_g orbitals, forming a high-spin ($S=1$) state. Then the experimental value of the ordered magnetic moment, $1.2\mu_B$, is naturally explained by the reduction of the high-spin moment ($2\mu_B$) due to a covalency effect. Indeed, the nearest-neighbor V-V distance is elongated compared to that of the ideal corundum structure, implying that the neighboring V ions do not form a chemical bond. This model was supported by recent V $2p$ x-ray absorption spectroscopy (Park *et al.*, 1997b). If this model is correct, the whole scenario of V_2O_3 should be fundamentally modified. Further experimental and theoretical studies are necessary to confirm this point in the future.

2. $NiS_{2-x}Se_x$

The pyrite system $NiS_{2-x}Se_x$ has long been one of the typical compounds for BC-MIT systems. The progress up to the mid 1980s was thoroughly reviewed by Wilson (1985). A more concise review on the MIT in $NiS_{2-x}Se_x$ was also given by Ogawa (1979), who with his co-workers had done pioneering work on this system. Here, let us confine ourselves to the nature of the metallic state on the verge of the BC-MIT in $NiS_{2-x}Se_x$.

The end member NiS_2 shows a pyrite structure, in which Ni and S_2 form a NaCl-type lattice. Due to strong intradimer bonding, the S_2 pair accepts only two electrons in the bonding state and hence serves as a single anion $S_2{}^{2-}$. Ni in the pyrite is hence formally divalent with two $d\gamma$ electrons. As we shall discuss below, according to the renewed view on the correlated electronic structure, NiS_2 is a charge-transfer insulator (Fujimori, Mamiya, *et al.*, 1996). The other end compound $NiSe_2$, which is isostructural with NiS_2, is a paramagnetic metal over the whole temperature range. This is because the p orbital of the $Se_2{}^{2-}$ ion has larger spatial extent than that of $S_2{}^{2-}$ and hence larger p-d and p-p transfer interactions. Thus $NiSe_2$ may be viewed as derived from a charge-transfer insulator by closing of the CT gap.

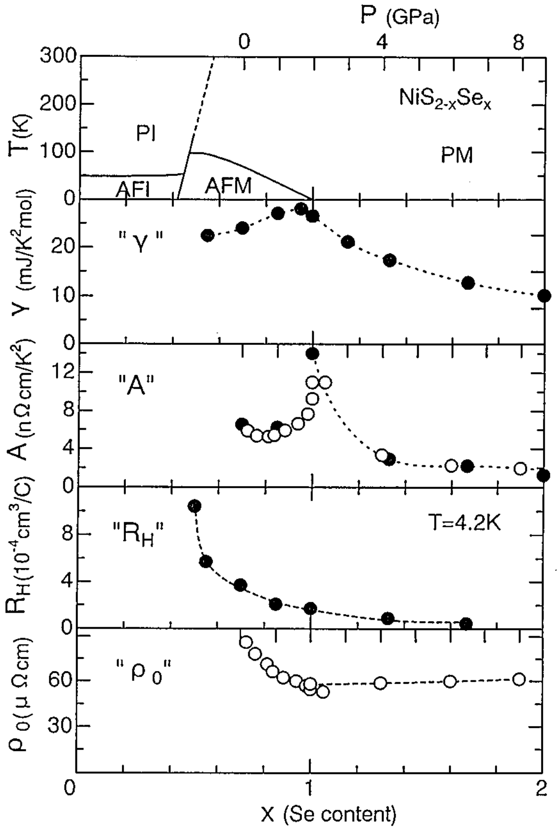

FIG. 77. The x dependence of χ, A, and residual resistivity (ρ_0) for NiS$_{2-x}$Se$_x$. From Miyasaka *et al.*, 1997.

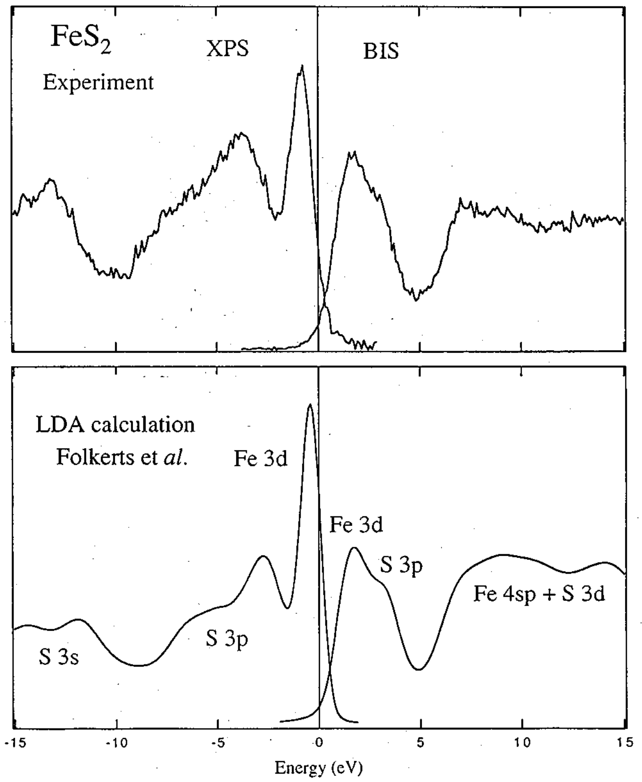

FIG. 78. Photoemission and inverse-photoemission (BIS) spectra of FeS$_2$ (Mamiya *et al.*, 1997b) compared with the band-structure calculation (Folkerts *et al.*, 1987). Good agreement is found between theory and experiment.

The solid solution NiS$_{2-x}$Se$_x$ with amalgamated p bands undergoes the BC-MIT around $x=0.8$ at room temperature and around $x=0.45$ at low temperatures below about 100 K (Wilson and Pitt, 1971; Bouchard *et al.*, 1973; Jarrett *et al.*, 1973; Czjzek *et al.*, 1976), as shown in Fig. 60 and also reproduced in the top panel of Fig. 77 (Miyasaka *et al.*, 1998). The antiferromagnetic metal phase is present in between the antiferromagnetic insulator and paramagnetic metal phases, which bears some analogy to the case of V$_2$O$_3$ (see Sec. IV.B.1). The AFI-AFM transition is weakly first order, while the AFM-PM transition is second order. The AFI state of NiS$_2$ shows a complicated spin structure (Miyadai *et al.*, 1978; Panissod *et al.*, 1979), which is a superposition of two kinds of sublattice structures, M1 and M2. In the AFM phase, only the M1-type (MnTe$_2$-type) magnetic structure appears to be preserved through the AFI-AFM transition and the averaged staggered moment shows a gradual decrease with x, for example, from $\approx 1.0\mu_B$ for $x=0$ (AFI) to $\approx 0.5\mu_B$ for $x=0.65$ (AFM) (Miyadai *et al.*, 1983).

The electronic structure of NiS$_2$ and NiS$_{2-y}$Se$_y$ as well as of the pyrite-type chalcogenides of Fe and Co has been studied by photoemission and inverse-photoemission spectroscopy for decades. Figure 78 shows combined photoemission and BIS spectra of the nonmagnetic semiconductor FeS$_2$ (Mamiya *et al.*, 1997b). There is a large gap between the occupied $p\pi$ band and the unoccupied antibonding $p\sigma^*$ band, both originating from the corresponding molecular orbitals of the S$_2^{2-}$ molecule. The narrow t_{2g} band of Fe $3d$ origin is completely filled and located within the $p\pi$-$p\sigma^*$ gap; the relatively wide e_g band is empty and overlaps the empty $p\sigma^*$ band. In going from FeS$_2$ to CoS$_2$ to NiS$_2$, the t_{2g} band is progressively broadened and an additional feature due to the occupation of the e_g band appears near E_F. The transition-metal ions in the pyrite-type compounds tend to take low-spin configurations: $S=0$ for Fe^{2+}(d^6), $S=1/2$ for the Co^{2+}(d^7) ion, and $S=1$ for Ni^{2+}(d^8). [No low-spin ($S=0$) ground state is possible for the d^8 ion in a cubic crystal field.] Earlier photoemission studies utilized ligand field theory (van der Heide *et al.*, 1980), molecular-orbital calculations on MS$_6$ clusters (E. K. Li *et al.*, 1974) and band-structure calculations (Krill and Amamou, 1980; Folkerts *et al.*, 1987) and the structures within $\sim$4 eV from E_F, were attributed to metal $3d$ states. A recent resonant photoemission study of NiS$_2$ (Fujimori, Mamiya, *et al.*, 1996), however, showed that $3p$-to-$3d$ resonance enhancement occurs at 5–10 eV below E_F rather than in the "d-band" region near E_F, indicating that NiS$_2$ is a charge-transfer insulator. In going from NiS$_2$ through CoS$_2$ to FeS$_2$, the near-E_F region becomes more strongly enhanced, indicating that the system gradually changes from charge-transfer-like to Mott-Hubbard-like because of the increasing Δ (and decreasing U). The photoemission spectra of NiS$_2$ were analyzed using the CI cluster model

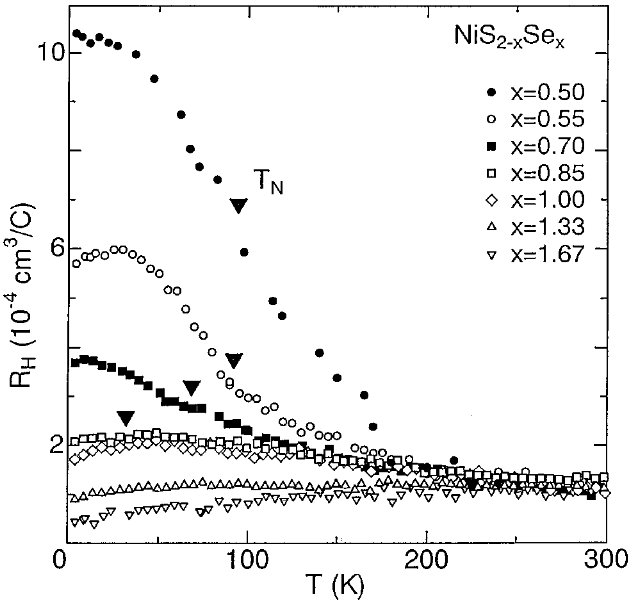

FIG. 79. Temperature dependence of Hall coefficient in the PM phase for $x > 1$ of $NiS_{2-x}Se_x$. From Miyasaka *et al.*, 1998.

(Fujimori, Mamiya, *et al.*, 1996). The electronic structure parameters were obtained as $\Delta = 1.8$ eV, $U = 3.3$ eV, and the charge transfer energy $(pd\sigma) = 1.5$ eV, confirming the $p \rightarrow d$ charge-transfer nature of the band gap. We note that the global spectral line shape does not change very much across the Se-substitution-induced MIT except for a slight narrowing of the photoemission main ($d^8\underline{L}$ final-state) peak in the metallic phase and overall shifts of the empty d and $p\sigma^*$ bands in the inverse-photoemission spectra toward E_F in going from the metallic to the insulating phase by 0.2–0.3 eV (Mamiya *et al.*, 1997b) due to closure of the band gap.

Viewed from the paramagnetic metallic side, the MIT is accompanied by strong enhancement of the electronic specific heat(γ), the paramagnetic susceptibility (χ), and the coefficient of the T^2 term (A) in the temperature-dependent resistivity, as noted by Ogawa (1979) and recently reinvestigated by Miyasaka *et al.* (1998). The x dependence of χ, A, and the residual resistivity (ρ_0) is summarized in Fig. 77 (Miyasaka *et al.*, 1998). In the PM phase ($1.0 < x < 2.0$), γ increases critically with decreasing x down to the PM-AFM phase boundary ($x = 1.0$) from 10 mJ/mol K^2 for $x = 2.0$ ($NiSe_2$) to 28 mJ/mol K^2. On the other hand, the Hall coefficient in the PM phase is almost temperature independent and approximately 10^{-4} cm^3/C with positive sign, as shown in the $x > 1$ data of Fig. 79, which is consistent with a large Fermi surface containing ≈ 2 carriers per atom of Ni. These results clearly indicate mass renormalization as the insulator phase is approached, while the Fermi surface is preserved in volume. In accord with this, the nearly temperature-independent χ is also enhanced (Ogawa, 1979) and the Wilson ratio χ/γ is around 2, nearly constant against x.

The T^2 coefficient A of the resistivity also reflects such an x-dependent mass-renormalization effect, as shown in the third panel of Fig. 77. Except for the region near the AFM-PM phase boundary, A is nearly proportional to γ^2, obeying the Kadowaki-Woods relation for a strongly correlated Fermi liquid (Kadowaki and Woods, 1986). The T^2 dependence of the resistivity in the PM phase is seen up to relatively high temperatures (say, 200 K), yet the deviation of the T^2 law above some temperature is conspicuous near the PM-AFM phase boundary ($x = 1.0$) and the resistivity follows the $T^{1.5}$ dependence rather than T^2 dependence down to low temperatures. In the immediate vicinity of the AFM-PM phase boundary, $T^{1.5}$ dependence persists down to liquid-helium temperatures and hence the T^2 coefficient tends to diverge (Ogawa, 1979), as seen in the third panel of Fig. 77. This is in line with the SCR theory (Ueda, 1977; Moriya, 1995) and can be ascribed to strong spin fluctuations, as discussed in Secs. II.D.1 and II.D.8. The $T^{1.5}$ dependence in this framework is derived in Eq. (2.118). All these observations are consistent with the canonical view of a Fermi liquid with strong electron correlation. Because A diverges while γ remains finite, the Kadowaki-Woods relation discussed in Sec. II.D.1 is clearly not satisfied near the AFM-PM boundary.

Let us now turn to the feature in the AFM phase near the MI phase boundary. Hall coefficients in the AFM phase (Fig. 79, Miyasaka *et al.*, 1998) show a remarkable increase with lowering of temperature. The low-temperature value increases with decrease of x, implying that in the AFM phase the carrier number decreases as the AFI phase is approached. It is worth noting that the temperature-dependent enhancement of the Hall coefficient is discernible in the high-temperature PM phase above T_N, perhaps due to antiferromagnetic spin fluctuations. Such a shrinkage of the Fermi surface in the AFM phase is also reflected in a change in the residual resistivity, as shown in the bottom panel of Fig. 77. The residual resistivity, which is free from renormalization effects of electron correlation, can be expressed with a Fermi surface area S_F and mean impurity distance L_i as (Rice and Brinkman, 1972)

$$\rho_0 = (e^2 S_F L_i / 12\pi^3)^{-1}. \tag{4.1}$$

In the high-pressure measurements, of which results are plotted with open circles in the figure, L_i was kept constant and hence ρ_0 directly probed the Fermi surface size S_F. In this system, the application of pressure was equivalent to Se substitution for bandwidth control, as the scaling relation indicates on the upper scale of Fig. 77 for the $x = 0.7$ crystal. The residual resistivity under pressure remained constant in the paramagnetic metal phase ($P > 2$ GPa) irrespective of the x-dependent mass renormalization, indicating that the carrier density was essentially unchanged in the PM phase. By contrast, the residual resistivity in the AFM phase ($P < 2$ GPa) increased rapidly towards the metal-insulator phase boundary, indicating shrinkage of the Fermi surface or reduction in carrier density, in accordance with the Hall coefficient.

As the AFI-AFM phase boundary ($x = 0.45$) is approached from the metallic side, the T^2 coefficient of the resistivity (A) is again enhanced by the Brinkman-Rice

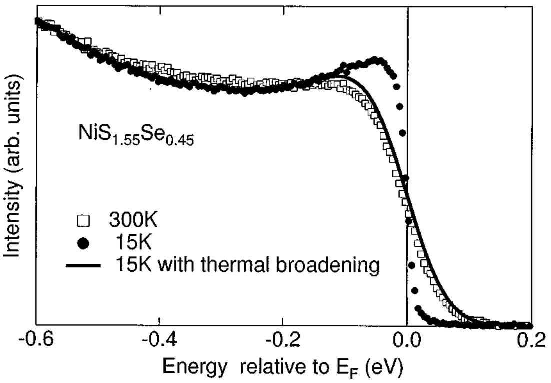

FIG. 80. Photoemission spectra of $NiS_{1.55}Se_{0.45}$ in the antiferromagnetic metallic state (15 K) and the paramagnetic insulating state (300 K) (Mamiya *et al.*, 1997a). The solid curve is the 15-K spectrum broadened with a Gaussian to "300 K."

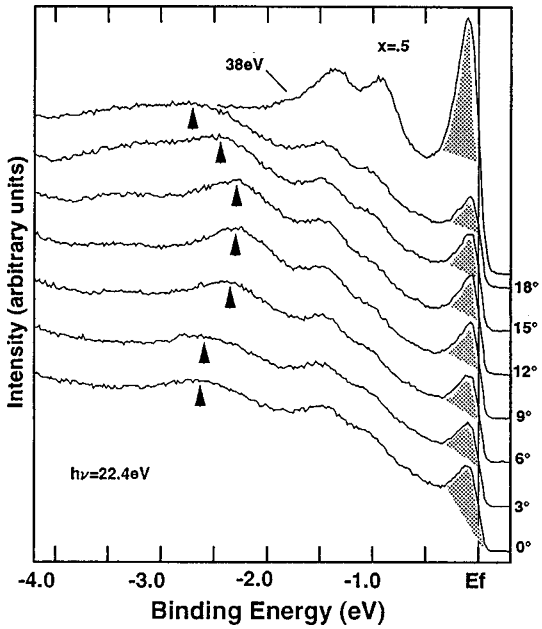

FIG. 81. Angle-resolved photoemission spectra of $NiS_{1.5}Se_{0.5}$ in the antiferromagnetic phase (Matsuura *et al.*, 1996). The spectra label the analyzer angle. The shaded feature due to a narrow Ni 3*d* band shows little dispersion.

mechanism (Husmann *et al.*, 1996). In the low-temperature region below 1 K near the MI phase boundary, however, the conductivity σ shows the $T^{1/2}$ dependence that is characteristic of a MIT by disorder due to Anderson localization under the electron-electron interactions, as discussed in Sec. II.G.2 (Lee and Ramakrishnan, 1985; Belitz and Kirkpatrick, 1994). However, in the pressure-tuned AFM phase on the verge of the MI phase boundary (at a distance with $\Delta P = P - P_c < 0.2$ Kbar), the conductivity shows a $T^{0.22}$ dependence. Husmann *et al.* (1996) argued that this supports violation of hyperscaling for the AFM-AFI transition. Such a violation had indeed been discussed in connection with the mapping to the random-field problem (Kirkpatrick and Belitz, 1995). For theoretical aspects of this issue, see Sec. II.G.2.

The temperature-induced MIT in $NiS_{2-y}Se_y$ with $x \sim 0.5$ has been the subject of recent high-resolution photoemission studies. The angle-integrated spectra of $NiS_{1.55}Se_{0.45}$ near E_F shown in Fig. 80 exhibit spectral weight transfer from the near-E_F region to 0.2–0.4 eV below it as the temperature increases from below $T_t \sim 60$ K (AFM) to above it (PI) (Mamiya *et al.*, 1997a). (This can be more clearly seen by comparing the solid curve, which represents the 15-K spectrum temperature-broadened to 300 K, with the actual 300-K spectrum in Fig. 80). The peak at ~ 50 meV below E_F in the AFM state may correspond to the quasiparticle spectral weight, as predicted by the calculations for the Hubbard model in three and higher dimensions discussed in Sec. II.E.6 for the infinite-dimensional approach (Georges *et al.*, 1996; Ulmke *et al.*, 1996). However, it should be noted that the calculations were done for the paramagnetic metal state and not for the AFM. A similar change in the spectrum near E_F can be identified in a composition-dependent MIT, between the AFM ($x > 0.5$) and AFI ($x < 0.5$). In the one-electron band picture, energy bands of the paramagnetic phase are folded into the antiferromagnetic Brillouin zone, and accordingly a gap or a pseudogap tends to open at E_F. Although this picture contrasts with the observation of the 50-meV peak, the pseudogap at E_F might collapse, if band narrowing due to electron correlation near E_F were strong enough. The 50-meV peak was observed to be even sharper and only very weakly dispersing in the angle-resolved photoemission study of $NiS_{1.5}Se_{0.5}$ by Matsuura *et al.* (1996; Fig. 81), indicating that the band narrowing is indeed very strong. The spectrum of the PI phase in Fig. 80 shows no gap at E_F in spite of the fact that the electrical conductivity is of the activated *p* type with an activation energy of ~ 75 meV. This means that the activated transport comes from the mobility, consistent with the observed low mobility $\ll 1\ \mathrm{cm^2\,V^{-1}\,sec^{-1}}$, which is in the range of small polaron hopping (Kwizera *et al.*, 1980; Thio and Bennett, 1994). Indeed, the Hall coefficient is small and temperature independent in the high-temperature paramagnetic insulator phase, meaning that the carrier number is large (~ 2 hole/Ni; Miyasaka *et al.*, 1997). For pure NiS_2 also, the photoemission spectrum shows almost no gap at E_F, implying that the transport activation energy (~ 300 meV at 300 K) is mostly due to the mobility.

3. *R*NiO$_3$

The interest in RNiO$_3$ has recently been revived by a systematic study on MITs by Torrance *et al.* (1992). The MI phase diagram as a function of the perovskite tolerance factor (or equivalently the *p*-*d* transfer interaction) was shown (Fig. 63) in Sec. III.C as a prototypical example of a BC-MIT. The metal-insulator phase diagram qualitatively resembles that of V_2O_3 (Fig. 68) or the theoretical prediction for the infinite-dimensional Hubbard model, although the insulating state of RNiO$_3$ should be classified as a charge-transfer (CT) insulator rather than a Mott-Hubbard insulator. Among charge-transfer-type

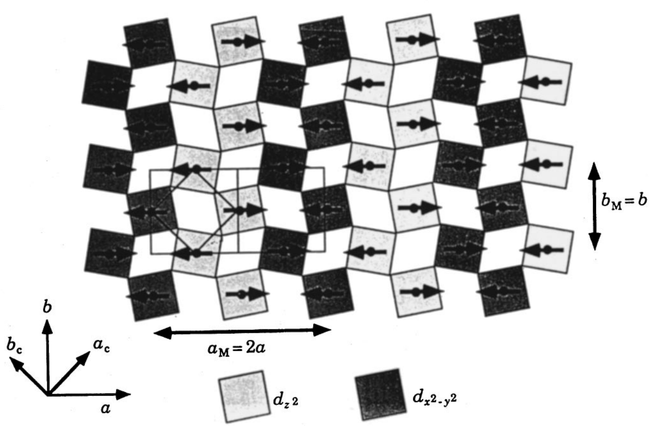

FIG. 82. The magnetic and orbital order structure of RNiO$_3$ determined by a neutron-scattering study by García-Muñoz *et al.* (1992).

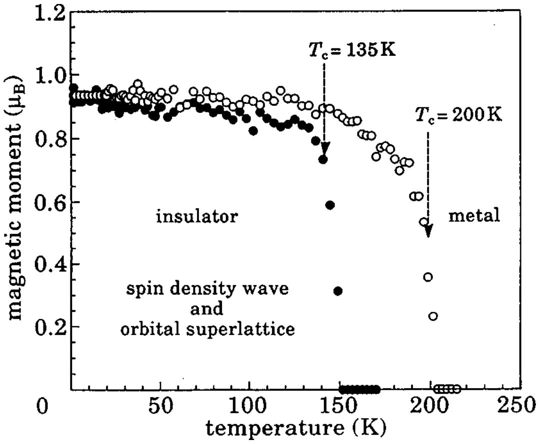

FIG. 83. Temperature dependence of the magnetic moment for RNiO$_3$. From Gracía-Muñoz *et al.*, 1992.

compounds, the high valency of the Ni^{3+} ions in RNiO$_3$ makes its charge-transfer energy Δ as small as ~ 1 eV and stabilizes its low-spin configuration $t_{2g\uparrow}^3 t_{2g\downarrow}^3 e_{g\uparrow}$, as shown by CI cluster-model analysis of photoemission spectra (Barman *et al.*, 1994; Mizokawa *et al.*, 1995). Because of the small Δ, the ground state is a strong mixture of d^7, $d^8\underline{L}$, and $d^9\underline{L}^2$ configurations, resulting in a net d-electron number as large as $n_d = 7.8$. On the other hand, the Ni magnetic moment is calculated to be $\sim 0.91\mu_B$, in good agreement with experiment, and is not strongly reduced from the ionic value, $1\mu_B$. This is because for the low-spin Ni^{3+} ion charge transfer occurs from O $2p$ orbitals to $e_{g\uparrow}$ and $e_{g\downarrow}$ orbitals.

Since there is nominally one electron in the e_g orbital, as in LaMnO$_3$, one may expect a Jahn-Teller distortion and associated orbital ordering in the insulating RNiO$_3$ compounds. Indeed, the unusual spin ordering structures in PrNiO$_3$ and NdNiO$_3$ was attributed to the formation of an orbital superlattice (García-Muñoz *et al.*, 1992), but so far no evidence for Jahn-Teller distortion has been found. The magnetic ground state, described by a commensurate $k = (1/2,0,1/2)$ spin-density wave, shown schematically in Fig. 82, was determined from a neutron-scattering study by García-Muñoz *et al.* (1992). The 3D magnetic ordering consists of alternating inverted bilayers: AA(AA)AA(AA)... along the [001] direction, with A representing the magnetic arrangement of Ni moments in one (001) plane (Fig. 82). The temperature dependence of the magnetic moment for both compounds is shown in Fig. 83. Reflecting the first-order nature of the transition, the abrupt appearance of the ordered moment ($\approx 0.9\mu_B$) is observed at the metal-insulator transition. The coexistence of F and AF interactions, which manifest themselves in the ordered spin structure, suggests the existence of an orbital superlattice, such as regular occupation of either $d_{3z^2-r^2}$ or $d_{x^2-y^2}$ type orbitals, as shown in Fig. 82. The nominal Ni^{3+} in RNiO$_3$ indicates one electron accommodated in the doubly degenerate e_g orbital. Thus one should consider the orbital degree of freedom (or orbital pseudospin; Kugel and Khomskii, 1973, 1982) on an equal footing with the spin ($S = 1/2$) degree of freedom, as discussed in Sec. II.I.1. Hartree-Fock band-structure calculations were made to investigate the possibility of orbital ordering in these materials using the parameters Δ, U, and $(pd\sigma)$ deduced from a cluster-model analysis of the photoemission spectra (Mizokawa *et al.*, 1995; Mizokawa and Fujimori, 1995). The ground states with various spin- and orbital-ordered structures (ferromagnetic and G-, A-, and C-type antiferromagnetic ordering) were found to fall within a narrow energy range of ~ 70 meV/Ni, indicating that the complicated orbital ordering proposed by the neutron study, which can be viewed as a combination of these spin-orbital ordered structures, is quite likely. However, the Hartree-Fock calculations predicted that an orbital superlattice of the x^2-$y^2$$-3z^2$-$r^2$-type would have an energy lower than the above spin-orbital-ordered states. A possible cause for the absence of Jahn-Teller distortion in RNiO$_3$ is hybridization of the e_g and t_{2g} orbitals as a result of the pair-transfer term ($c_{t_{2g}\uparrow}^\dagger c_{t_{2g}\downarrow}^\dagger c_{e_g\uparrow} c_{e_g\downarrow}$ and its Hermitian conjugate) in the degenerate Hubbard-model Hamiltonian [Eq. (2.6e)]: The Hartree-Fock approximation gives terms of the type $c_{t_{2g}\uparrow}^\dagger c_{e_g\uparrow}$, which cause a one-electron hybridization between the t_{2g} and e_g orbitals on the mean-field level. There is no pair-transfer contribution in the high-spin Mn^{3+} ion because the spin is fully polarized.

Torrance *et al.* (1992) discussed the metal-insulator transition in terms of a closing of the charge-transfer gap with increase of p-d hybridization. To substantiate this, Arima and Tokura (1995) investigated optical conductivity spectra at room temperature for a series of RNiO$_3$ (metallic for R = La and Nd and insulating for R = Sm and Y) as shown in Fig. 84. In accord with the metal-insulator phenomena in dc conductivity, the R = Sm and Y compounds showed decreasing optical conductivity as ω approached zero, that is, the gap feature. On the other hand, the optical conductivity appeared to remain at a finite value for the metallic (R = La and Nd) compounds. The spectral feature was not a simple Drude form, but the $2p$$-$$3d$ interband transitions seemed to contribute

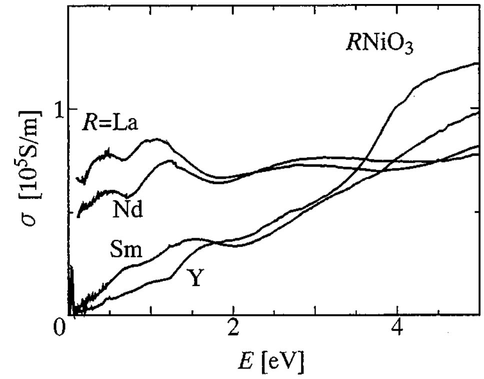

FIG. 84. Optical conductivity spectra at room temperature for a series of RNiO$_3$. From Arima and Tokura, 1995.

down to the low-energy part of the conductivity spectra. A point to be noted is the conspicuous change in the conductivity spectra over a wide energy region up to several eV with variation of R site: This change in the conductivity spectra is apparently accompanied by the isosbetic (namely, equal-absorption) point at 3.5–4.0 eV, across which the spectral weight is transferred from high- to low-energy regions upon closing of the CT gap. Such a large energy scale arises from the large-energy quantities that govern the opening and closing of the CT gap, namely, $3d$ electron correlation and the p-d transfer interaction. Thus collapse of the CT gap with increase of the tolerance factor (e.g., from $R=\mathrm{Sm}$ to $R=\mathrm{La}$) is obviously not a simple closing of the gap like that expected for a semiconductor-to-semimetal transition, but accompanies a reshuffle of the whole electronic structure relating to the $3d$–$2p$ states.

Among the RNiO$_3$ compounds, LaNiO$_3$ remains metallic down to low temperature, and shows features of a correlated metallic system (Mohan Ram *et al.*, 1984; Vasanthacharya *et al.*, 1984; Sreedhar *et al.*, 1992). The resistivity shows T^2 dependence, $\rho=\rho_0+AT^2$, below 50–70 K, although the (ρ_0,A) values are scattered in reports (Sreedhar *et al.*, 1992; Xu *et al.*, 1993), perhaps because of difficulty in the characterization of the sample quality (particularly the oxygen content). The heat capacity data below 10 K can be fitted to the relation (Sreedhar *et al.*, 1992)

$$C=\gamma T+\beta T^3+\delta T^3\ln T. \tag{4.2}$$

The last term arises as a consequence of spin fluctuations (Pethick and Carneiro, 1973). The electronic specific-heat coefficient $\gamma=14$ mJ/mol K^2 and the Pauli magnetic susceptibility $\chi=5.1\times10^{-4}$ emu/mol are enhanced well above their free-electron gas values. The Wilson ratio γ/χ for LaNiO$_3$ is 2.4, which is typical of a correlated system.

As shown in the MI phase diagram (Fig. 63), RNiO$_3$ metals ($R=$Pr, Nd, Sm, and Eu) undergo a MIT with decrease of temperature. Among them, PrNiO$_3$ and NdNiO$_3$ exhibit a transition from the paramagnetic metal (PM) to the antiferromagnetic insulator (AFI) at around 135 K and 200 K, respectively. The MIT is first order with thermal hysteresis (Granados *et al.*, 1992) and accompanied by a subtle increase in the cell volume by ≈0.02% (Torrance *et al.*, 1992). A more detailed neutron-diffraction study (García-Muñoz *et al.*, 1994) revealed that the lattice transition is accompanied by coupled tilts of NiO$_6$ octahedra, which implies changes in the Ni-O-Ni angles (by $-0.5°$) governing the transfer interaction between the Ni e_g and O $2p$ orbitals. However, the structural change with the transition is a subtle one and the MIT may be viewed as electronically driven.

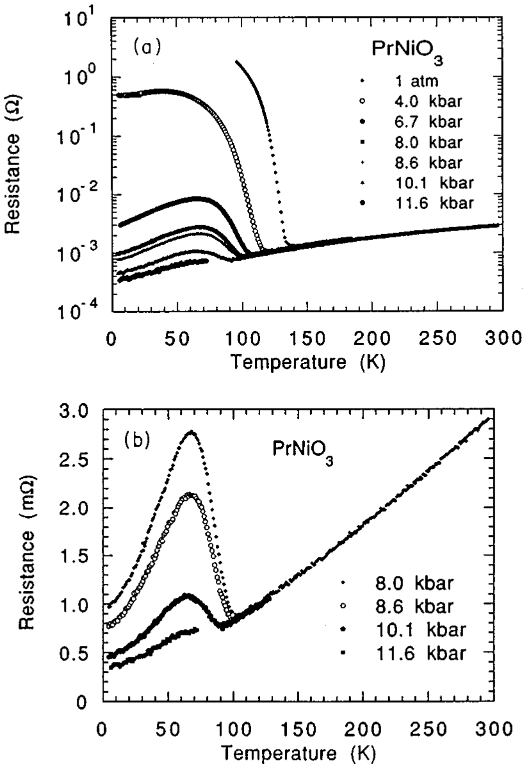

FIG. 85. Pressure dependence of $\rho(T)$ for PrNiO$_3$. From Obradors *et al.*, 1993.

The control of the p-d transfer interaction by changes in the tolerance factor can be mimicked by application of external pressure (Canfield *et al.*, 1993; Obradors *et al.*, 1993; Takagi *et al.*, 1995). We show an example of the pressure dependence of the $\rho(T)$ curves for PrNiO$_3$ (Obrandors *et al.*, 1993) in Fig. 85. The metal-insulator phase boundary under pressure for PrNiO$_3$ and NdNiO$_3$ can be related to the phase diagram shown in Fig. 63 by assuming that the pressure effectively increases the Ni-O-Ni angle (or tolerance factor). It is also noted in Fig. 85 that the $\rho(T)$ curve shows an apparent reentrant feature like the M-I-M transition in the vicinity of the pressure-induced disappearance of the AFI phase. This was ascribed to the nature of the first-order phase transition (Obradors *et al.*, 1993): The first-order phase transformation occurring at T_{MI} is incomplete due to a slowdown of the growth rate of the insulating phase, and the metallic phase remains dominant, producing reduced resistivity at low temperatures.

Another important aspect of the MIT to be kept in mind is the complicated ordered spin structure for the AFI phase of PrNiO$_3$ and NdNiO$_3$ and possible orbital

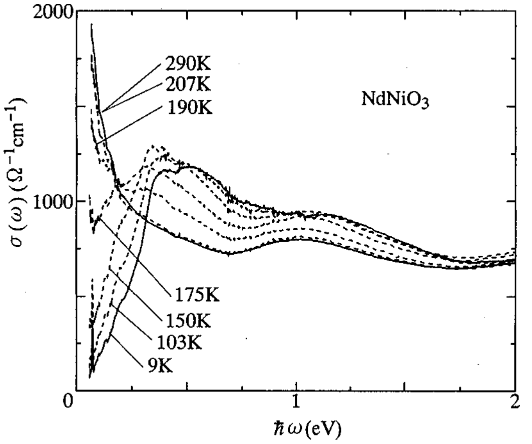

FIG. 86. Temperature dependence of optical conductivity spectra of $NdNiO_3$. From Katsufuji *et al.*, 1995.

ordering. It is essential to consider the orbital contribution to the total free energy not only for bandwidth-controlled MITs in RNiO$_3$ but also possibly for electron properties in the metallic phase.

We show in Fig. 86 the temperature dependence of the optical conductivity spectrum of $NdNiO_3$ (Katsufuji, Okimoto, Arima, Tokura, and Torrance, 1995), which undergoes the PM-to-AFI transition at $T_{MI}=200$ K. Drude-like increase of the optical conductivity as $\omega\to 0$ is suppressed, and the opening of the charge gap is observed below T_{MI}. The missing spectral weight in the low-energy part is redistributed over the energy region above 0.3 eV, but such a change in spectral features in the course of a thermally induced MIT is obviously different from the case of an MIT with variation of the R site (Fig. 84) affecting the energy scale for the spectral weight transfer. The evolution of the gap below T_{MI} is gradual with temperature, which appears to be well fitted with the BCS function (Katsufuji, Okimoto, Arima, Tokura, and Torrance, 1995). The feature is reminiscent of the SDW gap, whose ground-state magnitude should be $2\Delta(0)\approx 3.5k_B$ (Overhauser, 1962). However, what happens in $NdNiO_3$ is beyond this picture. In the case of Cr metal, which is a prototypical SDW system, the experimentally observed peak energy relevant to the gap structure in the conductivity spectrum is $5.2k_BT_c$. This was interpreted in terms of a slight modification of the mean-field theory by the phonon-scattering effect (Barker *et al.*, 1968). By contrast, the peak conductivity energy for $NdNiO_3$ at 9 K is $\approx 20k_BT_c$ as can be seen in Fig. 86. This is much larger than the value expected for a simple SDW transition and implies that electron correlation plays an important role in producing the AFI phase. The effect of the simultaneous formation of an orbital superlattice may also be relevant to the large-gap feature in the low-temperature phase of $NdNiO_3$.

4. NiS

The hexagonal form of NiS (β-NiS) undergoes a first-order phase transition from an antiferromagnetic nonmetal to a paramagnetic metal with temperature or under pressure (Sparks and Komoto, 1967; Anzai and Ozawa, 1968). Figure 87 shows the pressure-temperature phase diagram (McWhan *et al.*, 1972). The discovery of the MIT in NiS has attracted considerable attention because the transition is not accompanied by a change in the symmetry of the crystal structure and is therefore a candidate for a Mott transition driven by electron-electron interaction. The β-NiS, which is a metastable phase at room temperature and can only be obtained by quenching from high temperatures above ~600 K, crystallizes in the NiAs structure as shown in Fig. 88. Here the NiS_6 octahedra shares edges within the ab plane and share faces along the c direction. The Ni-Ni distance along the c direction is therefore short, $d_{\text{Ni-Ni}}=2.65-2.7$ A, making the Ni-Ni interaction along the c axis important. At the MIT, the hexagonal lattice

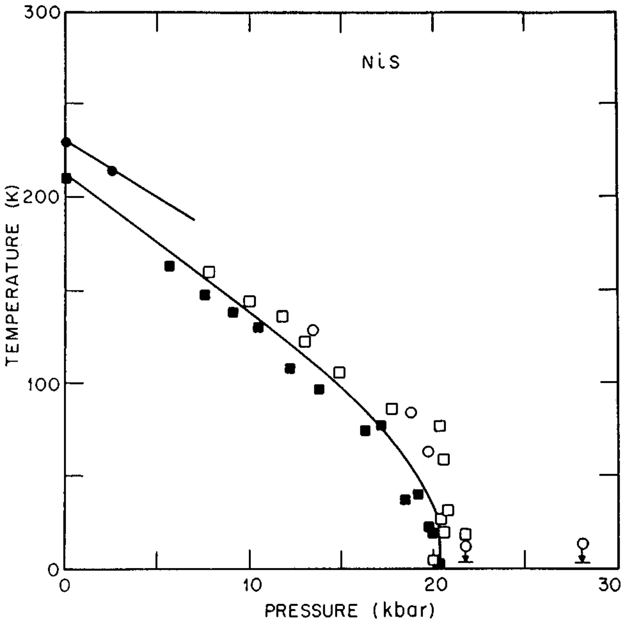

FIG. 87. Pressure-temperature phase diagram of NiS samples: circles, $T_t=230$ K; squares, $T_t=210$ K. Open symbols represent increasing pressures and closed symbols decreasing pressures. From McWhan *et al.*, 1972.

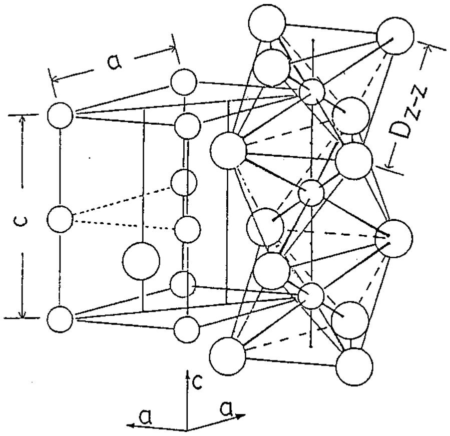

FIG. 88. Crystal structure of NiS (Matoba *et al.*, 1991). Small circles, Ni atoms; large circles, S atoms.

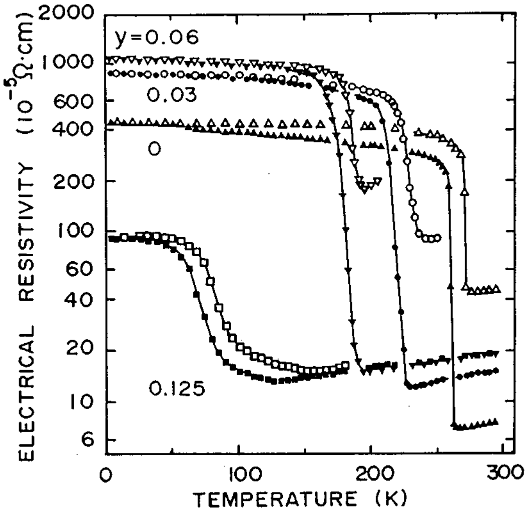

FIG. 89. Electrical resistivity of $NiS_{1-y}Se_y$: Open symbols are for heating runs, closed symbols for cooling runs. From Anzai *et al.*, 1986.

parameters a ($\simeq$3.45 A) and c ($\simeq$5.3–5.4 A) decrease by 0.3% and 1%, respectively, in going from the nonmetallic phase to the metallic phase, resulting in a volume collapse as large as ~2%.

Electrical resistivity as a function of temperature shows a jump by a factor of ~20 at the MIT temperature T_t, as shown in Fig. 89 (Anzai and Ozawa, 1968; Sparks and Komoto, 1968; Anzai *et al.*, 1986). Above T_t, the resistivity is as low as 10^{-5}–10^{-4} Ω cm and increases with temperature. Below T_t, the resistivity is nearly temperature independent in the 10^{-3} Ω cm range down to $T \sim 0$, in contrast to typical semiconductors or insulators, indicating that the low-temperature phase is a semimetal (White and Mott, 1971; Koehler and White, 1973) or a degenerate semiconductor (Ohtani, Kosuge, and Kachi, 1970; Barthelemy, Gorochov, and McKinzie, 1973). Accordingly, we refer to the low-temperature phase as the "nonmetallic" phase rather than the insulating or semiconducting phase. The nonmetallic phase is always doped with holes due to a small concentration of naturally present Ni vacancies (typically $x=0.002$ in $Ni_{1-x}S$). $T_t=260$ K for nearly stoichiometric samples and decreases with Ni vacancies.

The Hall coefficient R_H of $Ni_{1-x}S$ with small x ($0.004<x<0.017$) is positive in the nonmetallic phase and $n=1/eR_H$ is nearly equal to $2x$ per unit formula, which indicates that one Ni vacancy produces two hole carriers (Ohtani, Kosuge, and Kachi, 1970; Ohtani, 1974). The mobility is small ($=3\ \mathrm{cm}^2\,\mathrm{V}^{-1}\,\mathrm{sec}^{-1}$) and nearly temperature independent, indicating transport in a narrow band. The Hall coefficient in the metallic phase is smaller than in the nonmetallic phase by a factor of ~40 and becomes negative (Barthelemy, Gorochov, and McKinzie, 1973), meaning that in going from the nonmetallic to the metallic phase, the number of carriers dramatically increases. Presumably the character of the Fermi surfaces changes from "small" hole pockets to "large" electronlike (Luttinger) Fermi surfaces. Thermoelectric power is positive and relatively large below T_t and becomes negative and small above T_t, consistent with the sign of the Hall coefficient (Ohtani, 1974; Matoba, Anzai, and Fujimori, 1986). Below T_t, the Seebeck coefficient is roughly proportional to the temperature, a characteristic of a degenerate semiconductor, with some phonon-drag contribution. Above T_t, the Seebeck coefficient is negative and small, but again is proportional to the temperature, showing more typical metallic behavior. If there is one type of carrier in each of the metallic and nonmetallic phases, the jump of the resistivity at the MIT by a factor of ~20 and that of the Hall coefficient by a factor of ~40 means that the mobility in the metallic phase is similar to, or somewhat smaller than, that in the nonmetallic phase. However, according to band-structure calculations, the metallic phase has several Fermi surfaces (Mattheiss, 1974; Nakamura *et al.*, 1994b), and the simple relation $n=1/eR_H$ may not hold in the metallic phase.

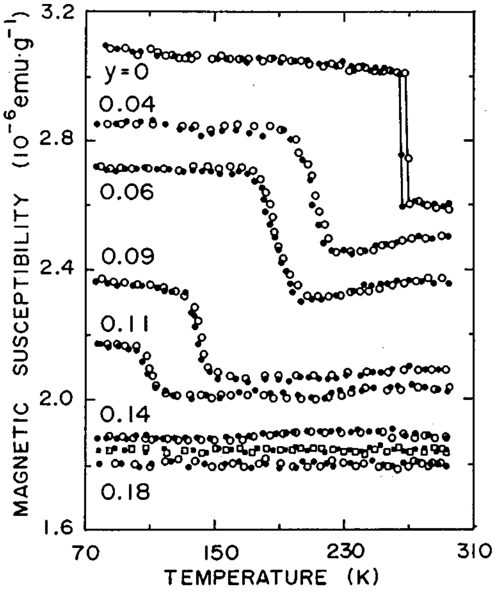

FIG. 90. Magnetic susceptibility of $NiS_{1-y}Se_y$. Open circles are for heating runs, filled circles for cooling runs. From Anzai *et al.*, 1986.

According to neutron-diffraction studies (Sparks and Komoto, 1968; Coey *et al.*, 1974), the magnetic moment of Ni in NiS is 1.5–1.7μ_B at $T=4.2$ K and it is ferromagnetically coupled within the ab plane and antiferromagnetically coupled along the c axis. The magnetic susceptibility of NiS is flat below T_t and abruptly decreases at $T=T_t$, as shown in Fig. 90 (Anzai *et al.*, 1986). The susceptibility above T_t is not typical Pauli paramagnetism and has a positive slope ($d\chi/dT>0$). (Unfortunately, measurements above ~300 K are prohibited by the phase instability). The magnetic susceptibility of single crystals has shown that the susceptibility $\chi_\perp$ perpendicular to the magnetization axis (c axis) is very small below T_t (Koehler and White, 1973); therefore the exchange coupling constant J between two Ni atoms along the c direction ($=N\mu_B^2/2z\chi_\perp$, where $z=2$ is the number of nearest-neighbor Ni ions) is as large as 0.14 eV. An in-

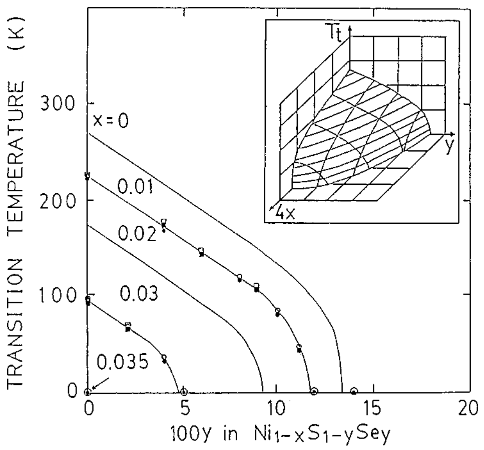

FIG. 91. Composition dependence of the transition temperature T_t in $Ni_{1-x}S_{1-y}Se_y$ (Matoba, Anzai, and Fujimori, 1991). Solid symbols are cooling runs and open symbols heating runs. The inset shows a schematic T-x-y phase diagram.

elastic neutron-scattering study indeed revealed a high spin-wave velocity along the c axis and $J=0.1$ eV was obtained (Hutchings, Parisot, and Tocchetti, 1978). From this J value, the Néel temperature was predicted to be $T_N\sim 1000$ K, which is much higher than $T_t=260$ K. This indicates that the antiferromagnetic-to-paramagnetic transition is not driven by a spin disordering along the c axis but by a spin disorder within the ab plane or by the appearance of the metallic phase itself. The strong exchange coupling J suggests the existence of antiferromagnetic correlation in the paramagnetic metallic state and is possibly the origin of the positive slope in the magnetic susceptibility of the metallic phase. This has some analogy with the metallic phase of high-T_c cuprates, although in NiS the electronic transport is three dimensional and the magnetic correlation is rather one dimensional.

A pressure-induced MIT is an ideal BC-MIT, for which interpretation of experimental data is most straightforward. On the other hand, it is rather difficult to obtain a set of accurate experimental data under high pressure. Substitution of Se for S causes an effect almost identical to pressure as far as the electronic phase diagrams are concerned (see Fig. 87 and the $x=0$ curve in Fig. 91). However, it should be noted that Se substitution increases the crystal volume rather than decreases it (Barthelemy *et al.*, 1976). $NiS_{1-y}Se_y$ is a charge-transfer-type compound (see below) whose band gap is formed between the occupied chalcogen p and empty Ni $3d$ states. Since the Se $4p$ band is higher than the S $3p$ band, Se substitution reduces the band gap and drives the system toward the metallic phase. The transition temperature T_t and the magnitude of the resistivity jump at T_t decrease with Se substitution in $NiS_{1-y}Se_y$. In fact, T_t is completely suppressed above $y\simeq 0.13$, where the electrical resistivity of the metallic phase can be studied down to $T\sim 0$. The resistivity of $Ni_{0.98}S_{1-y}Se_y$ shows a T^2 behavior at low temperatures and is analyzed using the formula $\rho=\rho_0+AT^2$ (Fig. 92) (Matoba and Anzai, 1987). The coefficient A, however, shows only a weak composition (y) dependence and does not show an increase towards the MIT ($y=0.1$ in $Ni_{0.98}S_{1-y}Se_y$). This is contrasted with the A of $NiS_{2-y}Se_y$ in the PM phase, which exhibits divergent behavior towards the PM-AFM transition, as predicted by spin-fluctuation theory (Moriya, 1985). Presumably, the first-order composition-dependent MIT in Se-substituted NiS has prevented our approaching the critical region. Indeed, the discontinuity of the lattice parameters at the y-dependent MIT is substantial at $T\sim 0$. Figure 90 shows that the magnetic susceptibility as well as the positive slope $d\chi/dT$ in the metallic phase decreases with Se concentration (Matoba, Anzai, and Fujimori, 1991). This may indicate that the antiferromagnetic spin fluctuations are weakened as the system is driven away from the MIT boundary into the metallic region. (The y dependence of ρ_0 was explained as due to disorder scattering.)

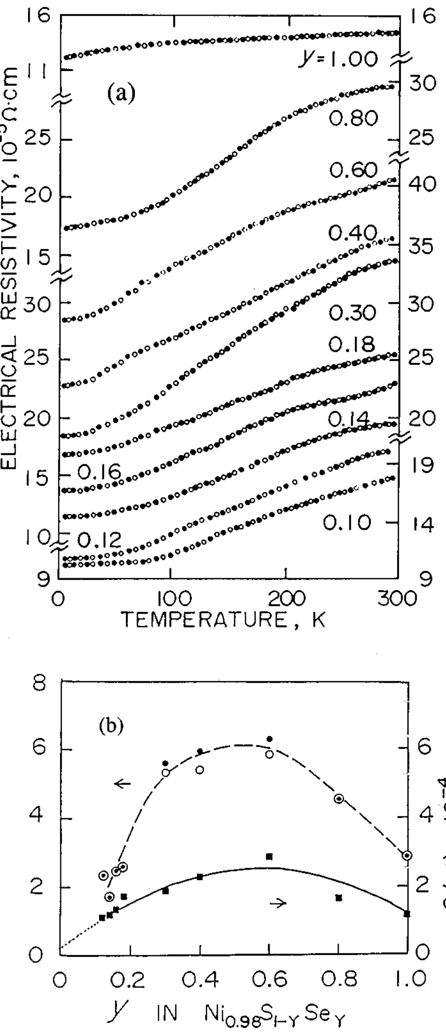

FIG. 92. Electrical resistivity of $Ni_{0.98}S_{1-y}Se_y$. (a) Temperature vs resistivity curves; (b) its low-temperature part is fitted to $\rho=\rho_0+AT^2$ and A and ρ_0 are plotted against Se concentration y. From Matoba and Anzai, 1987.

An FC-MIT in NiS can be studied in $Ni_{1-x}S$ (Sparks and Komoto, 1968). The MIT temperature T_t decreases with x in a manner analogous to that for pressure and Se substitution, and T_t is completely suppressed at $x \simeq 0.033$. This can be seen from the phase diagram of the $Ni_{1-x}S_{1-y}Se_y$ system shown in Fig. 91: $4x$ and y show almost the same effect on T_t. The changes in the thermoelectric power of $NiS_{1-y}Se_y$ with Se content (Matoba, Anzai, and Fujimori, 1991) are also almost identical to those of $Ni_{1-x}S$ (Ohtani, 1974) if "$4x$-y scaling" is applied. It should be noted that the Ni vacancies not only introduce holes but also decrease the volume, so that the $Ni_{1-x}S$ system is influenced by a combination of filling and bandwidth control. The volume contraction of $Ni_{1-x}S$ in going from $x=0$ to $x=0.033$ corresponds to that of NiS under pressure of ~ 10 kbar, which is half of the pressure (23 kbar) necessary to induce the MIT in NiS.

There have been studies of another type of substitution carried out on NiS, namely, $3d$ transition-metal substitution for Ni. It is not clear *a priori* whether this kind of substitution belongs to the BC type or the FC type; various experimental results and chemical considerations have been combined to estimate the number and sign of carriers in the substituted materials. Substituted Fe and Co are considered to form Fe^{2+} and Co^{2+} ions from the chemical point of view. This is consistent with the increase of T_t for Fe and the decrease of T_t for Co because FeS is more insulating and CoS more metallic (Coey and Roux-Buisson, 1979; Futami and Anzai, 1984). Substitution of Ti, V, or Cr for Ni is more subtle, since these elements can take various valence states in sulfides, although Ti and V tend to take valences higher than two (Anzai, Futami, and Sawa, 1981). Chemical shifts of core-level x-ray photoemission spectroscopy peaks indicated that Ti, V, and Cr are in the trivalent state and act as donors. Indeed, thermoelectric power in the nonmetallic phase changes the sign from positive to negative at around 2–5% V or Cr substitutions, indicating n-type doping to the NiS host (Matoba, Anzai, and Fujimori, 1994). Thermoelectric power in the metallic phase, on the other hand, remains negative, probably indicating that the transport properties of the metallic state with large Fermi surfaces is not sensitive to a small change in the band filling.

Now, we characterize more quantitatively the properties of conduction electrons in the metallic phase of NiS. The electronic contribution to the specific heat of NiS in the metallic phase is difficult to estimate because of the high MIT temperature. Brusetti *et al.* (1980) estimated the γT term by subtracting calculated lattice contributions from the measured entropy change at the MIT. The deduced value was $\gamma \simeq 6\ \mathrm{mJ\ mol^{-1}\ K^{-2}}$, which was incidentally close to the γ value of $Ni_{1-x}S$ with $x=0.04-0.05$, in which T_t is suppressed to zero. On the other hand, the magnetic susceptibility decreases with increasing Se concentration, as shown in Fig. 90. Thus the Wilson ratio $(\pi k_B^2/3\mu_B^2)(\chi/\gamma)$ decreases from ~ 2.9 for NiS ($\chi = 2.36\times 10^{-4}$ emu mol^{-1}) to ~ 2.1 for the 18% Se-substituted sample ($\chi = 1.75\times 10^{-4}$ emu mol^{-1}) if the same γ is assumed. The γ and χ of $Ni_{0.98}S_{1-x}Se_x$ were recently studied over the wide range of $0.1 < x \leqslant 1$ by Wada *et al.* (1997) and are plotted in Fig. 93, where one can see that the γ is constant and that the magnetic susceptibility is weakly enhanced near $x=0$, resulting in a weak enhancement of the Wilson ratio near $x=0$. If we compare the γ and the DOS at E_F deduced from an LDA band-structure calculation in the nonmagnetic state (Terakura, 1987), we obtain a mass enhancement factor $m^*/m_b = 1.7$. If A for $Ni_{0.98}S_{1-y}Se_y$ with $y \sim 0.1$ is employed, we obtain a Kadowaki-Woods ratio of $A/\gamma^2 \sim 5\times 10^{-5}\ \mu\Omega\ \mathrm{cm(mol\ K/mJ)^2}$, which is closer to (though significantly larger than) the strong-correlation limit 1.0×10^{-5} rather than the weak correlation limit 0.4×10^{-6}.

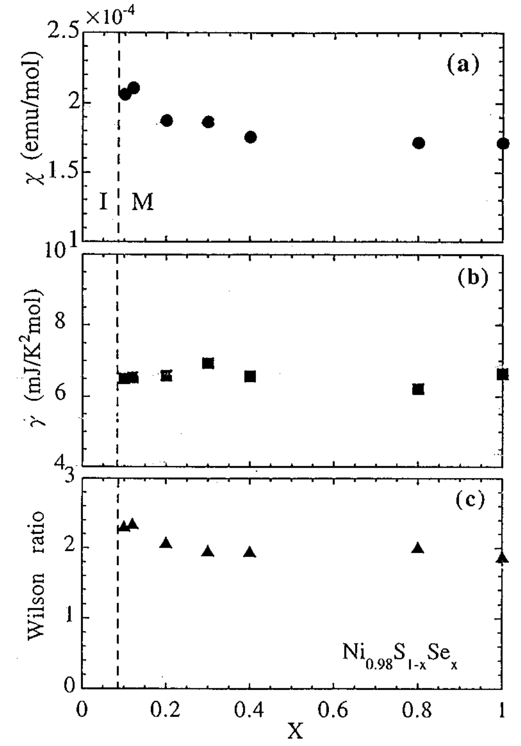

FIG. 93. Magnetic susceptibility χ at 300 K, the electronic specific-heat coefficient γ, and the Wilson ratio for $Ni_{0.98}S_{1-x}Se_x$. From Wada *et al.*, 1997.

Direct information about low-energy excitations was obtained in an infrared optical reflection study by Barker and Remeika (1974). Figure 94(a) shows the optical conductivity spectra obtained from the Kramers-Kronig analysis of the reflectivity data. The spectrum of the nonmetallic phase shows a threshold at 0.14 eV and a peak at 0.4 eV due to gap excitations. If the minimum band gap is an indirect one, the transport gap (indirect gap) can be much smaller than the optical gap. A non-self-consistent band-structure calculation by Mattheiss (1974) predicts a direct gap of 0.15 eV, whereas the minimum gap of indirect type is vanishingly small [Fig. 94(b)]. The ratio between the magnitude of the gap and that of the transition temperature, $2\Delta(0)/k_B T_t$, is ~ 6 if we take the threshold energy $2\Delta(0) = 0.14$ eV or ~ 18 if we take the peak energy $2\Delta(0) = 0.4$ eV. This indicates that the gap cannot be an ordinary SDW gap and that its opening involves electron correlation. Figure 94(a) also shows that the spectrum changes over a wide energy

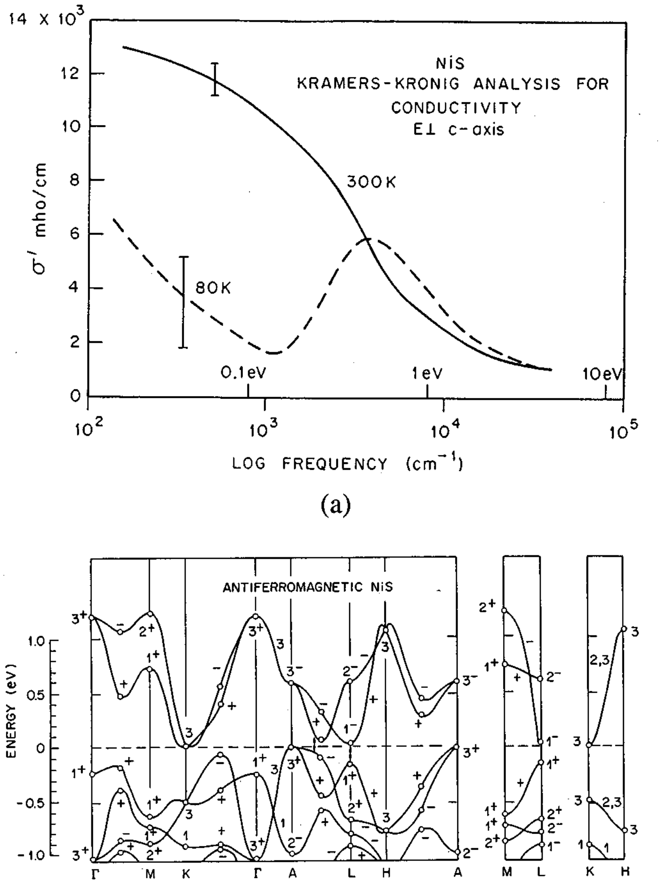

(a)

(b)

FIG. 94. Optical conductivity and band structure of NiS: (a) Optical conductivity. Solid curve, metallic phase; dashed curve, nonmetallic phase (Barker and Remeika, 1974). (b) Band structure of NiS in the antiferromagnetic state calculated by Mattheiss (1974). The arrows show direct gaps while the indirect gap is vanishingly small.

range (even above $h\nu \sim 1$ eV) between the two phases, indicating that the MIT reorganizes the electronic structure up to high energies. The Drude peak in the metallic phase is broad and the scattering rate of charge carriers is estimated to be as high as $1/\tau \sim 0.3$ eV (if one ignores the frequency dependence of $1/\tau$). The width of the Drude peak in the nonmetallic phase is an order of magnitude smaller than that in the metallic phase: $1/\tau \sim 0.03$ eV. From the mobility ratio between the metallic (M) and nonmetallic (NM) phases, $\mu_{\mathrm{M}}/\mu_{\mathrm{NM}} \sim 1/2$ (if we assume $n = 1/eR_H$ in both phases) and from the scattering rate ratio $\tau_{\mathrm{M}}/\tau_{\mathrm{NM}} \sim 1/10$, we may deduce the effective mass ratio $m^*_{\mathrm{M}}/m^*_{\mathrm{NM}} \sim 1/5$.

In order to explain the unusual transport and magnetic properties of NiS and its MIT mechanism, various models of the electronic structure have been proposed (White and Mott, 1971; Koehler and White, 1973). These models consider the e_g band of Ni near E_F in the nonmagnetic and magnetic states, with the t_{2g} and S $3p$ bands completely occupied. Earlier band-structure calculations (Tyler and Fry, 1971; Kasowski, 1973) did not take into account the magnetic ordering and were not able to predict the insulating behavior of the antiferromagnetic phase, whereas the calculated DOS well explains the overall line shape of the photoemission spectra (Hüfner and Wertheim, 1973). Mattheiss (1974) simulated the antiferromagnetic state within the non-self-consistent augmented plane-wave (APW) method by introducing a potential difference ($\pm V_s$) between the muffin-tin spheres of the spin-up and spin-down Ni sites and succeeded in opening a gap as described in Fig. 94(b). More recently, Terakura (1987) performed LSDA calculations for the antiferromagnetic as well as for the paramagnetic state, using the self-consistent linearized APW (LAPW) method. However, the self-consistent solution converged to a nonmagnetic state for the experimental lattice constants. In order to obtain the antiferromagnetic solution with a finite band gap, an external staggered magnetic field was applied, but the induced magnetic moment was still as small as $\sim 1\mu_B$, compared to the experimental value of $1.5-1.7\mu_B$ (Fujimori, Terakura, *et al.*, 1988). Figure 95(a) shows that although the calculated DOS of the paramagnetic state is in rather good agreement with experiment, the DOS for the antiferromagnetic state is quite different from the experimental line shape. The discrepancy was traced back to the exchange splitting as large as ~ 2 eV of the Ni $3d$ band in the calculated antiferromagnetic DOS, which vanishes in the nonmagnetic state.

As many difficulties are encountered in the band-theoretical description of the electronic structure of NiS, a different approach has been taken based on the NiS_6 cluster model, in which electron correlation is fully taken into account within a small cluster (Fujimori, Terakura, *et al.*, 1988), in analogy with the local cluster picture of NiO. Figure 95(b) shows that the theoretical photoemission spectrum calculated using the CI cluster model and the measured photoemission spectrum are in good agreement with each other. The result shows that the peak located from 0 to ~ 3 eV below E_F, which was previously assigned to the Ni $3d$ band, is now assigned to the $d^8\underline{L}$ charge-transfer final states, and the d^7 final states appear as satellites 5–10 eV below E_F (Hüfner, Riesterer, and Hulliger, 1985). Although the cluster model is too crude to describe the electronic structure near E_F, such as the semiconducting band gap of order 0.1 eV and the Fermi surfaces, it well describes the spectral weight distribution on the coarse energy scale of 1 eV to several eV. The calculated magnetic moment at the Ni site is found to be $1.7\mu_B$, in good agreement with experiment. This means that the reduction of the magnetic moment from the ionic value of Ni^{2+} ion is largely due to p-d covalency and we do not need to invoke itinerant-electron antiferromagnetism as previously suggested (Coey *et al.*, 1974).

Since the CI cluster model can describe localized electronic states with a finite local magnetic moment, the good agreement between the experimental and theoretical photoemission spectra and the magnetic moment indicates that the electronic structure of the nonmetallic phase of NiS is essentially that of a Mott insulator. On the other hand, the loss of local magnetic moment in the

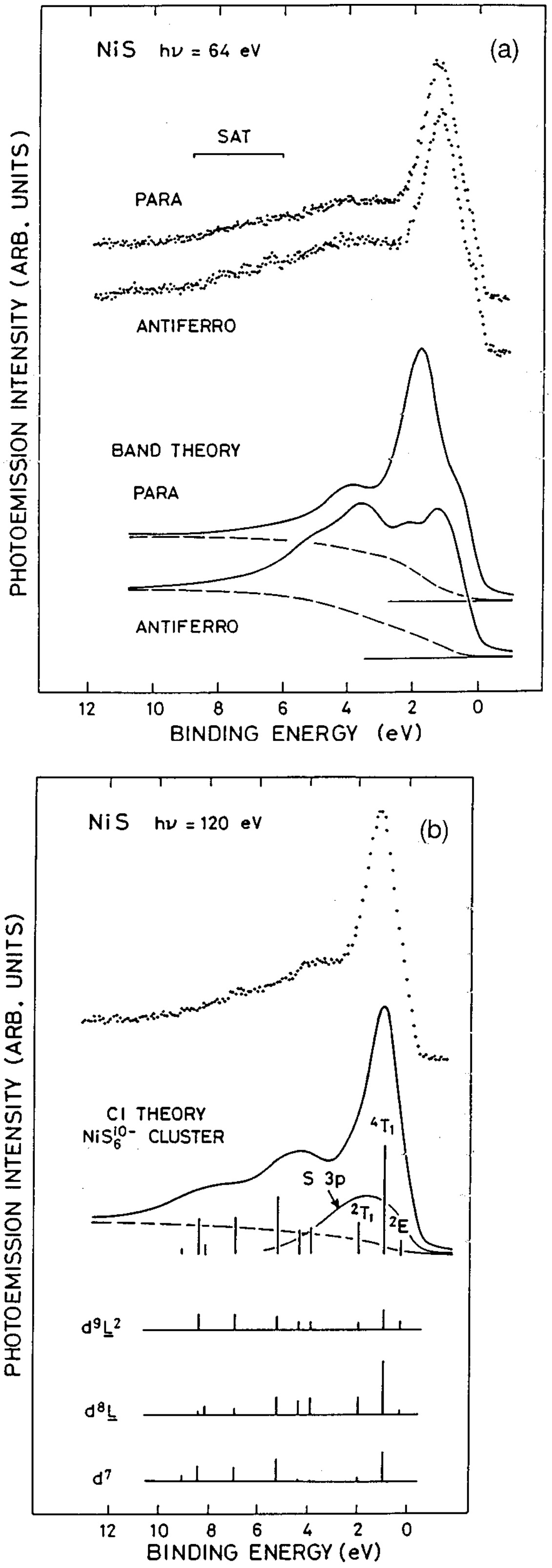

FIG. 95. Photoemission spectra of NiS in the metallic ($T = 300$ K) and nonmetallic ($T = 80$ K) phases compared with (a) the band-structure DOS of the nonmagnetic and antiferromagnetic states and (b) the CI cluster-model calculation (Fujimori *et al.*, 1988). Best-fit parameters are $\Delta = 2$, $U = 4$, and $(pd\sigma) = -1.5$ eV.

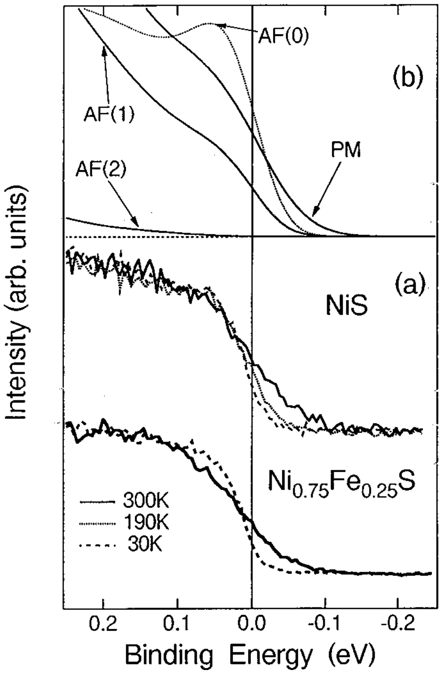

FIG. 96. Photoemission spectra of NiS ($T_t = 260$ K) and Fe-substituted NiS ($T_t \sim 350$ K) near the Fermi level compared with LDA (paramagnetic metal), LSDA [AF(1): metallic; AF(2): insulating], and LDA+U [AF(0)] band-structure calculations. From Nakamura *et al.*, 1994b.

metallic phase would naturally cast doubt upon the validity of the model in that phase, even though the calculated and measured photoemission spectra are in good agreement with each other. In order to reconcile the spectroscopic data and the nonmagnetic behavior, one could argue that the local magnetic moment exists on the time scale of photoemission (10^{-15} sec), but its fast quantum fluctuations lead to the Pauli paramagnetism. The unusual paramagnetic metallic state has been corroborated by an exact diagonalization study of a Ni$_4X_4$ cluster, where X is a sulfur atom in the present case and the degeneracy of the e_g orbitals is taken into account (Takahashi and Kanamori, 1991). Takahashi and Kanamori found that between the insulating phase (for large Δ), where the Ni ions are in the "high-spin" state ($\langle \mathbf{S}_{\mathrm{Ni}}^2 \rangle \sim 2$) and are antiferromagnetically coupled, and the metallic phase (for small Δ), where they are in the "low-spin" state ($\langle \mathbf{S}_{\mathrm{Ni}}^2 \rangle \sim 0.4$), there is an intermediate phase where the local moment remains substantial ($\langle \mathbf{S}_{\mathrm{Ni}}^2 \rangle \sim 1$) but the antiferromagnetic correlation between nearest neighbors is reduced. Calculated photoemission spectra do not significantly change between the insulating and intermediate phases, which may explain the result of the photoemission experiment.

The low-energy electronic structure and its temperature dependence were investigated using high-resolution photoemission spectroscopy by Nakamura *et al.* (1994b). Figure 96 shows the photoemission spectra near E_F taken with an energy resolution of ~25 meV. Starting from the thermally broadened Fermi edge of the metallic phase, a gap of ~10 meV is opened below T_t. A

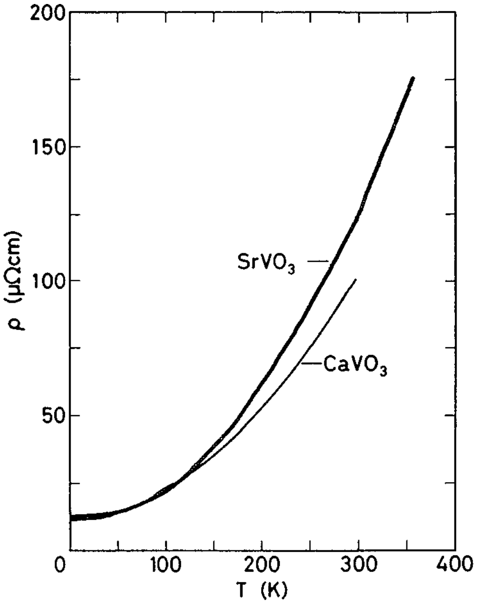

FIG. 97. Electrical resistivity of CaVO$_3$ and SrVO$_3$. From Onoda, Ohata, and Nagasawa, 1991.

remarkable feature in the spectra of the nonmetallic state is that the band edge is an almost resolution-limited step function, whereas the band-structure calculation (the LSDA calculation with the applied staggered magnetic field) predicts a much broader band edge. This means that actual energy bands near the top of the valence band are strongly narrowed compared to those predicted by band-structure calculations, most probably due to strong electron correlation. Comparison between the band DOS and the photoemission spectra of the nonmetallic phase shown in Fig. 96 suggests a band-narrowing factor (mass enhancement factor) of $m^*/m_b \gtrsim 10$. This value is larger than the mass enhancement factor in the metallic phase ($m^*/m_b = 1.7$) estimated from the electronic specific heat, and it is consistent with the relationship $m^*_{\rm M}/m^*_{\rm NM} \sim 1/5$ deduced from the transport and optical data above. It is tempting to view the very narrow quasiparticle bands near the band edge of the nonmetallic phase as reminiscent of a band structure with a nearly **k**-independent SDW gap, which is opened on the entire Fermi surfaces of the metallic states as in a BCS superconductor, even though the nonmetallic phase of NiS is not near a (hypothetical) second-order MIT. Recently, Miyake (1996) showed, using Luttinger's sum rule and the Ward identity, that in any spatial dimension, if a continuous phase transition occurs between a paramagnetic metal and an antiferromagnetic insulator, the Fermi surface should exhibit perfect nesting at the MIT on the metallic side.

5. $Ca_{1-x}Sr_xVO_3$

Both SrVO$_3$ and CaVO$_3$ exhibit metallic conductivity, as shown in Fig. 97, and nearly T-independent paramagnetism (apart from the increase at low temperatures probably due to impurities), as shown in Fig. 98 (Onoda, Ohta, and Nagasawa, 1991; Fukushima *et al.*, 1994; Inoue *et al.*, 1997b). Stoichiometric SrVO$_3$ crystallizes in a cubic perovskite structure, while CaVO$_3$, because of the small ionic radius of Ca^{2+} compared to Sr^{2+}, forms a GdFeO$_3$-type orthorhombic structure. Although they do not show a metal-insulator transition, magnetic ordering, or superconductivity, these compounds (and their alloy system Ca$_{1-x}$Sr$_x$VO$_3$) allow us to deduce important information about the nature of electron correlation in the normal metallic states when the d-band width is continuously varied. Both compounds are thought to be in the Mott-Hubbard regime (for details see below), and the V 3d bands are occupied by one electron per V atom. The on-site d-d Coulomb repulsion U is thought to be nearly the same for each of the two compounds because of the same valencies of the V ions. The difference between SrVO$_3$ and CaVO$_3$ lies in the different V-O-V bond angles, $\theta = 180°$ in SrVO$_3$ and $155°-160°$ in CaVO$_3$, which should lead to a decrease in the one-electron d-band width $W \propto \cos^2\theta$ by $\sim 15\%$ in going from SrVO$_3$ to CaVO$_3$, or equivalently an increase in the bare band mass m_b by $\sim 15\%$.

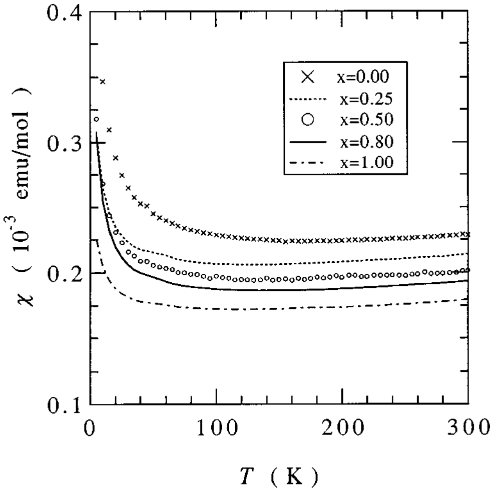

FIG. 98. Magnetic susceptibility of Ca$_{1-x}$Sr$_x$VO$_3$. From Inoue *et al.*, 1997b.

For CaVO$_3$, from the T-independent spin susceptibility $\chi = 2.3 \times 10^{-4}$ emu mol^{-1} (corrected for the core diamagnetism and the Van Vleck susceptibility) and the electronic specific-heat coefficient $\gamma = 9.25$ mJ mol^{-1} K^{-2} (Inoue *et al.*, 1997a), we obtain a Wilson ratio of $(\pi k_B^2/3\mu_B^2)(\chi/\gamma) = 1.8$, a value similar to those found for La$_{1-x}$Sr$_x$TiO$_3$ and Y$_{1-x}$Ca$_x$TiO$_3$ (Tokura, Taguchi, *et al.*, 1993; Taguchi *et al.*, 1993). As for SrVO$_3$, $\chi = 1.65 \times 10^{-4}$ emu mol^{-1} and $\gamma = 8.18$ mJ mol^{-1} K^{-2}, Inoue *et al.* (1997a, 1997b) give $(\pi k_B^2/3\mu_B^2)(\chi/\gamma) = 1.5$, which is smaller than the ratio of CaVO$_3$ by $\sim 20\%$. Electrical resistivity shows a nearly T^2 behavior (Fig. 97), indicating electron-electron scattering, but surprisingly the T^2 behavior persists up to room temperature. The Kadowaki-Woods ratio is $A/\gamma^2 = 0.9 \times 10^{-5}$ and 1.2×10^{-5} $\mu\Omega$ cm(mol K/mJ)^2 for CaVO$_3$ and SrVO$_3$, respectively, in the same range as heavy fermions in the case of perovskite-type Ti oxides (Tokura, Taguchi, *et al.*, 1993). In going from SrVO$_3$ to

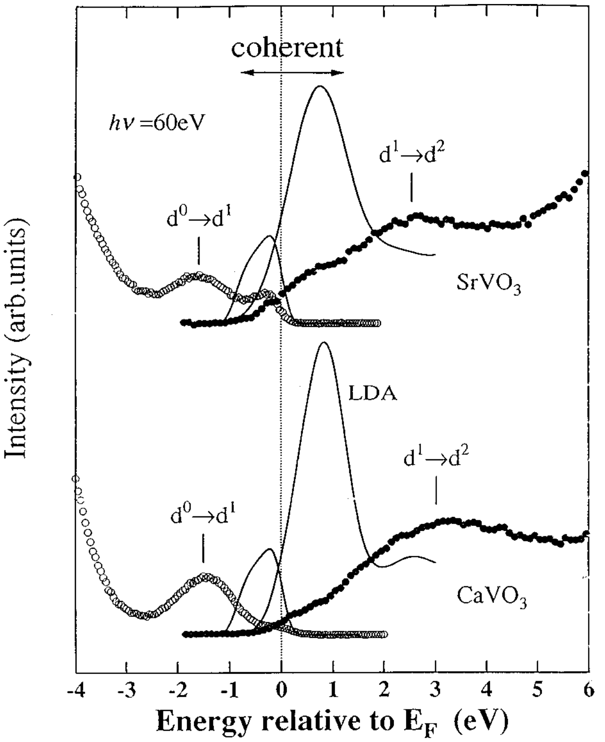

FIG. 99. Photoemission and inverse-photoemission spectra of $SrVO_3$ and $CaVO_3$ in the V $3d$ band region compared with a LDA band-structure calculation of Takegahara (1994). From Morikawa *et al.*, 1995.

$CaVO_3$, since the electronic specific heat indicates that the quasiparticle mass m^* increases by $\sim 15\%$ and the bare band mass m_b increases by $\sim 15\%$, the mass enhancement factor m^*/m_b does not increase. This is contrary to the general belief that the effective mass is enhanced (or even diverges) as one approaches the BC-MIT point with increasing U/W. As further evidence for normal Fermi-liquid behavior, the Hall coefficient of $SrVO_3$ is negative and has a nearly T-independent value, which corresponds to one electron per unit cell, as in $La_{1-x}Sr_xTiO_3$ with $x \gtrsim 1$ (Eisaki, 1991). An NMR study of $SrVO_3$ (Onoda, Ohta, and Nagasawa, 1991) showed a nearly T-independent Knight shift and a constant T_1T.

Further insight into the mass renormalization in $SrVO_3$ and $CaVO_3$ was obtained from a series of photoemission studies (Fujimori, Hase, *et al.*, 1992a; Inoue *et al.*, 1995; Morikawa *et al.*, 1995). Figure 99 shows combined photoemission and BIS spectra of $SrVO_3$ and $CaVO_3$. They show a typical Mott-Hubbard-type electronic structure as in V_2O_3: The V $3d$ band is located around E_F and the filled O $2p$ band well (3–10 eV) below E_F. It should be noted, however, that the "V $3d$ band" is not a simple V $3d$ band in the original Mott-Hubbard sense but is made up of states split off from the O $2p$ continuum due to strong p-d hybridization as in the case of V_2O_3. Since Δ's for V^{4+} compounds are smaller than those for V^{3+} compounds, $SrVO_3$ and $CaVO_3$ fall into the $\Delta < U$ region, meaning that the admixture of states with O $2p$ character into the "V $3d$ band" is even more substantial. A comparison between the photoemission spectra and the band-structure DOS of the t_{2g} subband of V $3d$ is made in Fig. 99. Spectral features from ~ -0.7 to $+1.5$ eV correspond to the V $3d$ band in the LDA band structure and are therefore attributed to the coherent contribution or the quasiparticle part of the V $3d$-derived spectral function. The peak at ~ -1.6 eV has no corresponding feature in the band-structure DOS and is therefore attributed to the incoherent part of the spectral function, reminiscent of the lower Hubbard band. The photoemission spectra of $Ca_{1-x}Sr_xVO_3$ shown in Fig. 100 indicate a systematic spectral weight transfer with increasing U/W. The V $3d$ spectral weight is transferred from the coherent part to the incoherent part of the spectral function (Inoue *et al.*, 1995), in good agreement with the dynamic mean-field calculation of the Hubbard model (Zhang, Rozenberg, and Kotliar, 1993). However, there is an important difference between the dynamic mean-field calculation and the experimental results. That is, with increasing U/W, the quasiparticle band is narrowed in the calculation whereas the overall intensity of the quasiparticle band decreases without significant band narrowing in the measured spectra. A high-resolution photoemission study has confirmed the absence of a sharp quasiparticle peak at E_F (Morikawa *et al.*, 1995).

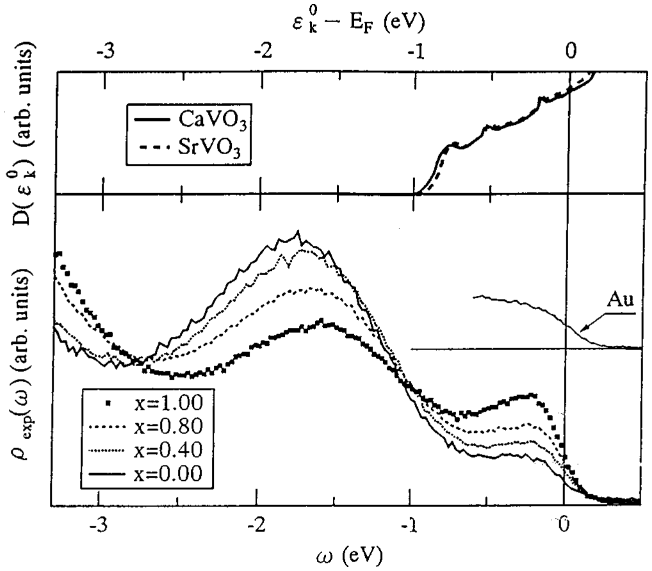

FIG. 100. Photoemission spectra of $Ca_{1-x}Sr_xVO_3$ in the V $3d$ band region (Inoue *et al.*, 1995). The upper panel shows the DOS derived from LDA band-structure calculation.

The deviation of the spectral function $\rho(\omega)$ from the LDA band structure can be expressed in terms of a self-energy correction $\Sigma(\mathbf{k},\omega)$ to the LDA eigenvalues $\varepsilon_0(\mathbf{k})$ as described in Sec. II.D.1. The spectral intensity at E_F, $\rho(\mu)$, differs from that of the LDA calculation by a factor m_k/m_b, where m_k is the k mass defined by the momentum derivative of the self-energy [Eq. (2.73e)]. The quasiparticle mass m^*, which is inversely proportional to the coherent bandwidth and is equal to the thermal (and transport) masses, is given by $m^*/m_b = (m_\omega/m_b)(m_k/m_b)$, where m_ω is the ω mass defined by the

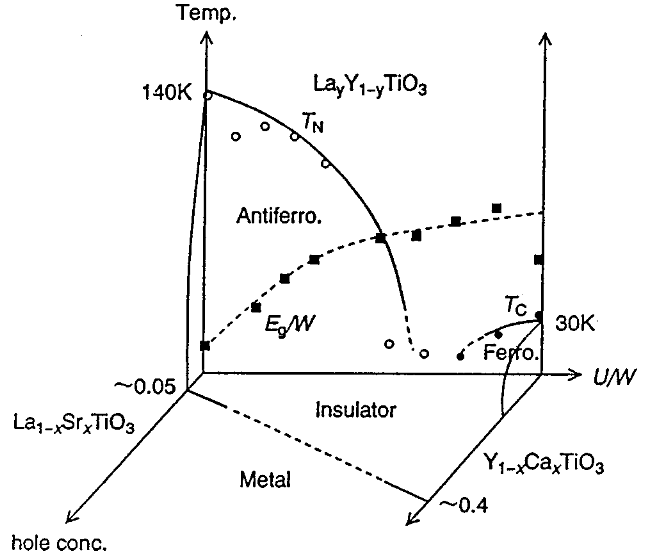

FIG. 101. Electronic and magnetic phase diagram for the $R_{1-x}Sr_xTiO_3$.

energy derivative of the self-energy [Eq. (2.73d)]. Here, we have assumed that the quasiparticle residue $Z_{\mathbf{k}}(\omega)$ [Eq. (2.70)] does not vary significantly within the quasiparticle band ($Z_{\mathbf{k}}(\omega) \equiv m_b/m_\omega$). Then the coherent-to-incoherent spectral weight ratio is given by $m_b/m_\omega:(1-m_b/m_\omega)$. The remarkable spectral weight transfer from the coherent part to the incoherent part in going from $SrVO_3$ to $CaVO_3$ means that m_ω increases as the system approaches the Mott transition from the metallic side. The observed simultaneous decrease in spectral intensity at E_F indicates that m_k decreases towards the Mott transition: for $SrVO_3$, $m_k/m_b \simeq 0.25$, $m_\omega/m_b \simeq 6$, and $m^*/m_b \simeq 1.5$; for $CaVO_3$, $m_k/m_b \simeq 0.07$, $m_\omega/m_b \simeq 20$, and $m^*/m_b \simeq 1.4$. Almost the same m^* for the two compounds is consistent with the specific heat γ and the effective electron numbers ($\propto 1/m^*$) deduced from an evaluation of the optical conductivity at about 1.5 eV (Dougier, Fan, and Goodenough, 1975).

B. Filling-control metal-insulator transition systems

1. $R_{1-x}A_xTiO_3$

The perovskitelike $RTiO_3$ (where R is a trivalent rare-earth ion) and its "hole-doped" analog $R_{1-x}A_xTiO_3$ (where A is a divalent alkaline-earth ion) are among the most appropriate systems for experimental investigations of the FC-MIT. The end member $RTiO_3$ is a typical Mott-Hubbard (MH) insulator with Ti^{3+} $3d^1$ configuration, and the A (Sr or Ca) content (x) represents a nominal "hole" concentration per Ti site, or equivalently the $3d$ band filing (n) is given by $n = 1-x$.

The electronic and magnetic phase diagram for $R_{1-x}Sr_xTiO_3$ is depicted in Fig. 101. The crystalline lattice is an orthorhombically distorted perovskite (of the $GdFeO_3$ type; see Fig. 61). As described in detail in Sec. III.C.1, the Ti-O-Ti bond angle distortion, which affects the transfer energy (t) of the $3d$ electron or the one-electron bandwidth (W), depends critically on the ionic radii of the (R,A) ions or the tolerance factor. For example, the Ti-O-Ti bond angle is 157° for $LaTiO_3$ but decreases to 144° (ab plane) and 140° (c axis) for $YTiO_3$ (MacLean *et al.*, 1979), which causes a reduction in W of the t_{2g} state by as much as 20%, according to an estimate by a simple tight-binding approximation (Okimoto *et al.*, 1995b). The W value can be finely controlled by use of the solid solution $La_{1-y}Y_yTiO_3$ or in $RTiO_3$ by varying the R ions. The abscissa in Fig. 101 thus represents the effective correlation strength U/W.

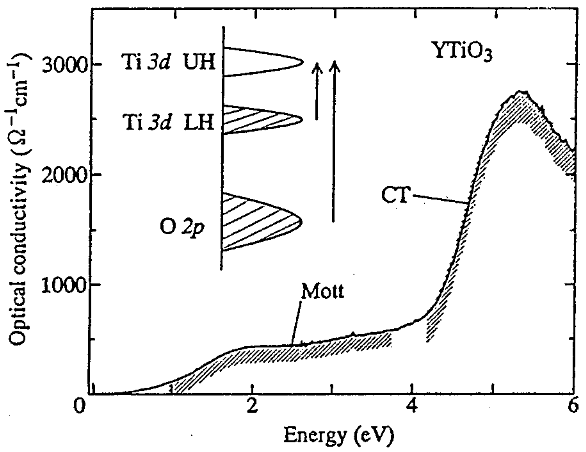

FIG. 102. Optical conductivity in $YTiO_3$. From Okimoto *et al.*, 1995b.

On the end ($x=0$) plane, the variation of the antiferromagnetic (AF) and ferromagnetic (F) transition temperatures is plotted for $La_{1-y}Y_yTiO_3$ (Goral, Greedan, and MacLean, 1982; Okimoto *et al.*, 1995b). Due to orbital degeneracy and orbital ordering, the $x=0$ insulators with large U/W value or a Y-rich ($y<0.2$) region show a ferromagnetic ground state. In fact, a recent study using polarized neutrons showed the presence of t_{2g} orbital ordering associated with a minimal Jahn-Teller distortion of TiO_6 octahedron (Akimitsu *et al.*, 1998).

Figure 102 shows the optical conductivity spectrum of the gap excitations in $YTiO_3$ (Okimoto *et al.*, 1995b): The onset of the Mott-Hubbard gap transition can be clearly seen around 1 eV, while the rise in optical conductivity around 4 eV is ascribed to the charge-transfer gap between the O $2p$ filled state and the Ti $3d$ upper Hubbard band. The observation of the two kinds of gap transition and their relative positions indicate that $RTiO_3$ is a Mott-Hubbard insulator rather than a CT insulator in the scheme of Zaanen, Sawatzky, and Allen. The U/W dependence of the Mott-Hubbard gap magnitude (E_g) normalized by W, which was obtained by optical measurements of $La_{1-y}Y_yTiO_3$ (Okimoto *et al.*, 1995b), is plotted in the $x=0$ end plane of Fig. 101. The Mott-Hubbard gap magnitude changes critically with a rather gentle change ($=20\%$) of W. A similar W dependence of the Mott-Hubbard gap was also observed for a series of $RTiO_3$ (Crandles *et al.*, 1994; Katsufuji, Okimoto, and Tokura, 1995; Katsufuji, Okimoto, Arima, Tokura, and Torrance, 1995).

Before considering the electronic structure of $R_{1-x}A_x\mathrm{TiO}_3$, it is necessary to understand the electronic structure of the parent Mott insulators $R\mathrm{TiO}_3$. Neither the local spin-density approximation nor the generalized gradient approximation is sufficient to explain the insulating nature of these compounds within one-electron band theory; calculations on the level of the Hartree-Fock or LDA+U approximation, in which the spin and orbital degrees of freedom are taken into account on an equal footing, are found to be necessary (Mizokawa and Fujimori, 1995, 1996b; Solovyev, Hamada, and Terakura, 1996b). With decreasing size of the R ion, $R\mathrm{TiO}_3$ changes from an antiferromagnetic insulator (LaTiO_3) to a ferromagnetic insulator (YTiO_3). According to the Hartree-Fock calculation (which includes the Ti $3d$ spin-orbit interaction), the t_{2g}^1 configuration in the nearly cubic LaTiO_3 is in the quadruply degenerate spin-orbit ground state, out of which two states with antiparallel orbital and spin moments [both directed in the (111) direction] are alternating between nearest neighbors, resulting in a G-type antiferromagnetic state (see Fig. 38). Larger GdFeO_3-type distortion [see Figs. 38(a) and 61] induces greater hybridization between neighboring xy, yz, and zx orbitals, which makes the antiferro-orbital exchange as well as ferromagnetic exchange larger through the Hund's-rule coupling. The ordering stabilizes the Jahn-Teller distortion of type d (see Fig. 38) and the t_{2g} level is split into two lower-lying levels and one higher-lying level (for example, for an octahedron elongated along the x direction, the energies of the xy and zx orbitals are lowered relative to the yz orbital). At each site, one of the two low-lying orbitals is occupied so that the neighboring orbitals are approximately orthogonal to each other with the spins ferromagnetically aligned. This is why the G-type antiferromagnetic order and the small Jahn-Teller distortion in LaTiO_3 is changed to ferromagnetic order with d-type Jahn-Teller distortion in YTiO_3. It has always been controversial whether orbital ordering is driven by electron-electron interaction or by electron-lattice interaction (the Jahn-Teller effect). Considering the small Jahn-Teller distortion in the present Ti perovskites, the orbital ordering would be largely of electronic origin.

Filling control in the $3d$ band can be achieved by partially replacing the trivalent ions with divalent Ca or Sr ions. The solid solution can be formed for an arbitrary R/A ratio and hence the filling (n) can be varied from 1 to 0. Figure 103 shows the temperature dependence of the resistivity for $\mathrm{LaTiO}_{3+\delta/2}$ or $\mathrm{La}_{1-x}\mathrm{Sr}_x\mathrm{TiO}_3$ and for $\mathrm{Y}_{1-x}\mathrm{Ca}_x\mathrm{TiO}_3$ near the FC-MIT. For LaTiO_3, which has relatively weak electron correlation, several % of hole-doping is sufficient to destroy the antiferromagnetic ordering and cause the MIT. To control the filling on a fine scale, nonstoichiometry ($\delta/2$) of oxygen is also utilized, as shown in the figure: $n=1-\delta$. The upturn or inflection point in the resistivity curve corresponds to the antiferromagnetic transition temperature. For YTiO_3 with larger U/W, by contrast, the insulating phase persists up to $x=0.4$, though ferromagnetic spin ordering disappears around $x=0.2$ (see also Fig. 101; Taguchi *et al.* 1993; Tokura, Taguchi, *et al.*, 1993). In the immediate vicinity of the MIT, the resistivity curve of $\mathrm{Y}_{1-x}\mathrm{Ca}_x\mathrm{TiO}_3$ shows a maximum around 150–200 K. The resistivity behavior below the temperature for the maximum is accompanied by thermal hysteresis, indicating the occurrence of a first-order insulator-metal transition, although this feature is blurred, perhaps due to the inevitable randomness of a mixed-crystal system. A similar temperature dependence or reentrant MIT with change of temperature was observed in $\mathrm{Sm}_{1-x}\mathrm{Ca}_x\mathrm{TiO}_3$ near the FC-MIT (Katsufuji, Taguchi, and Tokura, 1997). However, no structural transition has been detected so far near the hysteresis.

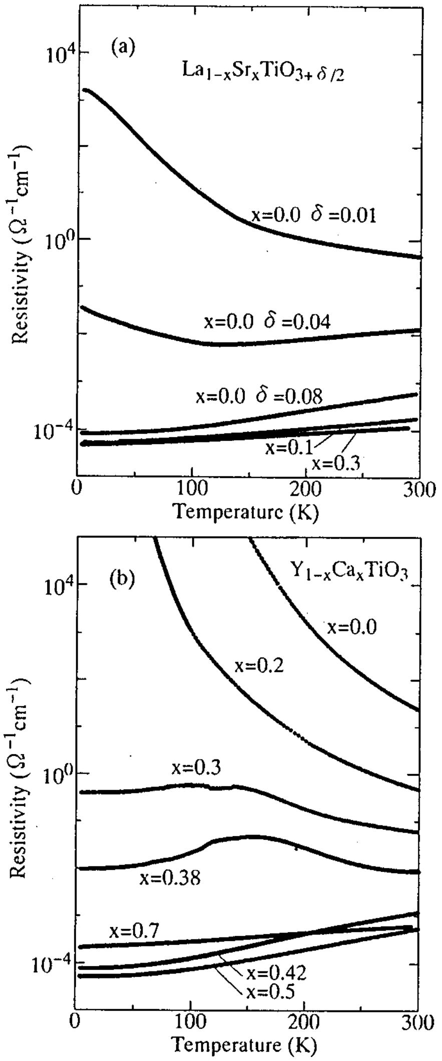

FIG. 103. Temperature dependence of the resistivity for $\mathrm{LaTiO}_{3+\delta/2}$ or $\mathrm{La}_{1-x}\mathrm{Sr}_x\mathrm{TiO}_3$ and for $\mathrm{Y}_{1-x}\mathrm{Ca}_x\mathrm{TiO}_3$. From Katsufuji and Tokura, 1994.

Metallic compounds, $\mathrm{La}_{1-x}\mathrm{Sr}_x\mathrm{TiO}_3$ for $x>0.05$ and $\mathrm{Y}_{1-x}\mathrm{Ca}_x\mathrm{TiO}_3$ for $x>0.4$, show strongly filling-dependent properties near the metal-insulator phase boundary (Kumagai *et al.*, 1993; Taguchi *et al.*, 1993; Tokura, Taguchi, *et al.*, 1993). The upper panel of Fig.

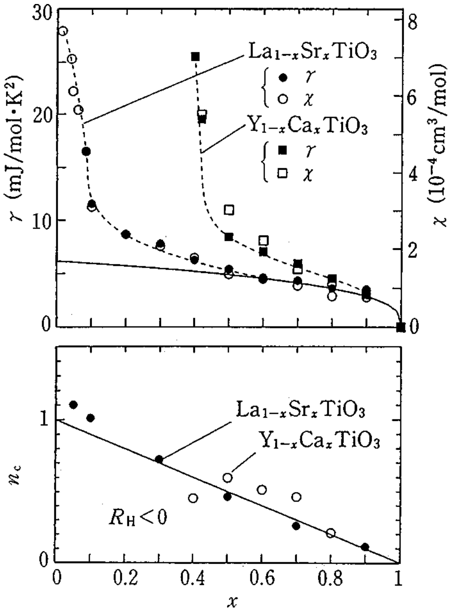

FIG. 104. Upper panel, x-dependence of the electronic specific-heat coefficient (γ) and the Pauli paramagnetic susceptibility (χ) in the metallic region of $La_{1-x}Sr_xTiO_3$ and $Y_{1-x}Ca_xTiO_3$; Lower panel, the effective carrier number per Ti-site (n_c), deduced from the Hall coefficient (R_H) as a function of $x=(1-n)$ (Tokura *et al.*, 1993; Taguchi *et al.*, 1993).

104 shows the x dependence of the electronic specific-heat coefficient (γ) and the Pauli paramagnetic susceptibility (χ) in the metallic region of $La_{1-x}Sr_xTiO_3$ and $Y_{1-x}Ca_xTiO_3$. In the lower panel of the figure, the effective carrier number per Ti site (n_c), deduced from the Hall coefficient (R_H) via the relation $R_H=1/n_cec$, is shown as a function of $x=(1-n)$. Thus the estimated value of n_c approximately equals the filling n, as indicated by a solid line in the lower panel of the figure. Such a relation is consistent with a simple band picture. On the other hand, γ shows a critical increase as the system approaches the Mott-Hubbard insulator phase ($x\simeq 0$). The x dependence of χ is almost parallel with that of γ, showing a nearly constant Wilson ratio of about 2. Provided that the band is parabolic with a constant effective mass m^*, γ or the density of states at the Fermi level (E_F) should be proportional to $n^{1/3}$, as shown by a solid line in the upper panel of Fig. 104. The critical enhancement of γ and χ as compared with this reference line is ascribed to the increase of m^* as the system approaches the Mott-Hubbard insulator phase. Such a filling-dependent mass renormalization is a generic feature of the FC-MIT, as predicted theoretically (Furukawa and Imada, 1992; Imada, 1993a; see Sec. II.G). The mass enhancement observed in the experiments also is consistent with the result in infinite dimensions (Rozenberg, Kotliar, and Zhang, 1994; see for a review, Georges *et al.*, 1996). The observed Wilson ratio is clearly not inconsistent with the $d=\infty$ result, as discussed in Sec. II.D.6. In the case of $Y_{1-x}Ca_xTiO_3$, a large mass enhancement in metals near $x\sim 0.4$ may be associated with orbital fluctuations instead of spin fluctuations.

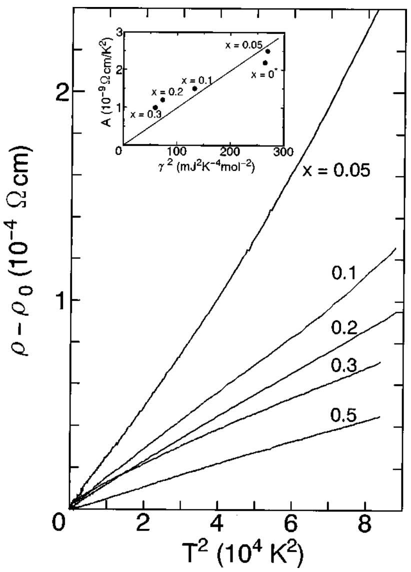

FIG. 105. Temperature dependence of the resistivity in metallic $La_{1-x}Sr_xTiO_3$. From Tokura *et al.*, 1993.

The temperature dependence of the resistivity in metallic $La_{1-x}Sr_xTiO_3$ can be well expressed up to 300 K by the relation $\rho=\rho_0+AT^2$, as can be seen in Fig. 105. The T^2 dependence of the resistivity is reminiscent of the dominant electron-electron scattering process as derived in Eq. (2.83) (see Sec. II.E.1). The coefficient A is also enhanced as the Mott-Hubbard insulator is approached from the metallic side. In the inset of the figure, the relation between A and γ is shown for the samples near the metal-insulator boundary. The well-known relation for heavy-fermion systems, $A=C\gamma^2$ (Kadowaki and Woods, 1986), also seems to hold approximately in this system, with $C[=1.0\times 10^{-11}\ \Omega\ \mathrm{cm(mol\ K/mJ)^2}]$, which is nearly the same as the universal constant (Tokura, Taguchi, *et al.*, 1993). This proportional constant seems to be in agreement with the infinite-dimensional result (Moeller *et al.*, 1995).

Such a critical enhancement of the carrier effective mass near the MIT phase boundary can also be probed by Raman spectroscopy. According to the theory of Mills, Maradudin, and Burstein (1970) for phonon Raman scattering in metals, the scattering cross section of an even-parity phonon is given by

$$\frac{d^2I}{d\Omega\, d\omega}\propto\{\gamma_{ph}/[\gamma_{ph}^2+(\omega-\omega_{ph})^2]\}|\delta\chi|^2, \tag{4.3}$$

where ω_{ph} is the phonon frequency and γ_{ph} is the width of the phonon spectrum. $\delta\chi$ is the modulation of the charge susceptibility caused by the atomic displacements. It was shown by a crude approximation (Katsufuji and Tokura, 1994) that $\delta\chi$ is proportional to the Drude weight, n_c/m^*. The Raman process in metals is mediated by particle-hole excitations across the Fermi level, while that in insulators is mediated by interband transitions. Thus, roughly speaking, the spectral intensity of the phonon is proportional to $(n_c/m^*)^2$ or the square of the Drude weight in metals. [However, we

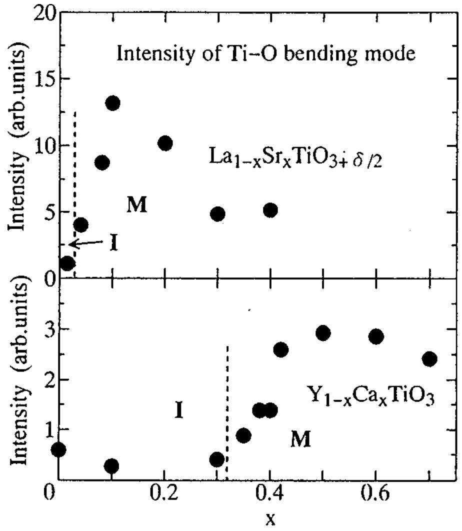

FIG. 106. Variation of phonon Raman intensities for the Ti-O bending A_{1g} mode as a function of x in $La_{1-x}Sr_xTiO_3$ and $Y_{1-x}Ca_xTiO_3$. From Katsufuji and Tokura, 1994.

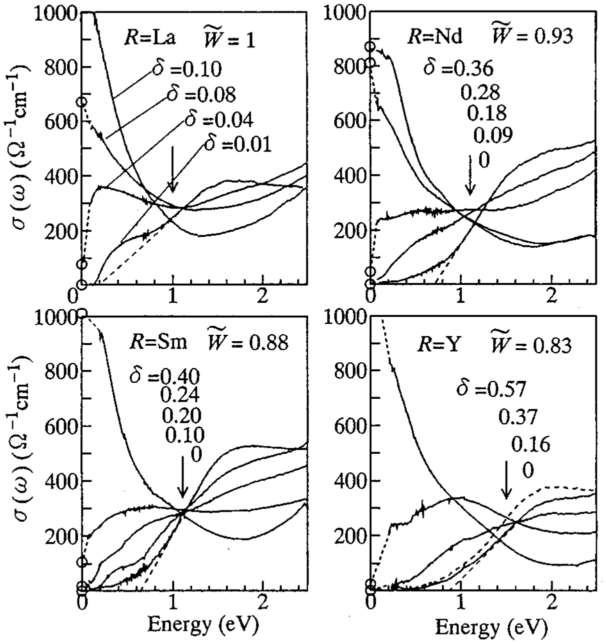

FIG. 107. Optical conductivity spectra in $R_{1-x}Sr_xTiO_{3+y}$ or $R_{1-x}Ca_xTiO_{3+y}$ (R=La, Nd, Sm, and Y). From Katsufuji, Okimoto, and Tokura, 1995.

need more careful analysis on the frequency dependence. As we shall discuss later, the true Drude weight is very small, with a presumably smaller frequency width than the phonon frequency ω_{ph} in the Raman process. In the frequency range out of the Drude-dominant frequency, $\sigma(\omega)$ is governed by the incoherent charge dynamics discussed in Secs. II.F.1 and II.G.9. Therefore, strictly speaking, the intensity picks up the incoherent weight of intraband excitations.] We show in Fig. 106 the variation of phonon Raman intensities for the Ti-O bending A_{1g} mode as a function of x in $La_{1-x}Sr_xTiO_3$ and $Y_{1-x}Ca_xTiO_3$. This mode becomes Raman active as a result of the orthorhombic distortion of the crystalline lattice, which is present for $x<0.4$ in $La_{1-x}Sr_xTiO_3$ and for the whole compositional range in $Y_{1-x}Ca_xTiO_3$. As can be seen in the figure, the spectral intensity in the metallic regions steeply decreases as the metal-insulator phase boundary (vertical dotted lines) is approached, and almost disappears in the insulating regions. This indicates that this phonon Raman mode is activated in the metallic state via coupling with the intraband excitation across the Fermi level, as described above, but not in the insulating state with a charge gap larger than the phonon energy. The phonon intensity can be corrected by the x-dependent orthorhombic distortion. It decreases to zero with decreasing x, indicating that the intraband response at ω_{ph} vanishes as the MIT is approached. As is noticed by Katsufuji and Tokura (1994), this x dependence of the phonon intensity is roughly scaled by $[(1-x)/\gamma]^2$ where γ is the specific-heat coefficient. Although the simple interpretation of $\delta\chi$ as the Drude weight needs caution as discussed above, it is interesting to note that $\delta\chi$ appears to follow the scaling $(1-x)/\gamma$, implying that the low-energy incoherent weight given by the ω-independent prefactor for the incoherent part of $\sigma(\omega)$ follows the same scaling as $1/\gamma$ near $x=0$.

The FC-MIT causes a change in electronic structure over a fairly large energy scale. In particular, spectral weight transfer from the correlation gap (Mott-Hubbard or CT gap) excitations to the inner gap excitations with carrier doping is a common feature of FC-MIT systems. The doping-induced changes in the optical conductivity spectra in $R_{1-x}Sr_xTiO_{3+y}$ or $R_{1-x}Ca_xTiO_{3+y}$ (where R=La, Nd, Sm, and Y and y is a small oxygen nonstoichiometry, mostly <0.02; Katsufuji, Okimoto, and Tokura, 1995) are shown in Fig. 107. The spectra of the respective samples are labeled with the nominal hole concentration δ, where $\delta=x+2y=1-n$, and with the value of the one-electron bandwidth $\widetilde{W}$ normalized by that of $LaTiO_3$. The open circles show the magnitude of the dc conductivity, $\sigma(\omega=0)$, at room temperature. In the case of R=Nd ($Nd_{1-x}Ca_xTiO_3$), for example, $\sigma(\omega)$ for $\delta=0$ ($n=1$) shows negligible spectral weight below 0.8 eV but steeply increases above 0.8 eV due to the onset of the Mott-Hubbard gap excitations. The spectral weight of the Mott-Hubbard gap excitations is reduced with increase of δ, while that inside the gap increases. The spectral weight appears to be transferred gradually one from the above-gap region to the inner-gap region across an isosbetic (equal-absorption) point around 1.2 eV.

It is remarkable in Fig. 107 that, though $\sigma(\omega)$ changes with δ in a similar way irrespective of the element R, the evolution rate of the inner-gap excitation (quasi-Drude part) with δ is critically dependent on the magnitude of W. That is, spectral weight transfer into the quasi-Drude part decreases with a decrease of W. In quantitative terms, the effective number of electrons is

$$N_{eff}(\omega)=\frac{2m_0}{\pi e^2 N}\int_0^{\omega}\sigma(\omega')d\omega \tag{4.4}$$

where m_0 is the free-electron mass and N the number of

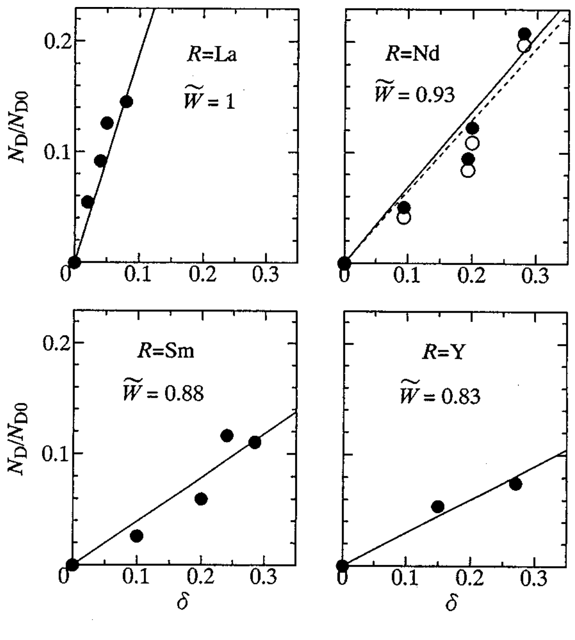

FIG. 108. N_D to N_{D0} as a function of δ (Katsufuji, Okimoto, and Tokura, 1995) for $La_{1-x}Sr_xTiO_3$.

Ti atoms per unit volume. $N_{eff}(\omega)$ is nearly independent of δ, with $\omega=2.5$ eV, which includes the spectral weight of both the inner-gap and the Mott-Hubbard-gap excitations. The sum of these two parts is nearly conserved under a variation of δ, but the spectral weight is transferred from the Mott-Hubbard part to the inner-gap part across the isosbetic point $\hbar\omega_c$ (≈ 1.1 eV for $Nd_{1-x}Ca_xTiO_3$). Thus the value defined as $N_D = N_{eff}(\omega_c)_\delta - N_{eff}(\omega_c)_{\delta=0}$ is the low-energy spectral weight transferred from the higher-energy region with doping. In Fig. 108, N_D, which is normalized to N_{D0}, the value of N_D for $U=0$ and $\delta=0$ ($n=1$), is plotted as a function of δ. The observed linear increase of N_D with δ,

$$N_D/N_{D0}=C\delta, \tag{4.5}$$

is consistent with theoretical studies of the Hubbard model in $d=\infty$ (Jarrell, Fredericks, and Pruschke, 1995), provided that N_D is interpreted as the Drude weight at $\omega=0$. However, because N_D also includes incoherent excitations up to ω_c, this δ dependence is dominated by that of the intraband kinetic energy and hence dominated by the incoherent charge response discussed in Sec. II.F.1. In fact, the optical conductivity shown in Fig. 107 shows a rather similar feature to the incoherent response $\sigma(\omega)\simeq(1-e^{-\beta\omega})/\omega$ discussed in Secs. II.F.1, II.G.9, and II.M.2 because both have a long tail at large ω roughly scaled as $1/\omega$, although $\sigma(0)\sim 1/T^2$ seen in Fig. 105 does not fit this form. This implies that the true Drude weight associated with T^2 resistivity is very small, only prominent around $\omega\sim 0$, while the dominant weight in the observed $\sigma(\omega)$ is exhausted in the incoherent part with the long tail up to large $\omega\sim 1$ eV. This is in contrast with the theoretical results in $d=\infty$ and similar to the incoherent response discussed in Secs. II.F.1 and II.G.9. The integrated intensity itself (namely, the kinetic energy of the intraband part containing both the true Drude and the incoherent responses) seems to be scaled by the doping level and is consistent with both the scaling theory in Sec. II.G.9 and the $d=\infty$ result (Kajueter and Kotliar, 1997).

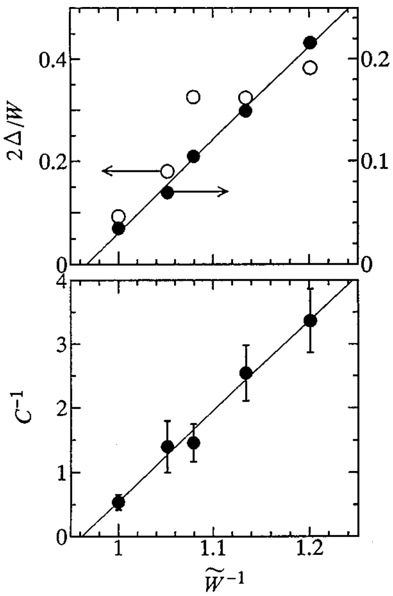

FIG. 109. Lower panel, the W^{-1} (strength of electron correlation) dependence of C^{-1}: upper panel, the value of $2\Delta/W$ (the optical energy gap normalized to the bandwidth) as well as the activation energy ($2\Delta_{act}$) of the resistivity for $R_{1-x}Ca_xTiO_3$. From Katsufuji, Okimoto, and Tokura, 1995.

Figure 109 (lower panel) shows the W^{-1} (strength of electron correlation) dependence of C^{-1}, while the upper panel shows the value of $2\Delta/W$ (the optical energy gap normalized to the bandwidth) as well as the normalized activation energy ($2\Delta_{act}/W$) of the resistivity. The solid line, which is a linear fit to the data points of $2\Delta_{act}/W$, crosses the $2\Delta=0$ line (abscissa) at a finite value of $W(\approx 0.97)$ corresponding to the critical value for the BC-MIT $[(U/W)_c]$ at which the charge gap closes and the Mott transition occurs. The relation $\Delta_{act} \propto [U/W-(U/W)_c]^\alpha$ with the exponent $\alpha\sim 1$ implies that the critical exponents of a BC-MIT here are characterized by $\nu z\sim 1$ where ν and z are the correlation length and dynamic exponents, respectively, as is discussed in Sec. II.F.4 [see Eq. (2.332)].

On the other hand, the lower panel of Fig. 109 indicates that C^{-1} decreases linearly with a decrease in W^{-1}. It is to be noted that the value of W^{-1} at which C^{-1} becomes zero nearly coincides with the value at which 2Δ becomes zero. This means that the rate of evolution of the low-energy incoherent part with δ is critically (divergently) enhanced as the electron correlation (U/W) approaches the critical value $(U/W)_c$ for the BC-MIT, following the relation

$$C\propto[(U/W)-(U/W)_c]^{-1}. \tag{4.6}$$

Strictly speaking, the MIT is defined as the point where the true Drude weight vanishes. However, it is interesting to note that the weight of the broad incoherent part

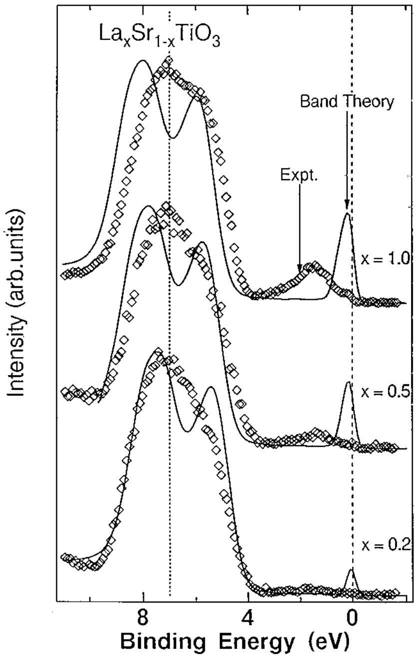

FIG. 110. Photoemission spectra of $La_{1-x}Sr_xTiO_3$. From Fujimori *et al.*, 1992b.

with the $1/\omega$ tail also more or less vanishes at the BC-MIT point because $N_{eff}(\omega_c)_{\delta=0}$ is small. Since N_{eff} measures the kinetic energy when ω is taken to be large, C measures approximately the singular part of the kinetic energy near the MIT. The exponent in Eq. (4.6) contradicts that in the Gutzwiller approximation given in Eq. (2.198), which implies the breakdown of the mean-field treatment in 3D.

A proper microscopic description of mass enhancement near the FC-MIT is an important step in elucidating the nature of the Mott transition, as reflected by the specific heat and the magnetic susceptibility mentioned above. Photoemission spectroscopy gives such information in the same way as was described for the bandwidth-control system $Ca_{1-x}Sr_xVO_3$ (Sec. IV.A.5). For filling-control systems, in addition to the spectral weight transfer between the coherent quasiparticle part and the incoherent part, spectral weight should be transferred between the occupied ($\omega<\mu$) and unoccupied ($\omega>\mu$) portions of the spectral function because of the sum rule that $\int_{-\infty}^{\mu} d\omega\rho(\omega)$ is equal to the number of electrons [see Eq. (2.58)].

Spectral weight transfer in the photoemission spectra has been studied for $La_{1-x}Sr_xTiO_3$ (Fujimori, Hase, *et al.*, 1992b; Aiura *et al.*, 1996), $R_{1-x}Ba_xTiO_3$ (R=Y, La, and Nd) (Robey *et al.*, 1993), $Nd_{1-x}Sr_xTiO_3$ (Robey *et al.*, 1995) and $Y_{1-x}Ca_xTiO_3$ (Morikawa *et al.*, 1996). These systems differ from each other in the magnitude of W and hence of U/W. Figure 110 shows the photoemission spectra of $La_{1-x}Sr_xTiO_3$ (Fujimori, Hase, *et al.*, 1992b). The $n=1$ ($x=0$) end member is a d^1 Mott insulator and shows a broad peak centered at $\sim$1.5 eV below E_F, which is assigned to the lower Hubbard band. (The weak intensity at the Fermi edge is due to the metallicity of the $LaTiO_{3+\delta}$ sample with excess oxygen studied in that work. Recent measurements on stoichiometric samples yielded a vanishing intensity at E_F.) With increasing x, i.e., with hole doping, the $\sim$1.5 eV peak loses its spectral weight without changing energy position or line shape down to $x\sim1$, at which composition the peak almost disappears. The lost spectral weight is transferred to above E_F, as observed by O 1s x-ray absorption and inverse photoemission spectroscopy. In the metallic region ($0\lesssim x\lesssim 1$ for $La_{1-x}Sr_xTiO_3$), a weak but finite Fermi-edge intensity is found, indicating that upon hole doping a small portion of the spectral weight is transferred from the lower Hubbard band to the quasiparticle band crossing E_F. Qualitatively the same spectral changes were observed for the other $R_{1-x}A_xTiO_3$ systems, but the quasiparticle spectral weight decreases with the decrease in ionic radius of the A-site ion and hence with increasing U/W (Morikawa *et al.*, 1996). The changes in spectral weight distribution as a function of both band filling n and interaction strength U/W are schematically depicted in Fig. 111.

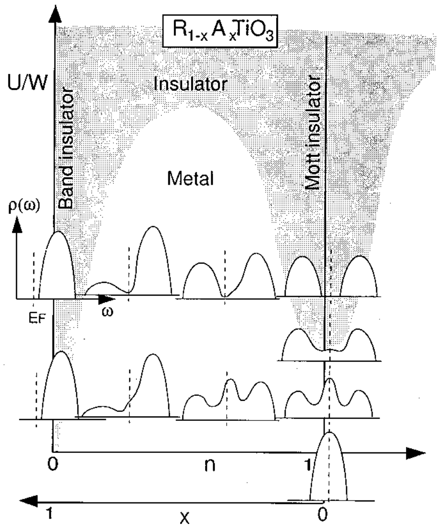

FIG. 111. Evolution of the single-particle density of states $\rho(\omega)$ as a function of U/W and band filling n, derived from the photoemission and inverse-photoemission studies of Ti and V perovskite oxides. From Morikawa *et al.*, 1996.

If we assume that the self-energy correction $\Sigma(\vec{k},\omega)$ is $\vec{k}$ independent and therefore that $m^*/n_b\sim Z^{-1}$ (where Z is the quasiparticle spectral weight), the experimentally observed low quasiparticle weight in every $R_{1-x}A_xTiO_3$ system is apparently incompatible with the electronic specific heat, which implies $m^*\sim m_b$ except for the vicinity of the Mott transition, where m^* becomes as large as $\sim5m_b$ (Tokura, Taguchi, *et al.*, 1993). This indicates the important role of nonlocal effects, i.e., of the momentum dependence of the self-energy correction, in the mass renormalization and enables us to evaluate not only $m^*=m_k m_\omega/m_b$ but also m_k and m_ω separately, as in the case of $Ca_{1-x}Sr_xVO_3$ (see Sec. IV.A.5). In the present case, because such a decomposition of the spectra into the coherent and incoherent parts is difficult owing to the weakness of the coherent part, the quasiparticle DOS at E_F, $N^*(\mu)$, obtained from the electronic specific-heat coefficient γ, is utilized to estimate Z, using the relationship $Z=\rho(\mu)/N^*(\mu)$ [Eq. (2.126)]. Because of the very low spectral intensity at E_F, one obtains $Z \lesssim 0.01$ and ~ 0.05, respectively, for metallic samples of $Y_{1-x}Ca_xTiO_3$ and $La_{1-x}Sr_xTiO_3$ (Morikawa *et al.*, 1996). Since $m_k/m_b=\rho(\mu)/N_b(\mu)$ [Eq. (2.125)], the reduction of the spectral weight $\rho(\mu)$ in going from $La_{1-x}Sr_xTiO_3$ to $Y_{1-x}Ca_xTiO_3$ means that Z and m_k decrease with U/W not only for $n=1$ ($Ca_{1-x}Sr_xVO_3$) but also for $0<n<1$.

The extremely low quasiparticle spectral weight observed in the photoemission study seems consistent with the overwhelmingly incoherent response in $\sigma(\omega)$. Although the results of finite-size calculations using the Hubbard model indicate a relatively sharp peak of large quasiparticle spectral weight (of order 0.1–1) for a realistic U/W (or U/t) values (Dagotto *et al.*, 1991; Bulut, Scalapino, and White, 1994a; Eskes *et al.*, 1994; Ulmke *et al.*, 1996), the real coherent weight of the quasiparticle near the Mott insulating phase could be only a tiny portion of this as discussed in Sec. II.F.2. This view seems to be consistent with the above observation, at least for a metal near the Mott insulator. However, this does not explain the low weight at small electron fillings. In order to explain the strong reduction of the spectral weight at E_F in the bandwidth control d^1 Mott-Hubbard system $Ca_{1-x}Sr_xVO_3$, Morikawa *et al.* (1995) proposed that it was the effect of the long-range Coulomb interaction, which is neglected in the Hubbard model. The effect of the long-range Coulomb force could be one origin of small Z even far away from the integer filling because the screening becomes progressively ineffective at low electron filling. Another origin of low Z could be disorder. A recent dynamic mean-field approach has shown that the typical quasiparticle weight can be reduced even far away from half filling if disorder and strong correlation coexist (Dobrosavljević and Kotliar, 1997).

Some remarks should be made on the experimental observation that the ~ 1.5 eV peak of the photoemission spectra persists in $x\sim 1$ ($n\sim 0$) samples, where the d band is nearly empty. This is an unexpected experimental result by itself, since in the limit of small band filling, $n \ll 1$, there should be only a small probability of electron-electron interaction. A similar peak was observed (but at somewhat lower binding energies of ~ 1.2 eV) for oxygen-deficient $SrTiO_{3-y}$ (Henrich and Kurtz, 1981; Barman *et al.*, 1996). In order to explain this behavior, two different models were proposed. One was based on the potential disorder caused by the substituted A-ion sites (Sarma, Barman, *et al.*, 1996). The substitution of La for Sr lowers the potential at neighboring Ti sites and, if the potential lowering is large enough, produces a peak ~ 1 eV below E_F even for a small band filling ($n \ll 1$). However, such a strong potential disorder may cause a localization of electrons and hence seems difficult to explain the metallic conductivity observed for the low n (especially for $La_{1-x}Sr_xTiO_3$). On the other hand, Dobrosavljević and Kotliar (1997) have shown, using dynamical mean-field theory, that metallic conductivity may remain finite up to a considerable degree of potential disorder. In the other model, one considers the interaction of doped electrons with the lattice distortion through both short-range and long-range interactions, which are usually described by the Holstein and Fröhlich Hamiltonians, respectively (Fujimori, Bocquet, *et al.*, 1996). In this model, a doped electron is self-trapped due to the polaronic effect with a small binding energy (and hence a small transport activation energy) but, when the electron is emitted in the photoemission process, the lattice is left with a large excess energy of ~ 1 eV, giving rise to the deep d-derived photoemission peak. This approach also has a problem, namely, that the observed metallic transport remains to be explained using models with the tendency for self-trapping.

2. $R_{1-x}A_xVO_3$

$La_{1-x}Sr_xVO_3$ has long been known as a FC-MIT system among the $3d$ transition-metal oxide perovskites and was discussed in the earlier version of Mott's text book (Mott, 1990). The end compound RVO_3, where R is a trivalent rare-earth ion, possesses V^{3+} ions with $3d^2$ configuration ($S=1$). The crystalline lattice of RVO_3 is tetragonal for $R=$La and Ce, while for the others it is of $GdFeO_3$ type with orthorhombic distortion (Sakai, Adachi, and Shiokawa, 1977). Therefore the one-electron bandwidth (W) must decrease with decreasing radius of the R ion, as in the case of $RTiO_3$ (Sec. IV.B.1). RVO_3 is typically a Mott-Hubbard insulator and undergoes an antiferromagnetic transition at 120–150 K. The antiferromagnetic phase is accompanied by a spin canting, giving rise to weak ferromagnetism.

The insulating nature of the parent RVO_3 compounds is again insufficiently explained by LSDA band-structure calculations. $LaVO_3$ and YVO_3 show C-type and G-type antiferromagnetic ordering, respectively. They are also accompanied by a Jahn-Teller distortion as in $RTiO_3$, but of the a type for $LaVO_3$ and d type for YVO_3. These phenomena were explained by Hartree-Fock (Mizokawa and Fujimori, 1996b) band-structure calculations. For the ideal cubic lattice, the lowest-energy Hartree-Fock solution is the C-type antiferromagnetic state in which two adjacent V atoms have $(xy)^1(yz)^1$ and $(xy)^1(zx)^1$ configurations, which favors the a-type Jahn-Teller distortion. Here, the occupation of the xy orbital at every site induces antiferromagnetic coupling within the ab plane, while the alternating occupation of the yz and zx orbitals induces ferromagnetic coupling along the c axis. (One can ignore the spin-orbit interaction, unlike the case of $LaTiO_3$, because the Jahn-Teller distortion is substantial in the RVO_3 compounds.) For the d-type Jahn-Teller distortion, either the yz or the zx orbitals are occupied along the c axis, resulting in antiferromagnetic coupling along the c direction and hence G-type antiferromagnetic ordering. Generalized density gradient band-structure calculations also explained the C-type antiferromagnetism

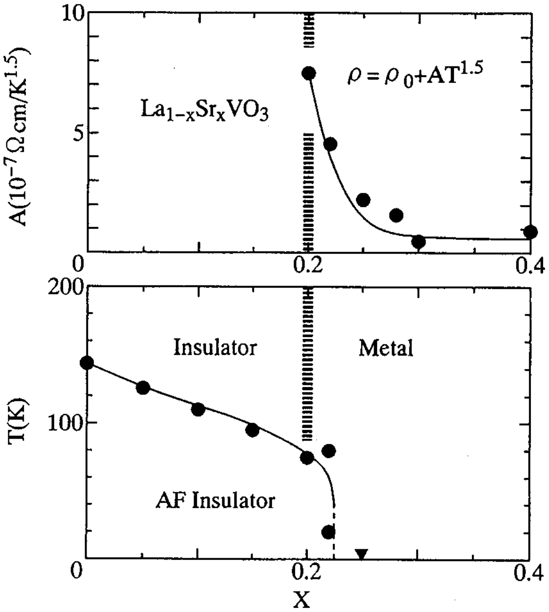

FIG. 112. Phase diagram of $La_{1-x}Sr_xVO_3$ (Mahajan *et al.*, 1992; Inaba *et al.*, 1995).

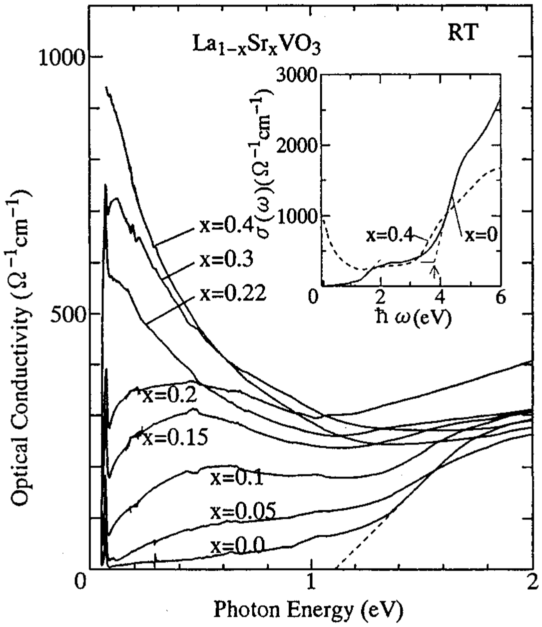

FIG. 114. Optical conductivity spectra at room temperature for $La_{1-x}Sr_xVO_3$. From Inaba *et al.*, 1995.

of $LaVO_3$ but failed to explain the G-type antiferromagnetism in YVO_3 (Sawada *et al.*, 1996).

With hole doping by partial substitution of divalent ions (Sr or Ca) for the rare-earth ions, the insulating antiferromagnetic phase eventually disappears, as shown in Fig. 112 for the case of $La_{1-x}Sr_xVO_3$ (Mahajan *et al.*, 1992; Inaba *et al.*, 1995). As compared with the case of V_2O_3 (Sec. IV.A.1), doping with more nominal holes is necessary to produce the metallic state. In the case of $La_{1-x}Sr_xVO_3$ the FC-MIT takes place around $x_c \approx 0.2$ (Dougier and Casalot, 1970; Dougier and Hagenmuller, 1975; Inaba *et al.*, 1995), while in $Y_{1-x}Ca_xVO_3$ it takes place around $x_c \approx 0.5$ with smaller W (Kasuya *et al.*, 1993).

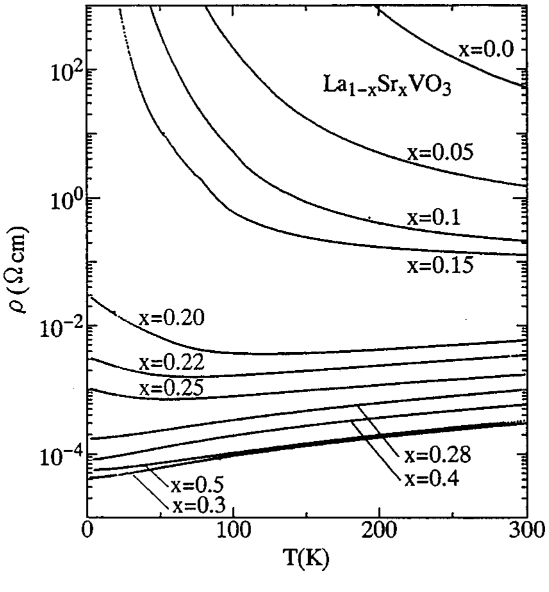

FIG. 113. Resistivity of $La_{1-x}Sr_xVO_3$. From Inaba *et al.*, 1995.

Figure 113 presents the data for the temperature dependence of the resistivity in arc-melted polycrystals (which suffer less from grain boundary effects than ceramics samples) of $La_{1-x}Sr_xVO_3$ (Inaba *et al.*, 1995). The conductivity in the insulating region ($x<0.15$) shows a thermal activation type at relatively higher temperatures above the antiferromagnetic transition temperature T_N (Fig. 112), and the thermal activation energy, ≈ 0.15 eV for $LaVO_3$, decreases steeply but continuously with x. Variation of the activation energy of $La_{1-x}Sr_xVO_3$ is shown to follow $(x_c-x)^{1.8}$ (Dougier and Hagenmuller, 1975). Mott (1990) argued that the critical variation in the form of $(x_c-x)^{\zeta}$ with $\zeta=1.8$ is in contradiction to the simple scenario, i.e., $\zeta=1$, of the Anderson localization and that some kind of mass enhancement, such as a consequence of the formation of spin polarons, must be taken into account. At lower temperatures below T_N in the region of $0.05<x<0.15$, the compound shows a variable-range hopping type of conduction. Again, Sayer *et al.* (1975) reported that the critical exponent for the localization length is $\zeta=0.6$ instead of the expected value $\zeta=1$.

The FC-MIT and resultant change of the electronic structure show up clearly in the optical spectra. Figure 114 shows the low-energy part of the optical conductivity spectra at room temperature for $La_{1-x}Sr_xVO_3$ together with the inset for a broader energy region (Inaba *et al.*, 1995). In $LaVO_3$ a Mott-Hubbard gap between the lower and upper Hubbard bands and a charge-transfer (CT) gap between the occupied O $2p$ band and the upper Hubbard band are observed at 1.1 eV and 3.6 eV, respectively; these can be discerned as rises in the optical conductivity in the inset of Fig. 114. With hole doping by substitution of Sr (x), the CT gap shifts to lower

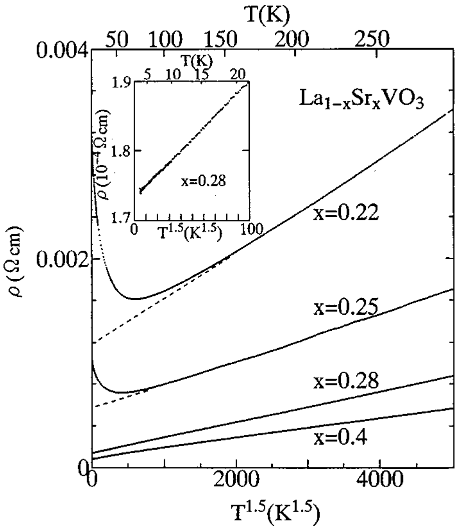

FIG. 115. Resistivity of $La_{1-x}Sr_xVO_3$ near the MI phase boundary as a function of $T^{1.5}$. From Inaba *et al.*, 1995.

energy mainly due to the shift in the $2p$ band, and the Mott-Hubbard gap is closed. As for the doping-induced change in the low-energy region, the spectral weight is first increased in the gap region and eventually forms the inner-gap absorption band. In barely metallic samples ($x=0.20$ and 0.22) at room temperature (see Fig. 113), the conductivity spectra show a non-Drude-like shape, indicating a dominant contribution from the incoherent motion of the charge carriers. However, the spectra for $x>0.3$ are typical of a metal. In contrast with the case of $R_{1-x}A_xTiO_3$ (Sec. IV.B.1), the spectral weight does not appear to be transferred from the gap excitation but from a higher-lying p-d interband transition, since no isosbetic point can be observed near the Mott-Hubbard gap energy. A similar feature of the evolution of the inner-gap excitation with doping is observed for $Y_{1-x}Ca_xVO_3$ (Kasuya *et al.*, 1993) but at a higher doping level, probably reflecting stronger electron correlation.

Figure 115 shows the resistivity of the compounds near the metal-insulator phase boundary as a function of $T^{1.5}$ (Inaba *et al.*, 1995). Apart from the upturns at low temperatures (probably below T_N), the temperature dependence of the resistivity (ρ) can be well expressed by the relation $\rho=\rho_0+AT^{1.5}$ in the metallic region. The inset of Fig. 115 shows a magnification of the low-temperature region for the $x=0.28$ sample, indicating that the above relation holds good at least down to 2.5 K. The coefficient A critically increases as the metal-insulator phase boundary is approached from the higher-x (metallic) region. Inaba *et al.* (1995) interpreted this to mean that the enhanced $T^{1.5}$ dependence was due to antiferromagnetic spin fluctuations. The self-consistent renormalization (SCR) theory (Moriya, 1995; Ueda, 1977; see also Secs. II.E.1 and II.E.8) indicates that the low-temperature resistivity near the critical boundary between the antiferromagnetic metal and normal metal deviates from the normal T^2 law and shows $T^{1.5}$ dependence, as discussed in Sec. II.E.8. The $T^{1.5}$ dependence of the resistivity can be interpreted in terms of the strong Curie-like enhancement of the spin susceptibility $\chi(Q)$ as derived in Eq. (2.118). This $T^2-T^{1.5}$ crossover has clearly been observed near the antiferromagnetic metal-normal metal phase boundary, for example in the case of the BC-MIT system $NiS_{2-x}Se_x$, as described in Sec. IV.B.2. In $La_{1-x}S_xVO_3$, however, it is not yet clear whether the antiferromagnetic metallic state is present around $x\approx0.2$. Furthermore, the measurement of the NMR relaxation rate T_1^{-1} by Mahajan *et al.* (1992) shows a conventional Korringa behavior and no indication of antiferromagnetic fluctuation, at least for $x\geqslant0.4$. Detailed neutron-scattering and NMR measurements using single-crystalline $La_{1-x}Sr_xVO_3$ samples in the immediate vicinity ($x\approx0.2$) of the MIT are obviously needed to detect and characterize possibly anomalous magnetic fluctuations near the FC-MIT.

The evolution of electronic states in the $R_{1-x}A_xVO_3$ system with x should be different from that in $R_{1-x}A_xTiO_3$ in that the parent insulator RVO_3 is a Mott insulator with d^2 configuration, where there is a Hund's rule coupling between the d electrons, and the $x\rightarrow1$ (100% hole doping) limit still has one d electron per V site. The photoemission and oxygen $1s$ x-ray absorption spectra of RVO_3 ($R=$La,Y) revealed lower and upper Hubbard bands, respectively, corresponding to the $d^2\rightarrow d^1$ and $d^2\rightarrow d^3$ spectral weight (Edgell *et al.*, 1984; Eisaki, 1991; Pen *et al.*, 1998). Upon hole doping, new spectral weight grows rapidly just above E_F, which corresponds to the $d^1\rightarrow d^2$ spectral weight induced by hole doping, as in the high-T_c cuprates. At the same time the lower Hubbard band loses its spectral weight. As the system becomes metallic ($x>0.5$ for $R=$Y and $x>0.2$ for $R=$La), a Fermi edge is developed in the photoemission spectra. If one starts from the $x=1$ (d^1) limit of the system $La_{1-x}Sr_xVO_3$ and increases the band filling, the remnant of the lower Hubbard band increases its intensity while the quasiparticle band in the photoemission and inverse photoemission spectra loses its intensity (Tsujioka *et al.*, 1997). The decrease of the quasiparticle weight as the system deviates from integer filling is opposite to what has been theoretically predicted for a fixed U/W (Kotliar and Kajueter, 1996; Rozenberg *et al.*, 1996), and would be attributed to the increase in U/W with decreasing x. Here it should be noted that in $R_{1-x}A_xVO_3$ not only does the band filling n ($\equiv2-x$) decrease but also U/W decreases with x, since $U/W<1$ in the metallic AVO_3 while $U/W>1$ in the insulating RVO_3.

C. High-T_c cuprates

1. $La_{2-x}Sr_xCuO_4$

The discovery of high-T_c cuprate superconductors was brought about by the observation of a superconducting transition for the compound $La_{2-x}M_xCuO_4$ with $M=$Ba by Bednorz and Müller (1986). The lattice structure of this compound was soon identified as the K_2NiF_4 type, namely, the layered perovskite structure shown in Fig. 116 (Takagi, Uchida, Kitazawa, and Tanaka, 1987).

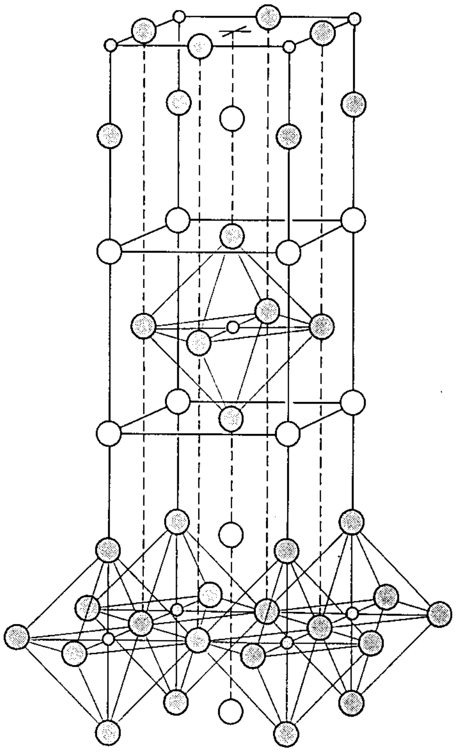

FIG. 116. The layered perovskite structure of $La_{2-x}M_xCuO_4$; large open circles, La(M); small open circle, Cu; large filled circle, O.

Although a large number of compounds have been discovered as high-T_c cuprate superconductors since then, they all have a common structure of stacking of CuO_2 layers sandwiched by block layers, as shown schematically in Fig. 117. The superconductivity itself has been an attractive and extensively studied subject. The symmetry of the pairing order parameter of the high-T_c cuprates now appears to be settled as the $d_{x^2-y^2}$ symmetry after enormous combined effort involving magnetic resonance experiments, Josephson junctions, etc. (see for a review Scalapino, 1995; Annett *et al.*, 1996). However, in this review article, we focus on the unusual normal-state properties of high-T_c compounds; properties in the superconducting state are beyond the scope of this article.

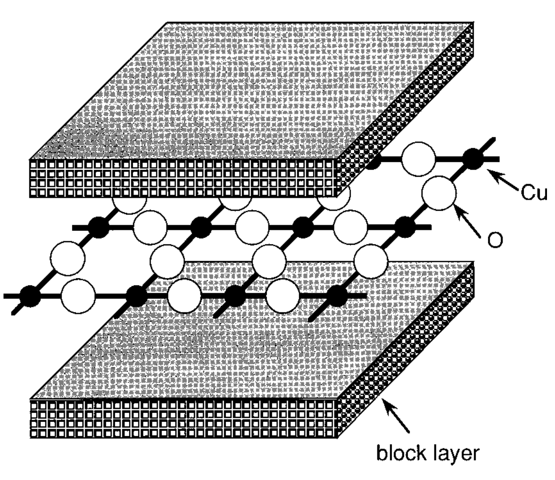

FIG. 117. Conceptual illustration of stacking of CuO_2 layers sandwiched by block layers.

Before going into a detailed discussion of experimental data, we first outline the basic electronic structure and the phase diagram in the plane of doping concentration x and temperature T. Because of the two-dimensional anisotropy of this lattice structure, CuO_6 octahedra are slightly elongated along the direction perpendicular to the CuO_2 layer. This means that the distance from Cu to the apex oxygen is slightly longer than the distance to the in-plane oxygen, which may be viewed as a Jahn-Teller-type distortion. This distortion lifts the degeneracy of the e_g orbitals of Cu $3d$ electrons to the lower-lying $d_{z^2-r^2}$ and higher-lying $d_{x^2-y^2}$ orbitals. Because the parent compound La_2CuO_4 has the valence of Cu^{2+}, and hence as the nominal d^9 state the above crystal-field splitting leads to fully occupied t_{2g} orbitals and $d_{3z^2-r^2}$ orbital, while the $d_{x^2-y^2}$ orbital remains half-filled, the Fermi level lies in a band constructed mainly from the $d_{x^2-y^2}$ orbital, relatively close to the level of the $2p_\sigma$ oxygen orbital, compared with other transition-metal oxides. In La_2CuO_4, since the $2p_\sigma$ band lies within the Mott-Hubbard gap, it is a charge-transfer (CT) insulator, as discussed in Secs. II.A and III.A. La_2CuO_4 is a typical insulator with antiferromagnetic long-range order. Up to the present time, all the cuprate superconductors with high critical temperatures are known to be located near the antiferromagnetic Mott insulating phase. La_2CuO_4 is, in fact, a Mott insulator with the Néel temperature $T_N \sim 300$ K. Because the $d_{x^2-y^2}$ band is half-filled, it is clear that the insulating behavior experimentally observed even far above T_N is due to strong correlation effects.

$La_{2-x}M_xCuO_4$ with $M=$Sr and Ba provides a typical example, with a wide range of controllability of carrier concentration, from the antiferromagnetic Mott insulating phase to overdoped good metals, by the doping of Sr, Ba, or Ca. Therefore $La_{2-x}M_xCuO_4$ is a good example of an FC-MIT system with 2D anisotropy. The basic electronic structure of the cuprate superconductors in all regions, from insulator to metal, is believed to be described by the d-p model defined in Eqs. (2.11a)–(2.11d). The parameters deduced from photoemission (Shen *et al.*, 1987; Fujimori, Takekawa, *et al.*, 1989), LDA calculations (Park *et al.*, 1988; Stechel and Jennison, 1988; Hybersten, Schlüter, and Christensen, 1989; McMahan, Martin, and Satpathy, 1989), and $\sigma(\omega)$ give overall consistency with $U_{dd} \simeq 6-10$ eV, $t_{pd} \simeq 1-1.5$ eV, $\Delta \simeq 1-3$ eV, $U_{pp} \simeq 1$ eV, and $V_{pd} \sim 1-1.5$ eV. The details of methods for determining the model parameters are given in Sec. III.B.

With increasing x, $La_{2-x}Sr_xCuO_4$ very quickly undergoes a transition from an antiferromagnetic insulator to a paramagnetic metal with a superconducting phase at low temperatures. The phase diagram of $La_{2-x}SrCuO_4$ is shown in Fig. 118. At sufficiently low temperatures, it is believed that the MIT with x is actually a

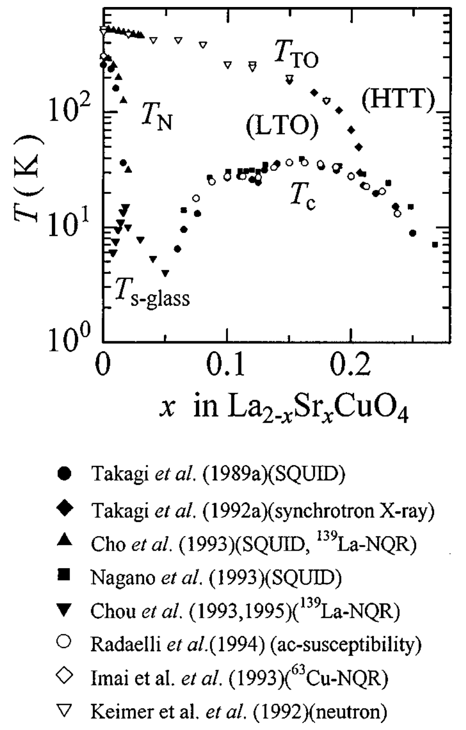

FIG. 118. The phase diagram of $La_{2-x}Sr_xCuO_4$ in the plane of the doping concentration x and temperature T. The Néel temperature T_N, superconducting transition temperature T_c, transition temperature between high-temperature tetragonal (HTT) and low-temperature orthorhombic (LTO) structures, T_{TO}, and spin-glass transition temperature $T_{s\text{-glass}}$ are plotted from various experimental data (by courtesy of T. Sasagawa and K. Kishio).

superconductor-insulator transition. Above the superconducting transition temperature, the normal metallic phase shows various unusual properties which are far from the standard Fermi-liquid behavior, especially for small x. These anomalous aspects will be described in detail below. The superconducting transition temperature T_c has the maximum $T_c \sim 40$ K around $x \sim 0.15$ for $La_{2-x}Sr_xCuO_4$ and decreases with further doping. The doping concentration $x = x_m$ which shows the maximum T_c is frequently called the optimum concentration while the region $x < x_m$ is called the underdoped region and $x > x_m$ the overdoped region. Anomalous metallic behavior observed in the underdoped region gradually crosses over to more or less standard Fermi-liquid behavior in the overdoped region. Another point to be discussed in the global phase diagram is the existence of structural phase transitions between the tetragonal structure at high temperatures and the orthorhombic one at low temperatures, as illustrated in Fig. 118. At $x = 0$, the transition occurs at around 560 K and it quickly decreases with increasing x. In the orthorhombic phase, the unit of octahedron CuO_6 is slightly tilted in a staggered way. In the overdoped region, $x > x_m$, T_c decreases continuously at least up to $x = 0.20$ (see the phase diagram). On the other hand, the possibility of phase separation and a discontinuity between underdoped and heavily doped regions around $x = 0.20$ on a microscopic level was discussed by Fukuzumi *et al.*, (1996).

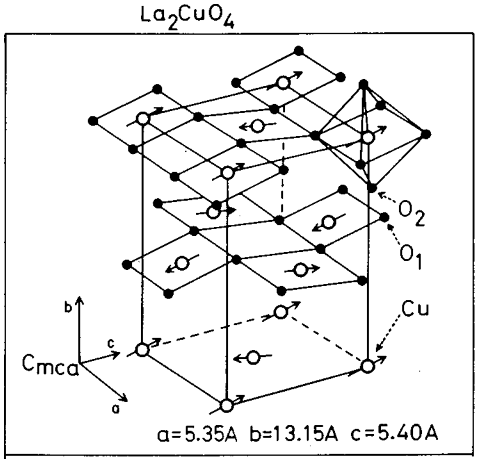

FIG. 119. The structure of the antiferromagnetic order in $La_{2-x}Sr_xCuO_4$. From Yamada *et al.*, 1989.

Below we discuss physical properties in the plane of x and T in more detail. The existence of antiferromagnetic long-range order below $T_N \sim 300$ K at $x \sim 0$ is clearly observed in neutron-scattering experiments as well as in magnetic susceptibility measurements. Other quantities such as NMR and Raman scattering also show anomalies. The structure of the antiferromagnetic order was determined by neutron-scattering experiments, as shown in Fig. 119. The driving force of the antiferromagnetic order is of course the superexchange interaction of neighboring Cu spins mediated by intermediate states of the bridging $2p_\sigma$ orbital. The localized spins at the Cu site have a moment $\sim 0.4\mu_B$, which is a consequence of the reduction due to a strong quantum effect and strong covalency. The ordered spins are primarily aligned in the basal CuO_2 plane (Vaknin *et al.*, 1987; Yamada *et al.*, 1987). To understand the detailed structure of the ordering vector, however, we need to consider small tilting of the CuO_6 octahedron as well as the spin-orbit interaction to generate a small Dzyaloshinski-Moriya interaction, which leads to an anisotropic interaction for the ordering vector. This leads to a slight canting of the spin vector out of the CuO_2 plane with a small ferromagnetic moment. (Fukuda *et al.*, 1988; Kastner *et al.*, 1988; Thio *et al.*, 1988; Yamada *et al.*, 1989; Koshibae, Ohta, and Maekawa, 1993, 1994).

Aside from this slight anisotropy, the basic magnetic interaction in the Mott insulating phase is well described within the framework of the spin-1/2 Heisenberg model. The antiferromagnetic exchange interaction J determined from two-magnon Raman scattering is $J \sim 1100\ \mathrm{cm}^{-1} = 1600$ K (Lyons, Fleury, Remeika, Cooper, and Negran, 1988; Cooper *et al.*, 1990b; Tokura, Koshihara, *et al.*, 1990), while $J = 135$ meV, equivalent to 1570 K, is identified from the dispersion in the neutron-scattering data (Aeppli *et al.*, 1989), which has one of the largest antiferromagnetic exchanges among d-electron systems. There are two reasons for the large J. One is that the transfer between the neighboring Cu $d_{x^2-y^2}$ orbital and O2p_σ orbital t_{pd} is large, $\sim$1 eV because of the large overlap of these two orbitals. The second is that the level splitting $\Delta=|\varepsilon_d-\varepsilon_p|$ is relatively small, $\sim$1–3 eV, as shown in Eqs. (2.11a)–(2.11d) and the paragraph below these equations. Then in the fourth-order perturbation, J may be large because it is proportional to $t_{pd}^4/|\varepsilon_d-\varepsilon_p|^3$ when the Coulomb interaction at the oxygen site, U_{pp}, and the intersite Coulomb interaction V_{pd} are neglected while U_{dd} is taken large enough. The Néel temperature T_N is much smaller than J because of the strong two-dimensionality and resulting quantum fluctuation effects. In fact, in single-layer 2D systems, T_N is theoretically expected to be zero, while small interlayer exchange coupling drives T_N to a finite temperature. Short-ranged antiferromagnetic correlations are developed even well above T_N, as observed in neutron-scattering experiments and NMR measurements. The growth of antiferromagnetic correlations with decreasing temperature is qualitatively described both by a renormalization-group study of the nonlinear sigma model (Chakravarty, Halperin, and Nelson, 1989) and by a modified spin-wave theory (Takahashi, 1989) as discussed in the neutron-scattering results (Aeppli *et al.*, 1989; Yamada *et al.*, 1989; Keimer *et al.*, 1992). (The prefactor of the exponential dependence is not reproduced by the spin-wave theory). At low temperatures above T_N, as discussed in Sec. II.E.4, the antiferromagnetic correlation length is expected to grow as

$$\xi\sim\frac{0.27\hbar c}{2\pi\rho_s}\exp\left(\frac{2\pi\rho_s}{T}\right)\left(1-\frac{T}{4\pi\rho_s}+\cdots\right) \tag{4.7}$$

with the spin stiffness constant $\rho_s\simeq1.15J$ (Chakraverty, Halperin, and Nelson, 1989; Hasenfratz and Niedermayer, 1991, 1993). The experimentally observed temperature dependence of ξ appears to agree with the above prediction of the nonlinear sigma model in the renormalized classical regime (Keimer *et al.*, 1992; Birgeneau *et al.*, 1995). The energy dispersion of spin excitations determined by high-energy inelastic neutron-scattering experiments shows overall agreement with the spin-wave theory of the Heisenberg model (Hayden *et al.*, 1991b; S. Itoh *et al.*, 1994).

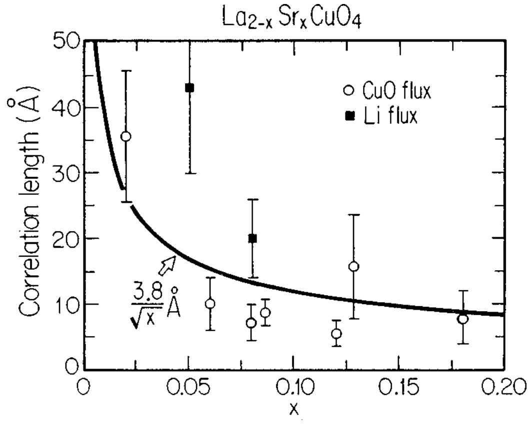

FIG. 120. Doping concentration dependence of antiferromagnetic correlation length ξ suggested by neutron scattering of La$_{2-x}$Sr$_x$CuO$_4$ (Birgeneau *et al.*, 1988). ξ appears to follow the mean hole distance 3.8 Å/$\sqrt{x}$.

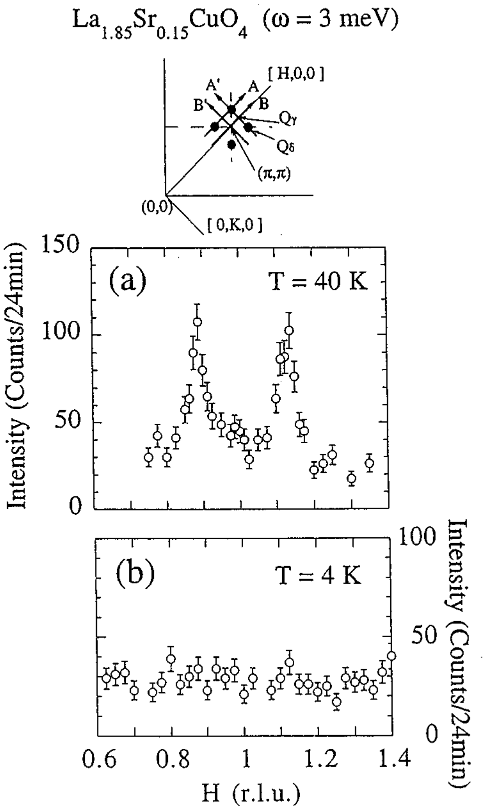

FIG. 121. Short-ranged incommensurate spin correlation observed by neutron-scattering experiments for Im $\chi(q,\omega)$ in La$_{2-x}$Sr$_x$CuO$_4$ above T_c at $\omega=3$ meV taken from the scan A illustrated in the top panel. The closed circles in the top panel denote the peak positions of the incommensurate structure. The incommensurate peak observed above T_c (top panel) becomes invisible below T_c (lower panel) at this energy $\omega=3$ meV. From Yamada *et al.*, 1995.

When Sr, Ba, or Ca are substituted for La, as in La$_{2-x}A_x$CuO$_4$ with A=Sr or Ba, holes are doped into CuO$_2$ planes. A remarkable feature of the hole doping is that it causes a quick collapse of the antiferromagnetic order and a MIT. When the doping concentration is low enough, the system is still insulating for $x\leq0.05$, as illustrated in the phase diagram Fig. 118, while antiferromagnetic long-range order is destroyed around $x=0.02$, where the localization effect due to disorder is serious. For $0.02<x<0.05$, the spin-glass state is realized at low temperatures (see, for example, Chou *et al.*, 1995). In any case, antiferromagnetic long-range order is absent in the metallic region, $x>0.05$. The antiferromagnetic correlation length ξ becomes progressively shorter and shorter when the doping concentration is increased. In the early stage of neutron studies on La$_{2-x}$Sr$_x$CuO$_4$, it was shown that ξ is approximately given by $\xi\sim a/\sqrt{x}$, where a is the lattice constant, and hence ξ is nothing but the mean hole distance, as shown in Fig. 120 (Birgeneau *et al.*, 1988).

In the metallic region $x>0.05$, the periodicity of short-ranged antiferromagnetic correlations is known to

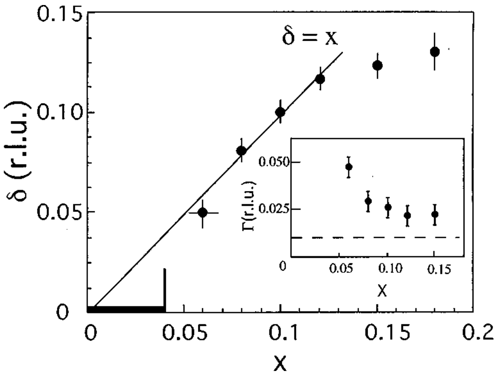

FIG. 122. The doping concentration (x) dependence of the incommensurability δ [deviation of the peak position from (π,π)] in spin correlations observed in neutron-scattering experiments for $La_{2-x}Sr_xCuO_4$ (Yamada *et al.*, 1998). Incommensurability appears in the metallic phase. The inset shows the half width at half-maximum Γ.

shift from (π,π) to fourfold-incommensurate wave vectors $[\pi(1\pm\delta),\pi]$ and $[\pi,\pi(1\pm\delta)]$, as can be seen in Fig. 121 (Yoshizawa *et al.*, 1988; Thurston *et al.*, 1989, 1992; Cheong *et al.*, 1991; Yamada, Endoh, *et al.*, 1995; Yamada, Wakimoto, *et al.*, 1995). The hole doping quickly increases δ at $x>0.05$ upon metallization; it seems that δ approaches the value $\delta=x$ at $0.05\leqslant x\leqslant 0.1$, as can be seen in Fig. 122 (Yamada *et al.*, 1998). At $x=0.15$ and 0.075, inelastic neutron-scattering experiments show that the width Δ, the peak height $S(Q,\omega)$, and the intensity $\int dq\, S(q,\omega)$ around the incommensurate peak depend on temperature for the energy $\omega<4$ meV, that is, the peak grows and is sharpened with lowering temperature when measured at $T<100$ K, while the incommensurate peak structure is more or less independent of temperature for $\omega\geqslant 4$ meV (Cheong *et al.*, 1991; Thurston *et al.*, 1992; Yamada, Wakimoto, *et al.*, 1995) above T_c. This suggests that rather sharp incommensurate peaks grow only in the low-energy range $\omega<4$ meV at $x\sim 0.15$ due presumably to a Fermi-surface effect combined with imperfect but finite nesting effects of the Fermi surface. This growth of incommensurate peaks may be ascribed to the growth of the coherent part of the magnetic response, as discussed in Secs. II.E.4 and II.F.10. Recent studies using high-quality samples show that the incommensurate peak decreases and disappears with decreasing temperatures below T_c at low energies (Mason *et al.*, 1992, 1993; Yamada, Wakimoto, *et al.*, 1995). This is consistent with the opening of a superconducting gap at the incommensurate wave number. The wave-number dependence appears to be consistent with $d_{x^2-y^2}$ symmetry of the superconducting gap. Another remarkable feature below T_c is that the incommensurate peak grows and becomes more prominent and sharpened on the high-energy side ($\gtrsim 7$ meV) with very long correlation length (>50 Å; Mason *et al.*, 1996). This may be related to the compatibility of antiferromagnetic correlation, especially in the d-wave superconductor (see, for example, Assaad, Imada, and Scalapino, 1997; Assaad and Imada, 1997).

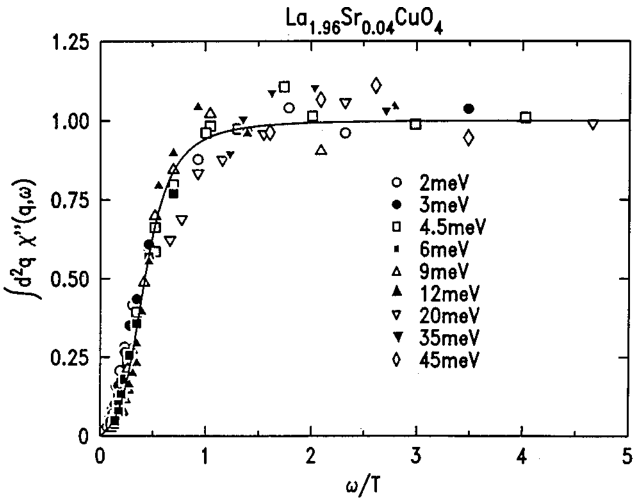

FIG. 123. Single-parameter scaling of $\int$ Im $\chi(q,\omega)dq$ for various choices of T and ω for $La_{1.96}Sr_{0.04}CuO_4$. From Keimer *et al.*, 1992.

An overall feature of Im$\chi(q,\omega)$ for La_2CuO_4 and $La_{1.85}Sr_{0.15}CuO_4$ up to high energies was measured by high-energy pulsed neutron inelastic scattering (Yamada, Endoh, *et al.*, 1995; Hayden *et al.*, 1996). The magnetic scattering intensities around (π,π) due to antiferromagnetic fluctuations were clearly observed up to $\omega=120$ meV. In addition, when the nonmagnetic component was subtracted, the magnetic signals remained up to 300 meV.

Here, it should be noted that a careful analysis of the neutron and NMR data is required for interpretation of spin fluctuations. As clarified in Secs. II.E.4 and II.F.10, the dynamic spin susceptibility is phenomenologically given as the sum of coherent and incoherent contributions. Although the coherent part may depend on temperature due to the Fermi-surface effect, the antiferromagnetic correlation length ξ must be determined from the incoherent part, and it appears to be temperature insensitive, as discussed in Sec. II.E.4. The incoherent contribution becomes more and more dominant over the coherent contribution as the doping concentration is lowered.

At low doping concentration, $\int$Im$\chi(q,\omega)dq$ follows a single-parameter scaling

$$\int \mathrm{Im}\,\chi(q,\omega)dq=g(\beta\omega), \tag{4.8}$$

with $g(x)\sim 1-e^{-x}$ or $\tanh x$ as in Fig. 123 (Keimer *et al.*, 1992; Hayden *et al.*, 1991a). The same scaling was also observed in a $YBa_2Cu_3O_{7-y}$ compound, as discussed in Sec. IV.C.3. As discussed in Secs. II.E.4 and II.G.2, this scaling is consistent with both a marginal Fermi liquid (see Sec. II.G.2; Varma *et al.*, 1989) and a view in terms of a totally incoherent response as in Eqs. (2.294) and (2.362) (see Secs. II.F.10 and II.E.4; Imada, 1994a; Jaklič and Prelovšek, 1995a). It should be noted that this single-parameter scaling is experimentally not satisfied at higher doping at low temperatures (Matsuda *et al.*, 1994). A general tendency appears to be that the single-parameter scaling by $\beta\omega$ is satisfied in the region of incoherent charge dynamics at low doping or at high temperatures, namely at $T > T_{\mathrm{coh}}$ (see Fig. 34), which is consistent with the region of incoherent charge and spin dynamics discussed in the theoretical argument in Secs. II.E.4 and II.F.10. In addition, it is clear that this single-parameter scaling is not satisfied when the superconducting gap (or pseudogap with nodes) is open, as is observed by (Yamada, Wakimoto, *et al.*, 1995). The scaling appears not to be satisfied in the pseudogap region above T_c in the Y compounds, as discussed in Sec. IV.C.3. However, the boundary of the region of single-parameter scaling by $\beta\omega$ in the plane of x and T has not yet been completely clarified experimentally, although it is important to establish the correct interpretation and theory.

When the doping concentration x is around 1/8, $\mathrm{La}_{2-x}\mathrm{Ba}_x\mathrm{CuO}_4$ and $\mathrm{La}_{2-x}\mathrm{Sr}_x\mathrm{CuO}_4$ are known to show anomalies in their transport properties. In particular, $\mathrm{La}_{2-x}\mathrm{Ba}_x\mathrm{CuO}_4$ with $x \sim 0.125$ shows a marked decrease in T_c as compared with the other region, and it becomes even insulating in the region close to $x = 0.125$. This may be due to the charge ordering of doped holes accompanied by spin ordering, as observed by muon (Kumagai *et al.*, 1994), nuclear quadrupole resonance, and neutron-scattering measurements. The periodicity of the charge ordering is commensurate to the CuO_2 lattice structure. In particular, recent neutron measurements for $\mathrm{La}_{1.6-x}\mathrm{Nd}_{0.4}\mathrm{Sr}_x\mathrm{CuO}_4$ at around $x = 0.12$ showed that a commensurate charge- and spin-ordered stripe phase is stabilized (Tranquada, Sternlieb, *et al.*, 1995).

Nuclear magnetic resonance provides us with another powerful tool for investigating spin correlations in $\mathrm{La}_{2-x}M_x\mathrm{CuO}_4$. The longitudinal relaxation time of nuclear magnetization, T_1, is inversely proportional to the dynamic spin susceptibility as

$$\frac{1}{T_1} = \frac{\gamma_n^2 k_B T}{2\mu_B^2} \sum_q \sum_{\alpha = x,y} |A_q^\alpha|^2 \frac{\mathrm{Im}\,\chi_{\alpha\alpha}(q,\omega_0)}{\omega_0}, \tag{4.9}$$

where ω_0 is the frequency of the NMR field applied in the z direction. The frequency ω_0 is usually very small and it may be viewed as the limit $\omega \to 0$ for the magnetic response in which we are interested. The shift of the NMR frequency due to the hyperfine interaction between nuclei and electrons, called the Knight shift K, is given as the sum of the orbital part K_{orb} and the spin part K_{spin}. The spin part is given by

$$K_{spin} = \frac{1}{\mu_B} A_{q=0} \mathrm{Re}\,\chi(q=0,\omega=0), \tag{4.10}$$

where $\chi(q=0,\omega=0)$ is the uniform magnetic susceptibility. K_{orb} is usually assumed to be temperature independent. For the isolated Cu^{2+} ion, anisotropy of the $d_{x^2-y^2}$ wave function causes very anisotropic K_{orb}, which well accounts for the experimental data (Takigawa *et al.*, 1989). The nuclear form factor A_q is determined from the hyperfine interaction. The anisotropy between $A_{q=0}^c$ and $A_{q=0}^{ab}$ is accounted for by considering a transferred hyperfine interaction through the hybridization of the 4s orbital and the Wannier orbital of $d_{x^2-y^2}$ extended to the neighboring site, as proposed by Mila and Rice (1989). The q dependence of the nuclear form factor A_q has a large weight around $\mathbf{q} = (\pi,\pi)$ for the Cu site, while the weight around $\mathbf{q} = (\pi,\pi)$ is vanishing in the case of A_q at the in-plane O site. At the Cu site, the nuclear form factor is such that the antiferromagnetic fluctuation around (π,π) is selectively picked up in $1/T_1$.

Comprehensive measurements of the NMR nuclear spin-lattice relaxation time T_1 at the Cu site were performed in the range $0 \leqslant x < 0.15$ and $T \leqslant 900$ K, as shown in Fig. 124 (Imai *et al.*, 1993). At the moment its interpretation is not unique. However, at least several points should be noted concerning on the T_1 results. For the mother material $\mathrm{La}_2\mathrm{CuO}_4$, $1/T_1$ shows striking enhancement with decreasing temperature, in agreement with the exponential growth of the antiferromagnetic correlation length ξ in the renormalized classical regime of the nonlinear sigma model. As doping proceeds, the enhancement of $1/T_1$ is rapidly suppressed, giving way to more or less temperature independent $1/T_1$ for $T > 100$–200 K with gradual crossover to $1/(T_1 T) \sim \mathrm{const}$ at lower temperatures for $x \sim 0.1$–0.15. This temperature dependence has been interpreted from several different viewpoints. One interpretation is that $1/(T_1 T)$ follows the Curie-Weiss law $1/(T_1 T) \sim C/(T + \Theta)$ [see Eq. (2.115)] which comes from a temperature-dependent antiferromagnetic correlation length $\xi \sim 1/\sqrt{T + \Theta}$, as discussed in Secs. II.D.1 and II.D.8 and stressed by spin-fluctuation theories (Millis, Monien, and Pines, 1990; Moriya, Takahashi, and Ueda, 1990). Another is the interpretation from marginal Fermi-liquid theory (see Sec. II.G.2) where $\mathrm{Im}\,\chi \sim \tanh \beta\omega$ is consistent with $1/T_1 \sim \mathrm{const}$ for $T > 200$ K at $\delta \sim 0.1$–0.15. The NMR data are also consistent with the discussion of the neutron data above when we take the limit $\omega_0 \to 0$. A completely dif-

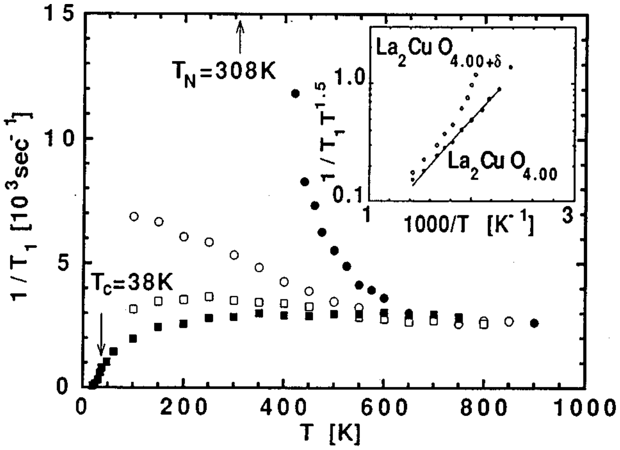

FIG. 124. Temperature dependence of inverse of NMR nuclear spin-lattice relaxation time T_1 at the Cu site for $\mathrm{La}_{2-x}\mathrm{Sr}_x\mathrm{CuO}_4$: filled circle, $x = 0$; open circle, $x = 0.04$; open square, $x = 0.075$; filled square, $x = 0.15$. The inset shows the scaling in the insulating phase. From Imai, Slichter, Yoshimura, and Kosuge, 1993.

ferent interpretation related to the marginal Fermi-liquid hypothesis is that the dynamic structure factor $S(\mathbf{q},\omega)$ is basically temperature independent and the temperature dependence of Im $\chi(q,\omega)=(1-e^{-\beta\omega})S(q,\omega)$ comes solely from the Bose factor $1-e^{-\beta\omega}$, as suggested from the temperature-independent ξ and the incoherent character of spin correlations in numerical studies (Imada, 1994a; Jaklič and Prelovšek, 1995b). This viewpoint is discussed in Secs. II.E.4 and II.F.10. The crossover from $1/T_1\sim$const to $1/(T_1T)\sim$const has been attributed to the crossover from the incoherent charge and spin dynamics to coherent dynamics, which are separated by an anomalously suppressed coherence temperature T_{coh} as discussed in Sec. II.F.10. $1/T_1$ at site O does not show appreciable influence from antiferromagnetic fluctuations because of the vanishing contribution from the part around (π,π), as is evident from the nuclear form factor of the oxygen site. This is more or less well described by Korringa-type behavior $1/(T_1T)\sim$const over a wide range of temperatures. However, a puzzle remains in the temperature dependence when the peak is at deeply incommensurate wave numbers, because the NMR at Cu and O sites both show a substantial contribution from those incommensurate wave numbers, while the temperature dependences of those sites are different.

The Gaussian decay rate $1/T_G$ associated with the nuclear spin-spin relaxation time measures the real part of the static spin susceptibility $\chi(\mathbf{q},\omega=0)$. In particular, $1/T_G$ at the Cu site was measured in $Tl_2Ba_2CuO_{6+\delta}$, $YBa_2Cu_3O_{7-y}$, and $YBa_2Cu_4O_8$, which selectively picks up $\chi(\mathbf{Q})$ with the staggered wave vector $\mathbf{Q}=(\pi,\pi)$. Except for the pseudogap region discussed below, the scaling $1/(T_1T)\propto\chi(\mathbf{Q})\sim(1/T_G)^2$ was suggested in a limited temperature range around 200 K (Y. Itoh *et al.*, 1994b; Y. Itoh, 1994). This behavior again can be interpreted in two ways. From the viewpoint of spin-fluctuation theories, this scaling is due to Eqs. (2.114) and (2.115), where $\chi(\mathbf{Q})\propto(T_1T)^{-1}$ is satisfied in 2D. The other interpretation is that both $\chi(\mathbf{Q},\omega=0)$ and $\mathrm{Im}\chi(\mathbf{q},\omega)/\omega$ are basically scaled by the above-mentioned Bose factor $\lim_{\omega\to 0}[(1-e^{-\beta\omega})/\omega]$, which leads to similar behavior between $\chi(\mathbf{Q})$ and $\mathrm{Im}\chi(\mathbf{Q},\omega)$. This is because the factor β also remains for $\mathrm{Re}\chi$ after the Kramers-Kronig transformation for T not much smaller than the frequency cutoff for the main contribution of Im χ. Since T_G and T_1 do not seem to follow a universal relation over a wide temperature range, the scaling does not uniquely determine the mechanism.

The uniform magnetic susceptibility $\chi(q=0,\omega=0)$ can be measured by bulk magnetization measurements as well as by the Knight shift. In an undoped compound, it has a pronounced peak at high temperatures $\geqslant$1000 K and decreases with decreasing temperatures, in agreement with the behavior of the 2D Heisenberg model (Okabe and Kikuchi, 1988). When carriers are doped, the peak temperature T_χ decreases ($T_\chi\sim$400–500 K at $\delta\sim0.15$). However the peak structure with a rather remarkable decrease at lower temperatures is retained, as shown in Fig. 125 (Johnston, 1989; Takagi, Ido, *et al.*, 1989; Takagi, Uchida, and Tokura, 1989; Nakano *et al.*, 1994). The peak structure and decrease at low temperatures appear to be more pronounced in the low-doping region $\delta\sim0.1$ than in the undoped case. The doping dependence of the peak temperature T_χ is similar to the crossover temperature T_H where the Hall coefficient shows a sharp increase with decreasing temperature, as discussed below. As a possible interpretation, this anomaly was analyzed as the effect of preformed singlet pairing fluctuations or antiferromagnetic fluctuations (Imada, 1993a, 1994b) which start below T_χ in the metallic region as is discussed in Sec. IV.C.3.

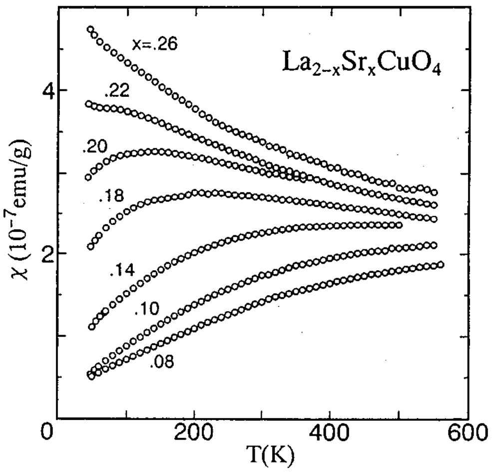

FIG. 125. Temperature dependence of the uniform magnetic susceptibility of $La_{2-x}Sr_xCuO_4$ for various x. From Nakano *et al.*, 1994.

This "pseudogap" behavior is seen in other quantities such as the specific heat γ. From far above T_c, γ and hence the electronic entropy itself are anomalously suppressed in the low-doping region as in Fig. 126. (Loram *et al.*, 1997). The crossover temperature T_γ is above 300 K at low doping. This suppression of γ at low temperatures $T\ll T_\gamma$ in the underdoped region was also pointed

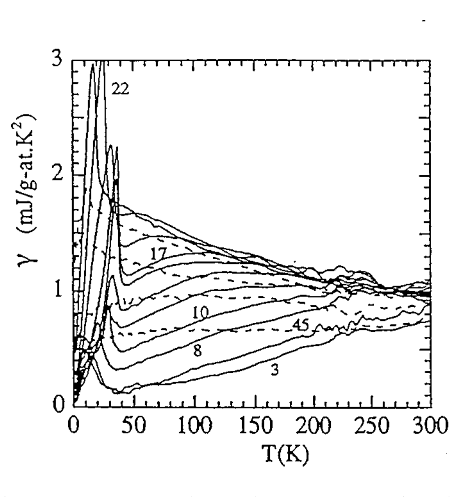

FIG. 126. Temperature dependence of specific heat γ for $La_{2-x}Sr_xCuO_4$. The numbers indicate the doping concentration in % (Loram *et al.*, 1997). The entropy is released at higher temperatures at lower dopings.

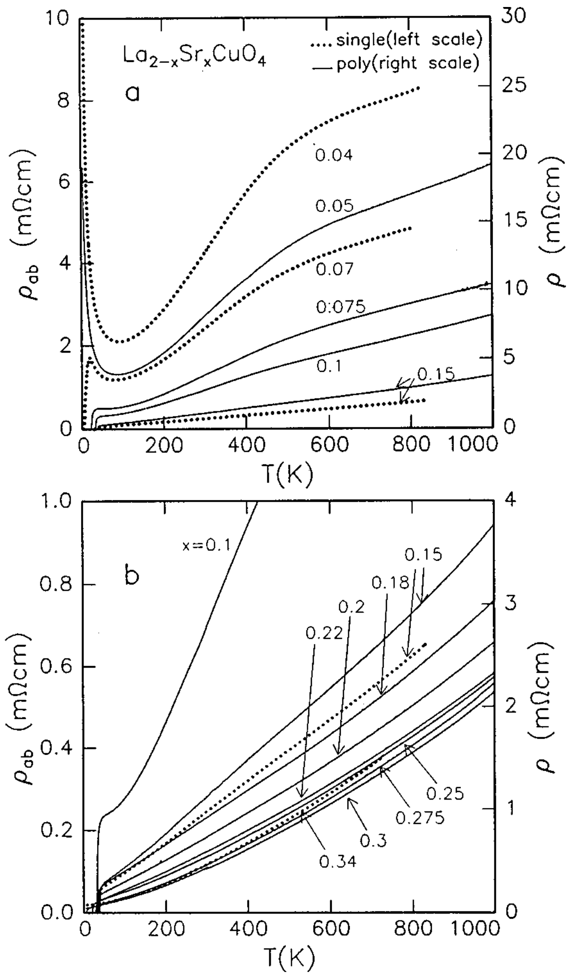

FIG. 127. Temperature dependence of the in-plane resistivity for various doping concentrations of $La_{2-x}Sr_xCuO_4$ for single and poly crystals (Takagi *et al.*, 1992a) T-linear resistivity is seen in a wide region.

out by Wada, Nakamura and Kumagai (1991) and by Nishikawa, Takeda, and Sato (1994). It is in striking contrast with the critical enhancement of γ for (La,Sr)TiO_3 discussed in Sec. IV.B.1. From the specific-heat data, a large entropy remaining above $T_\gamma \lesssim T_\chi$ is suggested from the picture of a mass-diverging Mott transition at higher temperatures with crossover to vanishing carrier number below T_γ due to the formation of a pseudogap, as discussed in Sec. II.F (Imada, 1993a, 1994b). This means a crossover of the scaling for the MIT between two different universality classes. We discuss the pseudogap behavior and the significance of T_χ and T_γ in greater detail for the case of Y compounds in Sec. IV.C.3.

The transport properties of this compound are also unusual in terms of standard Fermi-liquid theory (see, for other reviews, Iye, 1990; Ong, 1990). One of the most unusual properties is the temperature dependence of the resistivity. As we have discussed in Sec. II.D.1, standard Fermi-liquid theory predicts that the temperature dependence of the resistivity ρ is given as $\rho = \rho_0 + AT^2$ [see Eq. (2.83)] with correlation effects contained in the T^2 term. In contrast to this, this compound especially around optimum doping $x \sim 0.15$ shows robust T-linear dependence, $\rho \sim \rho_0 + A'T$, in a wide range from T_c to 800 K, as shown in Fig. 127. The residual resistivity ρ_0 appears to vanish for samples of higher quality. This T-linear behavior is widely observed in other high-T_c cuprates around optimum doping. In the overdoped region, the resistivity roughly follows the form

$$\rho = \rho_0 + A'' T^p, \tag{4.11}$$

with $2 \geqslant p > 1$, where p increases with increasing doping (Takagi, Batlogg, *et al.*, 1992a). In the underdoped region, ρ has a feature around T_χ, in which the linear law $\rho \sim \rho_0 + A'T$ changes slope: A' increases and ρ_0 decreases in going from the high-temperature region $T > T_\rho \simeq T_\chi$ to below T_ρ, as shown in Fig. 127. Recent measurements of ρ at low temperatures in the underdoped region revealed that ρ eventually shows insulating behavior (logarithimic T dependence) at sufficiently low temperatures if the superconductivity is suppressed (Ando *et al.*, 1995).

Various mechanisms for this T-linear behavior have been proposed. We discuss here only some of these suggestions. Although the mechanism is not yet fully understood, it is useful to list some of the proposed approaches to make connections with the recent extensive theoretical efforts discussed in Sec. II.

From the Fermi-liquid point of view, the spin fluctuation theory discussed in Secs. II.D.1 and II.D.8 ascribes this behavior to control of the carrier relaxation time τ by the scattering of carriers (quasiparticles) by paramagnetic excitations. The T-linear resistivity in this approach is obtained in Eq. (2.121) and, as discussed in the derivation of (2.121), is ascribed to the contribution of antiferromagnetic excitations which follows the Curie-Weiss form (2.114) (Millis, Monien, and Pines, 1990; Moriya, Takahashi, and Ueda, 1990). Near the critical point, $\Theta \sim 0$, Im Σ and hence the inverse relaxation time of the quasiparticles becomes proportional to T following the form of Eqs. (2.110), (2.111), and (2.114).

In the scenario of spin-charge separation, discussed in Sec. II.D.7, the slave-boson approximation with coupling between spinons and holons treated by the gauge field leads to the T-linear resistivity due to the incoherent character of the holons. (Ioffe and Wiegmann, 1990; Ioffe and Larkin, 1989; Lee and Nagaosa, 1992). The T-linear resistivity is also obtained from marginal Fermi-liquid theory, where Im Σ is indeed proportional to T, as discussed in Sec. II.G.2.

As discussed in Sec. II.E.1, recent numerical results of an exact diagonalization for the 2D t-J model by Jaklič and Prelovšek (1995a) succeeded in reproducing this T-linear behavior; the prefactor A' was in quantitative agreement with the experimental data shown in Fig. 127, although the temperature achieved by the numerical method was at least a few hundred K. It was suggested that this T-linear resistivity could be due solely to incoherent charge dynamics, which should be observed above the coherence temperature of the carriers. The conductivity is in fact consistent with incoherent charge dynamics of the form (2.274) with a broad $C(\omega)$, of the

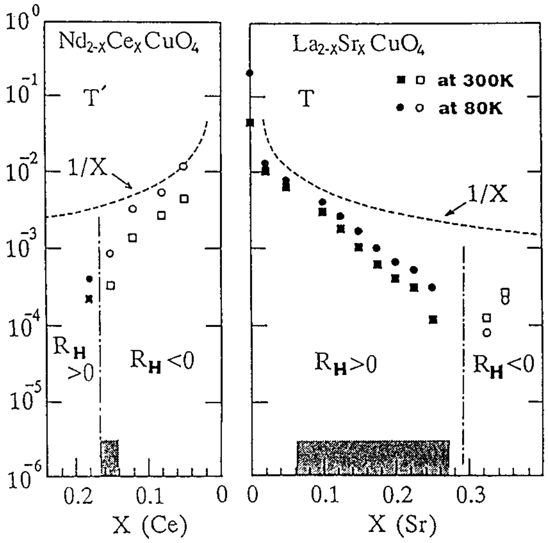

FIG. 128. Doping concentration dependence of the Hall coefficient at low temperatures for $La_{2-x}Sr_xCuO_4$ and $Nd_{2-x}Ce_xCuO_4$. Shaded windows show the superconducting phase at low temperatures (Uchida *et al.*, 1989). R_H roughly follows $1/x$ in the underdoped region.

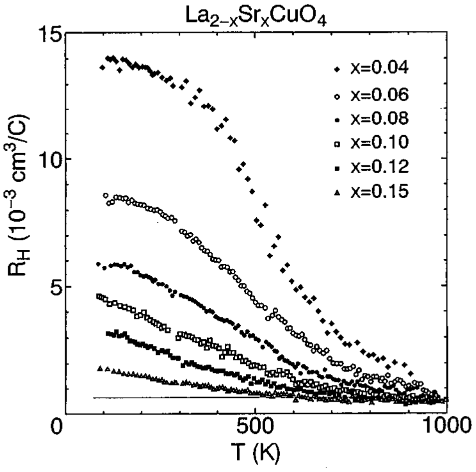

FIG. 129. Temperature dependence of the Hall coefficient for $La_{2-x}Sr_xCuO_4$ (Nishikawa, Takeda, and Sato, 1994). The thin line represents the nominal value of $1/nec$ at $n=1$ per Cu. Strong temperature dependence is seen in the underdoped region.

order of an eV, which implies that the current-current correlation decays very quickly over the time scale eV^{-1}. Such anomalous suppressions of coherence are consistent with the anomalous criticality of the Mott transition with the large dynamic exponent $z=4$, as discussed in Sec. II.E.9 (Imada, 1995b; see Sec. II.F.9).

The anisotropy of the resistivity shows another unusual property. The resistivity in the CuO_2 plane, ρ_{ab}, is smaller by a factor of 200 than that along the c axis (out-of-plane), ρ_c, at optimum doping in the room-temperature region (Ito *et al.*, 1991). The anisotropy increases for smaller x as well as for smaller T. Because the LDA calculation predicts a mass anisotropy of only 28 (Allen, Pickett, and Krauer, 1987), this large anisotropy has to be ascribed to strong electron correlations. Even more remarkable is that, in the low-doping and low-temperature region, there exists a region where ρ_{ab} shows metallic while ρ_c shows insulating temperature dependence. Roughly speaking this region is $T<T_\rho$. We discuss the anisotropy of ρ further in Sec. IV.C.3.

The Hall coefficient R_H also shows anomalous character in terms of standard Fermi-liquid theory. In the standard theory of weakly correlated systems, R_H is independent of temperature, and the amplitude is given by $R_H \sim 1/nec$ with carrier density n. However, at low temperatures, the observed R_H in this compound is holelike, that is, positive with large amplitude roughly scaled by $1/x$ for $x<0.3$, as shown in Fig. 128 (Ong *et al.*, 1987; Takagi, Ido, *et al.*, 1989). This contradicts a naive expectation from the Fermi-liquid picture because the carrier number is given by $1-x$ when the Luttinger theorem is satisfied and the carrier should be electronlike. The sign of R_H is determined from the average of the curvature over the Fermi surface in the weak-correlation picture and therefore the sign itself can be determined from a subtle balance of the electronic band structure. However, the large amplitude in the underdoped region is hard to explain from this approach. It has turned out that the temperature dependence of R_H is even more peculiar because a large positive R_H quickly decreases above a certain crossover temperature $T_H \simeq T_\chi$, as shown in Fig. 129 (Nishikawa, Takeda, and Sato, 1993, 1994; Hwang *et al.*, 1994). The crossover temperature T_H is close to T_χ for the uniform susceptibility and both show similar x dependence. Above $T_H \simeq T_\chi$, R_H decays to a small amplitude consistent with the large Luttinger volume given by $1-x$. As discussed above, this crossover at T_H was predicted to occur due to the gradual formation and fluctuations of a preformed singlet pair below T_H, as discussed in Sec. II.E.1 (Imada, 1993a, 1994b, 1995b), although the interpretation of the observed behavior has not been uniquely established. In other words, the crossover at T_H reflects a change in the character and the universality class of the Mott transition at small x, as discussed above for the anomalies of the specific heat T_γ and the susceptibility T_χ. Another interpretation of the existence of T_H is the anomalous Hall effect due to skew scattering arising from antiferromagnetic fluctuations. The effect of nesting has been discussed as the source of an anomalous contribution to R_H through a process similar to the Aslamazov-Larkin process in superconducting fluctuations (Miyake and Narikiyo, 1994a).

The optical conductivity $\sigma(\omega)$ shows a spectacular change with increasing doping concentration, as illustrated in Fig. 130 (Uchida, *et al.*, 1991). A charge-transfer gap of the order of 1.5–2 eV is clearly observed in La_2CuO_4, although it is accompanied by a tail up to $\sim$1 eV whose origin is not uniquely identified. Upon doping, the spectral weight is transferred from the region above the CT gap to the lower-frequency region. In the low-doping region, it appears to develop a broad structure around or below 0.5 eV, which is replaced by

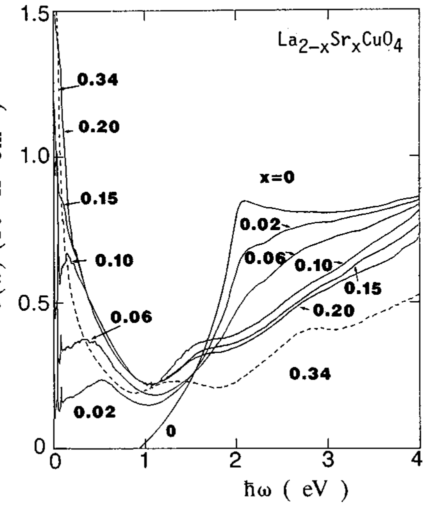

FIG. 130. The in-plane optical conductivity $\sigma(\omega)$ at room temperature for various choices of x in $La_{2-x}Sr_xCuO_4$. From Uchida *et al.*, 1991.

an overall $1/\omega$ dependence upon further doping. To understand the ω dependence, two phenomenological approaches have been attempted using extended Drude analyses (Thomas *et al.*, 1988; Collins *et al.*, 1989; see for a review Tajima, 1997). In the first approach, $\sigma(\omega)$ is fit with a single-oscillator model, while in the other approach a two-oscillator model has been employed. The advantage of the single-oscillator model is that the parameters—namely, the effective plasma frequency $\omega_p^* = 4\pi ne^2/m^*(\omega)$ and the relaxation time $\tau(\omega)$—are uniquely determined by assuming an ω-dependent effective mass m^* and τ, while the interpretation of the ω dependence is not straightforward for doped samples because of the mid-IR structure. On the other hand, the two-oscillator model fits the data better, while the parameters are not uniquely determined. Because the mid-IR peak is absent in an untwinned Y compound, the two-oscillator model probably needs to take account of the impurity localization effect and polaron effects (Thomas *et al.*, 1991). In any case, the overall $1/\omega$ dependence and the $1/T$ dependence at $\omega = 0$ are consistent with the form (2.274) and (2.275) with weak ω and T dependence for $C(\omega)$. The consistency of this form with numerical results is discussed in Sec. II.E.1. The connection to the scaling theory of the Mott transition and the marginal Fermi-liquid theory are given in Secs. II.F.9 and II.G.2, respectively. An important point is that experimental data that are well described by the form (2.274) with weakly ω-dependent $C(\omega)$ should be the consequence of incoherent charge dynamics with the complete lack of the true Drude weight. We discuss this incoherence further in the case of Y compounds in Sec. IV.C.3. The out-of-plane conductivity $\sigma_c(\omega)$ shows different charge dynamics from the in-plane one. A charge gap is developed from T above T_c (Tamasaku, Nakamura, and Uchida, 1992). Below T_c, it is rather difficult to observe the superconducting gap in the in-plane $\sigma_{a,b}(\omega)$, because the reflectivity is almost 100% around the gap energy, even in the absence of the superconducting gap. Since the c-axis reflectivity is lower, it is easier to distinguish from the gap region with 100% reflectivity. Because the cuprate superconductors can be viewed as layered superconductors of CuO_2 sheets coupled weakly by Josephson tunneling through the interlayer coupling, the plasma frequency ω_p of this Josephson-coupled system may have a smaller value than the superconducting gap Δ if the Josephson coupling is weak. This situation, $\omega_p < \Delta$, is in sharp contrast with the usual case where $\omega_p > 0.5\ \mathrm{eV} \gg \Delta$ is satisfied. Because ω_p is in the gap region, the Josephson plasma oscillation hardly decays. Various exotic electromagnetic phenomena due to this low ω_p were predicted by Tachiki, Koyama, and Takahashi (1994).

Below we shall discuss the electronic structure studied by first-principles calculations together with results of spectroscopic measurements. This compound is one of the hardest cases for reproducing the correct electronic states by band-structure calculation because of strong-correlation effects and strong p-d covalency. In order to explain the antiferromagnetic insulating state of the parent compound La_2CuO_4, standard LDA calculations are insufficient. The insulating state was correctly predicted by LDA+U calculations (Anisimov *et al.*, 1992), self-interaction-corrected (SIC)-LDA calculations (Svane and Gunnarsson, 1988a; Temmerman *et al.*, 1993), and parametrized Hartree-Fock calculations (Grant and McMahan, 1991). The effect of hole doping on an antiferromagnetic insulator, however, is usually beyond the scope of these band-structure calculations. The electronic structure of $La_{2-x}Sr_xCuO_4$ with static (self-trapped) holes was studied by Anisimov *et al.* (1992) using the LDA+U method applied to supercell calculations. They showed that, even without lattice distortion, a hole is self-trapped within a small ferromagnetic region where antiferromagnetic order is destroyed by the doped hole. Then a localized state is split off from the top of the valence band into the band gap. In spite of the structural simplicity and the presence of a well-defined parent insulator, $La_{2-x}Sr_xCuO_4$ is complicated in that doped holes enter not only the $p_{x,y}$-$d_{x^2-y^2}$ antibonding orbitals of the CuO_2 plane but also the p_z orbitals of the apical oxygen hybridized with the Cu $3d_{z^2}$ orbital, as suggested theoretically (Kamimura and Suwa, 1993) and observed experimentally (Chen *et al.*, 1992).

Experimentally, hole doping in La_2CuO_4 induces a new spectral weight (the so-called "in-gap spectral weight") within the charge-transfer gap, as first revealed by oxygen $1s$ core absorption spectroscopy (Romberg *et al.*, 1990; Chen, Sette, *et al.*, 1991). The in-gap spectral weight is distributed mostly above E_F, coming largely from the doped holes themselves (as $d^9\underline{L} \rightarrow d^9$ spectral weight) but is also transferred from the upper Hubbard band ($d^9 \rightarrow d^{10}$ spectral weight). A theoretical interpretation of the doping-induced spectral weight transfer above E_F is beyond the framework of the t-J model, since the model has no upper Hubbard band. Spectral weight transfer has been studied using a strong-coupling treatment (i.e., perturbation with respect to t/U) of the Hubbard model (Eskes and Oleś, 1994; Eskes *et al.*,

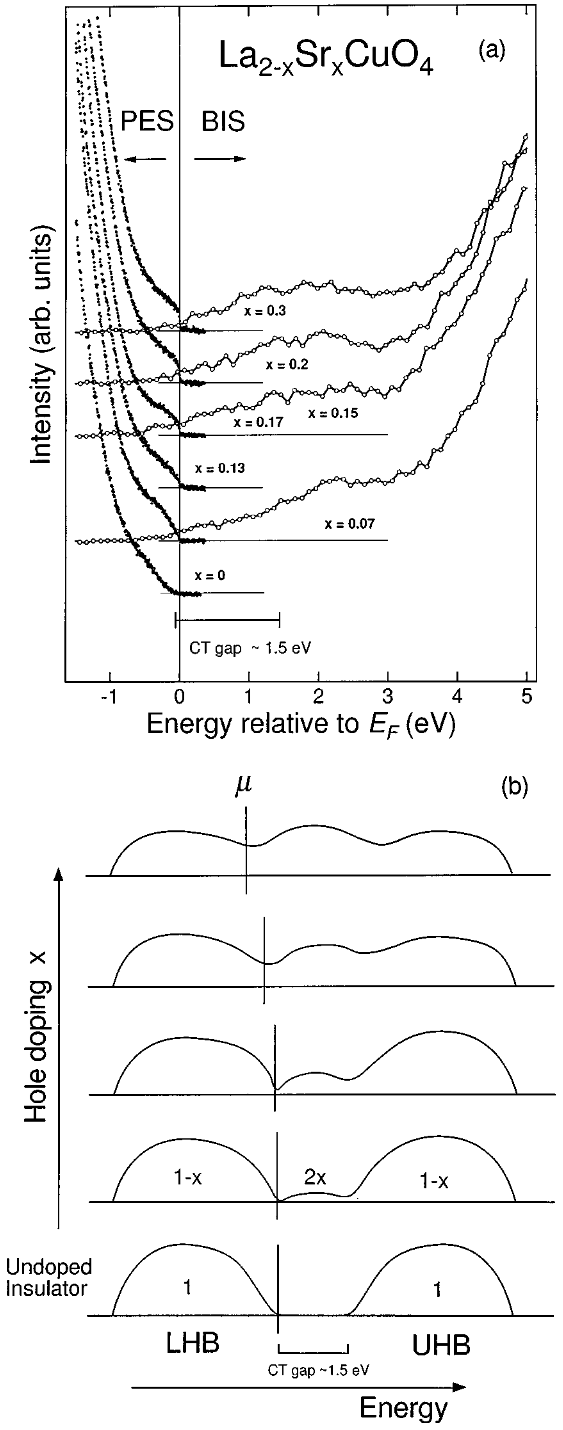

FIG. 131. Density of states of $La_{2-x}Sr_xCuO_4$. (a) Photoemission and inverse-photoemission spectra near the Fermi level (Ino *et al.*, 1997c); (b) Schematic representation of the evolution of spectral weight with hole doping.

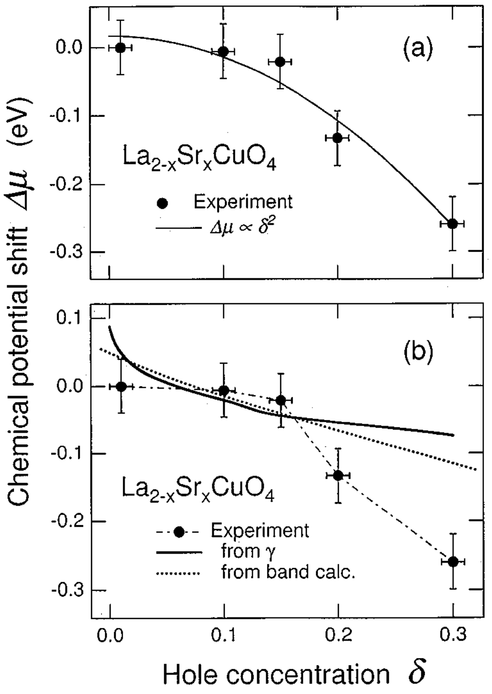

FIG. 132. Chemical potential shift as a function of hole concentration in $La_{2-x}Sr_xCuO_4$ (Ino *et al.*, 1997a). Shifts expected from band-structure calculation and the γT term in specific heat (which is proportional to the quasiparticle DOS at E_F) are also plotted in (b).

1994) and using numerical simulations of Hubbard clusters (Dagotto *et al.*, 1991; Li *et al.*, 1991; Bulut *et al.*, 1994a). Decrease of the spectral weight below E_F occurs in the Zhang-Rice singlet band [$d^9 \to d^9\underline{L}$ ($^1A_{1g}$) spectral weight], which was regarded as the effective lower Hubbard band when the high-energy part of the original p-d Hamiltonian is projected out and the Hubbard model or the t-J model is employed as the effective low-energy Hamiltonian. The decrease in the spectral weight of the Zhang-Rice singlet with hole doping is not easy to detect because of the overlapping intense oxygen $2p$ band. Figure 131(a) shows combined photoemission and inverse-photoemission spectra of $La_{2-x}Sr_xCuO_4$ (Ino *et al.*, 1997c). The doping-induced spectral weight is not concentrated just above E_F, as suggested by previous x-ray absorption studies, but is distributed over the whole band-gap region with the DOS peak ~1.5 eV above E_F. Thus spectral weight transfer occurs over a relatively wide energy range, within a few eV of E_F, and the Fermi level is located at a broad minimum of the DOS, as schematically shown in Fig. 131(b). The spectral DOS *at* E_F is much weaker than that given by LDA band-structure calculations even for optimally doped and overdoped samples, indicating that the quasiparticle weight is very small: $Z \ll 1$. In underdoped samples, there is even a pseudogap feature at E_F, which evolves into the insulating gap at $x=0$.

The E_F or the electron chemical potential in $La_{1-x}Sr_xCuO_4$ deduced from the shifts of various core levels exhibits an interesting behavior as a function of x (Ino *et al.*, 1997a). The chemical potential is shifted downward with hole doping as expected, but the shift is fast in the overdoped regime ($x \lesssim 0.15$) and slow in the underdoped regime ($x \gtrsim 0.15$), as shown in Fig. 132. It appears that $\partial\mu/\partial x$ becomes vanishingly small within experimental errors for small x, implying a divergence of charge compressibility/susceptibility towards $x \sim 0$ as predicted by Monte Carlo simulation studies of the 2D

Hubbard model (Otsuka, 1990; Furukawa and Imada, 1993). This is also consistent with the scaling theory with the dynamic exponent $z=4$ (see Sec. II.F). On the other hand, the electronic specific-heat coefficient γ is decreased towards $x\sim 0$ (Momono *et al.*, 1994), meaning that the effective mass of conduction electrons decreases as discussed above. In the overdoped region, the results of the chemical potential shift and the electronic specific heat are consistently interpreted within Fermi-liquid theory if the quasiparticle–quasiparticle repulsion is assumed to be $F_s^0\sim 7$. In the underdoped region, F_s^0 has to be assumed small or even negative: $F_s^0\rightarrow -1$ if $\partial\mu/\partial x\rightarrow 0$, invalidating the original Fermi-liquid assumption. Because the measurements were made in the normal state, the results indicate that the normal state of the underdoped cuprates is not a Fermi liquid but has a (charge) pseudogap at E_F. This observation would be closely related to other aspects of pseudogap behavior in the underdoped region discussed above as well as in Secs. IV.C.3 and IV.C.4. In accord with other measurements of the pseudogap discussed in other part of Sec. IV.C, possible microscopic mechanisms for the observed behavior may be (i) preformed Cooper pair fluctuations above T_c, (ii) spinon pairing in the resonating valence bond scenario, (iii) antiferromagnetic spin fluctuations strong enough to destroy Fermi-liquid behavior, and (iv) fluctuations of spin-charge stripes. Concerning of (iv), Zaanen and Oleś (1996) argued that spin-charge stripes pin the chemical potential for low hole concentrations if the stripes become static and may continue to do so even if the stripes are dynamic.

2. $Nd_{2-x}Ce_xCuO_4$

Since the discovery of electron-doping-induced superconductivity in $R_{2-x}Ce_xCuO_4$, where R may be Pr, Nd, Sm, or Eu (Tokura, Takagi, and Uchida, 1989), the existence of high-T_c superconductivity for both hole and electron doping has imposed a strong constraint on its mechanism (Anderson, 1992). $R_{2-x}Ce_xCuO_4$ has the so-called T' structure (Fig. 133) in which the single CuO_2 sheet without apical oxygen is sandwiched by fluorite-type $(R,Ce)_2O_2$ block layers. The Ce ion in the fluorite-type block is tetravalent (4+), and hence Ce doping (x) changes the band filling in the opposite direction to that in the so-called hole-doped superconductors such as $La_{2-x}Sr_xCuO_4$. In other words, high-T_c superconductivity emerges irrespective of the increase or decrease in band filling from the CuO_2-based half-filled Mott insulator. Electron doping can only be performed for this type of square CuO_2 sheet without apical oxygens, while the pyramidal or octahedral CuO_2 sheet with apical oxygens or halogens are mostly hole-dopable (Tokura and Arima, 1990; Tokura 1992a, 1992b), probably due to electrostatic reasons (i.e., Madelung-type energy origins from the valence change of Cu or O).

In spite of extensive studies on normal and superconducting properties in these electron-doped superconductors, much less physics has been clarified than in the cases of their hole-doped counterparts. This is simply because high-quality filling-controlled single crystals (in the sense of oxygen stoichiometry and distribution) have been difficult to prepare. In particular, only minute oxygen nonstoichiometry is determinant not only for the appearance of superconductivity but for normal-state transport and magnetic properties. For example, the 24–25-K superconductivity is known to show up around $x=0.15$ for $Nd_{2-x}Ce_xCuO_4$ and $Pr_{2-x}Ce_xCuO_4$, only when the compound is subject to a thermal annealing procedure under reducing conditions (Takagi, Uchida, and Tokura, 1989). In these compounds, the oxygen stoichiometry corresponding to increase of $\Delta y\approx 0.01$ is sufficient to quench superconductivity completely (Idemoto *et al.*, 1990; Suzuki *et al.*, 1990). This implies that minute oxygen interstitials positioned on other than the in-plane O(2) sites (Fig. 133) may serve as very effective carrier scatterers or localization centers, in contrast with the other cases where slight oxygen offstoichiometry plays the role of fine filling control (see Sec. IV.B). According to single-crystal neutron-diffraction structural studies (Radaelli *et al.*, 1994; Schultz *et al.*, 1996), it is probable that in as-grown crystals without a reducing procedure interstitial oxygens may sit on the apical O(3) site immediately above the Cu site.

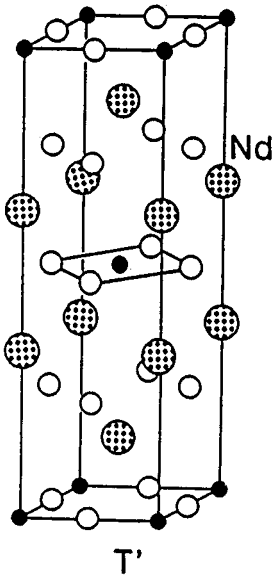

FIG. 133. Crystal structure of T' phase.

Keeping in mind the remarkable but still puzzling role of minute oxygen interstitials, let us survey the MIT-related properties in $R_{2-x}Ce_xCuO_4$ (where $R=$Nd and Pr). Figure 134 (Matsuda *et al.*, 1992) shows the evolution of 3D antiferromagnetic (AF) spin order ($T_N=160$ K) for an as-grown $Nd_{2-x}Ce_xCuO_4$ ($x=0.15$) crystal (nonsuperconducting) and its near disappearance for the reduced crystal (24-K superconducting). The (1,0,1) Bragg-peak intensity is contributed to by both Cu and Nd moments and its decrease below 50 K is due to the onset of the Nd spontaneous moment. By the decomposition procedure with the respective form factors, the saturation Cu moment at the lowest temperature was estimated as around $0.2\mu_B$ or less (Matsuda *et al.*,

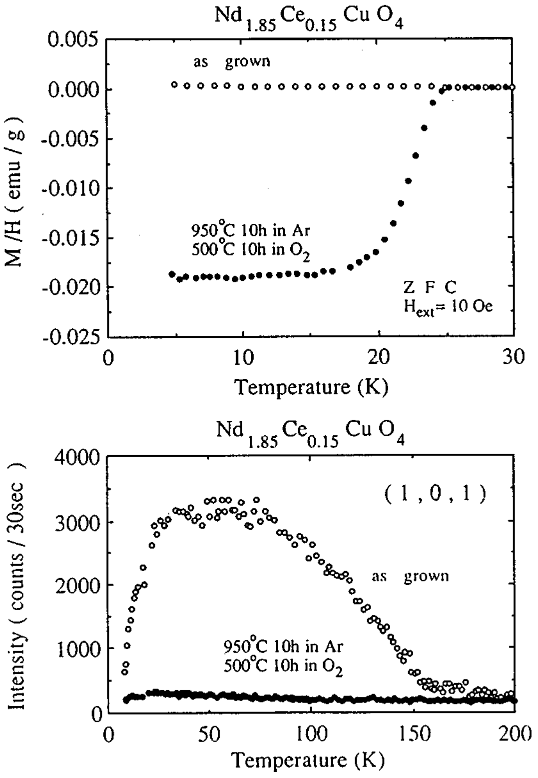

FIG. 134. Upper panel: M/H vs temperature both before and after reduction and annealing. The samples were cooled in zero magnetic field. Lower panel: (101) Bragg-peak intensity before and after reduction and annealing.

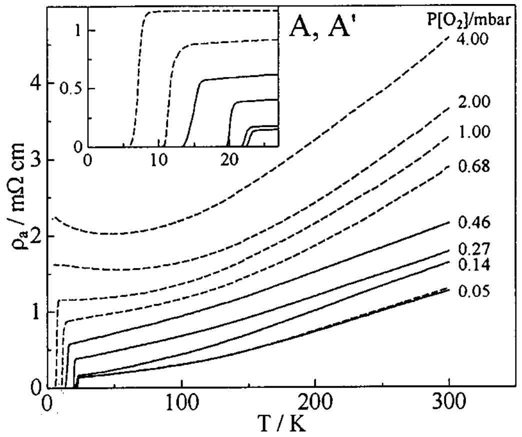

FIG. 135. Electrical resistivity vs temperature for the $Pr_{1.85}Ce_{0.15}CuO_{4+\delta}$ crystals A (drawn lines) and A' (dashed lines) annealed in different oxygen atmospheres as given in the figure. The inset shows the resistive superconducting transitions for samples A and A'.

1992). The as-grown $x=0.15$ crystal shows metallic behavior with resistivity ρ less than 10^{-3} Ω cm, but the ρ shows an upturn around the temperature corresponding to T_N (usually ranging from 120 to 160 K for the as-grown $x=0.15$ crystal). As shown in Fig. 134 and also demonstrated by earlier μSR (Luke *et al.*, 1989) and NMR (Kambe *et al.*, 1991) measurements, antiferromagnetic order is extinguished by the reducing procedure, which gives rise to superconductivity below $T_c \approx 24$ K.

Such a robust behavior of the antiferromagnetic order with electron-doping level x is in sharp contrast to the case of hole-doped superconductors, $La_{2-x}Sr_xCuO_4$. In the latter compound, T_N decreases at a rate of 160 K/at. %, while in the T'-phase compounds (as-grown) the rate of decrease is only ≈ 9 K/at. % (Thurston *et al.*, 1990). The slower collapse rate of the antiferromagnetic order with doping in the T'-phase compounds is seemingly in accordance with the simple site dilution model (Matsuda *et al.*, 1992), or intuitive scenario that a doped electron forms the local nonmagnetic Cu^{+1} species and dilutes the original $S=1/2$ Cu^{2+} spins. However, such a simplified model should not in principle be applicable to the metallic state induced by electron-doping. In fact, the minute change in the oxygen content brought about by the reduction procedure seems to drive a weakly localized doped (or site-diluted) Mott antiferrromagnet to a highly correlated metallic (at low temperatures, superconducting) state. The local square symmetry of the Ce dopant may be broken by disorder, or a small amount of interstitial oxygen may trigger long-range antiferromagnetic order, which is incompatible with superconductivity, as observed in the spin-gapped Cu-O ladder compounds (Sec. IV.D.1).

Figure 135 shows the temperature dependence of the in-plane resistivity on single crystals of $Pr_{2-x}Ce_xCuO_{4+y}$ ($x=0.15$) after several annealing steps at low-oxygen partial pressure (Brinkmann *et al.*, 1996). With a reduction procedure, the superconducting transition temperature T_c steadily increases, accompanying a gradual decrease in residual resistivity (defined by the resistivity immediately above T_c). In fact, the change of residual resistivity scales linearly with that of T_c, implying that the oxygen interstitials in the less reduced crystals play the role of strong carrier scatterers as well as pair-breaking impurities.

The resistivity in the normal state of 24-K superconductor $Nd_{2-x}Ce_xCuO_{4-y}$ is quadratic with temperature at relatively low temperatures below 200 K and, at higher temperatures, subject to the logarithmic correction characteristic of a 2D Fermi liquid (Tsuei, Gupta, and Loren, 1989). This is in contrast with the well-known T-linear behavior for optimally hole-doped superconductors. Brinkmann *et al.* (1995) succeeded in extending the superconducting composition range to $0.04 \leqslant x \leqslant 0.17$ for $Pr_{2-x}Ce_xCuO_{4-y}$ using an improved reduction technique. In those crystals, they observed for the normal state in the reduced superconducting crystals that the resistivity was fitted using the empirical formula $\rho(T)=\rho_0+bT^n$ and that the exponent n changed from $n \approx 1.7$ for high Ce concentration to $n \approx 1.3$ for lower Ce concentrations. A similar systematic change is known for the overdoped concentration range of the hole-doped superconductors (Takagi, Batlogg, *et al.*, 1992a; Kubo *et al.*, 1991).

The long-standing problem is the nature of superconducting carriers in the electron-doped cuprates. The Hall coefficient R_H is quite sensitive, not only to the

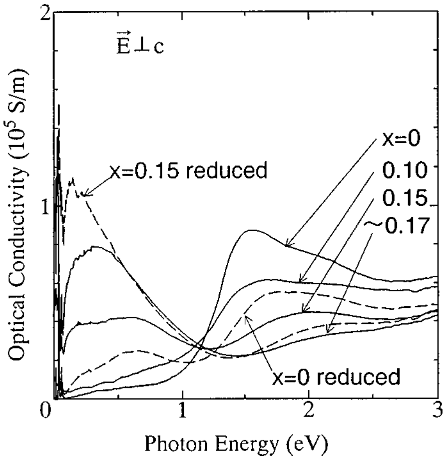

FIG. 136. Optical conductivity spectra of $Pr_{2-x}Ce_xCuO_{4-y}$ with light polarization perpendicular to the c axis (in-plane).

doping x as in the hole-doped superconductors, but also to the reduction procedure. In general, the R_H is negative and its absolute magnitude scales roughly with x in the lightly doped region, whereas in the nonsuperconducting overdoped region $x>0.17$ the sign of R_H is reversed to positive (Takagi, Uchida, and Tokura, 1989). Apart from the opposite sign, the behavior is analogous to the case of $La_{2-x}Sr_xCuO_4$ (Ong *et al.*, 1987; Takagi, Ido, *et al.*, 1989). However, it has been occasionally observed for superconducting $R_{2-x}Ce_xCuO_{4-y}$ (R=Nd or Pr) crystals with $x\approx0.15$ that R_H increases steeply to *positive* values with lowering temperature, say below 80 K (Wang *et al.*, 1991; Jiang *et al.*, 1994). These were interpreted in terms of the two-band model in which both holes and electrons participate in charge transport for the superconducting phase.

Figure 136 displays the in-plane optical conductivity spectra (at room temperature) of $Pr_{2-x}Ce_xCuO_4$ with and without reduction procedures (Arima, Tokura, and Uchida, 1993). Spectroscopically, the reduction procedure appears to produce an effect similar to the electron-doping x. With electron-doping, the spectral weight arising from the CT gap transition around 1.5 eV is transferred to the in-gap region (Cooper *et al.*, 1990a), as observed in the hole-doping case, $La_{2-x}Sr_xCuO_4$ (Uchida *et al.*, 1991). However, the broad infrared band (the so-called in-gap state absorption) is far from the conventional Drude spectrum and the charge dynamics appears highly incoherent. The doping-induced change was also observed in the O $2p$-Cu $4s$ interband transition region (Arima, Tokura, and Uchida, 1993). A single band around 5.0 eV in the $x=0$ parent compound is split and the spectral weight is gradually shifted to the lower-lying band around 4.2 eV with doping. This was interpreted in terms of the formation of an occupied in-gap state below the Fermi level. Therefore the energy difference between the upper edge of the occupied O $2p$ state and the in-gap state is about 0.8 eV, nearly half of the original CT band gap. This is contrary to the case of hole doping, in which the in-gap state is formed predominantly above the Fermi level and hence is observable, e.g., in the O $1s$ absorption spectroscopy, as the unoccupied state (Chen *et al.*, 1991).

Doping-induced changes in the single-particle DOS of $Nd_{2-x}Ce_xCuO_4$ are thus different from those in $La_{2-x}Sr_xCuO_4$ in that the in-gap spectral weight appears largely below E_F (Anderson *et al.*, 1993). It is then expected that the upper Hubbard band ($d^9\rightarrow d^{10}$) loses its spectral weight, although an increase of the spectral weight was indeed observed by oxygen $1s$ x-ray absorption spectroscopy (Pellegrin *et al.*, 1993). The position of the Fermi level of the doped sample with respect to the band gap of Nd_2CuO_4 has been a long-standing puzzle: It was pointed out that E_F is located below the mid-gap of the parent compound if we consider the band gap of

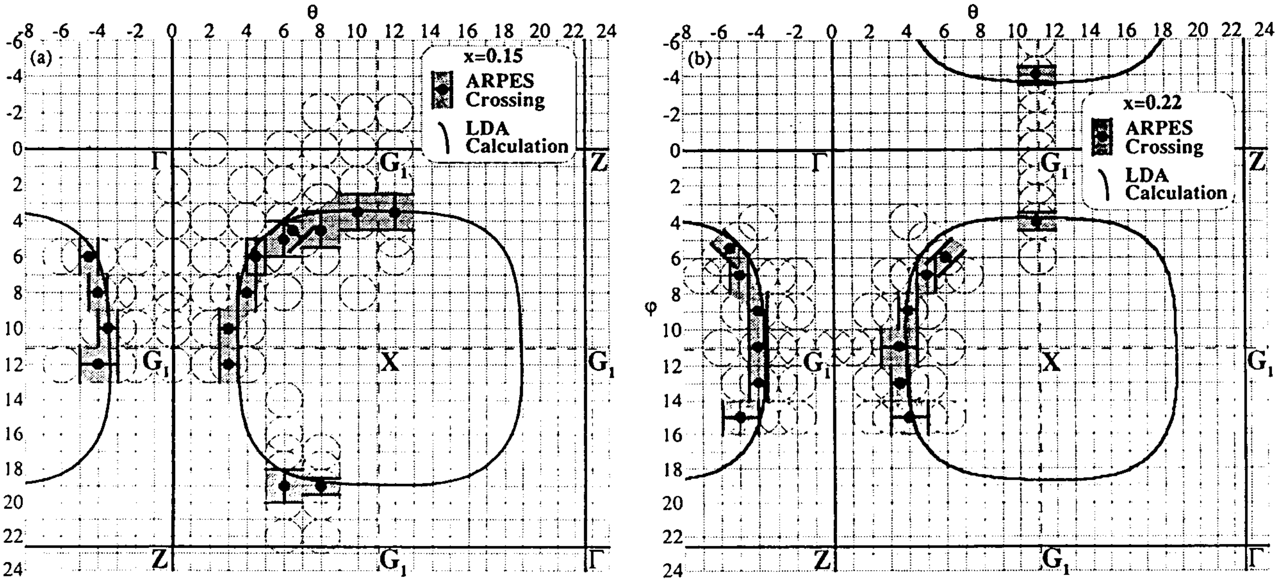

FIG. 137. Fermi surface of $Nd_{2-x}Ce_xCuO_4$ determined by angle-resolved photoemission spectroscopy (King *et al.*, 1993). Solid curves are results of LDA band-structure calculations (Massida *et al.*, 1989). G: $(\pi,0)$; X: (π,π).

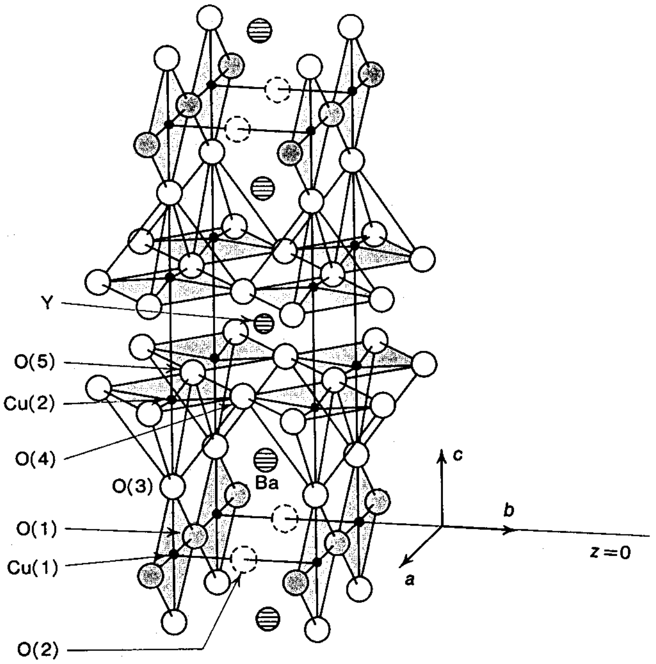

FIG. 138. Lattice structure of $YBa_2Cu_3O_7$.

Nd_2CuO_4 to be the optical gap of 2.0 eV (Allen *et al.*, 1990; Namatame *et al.*, 1990). This is obviously incompatible with the common notion that the bottom of the conduction band is the affinity level of the parent insulator.

Angle-resolved photoemission studies of $Nd_{1.85}Ce_{0.15}CuO_4$ revealed a dispersing band which crosses E_F (Anderson *et al.*, 1993; King *et al.*, 1993). As shown in Fig. 137, the Fermi surface thus determined is a hole-like one centered at the (π,π) point of the Brillouin zone, in excellent agreement with band-structure calculations for the nonmagnetic metallic state. The results also show that the Fermi surface volume changes following the Luttinger sum rule with varying doping level. There is a saddle point, not in the band dispersions near E_F, but a few hundred meV below it, unlike the hole-doped cuprate superconductors. The angle-resolved photoemission spectra show intense high-binding-energy tails and background, indicating that the spectral weight of the coherent quasiparticle Z is very small.

3. $YBa_2Cu_3O_{7-y}$

This compound has the same layered structure as $La_{2-x}Sr_xCuO_4$ in the sense that it has a stacking of the CuO_2 planes and the block layers. The lattice structure is shown in Fig. 138. A complexity in this compound is that it has a chain structure of Cu and O embedded in the so-called block layer sandwiched by the CuO_2 planes. This Cu-O chain structure makes a minor contribution to the dc conductivity.

The insulating compound of $YBa_2Cu_3O_{7-y}$ with $y \geqslant 0.6$ has antiferromagnetic long-range order. The first signature of the antiferromagnetic order was detected by the muon-spin-rotation measurements (Nishida *et al.*, 1987). An ordered structure similar to the case of La_2CuO_4 was confirmed by subsequent neutron-diffraction measurements (Tranquada *et al.*, 1988). In the region $0.6<y<1.0$, holes are mainly doped into the CuO chain sites, where excess oxygen added to $y=1.0$ is indeed introduced to the layers composed of separated CuO chains. Therefore the doping concentration in the CuO_2 plane changes little by basically retaining the Cu^{2+} valence and thereby retaining the antiferromagnetic insulating phase. Below $y=0.6$, holes start to be transferred to the CuO_2 plane, which immediately destroys

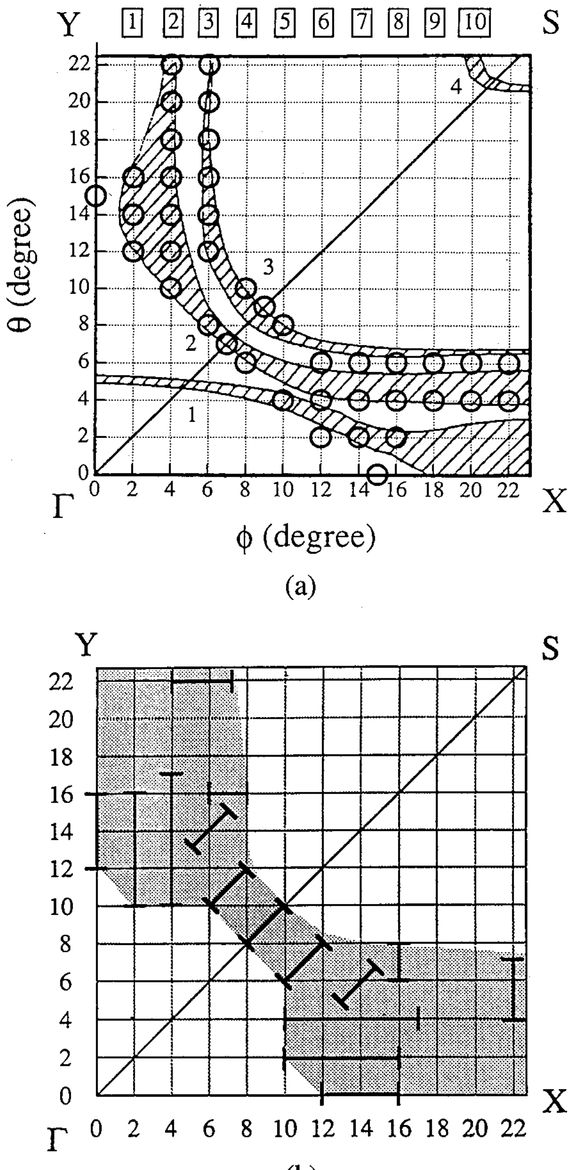

(a)

(b)

FIG. 139. Fermi surfaces of $YBa_2Cu_3O_{6.9}$ determined by angle-resolved photoemission spectroscopy. (a) Results by Liu *et al.*, 1992a. Open circles denote Fermi level crossings and shaded regions are calculated Fermi surfaces (Pickett *et al.*, 1990). The finite width of the shaded regions represents finite k_z dispersion. The measurements on twinned samples have been done for the half of the Brillouin zone shown here. X: $(\pi,0)$, Y: $(0,\pi)$, S: (π,π). (b) Another interpretation of the same data by Shen and Dessau (1995).

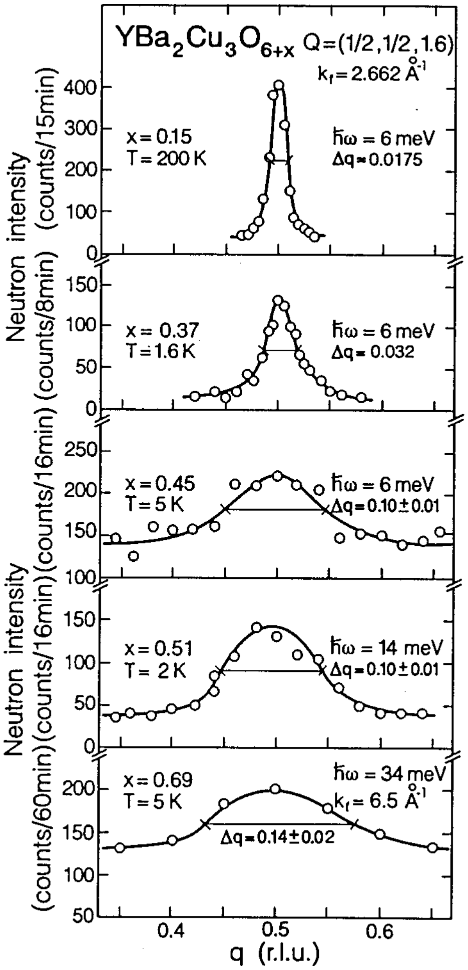

FIG. 140. Antiferromagnetic correlation observed in peak structures of Im $\chi(q,\omega)$ by neutron scattering for $YBa_2Cu_3O_{6+x}$. From Rossat-Mignod *et al.*, 1991a.

the antiferromagnetic order and is accompanied by metallization. The Néel temperature in the insulating phase is as high as 400 K. Because the electronic structure calculation using the LDA shows the Fermi surface more or less tilted by 45° from the case of La_2CuO_4, as illustrated in Fig. 139 (Liu *et al.*, 1992a), simple nesting condition is not satisfied in this case and thus strong correlation effects should be crucial in realizing the antiferromagnetic insulator. A pulsed high-energy neutron measurement performed up to 250 meV shows that the spin-wave theory of the Heisenberg model well describes the spin-wave dispersion with the in-plane exchange constant $J_{\parallel}=125\pm5$ meV and the inter-layer exchange $J_{\perp}=11\pm2$ meV (Hayden *et al.*, 1996).

Around $y=0.6$, the compound becomes metallic and the hole concentration in the CuO_2 layer increases with further decreasing y. This compound in the metallic phase shows a unique process of doping due to the transfer of holes between the Cu-O chain site and the CuO_2 layer (Tokura, Torrance, *et al.*, 1988). In the region $0.3\leqslant y\leqslant0.6$, the hole concentration in the CuO_2 plane is kept low with relatively low superconducting transition temperature $T_c\sim60$ K. Around $y=0.3$ the hole concentration is increased quickly to the overdoped or optimally doped region with $T_c\sim90$ K. Similarly to the case of $La_{2-x}Sr_xCuO_4$, short-range antiferromagnetic correlations survive in the metallic phase. This enhancement of antiferromagnetic correlations is seen in the diffuse neutron-scattering measurement around (π,π). However, in contrast to the case of $La_{2-x}Sr_xCuO_4$, $\mathrm{Im}\chi(q,\omega)$ resulting from the neutron data does not show clear incommensurate peaks in the metallic phase. Instead, it has a broad peak around (π,π), as is shown in Fig. 140 (Rossat-Mignod *et al.*, 1991a; Sternlieb *et al.*, 1994). The origin of this difference in the peak structure between La and Y compounds was ascribed to the difference in the shape of the Fermi surface (Furukawa and Imada, 1992; Si *et al.*, 1993; Tanamoto, Kohno, and Fukuyama, 1993, 1994). However, a signature of incommensurate structure was recently detected also in *Y* compounds (Dai *et al.*, 1998).

A single-parameter scaling by $\beta\omega$ for $\int dq\,\mathrm{Im}\chi(q,\omega)$, analogous to the case of $La_{2-x}Sr_xCuO_4$ as discussed in Sec. IV.D.1, is observed in the underdoped region (Sternlieb *et al.*, 1993). However this single-parameter scaling seems to break down at lower energies below ~12 meV at low temperatures. This may be related to pseudogap formation, as discussed below.

Magnetic properties show rather different features between the underdoped $(0.6\geqslant y\geqslant0.3)$ and the optimally or overdoped $(0.3\geqslant y\geqslant0)$ samples. The Knight-shift measurement in NMR clearly shows this difference. In overdoped samples with $T_c\sim90$ K, the Knight shift is more or less constant at $T>T_c$, indicating that the uniform magnetic susceptibility $\chi(q=\omega=0)$ follows the T-independent Pauli susceptibility of standard metals. On the other hand, in the underdoped material, $0.3<y<0.6$, the uniform magnetic susceptibility derived from the spin part of the Knight shift shows a rapid decrease with decreasing temperatures, as shown in Fig. 141 (Takigawa *et al.*, 1991). The observed decrease with lowering temperatures is in fact much more pronounced than that seen in the 2D or 1D spin-1/2 Heisenberg model (Bonner and Fisher, 1964; Okabe and Kikuchi, 1988; Makivić and Ding, 1991). This decrease appears to be continuously and smoothly connected with the decrease below T_c, as seen in Fig. 141. Therefore it is natural to speculate that formation of the pseudogap structure due to preformed singlet pairing fluctuations begins well above T_c. The peak structure of $\chi(q=\omega=0)$ at $T=T_\chi\sim500$ K is qualitatively similar to that for the case of $La_{2-x}Sr_xCuO_4$ in the underdoped region.

However, if we look at $1/T_1$, we notice that the situation is not so simple as naively expected from s-wave preformed pairing. In overdoped or optimally doped samples with $T_c\sim90$ K, $1/T_1T$ at the copper site is more or less similar to the case of $La_{1.85}Sr_{0.15}CuO_4$, although the experimentally accessible temperature range is limited to below 400–500 K because of the difficulty of controlling oxygen concentration above it. A gradual crossover from $1/T_1T\sim$const to $1/T_1\sim$const appears to take place from low to high temperatures. The underdoped samples with $T_c\sim60$ K show remarkably different behavior, as shown in Fig. 142, where $1/T_1T$ decreases be-

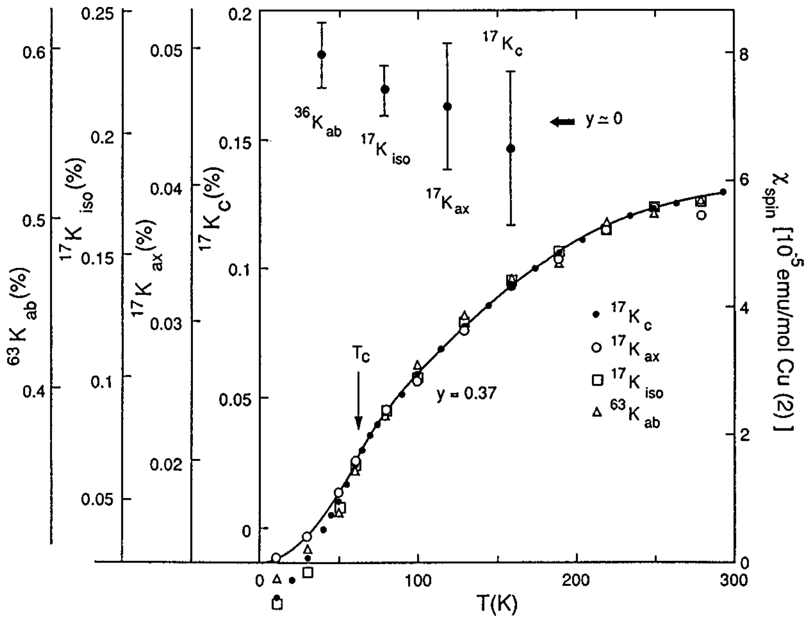

FIG. 141. Temperature dependence of the Knight shift for $YBa_2Cu_3O_{7-y}$ at $y=0$ and $y=0.37$. Various components of the Cu and O Knight shift are plotted with different vertical scales and origins. Anisotropy obtained from the direction of the applied magnetic field in *ab*, the *ab*-plane; *c*, *c*-axis; *ax*, the axial part; *iso*, the isotropic part (Takigawa *et al.*, 1991). The Knight shift starts decreasing from much higher temperature than T_c.

low 150–200 K as if it were under the influence of pseudogap formation (Yasuoka *et al.*, 1989). In fact, these $1/T_1T$ data were the first pioneering indication of pseudogap behavior in the high-T_c cuprates well above T_c. Similar pseudogap formation behavior is also observed in other underdoped compounds such as $YBa_2Cu_4O_8$, and $HgBa_2CuO_{4+\delta}$ (Itoh *et al.*, 1996). So far, in $La_{2-x}Sr_xCuO_4$, this pseudogap behavior in $1/T_1T$ is not clearly visible. The possible effect of randomness was discussed for the suppression of the pseudogap in $1/T_1T$. In any case, the anomaly in the underdoped Y compound appears to show up below $T_R \sim 200$ K, which is substantially lower than T_χ in the uniform magnetic susceptibility but markedly higher than T_c. The same type of anomaly has also been confirmed in neutron-scattering experiments (Rossat-Mignod *et al.*, 1991a, 1991b; Sternlieb *et al.*, 1993), where $\mathrm{Im}\,\chi(q,\omega)$ shows pseudogap behavior for $q \sim (\pi,\pi)$ below $T \sim 200$ K for the underdoped compound with $T_c \sim 60$ K, as shown in Fig. 143.

The origin of the difference between T_χ in $\chi(q=\omega=0)$ and T_R in $1/T_1T$ is not clear enough at the moment and further studies are clearly necessary. Another puzzling feature of the pseudogap behavior is that the Gaussian decay rate $1/T_G$ does not show a gaplike decrease either at T_χ or at T_R (Itoh *et al.*, 1992). This may be related to the compatibility of antiferromagnetic correlations and superconductivity; see Assaad, Imada, and Scalapino (1997), where the above two puzzling features are reproduced in a theoretical model.

Other indications of a pseudogap below $T \sim 200$ K were also suggested from the anomaly of the B_{2u} phonon mode (Harashina *et al.*, 1995) as well as from anomalies in the Raman mode coupled to phonons

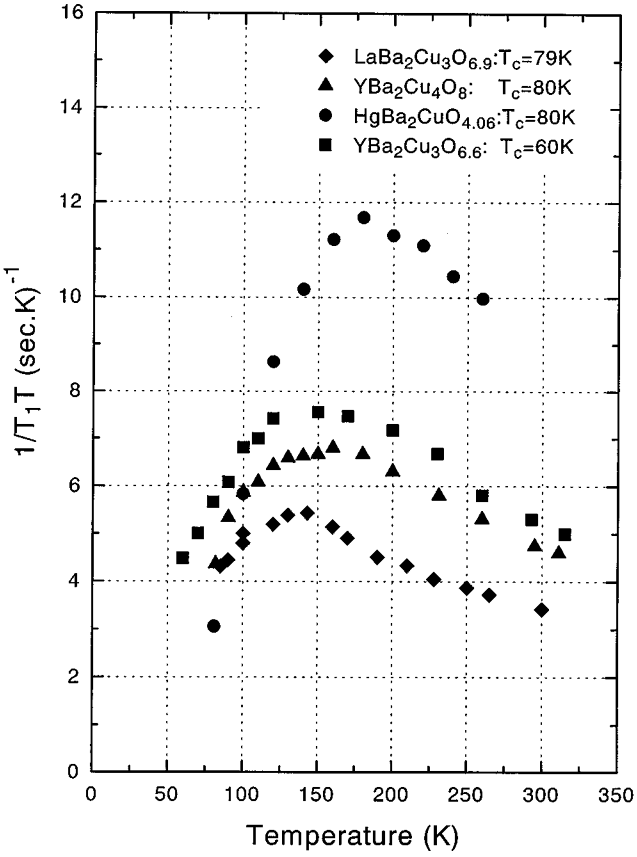

FIG. 142. Temperature dependence of $1/T_1T$ at the Cu site for several high-T_c compounds (by courtesy of H. Yasuoka, who replotted various available data). They show indications of pseudogap behavior well above T_c. The data are taken from Machi *et al.*, 1991; T. Imai *et al.*, 1989; Goto *et al.*, 1996; Warren *et al.*, 1989; Takigawa *et al.*, 1991; Y. Itoh *et al.*, 1996.

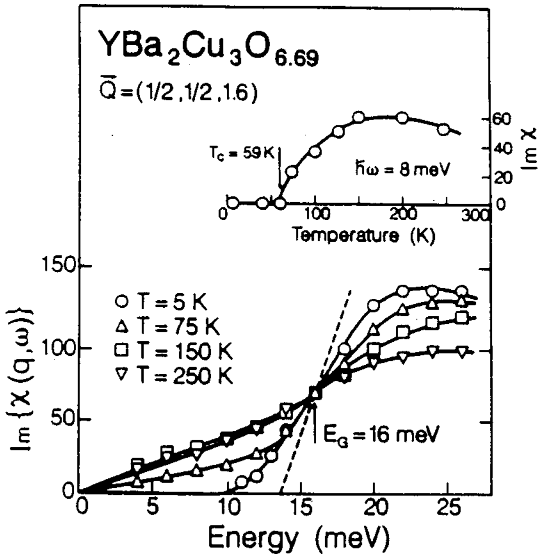

FIG. 143. Im $\chi(q,\omega)$, in arbitrary units, as a function of ω at $q=(\pi,\pi)$ for the underdoped compound YBa$_2$Cu$_3$O$_{6.69}$. The pseudogap structure is seen from the temperature above T_c. The inset shows the temperature dependence or fixed $\hbar\omega=8$ meV. From Rossat-Mignod *et al.*, 1991b.

(Litvinchuk, Thomsen, and Cardona, 1993), where consistency with coupling to d-wave pairing was proposed theoretically (Normand, Kohno, and Fukuyama, 1995). The energy shift of the phonons due to coupling to the superconducting order parameter has been discussed from a more general point of view by Zeyer and Zwicknagl (1988).

The origin of this pseudogap behavior is not fully understood. Experimentally, however, it has been confirmed in various cases, including the so-called single-layer compound HgBa$_2$CuO$_{4+\delta}$. The formation of a pseudogap has also been detected by photoemission measurements for underdoped Bi and La compounds, as discussed in Secs. IV.C.1 and IV.C.4. Another important indication of pseudogap behavior is a reduction of the specific-heat coefficient γ at low doping similar to the case of La$_{2-x}$Sr$_x$CuO$_4$ (Loram *et al.*, 1994; Momono *et al.*, 1994; Liang *et al.*, 1996).

Theoretically, several different explanations for this unusual behavior have been proposed. The possibility of preformed pairing fluctuations above T_c as the origin of pseudogap behavior has been examined from various approaches. This is a natural idea because the temperature for singlet pairing may in general be higher than T_c itself when the MIT point is approached. Near a continuous MIT point, the coherence temperature T_{coh} has to decrease to vanish, while the energy scale for the pairing energy may be independent of this reduction. This idea is supported by the small coherence length of the Cooper pair observed experimentally in the high-T_c cuprates. The short coherence length ξ_{coh} is easily deduced from a large critical magnetic field H_{c2} and the relation $\xi_{coh}=1/\sqrt{2\pi H_{c2}}$. In YBa$_2Cu_3O_7$, ξ_{coh} in the CuO$_2$ plane was estimated as ~10–20 Å, that is, only a few lattice spacings, even in the plane direction. It is known that weak-coupling BCS superconductors may be continuously connected to a strong-coupling region where the picture of Bose condensation by preformed pairs becomes appropriate (Nozières and Schmitt-Rink, 1985). When ξ_{coh} is small, the superconductivity is rather close to the picture of the condensation of bosons. If this is the case, the pairing temperature should be separated from T_c itself. However, the naive picture of Bose condensation is not appropriate because the preformed pair has d-wave character accompanied by antiferromagnetic correlations with strong momentum dependence.

One scenario for preformed singlet pair fluctuations is given by an unusual criticality near the Mott transition, as discussed in Sec. II.F. Because of unusual suppression of the coherence of the single-particle transfer process due to strong spin and charge fluctuations near the Mott transition point, we have to consider a higher-order process of the transfer. In the Mott insulating phase, this indeed makes the superexchange interaction in the order of t^2/U relevant. If the system is close to the Mott insulator but in the metallic phase, other higher-order processes of two-particle transfer contributes equally, while the single-particle process is still suppressed due to a large dynamical exponent $z=4$ (Assaad, Imada, and Scalapino, 1996). Near the Mott insulator this two-particle process can be more relevant than the single-particle process because of its small dynamical exponent $z=2$ (Imada, 1994c, 1995b). This means that, in contrast to the single-particle process, the two-particle process is not anomalously suppressed leading to a gain in the kinetic energy. This necessarily yields a pairing effect. An important point here is a strong momentum dependence of pairing fluctuations. The precursor of pairing starts around $(\pi,0)$ and $(0,\pi)$ in the momentum space at higher temperatures. For more detailed discussion of this mechanism, see Sec. II.F.

There are several completely different ways of interpreting pseudogap behavior as an effect of preformed pairing. Pairing through the magnetic polaron or conventional lattice polaron effect was studied as a bipolaron mechanism (Micnas *et al.*, 1990; Alexandrov, Bratkovsky, and Mott, 1994; Alexandrov and Mott, 1994). In the cuprate superconductors, it is not likely that bipolaronic mechanisms and local-pairing mechanisms can be compatible with the principal features of strong-correlation effects. Fluctuating phase-separation effects and dynamic charge-ordering effects (Emery and Kivelson, 1995, 1996; Zaanen and Oleś, 1996) were proposed as sources of preformed pairing. A more general argument from the separation of the optimized Bose condensation temperature and the pairing energy, as well as a comparison of cuprate superconductors with other cases such as heavy-fermion superconductors and C$_{60}$ compounds, was stressed by Uemura *et al.* (1989, 1991).

Another interpretation of pseudogap behavior is the scenario assuming spin-charge separated excitations at the low-energy level. Pseudogap formation is attributed to the pairing of spinons without Bose condensation of holons in the picture of the slave-boson formalism discussed in Sec. II.D.7 (Baskaran, Zou, and Anderson,

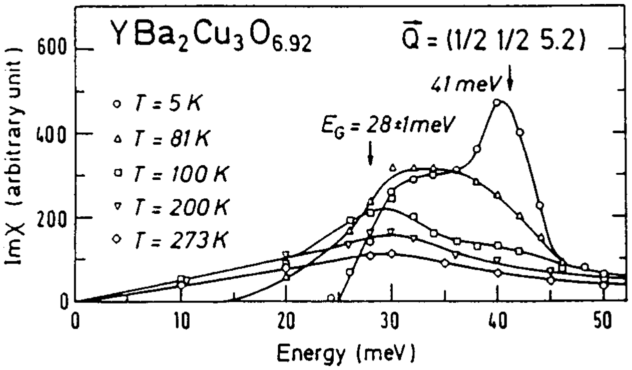

FIG. 144. Im $\chi(q,\omega)$, in arbitrary units, as a function of ω at $q=(\pi,\pi)$ for the optimally doped compound $YBa_2Cu_3O_{6.92}$ (Rossat-Mignod *et al.*, 1991b). A prominent 41-meV peak is observed below T_c.

1987; Kotliar and Liu, 1988; Suzumura, Hasegawa, and Fukuyama, 1988; Tanamoto, Kohno, and Fukuyama, 1994). The spinon pairing is basically due to singlet formation by the mean-field-type decoupling of the superexchange interaction $J\mathbf{S}_i\cdot\mathbf{S}_j$. From the Fermi-liquid approach the nesting condition has also been proposed as the origin of pseudogap behavior (Miyake and Narikiyo, 1994b).

In neutron scattering at higher energies, as shown in Fig. 144, another unusual behavior has been observed in Im $\chi(q,\omega)$, namely, a remarkable peak around $\omega=41$ meV with dramatic growth below T_c (Mook *et al.*, 1993; Fong *et al.*, 1995, 1997). The resonance energy decreases monotonically with decreasing doping concentration. It is clear that this excitation is strongly coupled to the superconducting order parameter. Demler and Zhang (1995) have proposed that this peak is related to a special type of triplet pairing excitation, namely, the rotational mode connecting the antiferromagnetic order parameter and the *d*-wave superconducting order parameter under SO(5) symmetry (Zhang, 1997). The enhancement of the resonance below T_c has some similarity to the result in La compounds above 7 meV. These all seem to indicate the compatibility of antiferromagnetic correlation in the superconducting state. Similar and consistent theoretical results were obtained in numerical studies attempting to account for the two-particle process explicitly (Assaad, Imada, and Scalapino, 1997; Assaad and Imada, 1997). The peak appears to be the remnant of the antiferromagnetic Bragg peak shifted to a finite frequency. In this context, the pseudogap formation widely observed appears to start at high temperatures as undifferentiated signatures of antiferromagnetic and *d*-wave preformed pair fluctuations.

The transport properties of $YBa_2Cu_3O_{7-y}$ show, roughly speaking, behaviors similar to that of $La_{2-x}Sr_xCuO_4$ as described in Sec. IV.C.1 (Iye, 1990; Ong, 1990). The in-plane resistivity ρ_{ab} is approximately proportional to T near $y=0$, that is, near the optimum doping concentration, in the same way as in $La_{1.85}Sr_{0.15}CuO_4$. However, in the underdoped region it shows substantial deviation from T-linear behavior. This deviation may be viewed as the reduction of ρ below the temperature T_ρ, which increases with decreasing doping concentration as seen in Fig. 145 (Ito, Takenaka, and Uchida, 1993; Takenaka *et al.*, 1994). As compared to $T_\chi\simeq T_\rho$ in the case of $La_{2-x}Sr_xCuO_4$, T_ρ in the Y compounds appears to be low with weaker effects. Similarly to the case of La_{2-x} Sr_xCuO_4, the Hall coefficient shows a rather sharp increase with decreasing temperature below a similar temperature T_ρ or T_χ (Ito *et al.*, 1993; Takeda *et al.*, 1993; Nishikawa, Takeda, and Sato, 1994).

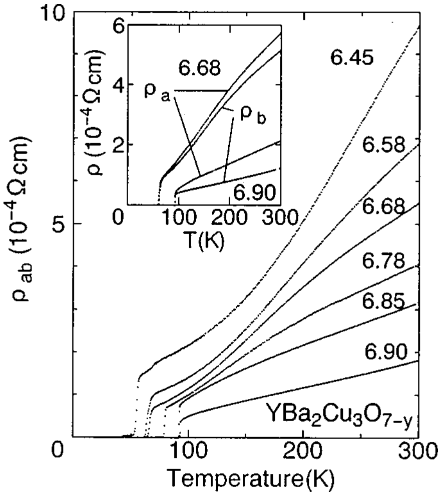

FIG. 145. Temperature dependence of in-plane resistivity for various choices of y for $YBa_2Cu_3O_{7-y}$, where the numbers in the figure indicate $7-y$ (Ito, Takenaka, and Uchida, 1993). The CuO_2-plane contribution is obtained by subtracting the chain contribution deduced from the a- and b-axis resistivities shown in the inset.

The temperature dependence of the Hall angle defined by

$$\cot\Theta_H=\frac{\sigma_{xx}}{\sigma_{xy}} \tag{4.12}$$

was measured for $YBa_2Cu_{3-p}Zn_pO_{7-y}$ (Chien, Wang, and Ong, 1991; Ong *et al.*, 1991). For $p=0$ and $\delta\sim 0$, cot Θ_H appears to follow

$$\cot\Theta_H\simeq\alpha T^2. \tag{4.13}$$

Anderson (1991a) introduced two different carrier relaxation rates, τ_{tr} and τ_H, where τ_{tr} is the longitudinal relaxation rate for motion perpendicular to the Fermi surface while τ_H is the transverse rate for the velocity component parallel to the Fermi surface. In the usual Fermi liquid, $\tau_{tr}=\tau_H$ must hold, while the above experimental result together with $\rho\sim T$ suggests $\tau_{tr}\sim 1/T$ and $\tau_H\sim 1/T^2$. Anderson interpreted this unusual temperature dependence as coming from a singular interaction of two electrons located perpendicular to the Fermi surface, and also proposed that it could yield similar behavior to a 1D Tomonaga-Luttinger liquid.

Around $y=0$, the c-axis transport is also metallic, indicating T-linear behavior of ρ_c, although the absolute value is much larger than ρ_{ab} due to anisotropy. However, it shows insulating temperature dependence in the

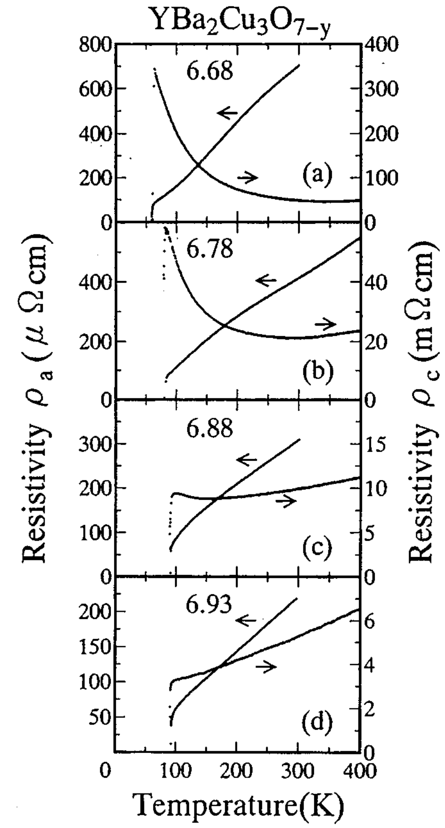

FIG. 146. Comparison of in-plane and c-axis resistivity vs temperature at several choices of doping concentrations $7-y$ for $YBa_2Cu_3O_{7-y}$. From Takenaka *et al.*, 1994.

low-doping region below certain temperatures. As temperatures are lowered, ρ_c decreases, with minima at a temperature slightly higher but similar to T_ρ, and increases as an insulating behavior below T_ρ as in Fig. 146 (Takenaka *et al.*, 1994). It should be noted that this anomaly occurs at a similar temperature to that for the deviation of ρ_{ab} from T-linear behavior discussed above and is again similar to the case of $La_{2-x}Sr_xCuO_4$. In the scenario of preformed singlet fluctuations, the reduction of ρ_{ab} below T_ρ can be ascribed to the increasing coherence of the fluctuating preformed pairs, while the charge excitation in the c direction has a pseudogap because interlayer hopping has to break the pair once if the pairing originates from two-dimensionality, as in the scenario of pairing due to large dynamic exponent z of the 2D Mott transition, discussed in Sec. II.F.9.

The effects of Zn doping on the anomalies below T_ρ were examined (Mizuhashi, Takenaka, Fukuzumi, and Uchida, 1995). There exists a range of Zn concentration around 2% where the metallic and pseudogap-type temperature dependence of the resistivity is retained while a Curie-like enhancement in the uniform magnetic susceptibility appears. This implies that the local spin moment appears despite the metallic conduction of carriers. This was interpreted from the scenario of spin-charge separation in the slave-boson formalism (Nagaosa and Ng, 1995).

An alternative scenario is given by a non-Fermi-liquid state sandwiched between the Fermi liquid and the Anderson localized phases (see, for example, Dobrosavljević and Kotliar, 1997). A key point to understand this result may lie in the strong wave-number dependence of carriers, which has been ignored in the above arguments. The preformed singlet pair fluctuations around $(\pi,0)$ may to some extent contribute to the "metallic" conduction, though they remain rather incoherent well above T_c. This small "metallic" contribution may explain the small reduction in the resistivity upon pseudogap formation. While the single-particle excitations may easily be localized by Zn substitution or induce the local moment, the Anderson localization may take place predominantly in the single-particle excitations because of the underlying large dynamic exponent of the MIT.

The residual resistivity ρ_0 by Zn doping in the unitarity limit depends on the carrier density n and the carrier charge e as $\rho_0 \propto 1/(ne^2)$. Therefore one might think that one could distinguish the following three cases: The first is the usual Fermi-liquid conduction with charge e and $n=1-x$, the second is a complicated situation in which the preformed pair with $n=x/2$ and charge $2e$ makes a minor contribution to the transport while the major contribution is from the part around $(\pm\pi/2,\pm\pi/2)$. The third is the spin charge separation scenario where the holon conduction gives the charge e with $n=x$ (Nagaosa and Lee, 1997). Experimentally, the increase of ρ_0 is large in the underdoped region and roughly scaled by $1/n=1/x$ (Fukuzumi *et al.*, 1996). However, a complexity exists because of the strong wave-number dependence of carriers in the underdoped region. Carriers in a region around $(\pi/2,\pi/2)$ remain unpaired, while carriers around $(\pm\pi,0)$ and $(0,\pm\pi)$ stay strongly damped due to $z=4$ with instability to gradual pseudogap formation. If the transport is still dominated by single-particle transport mainly coming from a small region around $(\pi/2,\pi/2)$ over other transport channels, the residual resistivity can be large because the effective carrier number is given by that small region around $(\pm\pi/2,\pm\pi/2)$ as if the Fermi volume were small. [This is clearly different from the scenario of small-pocket formation around $(\pm\pi/2,\pm\pi/2)$]. This may account for the experimental result. Even when we consider this complexity, the experimentally observed large residual resistivity induced by Zn doping does not seem to be compatible with the first case, while it seems to be hard to judge the superiority of one to the other in the latter two cases.

The optical conductivity $\sigma(\omega)$ of untwinned crystals shows a broad tail roughly proportional to $1/\omega$, as in Fig. 147 (Schlesinger *et al.*, 1990; Azrak *et al.*, 1994). At the optimum doping concentration $y\sim 0$, $\sigma(\omega)$ basically follows the scaling $\sigma(\omega)\sim\sigma_0(1-e^{-\beta\omega})/\omega$ with a constant σ_0 indicating the absence of coherent charge dynamics, as already discussed in Secs. II.E.1, II.F.9, and II.G.2 from the theoretical point of view. In untwinned samples, the broad mid-IR peak structure observed in La compounds is not visible, implying that the peak structure itself is not an intrinsic property of the high-T_c cuprates. The significance of the absence of the true

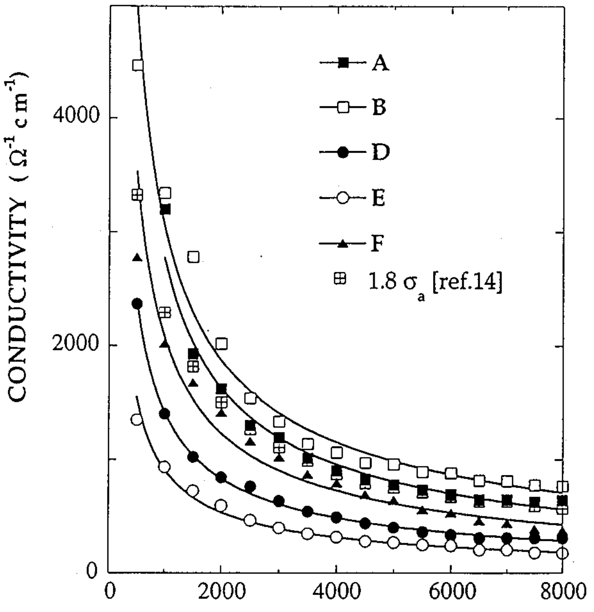

FIG. 147. Optical conductivity $\sigma(\omega)$ for several different untwinned film samples (denoted as A,B,D,E,F) of $YBa_2Cu_3O_7$ by Azrak *et al.* (1994). Solid lines are fitting curves in the form of ω^{-a}. Cross-square points are σ_a by Schlesinger *et al.* (1990). They roughly follow the scaling $1/\omega$.

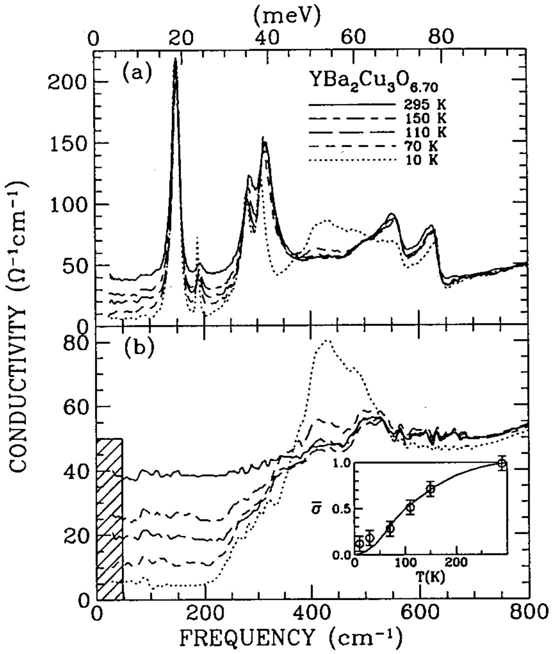

FIG. 148. Pseudogap observed in c-axis $\sigma(\omega)$ of $YBa_2Cu_3O_{7-y}$ for $y=0.3$. The upper panel (a) shows the data with the phonons, while the lower panel shows the data of the electronic part by subtracting the phonon contribution. The inset in the lower panel shows the conductivity at 50 cm^{-1} normalized by the room-temperature conductivity (open circles) and the normalized Knight shift for Cu(2) (solid line) at $y=0.37$. From Homes *et al.*, 1993.

Drude weight, common to all the cuprate superconductors, is also discussed in Sec. IV.C.1. The extended Drude analysis of the Y compound also supports the consistency of Eq. (2.274) with weakly ω-dependent and T-dependent $C(\omega)$ (Thomas *et al.*, 1988; Schlesinger *et al.*, 1990; El Azrak *et al.*, 1994).

A remarkable feature in the c-axis conductivity $\sigma_c(\omega)$ is also seen at low doping concentration. Corresponding to the insulating temperature dependence of ρ_c below T_ρ, a pseudogap structure grows in $\sigma_c(\omega)$ in the region $\omega < 600$ cm^{-1}, as shown in Fig. 148 (Homes *et al.*, 1993; Tajima *et al.*, 1995; see also the review by Tajima, 1997). Even in the ab plane, the pseudogap structure was detected well above T_c, as shown in Fig. 149 (Orenstein *et al.*, 1990; Rotter *et al.*, 1991; Schlesinger *et al.*, 1994; Basov *et al.*, 1996; Puchkov *et al.*, 1996). The pseudogap structure seems to be continuously connected with the superconducting gap observed below T_c. It may be associated with the pseudogap observed in angle-resolved photoemission spectra as discussed in Sec. IV.C.4. This pseudogap in the ab plane manifests itself as the spectral weight transfer from the incoherent part roughly scaled by $1/\omega$ to the coherent part. If we considered the optical spectra only for the coherent part (though it is actually absent, as discussed above), it would be difficult to identify this pseudogap structure because the gap energy is above the anticipated scale of inverse relaxation time of charge dynamics ($\sim T$) as represented by the conventional clean-limit theory. On the other hand, if we take the incoherent response as the intrinsic and dominant part of this "incoherent metal," in contrast to the conventional Drude theory, the pseudogap is indeed observable in this metallic response, as analyzed by Rotter *et al.* (1991), Schlesinger *et al.* (1994), Basov *et al.* (1996), and Puchkov *et al.* (1996).

When the preformed pair is formed by a mechanism of in-plane origin below the pseudogap temperature, it is expected that in-plane transport will become more coherent, as is discussed by Tsunetsugu and Imada (1997), while the c-axis resistivity should increase because the interplane transport has to break preformed pairs unless Josephson tunneling of pairs becomes possible in the superconducting state. Therefore the pseudogap in $\sigma(\omega)$ has the opposite effect. The in-plane spectra should show spectral weight transfer from the incoherent to coherent part and thus a decrease in dc resistivity while the c-axis spectra may show transfer to a higher-energy part and thus an increase in dc resistivity. This is consistent with the observed results. The reduction of the in-plane resistivity below T_ρ is gradual. In this context, we note the complexity due to strong momentum dependence between two regions, namely, around $(\pi,0)$ and $(\pi/2, \pi/2)$ as described above.

In $YBa_2Cu_4O_8$, it was observed that even the c-axis conductivity σ_c has a metallic temperature dependence in the pseudogap region (Hussey *et al.*, 1997, 1998). This appears to be associated with extremely good conduction in the double-chain structure specific to this compound. However, the origin of this exceptional behavior is not clear enough at the moment.

The unusual normal-state properties of $YBa_2Cu_3O_{7-y}$

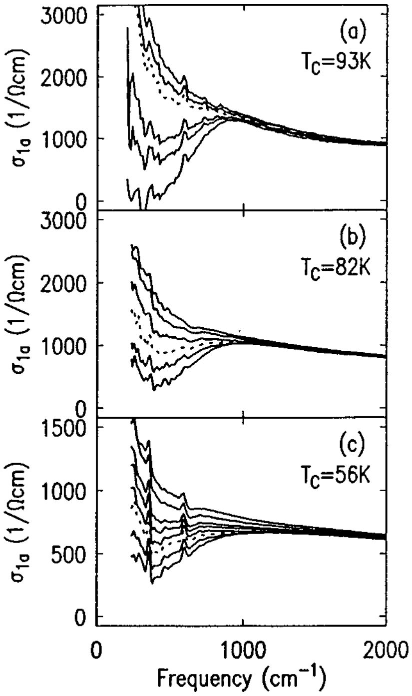

FIG. 149. Pseudogap observed in in-plane $\sigma(\omega)$ of $YBa_2Cu_3O_{7-y}$: (a) $T_c=93$ K at, from top to bottom, $T=120$, 100, 90, 80, 70, and 30 K; (b) $T_c=82$ K at $T=150$, 120, 90, 80, 70, and 20 K; (c) $T_c=56$ K at $T=200$, 150, 120, 100, 80, 60, 50, and 20 K. From Rotter *et al.*, 1991.

have many aspects in common with $La_{2-x}Sr_xCuO_4$. These common properties may be summarized as the suppressed coherence and the pseudogap behavior. Suppression of the coherence is typically observed in the T-linear resistivity and the $1/\omega$ dependence in $\sigma(\omega)$. The pseudogap behavior is observed at low doping below certain temperatures, namely, T_χ in the uniform susceptibility χ and T_γ in the specific heat. The anomalies in the Hall coefficient observed below T_H, and T_ρ in the resistivity, as well as in $\sigma_{ab}(\omega)$ and $\sigma_c(\omega)$, also appear to be related. The NMR relaxation rate $1/T_1$ shows pseudogap behavior below T_R in the Y compounds, as well as in some other compounds, though it is not observed in $La_{2-x}Sr_xCuO_4$. These crossover temperatures T_χ, T_H, T_ρ, T_R, and T_γ have quantitatively different values and they are slightly different from compound to compound. However, dependence on doping concentration is similar in all, in the sense that it is more pronounced and enhanced in the underdoped region. The overall tendency towards pseudogap formation above T_c in the underdoped region is clear. We summarize this basic tendency in a schematic phase diagram with two typical crossover temperatures T_χ and T_R in Fig. 150.

The doping dependence of the electronic structure of $YBa_2Cu_3O_{7-y}$ is more complicated than that of the other high-T_c materials because of the presence of the Cu-O chains, which make the number of holes in the CuO_2 plane somewhat ambiguous. Electron-energy-loss measurements from the oxygen 1s core level were interpreted as indicating that holes doped in the CuO_2 plane having $p_{x,y}$ symmetry become itinerant carriers (Nücker *et al.*, 1989).

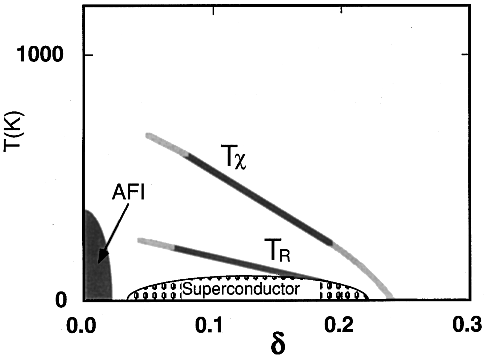

FIG. 150. Schematic phase diagram of pseudogap structure in the plane of temperature and the doping concentration in the high-T_c cuprates. Below T_χ or T_R, various indications of pseudogap formation are seen.

Fermi surfaces of $YBa_2Cu_3O_{7-y}$ ($0.1<y<0.65$) were studied by angle-resolved photoemission spectroscopy and generally good agreement with LDA band-structure calculations was obtained for optimally doped ($y\simeq0.1$) samples, as shown in Fig. 139 (Campuzano *et al.*, 1990; Liu *et al.*, 1992a, 1992b; Tobin *et al.*, 1992): The spectra were interpreted as indicating two hole-like Fermi surfaces centered at (π,π) (Liu *et al.*, 1992a), as shown in Fig. 139(a), or reinterpreted as indicating "universal" Fermi surfaces similar to those of $Bi_2Sr_2CaCu_2O_8$ (Shen and Dessau, 1995). The observed band dispersions near E_F are weaker by a factor of ~2 than the LDA band structure, indicating a moderate mass enhancement: $m^*/m_b\sim2$. Each spectrum shows an intense high-binding-energy tail and background, indicating that the spectral weight of the quasi-particle peak is small: $Z\ll1$. From these observations, it follows using Eqs. (2.125) and (2.126) that $m_k/m_b\ll1$, meaning that the energy bands crossing E_F are strongly renormalized by a **k**-dependent self-energy correction. The importance of the **k**-dependent self-energy is discussed in Sec. II.F.11.

In going from $y=0.1$ ($T_c\sim90$ K) to $y=0.5$ ($T_c\sim50$ K), the dispersions and the Fermi surfaces essentially do not change. However, while bands crossing E_F along the (π,π) direction remain unchanged, those crossing E_F along the (π,0) direction lose their spectral weight significantly [see Fig. 151(a) and 151(b)]. For an insulating $y=0.65$ sample, whose composition is in the vicinity of the MIT, bands do not cross E_F and some bands become less dispersive, whereas dispersions of other bands remain similar to those of the $y=0.1$ samples. Interestingly, bands dispersing toward E_F and crossing it along the (0,0)-(π,π) line remain in the insulating sample, although their peaks have become broader, as if the Fermi surface remains along this line, as shown in Fig. 151(c).

A closely related superconductor, $YBa_2Cu_4O_8$, with double chains was studied by angle-resolved photoemission spectroscopy in which band dispersions and Fermi surfaces are clarified as shown in Fig. 152 (Gofron *et al.*, 1994). Notably, a saddle-point behavior was found around the (π,0) point of the Brillouin zone, located

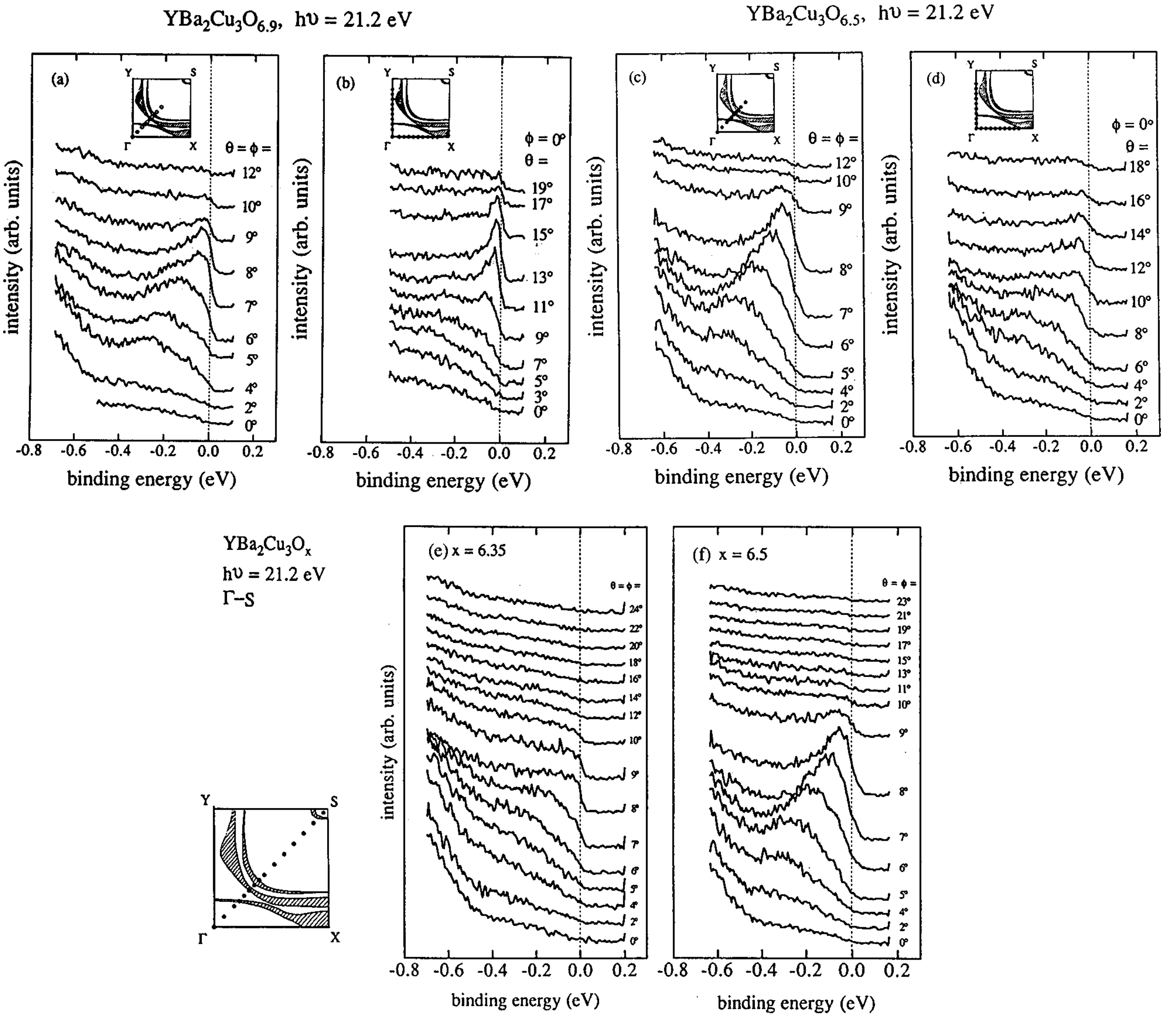

FIG. 151. Angle-resolved photoemission spectra of $YBa_2Cu_3O_{7-y}$ (Liu *et al.*, 1992a): (a) $y=0.1$ ($T_c \sim 90$ K); (b) $y=0.5$ ($T_c \sim 50$ K); (c) comparison between $y=0.5$ and $y=0.65$ (insulator).

~ 19 meV below E_F, as in $Bi_2Sr_2CaCu_2O_8$ and Sr_2RuO_4. The same behavior was found for $YBa_2Cu_3O_{7-y}$ (Tobin *et al.*, 1992; Liu *et al.*, 1992a). The experimental band dispersions are again weaker than calculated by a factor of ~ 2. A more remarkable discrepancy from the band-structure calculation is the very flat dispersion along the $(0,0)$-$(\pi,0)$ direction, compared to the calculated quadratic dispersion. A similar structure is discussed in Sec. IV.C.4. Theoretical aspects of this flat dispersion, which appears near the MIT point in 2D systems, are considered in Sec. II.F.11, and its importance is discussed in Sec. II.F.11 in terms of the scaling theory. The flatness is qualitatively different from the usual Van Hove singularity because the dispersion changes to a k^4 law consistent with a scaling theory that has a large dynamic exponent $z=4$. Because the chemical potential ($=E_F$) is determined from the level of the preformed pair, single-particle flat dispersion should be separated from this pair level by a distance equal to the binding energy of the pair. This is why the flat dispersion is shifted from E_F (which is 19 meV for $YBa_2Cu_4O_8$). The k^4 dispersion for the single-particle excitation is transformed to a k^2 dispersion for a pair excitation with a finite binding energy at the MIT edge.

4. $Bi_2Sr_2CaCu_2O_{8+\delta}$

$Bi_2Sr_2CaCu_2O_8$ and its derivatives have the strongest anisotropy in their transport properties between in-plane and out-of-plane behaviors (Ito *et al.*, 1991) and therefore are the best 2D conductors among the high-T_c cuprates. The idealized crystal structure of $Bi_2Sr_2CaCu_2O_8$ is shown in Fig. 153. It should be noted, however, that excess oxygen atoms are incorporated in the BiO plane, resulting in remarkable superstructure modulations (Yamamoto *et al.*, 1990). The T_c of $Bi_2Sr_2CaCu_2O_8$ can be controlled by changing the oxygen stoichiometry (annealing in oxygen or in a vacuum) or by substituting Y or other rare-earth elements for Ca. As-grown $Bi_2Sr_2CaCu_2O_{8+\delta}$ samples are close to the op-

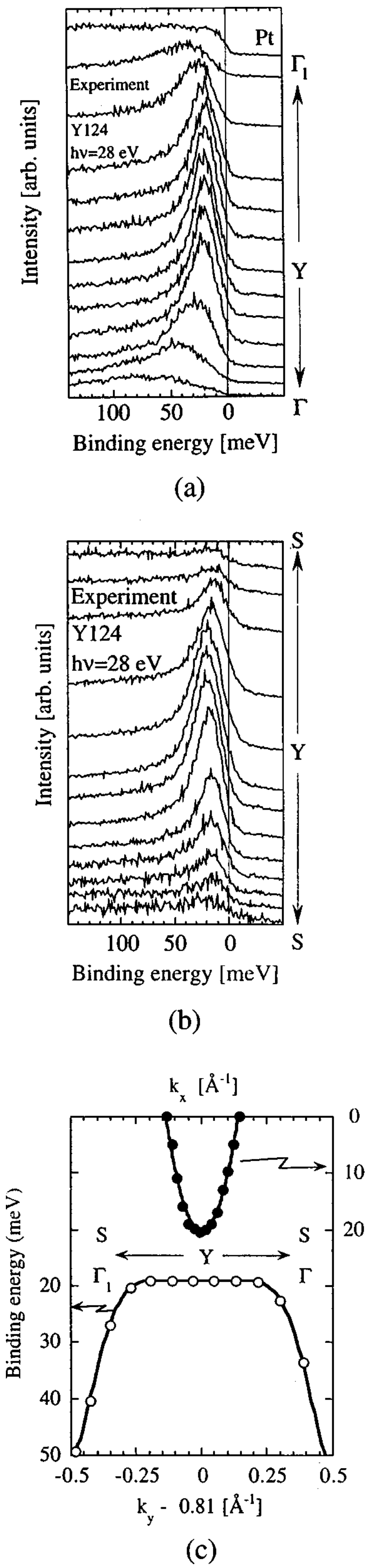

FIG. 152. Angle-resolved photoemission spectra of $YBa_2Cu_4O_8$ (a) along the Γ-Y [(0,0)-(0,π)] lines; (b) along the S-Y [(π,π)-(0,π)] lines; (c) band dispersions around the (0,π) point. From Gofron *et al.*, 1994.

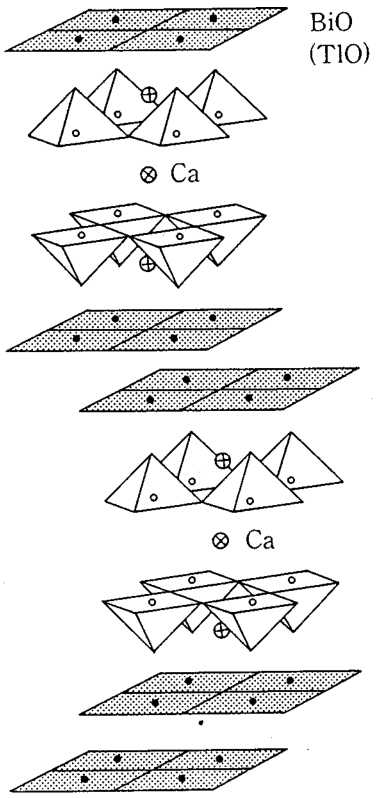

FIG. 153. Idealized cystal structure of $Bi_2Sr_2CaCu_2O_8$.

timum doping ($T_c \sim 90$ K), while oxygen-annealed ones are overdoped and have lower T_c. Holes are depleted in the Y-substituted samples $Bi_2Sr_2Ca_{1-x}Y_xCu_2O_{8+\delta}$ and they become semiconducting ($T_c = 0$) at $x \sim 0.5$.

The electronic structure of $Bi_2Sr_2CaCu_2O_{8+\delta}$ has been extensively studied by various electron spectroscopic techniques, including angle-resolved photoemission spectroscopy (Takahashi *et al.*, 1989) because of the high quality and stability of cleaved surfaces. According to oxygen 1s electron-energy-loss studies, doped holes in the CuO_2 plane have $p_{x,y}$ symmetry and occupy the p-$d\sigma$ antibonding band of the CuO_2 plane (Nücker *et al.*, 1989).

Angle-resolved photoemission studies of optimally doped and overdoped samples show band dispersions and Fermi surfaces similar to those given by band-structure calculations if the energy bands derived from the Bi-O plane are removed from E_F. Angle-resolved photoemission spectra along various cuts in the Brillouin zone are shown in Fig. 154 (Dessau *et al.*, 1993). The clearest quasiparticle peak is observed along the (0,0)-(π,π) line. The quasiparticle peak disappears approximately at (π/2,π/2), unambiguously indicating a Fermi-level crossing. Along the (0,0)-(π,0) line, on the other hand, the quasiparticle peak disperses towards E_F but never crosses it; it crosses E_F along the (π,0)-(π,π) line. Thus the band shows a saddle point at (π,0) and a very flat dispersion around that point, which is occasionally called an extended saddle point or extended Van Hove singularity, although it is much flatter than the usual Van Hove singularity. The flat band is located within ~50 meV of E_F over a large portion of the Brillouin zone around the (π,0) points. The resulting Fermi sur-

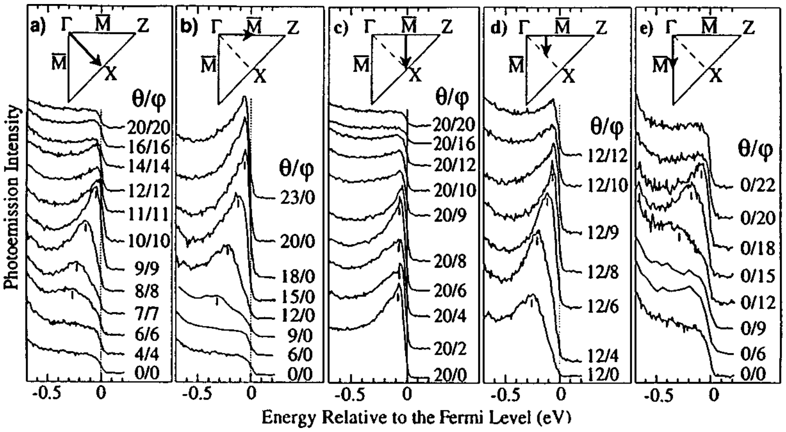

FIG. 154. Angle-resolved photoemission spectra of $Bi_2Sr_2CaCu_2O_8$ taken above 100 K ($>T_c=85$ K). $\bar{M}$: (π,0), X: (π,π). From Shen and Dessau, 1995.

faces are shown in Fig. 155, which shows, in addition to the hole-like Fermi surface centered at the (π,π) point, an electronlike Fermi surface centered at (0,0). The presence of the latter electronlike Fermi surface has been controversial. Ding *et al.* (1996a) reported only the hole Fermi surfaces and attributed other features to the superstructure modulation of the Bi-O plane or to "shadow bands," as discussed below. The presence of the flat band is in agreement with numerical studies of the Hubbard and t-J models (see Sec. II.E.2). The flat dispersion may constitute a microscopic basis for scaling theory with a large dynamic exponent z (Sec. II.F.11). The fact that the Fermi level lies slightly away from the flat band ($\sim$50 meV) is interpreted as coming from the formation of a pseudogap due to spin fluctuations or to the preformed pair of binding energy $\sim$50 meV. In the latter scenario, the single-particle excitation needs a finite energy from the chemical potential around (π,0) because of the two-particle bound-state formation.

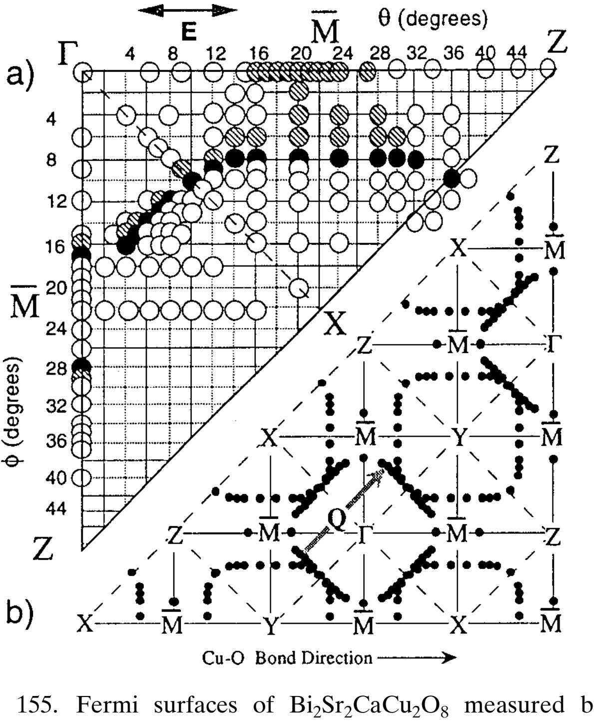

FIG. 155. Fermi surfaces of $Bi_2Sr_2CaCu_2O_8$ measured by angle-resolved photoemission spectroscopy (Dessau *et al.*, 1993): Filled circles, Fermi surface crossings; striped circles, locations where the band energy is indistinguishable from E_F.

The line shape of the angle-resolved photoemission spectra is unusual as in the other cuprates in that the high-binding-energy tail is intense, the background intensity is high, and consequently the quasiparticle weight is anomalously small. The unusually high background is not due to inelastically scattered secondary electrons, but must be an intrinsically incoherent part of the spectral function (Liu *et al.*, 1991). Indeed, angle-resolved photoemission spectra of a conventional 2D (semi)metal $TiTe_2$ show negligibly small background intensities (Claessen *et al.*, 1992). The large incoherent spectral weight means that the motion of the conduction electrons in the high-T_c cuprates is highly dressed by electron correlations. Even when the quasiparticle peak is located very close to E_F, it does not become a delta-function-like peak as predicted for a Landau Fermi liquid, but retains a highly asymmetric peak. In order to describe the unusual photoemission line shape, Varma *et al.* (1989) proposed the marginal Fermi-liquid phenomenology (see Sec. II.G2). Whether the quasiparticle spectral weight Z vanishes at E_F or not and whether the quasiparticle lifetime width is proportional to the energy from E_F ($1/\tau \propto |\omega - \mu|$) as in a marginal Fermi liquid are very subtle problems to be settled experimentally because of the limited energy and momentum resolution of photoemission spectroscopy. Nevertheless, the analysis by Olson *et al.* (1990) using a Lorentzian function with a Fermi cutoff favors a lifetime width that varies linearly in energy over a relatively large energy scale of a few 100 meV. Although the distinction between Fermi liquid and marginal Fermi liquid can in principle be made only in the low-energy limit, the high T_c's of $\sim$100 K practically make it meaningless to discuss energies lower than $\sim$30 meV; the unusual lifetime behavior and large incoherent spectral weight seen on the latter energy scale (of the order of the resolution of photoemission) are suffi-

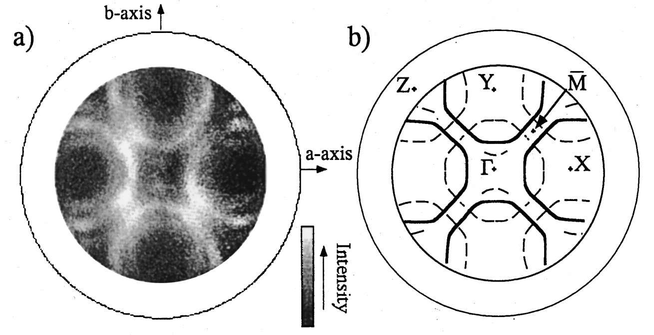

FIG. 156. (a) Angular distribution of photoelectrons from within 10 meV of the Fermi level in $Bi_2Sr_2CaCu_2O_8$ (Aebi *et al.*, 1994); (b) outline of (a), emphasizing the stronger and weaker lines.

cient to answer the above questions. Recently, the broad tail was interpreted as the $1/\sqrt{\omega}$ dependence. This phenomenological result is derived from the real part of the self-energy proportional to $\sqrt{\omega}$, which results from the enhanced antiferromagnetic susceptibility in the intermediate-energy region (Chubukov and Schmalian, 1997; for experimental results, see Norman *et al.*, 1998). The incoherent character of angle-resolved photoemission spectroscopy may be related to the suppression of coherence due to the large dynamic exponent $z=4$ of the MIT, as discussed in Sec. II.F.9.

The question of why antiferromagnetic fluctuations are strong in the superconducting cuprates has been frequently asked in the context of magnetic mechanisms of superconductivity. Kampf and Schrieffer (1990) predicted that antiferromagnetic fluctuations in the paramagnetic metallic state would induce scattering of electrons by the antiferromagnetic wave vector $\mathbf{Q}$ $[=(\pi,\pi)$ for the CuO_2 plane] and produce a "shadow band," which is shifted by $\mathbf{Q}$ from the original band. Aebi *et al.* (1994) observed "shadow Fermi surfaces" in optimally doped $Bi_2Sr_2CaCu_2O_{8+\delta}$ in the angular distribution of photoelectron intensities with a fixed energy (E_F), as shown in Fig. 156. According to that study, the original Fermi surface is centered at the (π,π) point and the shadow Fermi surface is centered at (0,0). Ding *et al.* (1996a) observed corresponding shadow bands in the standard angle-resolved photoemission mode, but also pointed out the possibility that the extra bands are due to superstructure modulation of the Bi-O planes. Theoretically the existence of the shadow bands and shadow Fermi surfaces has been quite controversial. Calculations using the "fluctuation exchange approximation" showed that the correlation length of antiferromagnetic fluctuation necessary to produce the shadow bands and shadow Fermi surfaces is only a few lattice spacings (Langer *et al.*, 1995). On the other hand, shadow Fermi surfaces are not visible in numerical studies of the $t-J$ and Hubbard models although shadow bands have been identified in the underdoped regime (Haas *et al.*, 1995; Moreo *et al.*, 1995; Preuss *et al.*, 1995).

The photoemission spectra of the antiferromagnetic insulator $Sr_2CuCl_2O_2$ shown in Fig. 157 clearly indicate the shadow band (Wells *et al.*, 1995; see also Fig. 24): Here, the antiferromagnetic Brillouin zone lies along the $(\pi,0)$-$(0,\pi)$ line, and therefore the band disperses back beyond the $(\pi/2,\pi/2)$ point. If the angle-resolved photoemission spectra of $Sr_2CuCl_2O_2$ are compared with those of $Bi_2Sr_2CaCu_2O_8$ along the same (0,0)-(π,π) line (Fig. 154), a strong similarity between the antiferromagnetic insulator and the metal/superconductor is noted. The flat band around $(\pi,0)$ in the metallic samples, on the other hand, is shifted well below ($\sim$0.3 eV) the valence-band maximum at $(\pi/2,\pi/2)$ (see also Sec. II.E.2). The evolution of the electronic structure from insulator to metal/superconductor has been systematically studied for underdoped $Bi_2Sr_2CaCu_2O_{8+\delta}$ in which a rare-earth element is substituted for Ca or oxygen is reduced (Loeser *et al.*, 1996; Marshall *et al.*, 1996). In underdoped samples, the energy band around the $(\pi,0)$ point is shifted away from E_F even above T_c, and the Fermi-level crossing along the (0,0)-$(\pi,0)$ line disappears, as shown in Fig. 158(a). That is, a "normal-state gap" opens around $(\pi,0)$ while the Fermi-level crossing near the $(\pi/2,\pi/2)$ point is not affected. The resulting band structure resembles that of a hole-doped antiferromagnetic insulator with a small Fermi surface at the $(\pi/2,\pi/2)$ point, although the inner half of the small Fermi surface is missing [Fig. 158(b)]. The latter observation contradicts the appearance of the shadow bands as a result of short-range antiferromagnetic correlation, since the correlation should be more significant in the underdoped regime and the whole small Fermi surface should be clearly visible. The normal-state gap which opens along the $(\pi,0)$ direction but not along the (π,π) direction has the same anisotropy as that of the supercon-

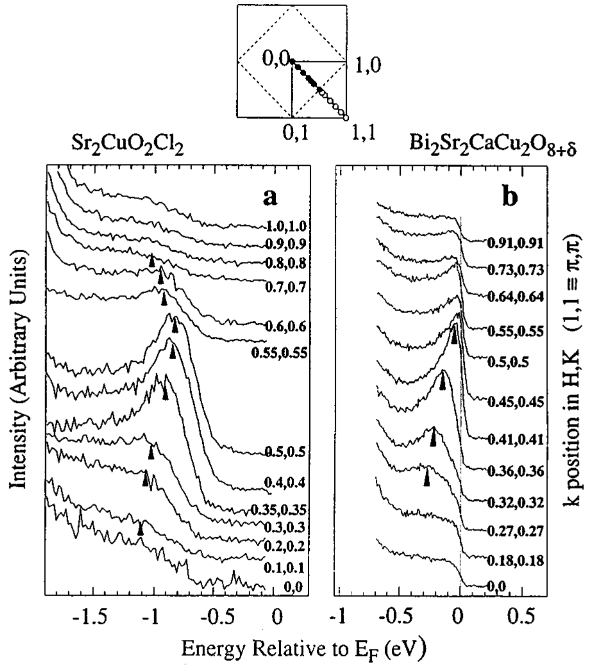

FIG. 157. Angle resolved photoemission spectra along the (0,0)-(π,π) line. Left panel, angle-resolved photoemission spectra of $Sr_2CuCl_2O_2$ (Wells *et al.*, 1995); right panel, corresponding spectra of $Bi_2Sr_2CaCu_2O_8$ (Dessau *et al.*, 1993).

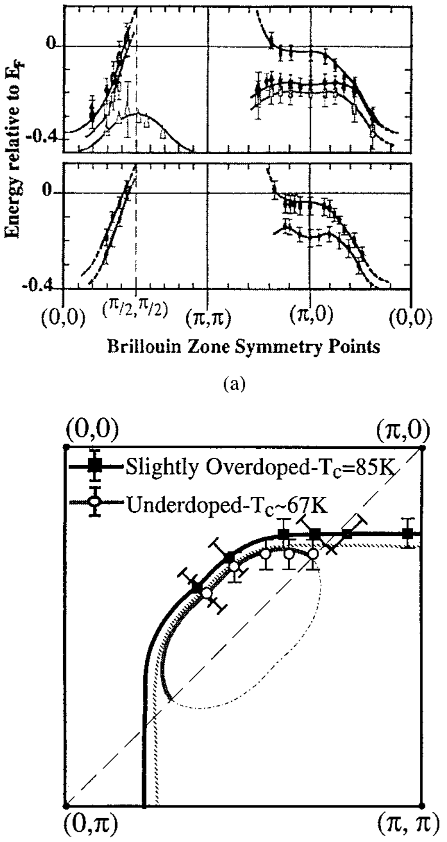

(a)

(b)

FIG. 158. Photoemission results of $Bi_2Sr_2CaCu_2O_8$. (a) Band dispersions of optimally doped and underdoped samples (Marshall *et al.*, 1996); (b) Fermi surfaces of slightly overdoped and underdoped samples.

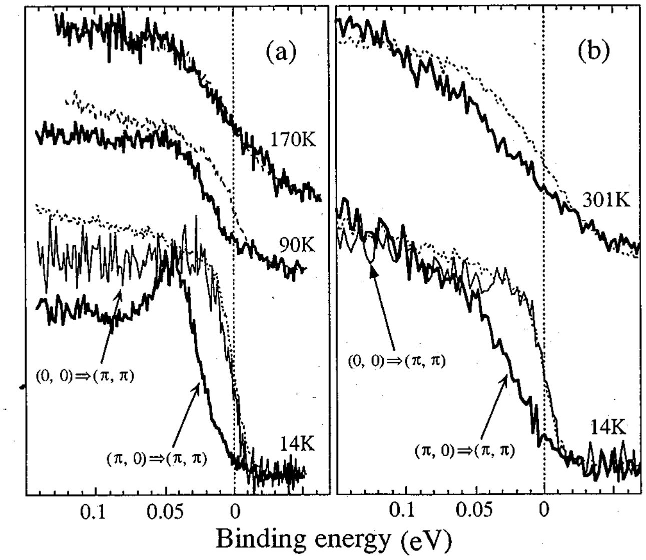

FIG. 159. The temperature dependence of angle-resolved photoemission spectra at Fermi surface crossings along the $(\pi,0)$-(π,π) line in oxygen-controlled $Bi_2Sr_2CaCu_2O_{8+\delta}$ (Ding *et al.*, 1996b): (a) $T_c=83$ K sample; (b) $T_c=10$ K sample. Spectra at the $(0,0)$-(π,π) Fermi-surface crossing are also shown. Broken lines are reference Pt spectra.

ducting gap below T_c. The temperature dependence of the normal-state gap was studied by Ding *et al.* (1996b), as shown in Fig. 159. The gap closes at a characteristic temperature T^*, which is well above T_c for underdoped samples and increases with decreasing hole concentration. The doping dependence of T^* seems to roughly follow the temperature T_R below which the Cu NMR relaxation rate shows a spin-gap behavior in $YBa_2Cu_3O_{7-y}$. Recent tunneling measurements on underdoped $Bi_2Sr_2CaCu_2O_{8+\delta}$ suggest an opening of the pseudogap at temperatures even higher than that observed in the photoemission (Renner *et al.*, 1998).

The origin of the normal-state gap has been discussed from different points of view, including antiferromagnetic correlation (for example, Preuss *et al.*, 1997), spinon pairing (Tanamoto *et al.*, 1992), and preformed Cooper pairs (Imada, 1993a, 1994b; see also Sec. IV.F.11). Ding *et al.* (1997) found that in underdoped $Bi_2Sr_2CaCu_2O_{8+\delta}$, the minimum gap locus below T^* coincides with the locus of gapless excitations above T^* and resembles the large Fermi surface of optimally doped and overdoped samples. The same scenario has been considered as an alternative to interpret the Fermi surface of Fig. 158(b) (Marshall *et al.*, 1996). This suggests that the normal-state gap is due to precursors of singlet pairs (including spinon pairing scenario) above T_c and not due to antiferromagnetic correlation, since the latter correlation would alter the Fermi surface considerably. The appearance of a normal-state gap conspicuous around $(\pi,0)$ above T_c is consistent with a pairing mechanism due to instability of the flat and incoherent dispersion around $(\pi,0)$ characterized by the $z=4$ universality class, as is discussed in Sec. II.F.9. The flat dispersion of single-particle process around $(\pi,0)$, generated from strong-correlation effects near the Mott insulator and characterized by a large dynamic exponent $z=4$, may be destabilized, leading to preformed pairs with k^2 dispersion with a binding energy indicated by the pseudogap, while the part around $(\pi/2,\pi/2)$ forms a more or less usual (but patchy) Fermi surface. Therefore, in the underdoped region with a pseudogap, the holes are predominantly doped into the $(\pi,0)$ region because of the flat dispersion and they are subject to binding to incoherent preformed pairs in this region.

The shift of the chemical potential with hole doping has been studied from the shifts of core levels and the valence band for $Bi_2Sr_2Ca_{1-x}Y_xCu_2O_{8+\delta}$ (van Veenendaal *et al.*, 1994) and from oxygen-controlled $Bi_2Sr_2CaCu_2O_{8+\delta}$ (Shen *et al.*, 1991a). The results showed a shift of ~1 eV/hole in metallic superconducting samples as in the overdoped region of $La_{2-x}Sr_xCuO_4$, whereas the shift is much larger (~8 eV/hole) in Y-rich semiconducting samples. The large shift in the semiconducting samples may be due to a finite DOS of Anderson-localized states within the band gap of the parent insulator.

D. Quasi-one-dimensional systems

1. Cu-O chain and ladder compounds

The 1D analog of the hole-doped cuprates may be very important, not only because the compounds can be

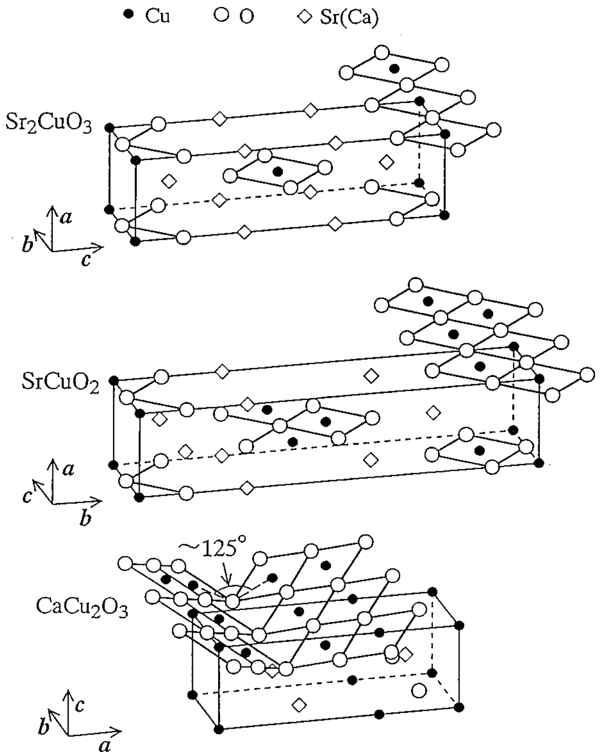

FIG. 160. Lattice structures of prototypical Cu-O chain compounds.

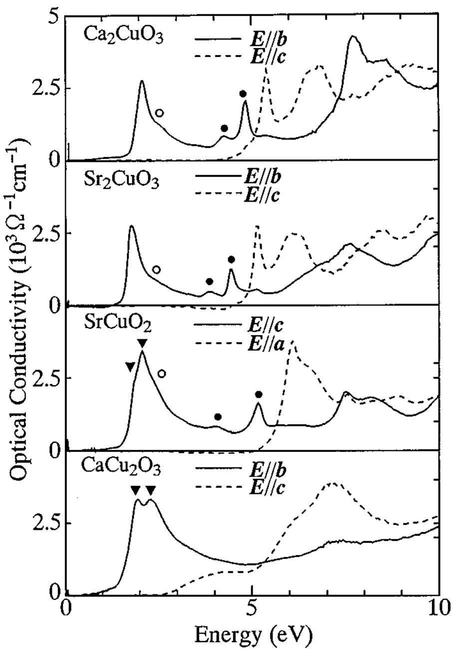

FIG. 161. Optical conductivity spectra (at room temperature) for the Cu-O chain compounds. Solid lines, spectra polarized parallel to the chain directions; dashed lines, spectra polarized perpendicular to the chain direction; closed triangles, splitting of the CT transitions due to interchain coupling; open circles, spin-excitation sideband of the CT transition; closed circles, the $2p-4s$ transitions. From Yasuhara and Tokura, 1998.

a touchstone for the theoretical models of high-T_c cuprates, but also because the 1D systems involve their own novel properties such as spin-charge separation, a spin-gapped metallic state, and associated superconductivity (see Secs. II.B and II.G.2). In this section, we show some examples of the Cu-O chain and ladder compounds whose electronic structures share many common features with those of the 2D CuO_2-based compounds (Sec. IV.C).

Lattice structures of prototypical Cu-O chain compounds are shown in Fig. 160. Sr_2CuO_3 or isostructural Ca_2CuO_3 can be viewed as derived from K_2NiF_4-type La_2CuO_4 by removing lines of oxygen in the CuO_2 sheet. In $SrCuO_2$ (in the ambient pressure phase), the Cu-O chains are doubled in the repeating unit, as shown in the figure, with the edge sharing of the CuO_4 square. The two Cu-O chains are magnetically nearly decoupled, since the exchange interaction between edge-sharing Cu spins is very weak compared with the corner-sharing ones and gives rise to frustration in the magnetic interaction between adjacent chains. In $CaCu_2O_3$, such edge-sharing double chains are connected via the corner oxygen but in a non-planar manner.

The electronic parameters and structures in these Cu-O chain compounds bear a close analogy to the 2D CuO_2 sheet compounds, that is, the parent compounds of high-T_c superconductors. Figure 161 shows the optical conductivity spectra for these compounds for the light E vector parallel and perpendicular to the respective chain axes (Yasuhara and Tokura, 1998). A clear gap structure polarized along the chain axis is seen around 1.6–1.8 eV, which is ascribed to the charge-transfer-type gap as in the layered cuprate compounds (see Secs. IV.C.1 and IV.C.2). The splitting of the CT gap peak (indicated by vertical bars), probably due to interchain coupling, is observed clearly for $CaCu_2O_3$ and also as a low-energy shoulder for $SrCuO_2$. Some sideband structures of the CT transition (marked with open circles) are also discernible at about 0.5 eV higher than the main peak, as in the CuO_2 sheet compounds (Tokura, Koshihara, *et al.*, 1990), which are supposed to arise from coupling of the charge-transfer excitation with the spin excitation via strong Kondo coupling between the $2p$ hole and the $3d$ spin in the final state. The higher-lying structures are assigned to the transitions relevant to Cu $4s$ and Sr (or Ca) $5d$ $(4d)$ states (Yasuhara and Tokura, 1998). Among them, the split peaks (closed circles) at 4–5 eV with $E_\parallel$ chain are assigned to transitions between the O $2p$ and Cu $4s$ states, whose energy separation may represent the binding energy of the Zhang-Rice singlet of the excited O $2p$ hole coupled with the Cu spin.

The energy of the exchange interaction (J) between adjacent Cu spins on the chain is extremely large, 2000–3000 K, in these Cu-O chain compounds (Motoyama *et al.*, 1996; Suzuura *et al.*, 1996; Yasuhara and Tokura, 1998). The μSR experiment (Keren *et al.*, 1993) and neutron-scattering experiment (Yamada, Wada, *et al.*, 1995) showed that 3D long-range antiferromagnetic order takes place only below $T_N = 5$ K for Sr_2CuO_3 and $T_N = 8$ K for Ca_2CuO_3. This means that the interchain exchange interaction $(J_\perp)$ is extremely small, $J_\perp/J \approx 10^{-5}$, and hence these Cu-O chain compounds should show an ideal 1D behavior for an $S=1/2$ Heisenberg antiferromagnet over a wide temperature range, from several K to 1000 K [$CaCu_2O_3$, shown in Fig. 160(c), shows the spin ordering below $T_N \approx 50$ K due to the appreciable interchain coupling between the corner-sharing double chains]. Motoyama, Eisaki, and Uchida (1996) estimated the J values for Sr_2CuO_3 and $SrCuO_2$ by fitting the T dependence of the magnetic susceptibility with the rigorous theoretical result of Eggert, Affleck, and Takahashi (1994). In particular, they observed an isotropic drop in susceptibility below 20 K (but obviously above T_N), which could be scaled to the asymptotic $(\ln T)^{-1}$ dependence clarified by the Eggert-Affleck-Takahashi theory but was not recognized in the well-known Bonner-Fisher curve.

An alternative method of determining the J value in a 1D antiferromagnet or 1D Mott-Hubbard insulator was developed by Suzuura *et al.* (1996). The spin excitation is observable as a sideband structure of an optical phonon in the midinfrared absorption spectrum below the CT gap energy. The absorption spectra of all these 1D Cu-O chain compounds show a λ-like cusp around 0.5 eV. A similar weak midinfrared absorption due to magnon-phonon coupled excitations is seen in the CuO_2-layered compounds (Perkins *et al.*, 1993; Lorenzana and Sawatzky, 1995), although the spectral profile is very different for the 1D and 2D cases. The distinct cusp structure of the Cu-O chain can be ascribed to the Van Hove singularity of the interband transition between spinon bands (corresponding to the $\pm\pi/2$ point of the 1D spin excitation dispersion) and its singular peak position corresponds to the sum of $\pi J/2$ and the optical phonon energy (0.05 eV of the oxygen stretching mode in the present case). The singularity is so clear in the absorption spectrum (Suzuura *et al.*, 1996; Yasuhara and Tokura, 1998) that one can determine the J value quite accurately to be 3000 K. The difference between the J values derived by these methods may be due to (1) an underestimate of the g value, assumed to be 2 in the analysis of the susceptibility (Motoyama *et al.*, 1996) or (2) the neglect of second-nearest-neighbor exchange interactions. In any case, the exchange interaction J in the 1D compounds is in the range of 2000–3000 K, considerably larger than in the 2D compounds (Cooper *et al.*, 1990b; Tokura, Koshihara, *et al.*, 1990; Tokura, 1992a, 1992b); e.g., $J \approx 1600$ K for La_2CuO_4 (Aeppli *et al.*, 1989). This is perhaps partly due to the smaller charge-transfer energy Δ in the 1D chain compounds than in the 2D sheet compounds because of the different Madelung energy, but still needs to be elucidated theoretically.

Hole doping or electron doping for these Cu-O chain compounds has been widely attempted, so far unsuccessfully, except for the ladder type Cu-O compounds described below. Nevertheless, the novel charge dynamics characteristic of correlated 1D systems show up in angle-resolved photoemission spectra in $SrCuO_2$ which virtually represent the charge dynamics of a single hole in the system.

The magnitudes of the various electronic structure parameters were estimated for $SrCu_2O_3$ and $CaCu_2O_3$ from analysis of core-level and valence-band photoemission spectra and inverse-photoemission spectra using the configuration-interaction cluster model (Maiti *et al.*, 1997). The deduced charge-transfer energies are indeed found to be small: $\Delta = 0.0$ eV for $SrCu_2O_3$ and $\Delta = 0.5$ eV for $CaCu_2O_3$. The band gaps deduced from the combined photoemission and inverse-photoemission spectra are 1.5 and 1.7 eV, respectively, in good agreement with the values deduced from optical studies. Okada *et al.* (1996) analyzed the photoemission data using a multi-impurity cluster model and gave slightly larger Δ's; the small difference is partly attributed to intersite charge-transfer screening.

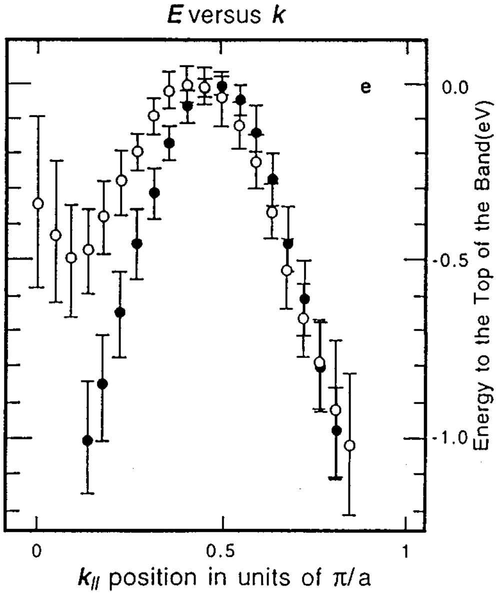

FIG. 162. Energy vs momentum curves of $SrCuO_3$. From Kim *et al.*, 1997.

Spin-charge separation is one of the most outstanding features of 1D systems. While Tomonaga-Luttinger-liquid behavior has been predicted and experimentally tested in the low-energy excitation spectra of quasi-1D metals (Sec. II.G.1), the spin-charge separation is predicted to be more clearly visible in the single-particle excitation spectra of insulating 1D systems. If one removes an electron from a 1D system in which one electron is localized at each site that is antiferromagnetically coupled with the nearest neighbors, the created hole can hop from site to site without disturbing the ordering of the spin arrangement; or two parallel spins adjacent to the initially created hole can propagate through the lattice without the motion of the hole. The former case corresponds to the elementary excitation of a positive charge (holon) and the latter is that of a spin (spinon), indicating the separation of a single hole into charge and spin excitations in the 1D system. This spin-charge separation was studied using angle-resolved photoemission spectroscopy in the two-chain compound $SrCuO_2$ (Kim *et al.*, 1996, 1997). The spectra show one band with strong dispersion and one with weak dispersion, the widths of which are 1.2 and 0.3 eV, respectively, as shown in Fig. 162. The observed bands are explained by peaks in the spectral function $A(k,\omega)$ of the 1D $t-J$ model calculated using exact diagonalization (with $t \sim 0.6$ eV and $J \sim 0.15$ eV). The peaks in $A(k,\omega)$ are assigned to "holon" and "spinon" bands from comparison with the k- and ω-dependent charge and spin susceptibilities: The energy scales of the holon and spinon bands are set by t and J, respectively. [The coupling between the two Cu-O chains in $SrCuO_2$ is negligible for $A(k,\omega)$.] The result for the 1D insulator is contrasted with that for the 2D insulator $Sr_2CuCl_2O_2$, which shows only a weakly dispersing feature whose width is of order J (Fig. 162). The different behaviors between the 1D and 2D systems have been attributed to strong coupling between the spin and charge excitations in the 2D system. There is, however, some controversy as to whether there is a spin-charge separation in the single-particle spectra of the 1D system. Suzuura and Nagaosa (1997) have examined the problem using the slave-boson formalism and found that the holon (boson) excitation and the spinon (fermion) excitation are strongly coupled with each other.

Let us turn to the Cu-O ladder compounds, which are natural extensions of the Cu-O chain compounds towards the CuO_2 sheet structure. Dagotto, Riera, and Scalapino (1992) proposed an electronic mechanism for the formation of spin gaps in the $S=1/2$ antiferromagnetically coupled double chains, or two-leg ladders, and argued that the ground state upon hole doping should be either superconducting or a charge-density wave. As discussed in Sec. II.B for the category [I-2↔M-2] of the MIT and also in Sec. II.G.2, the mechanism of superconductivity induced by doping of carriers into a spin-gapped Mott insulator is similar to that proposed in a dimerized system (Imada, 1991, 1993c). The pairing mechanism proposed in doped ladders shares the same origin as the dimerized case because coupled ladders and coupled dimerized chains are continuously connected in the parameter space of the models (Katoh and Imada, 1995). The most representative compounds to substantiate such an idea are a homologous series of ladder systems $Sr_{n-1}Cu_{n+1}O_{2n}$ ($n=$odd), as shown in Fig. 67 (Sec. III.B) for $n=3$ ($SrCu_2O_3$) and $n=5$ ($Sr_2Cu_3O_5$). In $Sr_{n-1}Cu_{n+1}O_{2n}$, $Cu_{n+1}O_{2n}$ sheets alternate with Sr_{n-1} sheets along the c axes of their orthorhombic cells (Hiroi *et al.*, 1991). In each ladder, strong antiferromagnetic interactions should occur through the linear Cu-O-Cu bonds along the a and b axes. By contrast, Cu-O-Cu bonds across the interface between ladders are formed with the right angle at the oxygen corner of the Cu-O-Cu bond and hence the exchange interaction in these bonds must be much weaker and be frustrated at the interface.

Rice and co-workers (Rice *et al.*, 1993; for a review, see also Dagotto and Rice, 1996) theoretically investigated the ground state of $S=1/2$ multileg spin ladders like $Sr_{n-1}Cu_{n+1}O_{2n}$ and concluded that the spin gap is open or closed according to whether the leg number $[=(n+1)/2]$ is even or odd. They further predicted that light hole doping into the even-leg ladder keeps the spin gap open and leads to singlet superconductivity.

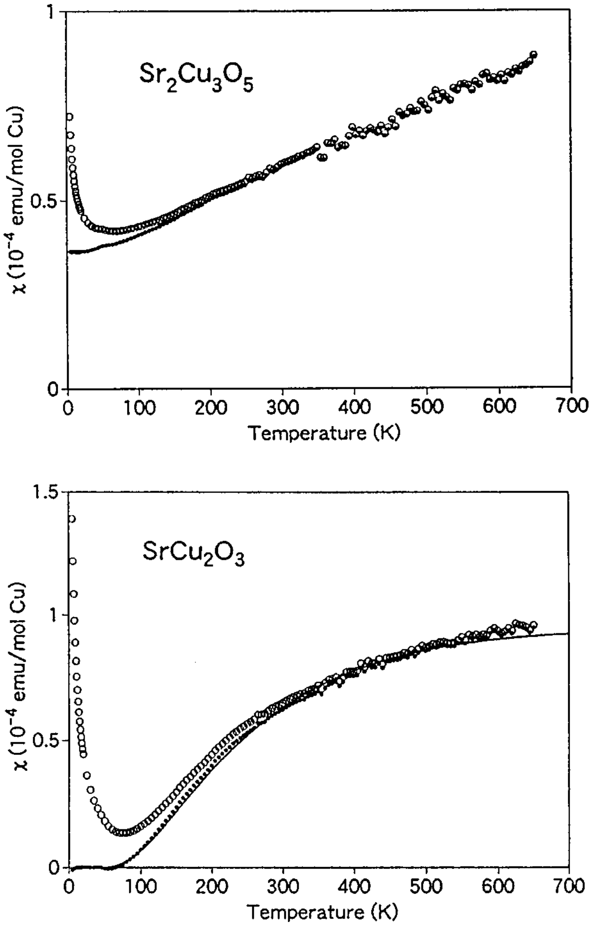

FIG. 163. Temperature dependence of magnetic susceptibility for $SrCu_2O_3$ (upper panel) and $Sr_2Cu_3O_5$ (lower panel): open circles, observed; closed circles, corrected by subtraction of the Curie component from the raw data. The solid line in the upper panel represents the calculated susceptibility assuming a spin gap of 420 K. From Azuma *et al.*, 1994.

The temperature dependence of the magnetic susceptibility (χ) of two-leg $SrCu_2O_3$ and three-leg $Sr_2Cu_3O_5$ is shown in Fig. 163. The data after subtraction of the Curie component, which is due to impurity phases, show a clear spin-gap behavior for $SrCu_2O_3$. The observed temperature dependence of χ in $SrCu_2O_3$ follows the theoretically predicted form for the two-leg ladder system (Troyer, Tsunetsugu, and Würtz, 1994), $\chi(T) = \alpha T^{-1/2}\exp(-\Delta_s/T)$, with the spin-gap energy $\Delta_s = 420$ K and the prefactor (relating to the dispersion of the excitation) $\alpha = 4 \times 10^{-3}$, as shown by a solid line in the figure. By contrast, χ remains with no spin gap for $Sr_2Cu_3O_5$ with a three-leg ladder structure, confirming the theoretical prediction.

The presence or absence of the spin gap depending on the number of legs is also confirmed by measurements of the nuclear spin-lattice relaxation rate $1/T_1$ in NMR (Azuma *et al.*, 1994). The Arrhenius plot of $1/T_1$ for $SrCu_2O_3$ at temperature $T \lesssim \Delta$ gave the spin-gap value 680 K. An apparent difference between spin-gap values deduced from the susceptibility (or Knight shift) and the NMR relaxation rate is due to the fact that the temperatures of the NMR data are too high to extract the true gap by fitting for $1/T_1$. When one takes the data at the lowest temperatures, the gap Δ_s extracted from $1/T_1$ agrees well with $\Delta_s \sim 420$ K. Alternatively, the large gap Δ_s deduced from $1/T_1$ at relatively high temperatures was interpreted in terms of the Majorana Fermion approach by Kishine and Fukuyama (1997), who clarified that higher-energy excitations contribute to $1/T_1$. Theoretically the spin gap is calculated to be about $J/2$ provided that the inter- and intra-chain exchange interactions are equal. Under the same assumption, J for $SrCu_2O_3$ is estimated to be about 840 K. However, thus deduced, the value of J in the ladder is considerably smaller than that of the Cu-O chain compounds described above, and even smaller than that for the CuO_2 sheet compounds. This is rather puzzling because the J value of the ladders is expected to be between the chain and sheet compounds and rather close to the chain compounds due to similarity of the structures. One possible origin of this discrepancy is interladder coupling; another is a larger J for leg bonds than for rung bonds in the ladder. In fact recent neutron results and susceptibility measurements are rather consistent with $J_\parallel \sim 2000$ K for legs and $J_\perp \sim 1000$ K for rungs (Johnston, 1996; Eccleston *et al.*, 1997; Hiroi *et al.*, 1997). A theoretical explanation of this effective exchange was proposed based on a correction due to next-nearest-neighbor and 4-spin exchange couplings (Nagaosa, 1997). In any case the reduction of Δ_s drives the system towards the quantum critical point of the antiferromagnetic transition. This problem was discussed in the context of Zn substitution for Cu in $SrCu_2O_3$ by Imada and Iino (1997).

Carrier doping has proved to be very difficult in the $Sr_{n+1}Cu_{n+1}O_{2n}$ series, yet some other Cu-O ladder compounds are promising for the FC-MIT. $La_{1-x}Sr_xCuO_{2.5}$ was the first system (Hiroi and Takano, 1995) in which holes were successfully introduced into the Cu-O ladder structures and the metallic state ($x \gtrsim 0.15$) emerged. However, superconductivity was not found in this compound. The crystal structure of $LaCuO_{2.5}$ can be derived from the 3D perovskite structure (e.g., $LaCuO_3$) by regularly removing oxygens in rows, as shown in Fig. 164. The ground state of the parent compound $LaCuO_{2.5}$ was suggested from susceptibility measurements to be the singlet spin liquid. The NMR (Matsumoto *et al.*, 1996) and μSR (Kadono *et al.*, 1996) experiments have, however, shown that the ground state is not the spin-gapped state but the antiferromagnetically ordered state below $T_N (\approx 110$ K), probably due to appreciable interladder interaction.

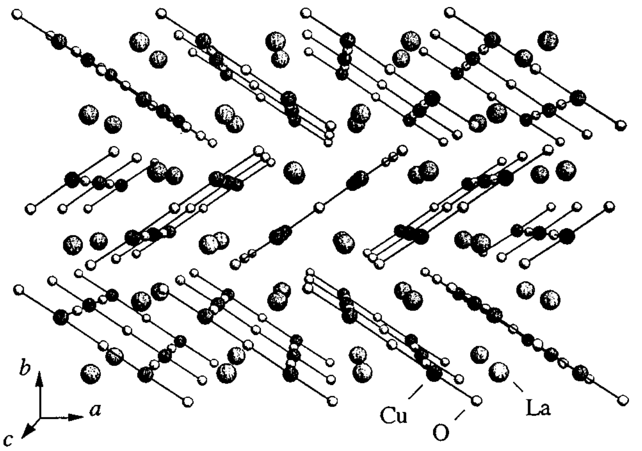

FIG. 164. Perspective view of the crystal structure of $LaCuO_{2.5}$. From Hiroi and Takano, 1995.

The hole-doped compounds $La_{1-x}Sr_xCuO_{2.5}$ exhibit a reduction in electrical resistivity with x by several orders of magnitude and become metallic for $x \geqslant 0.15$. The transport properties in the metallic region are those of conventional Fermi liquids (Nozawa *et al.*, 1997): The resistivity shows a T^2 dependence; the Hall coefficient is small and negative. As for the magnetic susceptibility, upon hole doping, it loses the spin-gap behavior and becomes nearly temperature independent: $\chi \sim 10^{-4}$ emu/mol for $x \geqslant 0.15$ (apart from Curie contributions from impurities). The electronic structure of $La_{1-x}Sr_xCuO_{2.5}$ was studied by photoemission and x-ray absorption (Mizokawa *et al.*, 1997). The evolution of the electronic structure with hole doping is qualitatively the same as that in $La_{2-x}Sr_xCuO_4$ (see, for example, Chen *et al.*, 1991), but the doping-induced spectral weight just above E_F—monitored by oxygen 1s absorption spectroscopy—is distributed at higher energies than in $La_{2-x}Sr_xCuO_4$, resulting in a lower spectral weight at E_F. Photoemission spectra show that the DOS at E_F is substantially lower than that in the 2D $La_{2-x}Sr_xCuO_4$, but still finite at E_F in the metallic samples. The low DOS at E_F may be a characteristic feature of quasi-1D metals (Sec. II.G.2). According to an LDA band-structure calculation of $LaCuO_{2.5}$ (Mattheiss, 1996a), the p-$d\sigma$ band of the Cu-O ladder shows a finite dispersion width of ~ 1 eV perpendicular to the ladder, compared to the ~ 2 eV dispersion along the ladder. This results in $\langle v_\parallel^2\rangle / \langle v_\perp^2\rangle \simeq 16$, which is substantially smaller than the $\langle v_\parallel^2\rangle / \langle v_\perp^2\rangle$ value of $\simeq 100$ for the 2D system La_2CuO_4.

Holes can be doped into another ladder compound with misfit structure, $(La, Sr, Ca)_{14}Cu_{24}O_{41}$ (McCarron *et al.*, 1988; Siegrist *et al.*, 1988). The compound, whose structure is schematically shown in Fig. 165, is composed of Cu_2O_3 planes with two-leg ladders alternating up the c axis with planes containing CuO_2 chains with edge-shared links of CuO_4, as $[(La,Sr,Ca)_2Cu_2O_2]_7[CuO_2]_{10}$. The Cu^{2+}-based compound $La_6Ca_8Cu_{24}O_{41}$ is viewed as the parent Mott insulator, and holes can be doped by substitution of Sr for La, as in $La_{6-y}Sr_yCa_8Cu_{24}O_{41}$. Carter *et al.* (1996) found that the $y=0$ parent compound showed a temperature dependence of the susceptibility consistent with weakly interacting $10(\pm 0.5)$ Cu^{2+} spins per formula unit, all contributed from the chain site. The Cu^{2+} spins on the ladder were virtually inert below 300 K due to the large spin gap. In fact, from the NMR measurement of $1/T_1$ and shift of ^{63}Cu, Magishi *et al.* (1998) deduced the spin gap for the ladder unit as $\Delta_{ladder} = 619 \pm 20$ K and for the related compound of $Sr_{14}Cu_{24}O_{41}$ as 510 ± 20 K. The Δ_{ladder} for the above $y=0$ compound is possibly even larger. Introduction of one hole by substitution of Sr for La is observed to re-

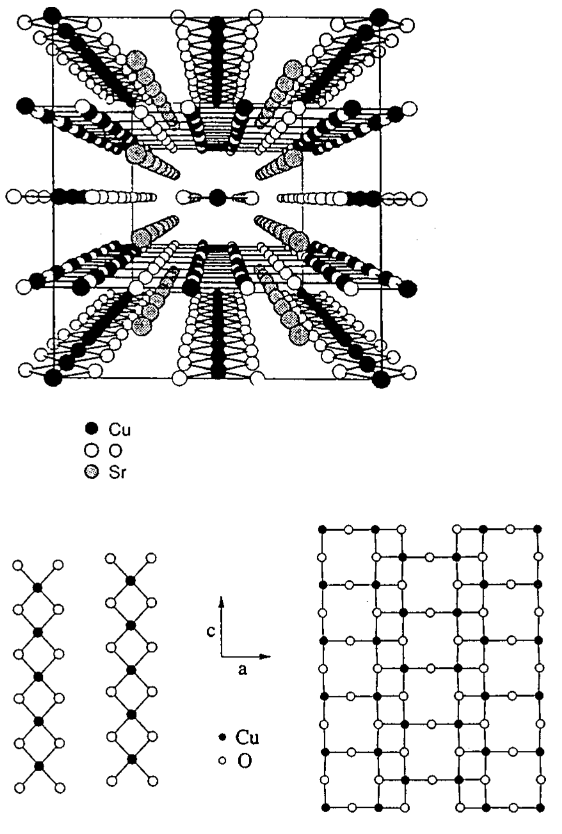

FIG. 165. Crystallographic structure (upper) of (La,Y,Sr,Ca)$_{14}$Cu$_{24}$O$_{41}$ (McCarron *et al.*, 1988), in which (a) the CuO$_2$ chain and (b) the Cu$_2$O$_3$ ladder stack along the *b* axis (vertical in this figure). The *a* axis is in the horizontal direction in this figure, while the ladder and chain axes are along the *c* axis.

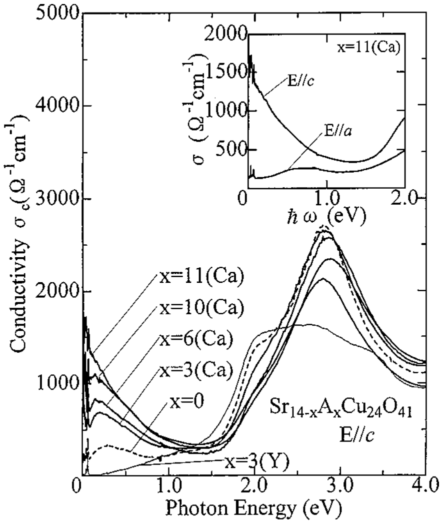

FIG. 166. The $E\perp$(ladder) optical conductivity at room temperature for single-crystalline samples of Sr$_{14-x}A_x$Cu$_{24}$O$_{41}$, A = Ca or Y. The anisotropic spectra with *a* and *c* polarization are shown for Sr$_3$Ca$_{111}$Cu$_{24}$O$_{41}$ in the inset. From Osafune *et al.*, 1997.

move one Cu spin, which means that the doped hole ($y\neq 0$) resides on the chain site, producing a nominal nonmagnetic Cu^{3+} site or Zhang-Rice singlet.

A rather complicated hole count is needed in the case of the solid solution Sr$_{14-x}$Ca$_x$Cu$_{24}$O$_{41}$, in which holes appear to be transferred into the ladder with increase of x (Kato *et al.*, 1996), although the average Cu valence is +2.25 and unchanged with x. In the $x=0$ compound Sr$_{14}$Cu$_{24}$O$_{41}$, most of the holes seem to reside on the chains, forming spin dimers. Below 240 K, the chain appears to be subject to charge ordering ($4k_F$ CDW), and at lower temperatures (below ≈60 K) undergoes a singlet pairing of the spin sites (Carter *et al.*, 1996; Matsuda *et al.*, 1996). The singlet-triplet gap (≈140 K) on the chain manifests itself in the temperature dependence of the χ (Carter *et al.*, 1996; Matsuda and Katsumata, 1996; McElfresh *et al.*, 1989) as well as in the inelastic neutron-scattering spectra (Eccleston *et al.*, 1998). As mentioned above, the spin gap on the ladder for Sr$_{14}$Cu$_{24}$O$_{41}$ is much larger; $\Delta_{ladder}=619\pm 20$ K (from the NMR rate $1/T_1$) or 510 ± 20 K (from the NMR shift; Magishi *et al.*, 1998).

With increasing Ca content x, the resistivity is much reduced (Yamane, Miyazaki, and Hirai, 1990; Kato *et al.*, 1994) yet remains semiconducting. The presence of mobile holes was confirmed by optical spectroscopy with single-crystalline samples of Sr$_{14-x}$Ca$_x$Cu$_{24}$O$_{41}$ (Osafune *et al.*, 1997). In Fig. 166, the $E\|c$ (ladder axis) optical conductivity spectrum is shown for single crystals of Sr$_{14-x}A_x$Cu$_{24}$O$_{41}$, where A is Ca or Y. The inset compares the $E\|c$ and $E\|a$ spectra for x(Ca) = 11. The $E\|c$ polarized quasi-Drude absorption below 1 eV gradually evolves with increase of x(Ca), indicating the quasimetallic responses of the doped holes on the ladder site. The x(Y) = 3 crystal should show minimal holes among the crystals investigated in Fig. 166, and its conductivity spectrum shows a clear onset around 1.6 eV due to a charge-transfer-type gap. As expected from the aforementioned transport and magnetic features, the $x=0$ crystal shows only a small weight of innergap absorption, ensuring a tiny fraction of holes on the ladder sites at this composition. However, a strong absorption band peaking around 3 eV emerges with decrease of x(Y) and hence has been attributed to excitation of the hole in the chain sites. Osafune *et al.* (1997) have further done a hole count on the ladder and chain sites as a function of Ca content x, by estimating the spectral weight in the inner gap region, using the assumption that the hole concentration is 1/2 on the chain site for the $x=0$ (Sr$_{14}$Cu$_{24}$O$_{41}$) compound. This assumption comes from the aforementioned fact that the CuO$_2$ chains show charge ordering perhaps at a rate of one hole per two Cu sites (Carter *et al.*, 1996; Matsuda *et al.*, 1996). According to such an estimate (Osafune *et al.*, 1997), the hole concentration increases up to ≈0.20 for the x(Ca) = 11 compound. The dominant feature of $\sigma(\omega)$ in the metallic phase is similar to that of the high-T_c cuprates—a broad tail indicating a strongly incoherent contribution in the transport. This feature is consistent with recent numerical studies of ladder systems (Tsunetsugu and Imada, 1997).

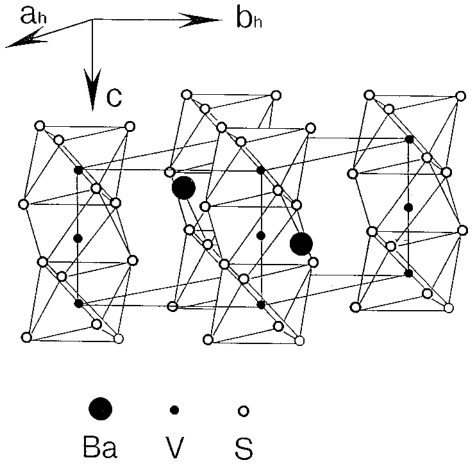

FIG. 167. Crystal structure of $BaVS_3$. From Nakamura *et al.*, 1994a.

Uehara *et al.* (1996) found that the resistivity ρ in the most Ca-substituted compound ($x=13.6$) still shows an upturn below 200 K but can be further reduced by the application of pressure. In fact, they discovered the occurrence of superconductivity at 9–12 K in the limited pressure range of 3–4.5 GPa. The quality of polycrystalline samples prepared under high oxygen pressure is not adequate for a discussion of the charge dynamics in superconducting $Sr_{14-x}Ca_xCu_{24}O_{41}$. The measurement of the anisotropic ρ in superconducting single crystals of $Sr_{14-x}Ca_xCu_{24}O_{41}$ under pressure is being attempted (Nagata, Uehara, *et al.*, 1998).

It is important to clarify whether the observed superconductivity in $Sr_{14-x}Ca_xCu_{24}O_{41}$ is truly relevant to such an exotic mechanism of carrier doping into the spin-gapped Mott insulator as was proposed by Imada (1991), Dagotto, Riera, and Scalapino (1992), and Rice *et al.* (1993). Kumagai *et al.* (1997) and Magishi *et al.* (1998) reported that the Δ_{ladder} deduced from the NMR Knight shift was reduced with hole doping on the ladder site, from 510 ± 20 K for x(Ca)$=0$ to 180 ± 10 K for $x=9$. The tentative linear extrapolation of the two (for $x=0$ and 9) experimental points appears to intersect zero around $x\approx13$. However, later NMR data for high-x (≈13) samples (Magishi *et al.*, 1998) indicated a persistent spin gap in such a high-x region where superconductivity was observed in the pressurized sample. Inelastic neutron scattering appears to show that the x dependence of the gap is weak (Nagata, Fujino, *et al.*, 1998), while recent NMR data at $x=11.5$ under a pressure of 29 kbar suggested collapse of the spin gap (Mayaffre *et al.*, 1997). Much work will be needed to clarify this intriguing new phenomenon in the spin-ladder compounds as well as its possible relevance to high-T_c superconductivity in the CuO_2-layered compounds.

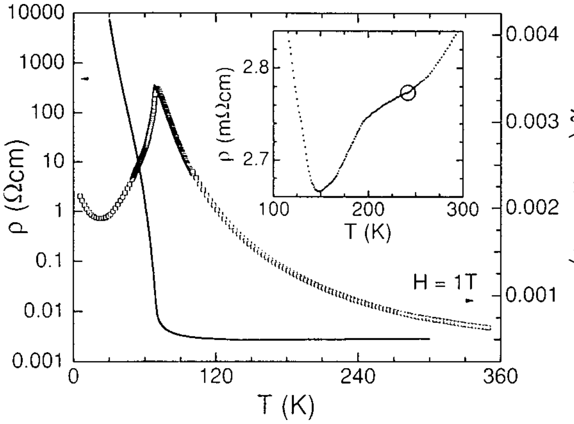

FIG. 168. Electrical resistivity and magnetic susceptibility of $BaVS_3$ (Graf *et al.*, 1995). The circle in the inset shows where the structural transition occurs.

2. $BaVS_3$

The crystal structure of $BaVS_3$ (Fig. 167) is based on the hexagonal NiAs type such as VS, from which 2/3 of the V atoms are removed or replaced by Ba atoms, resulting in well-separated V chains running along the c axis: The V-V distance along the c axis is 2.84 Å while that between the chains is as long as 6.72 Å (Sayetat *et al.*, 1982; Ghedira *et al.*, 1986). The formal valence of V is V^{4+} and hence the d-band filling is $n=1$. This compound has attracted much interest because it shows a temperature-dependent second-order phase transition at ~74 K between a paramagnetic conducting phase on the high-temperature side and a paramagnetic semiconducting phase on the low-temperature side. Below ~35 K, antiferromagnetic ordering has been suggested by NMR studies (Nishihara and Takano, 1981), neutron spin-flip scattering (Heidemann and Takano, 1980), and specific-heat (Imai *et al.*, 1996) studies, although there has been so far no experimental evidence for long-range order. Indeed, a recent NMR study has shown that the ground state is nonmagnetic with possible orbital ordering (Nakamura *et al.*, 1997). As shown in Fig. 168, the resistivity in the high-temperature phase is relatively low (in the 10^{-3} Ω cm range, which is high for a metal) and nearly temperature independent; it shows a minimum at ~150 K, above which it behaves as metallic ($d\rho/dT>0$) (Takano *et al.*, 1977; Massenet *et al.*, 1979; Matsuura *et al.*, 1991; Graf *et al.*, 1995). Below ~74 K, the resistivity rapidly increases by several orders of magnitude down to the lowest temperature studied (the activation energy being 100–300 K), with an inflection point at ~50 K. The Seebeck coefficient is negative and shows metallic temperature dependence above ~70 K. Below ~70 K, it becomes positive and semiconductor-like, indicating that the 74-K transition is between a p-type semiconductor and a metal (Matsuura *et al.*, 1991). The negative Hall coefficient at 100 K corresponds to an electron density of 2.5×10^{21} cm^{-3} or ~0.3 electrons per V atom.

The magnetic susceptibility above ~74 K, displayed in Fig. 168, shows Curie-Weiss behavior with an effective moment of 1.0–1.1 μ_B, which is smaller than the spin-only value of $1.73\mu_B$ (for $S=1/2$) or the free atomic value of $1.55\mu_B$ (for $J=3/2$); it also shows a positive Weiss constant of 20–40 K (Kebler *et al.*, 1980; Nakamura *et al.*, 1994a). This indicates that in going from

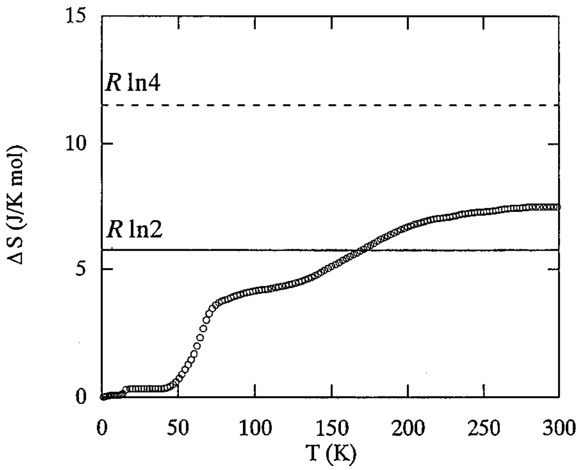

FIG. 169. Extra entropy ΔS due to conduction electrons in $BaVS_3$ obtained by subtracting the specific heat of $BaTiS_3$ from that of $BaTiS_3$. From Imai *et al.*, 1996.

high to low temperatures, the spin correlation changes its character from ferromagnetic to antiferromagnetic. The peak at the transition point ~74 K is reminiscent of an antiferromagnetic transition, but no magnetic order has been found down to ~35 K. Although the simultaneous decrease of the magnetic susceptibility and the electrical conductivity below ~74 K suggests a CDW formation or a spin Peierls transition, no corresponding pairing of V atoms has been detected in the structural studies. If the high-temperature conducting phase can be regarded as a metal, then the 74-K transition can be thought of as a genuine Mott transition in the sense that it occurs between paramagnetic phases without involving any long-range magnetic order or lowering of structural symmetry, although the transition is not of first order. The extra (magnetic and electronic) entropy ΔS of conduction electrons in $BaVS_3$ was obtained by subtracting the specific heat of $BaTiS_3$ from that of $BaVS_3$, as shown in Fig. 169. The figure shows that ΔS increases from $\sim 0\,\mathrm{J\,K^{-1}mol^{-1}}$ at ~40 K to $\sim 4.5\,\mathrm{J\,K^{-1}mol^{-1}}$ at ~74 K, and then reaches R ln 2 at ~170 K. The gradual increase of the entropy above ~35 K implies that short-range dynamic order gradually develops above ~35 K and even above ~74 K to a lesser extent. The increase in the resistivity with decreasing temperature above ~74 K (between ~74 K and the resistivity minimum at ~150 K) would be consistent with this picture, that is, with the fluctuation of the order parameter above the second-order phase transition: Such a fluctuation effect is characteristic of quasi-1D systems. The appearance of 3D antiferromagnetism below ~35 K may be caused by a weak but finite interchain interaction, since purely 1D systems should not show long-range order. The unusual magnetic behavior of $BaVS_3$ below ~74 K was attributed to frustrations due to the triangular arrangement of the V chains (Imai *et al.*, 1996). In addition to the 74-K and 35-K transitions, the magnetic susceptibility and the specific heat show an anomaly at ~160 K: Below ~160 K, the Curie constant slightly increases and the Weiss constant decreases from ~40 K to ~20 K, indicating that the magnetic correlation becomes less ferromagnetic.

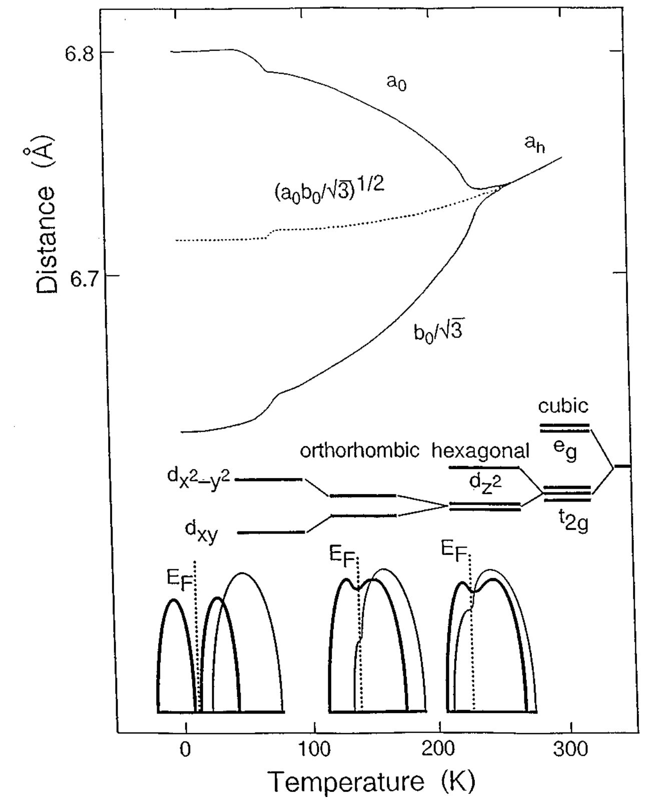

FIG. 170. Upper panel, orthorhombic lattice parameters of $BaVS_3$ as functions of temperature (Sayetat *et al.*, 1982); lower panel: corresponding changes of the electronic structures (Nakamura *et al.*, 1994a). The densities of state for the d_{z^2} and $d_{xy}-d_{x^2-y^2}$ bands are shown by thin and thick solid lines, respectively.

Apart from the electronic and magnetic phase transitions described above, $BaVS_3$ shows a second-order structural phase transition from the high-temperature hexagonal phase to the low-temperature orthorhombic phase at ~250 K, below which the linear V chains progressively become zigzag ones (Sayetat *et al.*, 1982; Ghedira *et al.*, 1986). It is suggested that the zigzag distortion remains as a dynamical fluctuation above ~250 K due to a large thermal ellipsoid for the V atom. As shown in Fig. 170, the orthorhombic distortion further increases below ~74 K.

The 74-K phase transition is sensitive to structural defects such as S vacancies and Ti substitution for V. The 74-K peak in the magnetic susceptibility disappears for S-deficient samples (typical compositions being $BaVS_{\sim 2.97}$), which become ferromagnetic with Curie temperatures of 16–17 K (Massenet *et al.*, 1978). The electrical resistivity is nearly constant, as in the stoichiometric $BaVS_3$, above ~150 K but gradually increases with decreasing temperature below it. As for Ti substitution for V, the 74-K peak in the magnetic susceptibility disappears for such a small Ti concentration as ~5%, while the resistivity above ~70 K gradually increases with Ti concentration and becomes semiconduc-

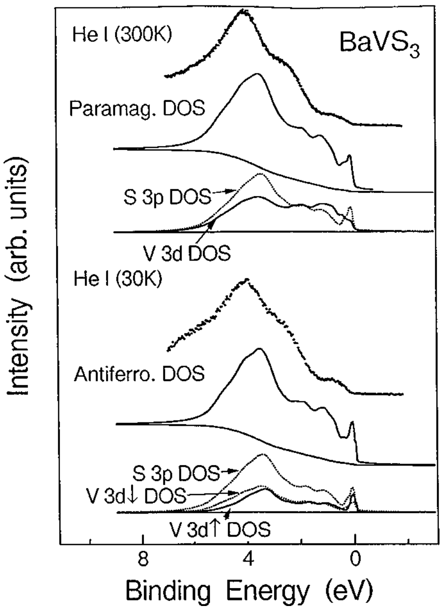

FIG. 171. Valence-band photoemission spectrum of BaVS$_3$ (Nakamura *et al.*, 1994b) compared with the DOS from a band-structure calculation (Itoh, Fujiwara, and Tanaka, 1994). The sharp Fermi edge is not observed in the photoemission spectrum.

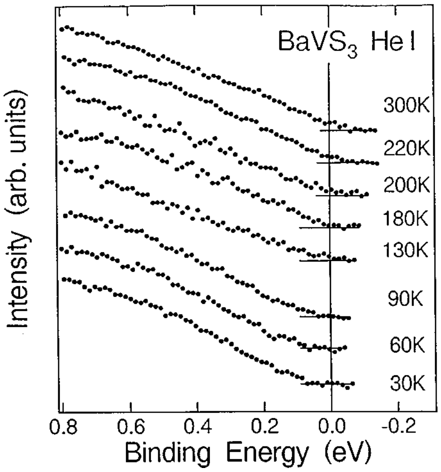

FIG. 172. High-resolution photoemission spectrum of BaVS$_3$ near E_F at various temperatures (Nakamura *et al.*, 1994b). The gap starts to open at ~90 K, somewhat above the transition temperature of ~74 K.

tive; in BaV$_{0.8}$Ti$_{0.2}$S$_3$, the resistivity becomes 1–3 orders of magnitude higher than that of BaVS$_3$ over the whole temperature range (Matsuura *et al.*, 1991). Beyond that composition, the resistivity decreases with Ti concentration (Massenet *et al.*, 1979). The origin of the increase in magnetic susceptibility below ~20–30 K is not clear at present. Because its magnitude is sample dependent and its contribution is not detected in the specific heat, it is likely that it is due to a magnetic impurity phase such as ferromagnetic BaVS$_{3-\delta}$ (Graf *et al.*, 1995). The 74-K transition is also sensitive to external pressure: The transition temperature decreases under pressure and appears to vanish around 20 kbar (Graf *et al.*, 1995).

From the systematic chemical trends of the electronic structure of transition-metal compounds, it is expected that the V $3d$-S $3p$ hybridization will be extremely strong (the charge-transfer energy being $\Delta \sim 0$). Indeed, LDA band-structure calculations have shown strongly hybridized V $3d$ and S $3p$ bands. Mattheiss (1995) made band-structure calculations on the low-temperature orthorhombic phase as well as on the high-temperature hexagonal phase without magnetic ordering and found no band-gap opening. Itoh, Fujiwara, and Tanaka (1994) made calculations on the antiferromagnetic state but also failed to open a band gap at E_F. These results indicate that electron-electron interaction has to be taken into account beyond the level of LDA or LSDA in order to account for the low-temperature insulating state, as in the cases of other Mott insulators. Apart from the electronic structure near E_F, which will be discussed below, the overall photoemission spectra are well described by the DOS given by the band-structure calculations, as shown in Fig. 171 (Itti *et al.*, 1991; Nakamura *et al.*, 1994a). As shown in Fig. 170, the distortion of the VS$_6$ octahedra along the hexagonal c axis splits the t_{2g} level into high-lying d_{z^2} and low-lying d_{xy} and $d_{x^2-y^2}$ levels. With the orthorhombic distortion below ~250 K, the degeneracy of the low-lying level is lifted, leading to a population imbalance between the split $d_{xy}-d_{x^2-y^2}$ levels. (Here, the z axis is taken along the c direction.) Further increase in the orthorhombic distortion below ~74 K may indicate that one of the split $d_{xy}-d_{x^2-y^2}$ levels is fully occupied, resulting in a Mott insulating state. In this picture, the multiband situation in the metallic phase would favor ferromagnetic coupling between the V atoms. According to the band-structure calculations, near E_F, the d_{xy} and $d_{x^2-y^2}$ orbitals form narrow energy bands while the d_{z^2} orbitals form relatively wide energy bands dispersing along the c axis. The Fermi level is pinned by the $d_{xy}-d_{x^2-y^2}$ bands.

Although quasi-1D metallic behavior of the d_{z^2} electrons is expected from the crystal and electronic structures, no anisotropic transport has been investigated so far on single crystals. On the other hand, it has been theoretically predicted that a 1D metal is not a Fermi liquid but behaves as a Tomonaga-Luttinger liquid. The single-particle spectral function of such a 1D metal should exhibit a characteristic non-Fermi-liquid behavior, as described above. Such an observation was recently made by high-resolution photoemission spectroscopy, as shown in Fig. 172 (Nakamura *et al.*, 1994a): As in other quasi-1D metals, the spectra exhibit an unusual suppression of photoemission intensity at E_F. From room temperature to ~90 K, the spectral function near E_F can be fitted to a power law: $\rho(\omega) \propto |\omega-\mu|^{\theta}$ [Eq. (2.376)] with $\theta \sim 0.8$–0.9. This value is well above the upper limit of 0.125 for the exponent of the single-band Hubbard model (Kawakami and Yang, 1990), indicating that the short-range interaction assumed in the Hubbard model is not sufficient to model electron-electron interactions in BaVS$_3$. According to Tomonaga-Luttinger liquid theory, the large exponent θ means that the $4k_F$

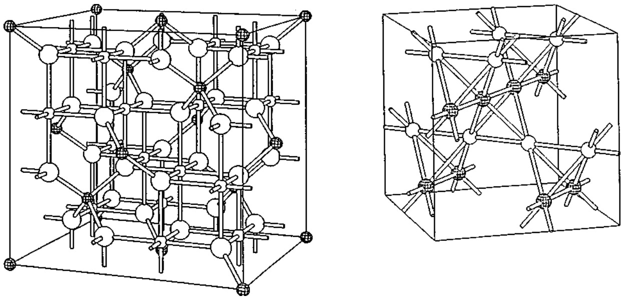

FIG. 173. Crystal structure and charge order in Fe_3O_4. Left panel, the structure of Fe_3O_4; right panel, the ordered structure of Fe^{2+} and Fe^{3+} at the B sites proposed by Verwey. From Tsuda *et al.*, 1991.

CDW correlation is the longest ranged and therefore a $4k_F$ CDW instability, i.e., localization of one electron per site, is most likely to occur in the real 3D material. This is consistent with the occurrence of the 74-K phase transition in $BaVS_3$, in which no antiferromagnetic order ($2k_F$ SDW) or Peierls distortion ($2k_F$ CDW) has been detected. In the low-temperature phase, a gap of ~ 50 meV is opened at E_F in the photoemission spectra (Fig. 172). Interestingly, the gap starts to open at ~ 90 K, well above the transition temperature of ~ 74 K, probably reflecting fluctuation effects above the transition point. It should be noted, however, that the mass anisotropy given by the Fermi velocity ratio, $\langle v_\parallel^2\rangle/\langle v_\perp^2\rangle$, is only ~ 3.8, which is much smaller than $\langle v_\parallel^2\rangle/\langle v_\perp^2\rangle \sim 100$ for the ideal 2D system La_2CuO_4 (Mattheiss, 1995). In spite of the small mass anisotropy, the photoemission spectra have exhibited 1D-like characteristics presumably because mass renormalization due to electron correlation is stronger for directions with a heavier band mass.

E. Charge-ordering systems

1. Fe_3O_4

Magnetite Fe_3O_4 forms in the spinel structure, in which one-third of the Fe ions are tetrahedrally coordinated with four oxygen ions and the remaining two-thirds are octahedrally coordinated with six oxygen ions, as shown in Fig. 173. The tetrahedral and octahedral sites are called A and B sites, respectively. In addition to its celebrated magnetic properties, which are utilized in permanent magnets, Fe_3O_4 has attracted much interest for its conductivity transition at $T_V \simeq 120$ K, called the Verwey transition (Verwey, 1939). In going from the high-temperature phase to the low-temperature phase, the electrical resistivity increases by two orders of magnitude at T_V, as shown in Fig. 174. The A-site Fe ions are stable trivalent, while the B-site Fe ions are of mixed valency with the ratio $Fe^{2+} : Fe^{3+} = 1 : 1$. Here, the Fe^{2+} and Fe^{3+} ions have $t_{2g\uparrow}^3 t_{2g\downarrow} e_{g\uparrow}^2$ ($S=2$) and $t_{2g\uparrow}^3 e_{g\uparrow}^2$ ($S=5/2$) configurations, respectively. The electrical conduction and the Verwey transition occur on the B-site sublattice. The Fe^{2+} and Fe^{3+} ions at the B sites are ordered below T_V. Fe_3O_4 is ferrimagnetic below T_C

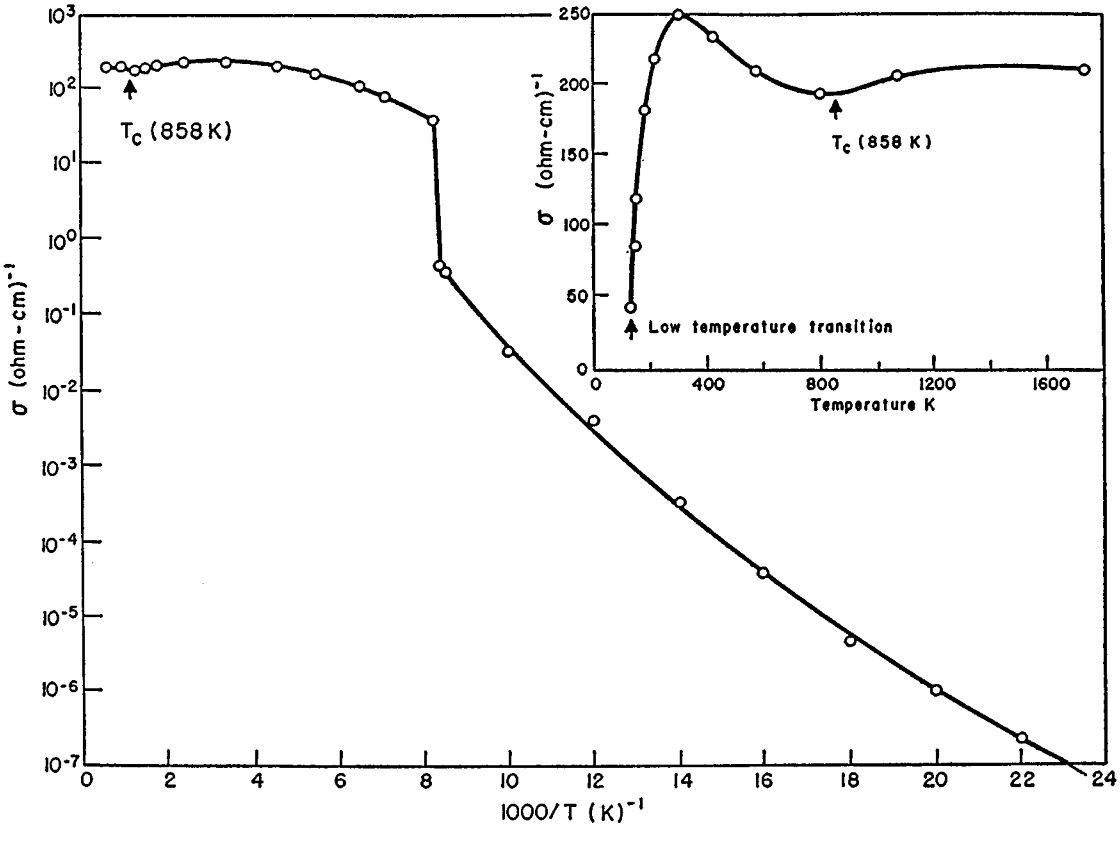

FIG. 174. Electrical conductivity of Fe_3O_4. From Miles *et al.*, 1957.

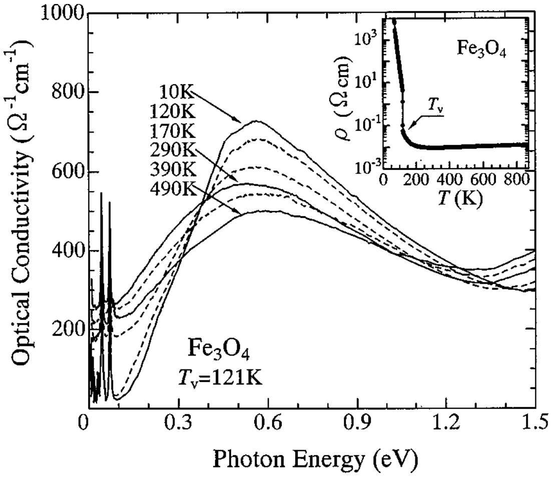

FIG. 175. Temperatures dependence of optical conductivity spectra of an Fe_3O_4 crystal. Inset shows the temperature dependence of the resistivity for the same crystal. From Park, Ishikawa, and Tokura, 1998.

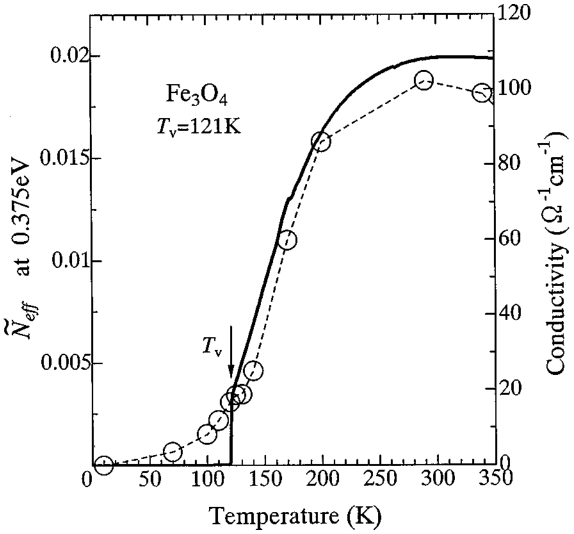

FIG. 176. Temperature variation of the spectral weight of the optical conductivity below the isobaric point energy 0.375 eV in comparison with the dc conductivity change. From Park, Ishikawa, and Tokura, 1998.

=858 K: the spins of the A and B sublattices are antiparallel, resulting in a net magnetization of $\sim 4\mu_B$ per unit formula. Since there are excellent review articles on Fe_3O_4 by Honig (1985) and by Tsuda *et al.* (1991), we shall mainly concentrate below on recent developments.

The ordered structure shown in Fig. 173 was first proposed by Verwey (Verwey and Haayman, 1941; Verwey *et al.*, 1947). Since then, however, there has been much controversy about the ordered structure from both experimental and theoretical points of view, and no consensus has been reached till now. Detailed descriptions of the structural studies are beyond the scope of this article and we refer the reader to the literature (e.g., Kita *et al.*, 1983). As for the charge-disordered phase above T_V, Anderson (1956) pointed out the importance of the short-range order, in which the total charge within a Fe_4 tetrahedron is conserved, i.e., two Fe^{2+} and two Fe^{3+} ions should form the Fe_4 octahedron. The electrical resistivity above T_V remains rather high ($\lesssim 10^{-2}$ Ω cm) and nonmetallic [$d\rho(T)/dT<0$] up to $\sim$300 K (Fig. 174), which may be due to the short-range order above T_V. The entropy change at the Verwey transition is close to $\Delta S_V = R$ ln 2 per mole Fe_3O_4, half of the value $\Delta S_V = 2R$ ln 2 expected for a random distribution of Fe^{2+} and Fe^{3+} at the B sites (Shepherd *et al.*, 1985). The role of the electron-phonon interaction or local lattice distortion in the high-temperature phase has been a matter of controversy. Yamada, Mori, *et al.* (1979) proposed, based on their diffuse neutron-scattering data, the existence of bipolarons above T_V, which they called "molecular polarons." In a molecular polaron, two Fe^{2+} ions induce the displacement of surrounding oxygen ions.

A gap opening below T_V, as well as possible short-range charge order, can be observed in the optical conductivity spectra. Figure 175 (Park, Ishikawa, and Tokura, 1998) displays the temperature dependence of the optical conductivity spectra below 1.5 eV, which was deduced from reflectance spectra on a single crystal. The spectra showing broad maxima around 0.5 eV are governed by transitions among the B sites, while transitions between the A-site and B-site Fe show up in a higher-energy region of 1.5–2.2 eV. Below T_V=121 K (see the inset for the resistive transition on the same crystal), the conductivity spectrum undergoes an abrupt change characteristic of a first-order phase transition and shows a clear gap structure in the low-energy part. Further decrease of temperature causes minimal change of the spectral shape, and the gap magnitude at the lowest temperature (10 K) is $\approx$0.12 eV, about 10 times $k_B T_V$.

Above T_V, the optical conductivity remains finite in the lower-energy region below 0.1 eV, but shows no conventional Drude features typical of metals. At temperatures between T_V and 300 K, a conspicuous spectral weight transfer is observed from the peak region around 0.5 eV to the lower-energy region with the increase of temperature, accompanying the isosbetic (equiabsorption) point at 0.375 eV. With further increase of temperature, the broad spectrum peaking at 0.5–0.6 eV gradually decreases and transfers spectral weight to the higher energy above 1.2 eV. The transferred spectral weight below the isosbetic point energy, as deduced by Eq. (4.4), is plotted in Fig. 176 as a function of temperature together with the dc conductivity (Park, Ishikawa, and Tokura, 1998). The transfer of spectral weight or the evolution of the pseudogap feature is nearly parallel with the change in conductivity. Such a spectral shape and conspicuous weight transfer above T_V up to near 300 K may be interpreted in terms of pseudogap formation due to the short-range charge order or polaron (or bipolaron) formation (Ihle and Lorentz, 1986).

When considering the charge ordering, transport, and optical properties of Fe_3O_4, only the d^5 (Fe^{3+}) and d^6 (Fe^{2+}) configurations are relevant because the on-site d-d Coulomb interaction is sufficiently large (U $\sim$5 eV) to prevent double occupancy of the B site by the extra electrons. Then the transport properties of Fe_3O_4 are governed by the intersite Coulomb interaction, which is orders of magnitude smaller than U. Because the spins are fully polarized below $T_C = 858$ K, the extra electrons at the B site enter the $t_{2g\downarrow}$ level. Therefore a "spinless" Fermion model with intersite Coulomb interaction (Cullen and Callen, 1973; Ihle and Lorenz, 1980) has often been employed:

$$\mathcal{H} = -t \sum_{\langle i,j \rangle} c_i^\dagger c_j + \frac{1}{2} \sum_{i \neq j} U_{ij} n_j n_j . \tag{4.14}$$

Here U_{ij} ($\ll U$) is the nearest-neighbor ($\equiv U_1$) or next-nearest-neighbor [$\equiv U_2$ ($\ll U_1$)] Coulomb energy, and the orbital degeneracy of the t_{2g} level has been neglected for simplicity. The parameter region $U_1 \gg U_2$ with $U_1 \sim 0.1$ eV is considered to be realistic for Fe_3O_4. The Hall coefficient (Siratori *et al.*, 1988) and Seebeck coefficient (Kuipers and Brabers, 1976) above T_V are negative, consistent with the small (1/6) filling of the $t_{2g\downarrow}$ band.

Below T_V, if $U_2 = 0$, U_1 determines only short-range order of the Anderson type, and a large number of configurations are degenerate in the ground state (Ihle and Lorenz, 1980). This degeneracy is lifted if $U_2 > 0$, and the Verwey order is stabilized. A finite transfer t or contributions from electron-lattice coupling, which arises from the different sizes of Fe^{2+} and Fe^{3+} ions, can stabilize other structures (Lorenz and Ihle, 1979, 1982). Recently, the relative stability of the Verwey structure and the more complicated "Mizoguchi structure" (Mizoguchi, 1978), which was determined through analysis of NMR data, has been studied by tight-binding band-structure calculations (Mishra and Satpathy, 1993). This study showed that the inclusion of the kinetic energy (band energy or transfer energy) favors the Mizoguchi structure, which has a higher second-neighbor Coulomb energy. Below T_V, if t is negligibly small, a gap of $2(U_1 + U_2)$ is opened between the occupied and empty B sites (Ihle and Lorenz, 1980). Above T_V, partial destruction of the short-ranged order creates new states in the middle of the gap and these states are partially filled by electrons. Ihle and Lorenz (1980) calculated the electrical conductivity using this model and obtained an excellent fit to the experimental data (with $t = 0$ and $U_1 = 0.11$ eV). The optical conductivity was calculated to show a peak at $\omega = U_1$, which may qualitatively explain the experimental data. The Seebeck coefficient above T_V was temperature independent, consistent either with the localized ($t = 0$) model or with strong correlation in Hubbard-like models.

First-principles calculations of the electronic structure of Fe_3O_4 in the ferrimagnetic state were performed using the LSDA (Zhang and Satpathy, 1991; Yanase and Siratori, 1984). Although the spin-polarized calculations were able to explain the magnetic structure, it was not possible to open a band gap within the $t_{2g\downarrow}$ band. In order to explain the insulating state of Fe_3O_4, LDA+U calculations were performed by Anisimov *et al.* (1996b). According to the LSDA calculation [Fig. 177(a)], the down-spin and up-spin bands from the A-site Fe are fully occupied and empty, respectively (corresponding to the high-spin Fe^{3+} ion), and the Fermi level is located within the $t_{2g\downarrow}$ band of the B-site Fe, resulting in the metallic state. In the LDA+U calculations, two sublattices for the B sites ($B1$ and $B2$ corresponding to the Fe^{3+} and Fe^{2+} sites, respectively) were assumed in a Verwey-type charge ordering, and the resulting DOS is shown in Fig. 177(b). While the local DOS of the $B1$ sublattice is similar to that of the A site (with the spin directions interchanged), the down-spin t_{2g} band of the $B2$ sublattice is split into a nondegenerate occupied band and a twofold degenerate unoccupied band due to the on-site U, as in Mott insulators. Thus a small gap of 0.34 eV is opened between the $B2$-site $t_{2g\downarrow}$ band below E_F and the $B1$-site $t_{2g\downarrow}$ band above E_F. Although the large on-site Coulomb interaction is a necessary condition for opening the gap in Fe_3O_4, the magnitude of the gap is determined by the smaller intersite d-d Coulomb interaction. The intersite Coulomb energy was estimated using the constrained LDA method to be 0.18 eV, which is an order of magnitude smaller than the bare point-charge value. This reduction is due to p-d covalency and dielectric polarization of the constituent ions.

The overall line shape of the valence-band photoemission spectra of Fe_3O_4 can be described as a superposition of that of the Fe^{2+} ion (at octahedral sites) and those of the Fe^{3+} ions (at both octahedral and tetrahedral sites) (Alvarado *et al.*, 1976; Siratori *et al.*, 1986; Lad and Henrich, 1989; Park *et al.*, 1997a). To be more exact, each of the Fe^{2+} and Fe^{3+} spectra consists of the main structure, which arises primarily from the $d^n\underline{L}$ final state, and a high-binding energy satellite, which arises primarily from the d^{n-1} final state, as described by the configuration-interaction cluster model (Sec. III.A.2; Fujimori, Saeki, *et al.*, 1986; Fujimori, Kimizuka, *et al.*, 1987). Here, $n = 6$ and 5 for the Fe^{2+} and Fe^{3+} components, respectively. According to this picture, the spectral feature just below E_F comes from the removal of a $t_{2g\downarrow}$ electron from the $B2$ site, which well corresponds to the band picture presented above. Detailed electronic structure near E_F and its temperature dependence were investigated by high-resolution photoemission studies. According to Park *et al.* (1997a), the spectra show no intensity at E_F either above or below $T_V \sim 120$ K, but the magnitude of the gap is reduced above T_V. They interpreted the result as an insulator-to-insulator transition. The resistivity jump at T_V is quantitatively explained by a change in the magnitude of the gap. Chainani *et al.* (1995) reported that, above T_V, the spectra show a finite DOS at E_F, as shown in Fig. 178, and concluded that the transition is indeed a metal-insulator transition. However, the broad peak at ~ 1 eV below E_F, which was assigned to the ${}^6A_{1g}$ ($t_{2g\uparrow}^3 e_{g\uparrow}^2$) final state at the Fe^{2+} site in the low-temperature phase, survives in the high-temperature phase. This implies that short-range order persists above T_V. The photoemission intensity at E_F is extremely weak and therefore, if the spectra are compared with the band DOS, an extremely small $m_k/m_b \ll 1$ and hence $Z \ll 1$ are implied (Sec.

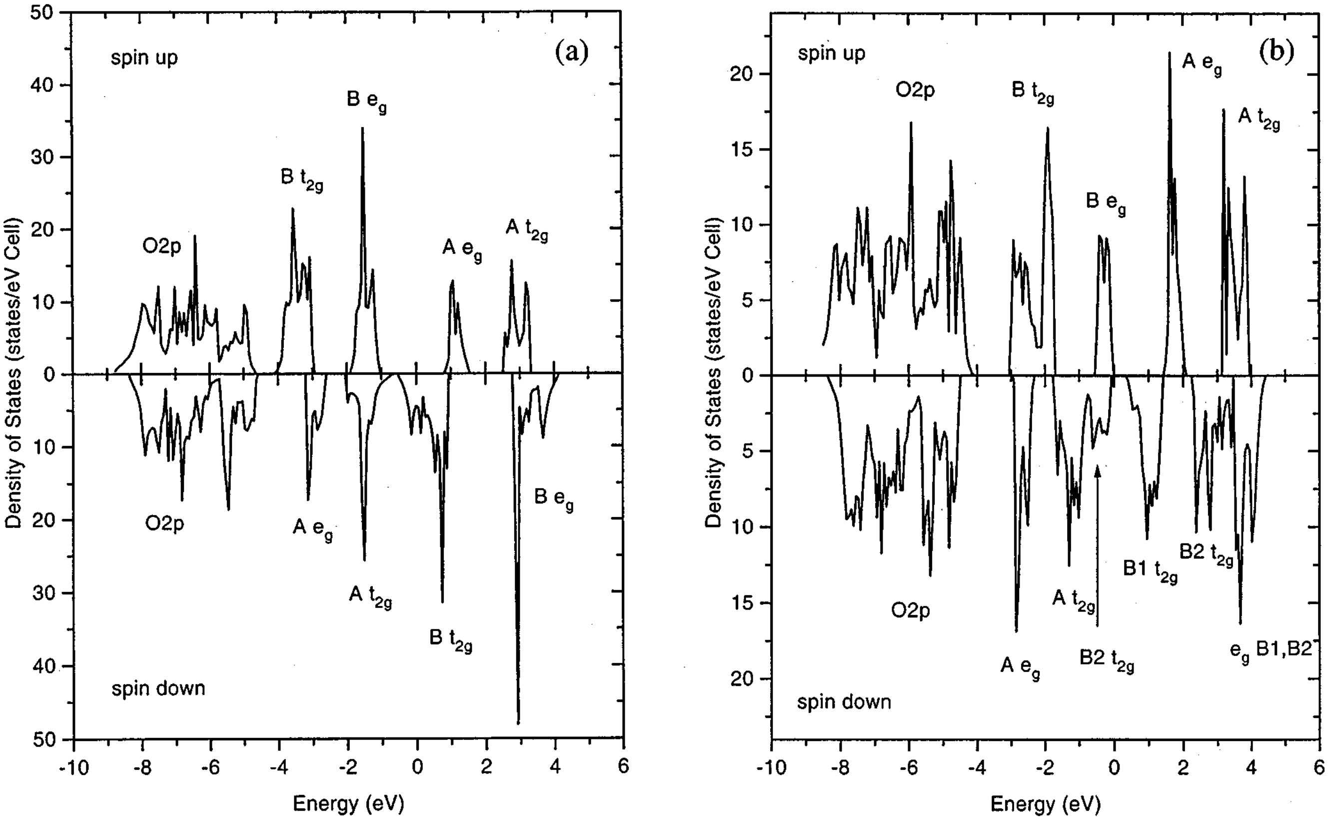

FIG. 177. Density of states of Fe_3O_4 in the ferrimagnetic state, calculated using (a) the LDA and (b) LDA+U methods (Anisimov *et al.*, 1996). The Fermi level is at 0 eV.

II.D.1). This is consistent with the poor/incoherent metallic state implied by the transport and optical studies.

2. $La_{1-x}Sr_xFeO_3$

A unique type of charge-ordering phenomenon is observed in $La_{1-x}Sr_xFeO_3$ below about 210 K around $x=2/3$, involving valence skipping of Fe sites as well as antiferromagnetic spin ordering (Takano and Takeda, 1983; Battle *et al.*, 1988, 1990). One end compound $LaFeO_3$ is an antiferromagnetic insulator with $3d^5$ ($S=5/2$) configuration of Fe that is characterized by high Néel temperature ($T_N=738\,\mathrm{K}$). The other end compound $SrFeO_3$ is an antiferromagnetic metal with $T_N=134$ K. In the solid solution system $La_{1-x}Sr_xFeO_3$, the Néel temperature decreases monotonically with x (Park, Yamaguchi, and Tokura, 1998). (To be precise, the antiferromagnetic state shows spin canting with weak ferromagnetism.) For $x>0.1$, the high-temperature paramagnetic phase above T_N is semiconducting or conducting, while the resistivity shows a steep increase at temperatures below T_N and insulating behavior in the antiferromagnetic phase, at least for $x\lesssim 0.7$. When the doping level x is around 2/3 (0.67), the resistivity shows an abrupt increase at around 207 K with a narrow thermal hysteresis, as shown in Fig. 179, signaling the occurrence of a first-order phase transition, that is, the charge-ordering (CO) phase transition with simultaneous antiferromagnetic spin ordering. This electronic phase change proved to be the simultaneous charge and spin ordering in a superlattice structure depicted in Fig. 180 (Battle *et al.*, 1990).

The charge disproportionation in the sample with near-$x=2/3$ was first detected by Mössbauer spectros-

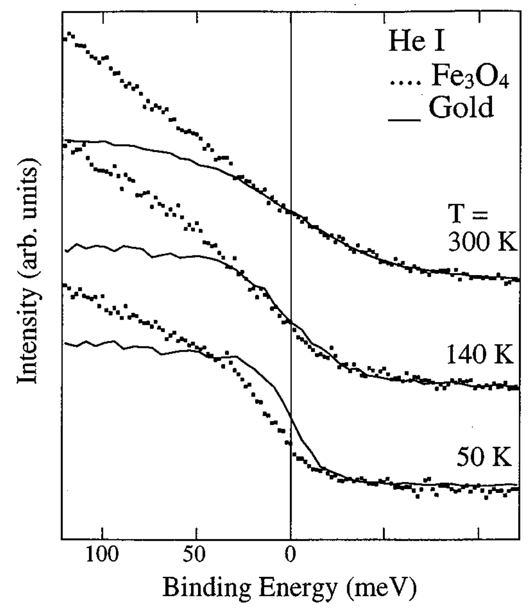

FIG. 178. Photoemission spectra of Fe_3O_4 near E_F (Chainani *et al.*, 1995). The gap opens below the Verwey transition of 121 K.

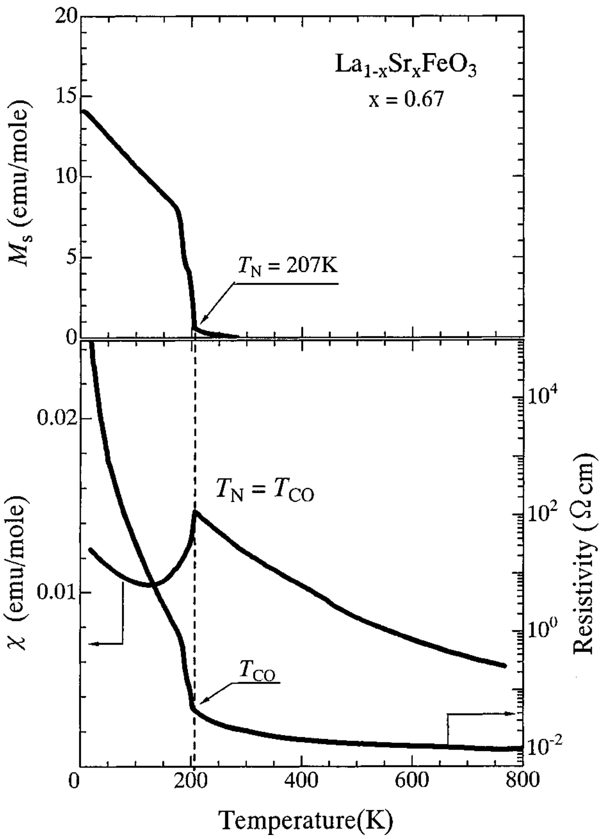

FIG. 179. Temperature dependence of spontaneous magnetization (M_S), resisitivity (ρ), and magnetic susceptibility (χ) for $La_{1-x}Sr_xFeO_3$ with $x=0.67$ (Park, Yamaguchi, and Tokura, 1998). The small spontaneous magnetization observed in the charge-ordered phase is due to the minimal spin canting in the essentially antiferromagnetic state.

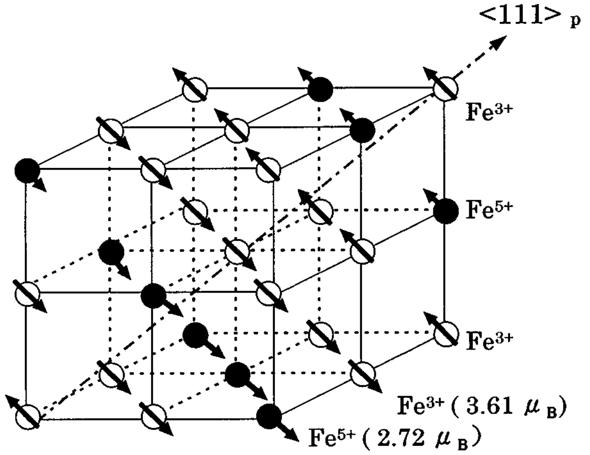

FIG. 180. Schematic structure of the charge- and spin-ordered state with charge disproportion in $La_{1-x}Sr_xFeO_3$ ($x=0.67$).

copy (Takano and Takeda, 1983). According to a profile analysis of temperature-dependent Mössbauer spectra, two kinds of Fe-site species with nominal valences of Fe^{3+} and Fe^{5+} were identified with number ratio of 2:1. The Fe^{5+} valence is unusually high and seldom realized. It is worth noting that Fe^{5+} shows the full spin-up occupancy of t_{2g} states, benefited by maximal Hund's-rule coupling energy without loss of crystal-field splitting (10 Dq) energy. Such an anomalous valence state as well as the real-space ordering of the valence-skipping sites was confirmed by neutron-scattering measurements (Battle *et al.*, 1990). The disproportionated charges are condensed within the (111) plane in the cubic perovskite setting. From the magnitudes of the respective staggered moments on the Fe sites, estimated by neutron diffraction, the Fe valence was estimated to be $+3.4$ and $+4.2$, respectively, perhaps corresponding to the Fe^{3+} and Fe^{5+} species detected by Mössbauer spectroscopy. The structural change of the lattice upon the CO transition, perhaps associated with breathing-type distortions of FeO_6 octahedra, was revealed by electron diffraction measurements (Li *et al.*, 1997), indicating a consistent superlattice structure, as shown in Fig. 180. The optical spectra also show a distinct splitting of the optical phonon modes due to folding of the phonon dispersion branch, caused by lattice distortion at the CO transition, as well as the opening of a small (<0.1 eV) charge gap (Ishikawa *et al.*, 1998).

The electronic structures of the end members, $LaFeO_3$ and $SrFeO_3$, are quite contrasting, as expected from the opposite consequences of multiplet effects in d^5 and d^4 compounds predicted in Sec. III.A.4. $LaFeO_3$ is a rather ionic insulator with a large band gap. Doped holes have relatively pure p-hole character, as demonstrated by O 1s x-ray absorption spectroscopy (Abbate *et al.*, 1992). On the other hand, $SrFeO_3$ is strongly covalent and the band gap is closed (see Fig. 56): the ground state is dominated by the $d^5\underline{L}$ configuration rather than the d^4 configuration (Bocquet *et al.*, 1992b). Therefore the net d-electron number is not much different in the nominally Fe^{3+} and Fe^{4+} (and probably Fe^{5+}) compounds. Because of this, the electrostatic energy of the system does not increase significantly with charge disproportionation, which is nominally denoted by $Fe^{4+}+Fe^{4+}\rightarrow Fe^{3+}+Fe^{5+}$, compared to other compounds. More importantly, the small charge-transfer energy $\Delta\sim0$ and the resulting small "band gap" ($E_{\text{gap}}\sim0$) for the Fe^{4+} oxides would favor charge disproportionation, as observed experimentally for $La_{1-x}Sr_xFeO_3$ with $x\sim0.7$ and for $CaFeO_3$ (Takano and Takeda, 1983; Takano *et al.*, 1991).

3. $La_{2-x}Sr_xNiO_4$

Hole-doped La_2NiO_4 also shows cooperative ordering of holes and Ni spins below some critical temperature (T_{co}). The behavior of doped holes in a 2D antiferromagnetic correlated insulator has been the subject of vital theoretical investigations concerned with the anomalous normal-state properties of the high-temperature superconducting cuprates. The charge-ordering (CO) phenomena of doped nickelates are one such example and may be viewed as a prototype of the

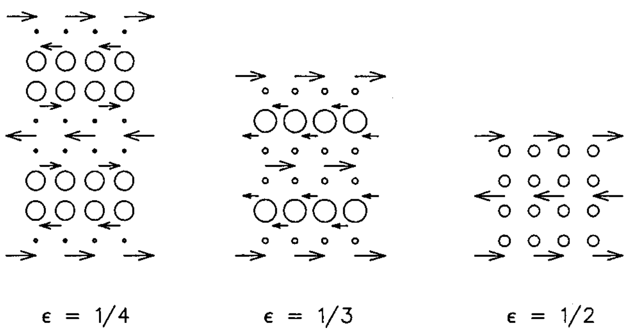

FIG. 181. Progression of spin and charge modulation in NiO_2 planes with increasing hole concentration proposed by Tranquada *et al.* (1995).

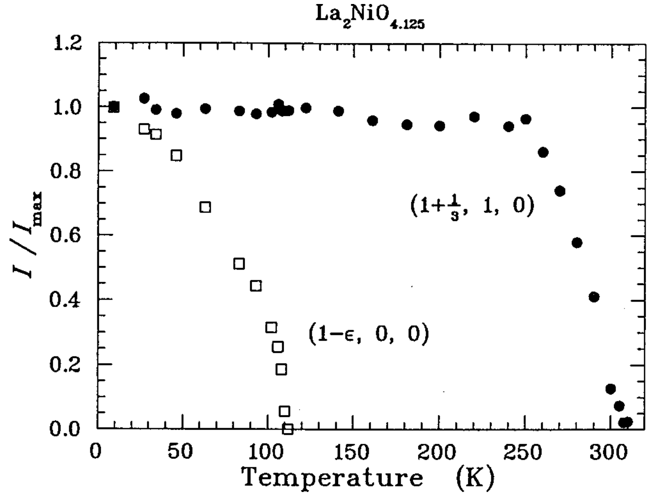

FIG. 182. Temperature dependence of normalized integrated intensities of g_1 and g_ϵ peaks, corresponding, respectively, to the oxygen and spin ordering, in $La_2NiO_{4.125}$. From Tranquada *et al.*, 1995.

microscopic phase separation that involves localization of holes in domain walls with an antiferromagnetic background.

Charge-ordering phenomena are seen at almost any doping level $(p=x+2y)$ in $La_{2-x}Sr_xNiO_{4+y}$ as long as the compound remains insulating $(p<0.7)$. The progression of spin and charge modulations in NiO_2 planes with increasing hole concentration p, which was proposed by Tranquada, Lorenzo, *et al.* (1995) on the basis of neutron-scattering results, is schematically shown in Fig. 181. In this model, it is assumed that the doped hole is of p orbital character, residing on the O site. In these spin- and charge-ordered states, the modulation wave vectors are, with use of the orthorhombic cell specified by $\sqrt{2}\vec{a}\times\sqrt{2}\vec{b}\times\vec{c}$ relative to the tetragonal, $g_\epsilon=(1-\epsilon,0,0)$ for the magnetic ordering and $g_{2\epsilon}=(2\epsilon,0,1)$ for the charge ordering. The charge-ordering superlattice peaks are of course not from the charge-density-modulation itself but likely to arise from the accompanied modulation of the Ni-O bond lengths. Here, the modulation wave number ϵ is expected to coincide with the doping level p, which was partly confirmed experimentally (Sachan *et al.*, 1995). As shown below, however, the commensurate locking at a particular modulation vector (mostly $\epsilon=1/3$ and 1/2 for Sr-doped compounds) is observed, suggesting mesoscopic hole-segregation behavior (Chen *et al.*, 1993; Cheong *et al.*, 1994).

The most thoroughly characterized case is for $\epsilon=1/4$, which was investigated by a single-crystal neutron-diffraction study for $La_2NiO_{4.125}$ $(p=0.25)$ (Tranquada *et al.*, 1993; Tranquada, Lorenzo, *et al.*, 1995). The interstitial oxygens form a superlattice with unit cell of $3\vec{a}\times5\vec{b}\times5\vec{c}$, which gives an ideal interstitial density of $y=2/15$ per unit formula. The compound shows a simultaneous ordering of dopant-induced holes and Ni spins, as modeled in the left panel of Fig. 181. Figure 182 displays the temperature dependence of the normalized intensity of superlattice peaks arising from interstitial oxygen ordering $(1+1/3,1,0)$ below 310 K and Ni spin ordering $(1-\epsilon,0,0)$ below 110 K. The modulation wave number is ideally $\epsilon=3/11$ but actually temperature dependent, varying from 0.295 at 110 K to 0.271 at 10 K.

It was proved from a detailed analysis of neutron-scattering patterns by Tranquada, Lorenzo, *et al.* (1995) that in the charge-ordered state in $La_2NiO_{4.125}$ the magnetic moments and the Ni-O bond lengths are both sinusoidally modulated within the NiO_2 plane. The maximum value of the Ni moment is comparable to that of the undoped compound (La_2NiO_4), and the moments point transverse to the modulation direction, as shown in Fig. 181, with nearest neighbors antiparallel. Therefore the ordering can be viewed as alternating stripes of antiferromagnetic and hole-rich regions. The hole-rich regions act as antiphase-domain boundaries. The position of the domain walls is staggered in neighboring layers for the case of $La_2NiO_{4.125}$.

Inelastic neutron scattering has been used to measure the low-energy spin excitations in the charge-stripe phase of $La_2NiO_{4.133}$. Spin-wave-like excitations were observed to disperse away from the incommensurate magnetic superlattice points with a velocity ~60% of that in La_2NiO_4 (Tranqnada, Wochner, and Buttery, 1997).

As described in Sec. II.H.3, the stability of charge ordering has been studied within the unrestricted Hartree-Fock approximation (Poilblanc and Rice, 1989; Zaanen and Gunnarsson, 1989; Schulz, 1990a). The observed diagonal domain-wall pattern in the Ni compound is in accord with the results of calculations by Zaanen and Littlewood (1994) which were derived from a multiband Hubbard model with parameters appropriate to the NiO_2 plane. They showed that Peierls-type electron-phonon coupling further stabilizes the formation of charged domain walls.

Charge ordering or formation of charged diagonal domain walls at higher doping levels, as shown in the center and right panels of Fig. 181, has been observed in Sr-doped La_2NiO_4 (Chen *et al.*, 1993; Cheong *et al.*, 1994). Chen *et al.* (1993) observed superlattice spots at the positions $(1,\pm\delta,0)$ or $(\pm\delta,1,0)$ in the [001] zone-axis electron-diffraction patterns. This coincides with the charge-ordering peaks of the aforementioned neutron diffraction in the $(hk0)$ zone of the reciprocal space. (Note that, even with the different choices of modulation vector in the neutron and electron-diffraction studies, the relation $\delta+2\epsilon=1$ still holds.) In measurements of the [100] zone-axis electron-diffraction pattern, diffuse streaks are observed along the $(00l)$ direction, peaked at $l=$odd with a coherence length $\leqslant 60$ Å. The modulation g is then $(1\pm\delta,0,1)$ or equivalently $(2\epsilon,0,1)$, which is in accordance with the charge-ordering peaks in the neutron scattering for $\mathrm{LaNiO}_{4.125}$.

The modulation wave vector $\epsilon=(1-\delta)/2$ increases generally as Sr doping increases (Chen *et al.*, 1993). The value of ϵ was found to increase rapidly from $\approx 1/4$ near $x=0$ to $\approx 1/3$ for $x>0.075$. Near $x=0$ the ordering is perhaps induced by excess oxygen, as typically seen for $\mathrm{La_2NiO_{4.125}}$ crystals. The modulation vector stays close to $\epsilon=1/3$ for a fairly wide x region of $0.075<x<0.4$ and around $\epsilon=1/2$ between $x=0.5$ and 0.6. However, the value of ϵ is known to be sensitive to oxygen stoichiometry (Sachan *et al.*, 1995).

The $\epsilon=1/2$ (or $\delta=0$) ordering is the most fundamental one, where one hole is present for every other Ni atom (or on its surrounding oxygen sites; see the right panel of Fig. 181). Chen *et al.* (1993), observed that this $\epsilon=1/2$ CO is essentially two dimensional without any intensity modulation of the (π,π) point superlattice peak along the c axis. This is perhaps because two breathing-type distortions cannot sit right next to each other and the coupling along the c axis is frustrated. In the picture of holes residing on Ni sites, the $\epsilon=1/3$ polaron lattice can be derived from the $\epsilon=1/2$ lattice by first removing holes (polarons) along the diagonal of the $\mathrm{NiO_2}$ square lattice (the x direction) and then repeating this process for every third polaron lattice unit cell along the y direction (Chen *et al.*, 1993). In the case of the $\epsilon=1/2$ state, intuitively and theoretically (Zaanen and Littlewood, 1994), a ferromagnetic spin arrangement with alternating $S=1$ and $S=1/2$ spins is expected to occur in the $\mathrm{NiO_2}$ plane. However, there is no sign of ferrimagnetism in the observed magnetic susceptibility (Cheong *et al.*, 1994). For $\mathrm{La}_{2-x}\mathrm{S}_x\mathrm{NiO}_4$ $(0.1<x<0.6)$, spin-glass-like behavior and weak ferromagnetism were observed below 150 K, presumably due to antiferromagnetic (short-range) ordering. However, the susceptibility above 200 K was field independent. Around $x=1/3$, the susceptibility decreased at 240 K, implying the onset of an electronic phase transition, that is, a charge-ordering transition.

A charge-ordering transition is clearly manifested in the transport and optical properties of $\mathrm{La}_{2-x}\mathrm{Sr}_x\mathrm{NiO}_4$ with $x=1/3$ and 1/2. Figure 183 displays the temperature dependence of the resistivity in polycrystalline samples of $\mathrm{La}_{2-x}\mathrm{Sr}_x\mathrm{NiO}_4$ with the inset showing the temperature derivative of the logarithmic resistivity (Cheong *et al.*, 1994). The $\rho(T)$ exhibits semiconducting behavior below room temperature and weak metallic behavior above 600 K for x between 0.2 and 0.5. For $x=0.3$, $\rho(T)$ increases abruptly at 240 K, indicative of a charge-ordering transition. The temperature derivative of the logarithmic resistivity, plotted in the inset of Fig. 183, shows a sharp dip at 240 K. A weaker and much broader feature for $x=0.5$ is also evident at 340 K, suggesting that the $\epsilon=1/2$ CO transition occurs around this temperature. The truly 2D nature of the $\epsilon=1/2$ state is responsible for the blurred nature of this transition.

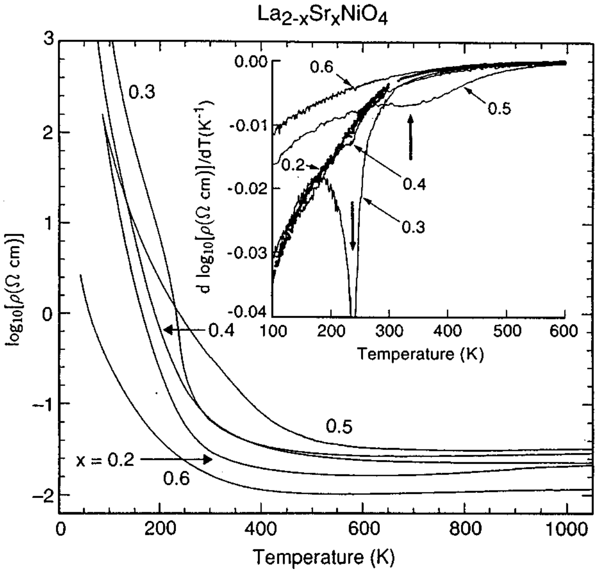

FIG. 183. Temperature dependence of resistivity for $\mathrm{La}_{2-x}\mathrm{Sr}_x\mathrm{NiO}_4$ with representative Sr concentrations (Cheong *et al.*, 1994). The inset displays the temperature derivative of the logarithmic resistivity. Vertical arrows indicate features in the derivative for $x=0.3$ and 0.5, indicative of the charge-ordering phase transitions.

In the following, let us focus on the $\epsilon=1/3$ CO transition in $\mathrm{La}_{2-x}\mathrm{Sr}_x\mathrm{NiO}_4$ $(x=0.33)$ and related compounds. The CO transition for $\epsilon=1/3$ is robust against the choice of divalent ions (Sr,Ba,Ca) (Cheong *et al.*, 1994) and of trivalent ions (La,Nd) (Katsufuji, Tanabe, and Tokura, 1998), ensuring that the transition is stabilized by the commensurate value of the hole number. Figure 184 shows the change in the sound velocity (top panel) due to the phase transition at 240 K, together with the specific heat and temperature derivatives of resistivity and magnetic susceptibility for $\mathrm{La_{1.67}Sr_{0.33}NiO_4}$ (Ramirez *et al.*, 1996). The temperature dependence of the sound velocity and the specific heat show a pronounced anomaly at the same temperature as observed in the resistivity and the susceptibility. This CO phase transition at 240 K is continuous in nature. The change in the sound velocity was observed to be insensitive to magnetic fields up to $9T$, not as in a typical antiferromagnet. This observation suggests that the CO transition for $x=0.33$ at $T_{co}=240$ K does not involve long-range ordering of the Ni spins. The entropy involved in the CO transition is obtained by subtracting a smooth background from the specific-heat data. It is estimated to be $\Delta\tilde{S}\equiv\Delta S/R\sim 0.25(\ln 2)=0.17$. The observed value is considerably smaller than that for the configurational (real-space ordering) hole entropy $(\Delta\tilde{S}=0.64)$ or for the $S=1$ spin ordering $(\Delta\tilde{S}=0.73)$, but obviously an order of magnitude larger than that of the weak-coupling

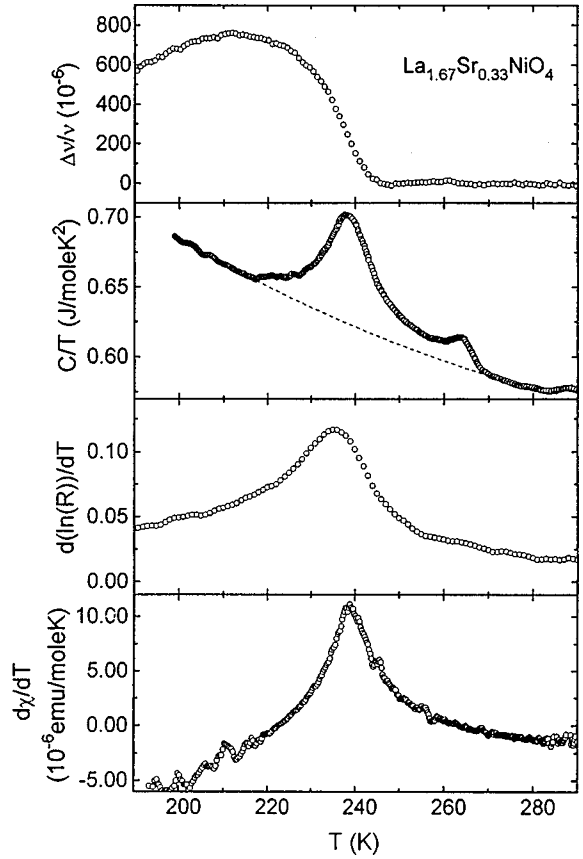

FIG. 184. The normalized sound velocity $\Delta\nu/\nu$, specific heat capacity (C), and temperature derivatives of resistivity (ρ) and magnetic susceptibility (χ) in $La_{2-x}Sr_xNiO_4$, with $x=0.33$ From Ramirez *et al.*, 1996.

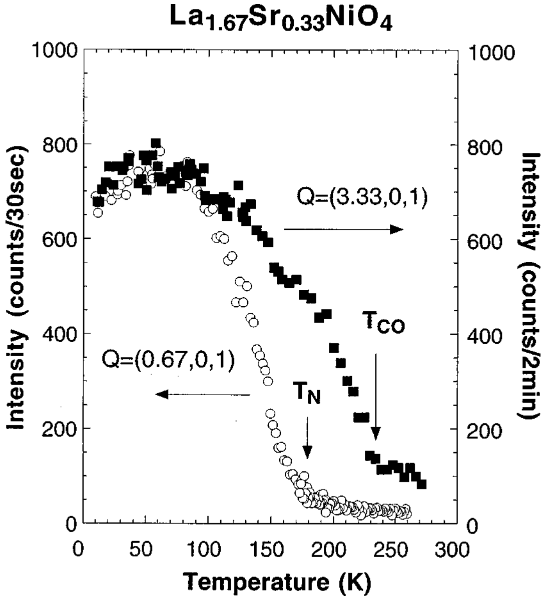

FIG. 185. Temperature dependence of normalized integrated intensities of g_ϵ (0.67,0,1) and $g_{2\epsilon}$ (3.33,0,1) peaks, corresponding, respectively, to spin and charge ordering, in $La_{2-x}Sr_xNiO_4$ $(x=0.33)$. From Kakeshita *et al.*, 1997.

CDW/SDW transition. Ramirez *et al.* (1996) argued this springs from independent hole-spin ordering.

Composition-tuned $(x=0.33)$ single crystals have subsequently become available. According to recent neutron-scattering studies (Lee and Cheong, 1997; Kakeshita *et al.*, 1998), the (static) charge and spin ordering in an $x(=\epsilon)=0.33$ crystal, which were probed by the $(4-2\epsilon,0,1)$ and $(3+\epsilon,0,1)$ superlattice peaks, takes place below $T_{co}=230$ K and $T_N=180$ K, respectively, as shown in Fig. 185. The temperature dependence of anisotropic transport and optical conductivity spectra were investigated by Katsufuji *et al.* (1996). The temperature dependence of the in-plane (ρ_{ab}) and out-of-plane (ρ_c) resistivity is displayed in Fig. 186 together with the inset for the conductivity (inversed resistivity) on a linear scale. The resistivity of the $x=0.33$ crystal shows a large anisotropy $(>10^2)$ between the in-plane and c-axis components, yet both show a simultaneously abrupt increase at T_{co}, as indicated by arrows in Fig. 186. An important point to be noticed is that the in-plane resistivity is metallic, i.e., $d\rho_c/dT>0$ above 500 K and then shows an upturn below 500 K, which is a much higher temperature than T_{co}, while the c-axis resistivity is semiconducting or insulating, namely, $d\rho_c/dT<0$, over the whole temperature region up to 800 K, as can be clearly seen in the inset. The Hall coefficient above 300 K is nearly constant and takes a small positive value, corresponding to ≈ 1 hole carrier per Ni site. However, the Hall coefficient decreases rapidly with cooling for temperatures ($\sim$300 K) near and above T_{co} and takes a negative value with a large absolute magnitude on entering the charge-ordered state below T_{co} (Tanabe *et al.*, 1998). The hole-type carrier conduction well above T_{co} is characterized by a large Fermi surface. As the charge-ordered state is approached with decreasing temperature, however, a small electron pocket is produced due to charge-ordering fluctuations and subsequent static ordering. For $x\lesssim 0.30$, on the other hand, the Hall coeffi-

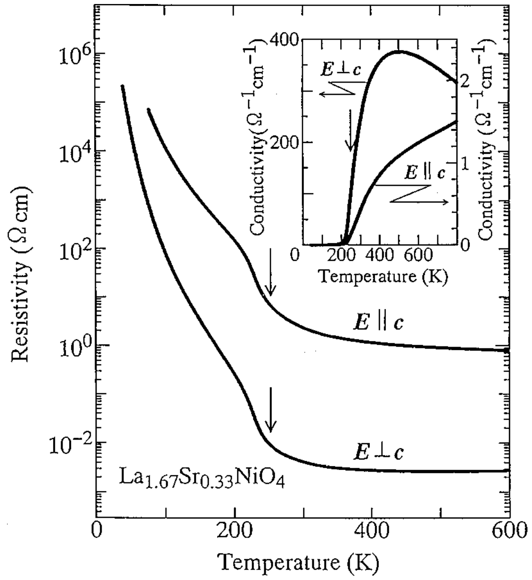

FIG. 186. Temperature dependence of in-plane and out-of-plane resistivity in single crystalline $La_{2-x}Sr_xNiO_4$ $(x=0.33)$. From Katsufuji *et al.*, 1996.

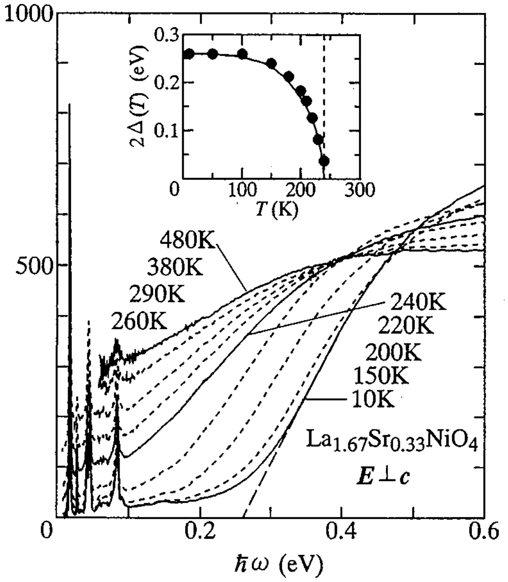

FIG. 187. Temperature-variation of the in-plane optical conductivity spectra in the gap region for $La_{2-x}Sr_xNiO_4$ ($x=0.33$) (Katsufuji *et al.*, 1996). The inset shows the variation of the charge gap in the charge-ordered state.

cient rises steeply as the temperature is lowered below T_{CO}, indicating the presence of a small hole pocket (Tanabe *et al.*, 1998).

The CO instability crucially affects the electronic structure over a fairly large energy scale, at least up to 2 eV in the case of a $La_{2-x}Sr_xNiO_4$ ($x=0.33$) crystal. The temperature variation of the low-energy part of the in-plane optical conductivity spectra (obtained by Kramers-Kronig analysis of the reflectivity spectra) is shown in Fig. 187 (Katsufuji *et al.*, 1996). Below T_{co}, a gradual opening of the charge gap as well as change in the gap magnitude 2Δ with temperature is clearly observed. At the lowest temperature ($=10$ K) shown here, 2Δ is estimated to be about 0.26 eV by a linear extrapolation from the onset of conductivity as indicated by a long-dashed line in the figure. There appears to be an appreciable amount of residual spectral weight below this estimated gap, which may arise from a slight deviation of the nominal hole concentration (p) from the commensurate value ($p=1/3$) or from a microscopic imperfection of the charge-ordered lattice. The temperature dependence of the gap 2Δ, shown in the inset, is in accordance with a BCS-like function represented by a solid line. Examples include the charge-density-wave (CDW) or spin-density-wave (SDW) transitions, which show BCS-like behavior both in wave amplitude and in the energy gap. However, the ratio of the energy gap at $T=0$ K [$2\Delta(0)$] to the transition temperature (k_BT_{co}) is ~ 13 in this compound, which is significantly larger than the theoretical value for a conventional weak-coupling CDW/SDW transition, $2\Delta(0)/k_BT_c \sim 3.5$. Such a large value of $2\Delta(0)/T_{co}$ implies that the charge gap in the charge-ordered state is affected by strong electron correlation effects or that the T_{co} is suppressed due to fluctuations arising from two dimensionality.

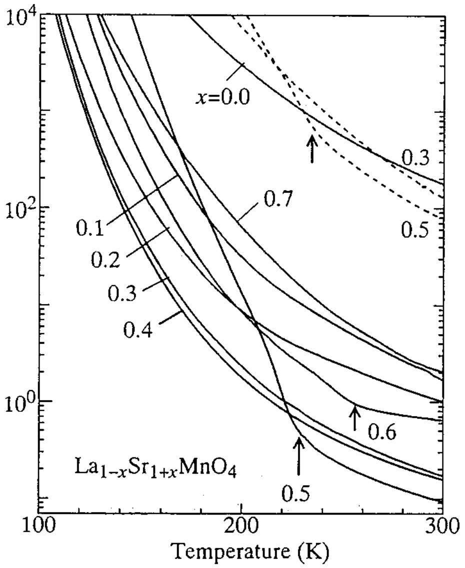

FIG. 188. Temperature dependence of resistivity (ρ) for single crystals of $La_{1-x}Sr_{1+x}MnO_4$ with various hole concentrations (x) (Moritomo *et al.*, 1995); Solid curves, in-plane (ρ_{ab}) components; dashed curves, out-of-plane (ρ_c) components. A steep increase in ρ as indicated by upward arrows is due to the charge-ordering transitions.

The optical conductivity spectra show considerable temperature dependence even above T_{co}: As signaled by the presence of the isosbetic (equi-absorption) point at 0.4 eV for the spectral change above $T_{co}(=240\,\text{K})$, the spectral weight below 0.4 eV is transferred to a higher-lying energy region (at least up to 2 eV, not shown here) with decreasing temperature, apparently producing a pseudogap feature in the low-energy side (Katsufuji *et al.*, 1996). This is contrasted with a nearly rigid shift of the optical conductivity spectrum below T_{co}. This effect is rather surprising but in accordance with the semiconducting behavior of the resistivity below 500 K. A charge-ordering fluctuation might be responsible for the anomalous spectral change and weight transfer above T_{CO}.

4. $La_{1-x}Sr_{1+x}MnO_4$

The manganite system $La_{1-x}Sr_{1+x}MnO_4$ with an $n=1$ layered perovskite (or K_2NiF_4-type) structure (see Fig. 66) also shows a charge-ordered state near $x=1/2$. The composition x represents the nominal hole number per Mn site, since the Mn^{3+} valence state ($LaSrMnO_4$; $x=0$) is viewed as the parent Mott insulator. Figure 188 displays the temperature dependence of the in-plane resistivity (ρ_{ab}) in $La_{1-x}Sr_{1+x}MnO_4$ crystals with $x=0-0.7$ (Moritomo *et al.*, 1995). In the figure, the temperature dependence of the c-axis resistivity (ρ_c, dotted curves) is displayed for $x=0.3$ and 0.5, showing highly anisotropic charge dynamics. In contrast to the case of the pseudocubic and $n=2$ layered perovskites (see Sec. IV.F), no ferromagnetic phase emerges, perhaps due to the reduced double-exchange interaction. It is to be noted in Fig. 188 that both ρ_{ab} and ρ_c curves for the x

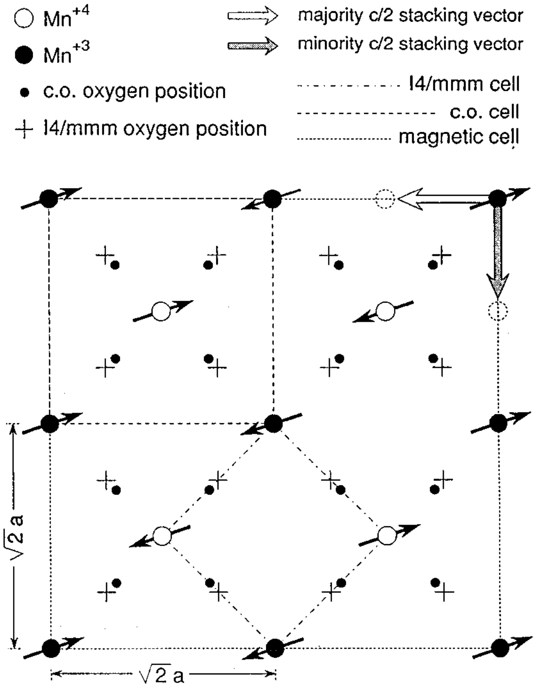

FIG. 189. The MnO_2 spin configuration in the charge-ordered state in $La_{1-x}Sr_{1+x}MnO_4$ $(x=0.5)$. From Sternlieb *et al.*, 1996.

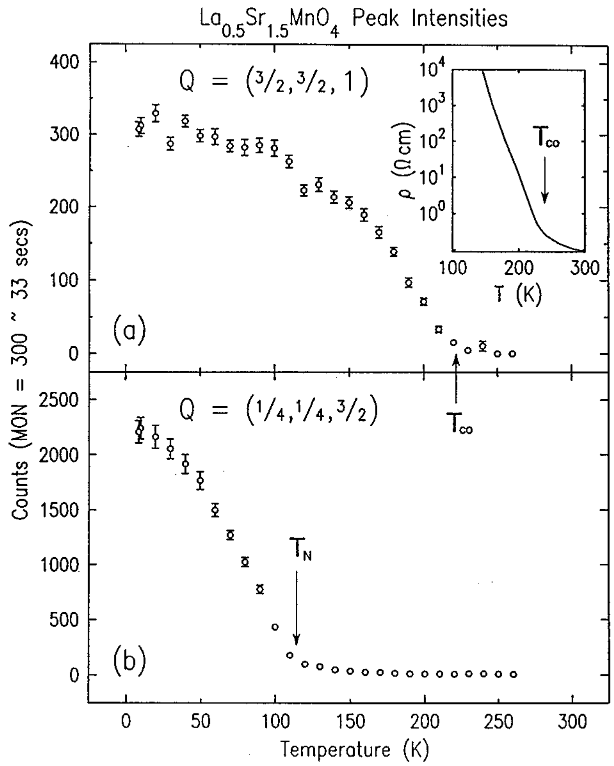

FIG. 190. Temperature dependence of the (a) charge and (b) magnetic order observed in a neutron-scattering study (Sternlieb *et al.*, 1996). Inset in (a) shows the resitivity vs T.

$=0.5$ crystal increase steeply at 220 K, as shown by upward arrows. A similar resistivity anomaly is also discernible for an $x=0.6$ crystal around 260 K.

Corresponding to the anomalies in the resistivity as well as in the magnetic susceptibility for $x=0.5$, electron-diffraction studies (Moritomo *et al.*, 1995; Bao, Chen, *et al.*, 1996) revealed (1/4,1/4,0) and (3/4,3/4,0) superlattice peaks which are thought to arise from the charge-ordered state. On the basis of the electron-diffraction patterns, Bao, Chen, *et al.* (1996) hypothesized the presence of diagonally ordered charged stripes, as in the case of $La_2NiO_{4.125}$ $(\epsilon=1/4$, Sec. IV.F.3), with modulation wave vector (1/4,1/4,0). This state can be viewed as a stripe-type ordering of Mn^{2+} $(3dt_{2g}^3e_g^2$; $S=5/2)$ and Mn^{4+} $(3dt_{2g}^3$; $S=3/2)$. By contrast, Moritomo *et al.* (1995) assumed a much simpler (1/2,1/2,0) ordering (or $\epsilon=1/2$), as in $La_{2-x}Sr_xNiO_4$ [$x=0.5$; see Fig. 181(c)], associated with the additional fourfold periodic distortion perhaps due to orbital ordering.

More recently, a single-crystalline neutron-scattering study was performed by Sternlieb *et al.* (1996), in which the aforementioned $\epsilon=1/4$ type scattering seen in the electron-diffraction studies was not observed, though it is observed in x-ray scattering. Sternlieb *et al.* (1996) viewed the $(1/4,1/4,l)$ peaks as spurious (tentatively attributing them to nonstoichiometry at the crystal surface) and presented the model of charge and spin order in the MnO_2 plane shown in Fig. 189. The temperature dependence of the charge and spin order as measured by superlattice intensities is also shown in Fig. 190. The charge shows an alternating Mn^{3+}/Mn^{4+} pattern with wave vector of (1/2,1/2,0), i.e., the $\epsilon=1/2$ charge ordering, below $T_{co}=217$ K. The onset of the charge ordering is in accordance with the steep increase in resistivity shown in Fig. 188. Below the Néel temperature, $T_N=110$ K, the magnetic moments form an ordered structure, shown in Fig. 189, with dimensions $2\sqrt{2}a\times2\sqrt{2}b\times2c$, relative to the underlying tetragonal chemical cell.

It is worth noting that the MnO_2 charge/spin order model for this $n=1$ layered perovskite is identical with the (001) face projection of the well-known CE-type charge/spin ordered pattern for pseudocubic (orthorhombic Pb_{nm}) perovskite manganites, $R_{1/2}A_{1/2}MnO_3$ (Goodenough, 1955; Wollan and Kohler, 1955). CE-type charge-ordering transitions and their modification under a magnetic field will be discussed in Sec.IV.F. Suffice it to say here that such a spin ordering must accompany ordering of the orbital. Apparently, the degeneracy of the e_g orbital is lifted by the tetragonal crystal field in a layered perovskite. In fact, the $x=0$ compound $LaSrMnO_4$ shows coherent elongation of the out-of-plane Mn-O(apical) bond length due to the Jahn-Teller effect. However, near $x=1/2$, the in-plane and out-of-plane Mn-O bond lengths are nearly equal (≈1.9 Å), indicating a minimal static Jahn-Teller effect in heavily hole-doped manganites, despite the layered structure. Orbital degrees of freedom should play an important role in producing a rather large magnetic unit cell, as shown in Fig. 189. In accordance with this expectation, the concomitant ordering of the orbital and charge with a charge-exchange-type projection onto the *ab* plane was recently demonstrated by Murakami *et al.* (1998)

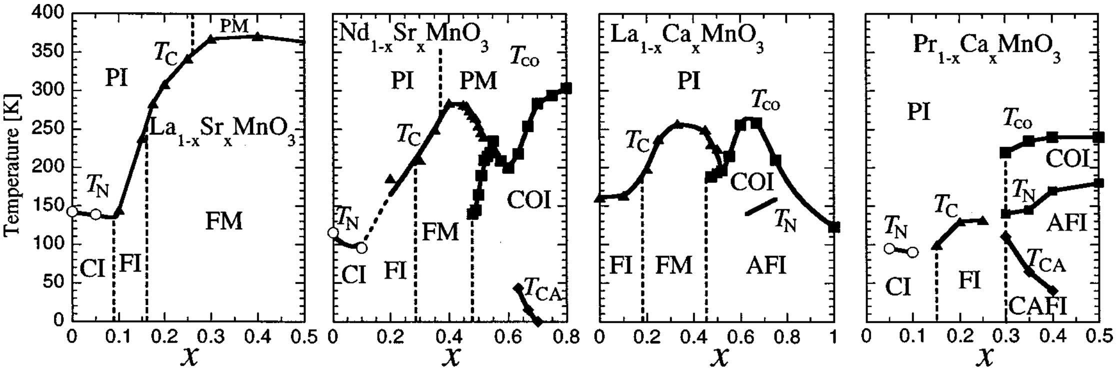

FIG. 191. Electronic phase diagrams in the plane of the doping concentration x and temperature for representative distorted perovskites of $R_{1-x}A_x\mathrm{MnO}_3$: (a) $\mathrm{La}_{1-x}\mathrm{Sr}_x\mathrm{MnO}_3$; (b) $\mathrm{Nd}_{1-x}\mathrm{Sr}_x\mathrm{MnO}_3$; (c) $\mathrm{La}_{1-x}\mathrm{Ca}_x\mathrm{MnO}_3$; and (d) $\mathrm{Pr}_{1-x}\mathrm{Ca}_x\mathrm{MnO}_3$. States denoted by abbreviations: PI, paramagnetic insulating; PM, paramagnetic metallic; CI, spin-canted insulating; COI, charge-ordered insulating; AFI, antiferromagnetic insulating (in the COI); CAFI, canted antiferromagnetic insulating (in the COI).

through x-ray resonant diffraction.

F. Double-exchange systems

1. $R_{1-x}A_x\mathrm{MnO}_3$

Giant negative magnetoresistance (MR) in the perovskite manganites near the Curie temperature (T_C) was first reported by Searle and Wang (1969) for a crystal of $\mathrm{La}_{1-x}\mathrm{Pb}_x\mathrm{MnO}_3$. Soon after, Kubo and Ohata (1972) gave an essential account of this phenomenon using the double-exchange Hamiltonian given in Eqs. (2.9a)–(2.9c). They calculated the magnetoresistance in the Hartree-Fock approximation with additional consideration of the lifetime effect of the quasiparticles scattered by spin fluctuations. This model contains the essential ingredient of the double-exchange mechanism elaborated by Zener (1951), Anderson and Hasegawa (1955), and de Gennes (1960).

A Mn^{3+} ion shows the electronic configuration of $t_{2g}^3 e_g^1$. The e_g-state electrons, hybridized strongly with the O $2p$ state, are subject to the correlation effect but can be itinerant when hole-doped, while the t_{2g} electrons, less hybridized with $2p$ states and stabilized by crystal-field splitting, are viewed as forming the local spin ($S=3/2$). In Eqs. (2.9a)–(2.9c), t stands for the transfer of e_g electrons between nearest-neighbor pairs (i,j) of sites, and J_H the on-site ferromagnetic (Hund's-rule) coupling between the e_g electron spin (s) and the t_{2g} local spin (σ). According to estimates from photoemission studies (Sarma, Shanthi, *et al.*, 1996) and optical spectroscopy (Arima and Tokura, 1995; Okimoto *et al.*, 1995a), J_H is about 2 eV and probably larger than the one-electron bandwidth $W(=2zt$, where z is the coordination number).

In the limit of large J_H/W, with classical treatment of S, the absolute magnitude of the effective transfer depends on the relative angle θ between neighboring t_{2g} spins at sites i and j (Zener, 1951; Anderson and Hasegawa, 1955; Millis *et al.*, 1995),

$$t_{eff}=t\cos(\theta/2). \tag{4.15}$$

Thus the ferromagnetic metallic state is stabilized by maximizing the kinetic energy of the conduction electrons for $\theta=0$. As was discussed in Sec. II.H.1, this effective transfer was treated using the average $\langle\cos\theta/2\rangle$ by the Hartree-Fock approach (Anderson and Hasegawa, 1955).

To understand the important features observed experimentally, we need to be aware of some factors that are missing from the simplified double-exchange model above. In the following, we focus on some experimental observations that may be relevant to anomalous metallic features, although the recent extensive research on the so-called "colossal" magnetoresistance has generated a huge number of reports in the scientific and technological literature.

We show in Fig. 191 electronic phase diagrams in the plane of the doping concentration x and temperature for representative distorted perovskites of $R_{1-x}A_x\mathrm{MnO}_3$ (Schhiffer *et al.*, 1995; Tokura, Tomioka, *et al.*, 1996b); these include (a) $\mathrm{La}_{1-x}\mathrm{Sr}_x\mathrm{MnO}_3$, (b) $\mathrm{Nd}_{1-x}\mathrm{Sr}_x\mathrm{MnO}_3$, (c) $\mathrm{La}_{1-x}\mathrm{Ca}_x\mathrm{MnO}_3$, and (d) $\mathrm{Pr}_{1-x}\mathrm{Ca}_x\mathrm{MnO}_3$. As the tolerance factor or equivalently the average ionic radius of the perovskite A site decreases from (La,Sr) to (Pr,Ca) through (Nd,Sr) or (La,Ca), orthorhombic distortion of the GdFeO_3 type increases, resulting in the decrease of the one-electron bandwidth W, as described in detail in Sec. III.C.1. With reduced transfer t_{ij} or W, other electronic instabilities, such as Jahn-Teller-type electron-lattice coupling, charge/orbital-ordering, and antiferromagnetic superexchange interactions, may become important and compete with the ferromagnetic double-exchange interaction. In fact, such a competition produces a number of intriguing magnetoresistive and magnetostructural phenomena, some of which will be introduced later in this section.

The compound $\mathrm{La}_{1-x}\mathrm{Sr}_x\mathrm{MnO}_3$ is the most canonical double-exchange system with the maximal one-electron bandwidth W. The parent compound LaMnO_3, with the $t_{2g}^3 e_g^1$ configuration of the Mn^{3+} ion, shows the ordering of the two e_g orbitals, $d_{3x^2-r^2}$ and $d_{3y^2-r^2}$, alternating from site to site on the (001) plane, in an "antiferro-

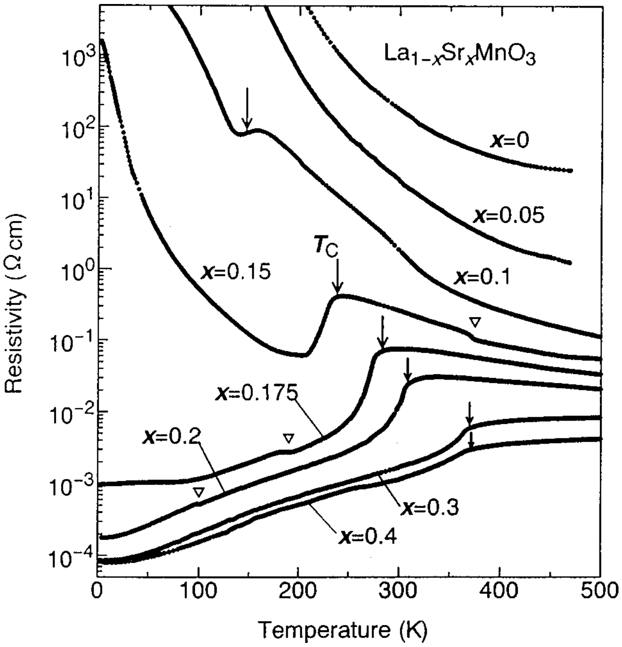

FIG. 192. Temperature dependence of resisitivity in crystals of $\mathrm{La}_{1-x}\mathrm{Sr}_x\mathrm{MnO}_3$ (Urushibara *et al.*, 1995): Arrows, the critical temperature for the ferromagnetic transition; triangles, critical temperature for the structural (rhombohedral-orthorhombic) transition.

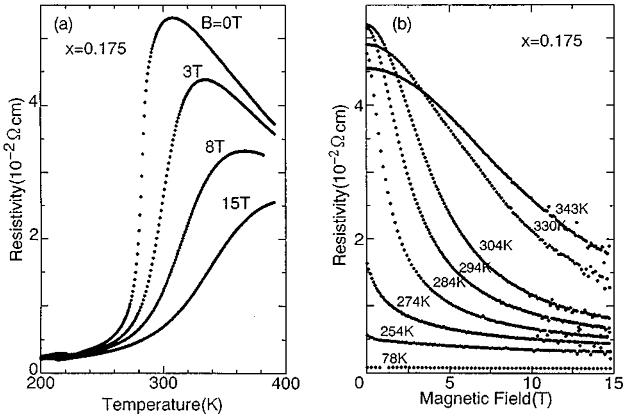

FIG. 193. Magnetic-field effect on the resistivity of a $\mathrm{La}_{1-x}\mathrm{Sr}_x\mathrm{MnO}_3$ ($x=0.175$) crystal (Tokura *et al.*, 1994): (a) T dependence of resistivity; (b) isothermal magnetoresistance.

orbital" fashion, as was discussed in Sec. II.H.1. This orbital ordering is accompanied by *collective* Jahn-Teller distortions (Kanamori, 1959). Such an orbital ordering produces ferromagnetic spin ordering within the (001) plane and antiferromagnetic coupling along the c-axis [A-type ordering in Fig. 38(c)]. Anisotropic dispersion of spin-wave excitations in LaMnO_3 was observed by single-crystal neutron scattering where the dispersion in the (001) plane was ferromagnetic while that alone in the (001) axis was antiferromagnetic (Hirota *et al.*, 1996).

The LaMnO_3 undergoes a phase transition to the spin-canted phase for $x<0.15$ (Kawano *et al.*, 1996), although for $x>0.10$ the spin-ordered phase is almost ferromagnetic. With further doping, a ferromagnetic phase appears below T_C which steeply increases with x up to 0.3 and then saturates. Figure 192 shows the temperature dependence of the resisitivity in crystals of $\mathrm{La}_{1-x}\mathrm{Sr}_x\mathrm{MnO}_3$ (Urushibara *et al.*, 1995). Arrows in the figure indicate the ferromagnetic transition temperature T_C. The ferromagnetic insulating (FI) phase is present in a fairly narrow x region ($x=0.10$–0.17), in which the double-exchange carrier is subject to (Anderson) localization but can still mediate the ferromagnetic interaction between neighboring sites and realize the ferromagnetic state in a bond-percolation manner. Around $x=1/8$, a possible ordering of polarons was observed in a single-crystal neutron-diffraction study (Y. Yamada *et al.*, 1996). Furthermore, the orthorhombic-to-rhombohedral structural transition also couples with the magnetic transition around $x=0.17$, giving rise to a unique magnetostructural transition or switching of the crystal structure upon application of an external magnetic field, as reported by Asamitsu *et al.* (1995, 1996). Various structual phase changes manifest themselves in anomalous resistivity curves, as indicated by triangles in Fig. 192. The possibility of phase separation in a simple double-exchange model was also examined theoretically by Yunoki *et al.* (1998).

The magnetic-field effect on the resistivity is shown in Fig. 193 for an $x=0.175$ crystal (Tokura, Urushibara, *et al.*, 1994; Urushibara *et al.*, 1995). The magnetic field greatly reduces the resistivity near T_C by shifting the resistivity maximum to a higher temperature due to suppression of the spin-scattering of e_g-state carriers. The change in resistivity appears to be scaled with the change in the magnetization of the system if the magnetization is small. Figure 194 shows the isothermal magnetoresistance near and above T_C as well as the temperature variation of the resistivity as a function of normalized magnetization, $m(T)\equiv M/M_s$ (where M_s is the saturation magnetization, about $3.8\mu_B$), for $\mathrm{La}_{1-x}\mathrm{Sr}_x\mathrm{MnO}_3$ ($x=0.175$). The good scaling of the magnetoresistance curves with $m(T)$ in the paramagnetic state as a function of the ferromagnetic magnetization indicates that the change in resistivity on the present scale is governed by temperature- or magnetic-field-dependent spin scattering of the e_g-state carriers. Solid lines in the figure represent the result calculated by Furukawa (1995a, 1995b, 1996), who applied the dynamic mean-field approximation, that is, the infinite-dimensional approach discussed in Sec. II.C.6, to the double-exchange model of Eqs. (2.9a)–(2.9c) with an additional approximation for the t_{2g} local spin, namely, a classical treatment in the limit $S=\infty$. In this limit, the t_{2g} spins provide as an external magnetic field in which one can solve for the dynamics of the e_g electrons are described in infinite dimensions. Although the spatial intersite correlations and the Coulomb repulsion effect of the e_g electrons responsible for the Mott insulator are ignored, this approximation improves upon the Hartree-Fock-type treatment of Kubo and Ohata by taking account of dynamic fluctuations. The result for $J_H/W=4$ well reproduces the experimental results, confirming that the double-exchange mechanism is a primary source

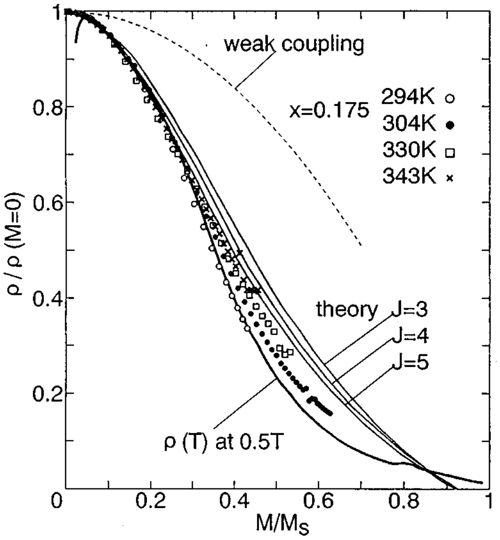

FIG. 194. Isothermal magnetoresistance near and above T_c as well as temperature variation of resistivity as a function of normalized magnetization, $m(T) \equiv M/M_s$ (where M_s is the saturation magnetization, about $3.8\mu_B$), for $La_{1-x}Sr_xMnO_3$ at $x=0.175$ (Tokura *et al.*, 1994): solid line, calculated results by the mean-field approach (Furukawa, 1995a); dashed line, the $J \rightarrow 0$ (weak-coupling) limit. Here J is the Hund's-rule coupling energy normalized by the bandwidth.

of the observed large negative magnetoresistance as well as of the temperature dependence of the resistivity around T_C.

However, fluctuations around the Curie temperature as well as the strongly incoherent character of the charge dynamics even at low temperatures, discussed below, cannot be well accounted for in the $d=\infty$ approach within single-orbital and rigid lattice systems. A controversial issue is the semiconducting or insulating behavior above T_C in the rather low-x region, e.g., $x=0.15-0.20$ for $La_{1-x}Sr_xMnO_3$, as shown in Fig. 192, or in a wider x region for narrower-W systems such as $La_{1-x}Ca_xMnO_3$ [see Fig. 191 where the ferromagnetic metallic phase is very limited (Schiffer *et al.*, 1995)]. In such a region of x, the negative magnetoresistance effect is most pronounced around T_C and hence the origin of the semiconducting transport is of great interest. Millis *et al.* (1995) pointed out that the resistivity of the low-doped crystals above T_C is too high to be interpreted in terms of the simple double-exchange model and ascribed its origin to a dynamic Jahn-Teller distortion. Static and coherent Jahn-Teller distortions disappear above $x=0.1$ in $La_{1-x}Sr_xMnO_3$, judging from the crystal structural phase changes between orthorhombic forms (Kawano *et al.*, 1996). However, Jahn-Teller coupling energy is large (of order 1 eV), and the distortion should remain finite when carrier itinerancy is reduced by disordered spin configurations above T_C. Therefore the mean amplitude of the Jahn-Teller distortion is critically reduced as the temperature is lowered below T_C. This idea was examined theoretically by Millis *et al.* (1996) in a classical approximation of a Jahn-Teller fluctuation. Millis *et al.* solved the double-exchange model with an orbital degeneracy in the limit $d=\infty$ by taking account of the coupling to dynamic but classical local lattice distortions. From this treatment an enhancement of the resistivity around T_C with suppressions both above and below it is obtained, in agreement with the experimental results. In fact, the presence of a dynamic Jahn-Teller distortion has been supported indirectly in some experiments, in particular for the narrower-bandwith system $La_{1-x}Ca_xMnO_3$ (Dai *et al.*, 1996).

Another possible origin of the increased resistivity near and above T_C as well as of the effective suppression of resistivity by an external magnetic field is Anderson localization of the double-exchange carriers arising from the random potential which is inevitably present in the solid solution system (Varma, 1996), or to antiferromagnetic fluctuations which compete with the double-exchange interaction (Kataoka, 1996). One of the important issues relating to all these instabilities is how we take into account the orbital degrees of freedom of the e_g-state electrons and their possibly strong intersite correlation or coupling to the lattice degrees of freedom for metals near the Mott insulator phase. In the Mott insulating phase, antiferromagnetic order, orbital order, and Jahn-Teller distortions are all present, while the primary origin of the insulating phase is the strong-correlation effect due to a charge gap of the order of 1 eV. Therefore the metallic phase near this insulator is under the critical fluctuation of the Mott transition even when the saturated ferromagnetic moment appears. Strong fluctuations toward orbital, spin, and Jahn-Teller ordering have to be considered. The importance of orbital degeneracy was stressed in studies in infinite dimensions (Rozenberg, 1996b) and in the slave-boson approximation (Frésard and Kotliar, 1997). In particular, the former emphasized the proximity of the Mott insulating phase to the experimentally observed ferromagnetic metal phase within the treatment in $d=\infty$.

Strong on-site coupling betweeen the e_g-electron spin and t_{2g} local spin and the resultant critical dependence of the electronic structure on spin polarization shows up in the temperature variation of the optical conductivity spectra (Okimoto *et al.*, 1995a, 1997). We show in Fig. 195 the temperature dependence of the optical conductivity spectrum for a $La_{1-x}Sr_xMnO_3(x=0.175)$ crystal (Okimoto *et al.*, 1995a). At high temperatures near and above T_C, the spectrum is characterized by an interband-like transition centered on 0.9 eV, while at low enough temperatures it shows an intraband-like transition. The spectral weight appears to be transferred from interband to intraband region with decrease of temperature. This unconventional temperature dependence of the optical conductivity spectrum below about 3 eV is ascribed to a change in the electronic structure of the e_g electrons with the spin polarization. The e_g conduction band is split into two bands due to J_H being larger than the bandwidth W (Furukawa, 1995a; Hamada *et al.*, 1995; Pickett and Singh, 1995). Above T_C, in the absence of net spin polarization, the up-spin and down-spin bands overlap, with identical density-of-states profiles and equal populations. For $T \ll T_C$, however,

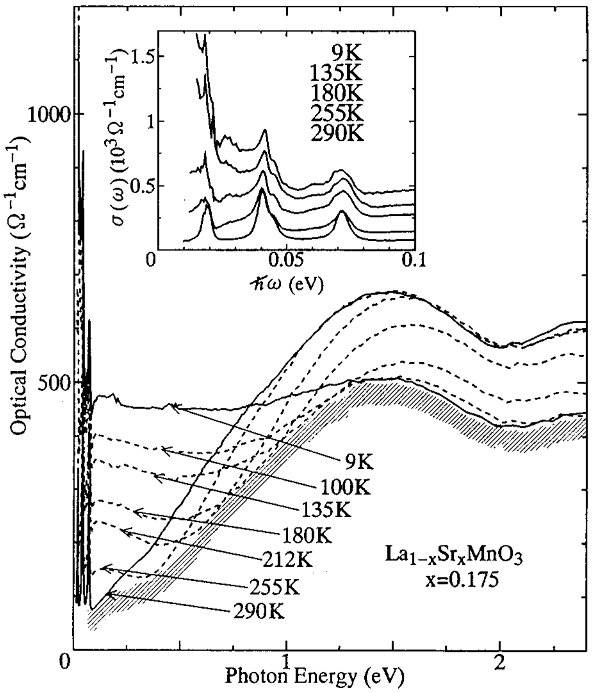

FIG. 195. Temperature dependence of the optical conductivity spectra of a $La_{1-x}Sr_xMnO_3$ ($x=0.15$) crystal (Okimoto *et al.*, 1995a). The hatched curve represents the temperature-independent part mainly arising from $2p$-$3d$ interband transitions. The inset shows magnified spectra in the low-energy region.

the only up-spin band is filled with saturated (100%) polarization, as shown in the inset. (This situation is in contrast with the case of conventional ferromagnetic transition metals; for example, in Ni metal the exchange splitting of the conduction band is incomplete and the maximum spin polarization of the conduction electrons is only 11%.) In accordance with such a sensitive dependence of electronic structure on the spin-polarization, low-energy optical conductivity spectra are expected to show a drastic change over the energy scale of J_H. The excitation band around 1.7 eV observed at higher temperatures corresponds to an interband transition between the exchange-split conduction bands, while the lower-energy excitation observed at low temperatures is assigned to an intraband excitation within the up-spin band. Thus the maximum of the interband transition should correspond to the exchange splitting of the conduction band or to SJ_H (where $S=3/2$ is the magnitude of t_{2g} local spins) which is about 1.7 eV for $La_{1-x}Sr_xMnO_3$ at $x=0.175$. The observed value is in accordance with an estimate ($SJ_H \sim 2$ eV) obtained by photoemission (Saitoh, Bocquet, *et al.*, 1995b; Park, Chen, *et al.*, 1996) and other optical spectroscopies (Arima and Tokura, 1995). On the other hand, a similar analysis of the spectrum for a $La_{1-x}Sr_xMnO_3$ ($x=0.3$) crystal (Okimoto *et al.*, 1997) gives a small value, about 0.9 eV, indicating that the apparent value is dependent on the doping level x. One plausible reason for this is that the oxygen $2p$ hole character of the doped carrier increases with x and hence effectively reduces the on-site exchange coupling originating from the $3d$ Hund's-rule coupling (Okimoto *et al.*, 1997).

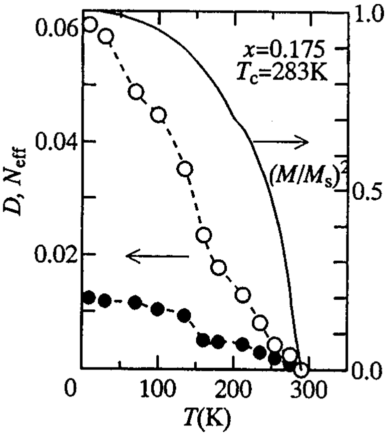

FIG. 196. Temperature dependence for intraband excitations: closed circles, dependence of the Drude weight D; open circles, dependence of the total low-energy spectral weight N_{eff} (Okimoto *et al.*, 1995a, 1997). The change in the square of the magnetization $(M/M_s)^2$ (where M_s is the saturation magnetization) is about $3.8\mu_B$.

It is worth pointing out here some puzzling features of the ferromagnetic metallic state at low temperatures. From the perfect spin polarization in the metallic ground state, we might expect the simplest spinless (perfectly spin-polarized) Fermi-liquid behavior. However, the optical conductivity spectra at low temperatures are far from the simple Drude type: As an example, a low-energy spectrum of the optical conductivity is shown in the inset of Fig. 195 for the ferromagnetic ground state (taken at 9 K) of a barely metallic $La_{1-x}Sr_xMnO_3$ ($x=0.175$) crystal. The coherent contribution is present only in the far-infrared region, say below 20 meV, as a sharp peak centered at zero energy, while most of the low-energy spectral weight is dominated by the slowly ω-dependent incoherent contribution. With decreasing temperatures these low-energy spectral weights in total are transferred from the aforementioned interband transitions between the exchange-split bands. The main panel of Fig. 196 shows the temperature dependence of the Drude weight D and of the total low-energy spectral weight N_{eff} for intraband excitations (Okimoto *et al.*, 1995a, 1997). The N_{eff}, keeps on changing, even in the low-temperature regions, say below 50 K, implying the presence of a persistent carrier-scattering mechanism even in the almost fully spin-polarized state. This is in contradiction with the expectation of the simple double-exchange model because $N_{eff} \sim D$ should be scaled by M^2 in the treatment by Kubo and Ohata (1972) as well as in that by Furukawa (1995a).

Importantly, the Drude weight D (i.e., the spectral weight of the coherent contribution) also increases with decrease of temperature, but remains about 1/5 of the total low-energy spectral weight. This means that carrier motion in the fully spin-polarized ground state is mostly incoherent. The ordinary Hall coefficient observed for the ferromagnetic metallic state in $La_{1-x}Sr_xMnO_3$ (x

$=0.175$) gives the carrier number $n\sim1$ hole/Mn site (Asamitsu and Tokura, 1998; Matl *et al.*, 1997). The nominal value of m^*/n is given as the inverse of D in terms of the Drude model, that is, about 80 in the present case, and hence m^*/m_0 should be as large as 80. This is, however, obviously in contradiction with the fairly small value ($\approx 3-5$ mJ/mol K^2) of the electronic specific-heat constant (Woodfield, 1997), which corresponds to the unrenormalized band mass between $2m_0$ and $3m_0$. The conventional Drude model is not applicable to the ferromagnetic metallic state in $La_{1-x}Sr_xMnO_3$ for small x, where carrier motion is mostly incoherent. The broad structure of $\sigma(\omega)$ is similar to many other transition-metal compounds near the Mott insulator, as we notice from the cases in other compounds discussed in this section, although Fig. 195 shows even broader and less structured features than the other cases. (Compare, for example, with Figs. 75, 86, 94, 102, 107, 114, 130, 136, 147, 161, 166, 175, 187, 210, 221, and 228.) In the case of $La_{1-x}Sr_xMnO_3$, discussed in Secs. II.H.1 and II.H.2, strong scattering in the fully spin-polarized ground state may be ascribed to the orbital degrees of freedom in the e_g state. Interband transitions within two e_g bands were examined as a possible origin of the broad structure at relatively large ω (Shiba, Shiina, and Takahashi, 1997). An exotic framework for the spin-charge separation in 3D was applied, and the flat structure of the band dispersion leading to an orbitally disordered state was claimed to be the origin of a broad incoherent response (Ishihara, Yamanaka, and Nagaosa, 1997). However, the weak mass renormalization observed in the small specific-heat coefficient γ is not easily explained when we simply assume an orbitally disordered state, because the entropy due to orbital degrees of freedom would remain large at low temperatures in the orbital disordered phase, as discussed in the case of $Y_{1-x}Ca_xTiO_3$ in Sec. IV.B.1. In any case, a crucial puzzling feature is the extremely small Drude weight, with the nominal effective mass of $m^*/m_0\sim80$. We need further studies, both experimental and theoretical, to elucidate this issue. Recently, the incoherent charge dynamics of $La_{1-x}A_xMnO_3$ with small Drude weight and small γ were derived from the scaling theory by anisotropic hyperscaling generated from the criticality of the orbital fluctuation of two e_g orbitals (Imada, 1998). This approach, derived from strongly wave-number-dependent renormalization, appears to be important for an understanding of the universally observed tendency towards incoherence in a variety of d-electron and other compounds near the Mott insulator.

A large-energy-scale reshuffle like that observed in the temperature and magnetic-field dependence of the optical spectra near T_C (Kaplan *et al.*, 1996) can also be due to a change of the Jahn-Teller coupling, which forms an intense mid-infrared polaronic band (Kaplan *et al.*, 1996; Millis *et al.*, 1996; Okimoto *et al.*, 1997) whose spectral weight and energy positions vary with temperature and applied magnetic field.

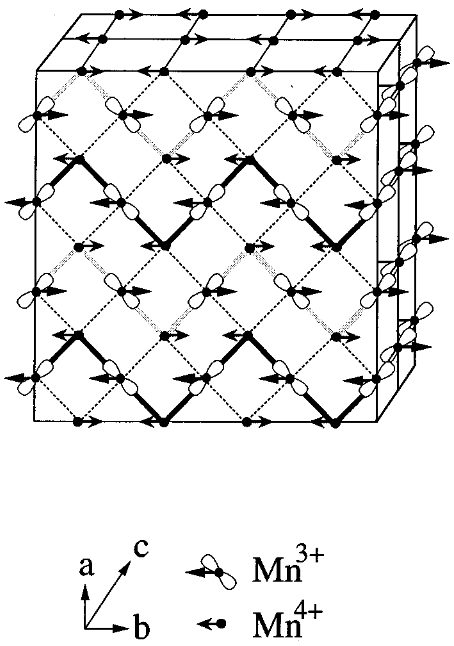

FIG. 197. CE-type charge ordering with orbital and antiferromagnetic spin ordering.

Let us come back to the electronic phase diagram shown in Fig. 191. With a decrease of W, other instabilities competing with the double-exchange interaction complicate the phase diagram. In particular, when the doping x is close to the commensurate value $x=1/2$, a charge-ordering instability occasionally shows up. In the case of $Nd_{1-x}Sr_xMnO_3$ [Fig. 191(b)], the ferromagnetic metallic phase emerges for $x>0.3$, yet in the immediate vicinity of $x=1/2$ the ferromagnetic state changes into a charge-ordered insulating (COI) state with decrease of temperature below $T_{CO}=160$ K. This charge-ordered insulating state accompanies a concomitant orbital and antiferromagnetic spin ordering of the CE type (Goodenough, 1955; Wollan and Koehler, 1955; Jirak *et al.*, 1985; Yoshizawa *et al.*, 1995, 1997) as illustrated in Fig. 197. The nominal Mn^{3+} and Mn^{4+} species with 1:1 ratio show the real-space ordering in the (001) plane of the orthorhombic lattice (P_{bnm}), while the e_g orbital shows the 1×2 superlattice on the same (001) plane. Reflecting such an orbital ordering, the spin ordering shows a complicated sublattice structure extending over a larger unit cell.

Such a concomitant charge and spin ordering is also seen in other transition-metal oxides, as described in Sec. IV.G, yet the most notable feature in the perovskite manganites is that the charge-ordered state can be relaxed to a ferromagnetic state by application of an external magnetic field. Figure 198 displays the temperature dependence of the resistivity under various magnetic fields in $Nd_{1-x}Sr_xMnO_3$ ($x=0.5$) (Kuwahara *et al.*, 1995; Tokura, Kuwahara, *et al.*, 1996a). The field-dependent change in resistivity around $T_C(=250\,\mathrm{K})$ represents the conventional magnetoresistance effect, as described above. A much more notable feature is that the MIT due to the charge ordering transition around 160 K at zero field, which accompanies the thermal hysteresis characteristic of a first-order phase transition, is shifted to the lower-temperature side, and above $7T$ the

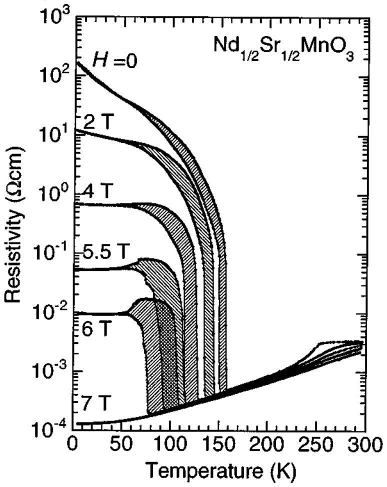

FIG. 198. Temperature dependence of the resistivity under various magnetic fields in $Nd_{1-x}Sr_xMnO_3$ ($x=0.5$). From Kuwahara *et al.*, 1995, 1997.

crystal eventually remains metallic down to the lowest temperature without a trace of a charge-ordered phase. The metal-insulator phase diagram derived in the plane of H (magnetic field) and T (temperature) shows a large hysteretic region arising from the metastability of the ferromagnetic metal and charge-ordered insulating states at low temperatures in the course of the first-order phase transition (Kuwahara *et al.*, 1995; Tokura, Kuwahara, *et al.*, 1996a). A quite similar behavior was observed for $La_{1-x}Ca_xMnO_3$ with $x\sim0.5$ (Schiffer *et al.*, 1995).

Increasing x beyond 0.5 for $R_{1-x}Sr_xMnO_3$ ($R=$La, Pr, and Nd; $x=0.5$–0.6) seems to produce a unique ferromagnetic state, which is an A-type layered antiferromagnet like $LaMnO_3$ but is conducting within the ferromagnetic basal plane (Kawano *et al.*, 1997). The resultant confinement of the spin-polarized carriers within the ferromagnetic sheets gives rise to large anisotropy in the resistivity, in spite of the nearly cubic lattice structure (Kuwahara *et al.*, 1998). When x is increased further above 0.6, e.g., in $La_{1-x}Ca_xMnO_3$, a new pattern of charge ordering different from the CE type is observed (Chen, Cheong, and Hwang, 1997).

The charge-ordered insulating state appears to be extended over a wider doping region (x) when W is further narrowed, as can be seen for $x>0.3$ in the case of $Pr_{1-x}Ca_xMnO_3$ [Fig. 191(c); Jirak *et al.*, 1980, 1985]. The charge and orbital ordering take place at first in the same commensurate pattern, as shown in Fig. 197 below $T_{CO}=220$–250 K when $x>0.3$. The onset of spin ordering emerges at a lower temperature than charge ordering. The crystal at $x=0.5$ undergoes a spin-collinear antiferromagnetic transition of the CE type at 160 K. With deviation of x from 0.5, the coupling of the spins along the c axis becomes ferromagnetic in the antiferromagnetically ordered state, and then the spin-canted phase arises in the lower temperature region. The spin-canting transition temperature (T_{CA}) and the spin-canting angle tend to increase with deviation of x from 0.5 (see Fig. 191). These features were interpreted in terms of the role of the double-exchange electrons extending along the c-axis direction, i.e., the charged-stripe direction (Jirak *et al.*, 1985).

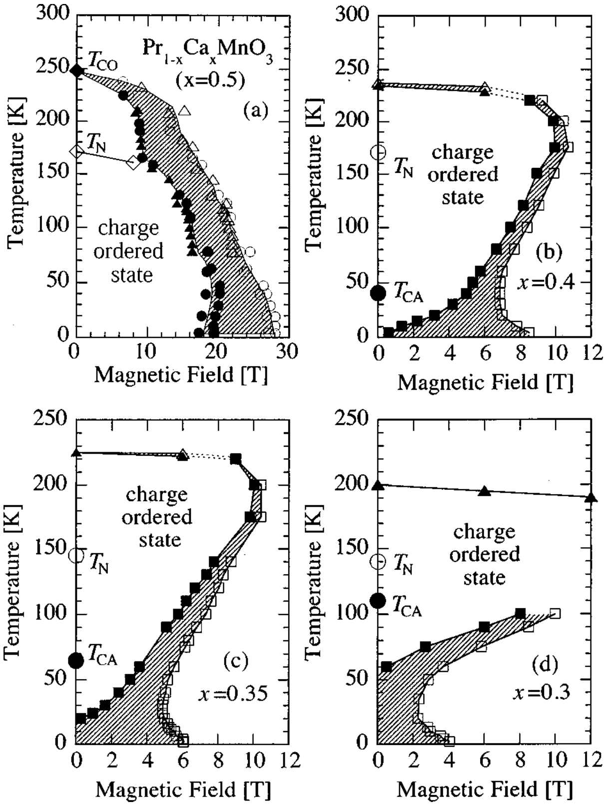

FIG. 199. MI phase diagrams for $Pr_{1-x}Ca_xMnO_3$ ($x=0.3$–0.5) in the H-T plane (Tomioka *et al.*, 1996, Tokunaga *et al.*, 1997).

The metal-insulator phase diagram for $Pr_{1-x}Ca_xMnO_3$ ($x=0.3$–0.5) is shown in Fig. 199 in the H-T plane (Tomioka *et al.*, 1996; Tokunaga *et al.*, 1998). The ferromagnetic metal/charge-ordered insulator phase boundaries, accompanied by a metamagnetic change in the magnetization, were determined by studies of isothermal magnetoresistance in which a change in resistivity of several orders of magnitude was observed (Tomioka *et al.* 1995, 1996). A larger external field is needed to destroy the charge-ordered insulating state in $Pa_{1-x}Ca_xMnO_3$ ($x=0.5$) crystals than in the corresponding Nd-Sr compound (see Fig. 198) with a larger W. The field hysteresis (hatched region) expands at low temperatures, which represents the supercooling (superheating) phenomena characteristic of a first-order phase transition. With deviation of x from 0.5, however, the ferromagnetic metal/charge-ordered insulator phase boundary is shifted to the low-magnetic-field side, in particular at low temperatures, reflecting perhaps a spin-canting tendency. The reentrant behavior of the charge-ordered transition, e.g., in the field-cooled run at $x<0.5$, may arise from large entropy in the discommensurate charge-ordered state. In particular, for $x=0.3$ the field-induced transition from ferromagnetic metal to charge-ordered insulator in the isothermal process becomes irreversible below 40 K, accompanying a persistent change of resistivity by more than 10 orders of magnitude.

It is worth noting that the irreversible transition of the metastable charge-ordered insulator state in $\mathrm{Pr}_{1-x}\mathrm{Ca}_x\mathrm{MnO}_3$ ($x=0.3$) crystals can be triggered not only by an external magnetic field or pressure (Tokura, Tomioka, *et al.*, 1996b; Moritomo *et al.*, 1997) but also by x-ray (Kiryukhin *et al.*, 1997) and light irradiations (Miyano *et al.*, 1997) and by an electric field (Asamitsu, Tomioka, *et al.*, 1997). These field- or photo-induced transitions have potential applications in new magnetoelectronic devices.

The electronic structure parameters for $R\mathrm{MnO}_3$ and $A\mathrm{MnO}_3$ have been derived from configuration-interaction cluster-model analysis of photoemission spectra (Saitoh, Bocquet, *et al.*, 1995b; Chainani, Mathew, and Sarma, 1993) and from first-principles band-structure calculations (Satpathy, Popović, and Vukajlović, 1996). The deduced values for LaMnO_3 are $U\sim 7$ eV and $\Delta\sim 4.5$ eV, which characterize $R\mathrm{MnO}_3$ as a charge-transfer-type insulator and hence mean that doped holes enter primarily oxygen p-like orbitals. The doped p hole is coupled with the high-spin ($S=2$) Mn d^4 ($t_{2g\uparrow}^3 e_{g\uparrow}$) configuration antiferromagnetically to form a $d^4\underline{L}$ ($S=3/2$) object (Saitoh, Bocquet, *et al.*, 1995b), analogously to the Zhang-Rice singlet ($d^9\underline{L}$ with $S=0$) in the high-T_c cuprates. The p hole has e_g symmetry with respect to the Mn site, and therefore the orbital and spin symmetry of the $d^4\underline{L}$ state is identical to the high-spin Mn d^3 ($t_{2g\uparrow}^3$) configuration. This justifies the use of an effective degenerate Hubbard model for the Mn e_g bands (Ishihara, Inoue, and Maekawa, 1997) instead of the full d-p multiband Hubbard model (Mizokawa and Fujimori, 1995), as long as values for the effective parameters are properly chosen. The exchange interaction between the localized $t_{2g\uparrow}^3$ spin and the itinerant e_g electron is estimated to be $J_H^{eff}\sim 1$ eV. The Jahn-Teller splitting of the e_g orbital is rather difficult to estimate empirically because not only the change in the p-d transfer integrals but also the change in the Madelung potential caused by lattice distortion contributes to this splitting. The crystal-field splitting is large enough to open a band gap in the LSDA calculation. In SrMnO_3, the $e_{g\uparrow}$ band is empty and the highest occupied states are $t_{2g\uparrow}$-like.

Jahn-Teller distortion and orbital ordering, which play essential roles in the physical properties of $R_{1-x}A_x\mathrm{MnO}_3$, are well described by Hartree-Fock band-structure calculations on the d-p multiband Hubbard model, where the parameters derived from photoemission studies are used (Mizokawa and Fujimori, 1995). The LDA+U method is also successful because the self-interaction has been eliminated by applying Hartree-Fock-type corrections to the LDA potential (Satpathy, Popović, and Vukajlović, 1996). The LSDA is successful in predicting the insulating nature of LaMnO_3 if the Jahn-Teller distortion is taken into account (Solovyev, Hamada, and Terakura, 1996a). In the LSDA calculations, however, the band gap is underestimated, whereas in the Hartree-Fock and LDA+U calculations the band gap already exists in a hypothetically cubic LaMnO_3. Starting from the Hartree-Fock or LDA+U band structure, inclusion of correlation effects through the self-energy correction reduces the band gap, resulting in better agreement with experiment (Mizokawa and Fujimori, 1996b). The charge-ordering phenomena in $R_{1-x}A_x\mathrm{MnO}_3$ have been studied theoretically using the LAD+U and Hartree-Fock methods. The correct CE-type magnetic structure with charge ordering, observed for $\mathrm{Pr}_{0.5}\mathrm{Ca}_{0.5}\mathrm{MnO}_3$, can indeed be reproduced in these calculations in the presence of Jahn-Teller distortion (Anisimov *et al.*, 1997; Mizokawa and Fujimori, 1997). However, different types of ordered structures (CE-type, antiferromagnetic, A-type antiferromagnetic, and ferromagnetic) are nearly degenerate in energy, and therefore it is a subtle problem which of these structures is realized under which conditions. There has also been controversy as to whether the Jahn-Teller distortion is necessary for the correct prediction of magnetically and orbitally ordered structures. Although band-structure calculations have shown that the Jahn-Teller distortion is necessary, mean-field solutions (Ishihara, Inoue, and Maekawa, 1997; Maezono *et al.*, 1998; Shiina, Nishitani, and Shiba, 1997) as well as exact diagonalization studies of small clusters (with $2\times 2\times 2$ Mn ions; Koshibae *et al.*, 1997) have also shown that correct spin-orbital structures can be obtained by including correlation effects without the lattice distortion for a certain parameter range.

The changes in electronic structure with composition in the $\mathrm{La}_{1-x}\mathrm{Sr}_x\mathrm{MnO}_3$ systems can be seen in Fig. 200. As holes are doped into LaMnO_3, spectral weight transfer occurs from the occupied $e_{g\uparrow}$ band, whose peak is located $\sim$1.5 eV below E_F, to the unoccupied $e_{g\uparrow}$ band. The spectral intensity at E_F remains low for all x, however. Therefore it can be said that the overall $e_{g\uparrow}$ spectral distribution exhibits a wide ($\sim$1 eV) pseudogap at E_F. The intensity at E_F is an order of magnitude smaller than in another ferromagnetic metal, $\mathrm{La}_{1-x}\mathrm{Sr}_x\mathrm{CoO}_3$, indicating an unusually small quasiparticle spectral weight Z. This nonrigid band behavior is qualitatively similar to that of $R_{1-x}A_x\mathrm{TiO}_3$, although the spectral intensity at E_F is much weaker in the Mn compounds. Even more unusual is the strong temperature dependence of the intensity at E_F (Sarma, Shanthi, *et al.*, 1996), as shown in Fig. 201, a behavior that has not been seen in any other metals so far. The E_F intensity decreases with temperature and almost disappears somewhat below T_C. Essentially the same behavior was observed for $\mathrm{La}_{1-x}\mathrm{Ca}_x\mathrm{MnO}_3$ (Park, Chen, *et al.*, 1996). The extremely low intensity at E_F ($m_k/m_b\ll 1$ and hence $Z\ll 1$ because the effective mass m^* is not so great) may correspond to the extremely small Drude weight (Okimoto *et al.*, 1997). The strong deviation of the spectral function from that of the Hubbard model, for which hole doping creates a rather intense peak around E_F, indicates that interactions neglected in the Hubbard model are probably important. A possible origin is the electron-phonon interaction associated with the local, dynamic Jahn-Teller distortion in doped com-

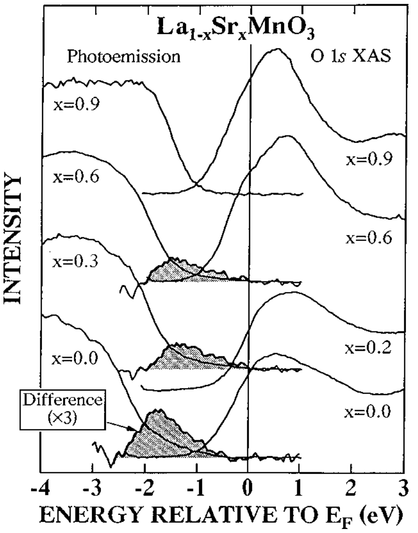

FIG. 200. Photoemission and oxygen 1s core-level x-ray absorption spectra of $La_{1-x}Sr_xMnO_3$ near E_F as a function of x (Saitoh, Bocquet, *et al.*, 1995b). The shaded area represents the occupied part of the $e_{g\uparrow}$ component estimated as the difference from $SrMnO_3$.

pounds discussed above (Millis, 1996). Alternatively, another type of atomic displacement that is symmetric around the electron, as discussed for lightly doped d^0 systems such as $La_{1-x}Sr_xTiO_3$ with $x\sim1$ (Sec. IV.B.1), may produce a pseudogap over an energy range of ~1 eV.

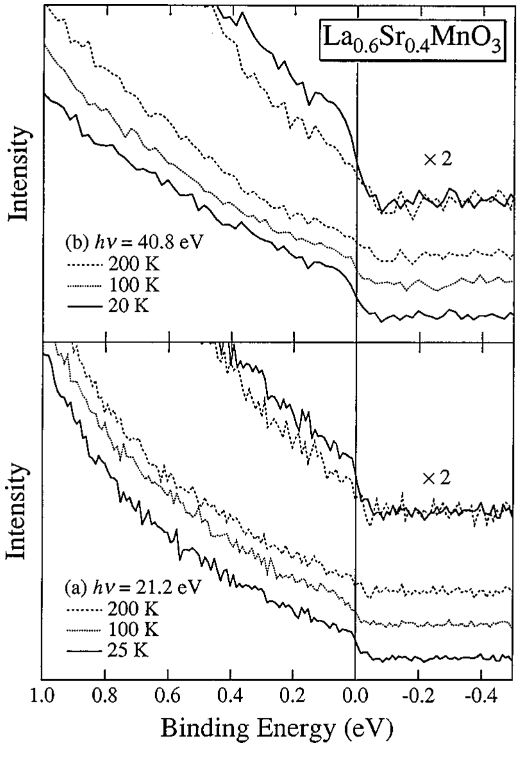

FIG. 201. Photoemission spectra of $La_{0.6}Sr_{0.4}MnO_3$ near E_F at different temperatures. From Sarma, Shanthi, *et al.*, 1996.

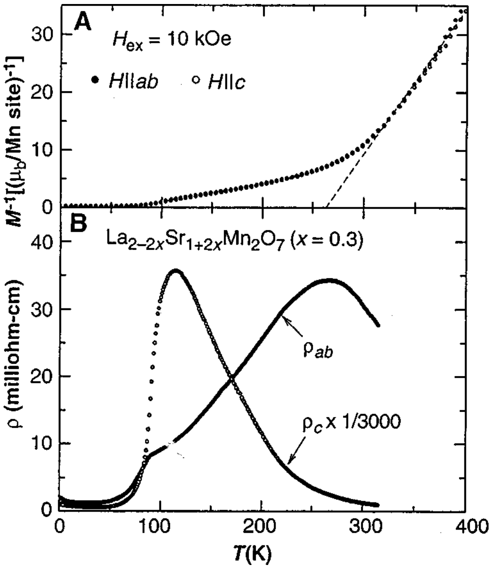

FIG. 202. Temperature dependence of in-plane resistivity (ρ_{ab}) and c-axis resistivity (ρ_c) as well as inverse of the magnetization for a $La_{2-x}Sr_{1+x}Mn_2O_7$ ($x=0.3$) crystal. From Kimura *et al.* 1996.

2. $La_{2-2x}Sr_{1+2x}Mn_2O_7$

The title compounds correspond to the $n=2$ layered perovskite structures (Ruddlesden-Popper series) (Fig. 66) with the MnO_2 bilayer in a repeated unit. Taking the Mn^{3+}-based $La_2Sr_1Mn_2O_7$ ($x=0$) as the parent Mott insulator, the composition x for $La_{2-2x}Sr_{1+2x}Mn_2O_7$ stands for the nominal hole number per Mn site. We show in Fig. 202 the temperature dependence of the in-plane resistivity (ρ_{ab}) and the c-axis resistivity (ρ_c) as well as the inverse of the magnetization for an $x=0.3$ single crystal (Kimura *et al.*, 1996). ρ_c shows a sharp maximum at $T^c_{max}\sim100$ K and a semiconducting behavior above T^c_{max}, with metallic-like behavior below T^c_{max}. Compared with the magnetization data, the steep drop of ρ_c below T^c_{max} has an intimate connection to the 3D spin ordering, where the weak antiferromagnetic interlayer coupling was confirmed by magnetization and neutron scattering studies (Kimura *et al.*, 1997; Perring *et al.*, 1998). By contrast, ρ_{ab} shows a broad maximum at $T^{ab}_{max}\sim270$ K, where the slope of inverse magnetization deviates from the Curie-Weiss law (a dotted line in Fig. 202). This implies that the in-plane 2D ferromagnetic correlation occurs for temperatures below T^{ab}_{max}, which is far above T^c_{max}. In between these two temperatures, the $x=0.3$ compound shows a 2D ferromagnetic metal behavior. This of course arises from the fact that the ferromagnetic interaction is mediated by hole motion, which is strongly confined within the MnO_2 bilayers.

The anisotropy of the resistivity ρ_c/ρ_{ab} is already as large as $\sim10^3$ at room temperature, and further increases with decrease of temperature, reaching as large a value as $\sim10^4$ at T^c_{max}. Below T_C, ρ_c steeply decreases with decreasing temperature. Such a change of the interplane charge dynamics from incoherent to coherent has rarely been encountered even among the highly aniso-

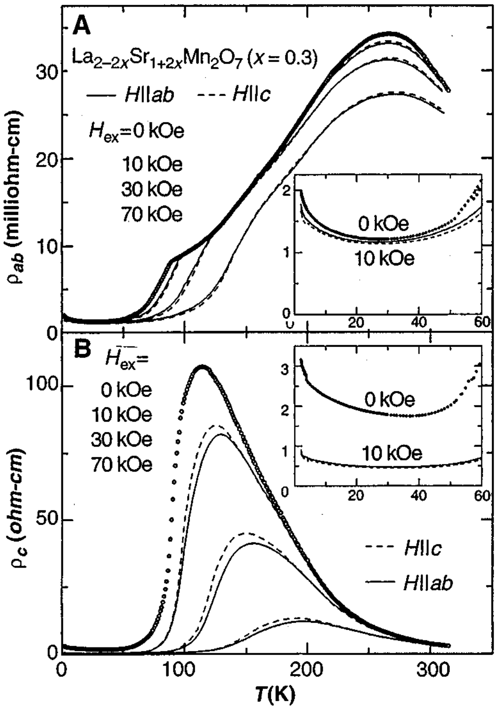

FIG. 203. Magnetic-field effect on ρ_{ab} and ρ_c for a $La_{2-x}Sr_{1+x}Mn_2O_7$ crystal with $x = 0.3$. From Kimura *et al.*, 1996.

tropic compounds, except for the high-T_c cuprates (see Sec. IV.C.) and Sr_2RuO_4 (see Sec. IV.H.).

In Fig. 203, the effect of the magnetic field on ρ_{ab} and ρ_c is shown for an $x = 0.3$ crystal (Kimura *et al.*, 1996). The magnetoresistance (MR) was found to depend weakly on the relative orientation of the field. The magnetoresistance for the in-plane component is enhanced in the vicinity of both T_{max}^{ab} and T_{max}^{c}, while for the interplane component T_{max}^{c} is apparently shifted to a higher temperature with a magnetic field, and the maximum resistivity value is remarkably suppressed. Another important feature is seen in anisotropic low-field magnetoresistance effects: Below T_{max}^{c}, the effect of magnetoresistance in ρ_c is appreciably large, even at $1T$, but saturated at higher fields. By contrast, the magnetoresistance in ρ_{ab} is much smaller than that in ρ_c.

The isothermal magnetoresistance curves (with application of a magnetic field along the c axis) are shown in Fig. 204 (Kimura *et al.*, 1996) for the in-plane and interplane components together with the magnetization curves at characteristic temperatures; around T_{max}^{ab} (273 K), T_{max}^{c} (100 K), and at a rather low temperature (4.2 K) with almost full spin polarization. Large magnetoresistance is observed for both components due to the enhanced in-plane and interplane ferromagnetic correlations at 273 K and more conspicuously at 100 K. In particular, the interplane magnetoresistance at 100 K is extremely large ($\rho_c(0)/\rho_c(H) \sim 10^{-4}$ at $5T$) due to the field-induced incoherent-coherent transition for c-axis charge transport at this temperature. In other words, magnetic 2D confinement of highly spin-polarized electrons (or holes) is realized due to uncorrelated interplane magnetization but can be removed by an external magnetic field.

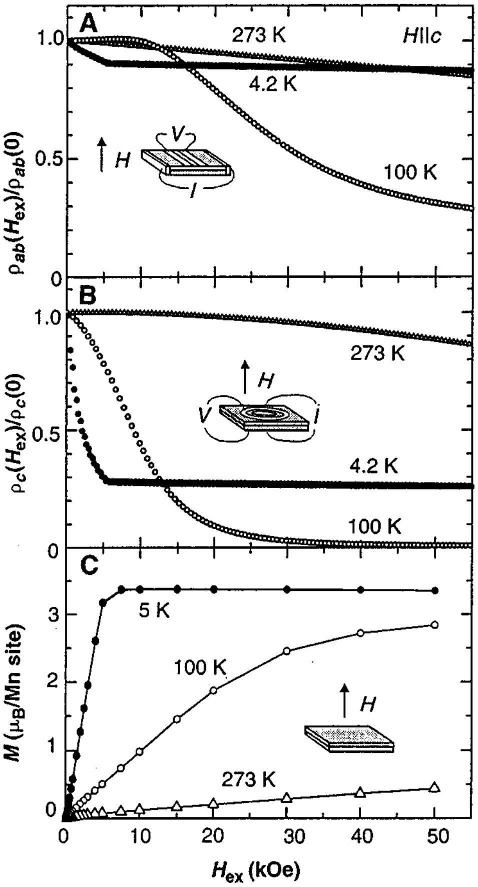

FIG. 204. Isothermal MR curves (with application of magnetic field along the c axis) for a $La_{2-x}Sr_{1+x}Mn_2O_7$ crystal with $x = 0.3$. From Kimura *et al.*, 1996.

In the low-temperature case at 4.2 K, ρ_c drastically decreases in the low-field region, in accordance with the magnetization process, and becomes constant when the magnetization saturates at an external field of about 0.5 T. Kimura *et al.* (1996) interpreted this behavior in terms of effects of interplane tunneling upon the magnetoresistance: Below T_{max}^{c}, the interplane antiferromagnetic correlation is established, producing many magnetic boundaries lying on the $(La,Sr)_2O_2$ layers (see Fig. 66). Such boundaries block interplane tunneling of spin-polarized electrons. By applying a magnetic field, however, one can increase the volume of the ferromagnetic domains and finally make a single domain with a field larger than the saturation field for magnetization, in which the carrier-blocking boundaries should disappear. It is worth noting that such a removal of the interlayer blocking domain boundary also affects the in-plane charge dynamics, as can be seen in the low-field magnetoresistance for the in-plane component (top panel of Fig. 204).

The charge-transport properties, including magnetoresistance characteristics in these bilayer manganites, are observed to be quite sensitive to the band-filling or hole-doping level, as in the aforementioned case of the

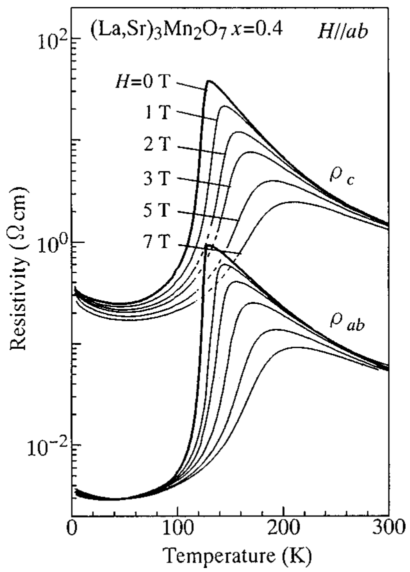

FIG. 205. Temperature dependence of ρ_{ab} and ρ_c for a $La_{2-x}Sr_{1+x}Mn_2O_7$ ($x=0.4$) crystal under various magnetic fields (applied perpendicular to the c axis). From Moritomo *et al.*, 1996.

pseudocubic perovskite manganites. Figure 205 shows the temperature dependence of ρ_{ab} and ρ_c for $La_{2-x}Sr_{1+x}Mn_2O_7$ ($x=0.4$) crystals under various magnetic fields (applied perpendicular to the c axis; Moritomo *et al.*, 1996). By contrast with the case of the $x=0.3$ crystal, both the in-plane and interplane resistivities show a semiconducting increase with decrease of temperature down to $T_C(=126\,\mathrm{K})$ and with activation energy of 30–40 meV, though the anisotropy ratio of the resistivity is still as large as 10^2. At around T_C ($=126\,\mathrm{K}$), both ρ_{ab} and ρ_c show a steep decrease by more than two orders of magnitude, showing a metallic behavior below T_C (but not below about 20 K due to some localization effect). By application of magnetic fields, the resistivity above T_C is appreciably suppressed, putting the resistivity maximum towards higher temperature.

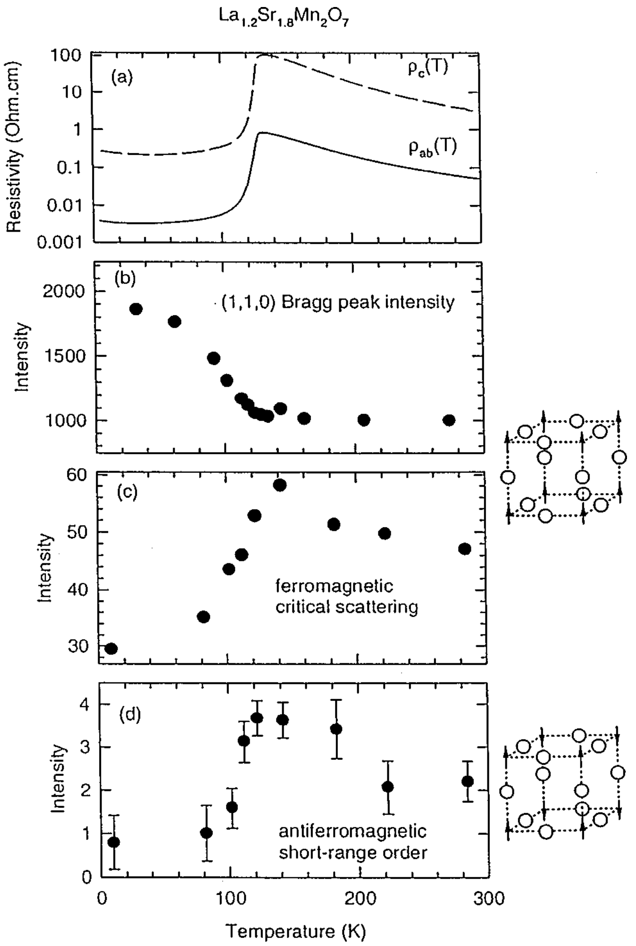

FIG. 206. Temperature dependence for a $La_{2-x}Sr_{1+x}Mn_2O_7$ ($x=0.4$) crystal of (a) resistivity; (b) the integrated intensity of the (110) Bragg peak; (c) ferromagnetic critical scattering; and (d) antiferromagnetic cluster scattering. From Perring *et al.*, 1997a.

An inelastic neutron-scattering study was performed (Perring *et al.*, 1997b) on an $x=0.4$ crystal. Figure 206 shows the temperature dependence of (a) the resistivity, (b) the integrated intensity of the (110) Bragg peak, (c) the ferromagnetic critical scattering, and (d) the antiferromagnetic cluster scattering. Due to growth in the magnetization below T_C, the (110) Bragg peak, which is also a nuclear reflection, increases in intensity as in the conventional ferromagnet. In accord with this, the ferromagnetic critical scattering displayed in Fig. 206, that is, the integrated intensity over an energy transfer range from $-5\,\mathrm{meV}$ to $+0.5\,\mathrm{meV}$ and over a momentum transfer range from 0.09 to $0.24\times(2\pi/a_0)$ along [110], is enhanced around T_C. This critical scattering disappears again below T_C, as it should. In addition to the above features expected for a conventional ferromagnet, Perring *et al.* (1997) found diffuse magnetic scattering that peaked at the zone boundary point (1/2,0,0). From an extensive survey of reciprocal space to characterize this peak and to find others, as well as from an analysis of momentum and energy transfer profiles, they concluded that this peak originated from the antiferromagnetic spin cluster depicted in Fig. 206(d), with a correlation length of about 9 Å and a lifetime of about 0.04 ps at 142 K, just above T_C. This diffuse scattering intensity, integrated over the energy-transfer range of $-5\,\mathrm{meV}$ to $+5\,\mathrm{meV}$ and momentum-transfer range 0.30 to 0.63 $(2\pi/a_0)$, as shown in Fig. 206, gradually increased with decreasing temperature down to T_C and then steeply decreased below T_C. The behavior was parallel to that of the ferromagnetic critical scattering shown in Fig. 206(c). Thus the paramagnetic state near T_C and just above it consisted of a slowly fluctuating mixture of ferro- and antiferromagnetic microdomains. The insulating behavior is perhaps due to the breaking of local symmetry by this anisotropic antiferromagnetic spin cluster and to the resultant localization effect. The magnetic field obviously suppresses carrier scattering by such an antiferromagnetic spin fluctuation, giving rise to the observed negative magnetoresistance of colossal magnitude (Fig. 205).

The above observation has significant implications for the origin of the colossal magnetoresistance (CMR) observed generally for doped manganites. As mentioned in the previous section, the scenario of local lattice distortions such as the dynamic Jahn-Teller distortion has been a favored potential source of colossal magnetoresistance in addition to the double-exchange mechanism. However, the orbital degree of freedom in the e_g state may give rise not only to Jahn-Teller electron-lattice coupling but also to strong and anisotropic antiferromagnetic fluctuations: The latter can arise from the orbital correlation between sites, as typically seen in the charge-exchange type charge-ordered state (see Sec. IV.F.1), and can compete with the double-exchange interaction. The anisotropic antiferromagnetic cluster above T_C for a $La_{2-x}Sr_{1+x}Mn_2O_7$ ($x=0.4$) crystal may also be a consequence of intersite orbital correlations. In fact, the static Jahn-Teller distortion, which is coherent along the c axis for the $x=0$ parent crystal, is minimal in such a heavily doped crystal as $x=0.4$: Typical bond length ratios at 300 K are Mn-O(1)/Mn-O(3)$\approx$1.001 and Mn-O(2)/Mn-O(3)$\approx$1.03, O(1),O(3),O(2), representing the inner and outer apex and equatorial oxygen, respectively (Mitchell *et al.*, 1997). However, the Jahn-Teller distortion was observed to increase in the low-temperature ferromagnetic-metallic phase (Mitchel *et al.*, 1997), implying the onset of orbital ordering at T_C.

The electronic structure of $La_{2-x}Sr_{1+x}Mn_2O_7$ was studied by angle-resolved photoemission spectroscopy by Dessau *et al.* (1998). Energy bands of $d_{3z^2-r^2}$ and $d_{x^2-y^2}$ character showed dispersions, consistent with the LDA band-structure calculation. Although the observed dispersions and Fermi-surface crossings were consistent with band-structure calculations, the spectral intensity was drastically reduced near E_F and there was practically no intensity as the bands crossed E_F (for the metallic $x=0.4$). Strong electron-phonon coupling (including Jahn-Teller-type coupling) was proposed as a possible origin of this very unusual behavior. The reduced intensity at E_F was also observed for 3D Mn oxides (Sec. IV.F.1), but was more dramatic here in that the spectral weight at E_F was totally suppressed in spite of the metallic conductivity.

G. Systems with transitions between metal and nonmagnetic insulators

1. FeSi

FeSi is a nonmagnetic insulator at low temperatures ($T\ll 500$ K). With increasing temperature, however, it gradually becomes a Curie-Weiss paramagnet (Benoit, 1955) with poor metallic conductivity at $T>500$ K (Wolfe *et al.*, 1965). In spite of the $\sim$500-K maximum in the magnetic susceptibility, no evidence for antiferromagnetic ordering has been found in neutron diffraction (Watanabe *et al.*, 1963), NMR, and Mössbauer (Wertheim *et al.*, 1965) studies. Because of its unusual magnetic and transport properties, FeSi has attracted much interest for many decades. Recently, Aeppli and Fisk (1992) pointed out the close similarity between the magnetic and transport properties of FeSi and those of Kondo insulators with rare-earth $4f$ or actinide $5f$ electrons, reviving interest in FeSi. Since then there has been controversy whether FeSi can be viewed as a d-electron Kondo insulator or not.

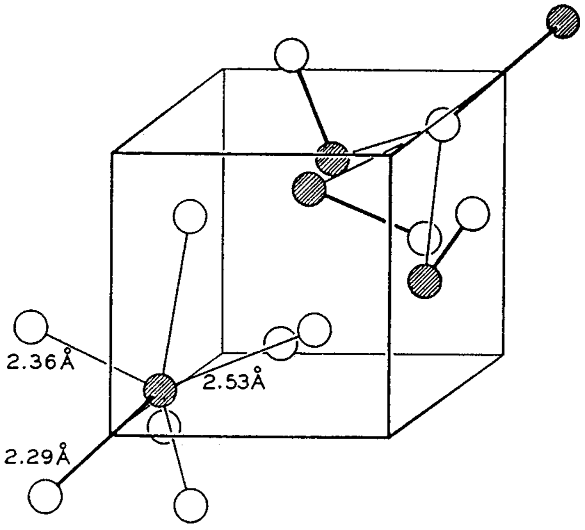

FIG. 207. Crystal structure of FeSi. From Jaccarino *et al.*, 1967.

FeSi crystallizes in a complicated cubic structure, shown in Fig. 207, in which the unit cell contains four molecules. The magnetic susceptibility, shown in Fig. 208, has been obtained and can be fitted with a Weiss temperature of $-(150-200)$ K and an effective moment of $2.6\pm 0.1\mu_B$/Fe. The crystal is semiconducting below $\sim$300 K and weakly metallic above it, as shown in Fig. 209 (Wolfe *et al.*, 1965). These data can be fitted to an activation law $\rho(T)\propto\exp(\Delta_{tr}/2kT)$ at relatively high temperatures (between $\sim$100 K and $\sim$150 K) with $\Delta_{tr}\simeq 550-700$ K, implying that the intrinsic gap is $\sim$50–60 meV. However, this temperature range may be too small to justify the activation fit; at lower temperatures (below a few tens of K), the resistivity has been fitted to power laws (see Fig. 209) or 3D variable-range hopping within Anderson-localized states, $\rho(T)\propto\exp(T_0/T)^{1/4}$ (S. Takagi *et al.*, 1981; Hunt *et al.*, 1994). FeSi shows a gigantic thermoelectric power of positive sign below $\sim$150 K (with a maximum of $S\sim 250-480$ μV/K at $\sim$50 K); it becomes negative above $\sim$150 K and then positive above $\sim$300 K (Wolfe *et al.*, 1965). Because the Hall coefficient is negative and increases with decreasing temperature (Kaidanov *et al.*, 1968), the semiconducting charge carriers must be predominantly n type. The different signs of the Hall coefficient and the Seebeck coefficient and the temperature dependence of the latter imply two types of carriers: n-type and p-type.

Optical measurements by Schlesinger *et al.* (1993) showed a gap of $\sim$60 meV, as shown in Fig. 210. The gap is gradually filled with increasing temperature up to

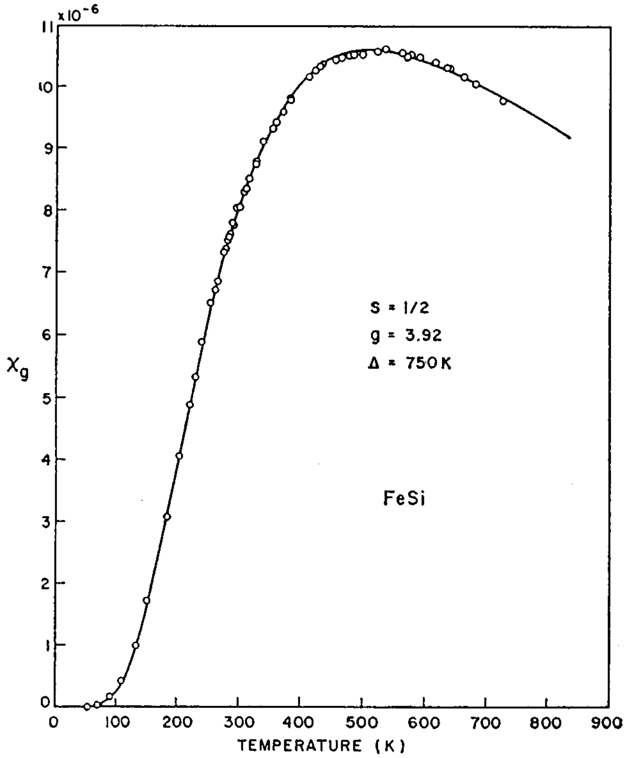

FIG. 208. Magnetic suceptibility of FeSi after subtraction of the low-temperature paramagnetic contribution by Jaccarino *et al.* (1967). The curve has been calculated using the local-moment model with parameters $S=1/2$, $g=3.92$, and $\Delta=750$ K (for definition, see text).

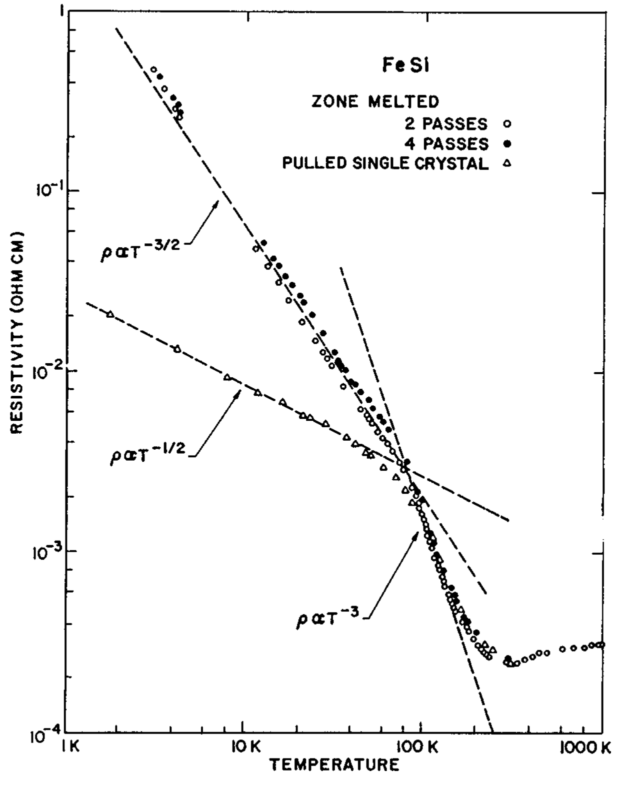

FIG. 209. Electrical resistivity of FeSi. From Wolfe *et al.*, 1965.

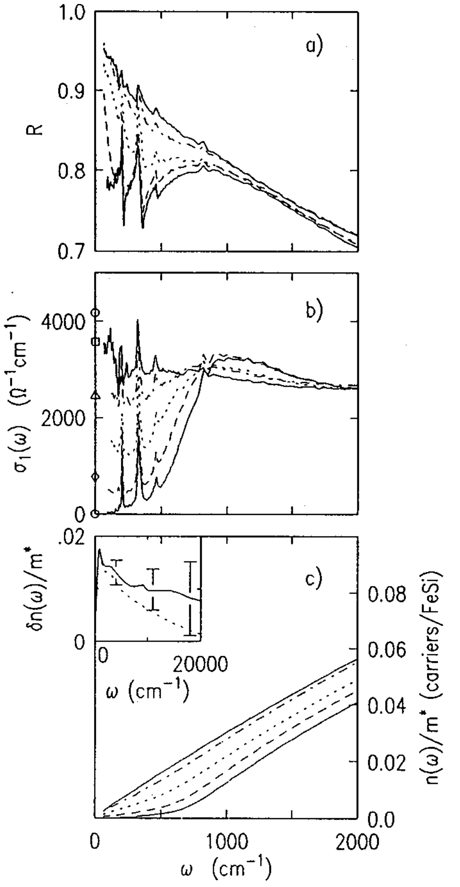

FIG. 210. Optical reflectivity R, optical conductivity $\sigma(\omega)$, and effective electron number $n(\omega)/m^*$ of FeSi (Schlesinger *et al.*, 1993): solid curve, $T=20$ K; dashed curve, $T=100$ K; dotted curve, $T=150$ K; dot-dashed curve, $T=200$ K; solid curve, $T=250$ K. DC conductivity values are also shown at $\omega=0$. The inset shows the difference in $n(\omega)/m^*$ between $T=250$ and 20 K.

250 K. The $\omega=0$ peak in the 250-K spectrum is very broad and is that of a "poor metal" or a dirty metal, far from being a typical Drude peak. It was pointed out that the gap starts to be filled at temperatures far below the temperature corresponding to the band gap (~ 600 K). Simulations assuming a rigid band and the Fermi-Dirac distribution failed to predict the complete filling of the optical gap at high temperatures, indicating the unusual nature of the optical gap (Ohta *et al.*, 1994). The $n(\omega)/m^*$ curves show that spectral weight integrated up to $\omega=2000\ \mathrm{cm}^{-1}$ is not conserved between different temperatures, meaning that spectral weight transfer occurs up to much higher energies (of order 1 eV). This picture was questioned, however, by a more recent infrared optical study (Degiorgi *et al.*, 1994), according to which the spectral weight sum rule is satisfied up to $\sim 3000\ \mathrm{cm}^{-1}$. The latter study confirmed the Anderson-localized nature of carriers at low frequencies, $\omega < 10\ \mathrm{cm}^{-1}$.

In order to explain the magnetic susceptibility of FeSi within the local-moment picture, Jaccarino *et al.* (1967) considered a model in which the nonmagnetic ($S=0$) ground state and an $S=1/2$ or 1 excited state were sepa-

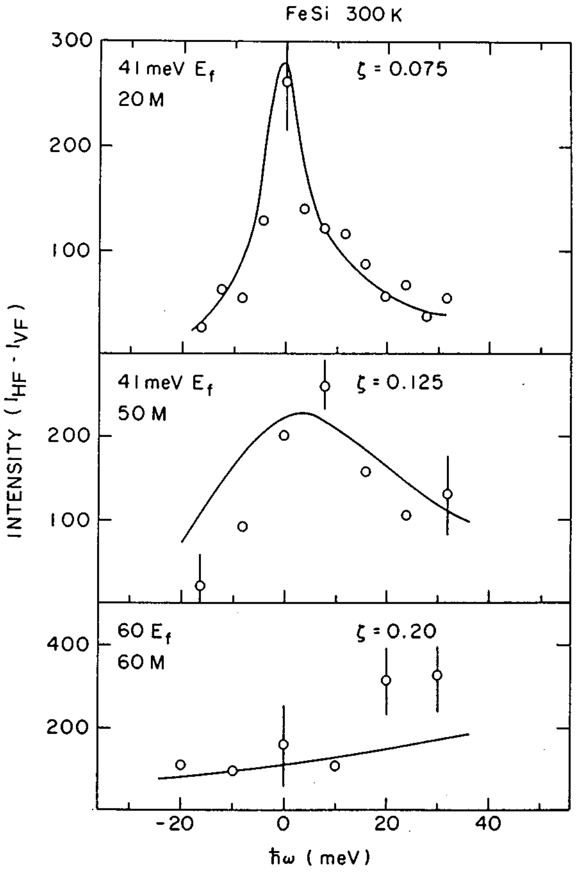

FIG. 211. Quasielastic magnetic scattering spectra of FeSi for different $\mathbf{q}$'s (Tajima *et al.*, 1988). The reciprocal-lattice points are $(1+\zeta,1+\zeta,0)$ in units of $2\pi/a$. Solid curves are the result of fitting using Eq. (4.16). $10M$ corresponds to 10 min counting time at $\hbar\omega=0$.

rated by a spin gap Δ. The solid curve in Fig. 208 shows a best fit with $S=1/2$, $\Delta=750$ K, and a g factor of 3.92. The magnetic contribution to the specific heat, which was estimated as the difference between FeSi and CoSi, was also well fitted with the same model, although there was a large ambiguity in the difference curve. Because the local-moment model is not compatible with the semiconducting properties, Jaccarino *et al.* also examined a band model in which conduction and valence bands of widths w were separated by a band gap of 2Δ. They had to assume, however, that $2w \ll 2\Delta$ (with $2\Delta = 760$ K) in order to reproduce the magnetic susceptibility. Such a narrow bandwidth is obviously unrealistic.

LDA band-structure calculations were performed by Mattheiss and Hamann (1993) and more recently by Fu *et al.* (1994) and predicted a small indirect gap of ~ 0.1 eV, which agrees with the experimental value of ~ 0.05 eV rather well. The band structure consists of wide bands of strongly hybridized Fe $3d$-Si $3p$ character (extending from ~ -12 eV to ~ 10 eV with respect to the Fermi level) and relatively narrow (~ 1 eV) bands of purely Fe $3d$ character. The ~ 1 eV widths of the energy bands near E_F is again inconsistent with the very narrow ($\leqslant 0.1$ eV) bands proposed by Jaccarino *et al.* and requires the inclusion of electron correlation effects for the bands near E_F. Takahashi and Moriya (1979) incorporated correlation effects using spin-fluctuation theory into the above band structure (with some simplification) and explained the peculiar magnetic and thermal properties of FeSi. They attributed the nonmagnetic ground state and the temperature-induced paramagnetism to a negative mode-mode coupling, and predicted the saturation of the temperature-induced local moment at high temperatures.

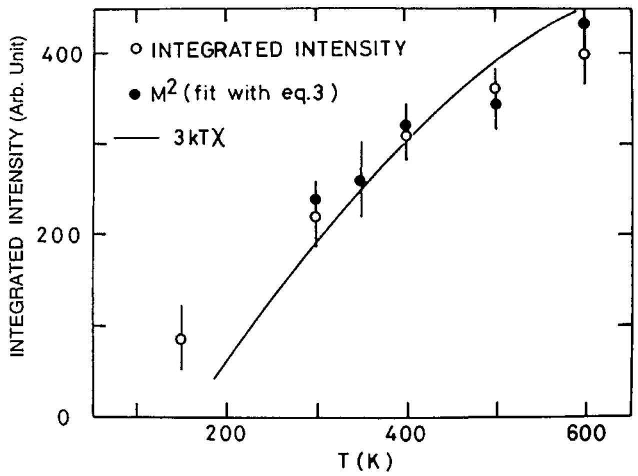

FIG. 212. Temperature dependence in FeSi: Open circles, integrated paramagnetic scattering intensity; closed circles, the paramagnetic moment $M(0)^2$ ($\mathbf{q}=0$) determined by fitting analysis using Eq. (4.16). The solild curve is $3kT\chi(0)$, where $\chi(0)$ is the uniform magnetic susceptibility. From Tajima *et al.*, 1988.

The question of whether local moments are induced at high temperatures according to the prediction of spin-fluctuation theory was addressed by inelastic neutron-scattering experiments, but these studies failed to observe paramagnetic moments (Kohgi and Ishikawa, 1981). Tajima *et al.* (1988) made a polarized neutron-scattering study on single crystals and indeed detected a temperature-induced local moment. The results show paramagnetic (quasielastic) scattering as described by

$$S(\mathbf{q},\omega)=M^2(\mathbf{q})\,\frac{\hbar/k_BT}{1-\exp(-\hbar/k_BT)}\,\frac{1}{\pi}\,\frac{\Gamma(\mathbf{q})}{\Gamma(\mathbf{q})^2+\omega^2}, \tag{4.16}$$

where $M(\mathbf{q})$ is the $\mathbf{q}$-dependent paramagnetic moment. The $\omega\sim 0$ scattering intensity shows a sharp increase towards the reciprocal-lattice points, as shown in Fig. 211, indicating ferromagnetic correlation. The $\omega\sim 0$ intensity as well as the integrated intensity show a temperature dependence which closely follows that of the static magnetic susceptibility, as shown in Fig. 212, a clear indication of temperature-induced paramagnetism. The unique feature of the scattering function of FeSi is that the ω-integrated intensity is $\mathbf{q}$ independent, i.e., $M(\mathbf{q})$ is $\mathbf{q}$ independent, while the $\omega\sim 0$ intensity is $\mathbf{q}$ dependent, as can be seen from the simultaneous sharpening of the spectrum and the increase in the $\omega\sim 0$ intensity as one approaches a reciprocal-lattice point. $M(\mathbf{q})$ is found to be as large as $(3.5\pm 2)\mu_B^2$ at 300 K.

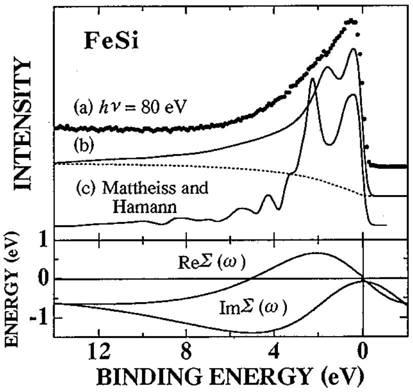

FIG. 213. Photoemission spectrum of FeSi (Saitoh, Sekiyama *et al.*, 1995) compared with the band DOS calculated using the LDA (Mattheiss and Hamann, 1993) and that modified by the self-energy correction. The employed local self-energy $\Sigma(\omega)$ is also shown.

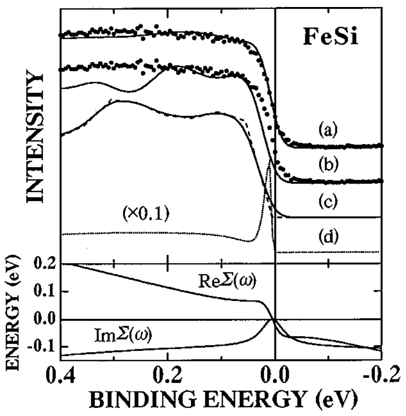

FIG. 214. Photoemission spectrum of FeSi near E_F compared with the band DOS calculated using the LDA (Mattheiss and Hamann, 1993) and that modified by the self-energy correction (Saitoh, Sekiyama, *et al.*, 1995): (a) Spectral function calculated using $\Sigma(\omega)$ shown in the lower panel; (b) spectral function calculated using only the high-energy part $\Sigma_h(\omega)$; (c) the LDA density of states; (d) density of quasiparticles.

The prediction of temperature-induced paramagnetism was also tested by Fe core-level photoemission spectroscopy (Oh *et al.*, 1987). Fe $3s$ core-level spectra, which show an exchange splitting when the Fe atom has a local moment, did not change between low and high temperatures. Valence-band photoemission studies were made by Kakizaki *et al.* (1982) and more recently by Saitoh, Sekiyama, *et al.* (1995), Chainani *et al.* (1994) and C. H. Park *et al.* (1995) with improved energy resolution. Since the Fe $3d$ and Si $3sp$ states are strongly hybridized and form wide bands, the configuration-interaction cluster model is certainly not a good starting point for FeSi. If one compared the band-theoretical DOS with the DOS $\rho(\omega)$ measured by photoemission, however, significant discrepancies would be found in the overall line shape, as shown in Fig. 213, as well as in the high-resolution spectra near E_F, as shown in Fig. 214. Therefore a local self-energy model was introduced to incorporate correlation effects in a phenomenological way: The model self-energy has the form $\Sigma(\omega) \equiv \Sigma_h(\omega) + \Sigma_l(\omega)$, where $\Sigma_h(\omega)$ is a self-energy correction of the type $g/(\omega + i\gamma)^2$ and is effective on the large energy scale of 1–10 eV, while $\Sigma_l(\omega)$ is a self-energy correction whose absolute magnitude is small but has a significant effect on the low-energy electronic structure on the scale of 10–100 meV (Saitoh, Sekiyama, *et al.*, 1995). $\Sigma(\omega)$ is assumed to have the Fermi-liquid property ($\mathrm{Im}\,\Sigma(\omega) \propto -\omega^2$) in the $\omega \to 0$ limit. Figure 213 shows that the application of $\Sigma_h(\omega)$ causes the narrowing of the Fe $3d$-derived DOS, the broadening of spectral features at higher binding energies, and the transfer of spectral weight towards higher binding energies. The same self-energy alone cannot reproduce the sharp rise of the band edge and the relatively flat line shape from the band edge to ~ 0.5 eV below it. The addition of $\Sigma_l(\omega)$, whose real part has a large negative slope near the band edge, introduces further band narrowing near E_F; through the Kramers-Kronig relation, the $|\mathrm{Im}\,\Sigma_l(\omega)|$ rapidly increases as one moves from E_F, smearing out the structures in $\rho(\omega)$. The quasiparticle density of states $N^*(\omega)$, calculated using Eq. (2.72), is also plotted in Fig. 214. Because of the increase in the negative slope of $\mathrm{Re}\,\Sigma_l(\omega)$ toward E_F, the quasiparticle DOS $N^*(\omega)$ is enhanced near the band edge. The angle-resolved photoemission study by C. H. Park *et al.* (1995) has found a sharp peak ~ 20 meV below E_F for a certain part of the Brillouin zone. The peak disperses only very weakly, again indicating the narrow quasiparticle band at the top of the valence band.

Thus the presence of the narrow bands at the band edges, originally suggested by Jaccarino *et al.* (1967), was corroborated by the microscopic experimental probe. The narrow bandwidths $W^* \sim 20$ meV naturally explain the poor metallic behavior as seen in the optical conductivity (Fig. 210), since charge transport should be incoherent at $T \gg W^*/k_B$. In the sense that the physical properties of f-electron Kondo insulators would have their origin in the presence of narrow f bands, which would be strongly renormalized, especially in the Kondo limit (Susaki *et al.*, 1996), FeSi and the f-electron Kondo insulators can be grouped in the same class of materials, although the underlying (high-energy) electronic structures are very different.

As for the microscopic origin of temperature-induced magnetism, on the basis of first-principles electronic calculations, Anisimov, Ezhov, *et al.* (1996) predicted a first-order nonmagnetic semiconductor-to-ferromagnetic metal transition as a function of magnetic field using the LDA$+U$ method. The transition was predicted to occur if the d-d Coulomb repulsion U was large enough (>3.2 eV). The ferromagnetic moment was predicted to be as large as $1\mu_B$ per Fe. The magnetic and thermal properties at finite temperatures were then calculated using a simplified model based on the first-principles results, yielding good agreement with experiment. This picture appears quite different from the correlated narrow-band picture, but the proximity of the ferromagnetic state to the ground state may be reflected in the ferromagnetic

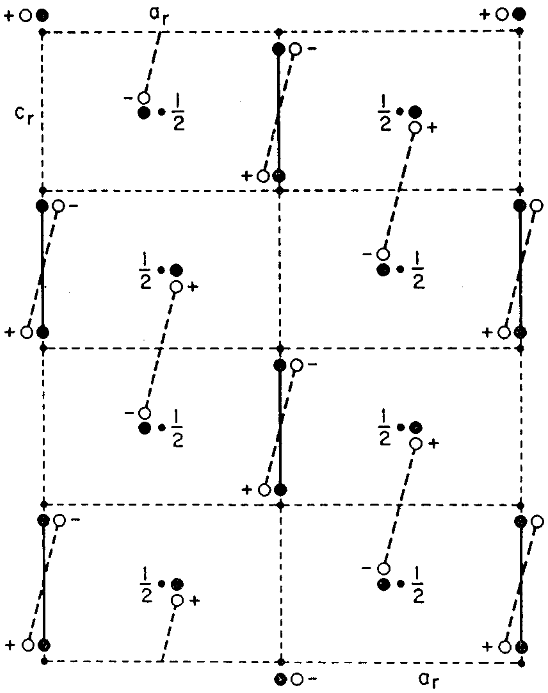

FIG. 215. Comparison of V-V pairing in the three phases, R, M_1, and M_2, in VO_2. In M_1 (open circles) all the vanadium atoms both pair and twist from the rutile positions. In M_2 (filled circles) one-half of the vanadium atoms pair but do not twist and the other half form unpaired zigzag chains. (The distortions are exaggerated by a factor of 2 for clarity.) From Marezio *et al.*, 1972.

correlations found in the neutron scattering study. Misawa and Tate (1996) explained the magnetic susceptibility of FeSi using a Fermi-liquid theory, according to which a singular contribution from the Fermi level (from the band edge in the case of FeSi) causes the susceptibility maximum as well as metamagnetism and ferromagnetic instability in other systems (Misawa, 1995). Recently, the transport properties of substituted compounds $FeSi_{1-x}Al_x$ have been studied and have been successfully interpreted in the conventional doped semiconductor picture (DiTusa *et al.*, 1997). How the correlation effects manifest themselves in FeSi still remains an open question, calling for further investigations.

2. VO_2

Many of the vanadium oxides exhibit temperature-induced MITs, as observed in V_2O_3 (Sec. IV.B.1) and the Magneli phases V_nO_{2n-1} ($4 \leqslant n \leqslant 8$). Among them VO_2, with a $3d^1$ configuration, differs from others, showing the nonmagnetic ground state without an antiferromagnetic phase. The MIT in VO_2 takes place at around 340 K, accompanying the lattice structural transition from a high-temperature rutile (TiO_2-type) structure (R phase) to a low-temperature monoclinic structure (M_1 phase), as illustrated in Fig. 215 (Marezio *et al.*, 1972). V-V pairing occurs in the M_1 phase together with tilting of the V-V pair.

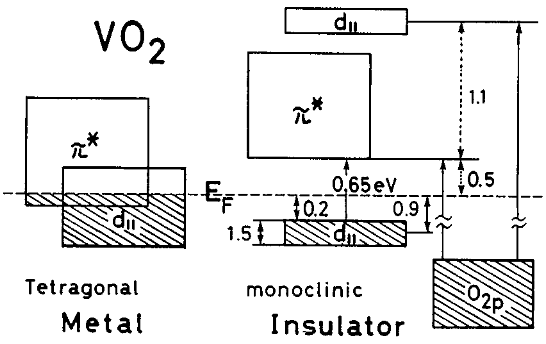

FIG. 216. Schematic energy diagram of the $3d$ bands around the Fermi level for VO_2. From Shin *et al.*, 1990.

The schematic electronic structures in metallic and insulating VO_2, corresponding to Goodenough's model (Goodenough, 1971), are shown in Fig. 216 (Shin *et al.*, 1990), in which some gap energies were derived by spectroscopic studies (Ladd and Paul, 1969; Shin *et al.*, 1990). In the R phase, the t_{2g} levels in the octahedral crystal field are further split into $d_\parallel$ and π^* levels in the R phase, comprising the electronic states near the Fermi level of the metallic state. Here, the $d_\parallel$ orbitals are rather nonbonding, while the π^* orbitals are strongly hybridized with the O $2p\pi$ state and hence lie higher than the $d_\parallel$ level. In the insulating M_1 phase, the pairing of the V atoms along the c_r axis (see Fig. 215) promotes $3d$-$2p$ hybridization and upshifts the π^* band off the Fermi level, as well as causing bonding-antibonding splitting of the $d_\parallel$ band (Goodenough, 1971), as shown in the right panel of Fig. 216.

The importance of the electron correlation for this lattice-coupled MIT has long been disputed. The issue is whether the essential nature of the insulating state is that of a Peierls insulator with the character of an ordinary band insulator or otherwise a Mott-Hubbard insulator. Recently, Wentzcovitch *et al.* (1994) pointed out that the LDA calculation can find a monoclinic distorted (M_1 phase) ground state in agreement with experiment and an almost opening of gap in charge excitations. Although it is conceptually difficult to distinguish the band and Mott insulators when there is a gap in the spin sector, Wentzcovitch *et al.*, (1994) concluded that VO_2 may be more bandlike than correlated.

Strong opposition to the band view (Rice *et al.*, 1994) is based on observation of the Mott-Hubbard insulator, that is, the insulator with no gap in the spin sector, in $V_{1-x}Cr_xO_2$ with very small x ($\geqslant 3 \times 10^{-3}$) (Pouget *et al.*, 1974) or in pure VO_2 when a small uniaxial pressure is applied along the $(110)_r$ direction (Pouget *et al.*, 1975). The $T-x$ phase diagram for $V_{1-x}Cr_xO_2$ (Marezio *et al.*, 1972; Villeneuve, Drillon, and Hagenmuller, 1973) is presented in Fig. 217. Two other distinct phases emerge, the insulating monoclinic M_2 and the triclinic T phase, in addition to the aforementioned metallic R and insulating (nonmagnetic) M_1 phases. Uniaxial pressure also gives rise to the M_2 and T phases and leads to a similar phase diagram (Pouget *et al.*, 1975).

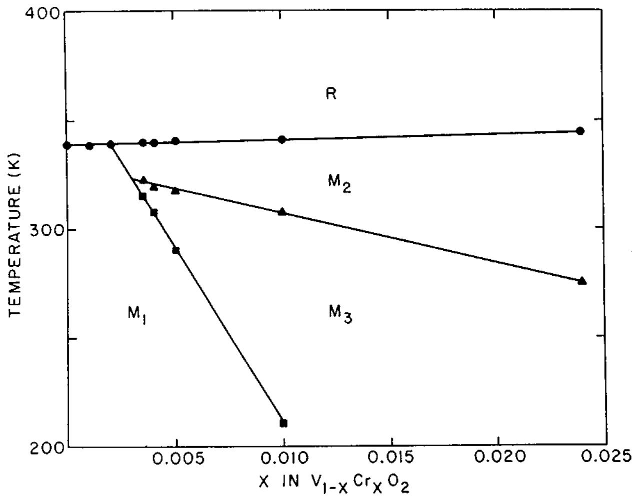

FIG. 217. The $T-x$ phase diagram for $V_{1-x}Cr_xO_2$ (Marezio *et al.*, 1972; Villeneuve, Drillon, and Hagenmuller, 1973).

The V-V pairing pattern for the M_2 phase is also shown in Fig. 215, which is composed of two kinds of V chains. In M_2 one half of the V^{4+} ions form equally spaced V chains, and NMR and EPR experiments (Pouget *et al.*, 1974) showed that they behave magnetically as $S=1/2$ Heisenberg chains ($J\approx 300$ K). Thus it is clear that these V chains in M_2 are Mott-Hubbard insulators. The insulating triclinic phase can be viewed as a spin Peierls state of the M_2 phase, although the transition between M_2 and T is weakly of the first order. In fact, further cooling leads to a continuous $M_2 \rightarrow M_1$ transition through the intermediate T phase, where the pairing (or dimerization) on one set of V chains grows. The Mott-Hubbard insulating M_2 phase is obviously a local minimum for VO_2, since the M_2 can be stabilized by minimal perturbations such as very light Cr-doping or a small uniaxial pressure. Rice *et al.* (1994) stressed again that all the insulating phases of VO_2, M_1, M_2, and T, are of the same type and should be classified as Mott-Hubbard and not band insulators.

The electron correlation effect should also show up in the metallic state in VO_2. The high-temperature metallic state in the R phase ($T \geqslant 330$ K) shows T-linear behavior up to 840 K (Allen *et al.*, 1996). The mean free path l (800 K)=3.3 Å is too short when the Bloch-Boltzman interpretation is applied for a metal such as is described by the LDA calculation. Allen *et al.* (1996) interpreted this in terms of either a sample problem, such as cracking at the phase transition, or of an indication of anomalous behavior of the metal close to the Mott-Hubbard insulator, which differs from the conventional Fermi liquid. To pursue the electron correlation effect in the metallic VO_2, however, it is desirable to realize the barely metallic state down to low enough temperatures, on which more detailed spectroscopic and transport investigations are possible.

A clear gap opening below the MIT temperature has been observed by photoemission spectroscopy (Sawatzky *et al.*, 1979; Shin *et al.*, 1990), as shown in Fig. 218. The results give some hint whether electron correlation plays an important role in the MIT or whether the one-electron band picture is sufficient. The V $3d$ band spectrum in the metallic phase is obviously much broader than predicted by the band-structure calculation and even shows a sign of the remnant of the lower Hubbard band, although weak, implying that electron correlation cannot be neglected in the metallic state (Fujimori, Hase, *et al.*, 1992a). In going from the metallic to the insulating state, the quasiparticle spectral weight disappears, and only the "lower Hubbard band" survives. Although no serious comparison has been made between the spectra of the insulating phase and the density of states of the LDA band (Wentzcovitch, Schulz, and Allen, 1994), it seems that the discrepancy between the measured spectra and the band DOS is substantial and that electron correlation is again important for realizing the insulating phase of VO_2.

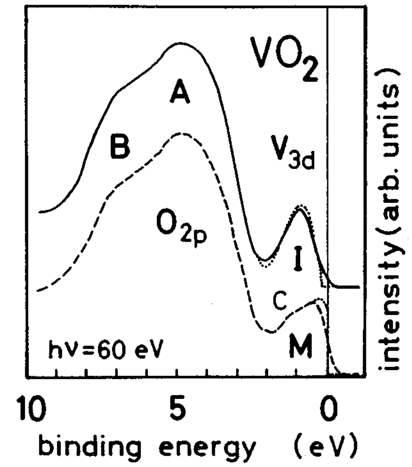

FIG. 218. Photoemission spectra of VO_2 in the insulating and metallic states (Shin *et al.*, 1990). The solid curve was taken at 298 K in the insulating phase and the dashed curve at 298 K in the metallic phase. The dotted curves are spectra after deconvolution with instrumental resolution.

3. Ti_2O_3

Corundum-type Ti_2O_3 undergoes a gradual metal-insulator transition around 400–600 K (for a review and comprehensive guide to the literature before 1975, see Honig and Van Zandt, 1975), as displayed in Fig. 219 together with the temperature dependence of the resistivity for the V-doped compound (Chandrashekhar *et al.*, 1970). In contrast to the perovskite analogs (e.g., $LaTiO_3$) of the $Ti^{3+}(3d^1)$-based oxide (Sec. IV.C.1) as well as to V_2O_3 with a similar corundum-type structure (Sec. IV.B.1), Ti_2O_3 has a low-temperature insulating state that is nonmagnetic. In fact, the magnetic susceptibility increases to the paramagnetic value at temperatures nearly corresponding to the MIT (Pearson, 1958). The conventional explanation for the nonmagnetic insulating ground state (Van Zandt, Honig, and Goodenough, 1968) is based on the splitting of the lower-lying t_{2g} level, depicted in Fig. 220. In a corundum-type struc-

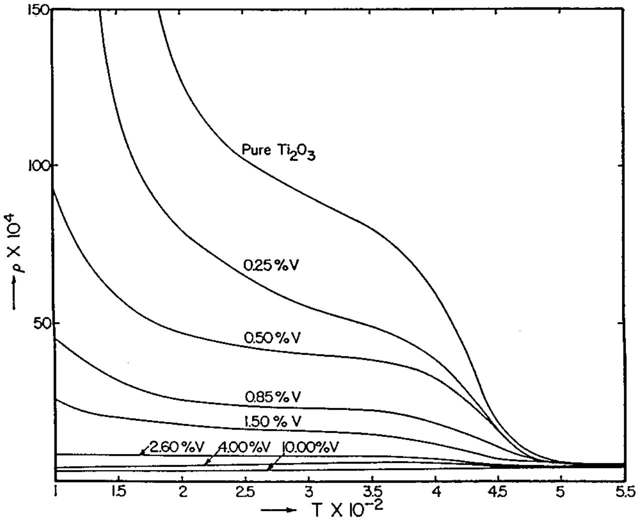

FIG. 219. Temperature dependence of resistivity for pure and V-doped Ti_2O_3. From Chandrashekhar *et al.*, 1970.

ture (see Fig. 68), the lower-lying t_{2g} manifold for the TiO_6 octahedron splits into bonding and antibonding states of a_{1g} and e_g^π levels. The a_{1g} orbitals, which have $d_{3z^2-r^2}$ character, form strong bonds between pairs of Ti atoms within the face-sharing octahedra along the c axis. Then the resulting bonding (a_{1g}) and antibonding (a_{1g}^*) bands are split and bracket the e_g^π and $e_g^{\pi*}$ bands. The minimum charge gap, or the semiconductor gap, is expected to occur between the filled a_{1g} and empty e_g^π subbands. According to this model, known as the Van Zandt-Honig-Goodenough model, the increase in the ratio c/a with increase of temperature reduces the bonding-antibonding splitting of the a_{1g} bands and promotes the collapse of the semiconductor gap between a_{1g} and e_g^π.

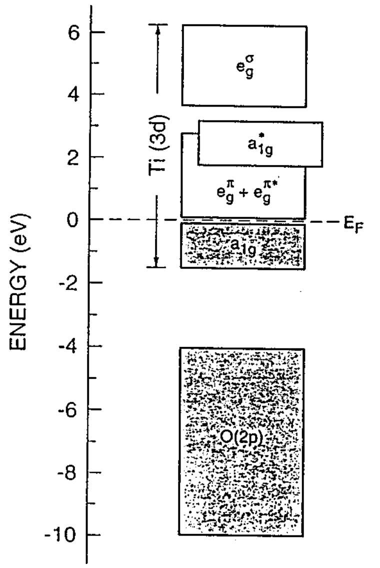

FIG. 220. Van Zandt–Honig–Goodenough model (1968) of electronic structure of Ti_2O_3. From Mattheis, 1994.

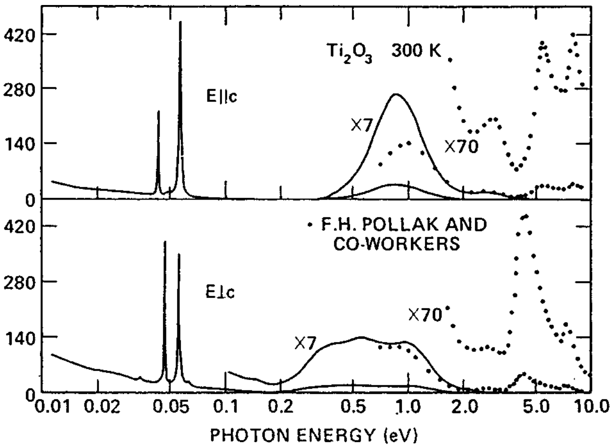

FIG. 221. Optical spectra for Ti_2O_3. From Lucovsky *et al.*, 1979.

In accord with the above scenario, the two types of gap transitions with corresponding polarization characteristics were observed in the optical spectra shown in Fig. 221 (Lucovsky *et al.*, 1979). The onset of the ϵ_2 spectrum at 0.2 eV with light polarization perpendicular to the c axis $(E \perp c)$ was assigned to the aforementioned semiconductor band gap, while the $E \| c$ band around 0.9 eV was assigned to the a_{1g} interband transition. The band peak corresponding to the $a_{1g}-a_{1g}^*$ transition shifts to lower energy (down to 0.6 eV) with increasing temperature, indicating a loosened c-axis Ti-Ti bond and hence supporting the Van Zandt-Honig-Goodenough model.

All the experimental results so far obtained appear to be consistent with the thermal closure of the semiconductor band gap, yet little is known about the electronic structures and properties in the high-temperature metallic state, which is likely to show strongly correlated electron behavior. Concerning this point, Mattheiss (1996b) recently pointed out, on the basis of an LDA band-structure calculation, the importance of the electron correlation effect on the MIT. The LDA calculation with the use of the LAPW (linearized argumented plane wave) method shows a partially filled t_{2g} complex near E_F which originates from overlapping a_{1g} and e_g^π subbands. Decreasing the c/a ratio, even beyond the observed low-temperature value, reduces but does not eliminate this $a_{1g}-e_g^\pi$ overlap as postulated in the model of Fig. 220. For example, to open a semiconductor gap in this system, an unphysically small Ti-Ti separation of about 2.2 Å along the c axis would be required. This may preclude the simplest band explanation for the MIT.

The electron correlation effect may show up explicitly when the MIT is driven by filling control and a low-temperature metallic state emerges. A Ti deficiency or excess oxygen in the chemical form of Ti_2O_{3+y} may correspond to hole doping, as in the case of $V_{2-\delta}O_3$ (Sec. IV.B.1). In fact, a nonstoichiometric sample up to $y = 0.03$ could be prepared that would show a greatly reduced resistivity value but still remain semiconducting or insulating at low temperatures, with fairly large Hall coefficient (Honig and Reed, 1968). Another method of

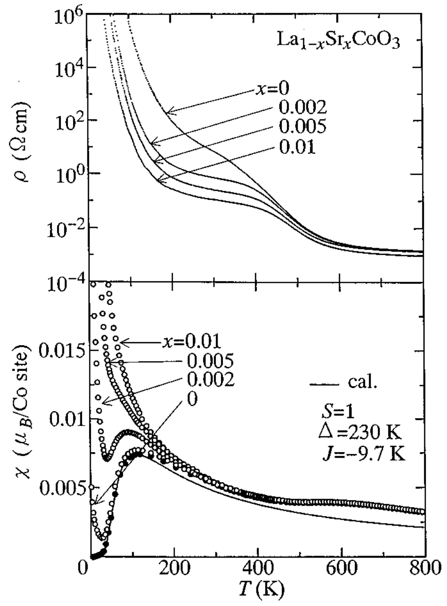

FIG. 222. Temperature dependence of resistivity (ρ, upper panel) and magnetic susceptibility (χ, lower panel) in $LaCoO_3$ and lightly hole-doped $LaCoO_3$ (Tokura *et al.*, 1997). A solid line in the lower panel represents the calculated curve based on the low-spin ($S=0$) and intermediate-spin ($S=1$) transition model (see text).

filling control is V doping, as exemplified in Fig. 219. The metal-site substitution may inherently contain complexity in assigning the effective valence of the doped and host metal cations. Recalling the parallel behavior of Ti doping with oxygen offstoichiometry in the case of V_2O_3, one may consider the V-doped Ti_2O_3 as an electron-doped system. As can be seen in Fig. 219, $x \gtrsim 0.02$ doping induces metallic conduction even at low temperatures (Chandrashekhar *et al.*, 1970; Dumas and Schlenker, 1976, 1979). However, the $Ti_{2-2x}V_{2x}O_3$ is a spin glass at low temperatures for above $x=0.005$ (Dumas and Schlenker, 1976, 1979; Dumas *et al.*, 1979). A large T-linear term in the specific heat (50–80 mJ/mol K) was observed for $x=0.02$–0.10 samples (Sjostrand and Keesom, 1973). This was first interpreted as an indication of a narrow conduction bandwidth or correlated electron behavior, as in Ti-doped V_2O_3. However, the large T-linear term was later reinterpreted in terms of the high entropy of the spin-glass state (Dumas and Schlenker, 1976, 1979; Dumas *et al.*, 1979). Nevertheless, correlated electron dynamics is evident in the enhanced temperature-independent (Pauli-like) component of the susceptibility, and some supplemental experimental work would be desirable for a more complete understanding of the Mott transition.

4. $LaCoO_3$

The thermally induced insulator-to-metal crossover phenomenon in $LaCoO_3$, as shown in the upper panel of Fig. 222, is quite unique because of its nonmagnetic ground state, distinguishing it from a conventional Mott insulator. The ground state of $LaCoO_3$ is a nonmagnetic insulator with a predominant configuration of $3d^6$ electrons of Co^{3+} fully occupying the t_{2g} level (Fig. 223), perhaps due to crystal-field splitting ($10Dq$), which slightly exceeds the Hund's-rule coupling energy. With increase of temperature, however, the compound undergoes a spin-state transition from a nonmagnetic ($S=0$) to a paramagnetic state, as signaled by a steep increase in the magnetic susceptibility around 100 K, shown in the lower panel of Fig. 222. Knight-shift measurements (Itoh *et al.*, 1995) and polarized neutron scattering (Asai *et al.*, 1989) have confirmed such a spin-state transition, arising from a change in the electronic state of the Co site. The nature of the high-temperature spin state, that is, the problem of whether it arises from the intermediate-spin ($S=1$) or the high-spin ($S=2$) state of the Co^{3+} ion (see Fig. 223), has not yet been settled, although the intermediate-spin-state model appears to be prevailing at the moment. Korotin *et al.* (1996) demonstrated, using the LDA+U method, the relative stability of the $S=1$ state rather than the $S=2$ state, as a result of strong p-d hybridization and orbital ordering in contrast to the behavior anticipated by the simple ionic model. Their proposed orbital ordering pattern is shown in Fig. 223. A recent finding of appreciable local lattice distortion during the spin-state transition (Yamaguchi *et al.*, 1997) suggests the presence of Jahn-Teller distortions in the high-temperature spin state, supporting the intermediate-spin-state model. An example of the fitting procedures for the magnetic susceptibility with the localized spin model (Yamaguchi *et al.*, 1997) is shown in Fig. 222. The Ising model molecular field calculation was done with assumption of a two-state model, i.e., $S=0$ and $S=1$ states with an energy gap of Δ and the antiferromagnetic exchange interaction J between thermally excited neighboring $S=1$ spins. An appropriate choice ($\Delta=230$ K and $J=9.7$ K) gives a reasonable account of the temperature dependence, although the high-spin model shows similar reproducibility, for example, with a

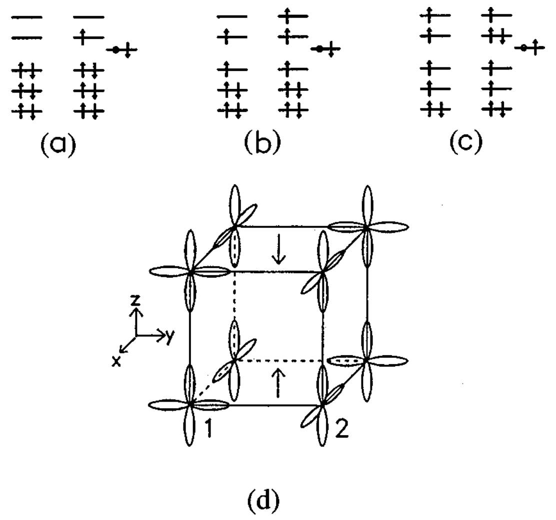

FIG. 223. Possible spin states in $LaCoO_3$: (a) low-spin (LS, $S=0$); (b) intermediate-spin (IS, $S=1$); (c) high-spin (HS, $S=2$); (d) diagram of the e_g orbital-ordered state in the IS state. From Korotin *et al.*, 1996.

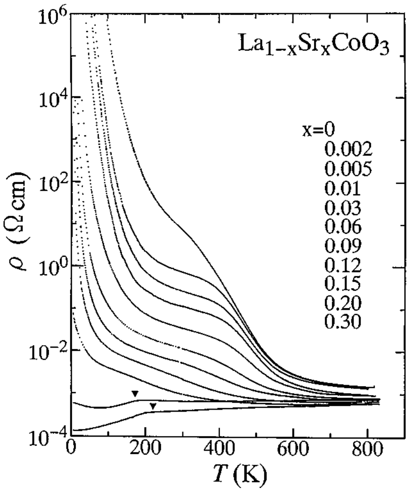

FIG. 224. Temperature dependence of $La_{1-x}Sr_xCoO_3$ with various doping levels. Closed triangles represent the ferromagnetic transition temperature.

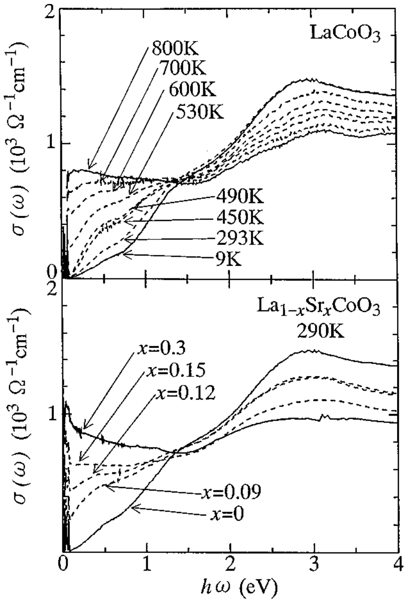

FIG. 225. Variations of optical conductivity spectra of $LaCoO_3$ with temperature (upper panel) and with doping x (by Sr substitution; lower panel) at 290 K. From Tokura *et al.*, 1997.

set of parameters, $\Delta = 299$ K and $J = 26.7$ K. Whichever model would be better, the spin-gap energy is 0.02–0.03 eV, and above room temperature an intermediate or high spin density exceeds 80% of the Co sites.

As can be seen in the lower panel of Fig. 222, a small amount of hole doping gives rise not only to a decrease in resistivity but also to a large Curie tail in the low-spin region at low enough temperatures. By measurements of the magnetization and fitting with the modified Brillouin function, it was demonstrated (Yamaguchi *et al.*, 1996a) that a doped single hole shows an extremely high spin number, $S = 10–16$. This means that a hole with O $2p$-state character causes a local spin-state transition (low-spin to intermediate-spin) over 10–16 Co sites around itself, perhaps due to strong $2p\sigma$-$3de_g$ hybridization. Such a gigantic spin polaron can be a precursor state for the ferromagnetic metallic state in $La_{1-x}Sr_xCoO_3$ ($x \gtrsim 0.2$; see Fig. 224, in which the ferromagnetic transition is indicated by closed triangles).

The resistivity of $LaCoO_3$ shows no anomaly around this spin-state transition near 100 K, with a nearly constant activation energy of about 0.2 eV. However, a large reduction in the resistivity takes place around 500 K (upper panel of Fig. 222), where the spin-state transition is almost complete. Furthermore, this continuous insulator-to-metal change is least affected by a small amount of hole-doping as shown in Fig. 222 and Fig. 224 (Yamaguchi and Tokura, 1998).

In the upper panel of Fig. 225, we show the temperature dependence of the optical conductivity spectra of $LaCoO_3$ in the range of 0–4 eV (Tokura, Okimoto, *et al.*, 1998). With increasing temperature up to 800 K through the metal-insulator crossover temperature around 500 K, the spectra show conspicuous change over a large energy region up to several eV. Such a huge spectral change cannot be accounted for by a simple band closing like that in a narrow-gap band insulator (semiconductor), in spite of the nonmagnetic nature of the insulating ground state. The optical conductivity spectrum shows a gap feature at low temperatures and undergoes minimal change even when temperature is increased up to 293 K and the spin-state transition is almost completed. The gap energy estimated from the onset of conductivity is more than 0.1 eV (Yamaguchi *et al.*, 1996b), in accord with the transport data, although the accurate determination of the gap energy is difficult because of the blurred onset of conductivity, perhaps due to the indirect-gap nature (Sarma *et al.*, 1995; Hamada, Sawada, and Terakura, 1995). With change of temperature around 500 K, the spectral weight is observed to be rapidly transferred from the higher-lying interband transition region to the lower-energy region, accompanying the well-defined isosbetic (equal-absorption) point at 1.4 eV.

A surprisingly similar change in the conductivity spectrum is observed for the case of hole doping, i.e., for $La_{1-x}Sr_xCoO_3$, when the doping level x is changed as shown in the lower panel of Fig. 225. Nominal hole doping by partial substitution of La with Sr drives the FC-MIT as shown in Fig. 224. The optical conductivity spectra at 290 K (the lower panel of Fig. 224) show a similar spectral weight transfer with increase of x, accompanying the isosbetic point around 1.4 eV as well. Most of the low-energy spectral weight is borne not by the conventional Drude component but by the incoherent part, both for the high-temperature $LaCoO_3$ and for $La_{1-x}Sr_xCoO_3$. This nearly parallel behavior for temperature increasing and hole doping indicates that the electronic structural change in both the insulator-metal transitions is also nearly identical in nature.

Figure 226 displays the inverse-temperature dependence of the Hall coefficient (R_H; lower panel) together with that of the resistivity coefficient in $LaCoO_3$ and the lightly hole-doped compounds $La_{1-x}Sr_xCo_3$ ($x = 0.005$

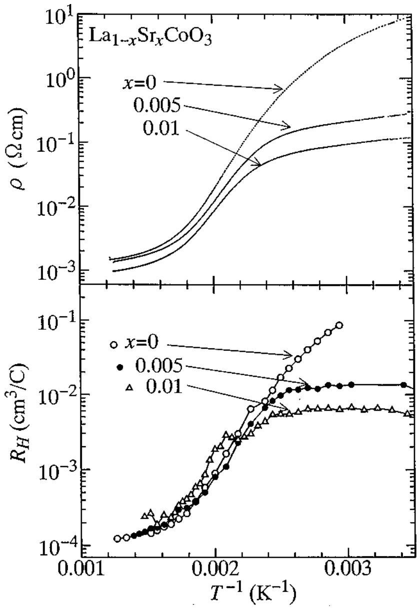

FIG. 226. Inverse-temperature dependence of resistivity (ρ, upper panel) and Hall coefficient (R_H, lower panel) in $LaCoO_3$ and lightly hole-doped $La_{1-x}Sr_xCoO_3$. From Tokura *et al.*, 1997.

and 0.01; Tokura, Okimoto, *et al.*, 1998). The R_H is positive, indicating hole-type conduction, over the whole temperature region and shows as steep a change as the resistivity with temperature. In particular, the carrier density $n = 1/R_H$ in $LaCoO_3$ shows a rapid increase at 400–600 K. This should be interpreted as a rapid decrease in the gap energy itself, with increase of temperature above 400 K, that is, after completion of the spin-state transition.

The light hole-doping effect manifests itself in the saturation of the increase of the resistivity and Hall coefficient below 400 K. The flat temperature dependence of the R_H in doped crystals implies the saturation behavior of impurity conduction. By contrast, the R_H value above 400 K shows approximately common values and temperature dependence irrespective of doping. The fully conducting state, e.g., at 800 K, shows a small R_H value corresponding to three holes per Co site. These facts clearly indicate the presence of a large Fermi surface in the high-temperature conducting phase, which is least affected by light doping as observed. Thus the observed insulator-metal crossover shows the essential features characteristic of a Mott transition at constant band filling.

The thermally induced MIT is also critically affected by changes of the one-electron bandwidth (W). The standard method of bandwidth control (BC) is to utilize the orthorhombic distortion of the perovskite, which depends on the A-site ionic radius, as described in detail in Sec. III.B. In the present case, $RCoO_3$ with R changing from La to Pr, Nd, Sm, Eu, and Gd causes an increase in the Co-O-Co bond distortion in the $GdFeO_3$-type orthorhombic lattice (apart from the rhombohedral $LaCoO_3$) and hence a decrease of W in this order. Figure 227 (Yamaguchi, Okimoto, and Tokura, 1996b) shows the T dependence of $d\log\rho/d(T^{-1})$ in the above series of $RCoO_3$ crystals. This quantity, if constant, would represent a thermal activation energy. The gradual MIT shows up as a broad peak for the respective compounds, which systematically shifts to higher temperature with decrease of the ionic radius of R or equivalently with decrease of W. The nearly constant value of $d\log\rho/d(T^{-1})$ at low temperatures represents the thermal activation energy, or half of the transport energy gap Δ_a, which also increases with decrease of W.

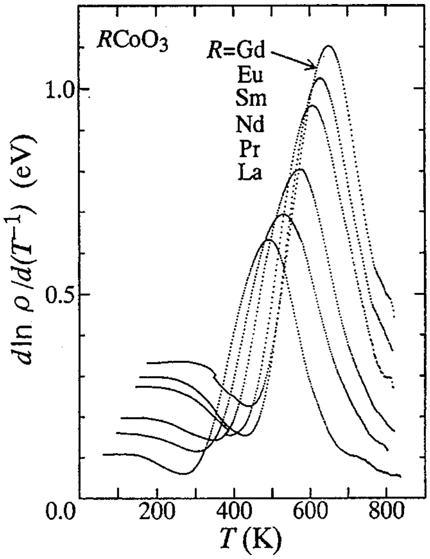

FIG. 227. Temperature (T) dependence of resistivity (ρ) and $d\log\rho/d(T^{-1})$ for crystals of $RCoO_3$ (R = La, Pr, Nd, Sm, Eu, and Gd). From Yamaguchi *et al.*, 1996b).

The variation of the charge gap is directly seen in the optical conductivity spectra for the ground state (low-spin state, e.g., at 9 K) for $RCoO_3$ shown in Fig. 228 (Yamaguchi, Okimoto, and Tokura, 1996b). The con-

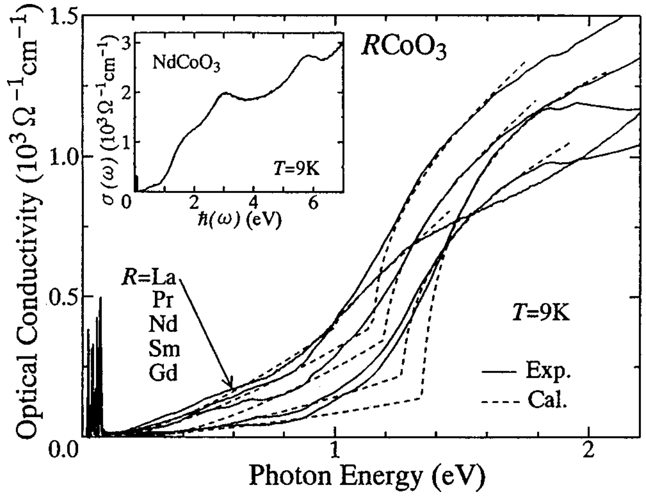

FIG. 228. Optical conductivity spectra $\sigma(x)$ for $RCoO_3$. Inset gives the overall features of $NdCoO_3$. Spiky peaks below 0.1 eV are due to optical phonons. Dashed lines are the best-fit results with the model function for the indirect-gap plus direct-gap transitions. From Yamaguchi *et al.*, 1996b.

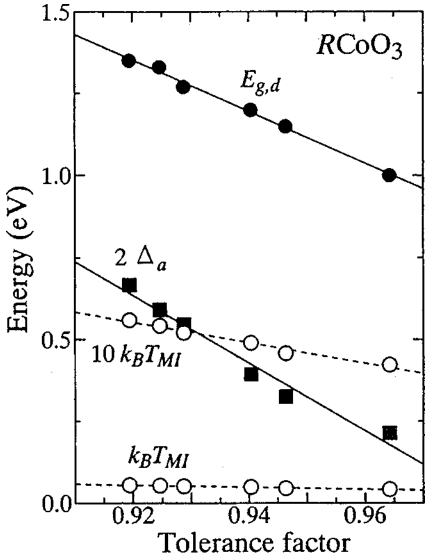

FIG. 229. Characteristic energies vs the tolerance factor for a series of RCoO$_3$. Solid circles, gap energies for the optical (direct-gap) transition ($E_{g,d}$); solid squares, gap energies for the charge transport ($2\Delta_a$) in the low-temperature insulating state. Open circles indicate temperatures (k_BT_{IM}) for the insulator-metal transition as well as their magnification ($10k_BT_{IM}$) for a better comparison. From Yamaguchi *et al.*, 1996b.

ductivity shows a gradual onset at 1–1.5 eV perhaps due to the indirect nature of the band gap (Sarma *et al.*, 1995), while a residual broad tail is present at 0.1–1 eV. With R substitution from La to Gd, the spectral shape and the onset shift as a whole to higher energy. Broken curves in the figure represent the fitting using the model functions for direct and indirect band-gap transitions. The lower-lying indirect gap is difficult to pinpoint due to the blurred feature, while the shift of the direct gap with R ions is quite clear.

Figure 229 (Yamaguchi, Okimoto, and Tokura, 1996b) shows the observed gaps and insulator-metal crossover temperature versus the tolerance factor (see Sec. III.B.1), which is related to the distortion of the perovskite lattice and hence the degree of p-d hybridization or W. Solid circles represent the optical gap $E_{g,d}$ for the direct transition (see Fig. 228), while solid squares and open circles the transport gap ($2\Delta_a$) and the metal-insulator crossover temperature k_BT_{IM} (as well as $10k_BT_{IM}$ for reference), respectively, as derived from Fig. 227. The energy scale of k_BT_{IM} is by far smaller than $2\Delta_a$ for all the RCoO$_3$ crystals, and the variation of k_BT_{IM} with R or the tolerance factor is not so significant as that of $2\Delta_a$ or $E_{g,d}$. The $E_{g,d}$ and $2\Delta_a$ show nearly parallel behavior as a function of tolerance factor. The change in the p-d transfer interaction t_{pd} should approximately scale with $\cos\theta$, θ being the Co-O-Co bond angle, as described in Sec. III.B.1. This means that t_{pd} changes almost linearly with the tolerance factor in this region and by about 10% between $R=$La and Gd in RCoO$_3$. The observed changes in both the transport and the optical gap magnitudes is quite large compared with the change in t_{pd}. Such a critical change in the charge gap with t_{pd}, as well as an anomalously low T_{IM} as compared with the charge-gap value, suggests again the important role of electron correlation in charge-gap formation below T_{IM} as well as in the MIT itself.

The electronic structure of LaCoO$_3$ has also been studied by photoemission spectroscopy and electronic structure calculations. These studies have invariably shown strong hybridization between Co $3d$ and O $2p$. An LDA band-structure calculation gave a semimetallic band structure, in which the bottom of the conduction band and the top of the valence band overlap (Hamada, Sawada, and Terakura, 1995). This is due to a common tendency of the local density approximation to underestimate band gaps; a finite gap was opened in a Hartree-Fock calculation of the multiband Hubbard model using parameters derived from photoemission spectroscopy (Mizokawa and Fujimori, 1996b). The density of states given by the LDA calculation and that from the photoemission spectra are in good agreement with each other (Sarma *et al.*, 1995), implying that LaCoO$_3$ is an ordinary semiconductor. Nevertheless, the presence of a weak but clear charge-transfer satellite indicates that electron correlation is also important (Saitoh *et al.*, 1997a). Indeed, the on-site d-d Coulomb energy is found to be as large as $U=5-7$ eV from cluster-model analysis of the Co $2p$ core-level photoemission spectra (Chainani, Mathew, and Sarma, 1992; Saitoh *et al.*, 1997a).

Concerning the phase transition from nonmagnetic semiconductor to paramagnetic semiconductor at $\sim$90 K, changes in the photoemission spectra in going from below to above $\sim$90 K are insignificant, ruling out the possibility that the transition is a low-spin–to–high-spin transition. While within the ligand-field theory the intermediate-spin state should be higher than the low-spin and high-spin states for any parameter set, the intermediate-spin state is found to be close to and in some cases lower than the low-spin state according to the cluster-model and band-structure calculations. Korotin *et al.* (1996) studied homogeneous solutions of the band model for LaCoO$_3$, that is, solutions with all the Co atoms in the identical electronic state, using the LDA$+U$ method. They found that, for an expanded lattice at high temperatures, the intermediate-spin state ($2.11\mu_B$) could be stabilized while the high-spin state ($3.16\mu_B$) always remained high in energy. Although the intermediate-spin state is an antiferromagnetic metal in the homogeneous solution, Korotin *et al.* (1996) also studied inhomogeneous solutions and found indications that orbital ordering with antiferromagnetism almost opens a gap and further lowers the energy. Hartree-Fock calculations (Mizokawa and Fujimori, 1996b) showed that the intermediate-spin state is ferromagnetic with antiferro-orbital ordering but a band gap is not opened. Since there is no long-range order in the high-temperature state, ferromagnetic correlation rather than

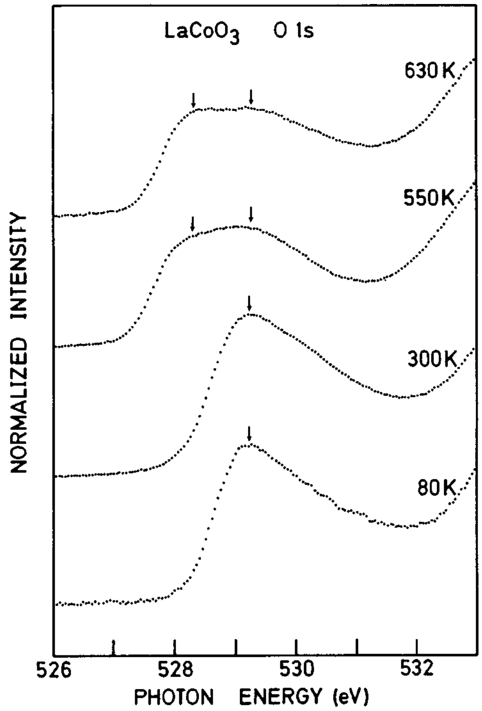

FIG. 230. Temperature dependence of the oxygen 1s x-ray absorption spectra of LaCoO$_3$ (Abbate *et al.*, 1993). The low-energy peak which appears above ~500 K may be assigned either to the t_{2g} band or to the coherent spectral weight of the metallic state.

ferromagnetic ordering is expected, in accordance with the results of a neutron-scattering study by Asai *et al.* (1997).

Concerning the 500–600-K insulator-to-(poor) metal transition, Abbate *et al.* (1993) observed a significant change in the oxygen 1s x-ray absorption spectra across the transition, as shown in Fig. 230, which is consistent with the large change expected for a transition from the low-spin ground state to the high-spin excited state but may also be consistent with an insulator-to-metal transition. According to both the LAD+U and Hartree-Fock calculations, however, the high-spin state is an insulator. Korotin *et al.* (1996) suggested that, above ~600 K, orbitals are disordered within the intermediate-spin state, driving the system metallic.

La$_{1-x}$Sr$_x$CoO$_3$ is a unique filling-control system in that doped holes not only act as metallic carriers but also induce a ferromagnetic moment. The doping-induced changes in the photoemission spectra are relatively small and indicate that the system is in the intermediate-spin state (Saitoh *et al.*, 1997b), unlike the high-spin La$_{1-x}$Sr$_x$MnO$_3$.

5. La$_{1.17-x}A_x$VS$_{3.17}$

La$_{1.17-x}A_x$VS$_{3.17}$, where A is the divalent Sr or Pb ion, is a "misfit-layer" compound consisting of alternating stacks of CdI$_2$-type VS$_2$ layers and rock-salt-type La$_{1-x}A_x$S layers, as shown in Fig. 231: (La$_{1-y}A_y$S)$_{1.17}$VS$_2$. In La$A_{0.17}$VS$_{3.17}$ ($x=0.17$), the V atoms are trivalent and the compound is an insulator with the d^2 configuration. The system becomes nonmagnetic below ~280 K, indicating a spin-singlet formation of some form at low temperatures (Yasui *et al.*, 1995). If the d^2 configuration is localized, it should be in the high-spin ($S=1$) state. Therefore the $S=1$ spins should somehow be coupled to form a singlet ground state. A most likely scenario is the formation of $S=0$ V$_3$ trimers as in LiVO$_2$ (Onoda, Naka, and Nagasawa, 1991); indeed, a structural deformation is involved in the 280-K transition, as revealed by thermal dilatation and ultrasound velocity measurements (Nishikawa *et al.*, 1996). If the d^2 configuration is not localized but forms band states, then the spin-gap behavior may be simply because the distorted La$A_{0.17}$VS$_{3.17}$ is a band insulator. In the band-insulator–to–metal transition, the disappearance of the spin gap and the appearance of metallic behavior should occur simultaneously. The latter possibility cannot be excluded from the resistivity and magnetic susceptibility data alone because the electrical resistivity is relatively low above ~280 K and nearly temperature independent, as shown in Fig. 232 (Nishikawa, Yasui,

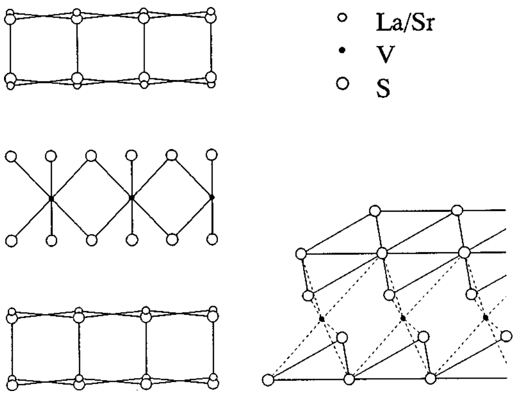

FIG. 231. Crystal structure of La$_{1.17-x}A_x$VS$_{3.17}$. From Nishikawa *et al.*, 1996.

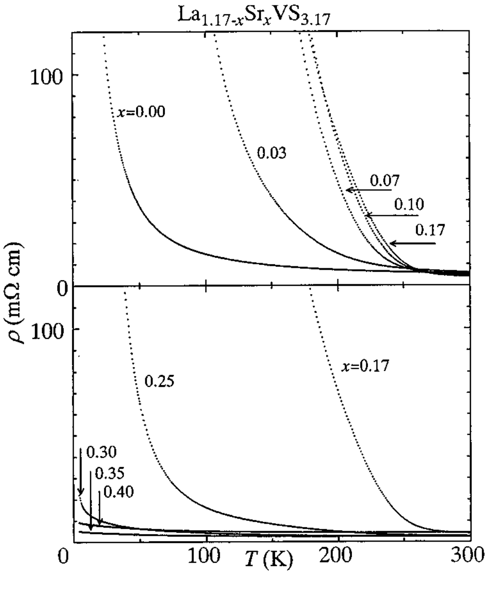

FIG. 232. Electrical resistivity of La$_{1.17-x}$Sr$_x$VS$_{3.17}$ (Nishikawa *et al.*, 1996). It becomes the largest for $x=0.17$.

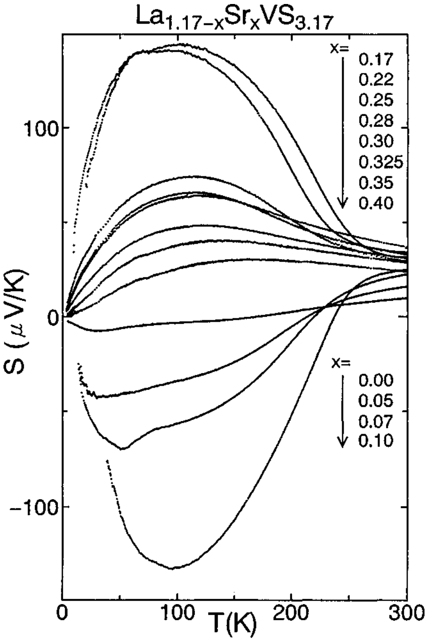

FIG. 233. Seebeck coefficient of $La_{1.17-x}Sr_xVS_{3.17}$ (Yasui *et al.*, 1995). It is negative for $x<0.17$ while it becomes positive for $x \geqslant 0.17$, indicating electron and hole doping, respectively.

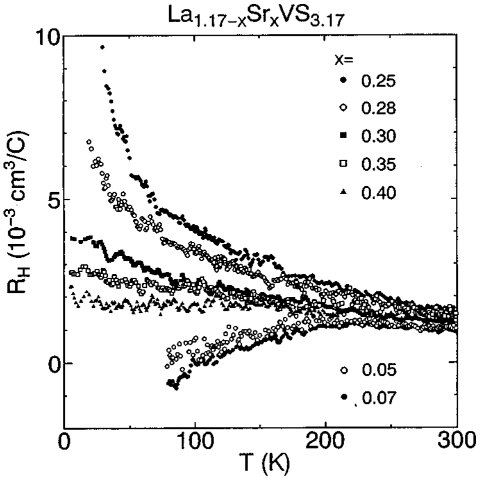

FIG. 234. Temperature dependence of the Hall coefficient for $La_{1.17-x}Sr_xVS_{3.17}$. From Yasui *et al.*, 1995.

and Sato, 1994; Nishikawa *et al.*, 1996).

$La_{1.17-x}A_xVS_{3.17}$ is a unique filling-control system in that it can be doped with either holes ($x>0.17$) or electrons ($x<0.17$). Its crystal structure implies that the electronic properties are highly two dimensional as in the cuprates. As shown in Fig. 232, the highest electrical resistivity indeed occurs at $x \sim 0.17$ and the material becomes more conductive with either decreasing or increasing x with respect to $x \sim 0.17$. Thermoelectric power is positive for $x \geqslant 0.17$ and negative for $x<0.17$, and its magnitude decreases as x deviates from 0.17, indicating that holes and electrons, respectively, are doped into the Mott insulator $LaSr_{0.17}VS_{3.17}$. Samples with the highest doping ($x \sim 0$ for n-type doping and $x \sim 0.35$ for p-type doping) still show a resistivity upturn at low temperatures, but the temperature dependence of the thermoelectric power (Fig. 233) indicates metallic behavior ($S \propto T$) below 50–100 K (Yasui *et al.*, 1995). Thermoelectric power, which is not influenced by intergrain transport, should reflect more intrinsic properties of the materials. It becomes semiconducting ($dS/dT<0$) above ~ 100 K and again metallic above ~ 250 K with smaller slope. The Hall coefficient (Fig. 234) is positive at high temperatures for all doping concentrations x, but in electron-doped samples it becomes negative at low temperatures ($\leqslant 100$ K). Its strong temperature dependence, especially in lightly doped samples, is similar to that found in the high-T_c cuprates.

The electronic specific heat decreases as $x \rightarrow 0.17$, that is, with decreasing carrier concentration (Nishikawa *et al.*, 1996), which means that the effective mass of the conduction electrons becomes lighter or the carrier number decreases as the system approaches the undoped insulator. This is analogous to the high-T_c cuprates (Loram *et al.*, 1989; Momono *et al.*, 1994) but opposite to the 3D Ti perovskite oxides (Tokura *et al.*, 1993).

Band-structure calculations have not been performed on this system because of the incommensurate crystal structure. The electronic structure of the VS_2 layer can be envisaged from the band structure of the layered material VS_2 (Myron, 1980), according to which the partially-filled V $3d$ band is located above the filled S $3p$ band and these bands are strongly hybridized with each other. Photoemission studies confirmed this electronic structure [Fig. 235(a); Ino *et al.*, 1997b], meaning that thecompound can be viewed as a Mott-Hubbard-type system (although it must be located near the boundary between the Mott-Hubbard and charge-transfer regimes). The doping dependence of the photoemission spectra reveals an interesting behavior of the spectral weight redistribution and chemical potential shift as functions of band filling. As shown in Fig. 235(a), the V $3d$ band (within ~ 1.5 eV of E_F) is shifted toward E_F with electron doping and away from E_F with hole doping, but the shift is slower than that of the S $3p$ band (located 1.5–1.7 eV below E_F). If the shift of the S $3p$ band reflects a chemical potential shift, the slower shift of the V $3d$ band would be interpreted as due to the repulsion between quasiparticles of V $3d$ character, as described in Sec. II.D.1. The shift of the chemical potential $\partial\mu/\partial n$, as reflected in the shift of the S $3p$ band, is slow for low hole/electron concentration and fast for high hole/electron concentration, as shown in Fig. 235(b). The suppression of $\partial\mu/\partial n$ near the Mott insulator may imply that the effective mass is enhanced, which excludes the simplest band-insulator picture for the undoped compound. The suppression of the chemical potential shift is apparently inconsistent with the decreasing electronic specific heat toward $x=0.17$, if one assumes the Fermi-liquid relations (2.74) and (2.75) with nonsingular behavior of the Landau parameters (Furukawa and Imada, 1993). The observations $\partial\mu/\partial n \rightarrow 0$ and $\gamma \rightarrow 0$ for $x \rightarrow 0.17$ can be reconciled with each other if the metallic state is not a Fermi liquid or if there is a pseudogap in the vicinity of the chemical potential. An-

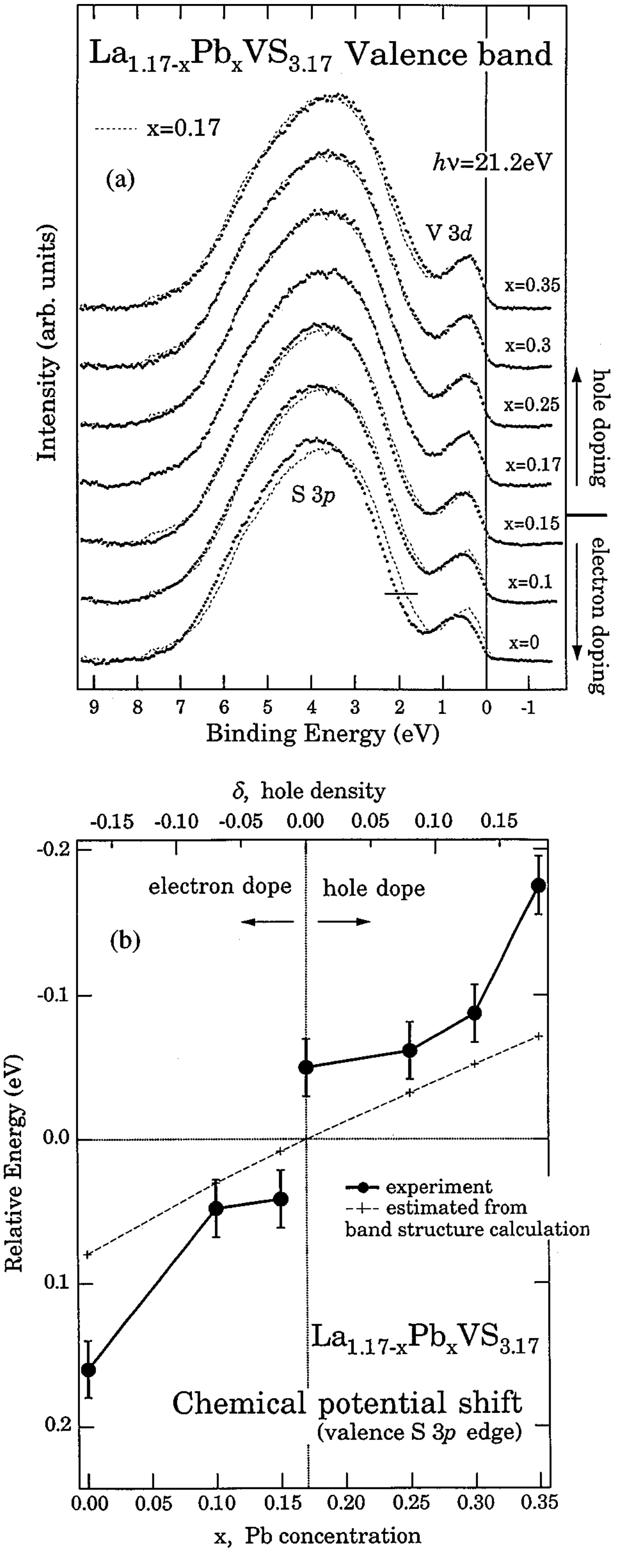

FIG. 235. Photoemission results of $La_{1.17-x}Pb_xVS_{3.17}$ (Ino *et al.*, 1997b). (a) Photoemission spectra; (b) shift of the chemical potential (deduced from the shift of the S 3p band) as a function of x. The dashed line is the shift expected from the band structure density of states.

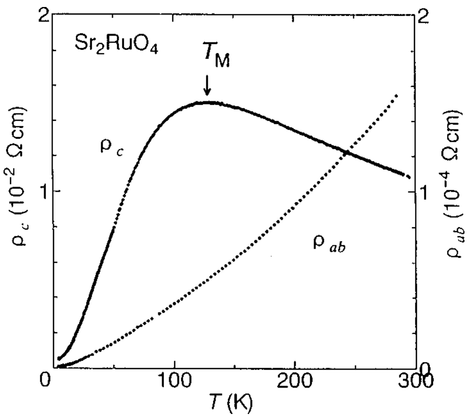

FIG. 236. Temperature dependence of anisotropic resistivity of Sr_2RuO_4 (Lichtenberg *et al.*, 1992; Maeno *et al.*, 1997).

other important feature of the chemical potential in the $La_{1.17-x}A_xVS_{3.17}$ system is a discontinuous jump of $\sim$0.08 eV between n-type and p-type doped samples, giving the first evidence for a chemical potential jump across the Mott-insulating gap. This gap is much larger than the temperature at which the spin gap is formed in the undoped compound, again disfavoring the band-insulator picture for undoped $LaA_{0.17}VS_{3.17}$.

H. 4*d* systems

1. Sr_2RuO_4

The ruthenium oxide compounds are among those showing the Ruddlesden-Popper series (layered and cubic perovskite) phase illustrated in Fig. 64. Sr_2RuO_4 has the K_2NiF_4-type structure and is isostructural with the cuprate superconductor $La_{2-x}Sr_xCuO_4$, apart from the absence of orthorhombic distortion. Maeno *et al.* (1994) discovered the $T_c \approx 1$ K superconductivity in this compound, which has stimulated studies on its anisotropic charge dynamics and electronic structures as well as on related layered ruthenates both for their possible relevance to the mechanism of high-T_c superconductivity and for the occurrence of exotic symmetry of superconductivity (Rice and Sigrist, 1996; Mazin and Singh, 1997; Agterberg, Rice, and Sigrist, 1997).

The temperature dependence of the in-plane and c-axis resistivity (ρ_{ab} and ρ_c, respectively) is shown in Fig. 236 (Maeno *et al.*, 1997). The in-plane conduction is typically metallic with a low residual resistivity just above T_c, reaching $\approx 1\ \mu\Omega$ cm. By contrast, the c-axis transport is nonmetallic above $T_M \approx 130$ K, but shows metallic behavior at lower temperatures (Lichtenberg *et al.*, 1992), indicating a crossover from a 2D to a 3D metal. The resistivity anisotropy ρ_c/ρ_{ab} reaches as large as 200 around T_M.

Below about 25 K, the resistivity follows the T^2 dependence both for ρ_{ab} and ρ_c, indicating the conventional Fermi-liquid behavior (Maeno, 1996). In fact, de Haas–van Alphen oscillations were observed by Mackenzie *et al.* (1996) and revealed some important Fermi surface parameters. The results could be well interpreted in terms of an almost 2D Fermi-liquid model, which is consistent with the LDA band structure (Oguchi, 1995; Singh, 1995). The observed (and LDA-calculated) Fermi surface consists of two large electron

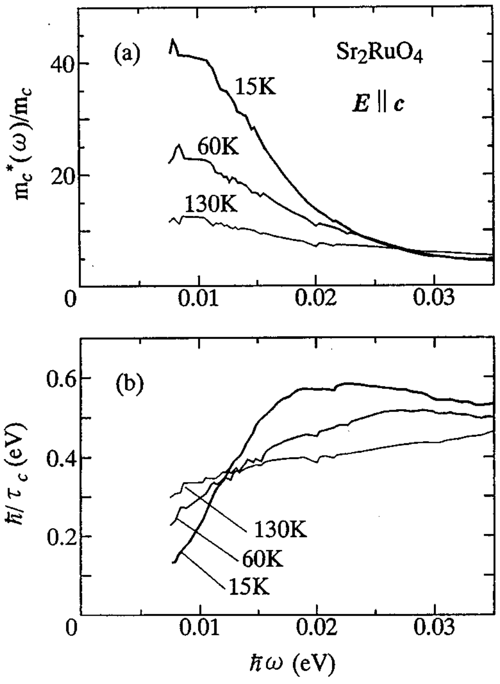

FIG. 237. Energy-dependent effective mass and scattering rate for the c-axis conduction, derived by extended Drude analysis of c-axis polarized optical conductivity spectra. From Katsufuji, Kasai, and Tokura, 1996.

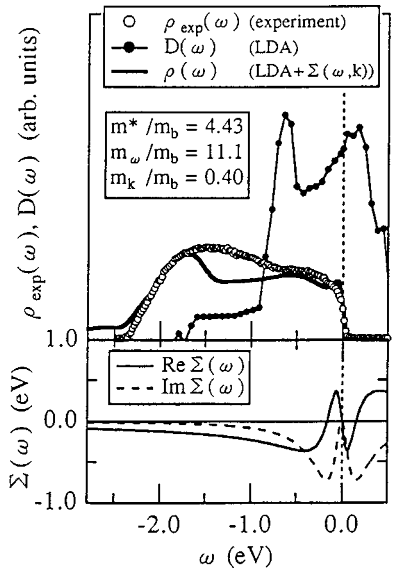

FIG. 238. Photoemission spectrum of Sr_2RuO_4 ($\rho_{exp}(\omega)$; Inoue *et al.*, 1996) compared with the DOS from a band-structure calculation [$D(\omega)$; Oguchi, 1995]. The solid curve represents the DOS modified by the self-energy correction $\Sigma(\mathbf{k},\omega)=g\omega[\Gamma/(\omega-i\Gamma)][\Delta/(\omega-i\Delta)]+a\varepsilon_{\mathbf{k}}$, where $g=10.1$, $\Gamma=0.102$ eV, $\Delta=0.246$ eV, and $a=1.5$.

cylinders (β and γ) centered on the ΓZ line and one narrow hole cylinder (α) running around the corner of the Brillouin zone (see dashed lines of Fig. 238 below). The metallic c-axis transport at low temperatures is dominated by β and γ sheets, for which the c-axis mean free path l_c ($\approx$30 Å at 1 K) can be substantially longer than the separation between adjacent RuO_2 sheets, $c/2=6.4$ Å (Mackenzie *et al.*, 1996).

The carrier electrons in Sr_2RuO_4 appear to be considerably renormalized due to the electron correlation. The electronic specific-heat coefficient (γ) is 37.5 mJ/K^2 mol (Maeno *et al.*, 1997), which gives rise to a density of states at the Fermi level enhanced by a factor of 3.6 over the LDA result. The Wilson ratio, $R_W=\chi/\gamma$, is 1.7–1.9, also typical of correlated metals.

A strong mass renormalization for the c-axis charge dynamics was observed in the strongly temperature-dependent c-axis spectra of the optical conductivity (Katsufuji, Kasai, and Tokura, 1996). In the c-axis spectra, the Drude band evolves below T_M with an apparent plasma edge around 0.01 eV at $T\ll T_M$. Figure 237 (Katsufuji, Kasai, and Tokura, 1996) shows the result of an analysis of the c-axis spectra in terms of the extended Drude model, in which the energy dependence of the mass and relaxation time of the conduction carriers was taken into account. Below $T_M\approx 130$ K, m_c^* for $\hbar\omega<0.02$ eV is enhanced and reaches about 30 times the unrenormalized c-axis mass m_c for $\hbar\omega<0.01$ eV at 15 K. On the other hand, $\hbar/\tau$ is suppressed for $\hbar\omega<0.012$ eV but increases for $\hbar\omega>0.012$ eV with a decrease in temperature. Such a conspicuous temperature dependence is similar to that of a heavy-fermion compound, e.g., URu_2Si_2 (Bonn, Garrett, and Timusk, 1988). By contrast, $m_{ab}^*(\omega)/m_{ab}$ is nearly independent of $\hbar\omega$, though a small mass enhancement is observed in a T-dependent manner below 0.3 eV. These results indicate that the 3D metallic conduction below $T_M\approx 130$ K is brought about by the onset of coherent motion of carriers for which the mass and scattering rate along the c axis are strongly renormalized. Such anisotropic mass renormalization may be considered as a generic feature of quasi-2D metals with strong electron correlation, but it is obviously distinct from the case of the cuprate superconductors.

The LDA band structure of Sr_2RuO_4 was calculated by Oguchi (1995) and Singh (1995). Their calculations predict that energy bands which cross the E_F are derived from the strong hybridization of the Ru $4d_{xy}$, $4d_{yz}$, and $4d_{zx}$ orbitals with the O $2p$ orbitals. The photoemission spectra are generally consistent with this picture, but the observed Ru $4d$ band feature is distributed over a wider energy range than the calculation, as shown in Fig. 238 (Inoue *et al.*, 1996). This may be interpreted as due to electron correlation effects within the Ru $4d$ band, as in the case of the V and Ti oxides described above, that is, as due to a transfer of spectral weight from the coherent quasiparticle band to the incoherent part of the spectral function. Also, the spectral weight *at* E_F is suppressed compared to the band DOS as in the V and Ti oxides. Thus Sr_2RuO_4 may be viewed as one of the strongly correlated electron systems like the $3d$ transition-metal oxides, and any interpretation of its various physical properties should take into account electron correlation.

Dispersions of the Ru $4d$-derived bands were investigated by angle-resolved photoemission studies (Yokoya *et al.*, 1996a, 1996b; Lu *et al.*, 1996). In spite of the wide energy distribution of the coherent plus incoherent spec-

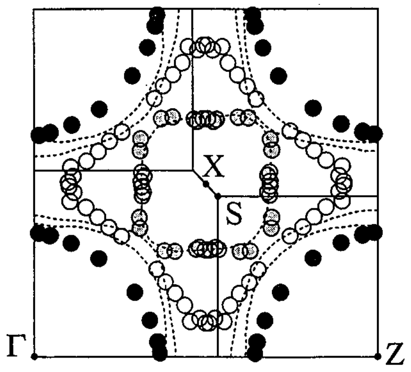

FIG. 239. Fermi surfaces of Sr_2RuO_4 measured by angle-resolved photoemission spectroscopy (Yokoya *et al.*, 1996a). The filled circles denote electronlike Fermi surfaces and the open and gray circles denote holelike Fermi surfaces. Fermi surfaces derived from band-structure calculations (Oguchi, 1995) are given by the dashed lines.

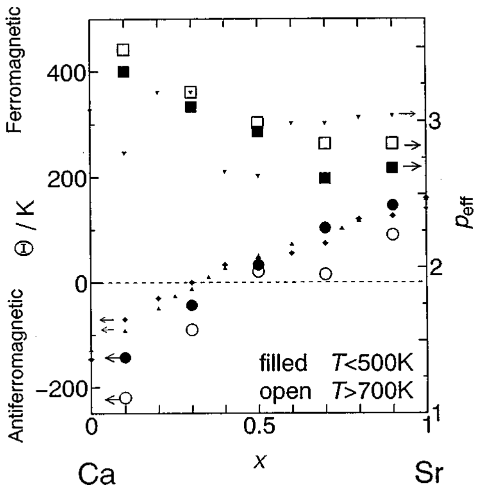

FIG. 240. Effective moment p_{eff} and Weiss temperature Θ of $Ca_{1-x}Sr_xRuO_3$ (Fukunaga and Tsuda, 1994). The open and filled symbols correspond to values deduced at high and low temperatures.

tral weight, the dispersions near E_F (reflecting only the coherent part) were generally weak compared with the band-structure calculations. In particular, they revealed a flat band with a saddle point, i.e., a so-called "extended van Hove singularity" around the $(\pi,0)$ point of the Brillouin zone, as in the high-T_c cuprates. The position of the flat band was ~20 meV below E_F. The calculations predicted an electron-like Fermi surface around the Γ point and two hole-like Fermi surfaces around the X $[(\pi,\pi)]$ point. Although the mass is more enhanced in the de Haas–van Alphen measurement than the LDA result, the volumes of the calculated Fermi surfaces are in agreement with those derived from the de Haas-van Alphen measurements to within 1% (Mackenzie *et al.*, 1996). On the other hand, the Fermi surfaces obtained by the angle-resolved photoemission studies are in disagreement with the band-structure calculations and the de Haas–van Alphen measurements, as shown in Fig. 239. It was found that the agreement is improved if the E_F is shifted upward by ~70 meV compared to the calculated band structure (Lu *et al.*, 1996), although it is difficult to justify such a procedure. Since this is the only case where ARPES experiments and LDA calculations have given different Fermi surfaces for a 2D metal, a more critical experimental check should be made in order to exclude, e.g., surface effects.

2. $Ca_{1-x}Sr_xRuO_3$

$SrRuO_3$ has a slightly distorted perovskite ($GdFeO_3$-type) structure and is metallic. It shows ferromagnetic order below $T_C \simeq 160$ K (Callagan *et al.*, 1966). The saturation magnetization is 1.1–1.3 μ_B/Ru, and a neutron-diffraction study gave the ordered moment of 1.4 ± 0.4 μ_B/Ru, which is the largest ordered magnetic moment among $4d$ transition-metal compounds (Longo *et al.*, 1968). While those values are smaller than that ($2\mu_B$) expected for the Ru^{4+} ion in the low-spin state (t_{2g}^4, $S=1$), the effective moment above T_C, $\sim 2.6\mu_B$, is rather close to the low-spin value of $2\sqrt{S(S+1)} = 2.83\mu_B$ (Callagan *et al.*, 1966; Longo *et al.*, 1968). The Rhodes-Wolfarth ratio is thus ~1.3, a value close to that of the itinerant ferromagnet Ni metal, implying that $SrRuO_3$ is an "intermediately localized" ferromagnet (Fukunaga and Tsuda, 1994). The T_C decreases under hydrostatic pressure at the rate of $dT_C/dP \simeq -(6-8)$ $\mathrm{K \cdot GPa^{-1}}$ (Neumeier *et al.*, 1994; Shikano *et al.*, 1994), as in other itinerant ferromagnets. The negative dT_C/dP is contrasted with the positive dT_N/dP in local-moment systems such as $LaTiO_3$ (Okada *et al.*, 1992) and the positive dT_C/dP in double-exchange systems such as $La_{1-x}Sr_xMnO_3$ (Moritomo *et al.*, 1995).

$CaRuO_3$ is also metallic. The crystal structure of $CaRuO_3$ is more distorted than $SrRuO_3$: the Ru-O-Ru bond angle is reduced from ~165° to ~150°, in going from $SrRuO_3$ to $CaRuO_3$ (Kobayashi *et al.*, 1994). The Weiss temperature is negative, indicating antiferromagnetic interaction between magnetic moments, but it remains paramagnetic down to the lowest temperature (Gibb *et al.*, 1974). In the solid solution $Ca_{1-x}Sr_xRuO_3$, the Curie temperature T_C decreases with Ca content and is completely suppressed at $x \simeq 0.4$ (Kanbayashi, 1978) [while a recent study on single crystals showed that T_C remains finite up to $x \lesssim 1$ (Cao *et al.*, 1997)]. The decrease of T_C with Ca substitution may appear consistent with the decrease of T_C under pressure, in the sense that the lattice constant shrinks in both cases. It should be remembered, however, that the reduction in the Ru-O-Ru bond angle with Ca substitution would normally reduce the d-band width and would therefore have an effect opposite to that of increased pressure. More studies are needed to explain both the pressure and Ca substitution effects in a consistent way.

With Ca substitution, the effective moment p_{eff} increases and the Weiss temperature θ decreases, as shown in Fig. 240 (Fukunaga and Tsuda, 1994): θ changes its sign at $x \simeq 0.4$. The χ^{-1}-T plot in a wide temperature range ($T < 100$ K) changes its slope above

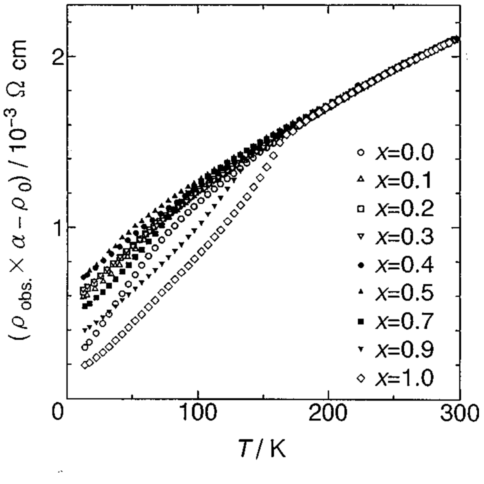

FIG. 241. Resistivity of $Ca_{1-x}Sr_xRuO_3$ normalized at 300 K (Fukunaga and Tsuda, 1994). ρ_0 is the residual resistivity and for $SrRuO_3$ ranges from $\rho_0 \sim 2\times10^{-5}$ Ω cm (Bouchard and Gillson, 1972; Klein *et al.*, 1996) to 2.3×10^{-6} Ω cm (Izumi *et al.*, 1997). Here $\rho(300\ \mathrm{K})=2-3\times10^{-4}$ Ω cm and α is a scaling parameter.

and below $T\sim600$ K for all x's: In the low-temperature region, θ is a little larger, indicating that ferromagnetic coupling increases at low temperatures, and p_{eff} is smaller, indicating that the magnetic electrons are more itinerant at low temperatures. These observations mean that metallic transport favors ferromagnetic coupling. The increased localized character at high temperatures may be a general property of narrow-band metals, in which there is no coherent transport above $T \sim W^*/3k_B$, where W^* is the renormalized bandwidth. The resistivity value of $\sim2\times10^{-4}$ Ω cm at high temperatures ($\sim$300 K) indicates $k_F l\sim1$, but no saturation is found up to 1000 K (Allen *et al.*, 1996). This indicates the breakdown of conventional metallic transport; Klein *et al.* (1996) attributed this to the "bad metallic behavior" discussed by Emery and Kivelson (1995). The optical spectra of $Ca_xSr_{1-x}RuO_3$ show great similarity to those of the high-T_c cuprates (Bozovic *et al.*, 1994). Nearly $\sigma(\omega)\sim1/\omega$ behavior is found up to $\omega\sim1$ eV; the electronic Raman scattering shows an energy-independent continuum up to $\sim$1 eV. These optical behaviors are characteristic of incoherent metals.

Coupling between the magnetic and transport properties is an interesting issue in metallic ferromagnets. $SrRuO_3$ shows negative magnetoresistance over the whole temperature range (Gasusepohl *et al.*, 1995; Izumi *et al.*, 1997). The Hall coefficient changes its sign from negative to positive at $\sim$50 K with increasing temperature (Gausepohl *et al.*, 1996), which implies that there are both electronlike and hole-like Fermi surfaces and that a large portion of the Fermi surfaces are very flat. Figure 241 shows that the resistivity drops at temperatures below T_C due to the disappearance of scattering from spin disorder. Above T_C, the temperature dependence of the normalized resistivity is nearly identical for all x's, probably because the same (spin-disorder) scattering mechanism dominates in the high-temperature range (Fukunaga and Tsuda, 1994). With Ca substitution, the resistivity below T_C increases as T_C decreases towards $x\sim0.4$, and with further substitution it decreases again: In particular, $CaRuO_3$ shows an unusual resistivity drop below $\sim$50 K, which may indicate the disappearance of scattering by magnetic fluctuations, possibly due to the opening of an excitation gap in the magnetic fluctuation spectrum. The critical behaviors around T_C give insight into the coupling between magnetic and transport properties. Anomalous critical transport behavior has been found, but is attributed to the "bad metallic" behavior and not to the coupling between the magnetic and transport properties, because the critical magnetic behavior is conventional (Klein *et al.*, 1996).

The band structure of ferromagnetic $SrRuO_3$ was calculated within the LSDA (Singh, 1996; Allen *et al.*, 1996). The results show very strong Ru $4d$-O $2p$ hybridization as in Sr_2RuO_4. Both electronlike and hole-like Fermi surfaces are indeed present. Flat bands cross E_F, giving rise to a high DOS at E_F and hence a ferromagnetic ground state through the Stoner mechanism. The obtained ordered moment of $\sim1.5\ \mu_B$/Ru is in good agreement with the experimental value of $1.4\pm0.4\ \mu_B$/Ru. The overall line shape of the photoemission spectra (Cox *et al.*, 1983; Fujioka *et al.*, 1997) agrees

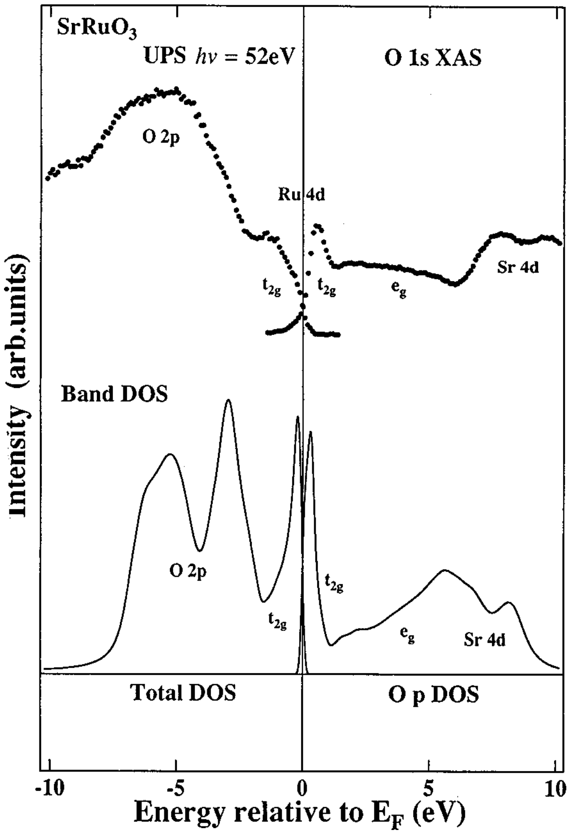

FIG. 242. Photoemission and O $1s$ x-ray absorption spectra of $SrRuO_3$ compared with the band DOS in the ferromagnetic state (Fujioka *et al.*, 1997). For the XAS spectra, the oxygen p partial DOS is presented.

well with the band DOS, as shown in Fig. 242. The Ru $4d$ band, however, is spread over a wider energy range than the calculation, and the spectral weight at E_F is suppressed compared to the band DOS, as in the case of Sr_2RuO_4. This may be interpreted as due to transfer of spectral weight from the coherent part to the incoherent part of the spectral function arising from electron correlation. From the reduced spectral intensity at E_F, one obtains $m_k/m_b \sim 0.3$ (Sec. II.D.1). Combining this value with the mass enhancement factor of $m^*/m_b = 3.7$ deduced from the electronic specific heat γ and the band-structure calculation (Allen *et al.*, 1996), one obtains the quasiparticle weight $Z = (m_k/m_b)/(m^*/m_b)m_b \sim 0.1$. Such a small weight should be related to the bad/incoherent metallic behavior discussed above.

Evolution of the spectral function in going from metallic to insulating Ru oxides was studied for various Ru oxides, including the Pauli-paramagnetic metal $Bi_2Ru_2O_7$, paramagnetic metal $CaRuO_3$, ferromagnetic metal $SrRuO_3$, and antiferromagnetic insulator $Y_2Ru_2O_7$ (Cox *et al.*, 1983). These oxides show qualitatively similar behavior to that of the V and Ti oxides with d^1 configuration (Sec. I.A.5), in that there is a transfer of spectral weight from higher binding energies (the "incoherent part") to lower binding energies (the "coherent part") with increasing U/W. From the shallower position of the incoherent peak, the Coulomb energy U is estimated to be somewhat smaller (~ 3 eV) than that of the Ti and V oxides (~ 4 eV).

V. CONCLUDING REMARKS

Almost localized electrons near the metal-insulator transitions are well described neither by a simple itinerant picture in momentum space nor by a localized picture in real space. Theoretical and experimental efforts to make bridges between the itinerant and localized or, in other words, coherent and incoherent pictures have been made for years and have been fruitful, as we have seen in this article. However, this is still a challenging subject and many open questions have yet to be answered. Marginally retained metals near the metal-insulator transition have offered interesting and rich phenomena for decades and will continue to do so in the future, presenting fundamental problems in condensed matter physics as well as potential sources of applications.

We first summarize the basic understanding of correlation effects of almost localized electrons near the metal-insulator transitions. In the Mott insulating state, a charge gap is formed and electrons are localized below the gap energy scale. Because of the local nature of the electron wave function in the insulator, the internal degrees of freedom (component degrees of freedom) such as spin and orbital fluctuations give rise to degeneracy, which, along with the resultant residual entropy, is released at low temperatures by intersite interactions such as superexchange and orbital exchange. In the strong-correlation regime, these exchange interactions can be much smaller than the charge gap and the bare bandwidth. Therefore the entropy due to the component remains unreleased above such low energy scales. When the system is slightly metallized, the coherent part is still small and the entropy related to the dominant incoherent part is also not released above the temperature of the intersite exchange interactions. This provides the background for the anomalous behavior of metals at low temperatures near the Mott insulator.

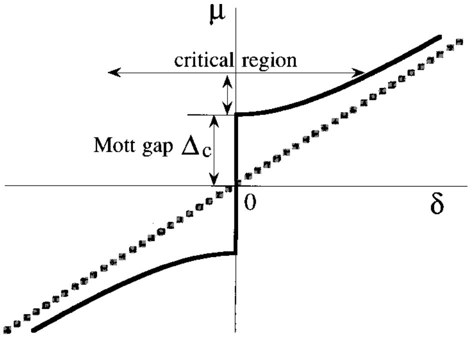

FIG. 243. The chemical potential μ and the doping concentration δ to illustrate the width of the critical region. The dotted line is the μ vs δ for a noninteracting system and the solid curve for an interacting system with the Mott insulating phase.

With this underlying residual entropy, in the lightly doped metallic region, more happens. At integer fillings, the states near the Fermi level for the noninteracting system are kicked out of the Mott gap region by strong Coulomb repulsion. The region reconstructed out of the Mott gap forms a flat band as in Fig. 243, causing degeneracy in momentum space, and constitutes another origin of degeneracy. The mobile carriers under this flat dispersion further strongly couple to the component degrees of freedom and disturb the process of entropy release for the spin and orbital degrees of freedom, when the carrier motion destroys the ordering of spins and orbitals. As a counteraction, the spin and orbital correlations also disturb the coherent carrier motion to make a flatter band with strong damping in a self-consistent fashion. Then the coupling of charge dynamics to the component destabilizes the charge coherence as well as the component ordering and compresses the process of residual entropy release into a much lower energy scale. This combined effect is the main origin of the various anomalous features of correlated metals near the metal-insulator transition that have been the main subject of this review article. As we have seen in various examples, the residual entropy and related fluctuations cause rich phenomena which are quite different from those of standard metals—for example, mass enhancement, unusual temperature dependence of the resistivity and spin susceptibility, obstinate incoherent responses in transport, optical, photoemission, and magnetic studies, and enhanced spin and orbital fluctuations.

These anomalous features are most distinctly described by the quantum critical phenomena of the Mott transition. In particular, coupling to the component degrees of freedom is able to cause a change even in the universality class of the metal-insulator transition, as in $z=4$ in the 2D systems. In terms of the critical exponents of the universality class, the degree of coherent carrier motion is characterized by the dynamic exponent z, which represents the dispersion of the charge carrier near the metal-insulator transition. Coupling to a component with large quantum fluctuations drives the ordinary exponent $z=2$ to a higher value, which qualitatively changes the character of a metal to a more incoherent liquid. Whether a metal can be described in terms of quantum critical phenomena depends on the width of the critical region. If the region is narrow, it will not influence experimental results. The critical region of a metal-insulator transition for filling control is roughly estimated from a simple argument. As discussed above, when the Mott gap Δ_c opens at an integer filling, the states of the noninteracting counterpart contained within the gap are reconstructed and pushed out from the gap region to the outer gap edge $E=\Delta_c$ roughly within the energy range of the gap, namely $\Delta_c \leqslant E \leqslant 2\Delta_c$. This energy range is transformed to the wave-number scale $k \sim \min(2\pi, 2\pi\Delta_c/t)$, which determines the area of flat dispersion due to many-body effects and characterizes the critical region (see Fig. 243). This is interpreted as the critical region of the doping concentration extended up to $\delta \sim \min(1, \Delta_c/t)$. In the strong-correlation regime, Δ_c could have the same order of magnitude as the bare bandwidth, which makes the critical region of the doping concentration wide. This is why Mott phenomena in the strong-correlation regime have a wide critical region and why treatments in terms of quantum critical phenomena are appropriate in experimentally observed metallic regions, in contrast to the case of simple magnetic transitions.

There are several different views of each anomalous feature of metals near the Mott insulator, in which different and individual aspects can be emphasized. They include Anderson localization due to disorder, localization transitions due to coupling to the lattice (polaron effects), instabilities to charge ordering and other local orders, as well as instabilities to superconductivity. We first note that these additional aspects are both repercussion effects of the Mott transition and at the same time inevitable products of it. When the Mott transition is approached from the metallic side, anomalously suppressed coherence with the vanishing renormalization factor generates slower and slower charge dynamics, which leads to the high sensitivity of charged carriers to various external fluctuations, and the system becomes subject to instabilities to localization or some type of symmetry breaking. This sensitive region is illustrated in Fig. 1 in the shaded area.

To understand the global features and the principal driving force of the Mott transition, we first have to understand its intrinsic nature. In this article, we have sketched various theoretical approaches for that purpose. In conjunction with experimental results, various mean-field approaches have succeeded in explaining some aspects of the anomalies. However, for unusual metals with increasingly incoherent responses toward the metal-insulator transition, it has been shown that temporal as well as spatial fluctuations have to be properly taken into account. In this context, the Fermi-liquid approaches must include strong wave-number and frequency dependences in the self-energy correction beyond the present level. It would be desirable for this Fermi-liquid framework to include a program for predicting the breakdown of the Fermi liquid itself as the Mott insulator is approached in a continuous fashion. The same requirement applies to first-principles calculations and spin-fluctuation theories. When spatial fluctuations are ignored, temporal fluctuations are correctly expressed by the dynamic mean-field theory, in contrast to other theoretical approaches such as the Gutzwiller, Hubbard, Hartree-Fock, and slave-particle approximations. When both spatial and temporal fluctuations become important, a prescription in low dimensions is established by the scaling theory. Further understanding along the lines of the scaling description, especially the singular wave-number dependence of the renormalization that it implies, has to be pursued. The flat band structure around $(\pi,0)$ in 2D relevant in the cuprates offers a particular example. Numerical methods have proven to be powerful when combined with an appropriate low-energy description of the scaling behavior. It would be desirable to further improve the method to reduce the limitation of finite system size and also to allow the calculation of dynamical quantities in large systems. The criticality of the Mott phenomena has been recognized as a subject to be studied in greater detail in real materials. Systematic studies have only just begun recently, and further experiments that fine-tune and control the parameters will be needed.

As mentioned above, the appearance of the strong correlation effects in real materials is accompanied by various other degrees of freedom. These secondary effects inevitably occur to some extent because of slow and incoherent charge dynamics generated by the Mott phenomena. Studies on these repercussion effects are all at a primitive stage of understanding at the moment and should be elucidated in the future. The first issue is *Anderson localization* near the Mott insulator. It remains to be clarified how the disorder effects appear just before a mass-diverging Mott transition. This is clearly beyond the presently available scenarios of the Anderson localization. The second issue is the *effect of polarons*, which may be particularly important when the lattice degrees of freedom are strongly coupled through the component, as in the case of dynamic Jahn-Teller distortion coupled to orbital fluctuations. Another secondary effect is the instability of incoherent metal near the Mott insulator to charge, spin, or orbital order and competition between these types of order. *Charge ordering* or stripe structure may happen more easily near the Mott insulator due to the mass enhancement. In particular, it has been proposed that the inherent instability of incoherent metal to the *superconducting state* is driven by the change in universality class connected with the mechanism of high-T_c superconductivity. This idea deserves elucidation in more detail.

For a better understanding of the d-electron systems, we need to study orbital degrees of freedom more systematically. Mean-field phase diagrams have been studied for the coupled spin and orbital systems and compared to the experimental results, but fluctuation effects are not well studied at the moment.

Here, we briefly summarize the effort to determine the overall electronic model parameters of correlated metals. The global electronic structure of $3d$ transition-metal compounds on the eV scale is now well understood from spectroscopic and first-principles studies. The electronic structure parameters such as the on-site Coulomb energy U, the charge-transfer energy Δ, and the transfer integrals T have been deduced and their systematic changes with chemical composition ranging from the Mott-Hubbard regime to the charge-transfer regime have been clarified. The LDA+U method provides a practical way to incorporate electron-electron interactions into first-principles band-structure calculations on the Hartree-Fock level. However, in many cases the U value has been determined not from first principles but empirically. That is, a true first-principles approach to strongly correlated systems is lacking so far, even on the mean-field level. To understand the spectroscopic properties, effects of interactions that are not included in the standard models such as the Hubbard and d-p models, namely, the long-range Coulomb interaction, electron-phonon interaction, impurity potentials, etc. need to be studied further in the future.

Experimentally, in this decade, many d-electron compounds have been studied with the idea of systematically controlling the parameters to tune the distance from the metal-insulator transition. Filling control, bandwidth control, and dimensionality control have been extensively studied. The compounds studied indeed show diverse properties of transport, optical and magnetic responses while theoretical analyses have provided useful schemes for classifying the anomalous properties surveyed in this article. In the last decade, interesting and surprising phenomena have been found in the region where the metallic state is retained close to the Mott insulator when instability to electron localization is suppressed. These include high-T_c superconductivity and colossal magnetoresistance. In future experimental studies, it is certainly hoped that metallic states as close as possible to the Mott insulator can be further realized in a variety of materials and that various instabilities can be controlled to obtain strongly nonlinear responses of charge, spin, orbital, and lattice properties, with the goal of developing useful devices for applications. Nonlinear responses also offer a rich array of dynamic properties in both equilibrium and nonequilibrium states, with metastabilities and slow relaxations as in the Mn perovskite compounds. These show great promise for useful optical or magnetic applications. It is certainly clear that our knowledge on the controllability of carrier dynamics close to the Mott insulator is still at a primitive stage compared to that in semiconductor devices. Correlated electron devices will have broad potential applications when properly developed, because of the cooperative and collective nature of electrons.

ACKNOWLEDGMENTS

The authors thank G. Aeppli, P. W. Anderson, S. Anzai, A. Asamitsu, F. F. Assaad, A. E. Bocquet, E. Dagotto, D. S. Dessau, H. Ding, N. Furukawa, J. M. Honig, I. H. Inoue, N. Katoh, T. Katsufuji, T. Kimura, K. Kishio, K. Kitazawa, G. Kotliar, Y. Kuramoto, H. Kuwahara, K. Matho, M. Matoba, T. Mizokawa, T. Moriya, Y. Motome, Y. Okimoto, J.-H. Park, T. M. Rice, D. D. Sarma, T. Sasagawa, G. A. Sawatzky, H. Tabata, H. Takagi, Y. Tomioka, H. Tsunetsugu, J. Wilkins, and H. Yasuoka for their help at various stages in the writing of this article, including fruitful discussions and preparation of figures. The authors thank J. Wilkins for his encouragement in writing this article. The authors are grateful for financial support by a Grant-in-Aid for Scientific Research on the Priority Area "Anomalous Metallic States near the Mott Transition" from the Ministry of Education, Science and Culture, Japan, and are also indebted to members of this project for valuable discussions. The authors also acknowledge support from Japan Society for Promotion of Science under the project JSPS-RFTP97P01103. The authors appreciate K. Fujii and N. Sasaki for their devotion and help during the preparation of this article.

REFERENCES

Preprint numbers refer to the archives cond-mat@xxx.lanl.gov

Abbate, M., F. M. F. de Groot, J. C. Fuggle, A. Fujimori, O. Strebel, F. Lopez, M. Domke, G. Kaindl, G. A. Sawatzky, M. Takano, Y. Takeda, H. Eisaki, and S. Uchida, 1992, Phys. Rev. B **46**, 4511.

Abbate, M., F. M. F. de Groot, J. C. Fuggle, A. Fujimori, Y. Tokura, Y. Fujishima, O. Strebel, M. Domke, G. Kaindl, J. van Elp, B. T. Thole, G. A. Sawatzky, M. Sacchi, and N. Tsuda, 1991, Phys. Rev. B **44**, 5419.

Abbate, M., J. C. Fuggle, A. Fujimori, L. H. Tjeng, C. T. Chen, R. Potze, G. A. Sawatzky, H. Eisaki, and S. Uchida, 1993, Phys. Rev. B **47**, 16124.

Abrahams, E., P. W. Anderson, D. C. Licciardello, and T. V. Ramakrishnan, 1979, Phys. Rev. Lett. **42**, 673.

Abrahams, E., and P. A. Lee, 1986, Phys. Rev. B **33**, 683.

Aebi, P., J. Osterwalder, P. Schwaller, L. Schlapbach, M. Shimoda, T. Mochiku, and K. Kadowaki, 1994, Phys. Rev. Lett. **72**, 2757.

Aeppli, G., *et al.*, 1988, Phys. Rev. Lett. **61**, 203.

Aeppli, G., and Z. Fisk, 1992, Comments Condens. Matter Phys. **16**, 155.

Aeppli, G., S. M. Hayden, H. A. Mook, Z. Fisk, S-W. Cheong, D. Rytz, J. P. Remeika, G. P. Espinosa, and A. S. Cooper, 1989, Phys. Rev. Lett. **62**, 2052.

Affleck, I. A., and J. B. Marston, 1988, Phys. Rev. B **37**, 3774.

Agterberg, D. F., T. M. Rice, and M. Sigrist, 1997, Phys. Rev. Lett. **78**, 3374.

Aiura, Y., H. Bando, I. Hase, Y. Nishihara, Y. Haruyama, and H. Suzuki, 1996, J. Electron Spectrosc. Relat. Phenom. **78**, 199.

Akimitsu *et al.*, 1998, unpublished.

Alexandrov, A. S., A. M. Bratkovsky, and N. F. Mott, 1994, Phys. Rev. Lett. **72**, 1734.

Alexandrov, A. S., and N. F. Mott, 1994, Rep. Prog. Phys. **57**, 1197.

Allen, P. B., H. Berger, O. Chauvet, L. Forro, T. Jarlborg, A. Junod, B. Revaz, and G. Santi, 1996, Phys. Rev. B **53**, 4393.

Allen, J. W., S-J. Oh, L. E. Cox, W. P. Ellis, M. S. Wire, Z. Fisk, J. L. Smith, B. B. Pate, I. Lindau, and A. J. Arko, 1985, Phys. Rev. Lett. **54**, 2635.

Allen, J. W., C. G. Olson, M. B. Maple, J.-S. Kang, L. Z. Liu, J.-H. Park, R. O. Anderson, W. P. Ellis, J. T. Markert, Y. Dalichaouch, and R. Liu, 1990, Phys. Rev. Lett. **64**, 595.

Allen, P. B., W. E. Pickett, and H. Krakauer, 1987, Phys. Rev. B **36**, 3926.

Alvarado, S. F., M. Erbudak, and P. Munz, 1976, Phys. Rev. B **14**, 2740.

An, G., and J. M. J. van Leeuwen, 1991, Phys. Rev. B **44**, 9410.

Anderson, P. W., 1952, Phys. Rev. **86**, 694.

Anderson, P. W., 1956, Phys. Rev. **102**, 1008.

Anderson, P. W., 1959, Phys. Rev. **115**, 2.

Anderson, P. W., 1963a, in *Magnetism*, edited by G. T. Rado and H. Suhl (Academic, New York), Vol. I, p. 25.

Anderson, P. W., 1963b, in *Solid State Physics*, edited by H. Ehrenreich, F. Seitz, and D. Turnbull (Academic, New York), Vol. 14, p. 99.

Anderson, P. W., 1984, *Basic Notions of Condensed Matter Physics* (Benjamin/Cummings, London).

Anderson, P. W., 1987, Science **235**, 1196.

Anderson, P. W., 1990, Phys. Rev. Lett. **64**, 1839.

Anderson, P. W., 1991a, Phys. Rev. Lett. **67**, 2092.

Anderson, P. W., 1991b, Phys. Rev. Lett. **67**, 3844.

Anderson, P. W., 1992, Science **256**, 1526.

Anderson, P. W., 1997, *The Theory of Superconductivity in the High-T_c Cuprate Superconductors* (Princeton University, Princeton, New Jersey).

Anderson, P. W., and H. Hasegawa, 1955, Phys. Rev. **100**, 675.

Anderson, R. O., R. Claessen, J. W. Allen, C. G. Olson, C. Janowitz, L. Z. Liu, J.-H. Park, M. B. Maple, Y. Dalichaouch, M. C. de Andrade, R. F. Jardim, E. A. Early, S.-J. Oh, and W. P. Ellis, 1993, Phys. Rev. Lett. **70**, 3163.

Ando, Y., G. S. Boebinger, A. Passner, T. Kimura, and K. Kishio, 1995, Phys. Rev. Lett. **75**, 4662.

Anisimov, V. I., I. S. Elfimov, N. Hamada, and K. Terakura, 1996, Phys. Rev. **54**, 4387.

Anisimov, V. I., I. S. Elfimov, M. A. Korotin, and K. Terakura, 1997, Phys. Rev. B **55**, 15494.

Anisimov, V. I., S. Yu. Ezhov, I. S. Elifimov, I. V. Solovyev, and T. M. Rice, 1996, Phys. Rev. Lett. **76**, 1735.

Anisimov, V. I., M. A. Korotin, J. Zaanen, and O. K. Andersen, 1992, Phys. Rev. Lett. **68**, 345.

Anisimov, V. I., A. I. Poteryaev, M. A. Korotin, A. O. Anokhin, and G. Kotliar, 1997, J. Phys.: Condens. Matter **9**, 7359.

Anisimov, V. I., J. Zaanen, and O. Andersen, 1991, Phys. Rev. B **44**, 943.

Annett, J. F., N. Goldenfeld, and A. J. Leggett, 1996, J. Low Temp. Phys. **105**, 473.

Anzai, S., T. Futami, and T. Sawa, 1981, J. Appl. Phys. **52**, 6270.

Anzai, S., M. Matoba, M. Hatori, and H. Sakamoto, 1986, J. Phys. Soc. Jpn. **55**, 2531.

Anzai, S., and K. Ozawa, 1968, J. Phys. Soc. Jpn. **24**, 271.

Arima, T., and Y. Tokura, 1995, J. Phys. Soc. Jpn. **64**, 2488.

Arima, T., Y. Tokura, and J. B. Torrance, 1993, Phys. Rev. B **48**, 17006.

Arima, T., Y. Tokura, and S. Uchida, 1993, Phys. Rev. B **48**, 6597.

Arovas, D. P., and A. Auerbach, 1988, Phys. Rev. B **38**, 316.

Aryasetiawan, F., 1992, Phys. Rev. B **46**, 13051.

Aryasetiawan, F. A., and O. G. Gunnarsson, 1997, cond-mat/9712013.

Asai, K., P. Gehring, H. Chou, and G. Shirane, 1989, Phys. Rev. B **40**, 10982.

Asai, K., O. Yokokura, N. Nishimori, H. Chou, J. M. Tranquada, G. Shirane, S. Higuchi, Y. Okajima, and K. Kohn, 1994, Phys. Rev. B **50**, 3025.

Asai, K., A. Yoneda, O. Yokokura, J. M. Tranquada, G. Shirane, and K. Kohn, 1997, unpublished.

Asamitsu, A., Y. Moritomo, R. Kumai, Y. Tomioka, and Y. Tokura, 1996, Phys. Rev. B **54**, 1716.

Asamitsu, A., Y. Moritomo, Y. Tomioka, T. Arima, and Y. Tokura, 1995, Nature (London) **373**, 407.

Asamitsu, A., and Y. Tokura, 1998, Phys. Rev. B **58**, 47.

Asamitsu, A., Y. Tomioka, H. Kuwahara, and Y. Tokura, 1997, Nature (London) **388**, 50.

Ashcroft, N. W., and N. D. Mermin, 1976, *Solid State Physics* (Saunders, Philadelphia).

Ashkenazi, J., and M. Weger, 1973, Adv. Phys. **22**, 207.

Assaad, F. F., and M. Imada, 1995, Phys. Rev. Lett. **74**, 3868.

Assaad, F. F., and M. Imada, 1996a, J. Phys. Soc. Jpn. **65**, 189.

Assaad, F. F., and M. Imada, 1996b, Phys. Rev. Lett. **76**, 3176.

Assaad, F. F., and M. Imada, 1998, Phys. Rev. B **58**, 1845.

Assaad, F. F., M. Imada, and D. Scalapino, 1996, Phys. Rev. Lett. **77**, 4592.

Assaad, F. F., M. Imada, and D. Scalapino, 1997, Phys. Rev. B **56**, 15001.

Azrak, A. El, *et al.*, 1994, Phys. Rev. B **49**, 9846.

Azuma, M., Z. Hiroi, M. Takano, K. Ishida, and Y. Kitaoka, 1994, Phys. Rev. Lett. **73**, 3463.

Bagno, P. G., O. Jepsen, and O. Gunnarsson, 1989, Phys. Rev. B **40**, 1997.

Bao, W., C. Broholm, S. A. Carter, T. F. Rosenbaum, G. Aeppli, S. F. Trevino, P. Metcalf, J. M. Honig, and J. Spalek, 1993, Phys. Rev. Lett. **71**, 766.

Bao, W., C. Broholm, J. M. Honig, P. Metcalf, and S. F. Trevino, 1996, Phys. Rev. B **54**, R3726.

Bao, W., C. H. Chen, S-W. Cheong, and S. A. Carter, 1996, Solid State Commun. **98**, 55.

Bao, W., *et al.*, 1997, Phys. Rev. Lett. **78**, 507.

Barker, A. S., Jr., B. I. Halperin, and T. M. Rice, 1968, Phys. Rev. Lett. **20**, 384.

Barker, A. S., Jr. and J. P. Remeika, 1974, Phys. Rev. B **10**, 987.

Barman, S. R., A. Chainani, and D. D. Sarma, 1994, Phys. Rev. B **49**, 8475.

Barman, S. R., N. Shanti, and D. D. Sarma, 1996, Europhys. Lett. **36**, 307.

Barnes, S. E., 1976, J. Phys. F **6**, 1375.

Barnes, S. E., 1977, J. Phys. F **7**, 2637.

Barthelemy, E., C. Chavant, G. Collin, and O. Gorochov, 1976, J. Phys. (Paris) **37**, C4-17.

Barthelemy, E., O. Gorochov, and H. McKinzie, 1973, Mater. Res. Bull. **8**, 1401.

Baskaran, G., Z. Zou, and P. W. Anderson, 1987, Solid State Commun. **63**, 973.

Basov, D. N., *et al.*, 1996, Phys. Rev. Lett. **77**, 4090.

Battle, P. D., T. C. Gibb, and P. Lightfoot, 1990, J. Solid State Chem. **84**, 271.

Battle, P. D., T. C. Gibb, and S. Nixon, 1988, J. Solid State Chem. **77**, 124.

Beard, B. B., and U.-J. Wiese, 1996, Preprint No. cond-mat/9602164.

Becke, A. D., 1988, Phys. Rev. A **38**, 3098.

Bednorz, J. G., and K. A. Müller, 1986, Z. Phys. B **64**, 189.

Belitz, D., and T. R. Kirkpatrick, 1994, Rev. Mod. Phys. **66**, 261.

Benoit, R., 1955, J. Chem. Phys. **52**, 119.

Bethe, H., 1928, Ann. Phys. (Leipzig) **87**, 55.

Bickers, N. E., and D. J. Scalapino, 1989, Ann. Phys. (N.Y.) **193**, 206.

Bickers, N. E., and S. R. White, 1991, Phys. Rev. B **43**, 8044.

Birgeneau, R. J., A. Aharony, N. R. Belk, F. C. Chou, Y. Endoh, M. Greven, S. Hosoya, M. A. Kastner, C. H. Lee, Y. S. Lee, G. Shirane, S. Wakimoto, B. O. Wells, and K. Yamada, 1995, J. Phys. Chem. Solids **56**, 1913.

Birgeneau, R. J., D. R. Gabbe, H. P. Jenssen, M. A. Kastner, P. J. Picone, T. R. Thurston, G. Shirane, Y. Endoh, M. Sato, K. Yamada, Y. Hidaka, M. Oda, Y. Enomoto, M. Suzuki, and T. Murakami, 1988, Phys. Rev. B **38**, 6614.

Bishop, D. J., E. G. Spencer, and R. C. Dynes, 1985, Solid-State Electron. **28**, 73.

Blankenbecler, R., D. J. Scalapino, and R. L. Sugar, 1981, Phys. Rev. D **24**, 2278.

Bloch, F., 1929, Z. Phys. **57**, 545.

Bocquet, A. E., A. Fujimori, T. Mizokawa, T. Saitoh, H. Namatame, and A. Fujimori, 1992a, Phys. Rev. B **46**, 3771.

Bocquet, A. E., A. Fujimori, T. Mizokawa, T. Saitoh, H. Namatame, S. Suga, N. Kimizuka, Y. Takeda, and M. Takano, 1992b, Phys. Rev. B **45**, 1561.

Bocquet, A. E., T. Mizokawa, K. Morikawa, A. Fujimori, S. R. Barman, K. B. Maiti, D. D. Sarma, Y. Tokura, and M. Onoda, 1996, Phys. Rev. B **53**, 1161.

Bocquet, A. E., T. Saitoh, T. Mizokawa, and A. Fujimori, 1992c, Solid State Commun. **83**, 11.

Bonn, D. A., J. D. Garrett, and T. Timusk, 1988, Phys. Rev. Lett. **61**, 1305.

Bonner, J. C., and M. E. Fisher, 1964, Phys. Rev. **135**, A640.

Bouchard, R. J., and Gillson, 1972, Mater. Res. Bull. **7**, 873.

Bouchard, R. J., *et al.*, 1973, Mater. Res. Bull. **8**, 489.

Bozovic, I., J. H. Kim, J. S. Harris, Jr., C. B. Eom, J. M. Phillips, and J. T. Cheung, 1994, Phys. Rev. Lett. **73**, 1436.

Brandow, B. H., 1977, Adv. Phys. **26**, 651.

Brandt, U., and C. Mielsch, 1989, Z. Phys. **75**, 365 (Part I); 1990, **79**, 295 (Part II).

Brinkmann, M., T. Rex, H. Bach, and K. Westerholt, 1995, Phys. Rev. Lett. **74**, 4927.

Brinkmann, M., T. Rex, M. Stief, H. Bach, and K. Westerholt, 1996, Physica C **269**, 76.

Brinkman, W. F., and T. M. Rice, 1970, Phys. Rev. B **2**, 4302.

Brückner, W., H. Oppermann, W. Reichelt, J. I. Terukow, F. A. Tschudnowski, and E. Wolf, 1983, *Vanadiumoxide Darstellung, Eigenschaften, Anwendung* (Akademie, Berlin).

Brusetti, R., J. M. D. Coey, G. Czjzek, J. Fink, F. Gomp, and H. Schmidt, 1980, J. Phys. F **10**, 33.

Bulut, N., D. J. Scalapino, and S. R. White, 1994a, Phys. Rev. Lett. **72**, 705.

Bulut, N., D. J. Scalapino, and S. R. White, 1994b, Phys. Rev. B **50**, 7215.

Buttrey, D. J., J. D. Sullivan, and A. L. Reingold, 1990, J. Solid State Chem. **88**, 291.

Byers, N., and C. N. Yang, 1961, Phys. Rev. Lett. **7**, 46.

Caffarel, M., and W. Krauth, 1994, Phys. Rev. Lett. **72**, 1545.

Callagan, A., C. W. Moeller, and R. Ward, 1966, Inorg. Chem. **5** 1573.

Campuzano, J. C., G. Jennings, M. Faiz, L. Beaulaigue, B. W. Veal, J. Z. Liu, A. P. Paulikas, K. Vandervoort, H. Claus, R. S. List, A. J. Arko, and R. J. Bartlett, 1990, Phys. Rev. Lett. **64**, 2308.

Canfield, P. C., J. D. Thompson, S-W. Cheong, and L. W. Rupp, 1993, Phys. Rev. B **47**, 12357.

Cao, G., S. McCall, M. Shepard, J. E. Crow, and R. P. Guertin, 1997, Phys. Rev. B **56**, R5740.

Capellmann, H., 1974, J. Phys. F **4**, 1466.

Capellmann, H., 1979, Z. Phys. B **34**, 29.

Carter, S. A., B. Batlogg, R. J. Cava, J. J. Krajewski, W. F. Peck Jr., and T. M. Rice, 1996, Phys. Rev. Lett. **77**, 1378.

Carter, S. A., T. F. Rosenbaum, J. M. Honig, and J. Spalek, 1991, Phys. Rev. Lett. **67**, 3440.

Carter, S. A., T. F. Rosenbaum, M. Lu, H. M. Jaeger, P. Metcalf, J. M. Honig, and J. Spalek, 1994, Phys. Rev. B **49**, 7898.

Carter, S. A., T. F. Rosenbaum, P. Metcalf, J. M. Honig, and J. Spalek, 1993, Phys. Rev. B **48**, 16841.

Castellani, C., C. Di Castro, and W. Metzner, 1992, Phys. Rev. Lett. **69**, 1703.

Castellani, C., C. Di Castro, and W. Metzner, 1998, Adv. Phys. **47**, 317.

Castellani, C., C. R. Natoli, and J. Ranninnger, 1978a, Phys. Rev. B **18**, 4945.

Castellani, C., C. R. Natoli, and J. Ranninnger, 1978b, Phys. Rev. B **18**, 4967.

Castellani, C., C. R. Natoli, and J. Ranninnger, 1978c, Phys. Rev. B **18**, 5001.

Cava, R. J., *et al.*, 1990, Nature (London) **345**, 602.

Cava, R. J., *et al.*, 1991, Phys. Rev. B **43**, 1229.

Ceperley, D. M., and B. J. Alder, 1980, Phys. Rev. Lett. **45**, 566.

Chainani, A., M. Mathew, and D. D. Sarma, 1992, Phys. Rev. B **46**, 9976.

Chainani, A., M. Mathew, and D. D. Sarma, 1993, Phys. Rev. B **47**, 15397.

Chainani, A., T. Yokoya, T. Morimoto, T. Takahashi, and S. Todo, 1995, Phys. Rev. B **51**, 17976.

Chainani, A., T. Yokoya, T. Morimoto, T. Takahashi, S. Yoshii, and M. Kasaya, 1994, Phys. Rev. B **50**, 8915.

Chakravarty, S., B. I. Halperin, and D. R. Nelson, 1989, Phys. Rev. B **39**, 2344.

Chandrasekhar, Q. Won Choi, J. Moyo, and J. M. Honig, 1970, Mater. Res. Bull. **5**, 999.

Chao, K. A., and M. C. Gutzwiller, 1971, J. Appl. Phys. **42**, 1420.

Chao, K. A., J. Spalek, and A. M. Oles, 1977, J. Phys. C **10**, L271.

Chayes, J., L. Chayes, D. S. Fisher, and T. Spencer, 1986, Phys. Rev. Lett. **57**, 2999.

Chen, C. H., S-W. Cheong, and A. S. Cooper, 1993, Phys. Rev. Lett. **71**, 2461.

Chen, C. H., S-W. Cheong, and H. Y. Hwang, 1997, J. Appl. Phys. **81**, 4326.

Chen, C. T., F. Sette, Y. Ma, M. S. Hybertsen, E. B. Stechel, W. M. C. Foulkes, M. Schluter, S.-W. Cheong, A. S. Cooper, L. W. Rupp Jr., B. Batlogg, Y. L. Soo, Z. H. Ming, A. Krol, and Y. H. Kao, 1991, Phys. Rev. Lett. **66**, 104.

Chen, C. T., L. H. Tjeng, J. Kwo, H. L. Kao, P. Rudolf, F. Sette, and R. M. Fleming, 1992, Phys. Rev. Lett. **68**, 2543.

Cheong, S-W., *et al.*, 1991, Phys. Rev. Lett. **67**, 1791.

Cheong, S-W., H. Y. Hwang, C. H. Chen, B. Batlogg, L. W. Rupp, and S. A. Carter, 1994, Phys. Rev. B **49**, 7088.

Chien, T. R., Z. Z. Wang, and N. P. Ong, 1991, Phys. Rev. Lett. **67**, 2088.

Cho, J. H., F. C. Chou, and D. C. Johnston, 1993, Phys. Rev. Lett. **70**, 222.

Chou, F. C., N. R. Belk, M. A. Kastner, R. J. Birgeneau, and A. Aharony, 1995, Phys. Rev. Lett. **75**, 2204.

Chou, F. C., F. Borsa, J. H. Cho, D. C. Johnston, A. Lascialfari, D. R. Torgeson, and J. Ziolo, 1993, Phys. Rev. Lett. **71**, 2323.

Chubukov, A. V., and J. Schmalian, 1998, Phys. Rev. B **57**, R11085.

Claessen, R., R. O. Anderson, J. W. Allen, C. G. Olson, C. Janowitz, W. P. Ellis, S. Harm, M. Kalning, R. Manzke, and M. Skibowski, 1992, Phys. Rev. Lett. **69**, 808.

Clarke, D. G., S. P. Strong, and P. W. Anderson, 1994, Phys. Rev. Lett. **72**, 3218.

Coey, J. M. D., R. Brusetti, A. Kallel, J. Schweizer, and H. Fuss, 1974, Phys. Rev. Lett. **32**, 1257.

Coey, J. M. D., and H. Roux-Buisson, 1979, Mater. Res. Bull. **14**, 711.

Coleman, P., 1984, Phys. Rev. B **29**, 3035.

Collins, R. T., *et al.*, 1989, Phys. Rev. B **39**, 6571.

Coluzza, C., H. Berger, P. Alméras, F. Gozzo, G. Margaritondo, G. Indlekofer, L. Forro, and Y. Hwu, 1993, Phys. Rev. B **47**, 6625.

Continentino, M. A., 1992, Phys. Rev. B **45**, 11312.

Continentino, M. A., 1994, Phys. Rep. **239**, 179, and references therein.

Cooper, S. L., G. A. Thomas, J. Orenstein, D. H. Rapkine, A. J. Millis, S-W. Cheong, A. S. Cooper, and Z. Fisk, 1990a, Phys. Rev. B **41**, 11605.

Cooper, S. L., *et al.*, 1990b, Phys. Rev. B **42**, 10785.

Cooper, S. L., *et al.*, 1992, Phys. Rev. B **45**, 2549.

Cox, P. A., R. G. Edgell, J. B. Goodenough, A. Kamnett, and C. C. Naishi, 1983, J. Phys. C **16**, 6221.

Crandles, D. A., T. Timusk, J. D. Garrett, and J. E. Greedan, 1994, Phys. Rev. B **49**, 16207.

Cullen, J. R., and E. R. Callen, 1973, Phys. Rev. B **7**, 397.

Czjzek, G., J. Fink, H. Schmidt, G. Krill, M. F. Lapierre, P. Paissod, F. Gautier, and C. Robert, 1976, J. Magn. Magn. Mater. **3**, 58.

Czyzyk, M. T., and G. A. Sawatzky, 1997, unpublished.

Dagotto, E., 1994, Rev. Mod. Phys. **66**, 763.

Dagotto, E., A. Moreo, F. Ortolani, D. Poilblanc, and J. Riera, 1992, Phys. Rev. B **45**, 10741.

Dagotto, E., A. Moreo, F. Ortolani, J. Riera, and D. J. Scalapino, 1991, Phys. Rev. Lett. **67**, 1918.

Dagotto, E., A. Nazarenko, and M. Boninsegni, 1994, Phys. Rev. Lett. **73**, 728.

Dagotto, E., and T. M. Rice, 1996, Science **271**, 618.

Dagotto, E., J. Riera, and D. J. Scalapino, 1992, Phys. Rev. B **45**, 5744.

Dai, P., H. A. Mook, and F. Doğan, 1998, Phys. Rev. Lett. **80**, 1738.

Dai, P., J. Zhang, H. A. Mook, S.-H. Liou, P. A. Dowben, and E. W. Plummer, 1996, Phys. Rev. B **54**, R3694.

Dai, P., Y. Zhang, and M. P. Sarachik, 1992, Phys. Rev. B **45**, 3984.

Dardel, B., D. Malterre, M. Grioni, P. Weibel, Y. Baer, D. Schlenker, and Y. Pétroff, 1992a, Europhys. Lett. **19**, 525.

Dardel, B., D. Malterre, M. Grioni, P. Weibel, Y. Baer, J. Voit, and D. Jérôme, 1992b, Europhys. Lett. **24**, 687.

Daré, A.-M., Y. M. Vilk, and A.-M. S. Tremblay, 1996, Phys. Rev. B **53**, 14236.

Davis, L. C., 1982, Phys. Rev. B **25**, 2912.

de Boer, J. H., and E. J. W. Verway, 1937, Proc. Phys. Soc. London, Sect. A **49**, 59.

de Gennes, P. G., 1960, Phys. Rev. **118**, 141.

Degiorgi, L., M. B. Hunt, H. R. Ott, M. Dressel, B. J. Feentrra, G. Grüner, Z. Fisk, and P. Canfield, 1994, Europhys. Lett. **28**, 341.

Deisz, J. J., D. W. Hess, and J. W. Serene, 1996, Phys. Rev. Lett. **76**, 1312.

Demler, E., and S.-C. Zhang, 1995, Phys. Rev. Lett. **75**, 4126.

Dessau, D. S., C.-H. Park, T. Saitoh, Z.-X. Shen, P. Villela, N. Hamada, Y. Moritomo, and Y. Tokura, 1998, Phys. Rev. Lett. **81**, 192.

Dessau, D. S., Z.-X. Shen, D. M. King, D. S. Marshall, L. W. Lombardo, P. H. Dickinson, J. DiCarlo, C.-H. Park, A. G. Loeser, A. Kapitulnik, and W. E. Spicer, 1993, Phys. Rev. Lett. **71**, 2781.

Ding, H., A. F. Bellman, J. C. Campuzano, M. Randeria, M. R. Norman, T. Yokoya, T. Takahashi, H. Katayama-Yoshida, T. Mochiku, K. Kadowaki, G. Jennings, and G. P. Brivio, 1996a, Phys. Rev. Lett. **76**, 1533.

Ding, H., M. R. Norman, T. Yokoya, T. Takeuchi, M. Randeria, J. C. Campuzano, T. Takahashi, T. Mochiku, and K. Kadowaki, 1997, Phys. Rev. Lett. **78**, 2628.

Ding, H., T. Yokoya, J. C. Campuzano, T. Takahashi, M. Randeria, M. R. Norman, T. Mochiku, K. Kadowaki, and J. Giapintzakis, 1996b, Nature (London) **382**, 51.

DiTusa, J. F., K. Friemelt, E. Bucher, G. Aeppli, and A. P. Ramirez, 1997, Phys. Rev. Lett. **78**, 2831.

Dobrosavljević, V., E. Abrahams, E. Miranda, and S. Chakravarty, 1997, Phys. Rev. Lett. **79**, 455.

Dobrosavljević, V., and G. Kotliar, 1997, Phys. Rev. Lett. **78**, 3943.

Dopf, G., A. Muramatsu, and W. Hanke, 1992, Europhys. Lett. **17**, 559.

Dopf, G., J. Wagner, P. Dieterich, A. Muramatsu, and W. Hanke, 1992, Phys. Rev. Lett. **68**, 2082.

Dougier, P., and A. Casalot, 1970, J. Solid State Chem. **2**, 396.

Dougier, P., J. C. C. Fan, and J. B. Goodenough, 1975, J. Solid State Chem. **14**, 247.

Dougier, P., and P. Hagenmuller, 1975, J. Solid State Chem. **15**, 158.

Dumas, J., and C. Schlenker, 1976, J. Phys. (Paris), Colloq. **37**, C4-41.

Dumas, J., and C. Schlenker, 1979, unpublished.

Dumas, J., C. Schlenker, J. L. Tholence, and R. Tournier, 1979, Phys. Rev. B **20**, 3913.

Eccleston, R., M. Uehara, J. Akimitsu, H. Eisaki, N. Motoyama, and S. Uchida, 1998, Phys. Rev. Lett. **81**, 1702.

Edgell, R. G., M. R. Harrison, M. D. Hill, L. Porte, and G. Wall, 1984, J. Phys. C **17**, 2889.

Edwards, P. P., and C. N. R. Rao, 1985, *The Metallic and Non-Metallic States of Matter* (Taylor & Francis).

Eggert, S., I. Affleck, and M. Takahashi, 1994, Phys. Rev. Lett. **73**, 332.

Eisaki, H., 1991, Ph.D. thesis (University of Tokyo).

Emery, V. J., 1979, in *Highly Conducting One-Dimensional Solids*, edited by J. T. Devreese *et al.* (Plenum, New York), p. 327.

Emery, V. J., 1987, Phys. Rev. Lett. **58**, 2794.

Emery, V. J., and S. A. Kivelson, 1995, Nature (London) **374**, 434.

Emery, V. J., and S. A. Kivelson, 1996, Physica C **263**, 44, and references therein.

Emery, V. J., S. A. Kivelson, and H. Q. Lin, 1990, Phys. Rev. Lett. **64**, 475.

Eskes, H., and A. Oleś, 1994, Phys. Rev. Lett. **73**, 1279.

Eskes, H., A. Oleś, M. B. Meinders, and W. Stephan, 1994, Phys. Rev. B **50**, 17980.

Eskes, H., L. H. Tjeng, and G. A. Sawatzky, 1990, Phys. Rev. B **41**, 288.

Evertz, H. G., G. Lana, and M. Marcu, 1993, Phys. Rev. Lett. **70**, 875.

Evertz, H. G., and M. Marcu, 1993, Nucl. Phys. B (Proc. Suppl.) **30**, 277.

Fabrizio, M., A. Parola, and E. Tosatti, 1992, Phys. Rev. B **46**, 3159.

Finkelstein, A. M., 1983, Zh. Eksp. Teor. Fiz. **84**, 168 [Sov. Phys. JETP **57**, 97 (1983)].

Finkelstein, A. M., 1984, Zh. Eksp. Teor. Fiz. **86**, 367 [Sov. Phys. JETP **86**, 367 (1984)].

Fisher, M. P. A., P. B. Weichman, G. Grinstein, and D. S. Fisher, 1989, Phys. Rev. B **40**, 546.

Folkerts, W., G. A. Sawatzky, C. Haas, R. A. de Groot, and F. U. Hillebrecht, 1987, J. Phys. C **20**, 4135.

Fong, H. F., B. Keimer, P. W. Anderson, D. Reznik, F. Doğan, and I. A. Aksay, 1995, Phys. Rev. Lett. **75**, 316.

Fong, H. F., B. Keimer, D. L. Milius, and I. A. Aksay, 1997, Phys. Rev. Lett. **78**, 713.

Fowler, R. H., 1933a, Proc. R. Soc. London, Ser. A **140**, 505.

Fowler, R. H., 1933b, Proc. R. Soc. London, Ser. A **141**, 56.

Frahm, H., and V. E. Korepin, 1990, Phys. Rev. B **42**, 10553.

Frésard, R., and G. Kotliar, 1997, Phys. Rev. B **56**, 12909.

Fu, C., M. P. C. M. Krijn, and S. Doniach, 1994, Phys. Rev. B **49**, 2219.

Fujimori, A., 1992, J. Phys. Chem. Solids **53**, 1595.

Fujimori, A., A. E. Bocquet, K. Morikawa, K. Kobayashi, T. Saitoh, Y. Tokura, I. Hase, and M. Onoda, 1996, J. Phys. Chem. Solids **57**, 1379.

Fujimori, A., A. E. Bocquet, T. Saitoh, and T. Mizokawa, 1993, J. Electron Spectrosc. Relat. Phenom. **62**, 141.

Fujimori, A., I. Hase, H. Namatame, Y. Fujishima, Y. Tokura, H. Eisaki, S. Uchida, K. Takegahara, and F. M. F. de Groot, 1992a, Phys. Rev. Lett. **69**, 1796.

Fujimori, A., I. Hase, M. Nakamura, H. Namatame, Y. Fujishima, Y. Tokura, M. Abbate, F. M. F. de Groot, M. T. Czyzyk, J. C. Fuggle, O. Strebel, F. Lopez, M. Domke, and G. Kaindl, 1992b, Phys. Rev. B **46**, 9841.

Fujimori, A., A. Ino, T. Mizokawa, C. Kim, Z.-X. Shen, T. Sasagawa, T. Kimura, K. Kishio, M. Takaba, K. Tamasaku, H. Eisaki, and S. Uchida, 1998, J. Phys. Chem. Solids, in press.

Fujimori, A., K. Kawakami, and N. Tsuda, 1988, Phys. Rev. B **38**, 7889.

Fujimori, A., N. Kimizuka, T. Akahane, T. Chiba, S. Kimura, F. Minami, K. Siratori, M. Taniguchi, S. Ogawa, and S. Suga, 1990, Phys. Rev. B **42**, 7580.

Fujimori, A., N. Kimizuka, M. Taniguchi, and S. Suga, 1987, Phys. Rev. B **36**, 6691.

Fujimori, A., K. Mamiya, T. Mizokawa, T. Miyadai, T. Sekiguchi, H. Takahashi, N. Môri, and S. Suga, 1996, Phys. Rev. B **54**, 16329.

Fujimori, A., and F. Minami, 1984, Phys. Rev. B **30**, 957.

Fujimori, A., F. Minami, and S. Sugano, 1984, Phys. Rev. B **29**, 5225.

Fujimori, A., M. Saeki, N. Kimizuka, M. Taniguchi, and S. Suga, 1986, Phys. Rev. B **34**, 7318.

Fujimori, A., S. Takekawa, E. Takayama-Muromachi, Y. Uchida, A. Ono, T. Takahashi, Y. Okabe, and H. Katayama-Yoshidda, 1989, Phys. Rev. B **39**, 2255.

Fujimori, A., K. Terakura, M. Taniguchi, S. Ogawa, S. Suga, M. Matoba, and S. Anzai, 1988, Phys. Rev. B **37**, 3109.

Fujioka, K., J. Okamoto, T. Mizokawa, A. Fujimori, I. Hase, M. Abbate, H. J. Lin, C. T. Chen, Y. Takeda, and M. Takano, 1997, Phys. Rev. B **56**, 6380.

Fukuda, K., S. Shamoto, M. Sato, and K. Oda, 1988, Solid State Commun. **65**, 1323.

Fukunaga, F., and N. Tsuda, 1994, J. Phys. Soc. Jpn. **63**, 3798.

Fukushima, A., F. Iga, I. H. Inoue, K. Murata, and Y. Nishihara, 1994, J. Phys. Soc. Jpn. **63**, 409.

Fukuzumi, Y., K. Mizuhashi, K. Takenaka, and S. Uchida, 1996, Phys. Rev. Lett. **76**, 684.

Furukawa, N., 1995a, J. Phys. Soc. Jpn. **64**, 2734.

Furukawa, N., 1995b, J. Phys. Soc. Jpn. **64**, 2754.

Furukawa, N., 1995c, J. Phys. Soc. Jpn. **64**, 3164.

Furukawa, N., 1996, J. Phys. Soc. Jpn. **65**, 1174.

Furukawa, N., and M. Imada, 1991a, J. Phys. Soc. Jpn. **60**, 810.

Furukawa, N., and M. Imada, 1991b, J. Phys. Soc. Jpn. **60**, 3604.

Furukawa, N., and M. Imada, 1991c, J. Phys. Soc. Jpn. **60**, 3669.

Furukawa, N., and M. Imada, 1992, J. Phys. Soc. Jpn. **61**, 3331.

Furukawa, N., and M. Imada, 1993, J. Phys. Soc. Jpn. **62**, 2557.

Futami, T., and S. Anzai, 1984, J. Appl. Phys. **56**, 440.

Fye, R. M., M. J. Martins, D. J. Scalapino, J. Wagner, and W. Hanke, 1991, Phys. Rev. B **44**, 6909.

Gansepohl, S. C., M. Lee, K. Char, R. A. Rao, and C. B. Eom, 1995, Phys. Rev. B **52**, 3495.

García-Muñoz, J. L., J. Rodriguez-Carvajal, and P. Lacorre, 1992, Europhys. Lett. **20**, 241.

García-Muñoz, J. L., J. Rodríguez-Carvajal, and P. Lacorre, 1994, Phys. Rev. B **50**, 978.

Georges, A., and G. Kotliar, 1992, Phys. Rev. B **45**, 6479.

Georges, A., G. Kotliar, W. Krauth, and M. J. Rozenberg, 1996, Rev. Mod. Phys. **68**, 13.

Georges, A., and W. Krauth, 1992, Phys. Rev. Lett. **69**, 1240.

Georges, A., and W. Krauth, 1993, Phys. Rev. B **48**, 7167.

Ghedira, M., M. Anne, J. Chenavas, and F. Sayetat, 1986, J. Phys. C **19**, 6489.

Giamarchi, T., and C. Lhuillier, 1990, Phys. Rev. B **42**, 10641.

Gibb, T. C., R. Greatrex, N. N. Greenwood, D. C. Puxley, and K. G. Snowdon, 1974, J. Solid State Chem. **11**, 17.

Gofron, K., J. C. Campuzano, A. A. Abrikosov, M. Lindroos, A. Bansil, H. Ding, D. Koelling, and B. Dabrowski, 1994, Phys. Rev. Lett. **73**, 3302.

Goodenough, J. B., 1955, Phys. Rev. **100**, 564.

Goodenough, J. B., 1971, J. Solid State Chem. **3**, 490.

Goral, J. P., J. E. Greedan, and D. A. MacLean, 1982, J. Solid State Chem. **43**, 244.

Goto, A., H. Yasuoka, and Y. Ueda, 1996, J. Phys. Soc. Jpn. **65**, 3043.

Graf, T., D. Mandrus, J. M. Lawrence, J. D. Thompson, P. C. Canfield, S.-W. Cheong, and L. W. Rupp, Jr., 1995, Phys. Rev. B **51**, 2037.

Granados, X., J. Fontcuberta, X. Obradors, and J. B. Torrance, 1992, Phys. Rev. B **46**, 15683.

Grant, J. B., and A. K. McMahan, 1991, Phys. Rev. Lett. **66**, 488.

Greeff, C. W., H. R. Glyde, and B. E. Clements, 1992, Phys. Rev. B **45**, 7951.

Greywall, D. S., 1990, Phys. Rev. B **41**, 1842.

Grilli, M., and G. Kotliar, 1990, Phys. Rev. Lett. **64**, 1170.

Gunnarsson, O., O. K. Andersen, O. Jepsen, and J. Zaanen, 1989, Phys. Rev. B **39**, 1708.

Gutzwiller, M. C., 1965, Phys. Rev. A **137**, A1726.

Haas, S., A. Moreo, and E. D. Dagotto, 1995, Phys. Rev. Lett. **74**, 4281.

Haldane, F. D. M., 1980, Phys. Rev. Lett. **45**, 1358.

Haldane, F. D. M., 1981, Phys. Rev. Lett. **47**, 1840.

Haldane, F. D. M., 1983a, Phys. Lett. A **93**, 464.

Haldane, F. D. M., 1983b, Phys. Rev. Lett. **50**, 1153.

Haldane, F. D. M., 1994, Proceedings of the International School of Physics Enrico Fermi Course CXXI, edited by R. A. Broglia and J. R. Schrieffer (North Holland, Amsterdam).

Hamada, N., 1993, J. Phys. Chem. Solids **54**, 1157.

Hamada, N., H. Sawada, and K. Terakura, 1995, in *Spectroscopy of Mott Insulators and Correlated Metals*, edited by A. Fujimori and Y. Tokura (Springer-Verlag, Berlin), p. 95.

Harashina, H., K. Kodama, S. Shamoto, M. Sato, K. Kakurai, and M. Nishi, 1995, J. Phys. Soc. Jpn. **64**, 1462.

Harrison, W. A., 1989, *Electronic Structure and the Properties of Solids* (Dover, New York).

Hase, M., I. Terasaki, and K. Uchinokura, 1993, Phys. Rev. Lett. **70**, 3651.

Hasegawa, H., 1997a, J. Phys. Soc. Jpn. **66**, 1391.

Hasegawa, H., 1997b, Phys. Rev. B **56**, 1196.

Hasenfratz, P., and F. Niedermayer, 1991, Phys. Lett. B **268**, 231.

Hasenfratz, P., and F. Niedermayer, 1993, Z. Phys. B **92**, 91.

Hatano, N., and M. Suzuki, 1993, in *Quantum Monte Carlo Methods in Condensed Matter Physics*, edited by M. Suzuki (World Scientific, Singapore), p. 13.

Hayden, S. M., G. Aeppli, H. Mook, D. Rytz, M. F. Hundley, and Z. Fisk, 1991a, Phys. Rev. Lett. **66**, 821.

Hayden, S. M., G. Aeppli, R. Osborn, A. D. Taylor, T. G. Perring, S-W. Cheong, and Z. Fisk, 1991b, Phys. Rev. Lett. **67**, 3622.

Hayden, S. M., G. Aeppli, T. G. Perring, H. A. Mook, and F. Doğan, 1996, unpublished.

Hayden, S. M., *et al.*, 1996, Phys. Rev. Lett. **76**, 1344.

Hedin, L., and S. Lundqvist, 1969, Solid State Phys. **23**, 1.

Heidemann, A., and M. Takano, 1980, Phys. Status Solidi B **100**, 343.

Hellberg, C. S., and E. Manousakis, 1997, Phys. Rev. Lett. **78**, 4609.

Henrich, V. E., and R. L. Kurtz, 1981, J. Vac. Sci. Technol. **18**, 416.

Herring, C., 1952, Phys. Rev. **87**, 60.

Herring, C., 1963, in *Magnetism*, edited by G. T. Rado and H. Suhl (Academic, New York), Vol. II.B, p. 2).

Hertel, P., and J. Appel, 1986, Phys. Rev. B **33**, 2098.

Hertz, J. A., 1976, Phys. Rev. B **14**, 1165.

Hida, K., 1992, Phys. Rev. B **45**, 2207.

Hida, K., M. Imada, and M. Ishikawa, 1983, J. Phys. C **16**, 4945.

Hiroi, Z. *et al.*, 1997, private communication.

Hiroi, Z., M. Azuma, M. Takano, and Y. Bando, 1991, J. Solid State Chem. **95**, 230.

Hiroi, Z., and M. Takano, 1995, Nature (London) **377**, 41.

Hirota, K., N. Kaneko, A. Nishizawa, and Y. Endoh, 1996, J. Phys. Soc. Jpn. **65**, 3736.

Hirsch, J. E., 1983, Phys. Rev. B **28**, 4059.

Hirsch, J. E., 1985a, Phys. Rev. Lett. **54**, 1317.

Hirsch, J. E., 1985b, Phys. Rev. B **31**, 4403.

Hirsch, J. E., and R. M. Fye, 1986, Phys. Rev. Lett. **56**, 2521.

Hohenberg, P., and W. Kohn, 1964, Phys. Rev. **136**, 864B.

Homes, C. C., T. Timusk, R. Liang, D. A. Bonn, and W. N. Hardy, 1993, Phys. Rev. Lett. **71**, 1645.

Honig, J., 1985, in *Metallic and Non-Metallic States of Matter*, edited by P. P. Edwards and C. N. Rao (Taylor & Francis, London), p. 226.

Honig, J. M., and T. B. Reed, 1968, Phys. Rev. **174**, 1020.

Honig, J. M., and L. L. van Zandt, 1975, Annu. Rev. Mater. Sci. **5**, 225.

Hubbard, J., 1963, Proc. R. Soc. London, Ser. A **276**, 238.

Hubbard, J., 1964a, Proc. R. Soc. London, Ser. A **277**, 237.

Hubbard, J., 1964b, Proc. R. Soc. London, Ser. A **281**, 401.

Hüfner, S., 1985, Z. Phys. B **61**, 135.

Hüfner, S., 1995, *Photoelectron Spectroscopy: Principles and Applications*, Springer Series in Solid-State Sciences No. 82, 2nd. Ed. (Springer, Berlin).

Hüfner, S., T. Riesterer, and F. Hulliger, 1985, Solid State Commun. **54**, 689.

Hüfner, S., and G. K. Wertheim, 1973, Phys. Lett. A **44**, 133.

Hunt, M. B., M. A. Chernikov, E. Felder, H. R. Ott, Z. Fisk, and P. Canfield, 1994, Phys. Rev. B **50**, 14933.

Husmann, A., D. S. Jin, Y. V. Zastavker, T. F. Rosenbaum, X. Yao, and J. M. Honig, 1996, Science **274**, 1874.

Hussey, N. E., M. Kibune, M. Nakagawa, N. Miura, Y. Iye, H. Takagi, S. Adachi, and K. Tanabe, 1998, Phys. Rev. Lett. **80**, 2909.

Hussey, N. E., K. Nozawa, H. Takagi, S. Adachi, and K. Tanabe, 1997, Phys. Rev. B **56**, R11423.

Hutchings, M. T., G. Parisot, and D. Tocchett, 1978, in *Neutron Inelastic Scattering 1977* (IAEA, Vienna), Vol. II, p. 123.

Hwang, H. Y., *et al.*, 1994, Phys. Rev. Lett. **72**, 2636.

Hybertsen, M. S., M. Schlüter, and N. E. Christensen, 1989, Phys. Rev. B **39**, 9028.

Hybertsen, M. S., E. B. Stechel, M. Schluter, and D. R. Jennison, 1990, Phys. Rev. B **41**, 11068.

Idemoto, Y., K. Fueki, and T. Shinbo, 1990, Physica C **166**, 513.

Igarashi, J., 1983, J. Phys. Soc. Jpn. **52**, 2827.

Ihle, D., and B. Lorenz, 1980, Philos. Mag. B **42**, 337.

Ihle, D., and B. Lorenz, 1986, J. Phys. C **19**, 5239.

Iino, Y., and M. Imada, 1995, J. Phys. Soc. Jpn. **64**, 4392.

Imada, M., 1991, J. Phys. Soc. Jpn. **60**, 1877.

Imada, M., 1992, J. Phys. Soc. Jpn. **61**, 423.

Imada, M., 1993a, J. Phys. Soc. Jpn. **62**, 1105.

Imada, M., 1993b, J. Phys. Soc. Jpn. **62**, 2557.

Imada, M., 1993c, Phys. Rev. B **48**, 550.

Imada, M., 1993d, in *Quantum Monte Carlo Methods in Condensed Matter Physics*, edited by M. Suzuki (World Scientific, Singapore), p. 299.

Imada, M., 1994a, J. Phys. Soc. Jpn. **63**, 851.

Imada, M., 1994b, J. Phys. Soc. Jpn. **63**, 3059.

Imada, M., 1994c, J. Phys. Soc. Jpn. **63**, 4294.

Imada, M., 1995a, J. Low Temp. Phys. **99**, 437.

Imada, M., 1995b, J. Phys. Soc. Jpn. **64**, 2954.

Imada, M., 1995c, in *Spectroscopy of Mott Insulators and Correlated Metals*, edited by A. Fujimori and Y. Tokura (Springer-Verlag, Berlin), p. 3.

Imada, M., 1995d, in *Computational Physics as a New Frontier in Condensed Matter Research*, edited by H. Takayama *et al.* (The Physical Society of Japan, Tokyo), p. 11.

Imada, M., 1998, J. Phys. Soc. Jpn. **67**, 45.

Imada, M., F. F. Assaad, H. Tsunetsugu, and Y. Motome, 1998, cond-mat/9808040.

Imada, M., N. Furukawa, and T. M. Rice, 1992, J. Phys. Soc. Jpn. **61**, 3861.

Imada, M., and Y. Hatsugai, 1989, J. Phys. Soc. Jpn. **58**, 3752.

Imada, M., and Y. Iino, 1997, J. Phys. Soc. Jpn. **66**, 568.

Imada, M., and M. Takahashi, 1986, J. Phys. Soc. Jpn. **55**, 3354.

Imai, H., H. Wada, and M. Shiga, 1996, J. Phys. Soc. Jpn. **65**, 3460.

Imai, T., C. P. Slichter, K. Yoshimura, and K. Kosuge, 1993, Phys. Rev. Lett. **70**, 1002.

Imai, T., H. Yasuoka, T. Shimizu, Y. Ueda, K. Yoshimura, and K. Kosuge, 1989, Physica C **162-164**, 169.

Inaba, F., T. Arima, T. Ishikawa, T. Katsufuji, and Y. Tokura, 1995, Phys. Rev. B **52**, R2221.

Inagaki, S., and R. Kubo, 1973, Int. J. Magn. **4**, 139.

Inagaki, S., and R. Kubo, 1975, J. Phys. Soc. Jpn. **39**, 596.

Ino, A., T. Mizokawa, A. Fujimori, K. Tamasaku, H. Eisuki, S. Uchida, T. Kimura, T. Sasagawa, and K. Kishio, 1997a, Phys. Rev. Lett. **79**, 2101.

Ino, A., T. Mizokawa, A. Fujimori, Y. Yasui, T. Nishikawa, and M. Sato, 1997b, unpublished.

Ino, A., T. Mizokawa, K. Kobayashi, A. Fujimori, T. Sasagawa, T. Kimura, K. Kishio, K. Tamasaku, H. Eisaki, and S. Uchida, 1997c, unpublished.

Inoue, I. H., Y. Aiura, Y. Nishihara, Y. Haruama, S. Nishizaki, Y. Maeno, T. Fujita, J. G. Bednorz, and F. Lichtenberg, 1996, J. Electron Spectrosc. Relat. Phenom. **78**, 175.

Inoue, I. H., I. Hase, Y. Aiura, A. Fujimori, Y. Haruyama, T. Maruyama, and Y. Nishihara, 1995, Phys. Rev. Lett. **74**, 2539.

Inoue, I. H., H. Makino, I. Hase, M. Ishikawa, N. E. Hussey, and M. J. Rozenberg, 1997a, unpublished.

Inoue, I. H., *et al.*, 1997b, Physica B **237-238**, 61.

Inoue, J., and S. Maekawa, 1990, J. Phys. Soc. Jpn. **59**, 2110.

Inui, M., and P. B. Littlewood, 1991, Phys. Rev. B **44**, 4415.

Ioffe, L. B., and G. Kotliar, 1990, Phys. Rev. B **42**, 10348.

Ioffe, L. B., and A. Larkin, 1989, Phys. Rev. B **39**, 8988.

Ioffe, L. B., and P. B. Wiegmann, 1990, Phys. Rev. Lett. **65**, 653.

Ishihara, S., J. Inoue, and S. Maekawa, 1997, Phys. Rev. B **55**, 8280.

Ishihara, S., Y. Yamanaka, and N. Nagaosa, 1997, Phys. Rev. B **56**, 686.

Ishikawa, T., S. K. Park, and Y. Tokura, 1998, Phys. Rev. B (in press).

Isobe, M., and Y. Ueda, 1996, J. Phys. Soc. Jpn. **65**, 1178.

Ito, T., H. Takagi, T. Ido, S. Ishibashi, and S. Uchida, 1991, Nature (London) **350**, 596.

Ito, T., K. Takenaka, and S. Uchida, 1993, Phys. Rev. Lett. **70**, 3995.

Itoh, M., M. Sugahara, I. Natori, and K. Motoya, 1995, J. Phys. Soc. Jpn. **64**, 3967.

Itoh, S., K. Yamada, M. Arai, Y. Endoh, Y. Hidaka, and S. Hosoya, 1994, J. Phys. Soc. Jpn. **63**, 4542.

Itoh, T., T. Fujiwara, and S. Tanaka, 1994, unpublished.

Itoh, Y., 1994, J. Phys. Soc. Jpn. **63**, 3522.

Itoh, Y., T. Machi, A. Fukuoka, K. Tanabe, and H. Yasuoka, 1996, J. Phys. Soc. Jpn. **65**, 3751.

Itoh, Y., H. Yasuoka, Y. Fujiwara, Y. Ueda, T. Machi, I. Tomeno, K. Tai, N. Koshizuka, and S. Tanaka, 1992, J. Phys. Soc. Jpn. **61**, 1287.

Itoh, Y., H. Yasuoka, A. Hayashi, and Y. Ueda, 1994, J. Phys. Soc. Jpn. **63**, 22.

Itti, R., T. Wada, K. Matsuura, T. Itoh, K. Ikeda, H. Yamauchi, N. Koshizuka, and S. Tanaka, 1991, Phys. Rev. B **44**, 2306.

Iye, Y., 1990, in *Properties of High-Temperature Superconductors*, edited by. P. M. Ginsberg (World Scientific, Singpore), Vol. 2, p. 459.

Izumi, M., K. Nakazawa, Y. Bando, Y. Yoneda, and H. Terauchi, 1997, J. Phys. Soc. Jpn. **66**, 3893.

Jaccarino, V., G. K. Wertheim, J. H. Wernich, L. R. Walker, and S. Arajs, 1967, Phys. Rev. **160**, 476.

Jaklič, J., and P. Prelovšek, 1994, Phys. Rev. B **49**, 5065.

Jaklič, J., and P. Prelovšek, 1995a, Phys. Rev. B **52**, 6903.

Jaklič, J., and P. Prelovšek, 1995b, Phys. Rev. Lett. **74**, 3411.

Jaklič, J., and P. Prelovšek, 1996, Phys. Rev. Lett. **77**, 892.

Jarrell, M., 1992, Phys. Rev. Lett. **69**, 168.

Jarrell, M., H. Akhlaghpour, and T. Pruschke, 1993, Phys. Rev. Lett. **70**, 1670.

Jarrell, M., J. K. Fredericks, and T. Pruschke, 1995, Phys. Rev. B **51**, 11704.

Jarrell, M., and T. Pruschke, 1993, Z. Phys. B **90**, 187.

Jarrell, M., and T. Pruschke, 1994, Phys. Rev. B **49**, 1458.

Jarrett, H. S., *et al.*, 1973, Mater. Res. Bull. **8**, 877.

Jiang, Wu, S. N. Mao, X. X. Xi, Xiuguang Jiang, J. L. Peng, T. Venkatesan, C. J. Lobb, and R. L. Greene, 1994, Phys. Rev. Lett. **73**, 1291.

Jichu, H., T. Matsuura, and Y. Kuroda, 1989, J. Phys. Soc. Jpn. **58**, 4280.

Jirak, Z., S. Krupicka, V. Nekvasild, E. Pollert, G. Villeneuve, and F. Zounova, 1980, J. Magn. Magn. Mater. **15-18**, 519.

Jirak, Z., S. Krupicka, Z. Simsa, M. Dlouha, and Z. Vratislav, 1985, J. Magn. Magn. Mater. **53**, 153.

Johnston, D. C., 1989, Phys. Rev. Lett. **62**, 957.

Johnston, D. C., 1996, Phys. Rev. B **54**, 13009.

Kadono, R., H. Okajima, A. Yamashita, K. Ishii, T. Yokoo, J. Akimitsu, N. Kobayashi, Z. Hiroi, M. Takano, and K. Nagamine, 1996, Phys. Rev. B **54**, R9628.

Kadowaki, K., and S. B. Woods, 1986, Solid State Commun. **58**, 507.

Kaidanov, V. I., V. A. Tselishchev, I. K. Iesalniek, L. D. Dudkin, B. K. Voronov, and N. N. Trusova, 1968, Sov. Phys. Semicond. **2**, 382.

Kajueter, H., and G. Kotliar, 1996, Preprint No. cond-mat/9609176.

Kajueter, H., and G. Kotliar, 1997, Int. J. Mod. Phys. B **11**, 729.

Kakeshita, T., R. Kajimoto, H. Yoshizawa, T. Tanabe, T. Katsufuji, and Y. Tokura, 1998, unpublished.

Kakizaki, A., H. Sugawara, I. Nagakura, Y. Ishikawa, T. Komatsubara, and T. Ishii, 1982, J. Phys. Soc. Jpn. **51**, 2597.

Kakizaki, A., K. Sugeno, T. Ishii, H. Sugawara, I. Nagakura, and S. Shin, 1983, Phys. Rev. B **28**, 1026.

Kambe, S., H. Yasuoka, H. Takagi, S. Uchida, and Y. Tokura, 1991, J. Phys. Soc. Jpn. **60**, 400.

Kamimura, H., and Y. Suwa, 1993, J. Phys. Soc. Jpn. **62**, 3368.

Kampf, A., and J. R. Schrieffer, 1990, Phys. Rev. B **41**, 6399.

Kanamori, J., 1959, J. Phys. Chem. Solids **10**, 87.

Kanamori, J., 1963, Prog. Theor. Phys. **30**, 275.

Kanbayashi, A., 1978, J. Phys. Soc. Jpn. **44**, 108.

Kanoda, K., 1997, Hyperfine Interact. **104**, 235.

Kaplan, S. G., S. Wu, H.-T. S. Lihn, H. D. Drew, Q. Li, D. B. Fenner, J. M. Phillips, and S. Y. Hou, 1996, Phys. Rev. Lett. **76**, 696.

Karlsson, K., O. Gunnarsson, and O. Jepsen, 1992, J. Phys.: Condens. Matter **4**, 895.

Kasowski, R. V., 1973, Phys. Rev. B **8**, 1378.

Kastner, M. A., R. J. Birgeneau, T. R. Thurston, P. J. Picone, H. P. Jenssen, D. R. Gabbe, M. Sato, K. Fukuda, S. Shamoto, Y. Endoh, K. Yamada, and G. Shirane, 1988, Phys. Rev. B **38**, 6636.

Kasuya, H., Y. Tokura, T. Arima, H. Eisaki, and S. Uchida, 1993, Phys. Rev. B **47**, 6197.

Katano, S., J. A. Fernandez-Baca, S. Funahashi, N. Mori, Y. Ueda, and K. Koga, 1993, Physica C **214**, 64.

Kataoka, M., 1996, Czech. J. Phys. **46**, Suppl. F4.

Katayama, M., S. Akimoto, and K. Asayama, 1977, J. Phys. Soc. Jpn. **42**, 97.

Kato, M., H. Chizawa, Y. Koike, T. Toji, and Y. Saito, 1994, Physica (Amsterdam) **235C-244C**, 1327.

Kato, M., K. Shiota, and Y. Koike, 1996, Physica C **258**, 284.

Kato, T., and M. Imada, 1998, J. Phys. Soc. Jpn. **67**, 2828.

Katoh, N., and M. Imada, 1993, J. Phys. Soc. Jpn. **62**, 3728.

Katoh, N., and M. Imada, 1994, J. Phys. Soc. Jpn. **63**, 4529.

Katoh, N., and M. Imada, 1995, J. Phys. Soc. Jpn. **64**, 4105.

Katoh, N., and M. Imada, 1998, J. Phys. Soc. Jpn. **67**, 564.

Katsufuji, T., M. Kasai, and Y. Tokura, 1996, Phys. Rev. Lett. **76**, 126.

Katsufuji, T., Y. Okimoto, T. Arima, Y. Tokura, and J. B. Torrance, 1995, Phys. Rev. B **51**, 4830.

Katsufuji, T., Y. Okimoto, and Y. Tokura, 1995, Phys. Rev. Lett. **75**, 3497.

Katsufuji, T., Y. Taguchi, and Y. Tokura, 1997, Phys. Rev. B **56**, 10145.

Katsufuji, T., T. Tanabe, T. Ishikawa, Y. Fukuda, T. Arima, and Y. Tokura, 1996, Phys. Rev. B **54**, R14230.

Katsufuji, T., T. Tanabe, and Y. Tokura, 1998, unpublished.

Katsufuji, T., and Y. Tokura, 1994, Phys. Rev. B **50**, 2704.

Kawabata, A., 1972, Prog. Theor. Phys. **48**, 1793.

Kawabata, A., 1975, Prog. Theor. Phys. **54**, 45.

Kawakami, N., and S.-K. Yang, 1990, Phys. Lett. A **148**, 359.

Kawakami, N., and S.-K. Yang, 1991, Phys. Rev. Lett. **67**, 2493.

Kawano, H., R. Kajimoto, M. Kubota, and H. Yoshizawa, 1996, Phys. Rev. B **53**, R14709.

Kawano, H., R. Kajimoto, H. Yoshizawa, Y. Tomioka, H. Kuwahara, and Y. Tokura, 1997, Phys. Rev. Lett. **78**, 4253.

Kebler, J., A. T. Aldred, G. H. Lander, M. H. Mueller, O. Massenet, and G. D. Stucky, 1980, J. Solid State Chem. **351**, 351.

Keimer, B., N. Belk, R. J. Birgeneau, A. Cassanho, C. Y. Chen, M. Greven, M. A. Kastner, A. Aharony, Y. Endoh, R. W. Erwin, and G. Shirane, 1992, Phys. Rev. B **46**, 14034.

Keren, A., L. P. Le, G. M. Luke, B. J. Sternlieb, W. D. Wu, Y. J. Uemura, S. Tajima, and S. Uchida, 1993, Phys. Rev. B **48**, 12926.

Kim, C., A. Y. Matsuura, Z.-X. Shen, N. Motoyama, H. Eisaki, S. Uchida, T. Tohyama, and S. Maekawa, 1996, Phys. Rev. Lett. **77**, 4054.

Kim, C., Z.-X. Shen, N. Motoyama, H. Eisaki, S. Uchida, T. Tohyama, and S. Maekawa, 1997, Phys. Rev. B **56**, 15589.

Kimura, T., Y. Tomioka, A. Asamitsu, and Y. Tokura, 1997, unpublished (submitted to Phys. Rev. Lett.).

Kimura, T., Y. Tomioka, H. Kuwahara, A. Asamitsu, M. Tamura, and Y. Tokura, 1996, Science **274**, 1698.

King, D. M., Z.-X. Shen, D. S. Dessau, B. O. Wells, W. E. Spicer, A. J. Arko, D. S. Marshall, J. DiCarlo, A. G. Loeser, C. H. Park, E. R. Ratner, J. L. Peng, Z. Y. Li, and R. L. Greene, 1993, Phys. Rev. Lett. **70**, 3159.

Kirkpatrick, T. R., and D. Belitz, 1995, Phys. Rev. Lett. **73**, 862.

Kirkpatrick, T. R., and D. Belitz, 1997, cond-mat/9707001.

Kiryukhin, V., D. Cax, J. P. Hill, B. Keimer, A. Vigliante, Y. Tomioka, and Y. Tokura, 1997, Nature (London) **386**, 813.

Kishine, J., and H. Fukuyama, 1997, J. Phys. Soc. Jpn. **66**, 26.

Kita, E., Y. Tokuyama, A. Tasaki, and K. Siratori, 1983, J. Magn. Magn. Mater. **31-34**, 787.

Kitaoka, Y., K. Ishida, S. Hiramatu, and K. Asayama, 1988, J. Phys. Soc. Jpn. **57**, 734.

Kittel, C., 1968, in *Solid State Physics 22* (Academic, New York), p. 1.

Klein, L., J. S. Dodge, C. H. Ahn, G. J. Snyder, T. H. Geball, M. R. Beasley, and A. Kapitulnik, 1996, Phys. Rev. Lett. **77**, 2774.

Kobayashi, H., M. Nagata, R. Kanno, and Y. Kawamoto, 1994, Mater. Res. Bull. **29**, 1271.

Koehler, R. F., Jr., and R. L. White, 1973, J. Appl. Phys. **44**, 1682.

Kohgi, M., and Y. Ishikawa, 1981, Solid State Commun. **37**, 833.

Kohn, W., 1964, Phys. Rev. A **133**, 171.

Kohn, W., and L. J. Sham, 1965, Phys. Rev. **140**, A1133.

Kohno, H., and K. Yamada, 1991, Prog. Theor. Phys. **85**, 13.

Kohno, M., 1997, Phys. Rev. B **55**, 1435.

Kopietz, P., V. Meden, and K. Schönhammer, 1995, Phys. Rev. Lett. **74**, 2997.

Korenman, V., J. L. Murray, and R. E. Prange, 1977a, Phys. Rev. B **16**, 4032.

Korenman, V., J. L. Murray, and R. E. Prange, 1977b, Phys. Rev. B **16**, 4048.

Korenman, V., J. L. Murray, and R. E. Prange, 1977c, Phys. Rev. B **16**, 4058.

Korotin, M. A., S. Yu. Ezhov, I. V. Solovyev, V. I. Anisimov, D. I. Khomskii, and G. A. Sawatzky, 1996, Phys. Rev. B **54**, 5309.

Koshibae, W., Y. Kawamura, S. Ishihara, S. Okamoto, J. Inoue, and S. Maekawa, 1997, J. Phys. Soc. Jpn. **66**, 957.

Koshibae, W., Y. Ohta, and S. Maekawa, 1993, Phys. Rev. B **47**, 3391.

Koshibae, W., Y. Ohta, and S. Maekawa, 1994, Phys. Rev. B **50**, 3767.

Kotani, T., 1997, cond-mat/9711062.

Kotliar, G., 1993, in *Correlated Electron Systems*, edited by V. J. Emery (World Scientific, Singapore), p. 118.

Kotliar, G., and H. Kajueter, 1996, Phys. Rev. B **54**, 14221.

Kotliar, G., and J. Liu, 1988, Phys. Rev. B **38**, 5142.

Koyama, T., and M. Tachiki, 1986, Phys. Rev. B **34**, 3272.

Kramers, H. A., 1934, Physica (Amsterdam) **1**, 1934.

Kravchenko, S. V., W. E. Mason, G. E. Bowker, J. E. Furneaux, V. M. Pudalov, and M. D'Iorio, 1995, Phys. Rev. B **51**, 7038.

Krill, G., and A. Amamou, 1980, J. Phys. Chem. Solids **41**, 531.

Kübert, C., and A. Muramatsu, 1996, Int. J. Mod. Phys. B **10**, 3807.

Kubo, K., and T. Kishi, 1988, Phys. Rev. Lett. **61**, 2585, and references therein.

Kubo, K., and N. Ohata, 1972, J. Phys. Soc. Jpn. **33**, 21.

Kubo, R., 1952, Phys. Rev. **87**, 568.

Kubo, R., 1957, J. Phys. Soc. Jpn. **12**, 570.

Kubo, Y., Y. Shimakawa, T. Manako, and H. Igarashi, 1991, Phys. Rev. B **43**, 7875.

Kugel, K. I., and D. I. Khomskii, 1973, Sov. Phys. JETP **37**, 725.

Kugel, K. I., and D. I. Khomskii, 1982, Sov. Phys. Usp. **25**, 231.

Kuipers, A. J. M., and V. A. M. Brabers, 1976, Phys. Rev. B **14**, 1401.

Kumagai, K., K. Kawano, I. Watanabe, K. Nishiyama, and K. Nagamine, 1994, J. Supercond. **7**, 63.

Kumagai, K., H. Matoba, N. Wada, M. Okaji, and K. Nara, 1991, J. Phys. Soc. Jpn. **60**, 1448.

Kumagai, K. I., T. Suzuki, Y. Taguchi, Y. Okada, Y. Fujishima, and Y. Tokura, 1993, Phys. Rev. B **48**, 7636.

Kumagai, K., S. Tsuji, M. Kato, and Y. Koike, 1997, Phys. Rev. Lett. **78**, 1992.

Kuramoto, Y., 1985, in *Theory of Heavy Fermions and Valence Fluctuations*, edited by T. Kasuya and T. Saso (Springer, Berlin), p. 152.

Kuramoto, Y., and N. Fukushima, 1998, J. Phys. Soc. Jpn. **67**, 583.

Kuramoto, Y., and K. Miyake, 1990, J. Phys. Soc. Jpn. **59**, 2831.

Kuramoto, Y., and T. Watanabe, 1987, Physica B **148**, 80.

Kuroki, K., T. Kimura, and H. Aoki, 1996, Phys. Rev. B **54**, R15641.

Kuwahara, H., Y. Tomioka, A. Asamitsu, Y. Moritomo, and Y. Tokura, 1995, Science **270**, 961.

Kuwahara, H., *et al.*, 1998, unpublished.

Kuwamoto, H., J. M. Honig, and J. Appel, 1980, Phys. Rev. B **22**, 2626.

Kwizera, P., M. S. Dresselhaus, and D. Adler, 1980, Phys. Rev. B **21**, 2328.

Lad, R. J., and V. E. Henrich, 1989, Phys. Rev. B **39**, 13478.

Ladd, L., and W. Paul, 1969, Solid State Commun. **7**, 425.

Landau, L. D., 1957a, Sov. Phys. JETP **3**, 920.

Landau, L. D., 1957b, Sov. Phys. JETP **5**, 101.

Landau, L. D., 1958, Sov. Phys. JETP **8**, 70.

Langer, M., J. Schmalian, S. Grabowsky, and K. H. Bennemann, 1995, Phys. Rev. Lett. **75**, 4508.

Langreth, D. C., and M. J. Mehl, 1983, Phys. Rev. B **28**, 1809.

Lee, P. A., and N. Nagaosa, 1992, Phys. Rev. B **46**, 5621.

Lee, P. A., and T. V. Ramakrishnan, 1985, Rev. Mod. Phys. **57**, 287.

Lee, S.-H., and S-W. Cheong, 1997, Phys. Rev. Lett. **79**, 2514.

Li, E. K., K. H. Johnson, D. E. Eastman, and J. L. Freeouf, 1974, Phys. Rev. Lett. **32**, 470.

Li, J. Q., Y. Matsui, S. K. Park, and Y. Tokura, 1997, Phys. Rev. Lett. **79**, 297.

Li, Q., J. Callaway, and L. Tan, 1991, Phys. Rev. B **44**, 10256.

Liang, W. Y., J. W. Loram, K. A. Mirza, N. Athanassopoulou, and J. R. Cooper, 1996, Physica C **263**, 277.

Lichtenberg, F., A. Catana, J. Mannhart, and D. G. Schlom, 1992, Appl. Phys. Lett. **60**, 1138.

Liechtenstein, A. I., V. I. Anisimov, and J. Zaanen, 1995, Phys. Rev. B **52**, 5467.

Litvinchuk, A. P., C. Thomsen, and M. Cardona, 1993, Solid State Commun. **83**, 343.

Liu, L.-Z., R. O. Anderson, and J. W. Allen, 1991, J. Phys. Chem. Solids **52**, 1473.

Liu, R., B. W. Veal, A. P. Paulikas, J. W. Downey, P. J. Kostić, S. Fleshler, U. Welp, C. G. Olson, X. Wu, A. J. Arko, and J. J. Joyce, 1992a, Phys. Rev. B **46**, 11056.

Liu, R., B. W. Veal, A. P. Paulikas, J. W. Downey, H. Shi, C. G. Olson, C. Gu, A. J. Arko, and J. J. Joyce, 1992b, Phys. Rev. B **45**, 5614.

Lloyd, P., and P. R. Best, 1975, J. Phys. C **8**, 3752.

Loeser, A., Z.-X. Shen, D. S. Dessau, D. S. Marshall, C.-H. Park, P. Founier, and A. Kapitulnik, 1996, Science **273**, 325.

Loh, E. Y., Jr., J. E. Gubernatis, R. T. Scalettar, S. R. White, D. J. Scalapino, and R. L. Sugar, 1990, Phys. Rev. B **41**, 9301.

Longo, J. M., P. M. Raccah, and J. B. Goodenough, 1968, J. Appl. Phys. **39**, 1327.

Loram, J. W., K. A. Mirza, J. R. Cooper, N. Athamassopoulou, and W. Y. Liang, 1997, unpublished.

Loram, J. W., K. A. Mirza, J. R. Cooper, and W. Y. Liang, 1994, Physica C **235-240**, 134.

Loram, J. W., K. A. Mirza, W. Y. Liang, and J. Osborne, 1989, Physica C **162-164**, 498.

Lorenz, B., and D. Ihle, 1979, Phys. Status Solidi B **96**, 659.

Lorenz, B., and D. Ihle, 1982, Phys. Status Solidi B **113**, 601.

Lorenzana, J., and G. A. Sawatzky, 1995, Phys. Rev. Lett. **74**, 1867.

Lu, D. H., M. Schmidt, T. R. Cummins, S. Schuppler, F. Lichtenberg, and J. G. Bednorz, 1996, Phys. Rev. Lett. **76**, 4845.

Lu, J. P., 1994, Phys. Rev. B **49**, 5687.

Lucovsky, G., J. W. Allen, and R. Allen, 1979, in *Physics of Semiconductors*, Conference Series No. 43, edited by B. L. H. Wilson (Institute of Physics, London), p. 465.

Luke, G. M., B. Sternlieb, Y. J. Uemura, J. H. Brewer, R. Kadono, R. F. Kiefl, S. R. Kreitzman, T. M. Riseman, J. Gopalakrishman, A. W. Sleight, M. A. Subramanian, S. Uchida, H. Takagi, and Y. Tokura, 1989, Nature (London) **338**, 49.

Lusher, C. P., B. P. Cowan, and J. Saunders, 1993, Phys. Rev. Lett. **67**, 2497.

Luther, A., and V. J. Emery, 1974, Phys. Rev. Lett. **33**, 589.

Luttinger, J. M., 1963, J. Math. Phys. **4**, 1154.

Lyons, K. B., P. A. Fleury, J. P. Remeika, A. S. Cooper, and T. J. Negran, 1988, Phys. Rev. B **37**, 2353.

Ma, S.-K., 1976, *Modern Theory of Critical Phenomena*, Frontiers in Physics Series No. 46 (Addison-Wesley, Reading, MA).

Machi, T., I. Tomeno, T. Miyatake, N. Koshizuka, S. Tanaka, T. Imai, and H. Yasuoka, 1991, Physica C **173**, 32.

Machida, K., 1989, Physica C **158**, 192.

Mackenzie, A. P., S. R. Julian, A. J. Diver, G. J. McMullan, M. P. Ray, G. G. Lonzarich, Y. Maeno, S. Nishizaki, and T. Fujita, 1996, Phys. Rev. Lett. **76**, 3786.

MacKinnon, A., and B. Kramer, 1993, Rep. Prog. Phys. **56**, 1469.

MacLean, D. A., Hok-Nam Ng, and J. E. Greedan, 1979, J. Solid State Chem. **30**, 35.

Maeno, Y., 1996, in *Advances in Superconductivity VIII*, edited by H. Hayakawa and Y. Enomoto (Springer, Tokyo), p. 15.

Maeno, Y., H. Hashimoto, K. Yoshida, S. Nishizaki, T. Fujita, J. G. Bednorz, and F. Lichtenberg, 1994, Nature (London) **372**, 532.

Maeno, Y., K. Yoshida, H. Hashimoto, S. Nishizaki, S. Ikeda, M. Nohara, T. Fujita, A. P. Machenzie, N. E. Hussey, J. G. Bednorz, and F. Lichtenberg, 1997, J. Phys. Soc. Jpn. **66**, 1405.

Maezono, R., S. Ishihara, and N. Nagaosa, 1998, Phys. Rev. B **57**, R13993.

Magishi, K., S. Matsumoto, Y. Kitaoka, K. Ishida, K. Asayama, M. Uehara, T. Nagata, and J. Akimitsu, 1998, Phys. Rev. B **57**, 11533.

Mahadevan, P., N. Shanthi, and D. D. Sarma, 1996, Phys. Rev. B **54**, 11199.
Mahajan, A. V., D. C. Johnston, P. R. Torgeson, and F. Borsa, 1992, Phys. Rev. B **46**, 10973.
Maiti, K., D. D. Sarma, T. Mizokawa, and A. Fujimori, 1997, Europhys. Lett. **37**, 359.
Makivić, M. S., and H.-Q. Ding, 1991, Phys. Rev. B **43**, 3562.
Mamiya, K., T. Mizokawa, A. Fujimori, N. Chandrasekaran, S. R. Krishnakumar, D. D. Sarma, T. Miyadai, H. Takahashi, N. Môri, and S. Suga, 1997a, Phys. Rev. B, in press.
Mamiya, K., T. Mizokawa, A. Fujimori, T. Miyadai, H. Takahashi, N. Môri, and S. Suga, 1997b, unpublished.
Marezio, M., D. B. McWhan, J. P. Remeika, and P. D. Dernier, 1972, Phys. Rev. B **5**, 2541.
Marezio, M., J. P. Remeika, and P. D. Dernier, 1970, Acta Crystallogr., Sect. B: Struct. Crystallogr. Cryst. Chem. **26**, 2008.
Marshall, D. S., D. S. Dessau, A. G. Loeser, C.-H. Park, A. Y. Matsuura, J. N. Eckstein, I. Bozovic, P. Fournier, A. Kapitulnik, W. E. Spicer, and Z.-X. Shen, 1996, Phys. Rev. Lett. **76**, 4841.
Mason, T. E., G. Aeppli, and H. A. Mook, 1992, Phys. Rev. Lett. **68**, 1414.
Mason, T. E., *et al.*, 1993, Phys. Rev. Lett. **71**, 919.
Mason, T. E., A. Schröder, G. Aeppli, H. A. Mook, and S. M. Hayden, 1996, Phys. Rev. Lett. **77**, 1604.
Massida, S., N. Hamada, J. Yu, and A. J. Freeman, 1989, Physica C **157**, 571.
Massenet, O., R. Buder, J. J. Since, C. Schlenker, J. Mercier, J. Kebler, and D. G. Stucky, 1978, Mater. Res. Bull. **13**, 187.
Massenet, O., J. J. Since, J. Mercier, M. Avignon, R. Buder, V. D. Ngyuyen, and J. Kebler, 1979, Solid State Commun. **40**, 573.
Matl, P., Y. F. Yan, N. P. Ong, Y. Q. Li, D. Studebaker, T. Baum, and G. Doubinina, 1997, unpublished.
Matoba, M., and S. Anzai, 1987, J. Magn. Magn. Mater. **70**, 213.
Matoba, M., S. Anzai, and A. Fujimori, 1991, J. Phys. Soc. Jpn. **60**, 4230.
Matoba, M., S. Anzai, and A. Fujimori, 1994, J. Phys. Soc. Jpn. **63**, 1429.
Matsuda, M., Y. Endoh, Y. Yamada, K. Kojima, I. Tanaka, R. J. Birgeneau, M. A. Kastner, and G. Shirane, 1992, Phys. Rev. B **45**, 12548.
Matsuda, M., and K. Katsumata, 1996, Phys. Rev. B **53**, 12201.
Matsuda, M., K. Katsumata, H. Eisaki, N. Motoyama, S. Uchida, S. M. Shapiro, and G. Shirane, 1996, Phys. Rev. B **54**, 12199.
Matsuda, M., K. Yamada, Y. Endoh, T. R. Thurston, G. Shirane, R. J. Birgeneau, M. A. Kastner, I. Tanaka, and H. Kojima, 1994, Phys. Rev. B **49**, 6958.
Matsumoto, S., Y. Kitaoka, K. Ishida, K. Asayama, Z. Hiroi, N. Kobayashi, and M. Takano, 1996, Phys. Rev. B **53**, R11942.
Matsumoto, S., *et al.*, 1997, unpublished.
Matsuura, A. Y., Z.-X. Shen, D. S. Dessau, C.-H. Park, T. Thio, J. W. Bennett, and O. Jepsen, 1996, Phys. Rev. B **53**, R7584.
Matsuura, K., T. Wada, T. Nakamizo, H. Yamauchi, and S. Tanaka, 1991, Phys. Rev. B **43**, 13118.
Mattheiss, L. F., 1972, Phys. Rev. B **5**, 290 (Part I); **5**, 306 (Part II).
Mattheiss, L. F., 1974, Phys. Rev. B **10**, 995.
Mattheiss, L. F., 1994, J. Phys.: Condens. Matter **6**, 6477.
Mattheiss, L. F., 1995, Solid State Commun. **93**, 791.
Mattheiss, L. F., 1996a, Solid State Commun. **97**, 751.
Mattheiss, L. F., 1996b, J. Phys.: Condens. Matter **8**, 5987.
Mattheiss, L. F., and D. R. Hamann, 1993, Phys. Rev. B **47**, 13114.
Mayaffre, H., P. Auban-Senzier, D. Jérome, D. Poilblanc, C. Bourbonnais, U. Ammerrahl, G. Dhalenne, and A. Revcolevschi, 1997, cond-mat/9710063.
Mazin, I. I., and D. J. Singh, 1997, Phys. Rev. Lett. **79**, 733.
McCarron, E. M., M. A. Subramanian, J. C. Calabrese, and R. L. Harlow, 1988, Mater. Res. Bull. **23**, 1355.
McElfresh, M. W., J. M. D. Coey, P. Strobel, and S. von Molnar, 1989, Phys. Rev. B **40**, 825.
McKane, A. J., and M. Stone, 1981, Ann. Phys. (N.Y.) **131**, 36.
McMahan, A. K., J. F. Annett, and R. M. Martin, 1990, Phys. Rev. B **42**, 6268.
McMahan, A. K., R. M. Martin, and S. Satpathy, 1989, Phys. Rev. B **38**, 6650.
McWhan, D. B., M. Marezio, J. P. Remeika, and P. D. Dernier, 1972, Phys. Rev. B **5**, 2552.
McWhan, D. B., A. Menth, J. P. Remeika, W. F. Brinkman, and T. M. Rice, 1973, Phys. Rev. B **7**, 1920.
McWhan, D. B., and J. P. Remeika, 1970, Phys. Rev. B **2**, 3734.
McWhan, D. B., J. P. Remeika, T. M. Rice, W. F. Brinkman, J. P. Maita, and A. Menth, 1971, Phys. Rev. Lett. **27**, 941.
Meden, V., and K. Schönhammer, 1993a, Phys. Rev. B **46**, 15753.
Meden, V., and K. Schönhammer, 1993b, Phys. Rev. B **47**, 16205.
Metzner, W., and D. Vollhardt, 1989, Phys. Rev. Lett. **62**, 324.
Metzner, W., P. Schmit, and D. Vollhardt, 1992, Phys. Rev. B **45**, 2237.
Micnas, R., J. R. Ranninger, and S. Robaszkiewicz, 1990, Rev. Mod. Phys. **62**, 113.
Mila, F., and T. M. Rice, 1989, Physica C **157**, 561.
Miles, P. A., W. B. Westphal, and A. von Hippel, 1957, Rev. Mod. Phys. **29**, 279.
Millis, A. J., 1993, Phys. Rev. B **48**, 7183.
Millis, A. J., 1996, Phys. Rev. B **53**, 8434.
Millis, A. J., P. B. Littlewood, and B. I. Shraiman, 1995, Phys. Rev. Lett. **74**, 5144.
Millis, A. J., H. Monien, and D. Pines, 1990, Phys. Rev. B **42**, 167.
Millis, A. J., B. I. Shraiman, and R. Mueller, 1996, Phys. Rev. Lett. **77**, 175.
Mills, D. L., A. A. Maradudin, and E. Burstein, 1970, Ann. Phys. (N.Y.) **56**, 504.
Misawa, S., 1995, Physica B **211**, 158.
Misawa, S., and A. Tate, 1996, J. Magn. Magn. Mater. **157-158**, 617.
Mishra, S. K., and S. Satpathy, 1993, Phys. Rev. B **47**, 5564.
Mitchell, J. F., D. N. Argyriou, J. D. Jorgensen, D. G. Hinks, C. D. Potter, and S. D. Bader, 1997, Phys. Rev. B **55**, 63.
Miyadai, T., K. Kikuchi, and H. Ito, 1978, Phys. Lett. A **67**, 61.
Miyadai, T., S. Sudo, Y. Tazuke, N. Môri, and Y. Miyao, 1983, J. Magn. Magn. Mater. **31-34**, 337.
Miyake, K., 1996, unpublished.
Miyake, K., and O. Narikiyo, 1994a, J. Phys. Soc. Jpn. **63**, 2042.
Miyake, K., and O. Narikiyo, 1994b, J. Phys. Soc. Jpn. **63**, 3821.
Miyano, K., T. Tanaka, Y. Tomioka, and Y. Tokura, 1997, Phys. Rev. Lett. **78**, 4257.

Miyasaka, S., H. Takagi, Y. Sekine, H. Takahashi, N. Môri, and R. J. Cava, 1998, Phys. Rev. B (in press).

Mizoguchi, M., 1978, J. Phys. Soc. Jpn. **44**, 1512.

Mizokawa, T., and A. Fujimori, 1995, Phys. Rev. B **51**, 12880.

Mizokawa, T., and A. Fujimori, 1996a, Phys. Rev. B **53**, R4201.

Mizokawa, T., and A. Fujimori, 1996b, Phys. Rev. B **54**, 5368.

Mizokawa, T., and A. Fujimori, 1997, Phys. Rev. B **56**, R493.

Mizokawa, T., A. Fujimori, T. Arima, Y. Tokura, N. Môri, and J. Akimitsu, 1995, Phys. Rev. B **52**, 13865.

Mizokawa, T., A. Fujimori, H. Namatame, K. Akeyama, and N. Kosugi, 1994, Phys. Rev. Lett. **49**, 7193.

Mizokawa, T., H. Namatame, A. Fujimori, K. Akeyama, H. Kondoh, H. Kuroda, and N. Kosugi, 1991, Phys. Rev. Lett. **67**, 1638.

Mizokawa, T., K. Ootomo, T. Konishi, A. Fujimori, Z. Hiroi, N. Kobayashi, and M. Takano, 1997, Phys. Rev. B **55**, R13373.

Mizuhashi, K., K. Takenaka, Y. Fukuzumi, and S. Uchida, 1995, Phys. Rev. B **52**, R3884.

Moeller, G., Q. Si, G. Kotliar, M. J. Rozenberg, and D. S. Fisher, 1995, Phys. Rev. Lett. **74**, 2082.

Mohan Ram, R. A., L. Ganpathi, P. Ganguly, and C. N. Rao, 1984, J. Solid State Chem. **63**, 139.

Momono, N., M. Ido, T. Nakano, M. Oda, Y. Okajima, and K. Yamaya, 1994, Physica C **233**, 395.

Momono, N., M. Ido, M. Oda, N. Yamada, and A. Onodera, 1991, Physica C **183**, 241.

Mook, H. A., M. Yethiraj, G. Aeppli, T. E. Mason, and T. A. Armstrong, 1993, Phys. Rev. Lett. **70**, 3490.

Moreo, A., and E. Dagotto, 1990, Phys. Rev. B **42**, 4786.

Moreo, A., E. Dagotto, T. Jolicoeur, and J. Riera, 1990, Phys. Rev. B **42**, 6283.

Moreo, A., S. Haas, A. W. Sandvik, and E. Dagotto, 1995, Phys. Rev. B **51**, 12045.

Moreo, A., D. J. Scalapino, and E. Dagotto, 1991, Phys. Rev. B **43**, 11442.

Moreo, A., D. J. Scalapino, R. L. Sugar, S. R. White, and N. E. Bickers, 1990, Phys. Rev. B **41**, 2313.

Mori, M., H. Fukuyama, and M. Imada, 1994, J. Phys. Soc. Jpn. **63**, 1639.

Morikawa, K., T. Mizokawa, A. Fujimori, Y. Taguchi, and Y. Tokura, 1996, Phys. Rev. B **54**, 8446.

Morikawa, K., T. Mizokawa, K. Kobayashi, A. Fujimori, H. Eisaki, S. Uchida, F. Iga, and Y. Nishihara, 1995, Phys. Rev. B **52**, 13711.

Moritomo, Y., A. Asamitsu, H. Kuwahara, and Y. Tokura, 1996, Nature (London) **380**, 141.

Moritomo, Y., H. Kuwahara, Y. Tomioka, and Y. Tokura, 1997, Phys. Rev. B **55**, 7549.

Moritomo, Y., Y. Tomioka, A. Asamitsu, Y. Tokura, and Y. Matsui, 1995, Phys. Rev. B **51**, 3297.

Moriya, T., 1979, J. Magn. Magn. Mater. **14**, 1.

Moriya, T., 1985, *Spin Fluctuations in Itinerant Electron Magnetism*, Springer Series in Solid-State Sciences No. 56 (Springer, Berlin).

Moriya, T., 1995, in *Spectroscopy of Mott Insulators and Correlated Metals*, edited by A. Fujimori and Y. Tokura (Springer, Berlin), p. 66.

Moriya, T., and H. Hasegawa, 1980, J. Phys. Soc. Jpn. **48**, 1490.

Moriya, T., Y. Takahashi, and K. Ueda, 1990, J. Phys. Soc. Jpn. **59**, 2905.

Motome, Y., and M. Imada, 1996, J. Phys. Soc. Jpn. **65**, 2135.

Motome, Y., and M. Imada, 1997, J. Phys. Soc. Jpn. **66**, 1872.

Motome, Y., and M. Imada, 1998, cond-mat/9808124.

Motoyama, N., H. Eisaki, and S. Uchida, 1996, Phys. Rev. Lett. **76**, 3212.

Mott, N. F., 1937, Proc. Phys. Soc. London, Ser. A **49**, 72.

Mott, N. F., 1949, Proc. Phys. Soc. London, Ser. A **62**, 416.

Mott, N. F., 1956, Can. J. Phys. **34**, 1356.

Mott, N. F., 1961, Philos. Mag. **6**, 287.

Mott, N. F., 1990, *Metal-Insulator Transitions* (Taylor and Francis, London/Philadelphia).

Müller-Hartman, E., 1989, Z. Phys. B **74**, 507.

Murakami, Y., H. Kawada, H. Kawata, M. Tanaka, T. Arima, Y. Moritomo, and Y. Tokura, 1998, Phys. Rev. Lett. **80**, 1932.

Muramoto, S., Y. Kitaoka, K. Magishi, K. Ishida, K. Asayama, M. Uehara, T. Nagata, and J. Akimitsu, 1997, unpublished.

Mutou, T., and D. S. Hirashima, 1996, Phys. Rev. B **54**, 9058.

Mutou, T., H. Takahashi, and D. S. Hirashima, 1997, J. Phys. Soc. Jpn. **66**, 2781.

Myron, H. W., 1980, Physica B **99**, 243.

Nagano, T., Y. Tomioka, Y. Nakayama, K. Kishio, and K. Kitazawa, 1993, Phys. Rev. B **48**, 9689.

Nagaoka, Y., 1966, Phys. Rev. **147**, 392.

Nagaosa, N., 1997, unpublished.

Nagaosa, N., and P. A. Lee, 1990, Phys. Rev. Lett. **64**, 2450.

Nagaosa, N., and P. A. Lee, 1997, cond-mat/9702103.

Nagaosa, N., and T-K. Ng, 1995, Phys. Rev. B **51**, 15588.

Nagata, T., H. Fujino, J. Akimitsu, M. Nishi, K. Kakurai, and S. Katano, 1998, private communication.

Nagata, T., M. Uehara, J. Goto, J. Akimitsu, N. Motoyama, H. Eisaki, S. Uchida, H. Takahashi, T. Nakanishi, and N. Môri, 1998, Phys. Rev. Lett. **81,** 1090.

Nakamura, M., A. Sekiyama, H. Namatame, A. Fujimori, H. Yoshihara, T. Ohtani, A. Misu, and M. Takano, 1994a, Phys. Rev. B **49**, 16191.

Nakamura, M., A. Sekiyama, H. Namatame, H. Kino, A. Fujimori, A. Misu, H. Ikoma, M. Matoba, and S. Anzai, 1994b, Phys. Rev. Lett. **73**, 2891.

Nakamura, M., H. Imai, and M. Shiga, 1997, Phys. Rev. Lett. **79**, 3779.

Nakano, T., M. Oda, C. Manabe, N. Momono, Y. Miura, and M. Ido, 1994, Phys. Rev. B **49**, 16000.

Namatame, H., A. Fujimori, Y. Tokura, M. Nakamura, K. Yamaguchi, A. Misu, H. Matsubara, S. Suga, H. Eisaki, T. Ito, H. Takagi, and S. Uchida, 1990, Phys. Rev. B **41**, 7205.

Narikiyo, O., 1996, Physica C **267**, 204.

Narikiyo, O., 1997, unpublished.

Narikiyo, O., and K. Miyake, 1994, J. Phys. Soc. Jpn. **63**, 4169.

Nazarenko, A., K. J. E. Vos, S. Haas, E. Dagotto, and R. J. Gooding, 1995, Phys. Rev. B **51**, 8676.

Negele, J. W., and H. Orland, 1988, *Quantum Many-Particle Systems* (Addison Wesley, Redwood City, CA).

Nersesyan, A. A., A. Luther, and F. V. Kusmartsev, 1993, Phys. Lett. A **176**, 363.

Neumeier, J. J., A. L. Cornelius, and S. Schilling, 1994, Physica B **198**, 324.

Neves, E. J., and J. F. Perez, 1986, Phys. Lett. A **114**, 331.

Newns, D. M., and N. Read, 1987, Adv. Phys. **36**, 799.

Nimkar, S., D. D. Sarma, and H. R. Krishnamurthy, 1993, Phys. Rev. B **47**, 10927.

Nishida, N., *et al.*, 1987, Jpn. J. Appl. Phys., Part 2 **26**, L1856.

Nishihara, H., and M. Takano, 1981, J. Phys. Soc. Jpn. **50**, 426.

Nishikawa, T., S. Shamoto, M. Sera, M. Sato, S. Ohsugi, Y. Kitaoka, and K. Asayama, 1993, Physica C **209**, 553.

Nishikawa, T., J. Takeda, and M. Sato, 1993, J. Phys. Soc. Jpn. **62**, 2568.

Nishikawa, T., J. Takeda, and M. Sato, 1994, J. Phys. Soc. Jpn. **63**, 1441.

Nishikawa, T., Y. Yasui, Y. Kobayashi, and M. Sato, 1996, J. Phys. Soc. Jpn. **65**, 2543.

Nishikawa, T., Y. Yasui, and M. Sato, 1994, J. Phys. Soc. Jpn. **63**, 3218.

Noack, R. M., N. Bulut, D. J. Scalapino, and M. G. Zacher, 1997, Phys. Rev. B **56**, 7162.

Norman, M. R., *et al.*, 1997, cond-mat/9710163.

Normand, B., H. Kohno, and H. Fukuyama, 1995, J. Phys. Soc. Jpn. **64**, 3903.

Nozaki, A., H. Yoshikawa, T. Wada, H. Yamauchi, and S. Tanaka, 1991, Phys. Rev. B **43**, 181.

Nozawa, K., M. Nohara, H. Takagi, Z. Hiroi, and M. Takano, 1997, in *Advances in Superconductivity IX*, edited by S. Nakajima and M. Murakami (Springer-Verlag, Tokyo, 1997), p. 69.

Nozières, P., and S. Schmitt-Rink, 1985, J. Low Temp. Phys. **59**, 195.

Nücker, N., H. Romberg, X. X. Xi, J. Fink, B. Gegenheimer, and Z.-X. Zhao, 1989, Phys. Rev. B **39**, 6619.

Obradors, X., L. M. Paulius, B. Maples, J. B. Torrance, A. I. Nazzal, J. Fontcuberta, and Y. Granados, 1993, Phys. Rev. B **47**, 12353.

Ogata, M., M. U. Luchini, and T. M. Rice, 1991, Phys. Rev. B **44**, 12083.

Ogata, M., and H. Shiba, 1990, Phys. Rev. B **41**, 2326.

Ogawa, S., 1979, J. Appl. Phys. **50**, 2308.

Ogawa, S., *et al.*, 1974, Int. J. Magn. **5**, 349.

Oguchi, T., 1995, Phys. Rev. B **51**, 1385.

Oh, S.-J., J. W. Allen, and J. M. Lawrence, 1987, Phys. Rev. B **35**, 2267.

Oh, S.-J., J. W. Allen, I. Lindau, and J. C. Mikkelsen, 1982, Phys. Rev. B **26**, 4845.

Ohata, N., and R. Kubo, 1970, J. Phys. Soc. Jpn. **28**, 1402.

Ohta, H., S. Kimura, E. Kulatov, S. V. Halilov, T. Nanba, M. Motokawa, M. Sato, and K. Nagasaka, 1994, J. Phys. Soc. Jpn. **63**, 4206.

Ohta, Y., T. Tohyama, and S. Maekawa, 1991a, Phys. Rev. B **43**, 2968.

Ohta, Y., T. Tohyama, and S. Maekawa, 1991b, Phys. Rev. Lett. **66**, 1228.

Ohtani, T., 1974, J. Phys. Soc. Jpn. **37**, 701.

Ohtani, T., K. Kosuge, and S. Kachi, 1970, J. Phys. Soc. Jpn. **28**, 1588 (Part I); **29**, 521 (Part II).

Okabe, Y., and M. Kikuchi, 1988, J. Phys. Soc. Jpn. **57**, 4351.

Okada, K., A. Kotani, K. Maiti, and D. D. Sarma, 1996, J. Phys. Soc. Jpn. **65**, 1844.

Okada, K., A. Kotani, and B. T. Thole, 1992, J. Electron Spectrosc. Relat. Phenom. **58**, 325.

Okada, K., T. Uozumi, and A. Kotani, 1994, J. Phys. Soc. Jpn. **63**, 3176.

Okimoto, Y., T. Katsufuji, T. Ishikawa, T. Arima, and Y. Tokura, 1997, Phys. Rev. B **55**, 4206.

Okimoto, Y., T. Katsufuji, T. Ishikawa, A. Urushibara, T. Arima, and Y. Tokura, 1995a, Phys. Rev. Lett. **75**, 109.

Okimoto, Y., T. Katsufuji, Y. Okada, T. Arima, and Y. Tokura, 1995b, Phys. Rev. B **51**, 9581.

Okuno, Y., O. Narikiyo, and K. Miyake, 1997, J. Phys. Soc. Jpn. **66**, 2389.

Olson, C. G., R. Liu, D. W. Lynch, R. S. List, A. J. Arko, B. W. Veal, Y. C. Chang, P. Z. Jiang, and A. P. Paulikas, 1990, Phys. Rev. B **42**, 381.

Olson, C. G., R. Liu, A.-B. Yang, D. W. Lynch, A. J. Arko, R. S. List, B. W. Veal, Y. C. Chang, P. Z. Jiang, and A. P. Paulikas, 1989, Science **245**, 731.

Ong, N. P., 1990, in *Properties of the High Temperature Superconductors*, edited by D. M. Ginsberg (World Scientific, Singapore), Vol. 2, p. 459.

Ong, N. P., T. W. Jing, T. R. Chien, Z. Z. Wang, T. V. Ramakrishnan, J. M. Tarascon, and K. Remschnig, 1991, Physica C **185-189**, 34.

Ong, N. P., Z. Z. Wang, J. Clayhold, J. M. Tarascon, L. H. Greene, and W. R. McKinnon, 1987, Phys. Rev. B **35**, 8807.

Onoda, M., T. Naka, and H. Nagasawa, 1991, J. Phys. Soc. Jpn. **60**, 2550.

Onoda, M., H. Ohta, and H. Nagasawa, 1991, Solid State Commun. **79**, 281.

Orenstein, J., G. A. Thomas, A. J. Millis, S. L. Cooper, D. H. Rapkine, T. Timusk, L. F. Schneemeyer, and J. V. Waszczak, 1990, Phys. Rev. B **42**, 6342.

Osafune, T., N. Motoyama, H. Eisaki, and S. Uchida, 1997, Phys. Rev. Lett. **78**, 1980.

Otsuka, H., 1990, J. Phys. Soc. Jpn. **59**, 2916.

Overhauser, A. W., 1962, Phys. Rev. **128**, 1437.

Panissod, P., G. Krill, C. Vettier, and R. Madar, 1979, Solid State Commun. **29**, 67.

Park, C.-H., Z.-X. Shen, A. G. Loeser, D. S. Dessau, D. G. Mandrus, A. Migliori, J. Sarrao, and Z. K. Fisk, 1995, Phys. Rev. B **52**, R16981.

Park, J.-H., and J. W. Allen, 1997, unpublished.

Park, J.-H., C. T. Chen, S.-W. Cheong, W. Bao, G. Meigs, V. Chakarian, and Y. U. Idzerda, 1996, Phys. Rev. Lett. **76**, 4215.

Park, J.-H., L. H. Tjeng, J. W. Allen, P. Metcalf, and C. T. Chen, 1997a, Phys. Rev. B **55**, 12813.

Park, J.-H., L. H. Tjeng, J. W. Allen, P. Metcalf, C. T. Chen, F. M. F. de Groot, and G. A. Sawatzky, 1997b, unpublished.

Park, K. T., K. Terakura, T. Oguchi, A. Yanase, and M. Ikeda, 1988, J. Phys. Soc. Jpn. **57**, 3445.

Park, S. K., T. Ishikawa, and Y. Tokura, 1998, Phys. Rev. B **58**, 3717.

Park, S. K., S. Yamaguchi, and Y. Tokura, 1998, unpublished.

Pearson, A. D., 1958, J. Phys. Chem. Solids **5**, 316.

Peierls, R., 1937, Proc. Phys. Soc. London, Ser. A **49**, 72.

Pellegrin, E., N. Nücker, J. Fink, S. L. Molodtsov, A. Gutiérrez, E. Navas, O. Strebel, Z. Hu, M. Domke, G. Kaindl, S. Uchida, Y. Nakamura, J. Markl, M. Klauda, G. Saemann-Ischenko, A. Krol, J. L. Peng, Z. Y. Li, and R. L. Greene, 1993, Phys. Rev. B **47**, 3354.

Pen, H. F., M. Abbate, A. Fujimori, Y. Tokura, H. Eisaki, S. Uchida, and G. A. Sawatzky, 1998 (unpublished).

Penn, D., 1966, Phys. Rev. **142**, 350.

Perdew, J. P., 1986, Phys. Rev. B **33**, 8822.

Perdew, J. P., and Y. Wang, 1986, Phys. Rev. B **33**, 8800.

Perdew, J. P., and A. Zunger, 1981, Phys. Rev. B **23**, 5048.

Perkins, J. D., J. M. Graybeal, M. A. Kastner, R. J. Birgeneau, J. P. Falck, and M. Greven, 1993, Phys. Rev. Lett. **71**, 1621.

Perring, T., G. Aeppli, T. Kimura, and Y. Tokura, 1998, unpublished.

Perring, T., G. Aeppli, Y. Moritomo, and Y. Tokura, 1998, Phys. Rev. Lett. **78**, 3197.

Pethick, C. J., and G. M. Carneiro, 1973, Phys. Rev. A **7**, 304.

Pickett, W. E., 1989, Rev. Mod. Phys. **61**, 433.

Pickett, W. E., R. E. Cohen, and H. Krakauer, 1990, Phys. Rev. B **42**, 8764.

Pickett, W. E., S. C. Erwin, and E. C. Ethridge, 1996, con-mat/9611225.

Pickett, W. E., and D. J. Singh, 1995, Europhys. Lett. **32**, 759.

Pines, D., and P. Nozières, 1989, *The Theory of Quantum Liquids* (Benjamin, New York).

Poilblanc, D., and T. M. Rice, 1989, Phys. Rev. B **39**, 9749.

Pouget, J. P., H. Launois, J. P. D'Haenens, P. Merender, and T. M. Rice, 1975, Phys. Rev. Lett. **35**, 873.

Pouget, J. P., H. Launois, T. M. Rice, P. Dernier, A. Gossard, G. Villeneuve, and P. Hagenmuller, 1974, Phys. Rev. B **10**, 1801.

Preuss, R., W. Hanke, C. Gröber, and H. G. Evertz, 1997, Phys. Rev. Lett. **79**, 1122.

Preuss, R., W. Hanke, and W. von der Linden, 1995, Phys. Rev. Lett. **75**, 1344.

Pruschke, Th., D. L. Cox, and M. Jarrell, 1993, Phys. Rev. B **47**, 3553.

Puchkov, A. V., P. Fournier, D. N. Basov, T. Timusk, A. Kapitulnik, and N. N. Kolesnikov, 1996, Phys. Rev. Lett. **77**, 3212.

Radaelli, P. G., D. G. Hinks, A. W. Mitchell, B. A. Hunter, J. L. Wagner, B. Dabrowski, K. G. Vandervoort, H. K. Viswanathan, and J. D. Jorgensen, 1994, Phys. Rev. B **49**, 4163.

Radaelli, P. G., J. D. Jorgensen, A. J. Schultz, J. L. Peng, and R. L. Greene, 1994, Phys. Rev. B **49**, 15322.

Rado, G. T., and H. Suhl, 1963, Eds., *Magnetism* (Academic, New York) Vol. I, p. 25.

Ramirez, A. P., P. L. Gammel, S-W. Cheong, D. J. Bishop, and P. Chandra, 1996, Phys. Rev. Lett. **76**, 447.

Reger, J. D., and A. P. Young, 1988, Phys. Rev. B **37**, 5978.

Renner, C., *et al.*, 1998, Phys. Rev. Lett. **80**, 149.

Rice, T. M., 1995, in *Spectroscopy of Mott Insulators and Corrrelated Metals*, edited by A. Fujimori and Y. Tokura (Springer, Berlin), p. 221.

Rice, T. M., and W. R. Brinkman, 1972, Phys. Rev. B **5**, 4350.

Rice, T. M., S. Gapalan, and M. Sigrist, 1993, Europhys. Lett. **23**, 445.

Rice, T. M., H. Launois, and J. P. Pouget, 1994, Phys. Rev. Lett. **73**, 3042.

Rice, T. M., and M. Sigrist, 1996, J. Phys.: Condens. Matter **7**, L643.

Rice, T. M., and F. C. Zhang, 1989, Phys. Rev. B **39**, 815.

Robey, S. W., V. E. Henrich, C. Eylem, and B. W. Eichhorn, 1995, Phys. Rev. B **52**, 2395.

Robey, S. W., L. T. Hudson, C. Eylem, and B. W. Eichorn, 1993, Phys. Rev. B **48**, 562.

Romberg, H., M. Alexander, N. Nücker, P. Adelmann, and J. Fink, 1990, Phys. Rev. B **42**, 8768.

Rossat-Mignod, J., *et al.*, 1991a, Physica B **169**, 58.

Rossat-Mignod, J., L. P. Regnault, C. Vettier, P. Bourges, P. Burlet, J. Bossy, J. Y. Henry, and G. Lapertot, 1991b, Physica C **185-189**, 86.

Roth, L. M., 1966, Phys. Rev. **149**, 306.

Roth, L. M., 1967, J. Appl. Phys. **38**, 1065.

Rotter, L. D., *et al.*, 1991, Phys. Rev. Lett. **67**, 2741.

Rozenberg, M. J., 1996a, Phys. Rev. B **55**, 4855.

Rozenberg, M. J., 1996b, Preprint No. cond-mat/9612089.

Rozenberg, M. J., I. H. Inoue, H. Makino, F. Iga, and Y. Nishihara, 1996, Preprint No. cond-mat/9603051.

Rozenberg, M. J., G. Kotliar, H. Kajueter, G. A. Thomas, D. H. Rapkine, J. M. Honig, and P. Metcalf, 1995, Phys. Rev. Lett. **75**, 105.

Rozenberg, M. J., G. Kotliar, and X. Y. Zhang, 1994, Phys. Rev. B **49**, 10181.

Rozenberg, M. J., X. Y. Zhang, and G. Kotliar, 1992, Phys. Rev. Lett. **69**, 1236.

Sachan, V., D. J. Buttrey, J. M. Tranquada, J. E. Lorenzo, and G. Shirane, 1995, Phys. Rev. B **51**, 12742.

Saitoh, T., A. E. Bocquet, T. Mizokawa, and A. Fujimori, 1995a, Phys. Rev. B **52**, 7934.

Saitoh, T., A. E. Bocquet, T. Mizokawa, H. Namatame, A. Fujimori, M. Abbate, Y. Takeda, and M. Takano, 1995b, Phys. Rev. B **51**, 13942.

Saitoh, T., T. Mizokawa, A. Fujimori, M. Abbate, Y. Takeda, and M. Takano, 1997a, Phys. Rev. B **55**, 4257.

Saitoh, T., T. Mizokawa, A. Fujimori, M. Abbate, Y. Takeda, and M. Takano, 1997b, Phys. Rev. B **56**, 1290.

Saitoh, T., A. Sekiyama, T. Mizokawa, A. Fujimori, K. Ito, H. Nakamura, and M. Shiga, 1995, Solid State Commun. **95**, 307.

Sakai, O., and Y. Kuramoto, 1994, Solid State Commun. **89**, 307.

Sakai, T., G. Adachi, and J. Shiokawa, 1977, J. Appl. Phys. **48**, 379.

Sarma, D. D., S. R. Barman, H. Kajueter, and G. Kotliar, 1996, Europhys. Lett. **36**, 307.

Sarma, D. D., N. Shanthi, S. R. Barman, N. Hamada, H. Sawada, and K. Terakura, 1995, Phys. Rev. Lett. **75**, 1126.

Sarma, D. D., N. Shanthi, S. R. Krishnakumar, T. Saitoh, T. Mizokawa, A. Sekiyama, K. Kobayashi, A. Fujimori, E. Weschke, R. Meier, G. Kaindl, Y. Takeda, and M. Takano, 1996, Phys. Rev. B **53**, 6873.

Satpathy, S., Z. S. Popović, and F. R. Vukajlović, 1996, Phys. Rev. Lett. **76**, 960.

Sawada, H., N. Hamada, K. Terakura, and T. Asada, 1996, Phys. Rev. B **53**, 12742.

Sawatzky, G. A., and J. W. Allen, 1984, Phys. Rev. Lett. **53**, 2339.

Sawatzky, G. A., and D. Post, 1979, Phys. Rev. B **20**, 1546.

Sayer, M., R. Chen, R. Fletcher, and A. Mansingh, 1975, J. Phys. C **8**, 2053.

Sayetat, F., M. Ghedira, J. Chenavas, and M. Marezio, 1982, J. Phys. C **15**, 1627.

Scalapino, D. J., 1990, in *High Temperature Superconductivity:* Proceedings—*The Los Alamos Symposium 1989*, edited by K. S. Bedell, D. Coffey, D. E. Meltzer, David Pines, and Robert Schrieffer (Addison-Wesley, Redwood City, CA), p. 400.

Scalapino, D. J., 1994, in *Proceedings of the International School of Physics, Enrico Fermi, Course CXXI*, edited by R. A. Broglia and J. R. Schrieffer (North-Holland, Amsterdam), p. 95.

Scalapino, D. J., 1995, Phys. Rep. **250**, 329.

Scalapino, D. J., S. R. White, and S. Zhang, 1993, Phys. Rev. B **47**, 7995.

Scalettar, R. T., D. J. Scalapino, R. L. Sugar, and D. Toussaint, 1989, Phys. Rev. B **39**, 4711.

Schiffer, P., A. P. Ramirez, W. Bao, and S.-W. Cheong, 1995, Phys. Rev. Lett. **75**, 3336.

Schiller, A., and K. Ingersent, 1995, Phys. Rev. Lett. **75**, 113.

Schlesinger, Z., R. T. Collins, F. Holtzberg, C. Feild, S. H. Blanton, U. Welp, G. W. Crabtree, Y. Fang, and J. Z. Liu, 1990, Phys. Rev. Lett. **65**, 801.

Schlesinger, Z., R. T. Collins, L. D. Rotter, F. Holtzberg, C. Feild, U. Welp, G. W. Crabtree, J. Z. Liu, Y. Fang, K. G. Vandervoort, and S. Fleshler, 1994, Physica C **235-240**, 49.

Schlesinger, Z., Z. Fisk, H.-T. Zhang, M. B. Maple, J. F. DiTusa, and G. Aeppli, 1993, Phys. Rev. Lett. **71**, 1748.

Schultz, A. J., J. D. Jorgensen, J. L. Peng, and R. L. Greene, 1996, Phys. Rev. B **53**, 5157.

Schulz, H. J., 1989, J. Phys. (Paris) **50**, 2833.

Schulz, H. J., 1990a, Phys. Rev. Lett. **64**, 1445.

Schulz, H. J., 1990b, Phys. Rev. Lett. **64**, 2831.

Schulz, H. J., 1990c, Phys. Rev. Lett. **65**, 2462.

Schulz, H. J., 1991, Int. J. Mod. Phys. B **5**, 57.

Searle, C. W., and S. T. Wang, 1969, Can. J. Phys. **47**, 2703.

Sega, I., and P. Prelovšek, 1990, Phys. Rev. B **42**, 892.

Sekiyama, A., A. Fujimori, S. Aonuma, H. Sawa, and R. Kato, 1995, Phys. Rev. B **51**, 13899.

Shastry, B. S., B. I. Shraiman, and R. R. P. Singh, 1993, Phys. Rev. Lett. **70**, 2004.

Shastry, B. S., and B. Sutherland, 1990, Phys. Rev. Lett. **65**, 243.

Shen, Z.-X., J. W. Allen, J. J. Yeh, J.-S. Kang, W. Ellis, W. Spicer, I. Lindau, M. B. Maple, Y. D. Dalichaouch, M. S. Torikachvili, J. Z. Sun, and T. H. Geballe, 1987, Phys. Rev. B **36**, 8414.

Shen, Z.-X., and D. S. Dessau, 1995, Phys. Rep. **253**, 1.

Shen, Z.-X., R. S. List, D. S. Dessau, B. O. Wells, O. Jepsen, A. J. Arko, R. Barttlet, C. K. Shih, F. Parmigiani, J. C. Huang, and P. A. P. Lindberg, 1991a, Phys. Rev. B **44**, 3604.

Shen, Z.-X., D. S. Dessau, B. O. Wells, C. G. Olson, D. B. Mitzi, L. Lombardo, R. S. List, and A. J. Arko, 1991b, Phys. Rev. B **44**, 12098.

Shepherd, J. P., J. W. Koenitzer, R. Aragón, C. J. Sanberg, and J. M. Honig, 1985, Phys. Rev. B **31**, 1107.

Shiba, H., R. Shiina, and A. Takahashi, 1997, J. Phys. Soc. Jpn. **66**, 941.

Shiina, R., T. Nishitani, and H. Shiba, 1997, J. Phys. Soc. Jpn. **66**, 3159.

Shikano, M., T.-K. Huang, Y. Inaguma, M. Itoh, and T. Nakamura, 1994, Solid State Commun. **90**, 115.

Shin, S., S. Suga, M. Taniguchi, M. Fujisawa, H. Kanzaki, A. Fujimori, H. Daimon, Y. Ueda, K. Kosuge, and S. Kachi, 1990, Phys. Rev. B **41**, 4993.

Shin, S., Y. Tezuka, T. Kinoshita, T. Ishii, T. Kashiwakura, M. Takahashi, and Y. Suda, 1995, J. Phys. Soc. Jpn. **64**, 1230.

Si, Q., and G. Kotliar, 1993, Phys. Rev. B **48**, 13881.

Si, Q., Y. Zha, K. Levin, and J. P. Lu, 1993, Phys. Rev. B **47**, 9055.

Siegrist, T., L. F. Schneemeyer, S. A. Sunshine, and J. V. Waszczak, 1988, Mater. Res. Bull. **23**, 1429.

Singh, D. J., 1994, Phys. Rev. B **49**, 1580.

Singh, D. J., 1995, Phys. Rev. B **52**, 1358.

Singh, D. J., 1996, J. Appl. Phys. **79**, 4818.

Singh, D. J., and W. E. Pickett, 1991, Phys. Rev. B **44**, 7715.

Siratori, K., S. Suga, M. Taniguchi, K. Soda, S. Kimura, and A. Yanase, 1986, J. Phys. Soc. Jpn. **55**, 690.

Siratori, K., S. Todo, and S. Kimura, 1988, J. Phys. Soc. Jpn. **57**, 2093.

Sjostrand, M. E., and P. H. Keesom, 1973, Phys. Rev. B **7**, 3558.

Slater, J. C., 1951, Phys. Rev. **82**, 538.

Slater, J. C., 1974, *Quantum Theory of Molecules and Solids* (McGraw-Hill, New York).

Smith, K. E., and V. E. Henrich, 1988, Phys. Rev. B **38**, 5965.

Smith, K. E., and V. E. Henrich, 1994, Phys. Rev. B **50**, 1382.

Solovyev, I., N. Hamada, and K. Terakura, 1996a, Phys. Rev. Lett. **76**, 4825.

Solovyev, I., N. Hamada, and K. Terakura, 1996b, Phys. Rev. B **53**, 7158.

Solyom, J., 1979, Adv. Phys. **28**, 201.

Sommerfeld, A., 1928, Z. Phys. **47**, 1.

Sorella, S., R. Car, S. Baroni, and M. Parrinello, 1989, Europhys. Lett. **8**, 663.

Sørensen, E. S., M. Wallin, S. M. Girvin, and A. P. Young, 1992, Phys. Rev. Lett. **69**, 828.

Sparks, J. T., and T. Komoto, 1967, Phys. Lett. **25**, 398.

Sparks, J. T., and T. Komoto, 1968, Rev. Mod. Phys. **40**, 752.

Sreedhar, K., J. M. Honig, M. Darwin, M. McElfresh, P. M. Shand, J. Xu, B. C. Crooker, and J. Spalek, 1992, Phys. Rev. B **46**, 6382.

Stafford, C. A., and A. J. Millis, 1993, Phys. Rev. B **48**, 1409.

Stechel, E. B., and D. R. Jennison, 1998, Phys. Rev. B **38**, 4632.

Stephan, W., and P. Horsch, 1990, Phys. Rev. B **42**, 8736.

Stephan, W., and P. Horsch, 1991, Phys. Rev. Lett. **66**, 2258.

Stephan, W., and P. Horsch, 1992, Int. J. Mod. Phys. B **6**, 589.

Sternlieb, B. J., J. P. Hill, U. C. Wildgruber, G. M. Luke, B. Nachumi, Y. Moritomo, and Y. Tokura, 1996, Phys. Rev. Lett. **76**, 2169.

Sternlieb, B. J., G. Shirane, J. M. Tranquada, M. Sato, and S. Shamoto, 1993, Phys. Rev. B **47**, 5320.

Sternlieb, B. J., J. M. Tranquada, G. Shirane, M. Sato, and S. Shamoto, 1994, Phys. Rev. B **50**, 12915.

Sugano, S., Y. Tanabe, and H. Kamimura, 1970, *Multiplets of Transition-Metal Ions in Crystals* (Academic, New York).

Susaki, T., A. Sekiyama, K. Kobayashi, T. Mizokawa, A. Fujimori, M. Tsunekawa, T. Muro, T. Matsushita, S. Suga, H. Ishii, T. Hanyu, A. Kimura, H. Namatame, M. Taniguchi, T. Miyahara, F. Iga, M. Kasaya, and H. Harima, 1996, Phys. Rev. Lett. **77**, 4269.

Suzuki, K., K. Kishio, T. Hasegawa, and K. Kitazawa, 1990, Physica C **166**, 357.

Suzuki, M., 1976, Prog. Theor. Phys. **56**, 1454.

Suzumura, Y., Y. Hasegawa, and H. Fukuyama, 1988, J. Phys. Soc. Jpn. **57**, 2768.

Suzuura, H., and N. Nagaosa, 1997, Phys. Rev. B **56**, 3548.

Suzuura, H., H. Yasuhara, A. Furusaki, N. Nagaosa, and Y. Tokura, 1996, Phys. Rev. Lett. **76**, 2579.

Svane, A., and O. Gunnarsson, 1988a, Europhys. Lett. **7**, 171.

Svane, A., and O. Gunnarsson, 1988b, Phys. Rev. B **37**, 9919.

Svane, A., and O. Gunnarsson, 1990, Phys. Rev. Lett. **65**, 1148.

Swendsen, R. H., and J. S. Wang, 1987, Phys. Rev. Lett. **58**, 86.

Tachiki, M., T. Koyama, and S. Takahashi, 1994, Phys. Rev. B **50**, 7065.

Taguchi, Y., Y. Tokura, T. Arima, and F. Inaba, 1993, Phys. Rev. B **48**, 511.

Tajima, K., Y. Endoh, J. E. Fischer, and G. Shirane, 1988, Phys. Rev. B **38**, 6954.

Tajima, S., 1997, *Superconductivity Review* (Gordon and Breach Science Publishers, in press).

Tajima, S., J. Schutzmann, and S. Miyamoto, 1995, Solid State Commun. **95**, 759.

Takagi, H., B. Batlogg, H. L. Kao, J. Kwo, R. J. Cava, J. J. Krajewski, and W. F. Peck, Jr., 1992a, Phys. Rev. Lett. **69**, 2975.

Takagi, H., R. J. Cava, M. Marezio, B. Batlogg, J. J. Krajewski, W. F. Peck, Jr., P. Bordet, and D. E. Cox, 1992b, Phys. Rev. Lett. **68**, 3777.

Takagi, H., H. Eisaki, S. Uchida, and R. J. Cava, 1995, in *Spectroscopy of Mott Insulator and Correlated Metals*, edited by A. Fujimori and Y. Tokura (Springer, Berlin), p. 185.

Takagi, H., T. Ido, S. Ishibashi, M. Uota, S. Uchida, and Y. Tokura, 1989, Phys. Rev. B **40**, 2254.

Takagi, H., S. Uchida, K. Kitazawa, and S. Tanaka, 1987, Jpn. J. Appl. Phys., Part 2 **26**, L123.

Takagi, H., S. Uchida, and Y. Tokura, 1989, Phys. Rev. Lett. **62**, 1197.

Takagi, S., H. Yasuoka, S. Ogawa, and J. H. Wernick, 1981, J. Phys. Soc. Jpn. **50**, 2539.

Takahashi, M., 1972, Prog. Theor. Phys. **47**, 69.

Takahashi, M., 1989, Phys. Rev. B **40**, 2494.

Takahashi, M., and J. Igarashi, 1996, Ann. Phys. (N.Y.) **5**, 247.

Takahashi, M., and J. Kanamori, 1991, J. Phys. Soc. Jpn. **60**, 3154.

Takahashi, T., H. Matsuyama, H. Katayama-Yoshida, Y. Okabe, S. Hosoya, K. Seki, H. Fujimoto, M. Sato, and H. Inokuchi, 1989, Phys. Rev. B **39**, 6636.

Takahashi, Y., and T. Moriya, 1979, J. Phys. Soc. Jpn. **46**, 1452.

Takano, M., H. Kosugi, N. Nakanishi, M. Shimada, T. Wada, and M. Koizumi, 1977, J. Phys. Soc. Jpn. **43**, 1101.

Takano, M., S. Nasu, T. Abe, K. Yamamoto, S. Endo, Y. Takeda, and J. B. Goodenough, 1991, Phys. Rev. Lett. **67**, 3267.

Takano, M., and Y. Takeda, 1983, Bull. Inst. Chem. Res., Kyoto Univ. **61**, 406.

Takeda, J., T. Nishikawa, and M. Sato, 1993, J. Phys. Soc. Jpn. **62**, 2571.

Takeda, J., *et al.*, 1994, J. Phys. Soc. Jpn. **63**, 3564.

Takegahara, K., 1994, J. Electron Spectrosc. Relat. Phenom. **66**, 303.

Takenaka, K., K. Mizuhashi, H. Takagi, and S. Uchida, 1994, Phys. Rev. B **50**, 6534.

Takigawa, M., E. T. Ahrens, and Y. Ueda, 1996, Phys. Rev. Lett. **76**, 283.

Takigawa, M., P. C. Hammel, R. H. Heffner, Z. Fisk, J. L. Smith, and R. B Schwarz, 1989, Phys. Rev. B **39**, 300.

Takigawa, M., and D. B. Mitzi, 1994, Phys. Rev. Lett. **73**, 1287.

Takigawa, M., A. P. Reyes, P. C. Hammel, J. D. Thompson, R. H. Heffner, Z. Fisk, and K. C. Ott, 1991, Phys. Rev. B **43**, 247.

Tamasaku, K., Y. Nakamura, and S. Uchida, 1992, Phys. Rev. Lett. **69**, 1455.

Tanabe, T., A. Katsufuji, and Y. Tokura, 1998, unpublished.

Tanamoto, T., H. Kohno, and H. Fukuyama, 1992, J. Phys. Soc. Jpn. **61**, 1886.

Tanamoto, T., H. Kohno, and H. Fukuyama, 1993, J. Phys. Soc. Jpn. **62**, 717.

Tanamoto, T., H. Kohno, and H. Fukuyama, 1994, J. Phys. Soc. Jpn. **63**, 2739.

Taniguchi, S., T. Nishikawa, Y. Yasui, Y. Kobayashi, M. Sato, T. Nishioka, M. Kontani, and K. Sano, 1995, J. Phys. Soc. Jpn. **64**, 2758.

Temmerman, W. M., Z. Szotek, and H. Winter, 1993, Phys. Rev. B **47**, 11533.

Terakura, K., 1987 (unpublished).

Terakura, K., T. Oguchi, A. R. Williams, and J. Kübler, 1984, Phys. Rev. B **30**, 4734.

Thio, T., and J. W. Bennett, 1994, Phys. Rev. B **50**, 10574.

Thio, T., T. R. Thurston, N. W. Preyer, P. J. Picone, M. A. Kastner, H. P. Jenssen, D. R. Gabbe, C. Y. Chen, R. J. Birgeneau, and A. Aharony, 1988, Phys. Rev. B **38**, 905.

Thomas, G. A., J. Orenstein, D. H. Rapkine, M. Capizzi, A. J. Millis, R. N. Bhatt, L. F. Schneemeyer, and J. V. Waszczak, 1988, Phys. Rev. Lett. **61**, 1313.

Thomas, G. A., D. H. Rapkine, S. A. Carter, A. J. Millis, T. F. Rosenbaum, P. Metcalf, and J. M. Honig, 1994, Phys. Rev. Lett. **73**, 1529.

Thomas, G. A., D. H. Rapkine, S. L. Cooper, S-W. Cheong, and A. S. Cooper, 1991, Phys. Rev. Lett. **67**, 2906.

Thouless, D. J., 1974, Phys. Rep., Phys. Lett. **13C**, 94.

Thuler, M. R., R. L. Benbow, and Z. Hurych, 1983, Phys. Rev. B **27**, 2082.

Thurston, T. R., R. J. Birgeneau, M. A. Kastner, N. W. Preyer, G. Shirane, Y. Fujii, K. Yamada, Y. Endoh, K. Kakurai, M. Matsuda, Y. Hidaka, and T. Murakami, 1989, Phys. Rev. B **40**, 4585.

Thurston, T. R., P. M. Gehring, G. Shirane, R. J. Birgeneau, M. A. Kastner, Y. Endoh, M. Matsuda, K. Yamada, H. Kojima, and I. Tanaka, 1992, Phys. Rev. B **46**, 9128.

Thurston, T. R., M. Matsuda, K. Kakurai, K. Yamada, Y. Endoh, R. J. Birgeneau, P. M. Gehring, Y. Hidaka, M. A. Kastner, T. Murakami, and G. Shirane, 1990, Phys. Rev. Lett. **65**, 263.

Tobin, J. G., C. G. Olson, C. Gu, J. Z. Liu, F. R. Solal, M. J. Fluss, R. H. Howell, J. C. O'Brien, H. B. Radousky, and P. A. Sterne, 1992, Phys. Rev. B **45**, 5563.

Tohyama, T., and S. Maekawa, 1992, Physica C **191**, 193.

Tokunaga, M., N. Miura, Y. Tomioka, and Y. Tokura, 1997, Phys. Rev. B **57**, 5259.

Tokura, Y., 1992a, Jpn. J. Appl. Phys. Ser. **7**, 14.

Tokura, Y., 1992b, Comments Condens. Matter Phys. **16**, 69.

Tokura, Y., 1994, Physica C **235-240**, 138.

Tokura, Y., 1997, unpublished.

Tokura, Y., and T. Arima, 1990, Jpn. J. Appl. Phys., Part 2 **29**, 2388.

Tokura, Y., S. Koshihara, T. Arima, H. Takagi, S. Ishibashi, T. Ido, and S. Uchida, 1990, Phys. Rev. B **41**, 11657.

Tokura, Y., H. Kuwahara, Y. Moritomo, Y. Tomioka, and A. Asamitsu, 1996a, Phys. Rev. Lett. **76**, 3184.

Tokura, Y., Y. Okimoto, S. Yamaguchi, H. Taniguchi, T. Kimura, and H. Takagi, 1998, Phys. Rev. B **58**, R1699.

Tokura, Y., Y. Taguchi, Y. Okada, Y. Fujishima, T. Arima, K. Kumagai, and Y. Iye, 1993, Phys. Rev. Lett. **70**, 2126.

Tokura, Y., H. Takagi, and S. Uchida, 1989, Nature (London) **337**, 345.

Tokura, Y., Y. Tomioka, H. Kuwahara, A. Asamitsu, Y. Moritomo, and M. Kasai, 1996b, J. Appl. Phys. **79**, 5288.

Tokura, Y., J. B. Torrance, T. C. Huang, and A. I. Nazzal, 1988, Phys. Rev. B **38**, 7156.

Tokura, Y., A. Urushibara, Y. Moritomo, T. Arima, A. Asamitsu, G. Kido, and N. Furukawa, 1994, J. Phys. Soc. Jpn. **63**, 3931.

Tomioka, Y., A. Asamitsu, H. Kuwahara, Y. Moritomo, and Y. Tokura, 1996, Phys. Rev. B **53**, R1689.

Tomioka, Y., A. Asamitsu, Y. Moritomo, and Y. Tokura, 1995, J. Phys. Soc. Jpn. **64**, 3626.

Tomonaga, S., 1950, Prog. Theor. Phys. **5**, 349.

Torrance, J. B., P. Lacorre, C. Asavaroengchai, and R. M. Metzger, 1991, Physica C **182**, 351.

Torrance, J. B., P. Lacorre, A. I. Nazzal, E. J. Ansaldo, and C. Niedermayer, 1992, Phys. Rev. B **45**, 8209.

Tranquada, J. M., *et al.*, 1988, Phys. Rev. Lett. **60**, 156.

Tranquada, J. M., D. J. Buttrey, V. Sachan, and J. E. Lorenzo, 1993, Phys. Rev. Lett. **73**, 1003.

Tranquada, J. M., J. E. Lorenzo, D. J. Buttrey, and V. Sachan, 1995, Phys. Rev. B **52**, 3581.

Tranquada, J. M., B. J. Sternlieb, J. D. Axe, Y. Nakamura, and S. Uchida, 1995, Nature (London) **375**, 561.

Tranquada, J. M., P. Wochner, and D. J. Buttrey, 1997, Phys. Rev. Lett. **79**, 2133.

Trotter, H. F., 1959, Proc. Am. Math. Soc. **10**, 545.

Troyer, M., H. Tsunetsugu, and D. Würtz, 1994, Phys. Rev. B **50**, 13515.

Tsuda, N., K. Nasu, A. Yanase, and K. Siratori, 1991, *Electronic Conduction in Oxides* (Springer, Berlin).

Tsuei, C. C., A. Gupta, and G. Koren, 1989, Physica C **161**, 415.

Tsujioka, T., T. Mizokawa, A. Fujimori, and Y. Tokura, 1997, unpublished.

Tsunetsugu, H., and M. Imada, 1997, J. Phys. Soc. Jpn. **66**, 1876.

Tsunetsugu, H., and M. Imada, 1998, J. Phys. Soc. Jpn. **67,** 1864.

Tsunetsugu, H., M. Troyer, and T. M. Rice, 1994, Phys. Rev. B **49**, 16078.

Tyler, J. M., and J. L. Fry, 1971, Phys. Rev. B **1**, 4601.

Uchida, S., T. Ido, H. Takagi, T. Arima, Y. Tokura, and S. Tajima, 1991, Phys. Rev. B **43**, 7942.

Uchida, S., H. Takagi, Y. Tokura, N. Koshihara, and T. Arima, 1989, in *Strong Correlation and Superconductivity*, edited by H. Fukuyama, S. Maekawa, and A. P. M. Malozemoff (Springer, Berlin), p. 194.

Ueda, K., 1977, J. Phys. Soc. Jpn. **43**, 1497.

Ueda, Y., K. Kosuge, and S. Kachi, 1980, J. Solid State Chem. **31**, 171.

Ueda, Y., K. Kosuge, S. Kachi, and T. Takada, 1979, J. Phys. (Paris), Colloq. **C2**, 275.

Uehara, M., T. Nagata, J. Akimitsu, E. Iiseki, N. Motoyama, S. Uchida, and R. Eccleston, 1997, unpublished.

Uehara, M., T. Nagata, J. Akimitsu, H. Takahashi, N. Môri, and K. Kinoshita, 1996, J. Phys. Soc. Jpn. **65**, 2764.

Uemura, Y. J., *et al.*, 1989, Phys. Rev. Lett. **62**, 2317.

Uemura, Y. J., *et al.*, 1991, Phys. Rev. Lett. **66**, 2665.

Ulmke, M., R. T. Scalettar, A. Nazarenko, and E. Dagotto, 1996, Phys. Rev. B **54**, 16523.

Uozumi, T., K. Okada, and A. Kotani, 1993, J. Phys. Soc. Jpn. **62**, 2595.

Uozumi, T., K. Okada, A. Kotani, Y. Tezuka, and S. Shin, 1996, J. Phys. Soc. Jpn. **65**, 1150.

Uozumi, T., K. Okada, A. Kotani, R. Zimmermann, P. Steiner, S. Hüfner, Y. Tezuka, and S. Shin, 1997, J. Electron Spectrosc. Relat. Phenom. **83**, 9.

Urushibara, A., Y. Moritomo, T. Arima, A. Asamitsu, G. Kido, and Y. Tokura, 1995, Phys. Rev. B **51**, 14103.

Usuki, T., N. Kawakami, and A. Okiji, 1989, Phys. Lett. A **135**, 476.

Vaknin, D., S. K. Sinha, D. E. Moncton, D. C. Johnston, J. M. Newsam, C. R. Safinya, and H. E. King, Jr., 1987, Phys. Rev. Lett. **58**, 2802.

van der Heide, H., R. Hemmel, C. F. van Bruggen, and C. Haas, 1980, J. Solid State Chem. **33**, 17.

van der Laan, G., C. Westra, and G. A. Sawatzky, 1981, Phys. Rev. B **23**, 4369.

van Dongen, P. G. J., 1991, Mod. Phys. Lett. B **5**, 861.

van Elp, J., R. H. Potze, H. Eskes, R. Berger, and G. A. Sawatzky, 1991, Phys. Rev. B **44**, 1530.

van Santen, J. H., and G. H. Jonker, 1950, Physica (Amsterdam) **16**, 337; **16**, 599.

van Veenendaal, M. A., G. A. Sawatzky, and W. A. Groen, 1994, Phys. Rev. B **49**, 1407.

Van Zandt, L. L., J. M. Honig, and J. B. Goodenough, 1968, J. Appl. Phys. **39**, 594.

Varma, C. M., 1996a, Phys. Rev. B **54**, 7328.

Varma, C. M., 1996b, Preprint No. cond-mat/9606086.

Varma, C. M., P. B. Littlewood, S. Schmitt-Rink, E. Abrahams, and A. E. Ruckenstein, 1989, Phys. Rev. Lett. **63**, 1996; **64**, 497(E).

Varma, C. M., S. Schmitt-Rink, and E. Abrahams, 1987, Solid State Commun. **62**, 681.

Vasanthacharya, N. Y., P. Ganguly, J. B. Goodenough, and C. N. R. Rao, 1984, J. Phys. C **17**, 2745.

Vergés, J. A., E. Louis, P. S. Lomdahl, F. Guinea, and A. R. Bishop, 1991, Phys. Rev. B **43**, 6099.

Verwey, E. J. W., 1939, Nature (London) **144**, 327.

Verwey, E. J. W., and P. W. Haaymann, 1941, Physica (Amsterdam) **8**, 979.

Verwey, E. J. W., P. W. Haaymann, and F. C. Romeijn, 1947, J. Chem. Phys. **15**, 174, 181.

Vilk, Y. M., L. Chen, and A.-M. S. Tremblay, 1994, Phys. Rev. B **49**, 13267.

Villeneuve, G., M. Drillon, and P. Hagenmuller, 1973, Mater. Res. Bull. **8**, 1111.

Virosztek, A., and J. Ruvalds, 1990, Phys. Rev. B **42**, 4064.

Visscher, P. B., 1974, Phys. Rev. B **10**, 943.

Voit, J., 1993, J. Phys.: Condens. Matter **5**, 8305.

Vojta, T., D. Belitz, R. Narayanan, and T. R. Kirkpatrick, 1996, Europhys. Lett. **36**, 191.

Vollhardt, D., 1984, Rev. Mod. Phys. **56**, 99.

von Barth, U., and L. Hedin, 1972, J. Phys. C **5**, 1629.

von der Linden, W., 1992, Phys. Rep. **220**, 53.

von Löhneysen, H., 1996, J. Phys.: Condens. Matter **8**, 9689.

Wada, H., G. Mori, H. Imai, and M. Shiga, 1997, Physica B **237-238**, 146.

Wada, N., Y. Nakamura, and K. Kumagai, 1991, Physica C **185-189**, 1177.

Wagner, J., W. Hanke, and D. J. Scalapino, 1991, Phys. Rev. B **43**, 10517.

Wallin, M., E. S. Sorensen, S. M. Girvin, and A. P. Young, 1994, Phys. Rev. B **49**, 12115.

Wang, Z. Z., T. R. Chien, N. P. Ong, J. M. Tarascon, and E. Wang, 1991, Phys. Rev. B **43**, 3020.

Warren, W. W., Jr., R. E. Walstedt, G. F. Brennert, R. J. Cava, R. Tycko, R. F. Bell, and G. Dabbagh, 1989, Phys. Rev. Lett. **62**, 1193.

Watanabe, H., H. Yamamoto, and K. Ito, 1963, J. Phys. Soc. Jpn. **18**, 995.

Watanabe, I., K. Kumagai, Y. Nakamura, and H. Nakajima, 1990, J. Phys. Soc. Jpn. **59**, 1932.

Watanabe, T., N. Môri, and T. Mitsui, 1976, Solid State Commun. **19**, 837.

Wegner, F., 1976, Z. Phys. B **25**, 327.

Wegner, F., 1979, Z. Phys. B **35**, 207.

Wells, B. O., Z.-X. Shen, A. Matsuura, D. M. King, M. A. Kastner, M. Greven, and R. J. Birgeneau, 1995, Phys. Rev. Lett. **74**, 964.

Wen, X.-G., and P. A. Lee, 1996, Phys. Rev. Lett. **76**, 503.

Wentzcovitch, R. M., W. W. Schulz, and P. B. Allen, 1994, Phys. Rev. Lett. **72**, 3389.

Werfel, F., G. Dräger, and U. Berg, 1981, Cryst. Res. Technol. **16**, 119.

Wertheim, G. K., V. A. Jaccarino, J. H. Wernick, J. A. Seitchik, H. J. WIlliams, and R. C. Sherwood, 1965, Phys. Lett. **18**, 89.

Wheatley, J. M., T. C. Hsu, and P. W. Anderson, 1988, Phys. Rev. B **37**, 5897.

White, R. M., and N. F. Mott, 1971, Philos. Mag. **24**, 845.

White, S. R., 1992, Phys. Rev. B **46**, 5678.

White, S. R., 1993, Phys. Rev. B **48**, 10345.

White, S. R., and D. J. Scalapino, 1996, Preprint No. cond-mat/9605143.

White, S. R., D. J. Scalapino, R. L. Sugar, E. Y. Loh Jr., J. E. Gubernatis, and R. T. Scalettar, 1989, Phys. Rev. B **40**, 506.

Wilson, A. H., 1931a, Proc. R. Soc. London, Ser. A **133**, 458.

Wilson, A. H., 1931b, Proc. R. Soc. London, Ser. A **134**, 277.

Wilson, J. A., 1985, in *The Metallic and Nonmetallic States of Matter*, edited by P. P. Edwards and C. N. R. Rao (Taylor and Francis, London), p. 215.

Wilson, J. A., and G. D. Pitt, 1971, Philos. Mag. **23**, 1297.

Wilson, K. G., 1975, Rev. Mod. Phys. **47**, 773.

Wolfe, R., J. H. Wernick, and S. E. Haszko, 1965, Phys. Lett. **19**, 449.

Wollan, E. O., and W. C. Koehlar, 1955, Phys. Rev. **100**, 545.

Woodfield, B. F., M. L. Wilson, and J. M. Byers, 1997, Phys. Rev. Lett. **78**, 3201.

Xu, X. Q., J. L. Peng, Z. Y. Li, H. L. Ju, and R. L. Greene, 1993, Phys. Rev. B **48**, 1112.

Yamada, K., *et al.*, 1987, Solid State Commun. **64**, 753.

Yamada, K., *et al.*, 1998, Phys. Rev. B **57**, 6165.

Yamada, K., Y. Endoh, C.-H. Lee, S. Wakimoto, M. Arai, K. Ubukata, M. Fujita, S. Hosoya, and S. M. Bennington, 1995, J. Phys. Soc. Jpn. **64**, 2742.

Yamada, K., K. Kakurai, Y. Endoh, T. R. Thurston, M. A. Kastner, R. J. Birgeneau, G. Shirane, Y. Hidaka, and T. Murakami, 1989, Phys. Rev. B **40**, 4557.

Yamada, K., J. Wada, Y. Endoh, S. Hosoya, S. Noguchi, S. Kawamata, and K. Okuda, 1995, Physica C **253**, 135.

Yamada, K., S. Wakimoto, G. Shirane, C. H. Lee, M. A. Kastner, S. Hosoya, M. Greven, Y. Endoh, and R. J. Birgeneau, 1995, Phys. Rev. Lett. **75**, 1626.

Yamada, K., and K. Yosida, 1986, Prog. Theor. Phys. **76**, 621.

Yamada, Y., O. Hino, S. Nohdo, R. Kanao, T. Inami, and S. Katano, 1996, Phys. Rev. Lett. **77**, 904.

Yamada, Y., M. Mori, Y. Noda, and M. Izumi, 1979, Solid State Commun. **32**, 827.

Yamaguchi, S., Y. Okimoto, H. Taniguchi, and Y. Tokura, 1996a, Phys. Rev. B **53**, 2926.

Yamaguchi, S., Y. Okimoto, and Y. Tokura, 1996b, Phys. Rev. B **54**, R11022.

Yamaguchi, S., Y. Okimoto, and Y. Tokura, 1997, Phys. Rev. B **55**, R8666.

Yamaguchi, S., and Y. Tokura, 1998, unpublished.

Yamaji, K., and Y. Shimoi, 1994, Physica C **222**, 349.

Yamamoto, A., M. Onoda, E. Takayama-Muromachi, F. Izumi, T. Ishigaki, and H. Asano, 1990, Phys. Rev. B **42**, 4228.

Yamane, H., Y. Miyazaki, and H. Hirai, 1990, J. Ceram. Soc. Jpn. **98**, 105.

Yanase, A., and K. Siratori, 1984, J. Phys. Soc. Jpn. **53**, 312.

Yasuhara, H., and Y. Tokura, 1998, unpublished.

Yasui, Y., T. Nishikawa, Y. Kobayashi, M. Sato, T. Nishioka, and M. Kontani, 1995, J. Phys. Soc. Jpn. **64**, 3890.

Yasuoka, H., T. Imai, and T. Shimizu, 1989, in *Strong Correlation and Superconductivity*, edited by H. Fukuyama, S. Maekawa, and A. P. Malozemoff (Springer, Berlin), 1989, p. 254.

Yokoya, T., A. Chainani, T. Takahashi, H. Ding, J. C. Campuzano, H. Katayama-Yoshida, M. Kasai, and Y. Tokura, 1996a, Phys. Rev. B **54**, 13311.

Yokoya, T., A. Chainani, T. Takahashi, H. Katayama-Yoshida, M. Kasai, and Y. Tokura, 1996b, Phys. Rev. Lett. **76**, 3009.

Yokoyama, H., and H. Shiba, 1987a, J. Phys. Soc. Jpn. **56**, 1490.

Yokoyama, H., and H. Shiba, 1987b, J. Phys. Soc. Jpn. **56**, 3582.

Yoshioka, D., 1989a, J. Phys. Soc. Jpn. **58**, 32.

Yoshioka, D., 1989b, J. Phys. Soc. Jpn. **58**, 1516.

Yoshizawa, H., H. Kawano, Y. Tomioka, and Y. Tokura, 1995, Phys. Rev. B **52**, R13145.

Yoshizawa, H., S. Mitsuda, H. Kitazawa, and K. Tatsumata, 1988, J. Phys. Soc. Jpn. **57**, 3686.

Yoshizawa, H., *et al.*, 1998, unpublished.

Yunoki, S., J. Hu, A. L. Malvezzi, A. Moreo, N. Furukawa, and E. Dagotto, 1998, Phys. Rev. Lett. **80**, 845.

Zaanen, J., and O. Gunnarsson, 1989, Phys. Rev. B **40**, 7391.

Zaanen, J., and P. B. Littlewood, 1994, Phys. Rev. B **50**, 7222.

Zaanen, J., and A. M. Oleś, 1996, Ann. Phys. (Leipzig) **5**, 224.

Zaanen, J., and G. A. Sawatzky, 1990, J. Phys. Chem. Solids **88**, 8.

Zaanen, J., G. A. Sawatzky, and J. W. Allen, 1985, Phys. Rev. Lett. **55**, 418.

Zener, C., 1951, Phys. Rev. **82**, 403.

Zeyer, R., and G. Zwicknagl, 1988, Solid State Commun. **66**, 617.

Zhang, F. C., and T. M. Rice, 1988, Phys. Rev. B **37**, 3759.

Zhang, S. C., 1997, Science **275**, 4126.

Zhang, S., J. Carlson, and J. E. Gubernatis, 1997, Phys. Rev. B **55**, 7464.

Zhang, S., N. Kawashima, J. Carlson, and J. E. Gubernatis, 1995, Phys. Rev. Lett. **74**, 1500.

Zhang, X. Y., M. J. Rozenberg, and G. Kotliar, 1993, Phys. Rev. Lett. **70**, 1666.

Zhang, Z., and S. Satpathy, 1991, Phys. Rev. B **44**, 13319.

Zotos, X., and P. Prelovšek, 1996, Phys. Rev. B **53**, 983.